2-P

MSC-04312

NATIONAL AERONAUTICS AND SPACE ADMINISTRATION

MSC CRYOGENICS SYMPOSIUM PAPERS

PRESENTED AT
NASA MANNED SPACECRAFT CENTER
HOUSTON, TEXAS
MAY 20 AND 21, 1971

MANNED SPACECRAFT CENTER
HOUSTON, TEXAS

514p

FOREWORD

During the past twelve months, intensive efforts in the areas of design, development, analysis and testing have been conducted to assure the timely redesign of the Apollo cryogenic oxygen storage and supply system. As a result of these activities, much useful information has been developed in the cryogenics area, and the purpose of the MSC Cryogenics Symposium is to share this information with others who have a need for it, whether they be designers of future spacecraft or of cryogenic systems for terrestrial applications.

The papers contained herein will hopefully assist symposium attendees in getting as much information as possible from the oral presentations. The papers are grouped into five major categories to assist the reader in readily identifying any topic of interest.

Grateful acknowledgement is extended to each of the authors, all of whom have contributed much of their own time in writing the papers; to Charles W. Glassburn, whose assistance and helpful suggestions have been invaluable in implementing preparatory plans; and to Stanley E. Jacobsen and Helen N. Foley for their perseverance and helpful assistance in preparation for the symposium.

William E. Simon

William E. Simon
Chairman

237

CONTENTS

Page

GROUP I: HARDWARE DEVELOPMENT

GROUP II: STRATIFICATION ANALYSES

GROUP III: SYSTEM MODELS

GROUP IV: TEST PROGRAMS

GROUP V: FLIGHT PERFORMANCE

N72-23786

REDESIGN OF THE APOLLO CRYOGENIC STORAGE SYSTEM

Author - C. P. Bouman
North American Rockwell, Inc.
Space Division

An assessment of the Apollo 13 mission resulted in establishing new and revised requirements for the design of the oxygen tanks and the associated spacecraft system.

Areas to be discussed include new system requirements, system changes to Apollo 14, revised operational requirements, instrumentation, operational redlines, component isolation modes, and return enhancement capabilities. In order to show the relationship of the cryogenic system to the spacecraft, a short description of the system may be useful.

General System Description and Requirements (Basic Apollo)

The basic Apollo cryogenic system consisted of two each oxygen tanks and hydrogen tanks. The system includes related controls, check valves, filters and shutoff valves as shown in Figure 1.

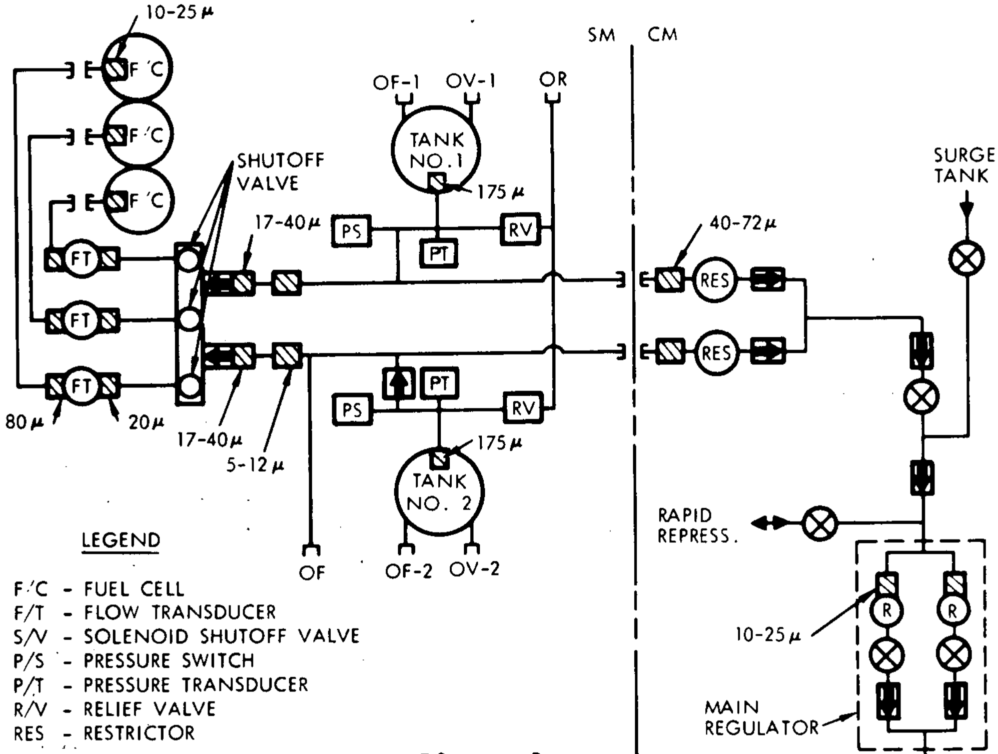

Figure 1

Oxygen is provided for pressurization of the command module and for crew metabolic consumption. Oxygen and hydrogen in an 8:1 ratio is also provided as reactants to the fuel cells for the generation of spacecraft electrical power. Useful stored consumables are 320 pounds of oxygen per tank, and 28 pounds of hydrogen per tank. The basic design concept for the cryogenic system allows for an emergency return with the loss of either one hydrogen tank, or one oxygen tank, or both. The hydrogen and oxygen systems for the basic Apollo are stored in Sector IV of the service module as shown on Figure 2.

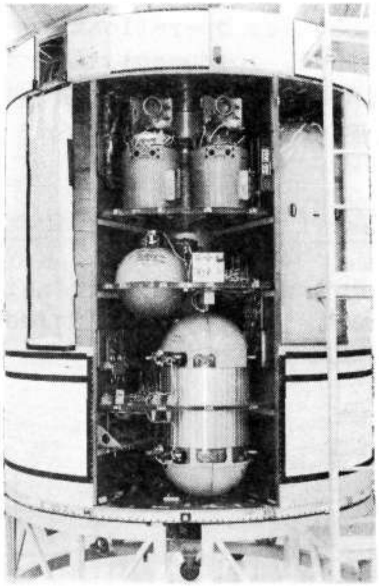

Figure 2

Detailed System Description

Following an oxygen fluid flow path from Tank Number 1, fluid from the tank passes through the system valve module which contains a pressure relief valve, a pressure transducer, a pressure control switch, and a check valve. The pressure control switch operates between a range of 865 to 935 psig. As the pressure in the tank decays due to fluid expulsion, the pressure control switch activates at the low setting, energizing the motor driven electrical transfer switch, which in turn provides electrical energy to the heaters located inside the oxygen tank. The process reverses as the pressure control switch reaches the upper limit setting. The pressure transducer provides pressure readout to the crew and to flight control. The pressure transducer readout is accurate within plus or minus 2.5 percent of full scale within a range of 50 to 1,050 psig. The system relief valve operates within a pressure band of 973 psig cracking pressure with full flow in excess of 100 lbs/hr at 1,010 psig.

Oxygen passing through the system valve module is transported to the fuel cells through check valves, solenoid shutoff valves, and the fuel cell flow meters. Fluid is also transported to the Environmental Control System (ECS) through flow restrictors, check valves and isolation valves. Components within the system are protected from contamination by the use of inline filters ranging from 12 μ absolute to 175 μ absolute.

Pressure and quantity readouts for each tank are displayed on the control and display panels in the command module, and are also provided through telemetry to flight operations. The cryogenic bulk fluid temperatures are also provided to flight operations. The two oxygen systems are completely independent in operation, the systems being interconnected downstream of the fuel cell system check valves and the ECS check valves. The primary purpose of the check valves is to prevent reverse flow from Tank Number 1 to Tank Number 2 and the reverse.

Controls are provided which allow the crew to select ON-OFF or AUTO selection for the O_2 and H_2 tank heaters and fans. Circuit breakers and/or fuses are provided for circuit protection for all electrical components and systems. Installation of the cryogenic system is of a modular concept; all components, including the tanks, are mounted on the equipment shelves which in turn are installed in the service module. Interconnecting lines are brazed, except for the connections to the fuel cells which are mechanical joints.

Apollo 13 Mission Assessment

As a result of the Apollo 13 incident, NR joined with NASA and other contractors in an immediate investigation, including a reassessment of the Command and Service Module (CSM) subsystems, and support equipment. Results of the joint reassessment suggested significant changes in the following two basic areas.

First, the knowledge that emerged from the investigation indicated that new requirements needed to be established for the spacecraft cryogenic system, as well as for the oxygen tank. These requirements resulted in a series of design changes known as the cryogenic system modification.

Second, the experience gained from the safe return of Apollo 13 indicated that, during certain abort-mission conditions, additional power, oxygen, and potable water would enhance the probability of a successful return to earth. This series of changes has come to be known as the return enhancement modification.

The new requirements established revised ground rules for the design of the cryogenic oxygen system as follows:

a) Eliminate or minimize the use of organic materials within tanks and components.

b) Eliminate or reduce blind installations.

c) Eliminate dynamic components exposed to oxygen.

d) Revise instrumentation and caution and warning system to provide for positive indication of system operational parameters.

Changes to the Apollo cryogenic system considered previous flight operational data, which resulted in maintaining changes to a minimum to avoid losing valuable mission experience. The above requirements resulted in the following changes to the spacecraft and components.

1) Redesign the oxygen tank.
2) Add oxygen tank heater instrumentation.
3) Provide for one, two or three oxygen tank heater operation.
4) Install oxygen tank feed line filters.
5) Replace fuel cell reactant shutoff valve.
6) Revise talk-back logic in F/C reactant shutoff valves.
7) Add reactant valve position to caution and warning system.
8) Revise hydrogen tank pressure caution and warning limits.
9) Install third oxygen tank in Apollo 14.
10) Add third oxygen tank isolation valve.
11) Add third oxygen tank check valve.
12) Add oxygen tank 2 and 3 manifold pressure transducer.
13) Install auxiliary battery.

Oxygen Tank Redesign and Related CSM Changes

The redesign of the oxygen tank resulted in some additional changes to the spacecraft associated with the electrical system, controls and displays, and instrumentation. The design of the modified tank incorporates three heater elements, versus two on the basic Apollo tank, plus the addition of a heater temperature sensor. The addition of the third heater element provides for additional redundancy, plus the capability of selecting either one, two or three heater element operation. The selection of single or multiple energy input sources becomes important for future missions where higher flow rates, at various fluid density levels are required.

Heater Temperature Sensor

Extensive testing and analysis showed that the bulk fluid temperature sensor installed in the basic Apollo oxygen tank did not reflect the highest temperatures of the fluid or materials within the tank. This was amplified by the removal of the destratification fans, which resulted in a higher degree of stratification of the fluid.

To provide more realistic temperature data, with reference to the highest temperatures within the tank, a heater temperature sensor was added. Comprehensive analysis and test programs have established that the location of the heater temperature sensor is within 30 F relative to the hottest spot on the heater assembly. The addition of the heater temperature sensor required the addition of temperature signal conditioners located on the oxygen shelf assembly as shown on Figure 3.

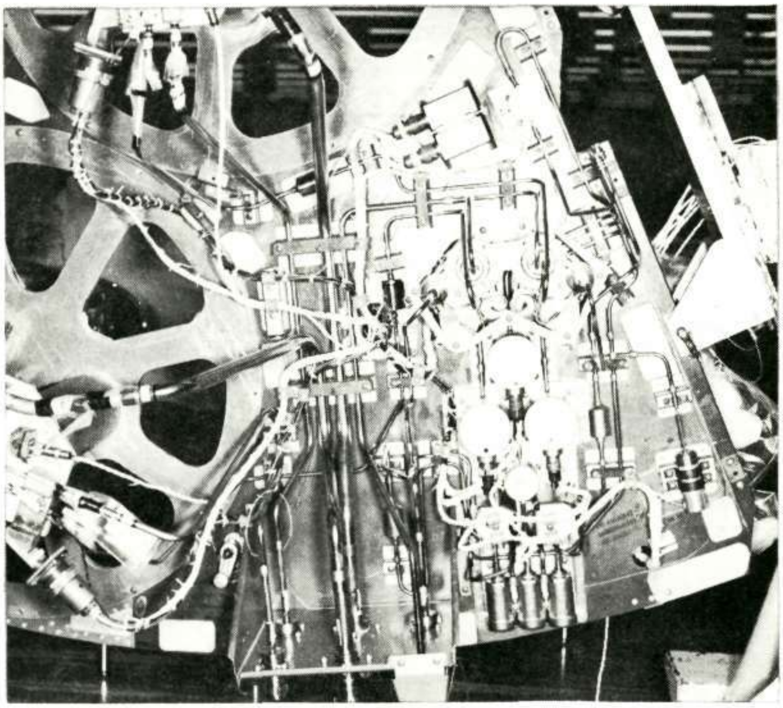

Figure 3

The temperature sensor output range is from -320 F to +600 F. Heater temperature data is available to flight operations for monitoring during the mission. Spacecraft wiring and switch panel modifications have been made to allow for crew selection of varied heater configuration. The establishment of a 350 F heater temperature redline was the result of extensive testing and analysis. The analysis indicated that the heater temperature should not approach the 350 F redline based on currently planned oxygen flow rates for the "H", "J", and Skylab missions. The material test programs have shown that there is no degradation or hazardous operating condition with heater temperatures up to 550 F. The 350 F redline considers the 30° temperature delta between location of the sensor and the hottest spot on the heater, instrumentation error, material limits plus a safety factor.

System Filters

Redesign of the oxygen tank also necessitated the installation of inline filters in the oxygen feed lines. The addition of a heater temperature sensor in the oxygen tank, coupled with relocation of the bulk fluid temperature sensor, resulted in a space limitation within the oxygen tank neck adapter area. This necessitated removing the filters from within the tanks and installing them in the tank feed line.

Replacement of Fuel Cell Reactant Shutoff Valves

The reactant shutoff valve assembly is composed of three solenoid valves and two check valves as shown on Figure 4.

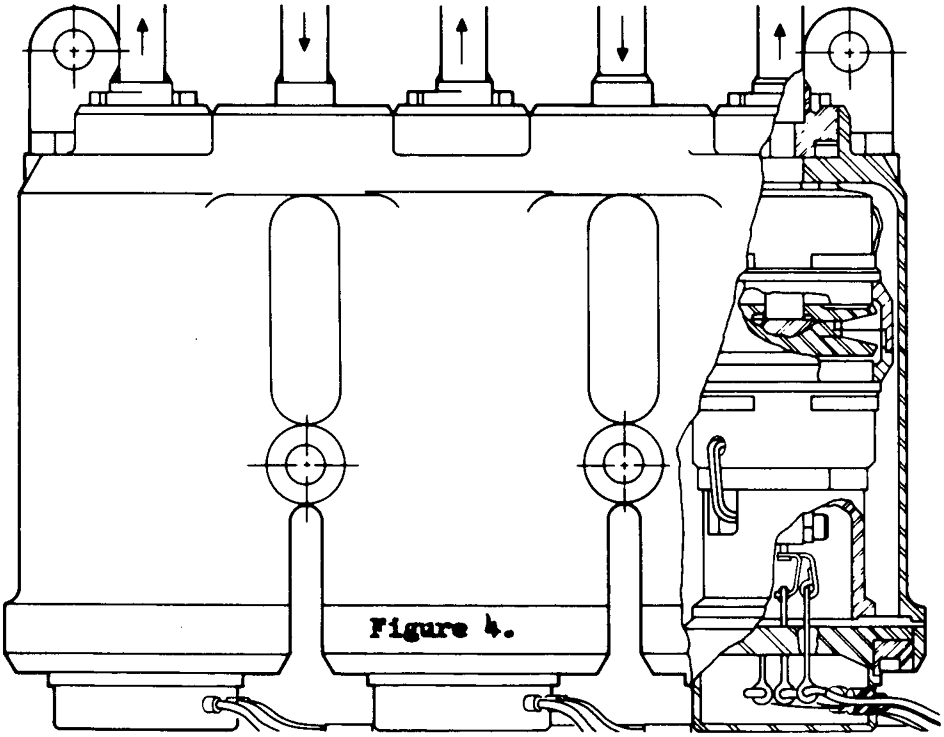

Figure 4.

The oxygen enters from each oxygen tank through the check valves into a plenum. The plenum allows for oxygen to flow from either tank to the fuel cells. Three latching solenoid shutoff valves are used to close off reactant flow to the fuel cells. A talk-back is displayed to the crew to indicate the open or closed valve position.

The replacement of the oxygen reactant shutoff valve was the result of the flammability analysis conducted on all components in the oxygen loop. The O_2 reactant shutoff valve was identified as having teflon coated electrical wiring, teflon material, and open terminals exposed to high pressure oxygen. Rework of the valve to provide an oxygen barrier was considered too extensive, requiring a complete redesign of the valve; therefore, the valve was modified by removing the solenoid shutoff valves from the housing. This maintained the manifold for fluid distribution to the fuel cells and the check valves. The replacement valve as shown on figure 5 was installed between the manifold and the fuel cell flow meters.

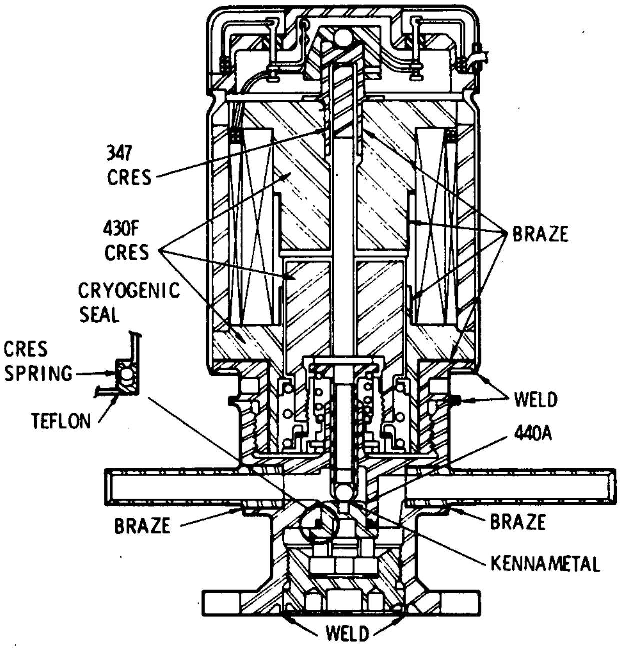

Figure 5

This valve was developed and is currently used on the Apollo reaction control system. All electrical components are shielded from high pressure oxygen. The only change to the valve was to replace a body seal to eliminate leakage at cryogenic temperatures. The valve was successfully subjected to an extensive test program, which included cryogenic operation, life cycling, thermal shock and magnetic latch holding capability. This valve was flown on Apollo 14. The installation of the valve is shown in figure 3.

Reactant Valve Talk-Back Logic

The talk-back logic on basic Apollo was such that both the H_2 and O_2 reactant shut-off valves were required to be closed to provide talk-back display. This was to ensure that for ground operation and checkout both valves were either closed or open. With the O_2 and H_2 system pressurized, closure of either the O_2 or H_2 valve places a high, damaging, pressure differential across the fuel cell. The Apollo 13 assessment indicated the requirement to provide inflight information of any reactant valve closure. This change was accomplished by wiring the H_2 and O_2 reactant switches in parallel. The talk-back logic was also added to the caution and warning system for early indication of valve closures. (Figure 6)

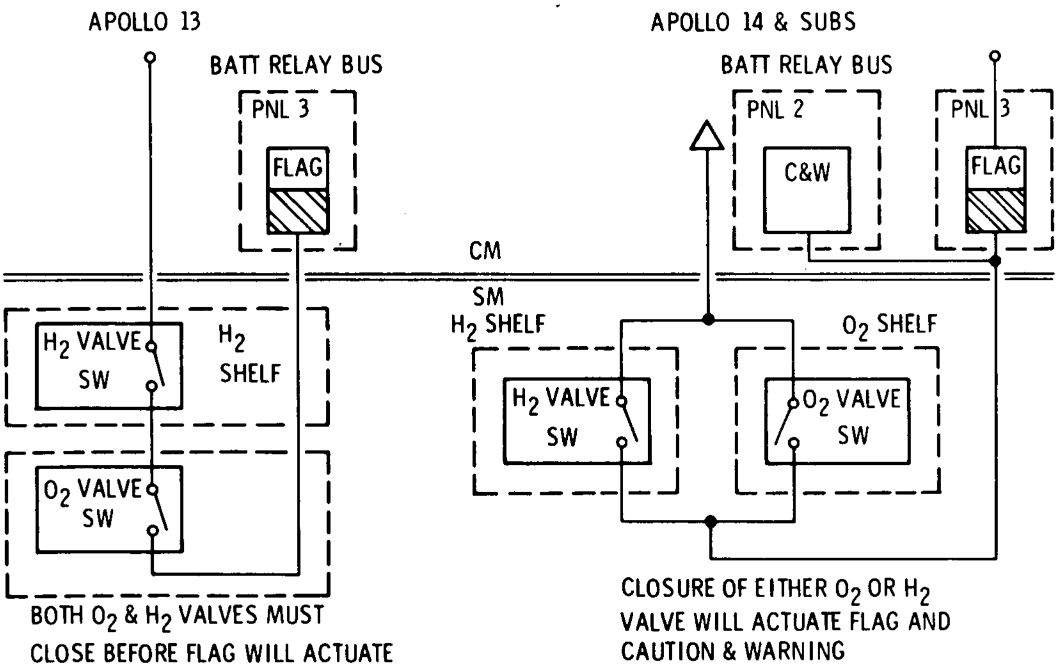

Figure 6

Hydrogen Tank Pressure Caution and Warning Limits

The low pressure caution and warning signal for the hydrogen tanks on basic Apollo was set at approximately 1.0 psi below the lower trip point pressure on the hydrogen tank pressure control switch. Due to a pressure imbalance between tanks, or a shift in pressure control switch setting, the alarm can be triggered when, in fact, system operation is normal. To delete the possibility of nuisance alarms, and the potential screening effect of the C&W system as related to the H_2 system pressure switch setting, the system was revised to lower the C&W low pressure actuation point to effectively reduce the chance of pressure switch and C&W interference.

Installation of Third Oxygen Tank in Apollo 14

The decision to install the oxygen tank in Apollo 14 was based on three factors.

First, to provide added confidence in mission success with redesigned tanks.

Second, to provide a return enhancement capability in the event anomalies would prevent making oxygen available from tanks 1 and 2.

Third, system performance in the low density regime, without destratification fans to provide forced convection, was not understood.

The "J" configuration Apollo vehicles are designed to provide for more extensive lunar exploration, which includes the Scientific Instrumentation Module. The extended operation required additional reactants for the fuel cells, plus oxygen for the command module. As a result, the "J" mission vehicles have been modified to accept one each additional hydrogen and oxygen tank and related controls as shown on figure 7.

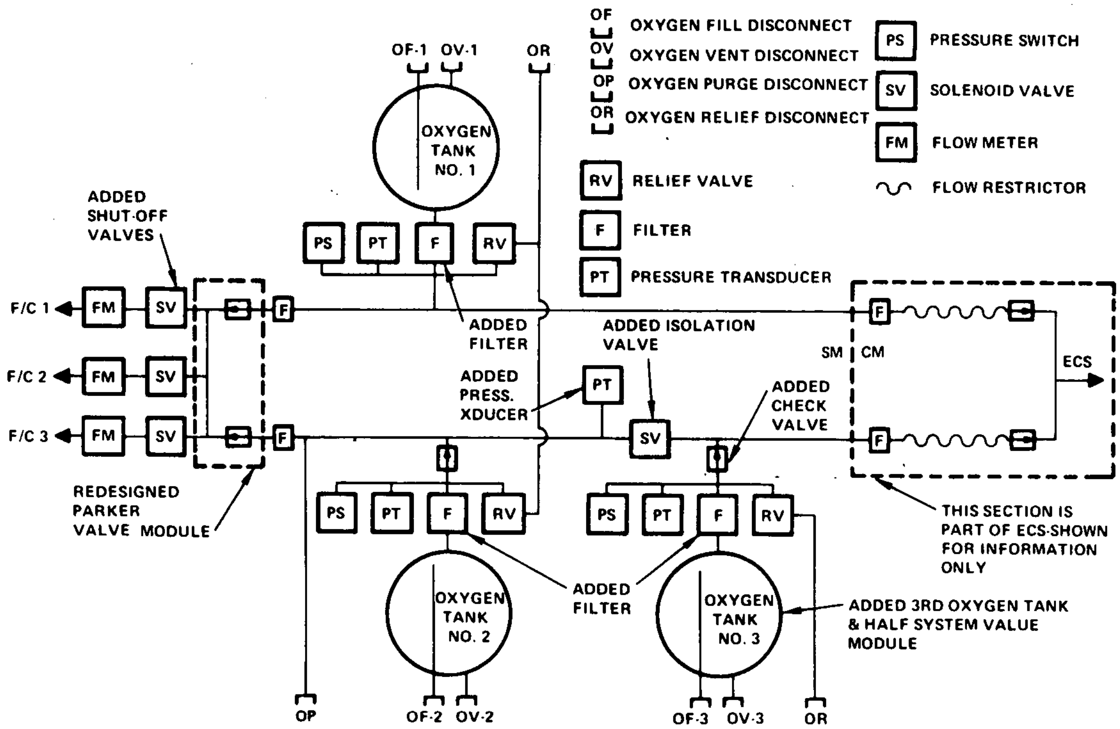

Figure 7

Because of additional crew activities, including external vehicle activity (EVA), operation of oxygen tanks in lower fluid density ranges is anticipated. In order to provide advance information on system response at low fluid density operation; and to provide added confidence in mission success, a decision was made in July 1970, to install a third oxygen tank on the Apollo 14 spacecraft. The third oxygen tank was installed as shown on figure 8 and is plumbed in parallel with oxygen tank number 2. A pressure switch, relief valve, and pressure transducer package is provided which is identical to the basic system components.

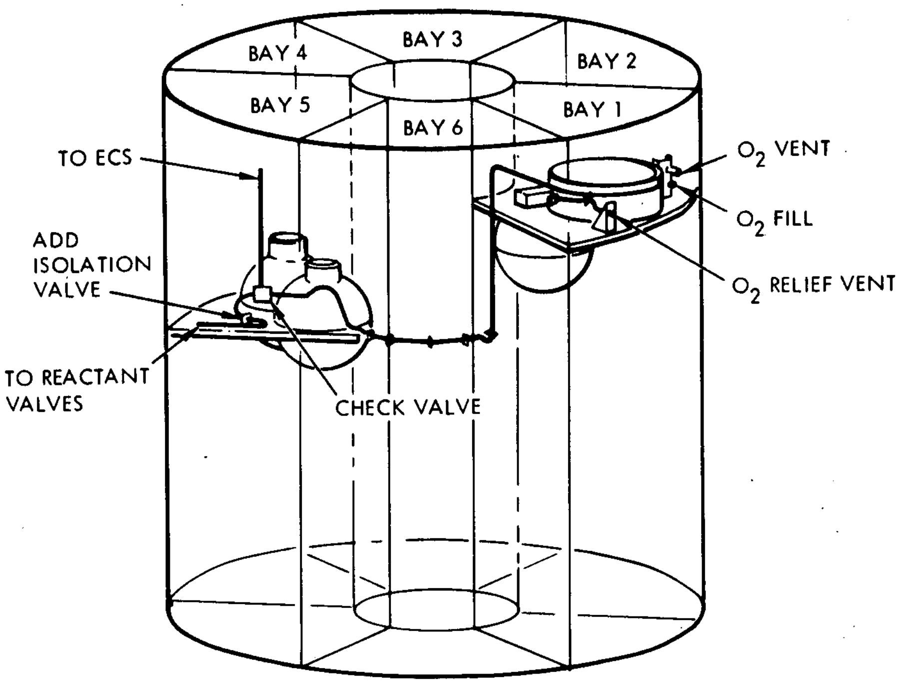

Figure 8

Isolation Valve

As part of the return enhancement capability, an isolation valve was installed which provides a means to isolate tank number 3 from the rest of the system, providing oxygen only to the command module. The isolation valve is identical to the new fuel cell reactant shut-off valves and carries the same part number. The isolation valve is wired to the battery bus to assure operation in the event of the loss of primary spacecraft electrical power.

Tank Number 3 Check Valve

The installation of the tank number 3 check valves is identical to tanks number 1 and 2 and serves the same purpose, i.e., preventing reverse flow between tanks during normal system operation and in the event of the loss of a system.

Return Enhancement Provisions

In addition to the third oxygen tank installed in Apollo 14, provisions were made to install a battery in the service module to provide emergency return electrical power in the event of total loss of the spacecraft primary electrical power system. The battery is rated at 400 amp hours and is identical to the LEM descent battery. The emergency return power profile, assuming total loss of the Apollo primary electrical power system, is such, that the spacecraft capability of a safe return from worst case condition is enhanced.

Testing

The redesigned components and the system were subjected to an extensive test program which considered all phases of environmental and operation conditions, including off-limits testing. The three tank system was subjected to two mission life cycle tests at the Beech Aircraft test facility in Boulder, Colorado. The system was also operated in parallel with the Apollo 14 mission, simulating actual mission oxygen flows, at established density ranges. The successful completion of the test program provided added confidence in the redesign of the components and the system.

The installation of the third oxygen tank in Apollo 14 allowed for performing a specific series of tests at fluid densities below 20% during the mission. Data from the test showed good temperature correlation with the zero "G" heat transfer models. The test demonstrated that with two heater element operation, flows up to 7.0 lb/hr can be provided while maintaining heater temperatures below 350 F.

The Apollo 14 flight test program also demonstrated that within the proposed flow regime for the Apollo 15 mission, pressurization of the system can be maintained without the use of destratification fans or external pumping loops to increase convective heat transfer. The test, and total system operation, verified that pressure drops associated with sudden mixing of stratified fluids is negligible.

Conclusion

The new requirements, test programs and attendent changes as implemented on the follow-on spacecraft have:

1) Extended the capability of the cryogenic system by providing a high degree of confidence and great flexibility in system operation.

2) Provided an extremely high confidence in a successful return to earth from worst case abort conditions.

3) Supplied data from the Apollo 14 mission which is directly applicable to future, more advanced Apollo missions; established analyses/flight correlation techniques applicable to future programs and systems.

4) Provided increased knowledge regarding ignition characteristics and burn rates of materials exposed to high pressure oxygen.

5) Established new design requirements for cryogenic systems relative to future programs and systems.

N72-23787

MODIFIED APOLLO CRYOGENIC OXYGEN TANK DESIGN

Kermit Van Leuven
Project Engineer
Beech Aircraft Corporation
Boulder, Colorado

ABSTRACT

Assessment of the Apollo 13 mission indicated that some design changes be incorporated into Apollo cryogenic oxygen storage tanks. These changes broadly fit into three categories. They were: deletion of the fluid equilibration motors and redesign of heater assembly, material changes for internal tank wiring and density sensor, and the addition of a heater assembly temperature sensor. Development of a cryogenic oxygen tank incorporating these changes is presented.

PRELIMINARY EVALUATION

Analysis of required design changes (reference Figure 1 which illustrates the original tank design), indicated that the heater assembly would be the key element and that the primary development problem was to incorporate metal sheathed wiring. A solution to this problem dictated the following general criteria for sheathed wiring:

1. Small diameter to:

    (a) mimimize conducted heat leak,

    (b) keep the containing conduit diameter small to allow installation in the existing pressure vessel neck opening and provide low conducted heat leak in short conduit lengths, and

    (c) provide maximum flexibility since the sheathed wires would have to be pulled through the containing conduit at installation.

2. Good handling resistance.

3. Completely compatible with silver solder brazing temperatures (1325°F).

4. LOX-GOX compatibility for all materials.

5. Appropriate electrical characteristics such as current carrying capacity with acceptable self-heating, insulation properties and capacitance.

These criteria were then used to screen available metal sheathed wiring and resulted in the selection of a sheathed wire produced by the Rosemount Engineering Company of Minneapolis. The wire produced by Rosemount had shown superior characteristics in the areas of flexibility, handling tolerance, and internal materials. An additional bonus was realized with this wire selection in that heater elements could be fabricated with integral cold leads inside a continuous metallic sheath. This capability eliminated the need for heater lead terminations on the heater assembly.

Construction details of the selected metal sheathed wiring are illustrated in Figure 2. Figure 2 also shows a cross section of the sheathed wire. The outer sheath material is 321 stainless steel. Nominal finished outside diameter is 0.059 inch with 0.010 inch wall thickness. The insulation material is crushed and compacted Refrasil which is fused silicon dioxide or quartz. The Refrasil is applied as a woven braid of fused quartz fibers and is crushed and compacted when the metallic sheath is drawn. The conductor materials are 0.0158 inch O.D. Nichrome V for heater elements and 0.020 inch O.D. nickel-clad copper for cold leads. Figure 2 illustrates the manufacturing process used to fabricate the sheathed wire and shows how cold leads and heater elements are joined so that they can be enclosed in a single continuous sheath. Figure 2 also illustrates how a completed heater element is terminated with hermetically sealed headers.

CONCEPT DEVELOPMENT AND SELECTION

The selection of a specific metal sheathed wire and preliminary compilations of its design application parameters allowed detailed engineering development of the required design changes. This in turn led to the comprehensive hardware development and design verification testing program presented in Table I. The resulting new design is illustrated in Figures 3 and 4.

In addition to the items shown in Table I, a development program to eliminate teflon materials from the tank density sensing probe was pursued. Two development density sensors were fabricated using insulating materials other than teflon. The materials were fused quartz and Alsimag ceramic. Subsequent testing of these two probes indicated that both materials were feasible; however, considerable further work would be required to perfect them to production design status. The main problem areas were: moisture sensitivity and particle generation.

DESIGN AND PRODUCTION DEVELOPMENT

BAC encountered four significant manufacturing process development problems during the fabrication of these initial tanks. They were:

1. Perfection of tooling and brazing techniques for installation of Rosemount heater elements on the heater assembly support tube. These spirally wrapped elements were difficult to keep in place and simultaneously allow a smooth continuous braze with uniform temperature distribution. The problem was resolved by more sophisticated retaining tools and the incorporation of a preheater into the brazing tool.

2. Maintenance of dry sheathed leads throughout the manufacturing cycle. The sheathed wiring readily wicked air moisture in any process which heated and cooled the leads in an unsealed condition. Moisture in the leads would result in their insulation resistance and dielectric strength being less than specification requirements. This problem was resolved by minimizing the occurrence and duration of leads being in an unsealed condition and when leads were required to be unsealed all work was done in dry boxes or under hot dry blanket purge conditions.

3. Brazing problems associated with installation of transition spline pins between sheathed wire hermetic headers and the original design Apollo main electrical connector. The problems

were primarily associated with small clearances between pins in the main electrical connector which made torch brazing very difficult and resulted in multiple reheat of some connector pins. This problem was eventually resolved by a new electrical connector design. The original and new design connectors are contrasted in Figure 5.

4. A problem occurred with the heater element platinum braze joint during component acceptance testing of heater assemblies. The problem was continuity failures in the platinum braze joints or close to the joint in the nickel-clad copper lead. Investigation of the problem traced the cause to inadequate wetting of the Nichrome V heater element wire during the joint braze operation, manual control of centering during the joint braze operation, and an extremely severe annealing operation following drawing of the wire sheath. All of these problems were resolved by changing the joint braze and annealing processes. The investigation also showed that the existing component acceptance tests would have screened out any heater assemblies with potentially defective heater elements. However, both BAC and Rosemount inspection and component acceptance tests were made more stringent as a result of this problem.

DESIGN QUALIFICATION

Qualification of the new design oxygen tank commenced in mid-October. Table II indicates the items qualified, the tests conducted and a brief synopsis of the test results. One failure was encountered during vibration qualification testing. The bulk fluid temperature sensor MI cable separated where it entered to the sensor housing. The failure resulted in severe degradation of the first qualification tank (XTA0033) vacuum when sorbed gases in the magnesium oxide insulation were released into the tank vacuum annulus. This failure occurred prior to running the last axis of random design proof vibration. Investigation of this failure included re-evaluation of the vibration test levels and exposure times. Results of this re-evaluation indicated that the test requirements were unnecessarily severe especially in the area of exposure time. The test levels were redefined and a second qualification tank, XTA0037, was subsequently exposed to the new test requirements without incident.

Successful qualification of the new design oxygen tank was completed just a matter of days before launch of Apollo 14. In fact, the mission simulation test setup being used for the last qualification test of the tanks was recycled and used to "fly" a parallel mission with the tank system in Apollo 14.

Performance of the new design oxygen tanks was completely satisfactory. The performance ratings of the original design oxygen tank and the new design oxygen tank are compared in Table III.

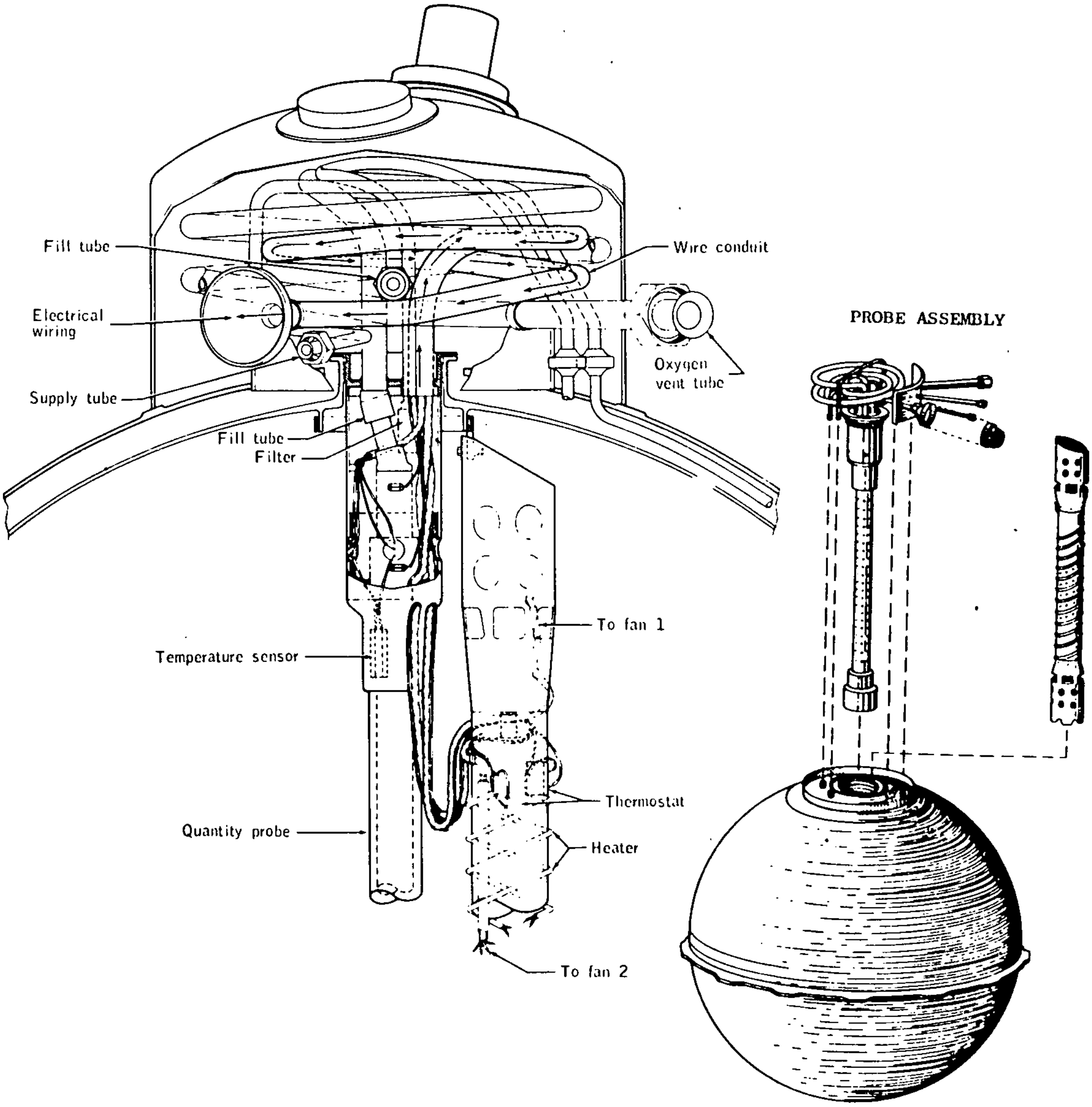

Figure 1

ORIGINAL BLOCK II OXYGEN TANK

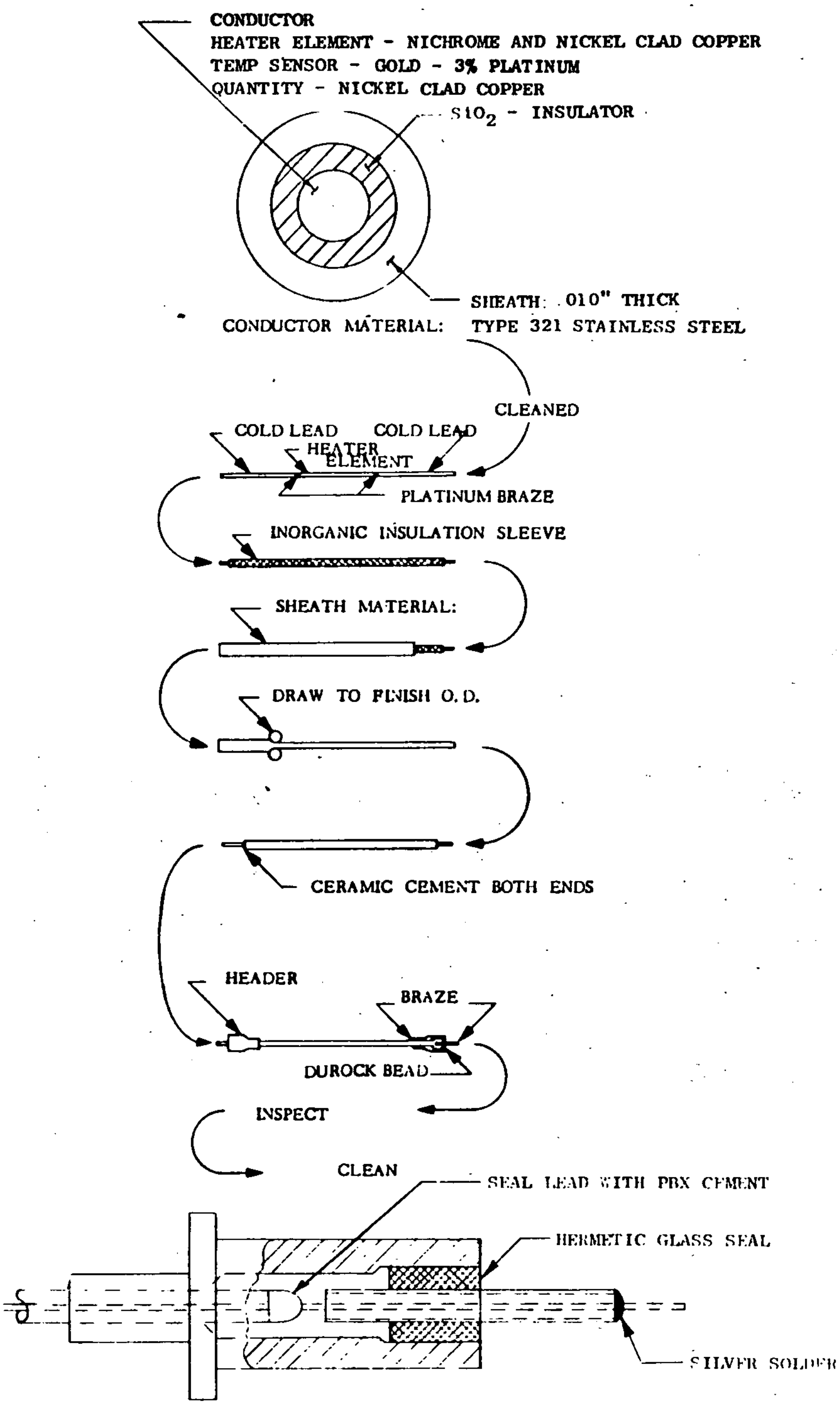

Figure 2

SHEATHED WIRING

TABLE I

SYNOPSIS OF NEW DESIGN DEVELOPMENT & DVT TESTING

TEST ITEM	TYPE OF TESTING	REMARKS
Sheathed Wiring & Heater Elements	1. Tensile tests with headers	150 lb - fails in sheathed lead.
	2. Leak test (length of lead)	10cc He in 80 minutes 15 psid.
	3. Vibration	Completely acceptable.
	4. Handling & flexibility	Triple 5/8 dia reverse rolling bend.
	5. Particle generation	Acceptable.
	6. Minimum bend radius & restraighten and ding effects	1/8 inch radius. 0.005 to 0.250. Radius dings to 50% of dia. pass.
	7. Thermal shock	$+140^{\circ}F$ to LN_2 no effect.
	8. Drying techniques	Is dryable without complications.
	9. Resistance & resistance temperature	Met design requirements.
	10. Capacitance	72.5 pf/ft.
	11. Dielectric strength	10 μa, one time 1000vdc, 500vdc unlimited.
	12. Ruptured heater in high pressure oxygen	No ignition or operation problems.
Hermetic Headers	1. Thermal shock	$+140^{\circ}F$ to LN_2 no effect.
	2. Leak tests	3×10^{-8} scc He.
	3. External & internal pressure	To 6200 psia no failure.

TABLE I (contd)

SYNOPSIS OF NEW DESIGN DEVELOPMENT & DVT TESTING

TEST ITEM	TYPE OF TESTING	REMARKS
	4. Resistance	Met design requirements.
	5. Humidity effects	Does not collect, dries readily.
	6. Brazing temperature distribution	Mfg. process causes no degradation.
Electrical Connector (extended pin)	1. Thermal shock	+140°F to LN_2 no effect.
	2. Vibration	Design proof, no problems.
	3. Shock	30 g's 11 milliseconds, no problems
	4. Pressurization	System burst, no failure.
	5. Leak test	Meets 1 x 10^{-4} scc He at 1357 psia.
	6. Dielectric strength	10 μa at 1000vdc.
Heater Assembly including Heater Temperature Sensor	1. Thermal shock	+140°F to LN_2, no effect.
	2. Vibration	Margin considerably above design proof.
	3. Acceleration	7 g's + X axis, 3 g's all others.
	4. Life cycle	400 hours 10% duty cycle & cryo shock.
	5. Temperature distribution	Verified design.
	6. Off-limits cryo shock	+700°F to LN_2, no failure.
	7. In tank operation	Development phase 755 hours, 425 cycles.

TABLE I (contd)

SYNOPSIS OF NEW DESIGN DEVELOPMENT & DVT TESTING

TEST ITEM	TYPE OF TESTING	REMARKS
Fluid Temperature Sensor	1. Thermal shock	+140°F to LN_2, no degradation.
	2. Pressurization	To 1537 psia, no failure.
	3. Vibration	Design proof, no failure.
	4. Acceleration	7 g's + X axis, all others 3 g's.
	5. Weld Temperatures	Mfg. process causes no degradation.
Density Probe	1. Thermal shock	+140°F to LN_2, no effect.
	2. Vibration	Design proof, no failure.
	3. Acceleration	7 g's + X axis, all other 3 g's.
	4. Capacitance effects	Sheathed leads & header cause no problem.
	5. Tensile test	Lowest tensile 515 lb inner tube.
Development Tank LO-19 with Harness Assembly	1. Cold shock & proof pressure	Tank met and is still meeting all design requirements. Has accumulated over 1087 hours. Cryogenic operating hours at pressure.
	2. Design verification function test	
	3. Optimum detanking	
	4. Standby heat leak (140°F & vacuum)	
	5. Design proof vibration	
	6. Optimum heater pressurization mode	
	7. Mission simulations	

TABLE I (contd)

SYNOPSIS OF NEW DESIGN DEVELOPMENT & DVT TESTING

TEST ITEM	TYPE OF TESTING	REMARKS
Heater Temperature Signal Conditioner	1. Temperature-vacuum functional and accuracy tests	No loss of accuracy or failure.
	2. Vibration	Eight times design proof, no failure.

Figure 3

OXYGEN TANK ASSEMBLY

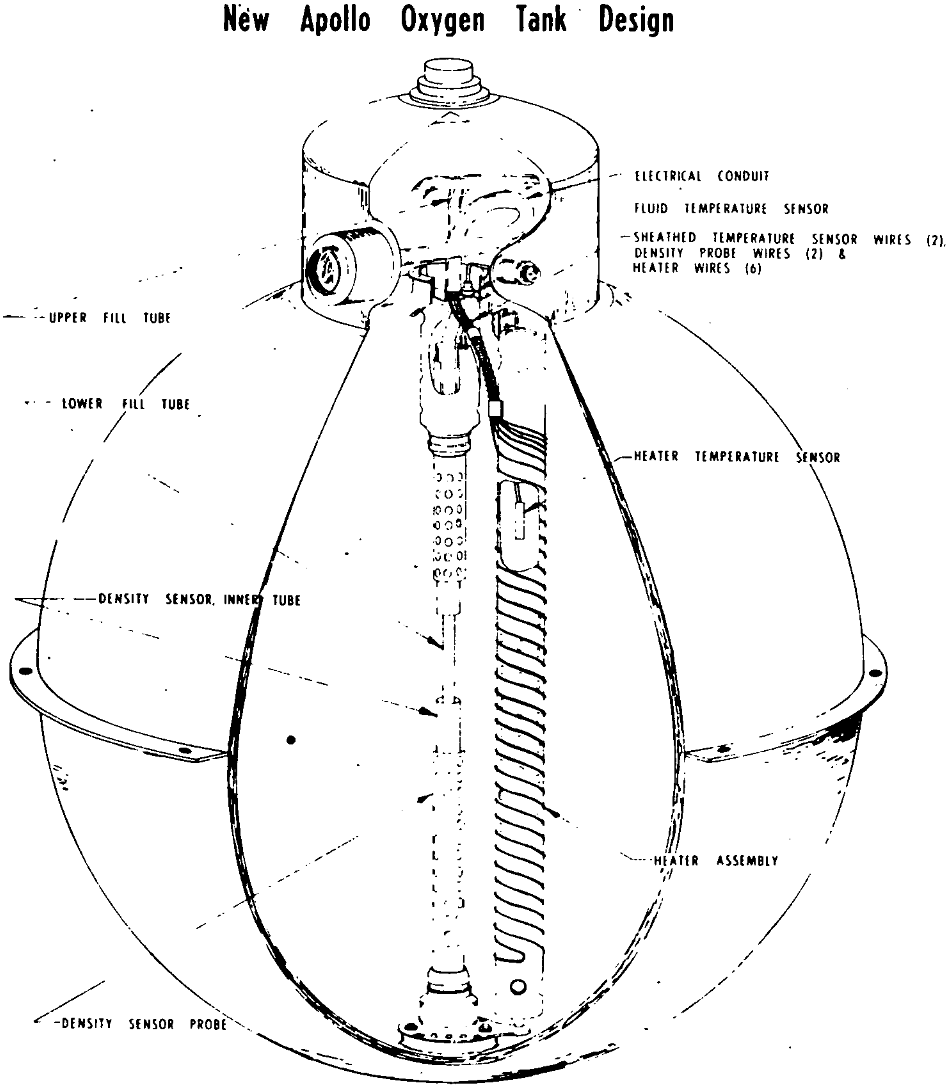

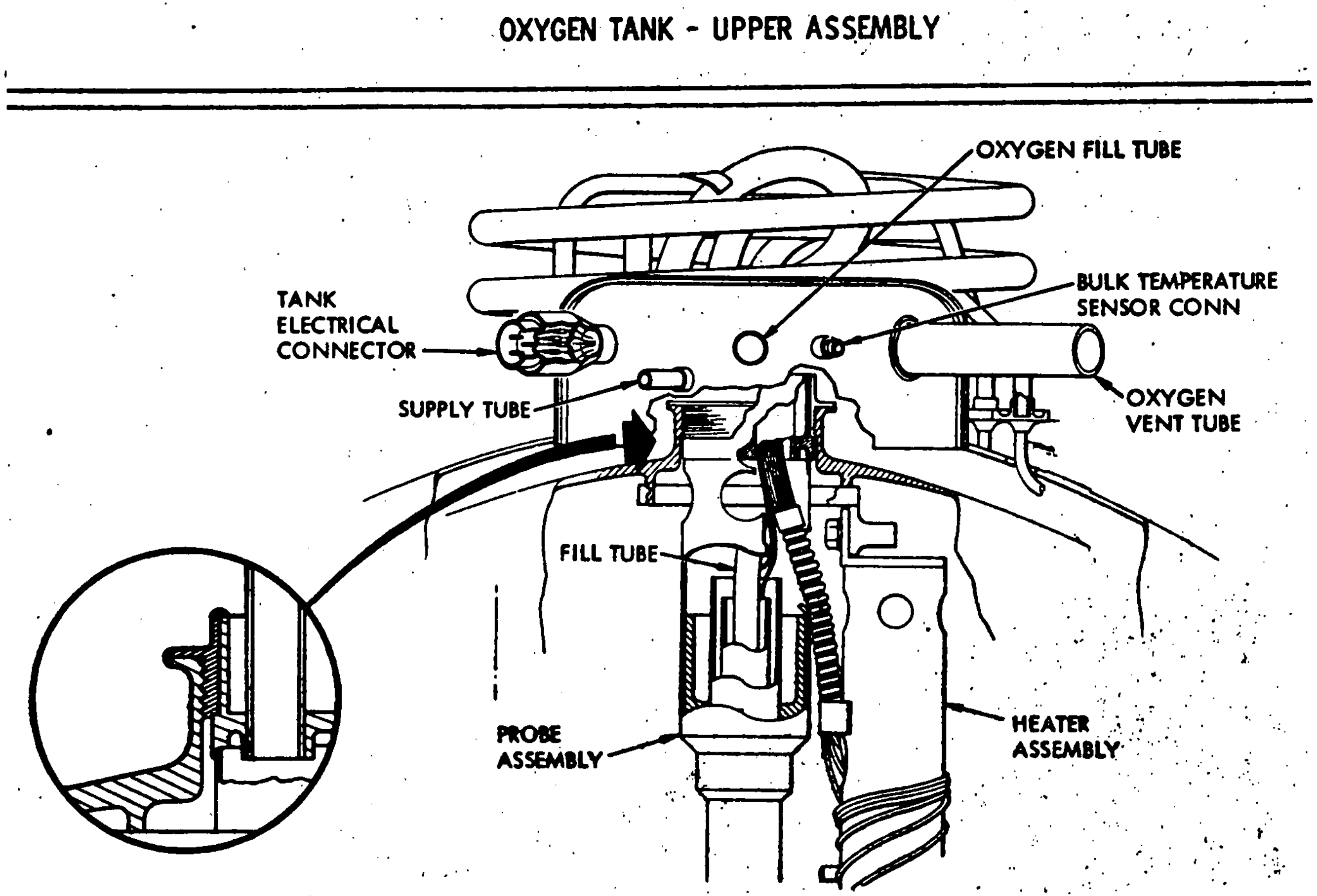

Figure 4

NEW DESIGN OXYGEN TANK NECK & PROBE DETAIL

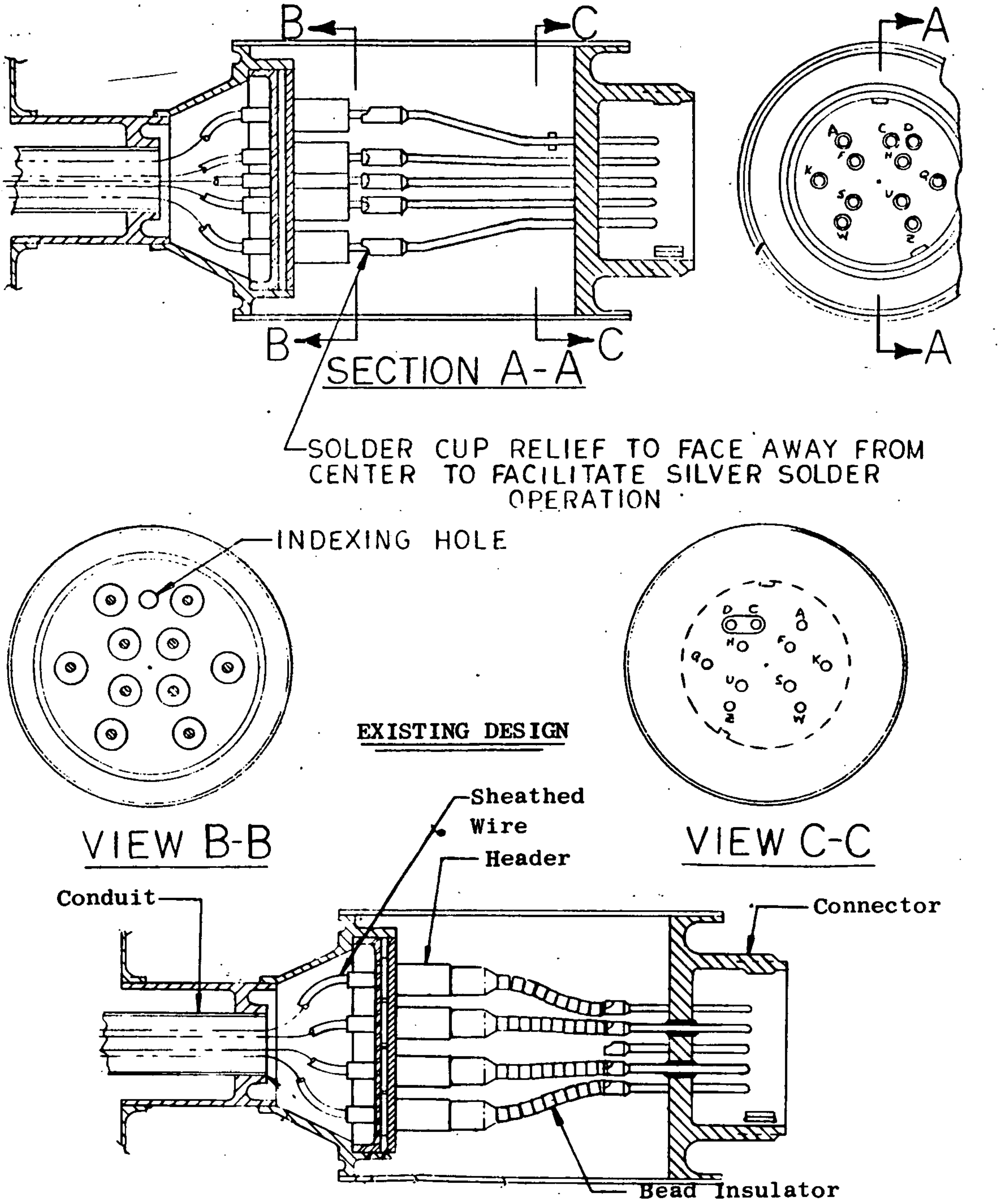

EXISTING DESIGN

DEVELOPMENT DESIGN

Figure 5

CONNECTOR ASSEMBLY

TABLE II

SYNOPSIS OF NEW DESIGN QUALIFICATION TESTING

QUALIFICATION ITEM	QUALIFICATION TESTS	REMARKS
New Design Tank Assembly	1. Transportation Vibration	Actual over the road, empty tank in shipping container.
	2. Sinusoidal Vibration	Filled tank & pressurized 5-30-5 Hz, ± 0.25 g peak.
	3. Random Vibration	
	a. Space Flight	Filled tank & pressurized. Increase 3 db/octave 20-15 Hz, constant 0.0075 g^2/Hz 150 to 2000 Hz. 12-1/2 minutes each axis.
	b. Atmospheric Flight	Filled tank & pressurized. Y & Z axes - increase 12 db/octave 20-35 Hz, constant 0.006 g^2/Hz. 35-105 Hz, increase 9 db/octave 105-200 Hz, constant 0.04 g^2/Hz 200-800 Hz, decrease 3 db/octave. 800-2000 Hz. For 75 seconds & +4 db increase for 10 seconds. X axis -- increase 6 db/octave 20-40 Hz, constant 0.01 g^2/Hz 40-125 Hz, increase 9 db/octave 125-200 Hz, constant 0.04 g^2/Hz 200-300 Hz, decrease 3 db/octave 300-2000 Hz. For 75 seconds & +4 db increase for 10 seconds.
	4. Acceleration	Filled tank & pressurized. +X = 6 g's 5 minutes. -X = 2 g's 1 minute. ±Y & ±Z = 1.5 g's 1 minute.

TABLE II (contd)

SYNOPSIS OF NEW DESIGN QUALIFICATION TESTING

QUALIFICATION ITEM	QUALIFICATION TESTS	REMARKS
	5. Mission Simulations	
	a. H-Mission	107 hours prelaunch 216.2 hours mission, 3 oxygen tanks. Qual tank off loaded to 60%.
	b. J-Mission	240 hours mission time 3 oxygen tanks.
Pressure Vessel Plug Assembly	1. Pressure Cycling	300 cycles each (fill to maximum relief pressure 1010 psig) at ambient and at LN_2 temperature. Proof pressure (1357 psia) and leak test each 300 cycles.
	2. Burst Pressure	Pressurized to 1537 psia for one minute then increase to rupture (3375 psig).
Heater Temperature Signal Conditioner	1. Salt Fog	MIL-STD-810, Method 509, Procedure 1 - 48 hours.
	2. Explosive Atmosphere	Hydrogen-oxygen explosive mixture. Included complete external electrical harness and signal conditioners.

TABLE III

PERFORMANCE RATINGS

ITEM	BLOCK II DESIGN	NEW DESIGN
Tank Weight (pounds)	80.85	79.7
Heater Watt Density (watts/sq.in.)	2.8	2.1
Maximum Heater Temperature (12.5% density & after 1 hr.) (Degree F)	580.0	490.0
Maximum Flow (lb/hr)	0.790	0.825 (measured LO-19)
Electrical Conduit Heat Leak (BTU/hr)	1.93	2.29
Fluid Temperature Sensor Heat Leak (BTU/hr)	0.0	1.53
Total Tank Heat Leak (BTU/hr)	28.05	29.26

N72-23788

THERMOPHYSICAL PROPERTY DATA AND SAFETY INFORMATION

R. H. Kropschot
Cryogenics Division
NBS-Institute for Basic Standards
Boulder, Colorado 80302

The accuracy of any calculation is usually dependent upon the quality of the input data. The National Bureau of Standards is the largest source of reliable data on the properties of materials and on bibliographic information at cryotemperatures. Precision measurements of the properties of oxygen over a wide range of temperature and pressure are complete. The primary remaining effort, which is in progress, is the representation of these data in the most usable format such as tables, equations, diagrams, and computer programs. In addition, safety data are essential to proper design, operation, and failure analysis. All of the available information on oxygen safety is being reviewed, evaluated and indexed for quick retrieval through the NASA Aerospace Safety Research and Data Institute program. This paper discusses the availability of data, where the major gaps in data occur, and retrieval of bibliographic information.

A prime function of the NBS-Cryogenic Division is to supply data for low temperature design and analysis. Table 1 shows the Functional Activities of the division and is intended to illustrate some of the resources available to the cryogenic engineer. The Cryogenics Division is the largest source of data on the properties of materials and bibliographic information at cryotemperatures. The Division is also the source of information on other areas of cryogenics such as safety, metrology, and process equipment. The primary objective of this paper, in relation to the Apollo program is to; a) summarize the sources of available data, b) discuss deficiencies in available data, c) review ongoing programs to alleviate these deficiencies, and d) discuss requirements for future space applications.

TABLE 1. Functional Activities of the NBS-Cryogenics Division

- Cryogenic Data Center
  - Documentation
  - Compilation and Critical Evaluation
- Cryogenic Properties of Solids
  - Electrical Properties
  - Thermal Properties
  - Mechanical/Metallurgical Properties
- Properties of Cryogenic Fluids
  - Pure Fluids
  - Mixtures
- Cryogenic Systems
  - Systems Evaluation
  - Consultation
  - Slush Cryogens
- Metrology
  - Flowmetering
  - Pressure/Temperature/Density/State
- Fluid Transport Processes
  - Heat Transfer
  - Infrared Properties
- Cryoelectronics

Data for Analysis and Design

A complete review of the information service provided by the Cryogenic Data Center for the field of cryogenics has recently been published by Olien.[1] A thorough and continuous search of current published literature is conducted. We review over 300 journals cover-to-cover, search other abstracting services, patents, conference proceedings, and report literature. Dissemination is made each week through the Current Awareness Service as illustrated in Figure 1. In addition, two specialized bibliographies are published quarterly, The Superconducting Devices and Materials Quarterly and the Liquefied Natural Gas Quarterly. Documents from these lists are then selected for entry into the information retrieval system. Punched cards in machine-readable form containing title, author, byline, reference, abstract reference, and indexing terms are prepared for each of the selected documents. Over 7500 new documents are added each year and our total file contains over 70,000 documents.

The availability of these data on magnetic tape permits rapid access to a vast amount of information. For example, Table 2 shows a list of bibliographies prepared for NASA and NASA contractors immediately after the Apollo 13 incident. Selected data from these references were scanned by the NBS staff and transmitted over the telephone. The entire bibliography was then forwarded, usually within hours after being requested. The rapid availability of these data saved many laborious manhours in conducting literature searches for creditable data and tended to assure the investigators that all pertinent sources of data had been utilized.

Thermophysical Properties of Oxygen

Data on the thermodynamic and transport properties of oxygen have been measured by NBS over a wide range of temperature and pressure.[2] These measurements were made at the request of NASA-OART.[3] Available tables, charts, graphs, and computer programs were supplied in copious quantities to assist in the Apollo investigation. The diverse nature of subsequent calculations (as illustrated by today's program) reemphasized the fact that the data, although available, were not always in the most usable format. In response to this need, NBS has undertaken a program for NASA-MSC to compile the thermophysical data in a format which is more readily usable by the design engineer.[4] The first of these documents is in final form for editorial

TABLE 2. Prepared Bibliographies Related to the Apollo 13 Incident

Compatibility of Oxygen with Various Materials and Contamination, Hazards and Safety with Liquid Oxygen

Handling and Safety with Liquid Oxygen

Liquid Oxygen Storage, Transfer, Loading, etc., Procedures and Equipment

Flow, Temperature and Pressure Measurement of Liquid and Supercritical Oxygen

Heat Transfer to Supercritical Oxygen at Zero Gravity

Properties of Thermal Insulation for Use at Cryogenic Temperatures

Critical Properties of Oxygen

Thermal Conductivity and Specific Heat of Inconel

Thermodynamic Diagrams of Oxygen

Thermodynamic Properties of Oxygen

Thermodynamic and Transport Properties of Teflon review and printing. R. D. McCarty and L. A. Weber[5] have compiled and critically evaluated the "Thermophysical Properties of Oxygen from the Freezing Liquid Line to 600 R for Pressures to 5000 psia." The tables include, entropy, enthalphy, internal energy, density, volume, speed of sound, specific heat, thermal conductivity, viscosity, $(\partial P/\partial V)_T$, $(\partial P/\partial T)_\rho$, $V(\partial H/\partial V)_P$, $V(\partial P/\partial U)_V$, $-V(\partial P/\partial V)_T$, $1/V(\partial V/\partial T)_P$, thermal diffusivity, Prandtl number and the dielectric constant for 79 isobars. In addition to the isobaric tables, tables for the saturated vapor and liquid are given which include all of the above properties, plus the surface tension. Tables for the pressure-temperature relationship of the freezing liquid and the derived Joule-Thomson inversion curve are also presented. The specific heat at constant saturation and the index of refraction are given in graphical form. Figures 2 and 3 show a representative table of data and a temperature entropy chart.

Thermodynamic Property Diagrams

Thermodynamic and phase diagrams permit the properties of a fluid to be visualized in a familiar frame of reference. They are often used for preliminary design and occasionally for final design, even though greater accuracy can be obtained from tables, computer routines or greatly enlarged charts. Diagrams are also useful in the analysis of malfunctions because they provide rapid access to property values without the difficulty of two-dimensional interpolation. Table 3 outlines the types of charts in most common use. Each chart has its adherents and, in general, each serves a slightly different purpose. Preparation of all of these charts for a given fluid would be very expensive. To be complete, all eight charts (in three, four and five variables) in SI, British, and modified units would require at least 30 different diagrams. In order to cover all ranges of temperature and pressure to adequate accuracy, some diagrams must be prepared in sections. Selected diagrams are currently in preparation by McCarty and Weber.

TABLE 3. Thermodynamic Diagrams

	3 variable charts	4 variable charts	5 variable charts
Variables	P, V or ρ, T	P, V or ρ, T, Z	P, V or ρ, T, H or U, S
Coordinate axes (the other variables are shown as constant property lines)	P vs T P vs V or ρ ρ vs T	Z vs log P	H vs S T vs S P or log P vs H P or log P vs U

Computer Programs for Thermophysical Properties of Oxygen

Several approaches to the development of computer programs for thermophysical properties of oxygen have been taken. The equation of state approach is very useful because it allows the direct calculation of the thermodynamic properties from an easily programmable mathematical function. The equation of state for oxygen developed by Stewart[6] has been used extensively, and although it does not give the best representation of existing experimental data, the accuracy is sufficient for many purposes. However, it is necessary to proceed with caution since equations of state often give erroneous results in the critical region and should not be used for extrapolation beyond the limits of experimental data.

Another method of computerizing thermodynamic properties is the so-called "Tab Code" method, which allows rapid calculations by interpolations of tables stored in the computer. This method was used for hydrogen,[7] but to this authors' knowledge no such program is available for oxygen. The primary problem with this method is interpolation error. If accurate calculations are required, the size of the tables to be stored in the computer becomes prohibitively large.

A third method of computerizing thermodynamic properties is by programming a series of independently derived mathematical functions (multifunction) such as isochores or isotherms or both. These functions are then joined together in the computer program by various means. Although this approach gives the most accurate results, it usually produces a program which allows very little, if any, versatility and the program is relatively slow on the computer. Because it is the most accurate way to present data, we have prepared the oxygen data in this manner for NASA-MSC under our present contract.[4] The problem of determining which calculational approach is best has no single answer but depends upon the individual user's requirements. The following table can be used as a guide. In addition, the National Bureau of Standards is constantly striving to fulfill the needs of the scientific and engineering community for computerized property data.

Type of Program	Speed	Versatility	Accuracy
Equation of State	medium	best	medium
Tab Code	best	very little	medium
Multifunction	slow	none	best

Radiation Properties of Oxygen

Measurement of the spectral transmission of infrared radiation in oxygen has been reported by several experimenters. These data are being compiled, critically evaluated and used to calculate total hemispherical radiation properties necessary for heat transfer calculations.[8]

Safety of Oxygen

An extensive program is underway to provide data for the safe handling of cryogenic fluid oxygen. Under the sponsorship of NASA Aerospace Safety Research and Data Institute (ASRDI) information on oxygen is being synthesized for quick retrieval through the NASA automated data processing system.[9] The technical objectives of the program are to:

(1) develop a thesaurus (dictionary) for information retrieval of safety related information,

(2) conduct an exhaustive literature search and acquire the documents,

(3) index and abstract these documents using the thesaurus,

(4) enter these documents into the NASA data bank for retrieval, and

(5) prepare a summary report on the properties of oxygen, giving "best values" for design.

An exhaustive search by our laboratory of both formal and informal sources of information is about 90 percent complete and has yielded over 3500 documents. Over half of these articles concern properties data and at least 400 are being evaluated in detail for the preparation of "best values."

The indexing thesaurus has been developed by the NBS and ASRDI staff and used to code a large number of cryogenic fluid safety papers. Coding is performed by members of the NBS senior staff which permits a critical evaluation by specialists in a particular field. The final input contains an abstract, major subject(s), minor subject(s), and links. The links are sequences of key words which permit retrieval (and sorting) of papers by a combination or words rather than single isolated words, i.e., a link is a set of indexing terms connected together to represent a detailed subject discussed in the report or paper.

Summary

Many of the thermophysical properties of oxygen below 5000 psi are extremely well known (relative to other fluids) and the development of "best values" along with tables, charts and computer programs should suffice for nearly all requirements. Future demands will require additional specialized data, data near the critical point, and most importantly, data above 5000 psi. The most severe and immediate problem to be solved is the criteria for compatibility as a function of temperature, pressure, density, etc., and the development of correlations between test procedures and service failure.

The Cryogenics Division is engaged in a program for NASA-MSC to compile the thermophysical properties of H_2, He, and N_2 in a format similar to the oxygen properties work of McCarty and Weber mentioned above.[4] Gaps in the data and uncertainties will, in many cases, limit the accuracy of calculations which can be made using these fluids. Details of these uncertainties will be given in the individual reports, but two potential problems should be outlined to this group. First, there exists a complete lack of data on helium in certain regions of the thermodynamic diagram, and in other regions, major discrepencies exist which can only be resolved by additional measurements. Secondly, no data on hydrogen exist at low temperatures above 5000 psi. This lack of data could be a severe problem for the shuttle engine design and, in collaboration with NASA-OART, we are planning on; (1) extrapolating existing data and estimating the uncertainties, and (2) evaluating the need for new measurements.

The author wishes to gratefully acknowledge the assistance of Dudley B. Chelton and Robert D. McCarty in the preparation of this manuscript.

References

[1] N. A. Olien, "The Cryogenic Data Center, an Information Service in the Field of Cryogenics," CRYOGENICS 11, 11 (1971).

[2] A synthesis of the oxygen properties data from all sources is given in Ref. 5.

[3] V. J. Johnson and D. E. Diller, "Thermodynamic and Transport Properties of Fluids and Selected Solids for Cryogenic Applications," Summary Report of work performed on NASA Contracts R-06-006-046 and W-12,745, unpublished.

[4] "Properties of Oxygen, Hydrogen, Helium and Nitrogen," NASA-MSC Contract T-1813A.

[5] Robert D. McCarty and Lloyd A. Weber, "Thermophysical Properties of Oxygen from the Freezing Liquid Line to 600 R for Pressures to 5000 PSIA." NBS Tech. Note (in press).

[6] R. B. Stewart, "The Thermodynamic Properties of Oxygen," University of Iowa, Iowa City, Ph.D. Thesis (1966).

[7] W. J. Hall, R. D. McCarty, and H. M. Roder, "Computer Programs for Thermodynamic and Transport Properties of Hydrogen," unpublished report.

[8] "Absorption Coefficients," NASA-Langley Research Center, Contract No. L-62,510.

[9] "Oxygen Safety and Cryogenic Fluids Safety Grid." NASA-Lewis Research Center Contract C-81608-B.

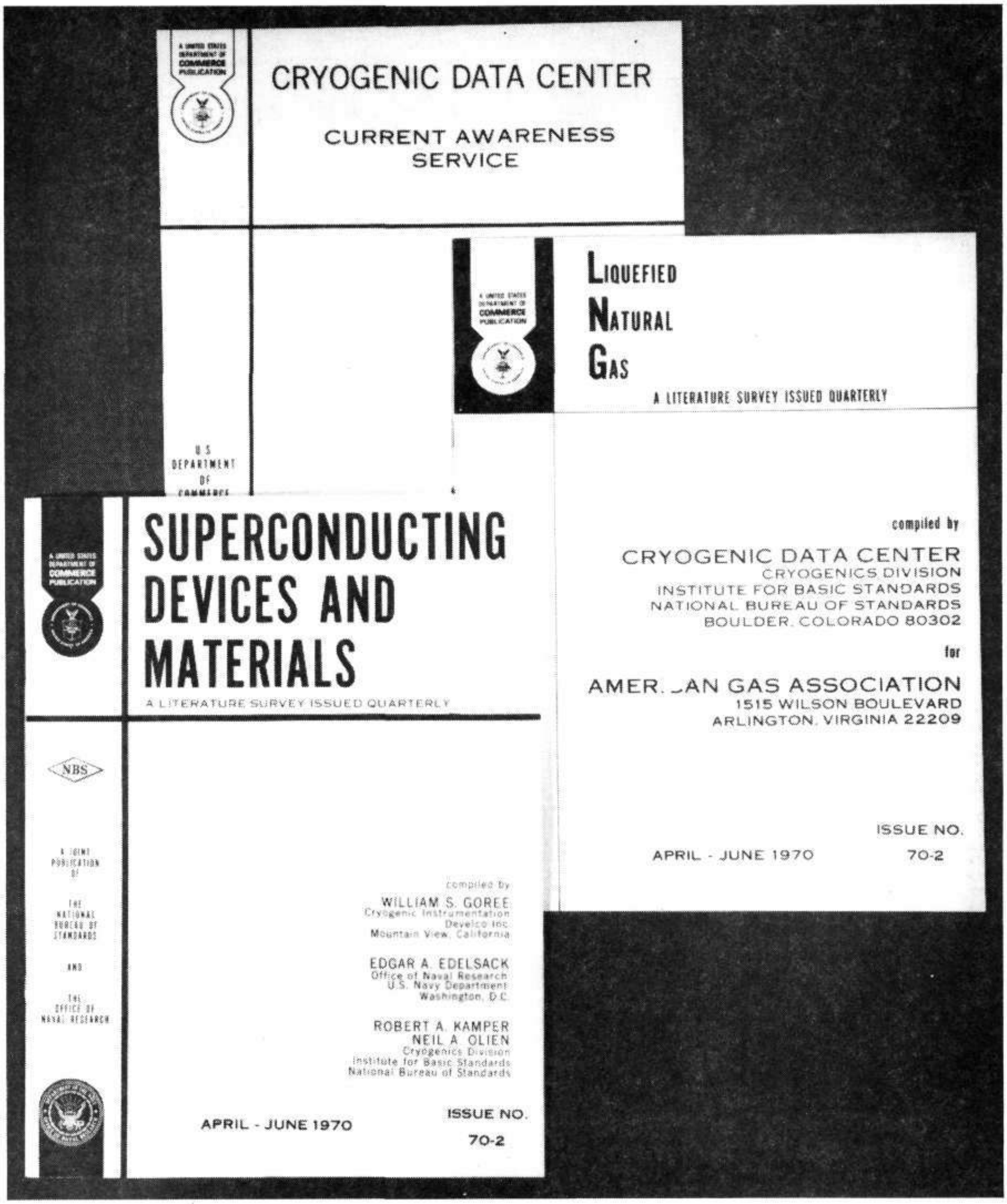

CRYOGENIC DATA CENTER

CURRENT AWARENESS
SERVICE

U.S.
DEPARTMENT
OF

LIQUEFIED
NATURAL
GAS

A LITERATURE SURVEY ISSUED QUARTERLY

compiled by

CRYOGENIC DATA CENTER
CRYOGENICS DIVISION
INSTITUTE FOR BASIC STANDARDS
NATIONAL BUREAU OF STANDARDS
BOULDER, COLORADO 80302

for

AMERICAN GAS ASSOCIATION
1515 WILSON BOULEVARD
ARLINGTON, VIRGINIA 22209

APRIL - JUNE 1970

ISSUE NO.
70-2

SUPERCONDUCTING
DEVICES AND
MATERIALS

A LITERATURE SURVEY ISSUED QUARTERLY

NBS

A JOINT
PUBLICATION
OF

THE
NATIONAL
BUREAU OF
STANDARDS

AND

THE
OFFICE OF
NAVAL RESEARCH

compiled by

WILLIAM S. GOREE
Cryogenic Instrumentation
Develco Inc.
Mountain View, California

EDGAR A. EDELSACK
Office of Naval Research
U.S. Navy Department
Washington, D.C.

ROBERT A. KAMPER
NEIL A. OLIEN
Cryogenics Division
Institute for Basic Standards
National Bureau of Standards

APRIL - JUNE 1970

ISSUE NO.
70-2

Figure 1. Three Subscription Services
of the Cryogenic Data Center

5000 PSIA ISOBAR

TEMPERATURE DEG. R	VOLUME CU FT/LB	ISOTHERM DERIVATIVE CU FT-PSIA/LB	ISOCHORE DERIVATIVE PSIA/R	INTERNAL ENERGY BTU/LB	ENTHALPY BTU/LB	ENTROPY BTU/LB-R	C_v BTU / LB -R	C_p	VELOCITY OF SOUND FT/SEC
* 104.777	0.01208	2390.44	320.1	-82.324	-71.151	0.50834	0.268	0.389	4010
105	0.01208	2386.51	319.5	-82.241	-71.064	0.50917	0.268	0.389	4008
110	0.01218	2299.59	307.6	-80.388	-69.120	0.52726	0.264	0.388	3958
115	0.01228	2215.35	296.1	-78.541	-67.180	0.54451	0.261	0.388	3907
120	0.01238	2133.71	285.0	-76.698	-65.243	0.56099	0.257	0.387	3855
125	0.01248	2054.63	274.3	-74.861	-63.310	0.57677	0.254	0.386	3803
130	0.01259	1978.03	254.0	-73.029	-61.381	0.59191	0.251	0.385	3750
135	0.01269	1903.88	254.0	-71.202	-59.456	0.60644	0.248	0.385	3697
140	0.01280	1832.10	244.4	-69.380	-57.533	0.62042	0.246	0.384	3643
145	0.01291	1762.65	235.1	-67.563	-55.615	0.63388	0.243	0.383	3589
150	0.01303	1695.46	226.2	-65.752	-53.699	0.64687	0.240	0.383	3535
155	0.01314	1633.48	217.7	-63.945	-51.787	0.65941	0.238	0.382	3481
160	0.01326	1567.66	209.4	-62.144	-49.878	0.67153	0.236	0.381	3427
165	0.01337	1506.93	201.5	-60.348	-47.973	0.68326	0.234	0.381	3374
170	0.01350	1448.24	193.9	-58.557	-46.070	0.69462	0.231	0.380	3320
175	0.01362	1391.54	186.6	-56.771	-44.170	0.70563	0.229	0.380	3267
180	0.01374	1336.78	179.6	-54.990	-42.273	0.71632	0.227	0.379	3214
185	0.01387	1283.88	172.9	-53.214	-40.379	0.72670	0.225	0.379	3163
190	0.01400	1232.82	156.5	-51.444	-38.487	0.73679	0.223	0.378	3111
195	0.01414	1183.52	150.3	-49.679	-36.598	0.74661	0.221	0.378	3061
200	0.01427	1135.95	154.5	-47.919	-34.711	0.75616	0.219	0.377	3012
205	0.01441	1090.04	148.8	-46.164	-32.827	0.76547	0.216	0.377	2964
210	0.01456	1045.76	143.4	-44.416	-30.945	0.77454	0.214	0.376	2918
215	0.01471	1003.05	138.3	-42.672	-29.066	0.78339	0.211	0.375	2873
220	0.01486	961.87	133.4	-40.935	-27.189	0.79202	0.209	0.375	2830
225	0.01501	922.17	128.7	-39.204	-25.315	0.80044	0.206	0.374	2789
230	0.01517	883.92	124.3	-37.480	-23.442	0.80866	0.202	0.374	2750
235	0.01534	852.76	119.4	-35.741	-21.552	0.81679	0.206	0.377	2669
240	0.01551	826.75	120.4	-33.982	-19.635	0.82487	0.205	0.392	2718
245	0.01568	788.34	110.8	-32.239	-17.733	0.83271	0.204	0.378	2599
250	0.01585	750.71	107.1	-30.498	-15.829	0.84040	0.203	0.381	2554
255	0.01604	719.26	105.0	-28.747	-13.908	0.84801	0.202	0.388	2529
260	0.01622	681.83	97.5	-27.023	-12.014	0.85537	0.201	0.377	2435
265	0.01642	651.07	97.3	-25.275	-10.085	0.86272	0.200	0.392	2432
270	0.01662	625.00	92.5	-23.527	-8.151	0.86995	0.199	0.388	2377
275	0.01683	598.70	89.5	-21.790	-6.223	0.87703	0.197	0.390	2342
280	0.01703	560.81	81.9	-20.072	-4.312	0.88391	0.196	0.376	2232
285	0.01726	550.11	75.6	-18.331	-2.363	0.89081	0.195	0.358	2165
290	0.01748	516.84	78.0	-16.523	-0.453	0.89745	0.198	0.391	2176
295	0.01771	496.88	75.7	-14.876	1.511	0.90417	0.196	0.393	2150
300	0.01795	479.62	73.2	-13.131	3.480	0.91079	0.195	0.395	2122
310	0.01846	444.22	67.7	-9.656	7.423	0.92372	0.194	0.396	2049
320	0.01899	407.72	61.6	-6.202	11.367	0.93624	0.193	0.392	1957
330	0.01956	380.41	58.1	-2.749	15.346	0.94849	0.192	0.400	1913
340	0.02016	354.16	53.6	0.672	19.321	0.96035	0.191	0.398	1850
350	0.02079	330.93	49.7	4.059	23.293	0.97187	0.189	0.398	1797
360	0.02145	307.04	45.6	7.385	27.231	0.98296	0.187	0.395	1733
370	0.02215	288.27	42.2	10.663	31.154	0.99371	0.185	0.393	1695
380	0.02289	277.37	42.2	13.912	35.095	1.00422	0.182	0.419	1718
390	0.02368	272.27	37.7	17.102	39.008	1.01438	0.180	0.391	1655
400	0.02445	258.76	33.6	20.192	42.813	1.02431	0.179	0.372	1579
410	0.02525	246.19	31.8	23.232	46.594	1.03335	0.178	0.376	1554
420	0.02608	235.52	29.1	26.204	50.331	1.04236	0.177	0.367	1506
430	0.02694	230.45	27.9	29.139	54.063	1.05114	0.176	0.371	1501
440	0.02786	236.33	27.6	32.057	57.831	1.05990	0.175	0.378	1540
450	0.02875	237.55	25.4	34.869	61.469	1.06798	0.174	0.361	1512
460	0.02962	233.99	23.5	37.588	64.998	1.07573	0.173	0.350	1480
470	0.03051	231.83	22.2	40.250	68.481	1.08323	0.172	0.344	1465
480	0.03141	230.84	21.1	42.851	71.912	1.09045	0.171	0.340	1458
490	0.03231	230.80	20.1	45.396	75.294	1.09743	0.170	0.335	1451
500	0.03322	231.62	19.2	47.889	78.626	1.10416	0.169	0.331	1449
510	0.03416	235.52	18.9	50.337	81.941	1.11072	0.168	0.336	1476
520	0.03509	239.60	17.9	52.730	85.192	1.11703	0.167	0.325	1470
530	0.03599	240.90	16.9	55.060	88.362	1.12307	0.166	0.316	1456
540	0.03690	243.09	16.2	57.351	91.493	1.12892	0.165	0.313	1460
550	0.03780	245.38	15.4	59.594	94.564	1.13456	0.164	0.304	1452
560	0.03869	248.24	14.9	61.799	97.598	1.14002	0.163	0.301	1457
570	0.03959	251.54	14.4	63.966	100.594	1.14533	0.162	0.298	1462
580	0.04048	255.15	13.9	66.096	103.551	1.15047	0.161	0.294	1469
590	0.04137	258.99	13.4	68.191	106.469	1.15546	0.160	0.291	1475
600	0.04226	262.99	13.0	70.251	109.350	1.16030	0.159	0.287	1482

Figure 2a. Thermodynamic Properties of Oxygen

5000 PSIA ISOBAR

TEMPERATURE DEG. R	DENSITY LB/CU FT	V(DH/DV) BTU/LB	V(DP/DU) PSIA-CU FT/BTU	-V(DP/DV) PSIA	-(DV/DT)/V DEG. R	THERMAL CONDUCTIVITY BTU/FT-HR-R	VISCOSITY LB/FT-SEC X 10^5	THERMAL DIFFUSIVITY SQ FT/HR	DIELECTRIC CONSTANT	PRANDTL NUMBER
* 104.777	82.80994	240.72	14.420	197952.53	0.0016169	0.11425	48.928	0.00354	1.57872	6.0009
105	82.73009	240.62	14.410	197555.14	0.0016175	0.11420	48.738	0.00354	1.57846	5.9796
110	82.11091	238.46	14.183	188821.79	0.0016293	0.11304	44.681	0.00354	1.57306	5.5272
115	81.44227	236.18	13.951	180423.02	0.0016414	0.11181	41.005	0.00354	1.56768	5.1184
120	80.77411	233.94	13.714	172348.63	0.0016539	0.11052	37.678	0.00354	1.56231	4.7486
125	80.10636	231.69	13.475	164588.53	0.0016667	0.10917	34.652	0.00353	1.55694	4.4139
130	79.43893	229.43	13.232	157132.81	0.0016800	0.10777	31.928	0.00352	1.55163	4.1107
135	78.77175	227.14	12.988	149971.76	0.0016937	0.10633	29.449	0.00351	1.54631	3.8358
140	78.10471	224.84	12.743	143095.78	0.0017080	0.10486	27.202	0.00350	1.54100	3.5864
145	77.43770	222.51	12.498	136495.47	0.0017228	0.10335	25.152	0.00348	1.53572	3.3631
150	76.77060	220.16	12.254	130161.62	0.0017382	0.10181	23.312	0.00347	1.53042	3.1545
155	76.10326	217.77	12.012	124085.16	0.0017542	0.10024	21.632	0.00345	1.52514	2.9678
160	75.43554	215.36	11.773	118257.23	0.0017710	0.09866	20.106	0.00343	1.51988	2.7982
165	74.75725	212.90	11.538	112669.13	0.0017886	0.09706	18.720	0.00341	1.51462	2.6441
170	74.09822	210.41	11.307	107312.37	0.0018070	0.09544	17.460	0.00339	1.50937	2.5047
175	73.42823	207.87	11.082	102178.65	0.0018264	0.09382	16.315	0.00337	1.50412	2.3766
180	72.75707	205.28	10.864	97259.86	0.0018468	0.09219	15.272	0.00334	1.49887	2.2069
185	72.08448	202.63	10.654	92548.09	0.0018683	0.09056	14.324	0.00332	1.49363	2.1557
190	71.41020	199.92	10.452	88035.65	0.0018911	0.08892	13.460	0.00329	1.48838	2.0602
195	70.73393	197.13	10.261	83715.07	0.0019153	0.08729	12.673	0.00327	1.48313	1.9734
200	70.05536	194.28	10.081	79579.10	0.0019409	0.08566	11.955	0.00324	1.47786	1.8446
205	69.37414	191.33	9.914	75620.70	0.0019681	0.08403	11.301	0.00322	1.47262	1.8231
210	68.68991	188.30	9.760	71833.08	0.0019970	0.08241	10.703	0.00319	1.46734	1.7581
215	68.00228	185.16	9.623	68209.69	0.0020278	0.08080	10.157	0.00315	1.46206	1.6992
220	67.31082	181.92	9.502	64744.24	0.0020606	0.07919	9.658	0.00314	1.45675	1.6453
225	66.61509	178.56	9.401	61430.68	0.0020957	0.07760	9.201	0.00311	1.45145	1.5974
230	65.91461	175.10	9.319	58263.22	0.0021331	0.07601	8.783	0.00309	1.44606	1.5536
235	65.20898	175.51	8.895	55607.62	0.0021475	0.07444	8.399	0.00303	1.44071	1.5309
240	64.49079	173.69	9.110	53317.99	0.0022587	0.07287	8.044	0.00288	1.43527	1.5592
245	63.78531	171.38	8.510	50284.57	0.0022031	0.07135	7.727	0.00295	1.42991	1.4727
250	63.07645	168.36	8.362	47352.01	0.0022628	0.06986	7.436	0.00291	1.42459	1.4599
255	62.35220	165.79	8.329	44447.35	0.0023404	0.06836	7.165	0.00283	1.41908	1.4542
260	61.64795	162.78	7.863	42033.29	0.0023189	0.06694	6.925	0.00288	1.41379	1.4053
265	60.91420	159.82	7.986	39059.46	0.0024525	0.06548	6.695	0.00274	1.40829	1.4427
270	60.17397	157.60	7.737	37058.52	0.0024602	0.06405	6.483	0.00275	1.40279	1.4128
275	59.43532	155.14	7.629	35583.75	0.0025162	0.06266	6.290	0.00277	1.39724	1.4106
280	58.70712	151.14	7.113	32923.64	0.0024882	0.06132	6.115	0.00278	1.39182	1.3506
285	57.94593	150.93	6.700	31476.57	0.0023724	0.05996	5.958	0.00289	1.38617	1.2609
290	57.22107	148.05	6.903	29574.41	0.0026385	0.05870	5.843	0.00263	1.38080	1.3991
295	56.45265	145.77	6.843	28055.17	0.0026971	0.05741	5.719	0.00259	1.37525	1.4097
300	55.69902	144.06	6.746	26714.40	0.0027404	0.05616	5.599	0.00255	1.36956	1.4176
310	54.17574	140.64	6.441	24005.91	0.0028124	0.05377	5.369	0.00251	1.35841	1.4219
320	52.66463	136.69	6.046	21472.53	0.0028684	0.05155	5.153	0.00250	1.34739	1.4197
330	51.13449	133.80	5.905	19451.93	0.0029864	0.04945	4.943	0.00242	1.33629	1.4379
340	49.61541	130.57	5.660	17571.70	0.0030516	0.04750	4.745	0.00240	1.32534	1.4329
350	48.10370	127.50	5.466	15919.15	0.0031238	0.04570	4.558	0.00239	1.31449	1.4301
360	46.62166	123.87	5.234	14314.75	0.0031876	0.04406	4.384	0.00234	1.30392	1.4146
370	45.15354	120.96	5.065	13016.44	0.0032454	0.04254	4.221	0.00240	1.29351	1.4423
380	43.67885	120.27	5.298	12115.04	0.0034819	0.04112	4.065	0.00225	1.28316	1.4963
390	42.23714	119.34	4.951	11499.81	0.0032749	0.03982	3.920	0.00241	1.27298	1.3651
400	40.90227	117.14	4.596	10583.71	0.0031761	0.03872	3.795	0.00254	1.26366	1.3127
410	39.60409	115.41	4.516	9749.97	0.0032604	0.03771	3.679	0.00253	1.25463	1.3215
420	38.35047	113.79	4.394	9032.27	0.0032269	0.03680	3.573	0.00261	1.24597	1.2533
430	37.12212	113.63	4.282	8554.64	0.0032622	0.03596	3.475	0.00261	1.23751	1.2892
440	35.89784	116.26	4.402	8483.62	0.0032517	0.03517	3.381	0.00259	1.22912	1.3082
450	34.78353	117.34	4.205	8262.91	0.0030759	0.03450	3.301	0.00275	1.22152	1.2432
460	33.75686	117.41	4.029	7898.62	0.0029792	0.03393	3.232	0.00287	1.21455	1.1997
470	32.77384	117.83	3.933	7598.00	0.0029203	0.03341	3.170	0.00295	1.20789	1.1754
480	31.83830	118.51	3.869	7349.69	0.0028703	0.03294	3.114	0.00304	1.20156	1.1575
490	30.94678	119.40	3.808	7142.37	0.0028091	0.03252	3.063	0.00313	1.19559	1.1372
500	30.09838	120.49	3.761	6971.32	0.0027489	0.03215	3.018	0.00322	1.18991	1.1193
510	29.27605	122.31	3.843	6895.15	0.0027450	0.03180	2.975	0.00324	1.18442	1.1313
520	28.50220	124.23	3.753	6829.22	0.0026193	0.03149	2.939	0.00340	1.17927	1.0931
530	27.78387	125.48	3.655	6693.27	0.0025211	0.03123	2.907	0.00355	1.1745	1.0599
540	27.03959	126.89	3.626	6587.67	0.0024641	0.03100	2.878	0.00365	1.16997	1.0452
550	26.45847	128.49	3.540	6492.35	0.0023693	0.03079	2.854	0.00382	1.16574	1.0155
560	25.84578	130.08	3.521	6416.02	0.0023160	0.03062	2.831	0.00393	1.16170	1.0033
570	25.26109	131.78	3.503	6354.12	0.0022632	0.03046	2.812	0.00405	1.15786	0.9899
580	24.70351	133.56	3.485	6303.12	0.0022038	0.03032	2.795	0.00417	1.15421	0.9766
590	24.17185	135.39	3.469	6260.33	0.0021477	0.03020	2.779	0.00430	1.15073	0.9634
600	23.66478	137.26	3.454	6223.71	0.0020928	0.03010	2.765	0.00443	1.14742	0.9504

Figure 2b. Thermodynamic Properties of Oxygen

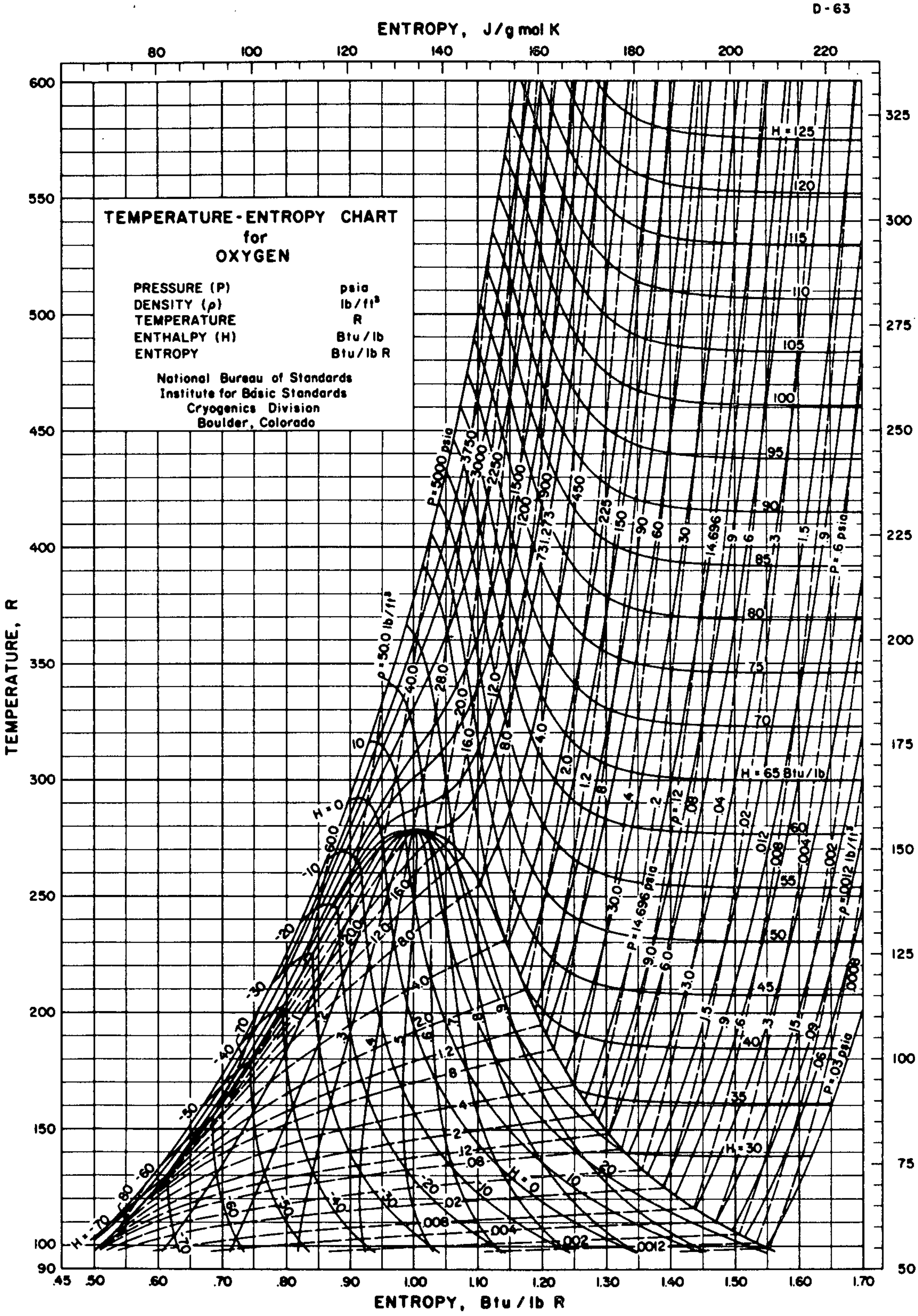

Figure 3. Temperature-Entropy Chart for Oxygen

N72-23789

PRESSURIZED EXPULSION OF NONISOTHERMAL SINGLE-PHASE CRYOGEN

Clifford K. Forester
Research Engineer
The Boeing Company
Seattle, Washington

The performance of single-phase storage and expulsion systems is strongly affected by temperature variations within the stored cryogen which are generated during heat transfer. Peculiar operating responses are indicated by spontaneous changes in fluid pressure which accompany "g" level changes, increased heater surface temperature, and durations of pressure cycles which differ considerably from that which is computed for an isothermal cryogen. The nonisothermal characteristics are predicted with a numerical model which includes the simultaneous solution of the time dependent conservation equations of mass, energy, and momentum in two space dimensions of Cartesian coordinates for boundary conditions which approximate those of the flight cryogenic system. The methodology of the numerical method and some comparisons between the predictions and the Apollo 12 flight data are included.

Acknowledgement

The boundary and initial conditions which are required for the application of the numerical simulation technique were established by H. W. Patterson who is associated with Boeing, Houston.

Table of Contents

Illustrations

Nomenclature

$\dot{P}_g$	Time derivative of the global pressure
P_g	Global pressure
P	Pressure
ρ	Mass density
ρ_c	Average mass density of the fluid in the container
ρ_p	Mass density of fluid in the external plumbing
h	Enthalpy
e	Specific internal energy
T	Temperature
k	Thermal conductivity
μ	Kinematic viscosity
g_x	x- direction acceleration component
u	x- direction velocity
A_x	Cross sectional area of a cell face normal to the x- direction
Δx	x-direction discrete distance
X	x- direction mass rate
HX	Discrete stress tensor, momentum convection and body force terms of the x-momentum equation
g_y	y- direction acceleration component
v	y- direction velocity

Y	y- direction mass rate
Δy	y- direction discrete distance
A_y	Cross sectional area of a cell face normal to the y- direction
HY	Discrete stress tensor, momentum convection, and body force terms of the y- momentum equation
θ	$\equiv(-\rho\,\partial h/\partial\rho)\big|_p$
Φ	$\equiv(1/\rho\;\partial p/\partial e)\big|_\rho$
V	Cell volume
V_c	Container volume
V_p	Volume of the external plumbing
Δt	Time increment
δ	A fraction of a time increment
EF	Container elastic factor
HCX	Thermal capacitance of a material located at a cell face
TWX	Temperature of a cell face
$\dot{Q}X$	The prescribed cell face heating rate
g	The magnitude of g acceleration vector
Q_{DA}	The adiabatic heat deficiency of a nonisothermal fluid system
Q_{DT}	The heat deficiency of a process in which a discrete amount of heat is added during the process

$\Delta P\|_{max}$	The pressure decay potential of a nonisothermal fluid system
Z	Compressibility
M	Mass
$\dot{m}$	Mass rate
n	The inverse of the polytropic exponent

References

1. Forester, C. K., "Numerical Integration of Conservation Equations for the Storage and Expulsion of Single-Phase Cryogen", M.S. Thesis, University of Washington, Seattle, Washington, 1969.

2. Forester, C. K., and Emery, A. F., "The Numerical Computation of the Free Convection of Cryogens with Variable Density", to be published.

3. Williams, G. P., "Numerical Integration of the Three-Dimensional Navier-Stokes Equations for Incompressible Flow", J. Fluid Mechanics, Vol. 37, Part 4, pp. 727-750, 1969.

4. Harlow, Francis H. and Welch, J. E., "Numerical Calculation of Time-Dependent Viscous Incompressible Flow of Fluid with a Free Surface", Physics of Fluids, No. 12, Vol. 8, 1965.

PRESSURIZED EXPULSION OF NONISOTHERMAL SINGLE-PHASE CRYOGEN

Clifford K. Forester
Research Engineer
The Boeing Company
Seattle, Washington

The single-phase storage concept has been employed in the design of the Gemini and Apollo atmosphere and fuel cell supply equipment. In the course of using these systems, some peculiar performance characteristics have been observed during flight operations. For example, shortly after the launch of Gemini II and Apollo 12, abrupt decreases in the oxygen storage pressure in excess of 100 psi have been noted. Additionally, the observed time required to complete a pressurization cycle has been both substantially shorter and longer than the duration predicted from calculations which assume the stored cryogen is isothermal.

In this paper, the methodology of a numerical model is presented which, for the comparisons this far made with Apollo 12 and 14 flight data, appears to predict the observed peculiarities. Several considerations comprise the numerical model:

1) the methodology of the General Elliptic Method - GEM
2) the 1/2 box model in which the GEM is applied
3) the method of accounting for the cryogenic container elasticity
4) the method of treating the gas trapped in the external volume

The first two of these are discussed in order after the introduction. The mathematical derivation of the last two are provided in Appendix A. These considerations are followed by a discussion of the physical characteristics of the Apollo oxygen system and a brief discussion of the flight data reduction considerations. Finally, a discussion is provided in which the comparison between Apollo 12 flight data and the 1/2 box model predictions for two problems is presented.

The Methodology of the General Elliptic Method (GEM)

Because of the length, no attempt is provided here to document the literature now available on numerical algorithms which model the conservation equations of mass, energy, and momentum in time and space. A review of this literature at the end of 1967 showed that the methods generally applied either to incompressible flow or high speed compressible flow. These algorithms are restrictive enough so that they eliminate from practical analysis one of the most intriging aspects of the problems at hand which is to compute the cryogen pressure history. As a result, a new algorithm, the General Elliptic Method (GEM), was developed by the author as a part-time effort and was documented in reference (1). Reference (2) includes a literature survey of those algorithms which depend upon an elliptical equation and some refinements of the GEM which was presented in reference (1). However, the GEM had to be modified to suit the special requirements which the problems at hand establish. Since these modifications are an intricate part of the computational method, a complete description of the methodology is necessary and is illustrated subsequently.

The conservation equations of mass, energy, and momentum for a Newtonian fluid may be written in the x- and y-directions of Cartesian coordinates respectively as

$$\frac{\partial \rho}{\partial t} + \frac{\partial(\rho u)}{\partial x} + \frac{\partial(\rho v)}{\partial y} = 0$$

$$\frac{\partial(\rho e)}{\partial t} + \frac{\partial(\rho u h)}{\partial x} + \frac{\partial(\rho v h)}{\partial y} = \frac{\partial}{\partial x}\left(k\frac{\partial T}{\partial x}\right) + \frac{\partial}{\partial y}\left(k\frac{\partial T}{\partial y}\right)$$

$$\frac{\partial(\rho u)}{\partial t} + \frac{\partial(\rho u^2)}{\partial x} + \frac{\partial(\rho v u)}{\partial y} + \frac{\partial P}{\partial x} + g_x \rho = \sigma_x$$

$$\frac{\partial(\rho v)}{\partial t} + \frac{\partial(\rho v^2)}{\partial y} + \frac{\partial(\rho u v)}{\partial x} + \frac{\partial P}{\partial y} + g_y \rho = \sigma_y$$

where

$$\sigma_x = \frac{\partial}{\partial x}\left[2\mu\frac{\partial u}{\partial x} - \frac{2}{3}\mu\left(\frac{\partial u}{\partial x} + \frac{\partial v}{\partial y}\right)\right] + \frac{\partial}{\partial y}\left[\mu\left(\frac{\partial u}{\partial y} + \frac{\partial v}{\partial x}\right)\right]$$

$$\sigma_y = \frac{\partial}{\partial y}\left[2\mu\frac{\partial v}{\partial y} - \frac{2}{3}\mu\left(\frac{\partial u}{\partial x} + \frac{\partial v}{\partial y}\right)\right] + \frac{\partial}{\partial x}\left[\mu\left(\frac{\partial v}{\partial x} + \frac{\partial u}{\partial y}\right)\right] \qquad (1)$$

and where ρ is the mass density, u is the x-direction velocity, v is the y- direction velocity, e is the specific internal energy, h is the enthalpy, k is the thermal conductivity, T is the temperature, P is the pressure, g_x is the x- direction acceleration component, g_y is the y-direction acceleration component, and μ is the kinematic viscosity.

Since

$e = e(P, \rho)$ and $h \equiv e + P/\rho$

$$\frac{\partial(\rho e)}{\partial t} = \frac{1}{\Phi}\frac{\partial P}{\partial \epsilon} + (h - \theta)\frac{\partial \rho}{\partial t} \qquad (2)$$

where

$$\Phi \equiv \frac{1}{\rho}\left.\frac{\partial P}{\partial e}\right|_{\rho}$$

and

$$\theta \equiv -\rho\left.\frac{\partial h}{\partial \rho}\right|_{P}$$

and the product of Φ and θ ($\Phi\theta$) is the speed of sound squared of the fluid.

Because the Mach number is less than about 10^{-3} for the problems to be considered, only pressure waves of the acoustic variety will dominate during the various flow processes of interest. But since, for the purposes here, modeling acoustic waves is unnecessary, and since each acoustic wave only subtly modifies the density field as it passes by any point of interest, the local time derivative of pressure ($\partial P/\partial t$) may be replaced with the time derivative of the global pressure (P_g) or ($\partial P_g/\partial t) \rightarrow \dot{P}_g$. (Note however that this simplification does not eliminate spatial gradients of pressure from the momentum equations.) Thus equation (2) may be simplified to read

$$\frac{\partial(\rho e)}{\partial t} = \frac{\dot{P}_g}{\phi} + (h-\theta)\frac{\partial \rho}{\partial t} \tag{3}$$

Now the mass rates which pass normal to and through the center of the sides of a cell are defined as

$$X \equiv \rho u A_x \text{ and } Y \equiv \rho v A_y \tag{4}$$

where A_x and A_y are the areas of the cell faces perpendicular to the x and y axes respectively. Equations (1, 3 and 4) can be combined as

$$\frac{\partial \rho}{\partial t} + \frac{1}{A_x}\frac{\partial X}{\partial x} + \frac{1}{A_y}\frac{\partial Y}{\partial y} = 0 \tag{5a}$$

$$\frac{P_g}{\phi} = (h-\theta)\left[\frac{1}{A_x}\frac{\partial X}{\partial x} + \frac{1}{A_y}\frac{\partial Y}{\partial y}\right] - \left[\frac{1}{A_x}\frac{\partial(Xh)}{\partial x}\right] - \left[\frac{1}{A_y}\frac{\partial(Yh)}{\partial y}\right] + \left[\frac{1}{A_x}\frac{\partial}{\partial x}\left(kA_x\frac{\partial T}{\partial x}\right)\right] + \left[\frac{1}{A_y}\frac{\partial}{\partial y}\left(kA_y\frac{\partial T}{\partial y}\right)\right] \tag{5b}$$

$$\frac{\partial X}{\partial t} + \frac{\partial(Xu)}{\partial x} + \frac{A_x}{A_y}\frac{\partial Yu}{\partial y} + A_x\frac{\partial P}{\partial x} + \beta_x A_x \rho = A_x \sigma_x \tag{5c}$$

$$\frac{\partial y}{\partial t} + \frac{\partial(Yv)}{\partial y} + \frac{A_y}{A_x}\frac{\partial(Xv)}{\partial x} + A_y\frac{\partial P}{\partial y} + \beta_y A_y \rho = A_y \sigma_y \tag{5d}$$

Now (5a) - (5d) are transformed into a discrete set of simultaneous algebraic equations with the use of a discrete grid network.

It should be noted that two types of grid networks are in general use:

1) a mathematical grid in which all dependent variables are defined at common points and

2) a physical grid in which the state and transport properties are defined in the centers of control volumes and the velocities are defined normal to and in the center of the faces which bound the volumes.

The physical grid possesses three important advantages:

1) a unique definition of local mass conservation is specified.

2) The resolution of thermal and velocity boundary layers are improved for the same grid density since the temperature and velocity points are $\Delta x/2$ or $\Delta y/2$ from solid boundaries rather than the usual Δx or Δy for the mathematical grid. This is achieved without the usual complication that nonlinear grid spacings involve.

3) The procedures for treating mathematical singularities (e.g., the center of a polar coordinate system) are not ambiguous.

For these reasons the physical grid is employed in the following discrete formulation. Figure (1) shows a typical computational cell which is imbedded in an array of such cells which altogether comprise the volume of the entire region of interest. For identification purposes, the subscripts i and j are used with the cell center variables P, ρ, T, h, e, k, and μ to denote their relative location in the complete cellular array. The whole integers, i and j, are counted with the increasing x- and y- directions, respectively. The velocities and mass rates which are defined at the cell sides are denoted by half integers and are counted similarly to the cell center values. Both the integer and half integer nodal points are defined to be separated by a cell width (Δx) and a cell height (Δy).

The difference approximations of equations (5a) - (5d) for a uniform two dimensional rectangular grid with an arbitrary depth in the third dimension, are

$$\rho_{ij}^{t+1} = \rho_{ij}^{t} + D_{ij}^{t+1}\frac{\Delta t}{V} \tag{6a}$$

$$\left.\begin{aligned} \dot{P}_g &= \theta_{ij}^{t+\delta}\left(E_{ij}^{t+\delta} + \phi_{ij}^{t+\delta}\, D_{ij}^{t+1}\right)\frac{\Delta t}{V} && (6b)\\ P_g^{t+1} &= P_g^{t} + \dot{P}_g\Delta t && (6c) \end{aligned}\right\}\text{ energy equation}$$

$$X_{i+\frac{1}{2}j}^{t+1} = X_{i+\frac{1}{2}j}^{t} + A_x\left[\left(\frac{P_{ij}-P_{i+1\,j}}{\Delta x}\right)^{t+1} + HX_{i+\frac{1}{2}j}^{t}\right]\Delta t \tag{6d}$$

$$Y_{ij+\frac{1}{2}}^{t+1} = Y_{ij+\frac{1}{2}}^{t} + A_y\left[\left(\frac{P_{ij}-P_{ij+1}}{\Delta y}\right)^{t+1} + HY_{ij+\frac{1}{2}}^{t}\right]\Delta t \tag{6e}$$

where

$$D_{ij}^{t+1} \equiv \left(X_{i-\frac{1}{2}j} - X_{i+\frac{1}{2}j} + Y_{ij-\frac{1}{2}} - Y_{ij+\frac{1}{2}}\right)^{t+1}$$

and $V = A_x\Delta x = A_y\Delta y$ (the cell volume) and the superscripts $t + 1$ and $t + \delta$ indicate an evaluation at the time $t + \Delta t$ and $t + \delta\ (\Delta t)$ respectively ($\delta = 1/2, 0$). For $\delta = 1/2$, ϕ_{ij}, θ_{ij}, $\dot{P}_g$ and the terms of the convection of heat are nearly time centered. Such an alternative has certain advantages which are provided together with the methodology for implementation in reference (2).

D_{ij} is the net added mass rate to an ij cell, E_{ij} is the net added heat rate to an ij cell by conduction and convection. $HX_{i+1/2j}$ and $HY_{ij+1/2}$ are the viscous, body force and the convection terms of momentum in the x- and y- directions respectively. The difference expressions for these terms are given in references (1) and (2) and are omitted because they are not essential to the illustration of the methodology of the GEM.

(6b) may be revised as

$$D_{ij}^{t+1} = \dot{P}_g \frac{V}{(\phi\theta)_{ij}^{t}} - \left(\frac{E}{\theta}\right)_{ij}^{t} \qquad (7)$$

Since D_{ij}^{t+1} summed over the total volume is equal to net mass rate inflow at the boundaries, and since $\dot{P}_g$ is a constant over the total volume, (7) may be integrated over the total volume to yield

$$\dot{P}_g = \frac{\sum\left(\frac{E}{\theta}\right)_{ij}^{t} - \left(\begin{matrix}\text{net mass rate outflow}\\ \text{at the boundaries}\end{matrix}\right)}{\sum\left(\frac{V}{\phi\theta}\right)_{ij}^{t}} \qquad (8)$$

where $\sum$ is the sum over all active cells.

Now (6a) and (7) may be combined to form

$$\rho_{ij}^{t+1} = \rho_{ij}^{t} + \frac{\Delta t}{V}\left[\frac{\dot{P}_g V}{(\phi\theta)_{ij}} - \left(\frac{E}{\theta}\right)_{ij}^{t}\right] \qquad (9)$$

Equations (6c, 8, and 9) apply only to a container whose walls are rigid. These equations may be modified in two ways to accomodate the elasticity effect of the container wall and the external volume. The first method involves simply the multiplication of (8) by (EF) where

$$EF = \frac{1}{1 + (\rho\phi\theta)_c\,(ESF)}$$

where

$$ESF \equiv \left[\frac{3r(1-\sigma)}{2bE} + \frac{V_p}{V_c}\,\frac{n}{P_g}\,\frac{\rho_p}{\rho_c}\right] \qquad (10)$$

which is the elastic factor derived in Appendix A. $(\rho\phi\theta)_c$ is evaluated at the average stored fluid density. $(\rho V)_p$ is the product of the external plumbing volume and the density of the fluid in the volume. n is the inverse of the polytropic coefficient and is unity for an isothermal process. This method of modifying $\dot{P}_g$ for the elastic effect is valid provided the ratio of the volume occupied by the thermal boundary layer to the total volume is small.

A general method of incorporating the elastic factor involves modifying (8) as

$$\dot{P}_{\emptyset} = \frac{\sum\left(\frac{E}{\theta}\right)^t_{ij} - \left(\begin{array}{c}\text{net mass rate outflow}\\ \text{at the boundaries}\end{array}\right)}{V\sum\left[\left(\frac{1}{\phi\theta}\right)^t_{ij} + \rho^t_{ij}\,(ESF)\right]} \tag{11}$$

and (9) may be modified as

$$\rho^t_{ij} = \rho^t_{ij} - \frac{\Delta t}{V} HH_{ij} \tag{12}$$

where

$$HH_{ij} = \left\{\left(\frac{E}{\theta}\right)^t_{ij} - V\dot{P}_{\emptyset}\left[\left(\frac{1}{\phi\theta}\right)^t_{ij} + \rho_{ij}\,(ESF)\right]\right\}$$

For convenience, equation (6c) is renumbered as

$$P^{t+1}_{\emptyset} = P^t_{\emptyset} + \Delta t\,(\dot{P}_{\emptyset}) \tag{13}$$

Equations (11, 12, and 13) are the discrete conservation equations of mass and energy which must be solved simultaneously with the momentum balances (6d) and (6e). To implement this, equations (6d and 6e) are discretely differentiated with respect to x and y respectively and combine to form

$$D^{t+1}_{ij} = D^t_{ij} + \Delta t\,(P12^{t+1}_{ij} - H12^t_{ij}) \tag{14}$$

where

$$P12^{t+1}_{ij} = \frac{A_x}{\Delta x}(P_{i-1\,j} - 2P_{ij} + P_{i+1\,j})^{t+1} + \frac{A_y}{\Delta y}(P_{i\,j-1} - 2P_{ij} + P_{i\,j+1})^{t+1}$$

and

$$H12^t_{ij} = HX^t_{i-\frac{1}{2}j} - HX^t_{i+\frac{1}{2}j} + HY^t_{ij-\frac{1}{2}} - HY^t_{ij+\frac{1}{2}}$$

The D^{t+1}_{ij} term is eliminated from (14) with the aid of (6a) and (12) to yield

$$0 = D^t_{ij} + HH^t_{ij} + \Delta t\,(P12^{t+1}_{ij} - H12^t_{ij}) \tag{15}$$

Equation (15) is an elliptic difference equation which may be solved by direct inversion, direct Fourier methods (see reference 3), and iterative methods. For generality and simplicity, the Liebmann iterative method is employed which is used in the MAC method of Harlow and Welch (reference 4). NIP is defined as the number of iterations used to solve equation (15). The pressures which result from the approximate solution of (15) are used in the momentum balances to obtain updated x- and y- direction mass rates in the active cells. With the use of the thermodynamic relations, the updated values of density and global pressure from equations (12 and 13) are used to find updated values of temperature, enthalpy, thermal conductivity, viscosity, θ and ϕ for all active cells.

The sequence of computations for the General Elliptic Method (GEM) is summarized as:

1) Prescribe the initial values of the mass rates $(X_{i+1/2j}, Y_{ij+1/2})$, the global pressure (P_g), and the density (ρ_{ij}) for all active cells including the border values. Compute the velocities (u_{ij} and v_{ij}) for all the field and border locations using the mass rate definitions. Evaluate the exterior velocities for the no-slip and free-slip conditions. Find T_{ij}, h_{ij}, k_{ij}, μ_{ij}, $(\theta\phi)_{ij}$, and θ_{ij} with P_g and ρ_{ij} from the thermodynamic and transport relations. These relations may be defined in terms of equations of state or tabular data. For the simulations reported, the thermodynamic properties are tabulated at three pressure levels; 850 psia, 900 psia, and 950 psia. Linear interpolation with density and pressure are used to find the other desired thermodynamic properties. The transport properties are determined from a linear interpolation with temperature in single arrays of thermal conductivity and viscosity at 900 psia.

2) Evaluate $HX_{i+1/2j}$, $HY_{ij+1/2}$, E_{ij}, D_{ij}, (EF), $\dot{P}_g$ and HH_{ij} for all active cells from the existing field values.

3) Compute ρ^{t+1}_{ij} and P_g^{t+1} from (12) and (13). With these values find T^{t+1}_{ij}, h^{t+1}_{ij}, k^{t+1}_{ij}, μ^{t+1}_{ij}, $(\theta\Phi)^{t+1}_{ij}$, and θ^{t+1}_{ij} from the linear table searches. Compute the border values of $X^{t+1}_{i+1/2j}$ and $Y^{t+1}_{ij+1/2}$ from the expulsion rate function.

4) Solve (15) approximately with NIP iterations for P^{t+1}_{ij} for all cells inside the border and immediately outside the border. The pressure P_{ij} in cells outside and adjoining the border are obtained directly from the momentum balances (6d) and (6e) and are recomputed each sweep of the field for new tentative values. Note that the border values of $HX_{i+1/2j}$ and $HY_{ij+1/2}$ used in (15), (6d), and (6e) must be the same but may be any desired value. It is best to set these to zero.

5) Use the values of pressure (P_{ij}) from step 4 in (6d) and (6e) to obtain the remaining unknown values of $X^{t+1}_{i+1/2j}$ and $Y^{t+1}_{ij+1/2}$ respectively.

6) The updated values then become the current values at time (t) and step 2 through step 5 may be repeated until the time (t) has been advanced to some value of interest.

Some discussion is now devoted to the various boundary conditions which are required to define all derivatives and quantities normal to the boundary. All mass rates normal to the border must be set to zero except where expulsion is specified. The velocities are computed from the mass rates, the normal cross sectional area through which the mass flows, and the average density of respective adjoining cells. Where mass rates are nonzero at the border, the velocity calculation requires a prescription of the density in the external receiver cell and is set equal to that in the supplier cell. This velocity enters into two viscous terms. Two other viscous terms require the prescription of velocities parallel to the boundary in all external cells. Where no-slip boundaries are required, the external velocity is set equal and opposite to the values in the active adjoining cell. Where free-slip boundary velocities are required, the external velocity is set equal to the values in the active adjoining cell. These velocities in external cells are computed <u>after</u> all the velocities have been computed which reside inside and on the border. The $HX_{i+1/2j}$ and $HY_{ij+1/2}$ terms required by the momentum balances on the border may be set to any value but for convenience are set to zero. This follows from the fact that since the mass rates at t+1 and t are prescribed on the border, the momentum balances are not required to generate these values at the border . For these to balance then it is only necessary that the values of $HX_{i+1/2j}$ and $HY_{ij+1/2}$ defined on the border which are used in the elliptic equation (15) be the same as those used in the border momentum balances to find the unknown external cell pressure which is required by equation (15) during the iterative solution.

The heat conduction terms involve gradients of temperature normal to the sides of a cell. Cell sides at which the heat rate is prescribed may be used to calculate these gradients. For generality, it is assumed that any cell face at which the heating rate is prescribed has an arbitrary thermal capacitance. The cell face temperature is determined with an implicit energy balance on a cell face of interest and for a left cell face is

$$\dot{Q}X^{t}_{i-\frac{1}{2}j} = \frac{(TWX^{t+1}_{i-\frac{1}{2}j} - TWX^{t}_{i-\frac{1}{2}j})(HCX_{i-\frac{1}{2}j})^{t}}{\Delta t} + (TWX^{t+1}_{i-\frac{1}{2}j} - T^{t}_{ij})(k_{i-\frac{1}{2}j} + k_{ij})^{t}\,\frac{A_X}{\Delta X} \qquad (16)$$

where $\dot{Q}X_{i+1/2j}$ is the prescribed cell face heat rate, $HCX_{i=1/2j}$ is the cell face thermal capacitance, $TWX_{i-1/2j}$ is the face temperature, $k_{i-1/2j}$ is the thermal conductivity at temperature $TWX_{i-1/2j}$ and T_{ij} is the cell temperature. Equation (6) may be solved for the unknown

$TWX^{t+1}_{i-1/2j}$ by algebraic manipulation and yields

$$TWX^{t+1}_{i-\frac{1}{2}j} = \frac{\dot{Q}X^{t}_{i-\frac{1}{2}j} + T^{t}_{ij}\,(k_{i-\frac{1}{2}j} + k_{ij})^{t}\left(\frac{A_x}{\Delta x}\right) + TWX^{t}_{i-\frac{1}{2}j}\,\frac{HCX_{i-\frac{1}{2}j}}{\Delta t}}{\frac{HCX}{\Delta t}^{t}_{i-\frac{1}{2}j} + (k_{i-\frac{1}{2}j} + k_{ij})\,\left(\frac{A_x}{\Delta x}\right)} \tag{17}$$

Similar expressions to equation (17) may be written for any other of the remaining cell faces. It should be noted that if (16) were not implicit in the heat conduction term, the time step would be restricted to

$$\Delta t \leqslant \frac{HCX_{i-\frac{1}{2}j}}{\frac{A_x}{\Delta x}\,(k_{i-\frac{1}{2}j} + k_{ij})} \tag{18}$$

which could be substantially more restrictive than that required by GEM. (A discussion of GEM stability conditions is given below). Since the computational efficiency of the algorithm is directly related to Δt, equation (18) could impose severe increases in computing time. This is especially important since practical problems frequently require hours of computer time. For this reason, equation (17) is a preferred form over the explicit alternatives. This situation offers a fine example of the reason why implicit schemes are preferred or essential compared to explicit schemes whether the model of the boundary conditions or the field conservation equations are concerned. Reference (2) has some additional details with regard to explicit modeling of the conservation equations.

Note that for $HCX_{i-1/2j}$ and $\dot{Q}X_{i-1/2j}$ equal to zero, equation (17) reduces to $TWX^{t+1}_{i-1/2j} = T^{t}_{ij}$ which is the boundary condition for an ideally insulated cell face. Where the biased differences for the convective terms, reference (2), are employed, the fundamental stability conditions for GEM are:

$$\frac{1}{\Delta t_1} \geqslant (1+\Phi)_{MAX}\left[2(A)\left(\frac{B+1}{\Delta x^2} + \frac{C+1}{\Delta y^2}\right) + \left(\frac{u}{\Delta x}, \frac{v}{\Delta y}\right)_{MAX}\right] \tag{19}$$

where

$A = (k/\rho cp)_{max}$

B = 0, 1, 2 for the x- direction, and

C = 0, 1, 2 for the y-direction
and

$$\frac{1}{\Delta t} \geqslant \left[2\left(\frac{\mu}{\rho}\right)_{MAX} \left(\frac{1}{\Delta x^2} + \frac{1}{\Delta y^2}\right) + \left(\frac{u}{\Delta x}, \frac{v}{\Delta y}\right)_{MAX} \right] \tag{20}$$

B and C depend upon the number of cell faces which have prescribed heat rates in equation (19). For "g" spikes,

$$\Delta t_3 \leqslant \sqrt{\frac{(\Delta x, \Delta y)_{MIN}}{2\beta}} \tag{21}$$

is used to insure that equations (19) and (20) are nearly satisfied during a "g" spike. For time integration accuracy, equation (21) is modified to read

$$\Delta t_4 = 0.03\sqrt{\frac{(\Delta x, \Delta y)}{\beta}} \tag{22}$$

In the calculations, equations (19) and (20) multiplied by about a factor of 1.5 in order to ensure small truncation errors in time while the "g" level is constant. Equations (19) and (20) are additionally superceded by the conditions
If $\dot{P}_g > 0$

then

$$\Delta t = \text{Min.}\ (\Delta t_1, \Delta t_2, 30) \tag{23a}$$

If $\Delta t > 1.3\ \Delta t^{t-1/2}$
then

$$\Delta t = 1.3\,\Delta t^{t-1/2} \tag{23b}$$

where

$\Delta t^{t-1/2}$ is the previous time step in seconds.

Equation (23a) has a thirty second value shown. It is used to minimize the truncation errors in time for pressurization strokes which are about four minutes long and which are simulated with coarse meshes.

Equation (23b) is used to limit the rate change of time step increases in order to promote time integration accuracy especially after "g" spikes or abrupt changes in the heating rate.

If there is a "g" spike, then

$$\Delta t = \text{Min}\ (\Delta t,\ \Delta t_4) \qquad (23c)$$

is imposed for ten time steps.

There are a number of integral relations which provide checks on the accuracy or correctness of the various local calculations and these are now discussed. The sum over the volume of the local heat conduction terms should equal the prescribed boundary heating rate. The sum over the volume of the local convection of energy or momentum terms should equal the boundary values. The sum of the cell densities divided by the total number of cells should equal the average density computed from the initial density and the time integral of the mass density loss due to fluid expulsion. The change in global fluid pressure should equal the potential pressure decay when the non-isothermal cryogen is adiabatically restored to an isothermal state. The adiabatic potential pressure decay is defined algebraically as

$$\Delta P|_{MAX} = \frac{\Phi_{\bar{\rho}}}{V_C} Q_{DA}\,(EF) \qquad (24)$$

$$Q_{DA} \equiv -\sum V\left[(\rho e)_{\bar{\rho},P_g} - (\rho e)_{ij}\right]$$

where $\Phi_{\bar{\rho}}$ is Φ at the average density and initial pressure, V is the cell volume, V_c is the container volume, (EF) is the elastic factor of the system, Q_{DA} is the adiabatic heat deficiency, $(\rho e)_{\bar{\rho},P_g}$ is the product of the average density and the specific internal energy which is evaluated at the average density and initial global pressure, and $(\rho e)_{ij}$ is the product of the cell density and specific internal energy. The validity of equation (24) is predicated upon the invariance of Φ over the pressure change $(\Delta P|_{max})$.

Single-phase helium, parahydrogen, nitrogen, and oxygen in the density region from about the solid density through the low gas density exhibit a very weak or no dependency of Φ upon P_g at any given density. Thus, equation (24) is a simple means of computing the adiabatic potential pressure decay. Where tank wall or heater tube, thermal capacitance is involved, and/or where boundary heating is prescribed, a pressure decay however abrupt may not be adiabatic. If the end state temperatures of the metal are known, the energy added to the system can be computed and for such a condition equation (24) may be modified as

$$\Delta P\Big|_{MAX} = \frac{\phi_{\bar{\rho}}\, Q_{DT}}{V_C}\,(EF)$$

$$Q_{DT} \equiv -\sum V\left[(\rho e)_{\bar{\rho},P_B} - (\rho e)_{ij}\right] - Q_B - Q_M \tag{25}$$

where Q_B is the total boundary heating and Q_M is the total energy from the metal for any short interval of time. Short here is taken to mean a time period in which the change of $\bar{\rho}$ is small enough so that the desired accuracy of equation (25) is maintained during the event.

If the GEM is properly coded, all of the integral relations are satisfied exactly except for the energy convection terms which have a small nonconservative error. There is also a time dependent truncation error. In spite of these errors, the integral equation (24) and (25) are very nearly satisfied during time dependent calculations which is shown in an example in the results section.

The 1/2 Box Model

In order to simulate a physical problem with the GEM certain boundary and initial conditions must be established. Figure (2a) shows a sketch of the cross section of a flight oxygen tank in the plane of the "g" vector which is taken to be perpendicular to the heater tube. Figure (2b) shows a sketch of the geometry used for the numerical model. The region shown has a depth dimension so that the walls of the model form a box. The left wall is assumed to be a plane of symmetry in order to reduce the total volume of region of interest by two. (This reduces the computer time by a factor of two). For this reason, the model is called the 1/2 box model. Only one half the values of the container volume, heat input, expulsion rate, the heater tube thermal capacitance (HTC), and plumbing volume are used in the calculations. The boundary conditions for the 1/2 box model are

1) freeslip left wall except where the heater element is

2) no-slip right, top, bottom and heater surfaces

3) uniform heat flux at the top, right and bottom wall for the heat leak simulation

4) insulated left wall except where the heater surface is

5) a flat plate heater surface midway up to the left wall, parallel to the left wall and extending the distance of the depth dimension

The initial conditions for the velocity and temperature fields, the global pressure, and the initial density, are chosen to be as consistent as possible with the conditions in the flight hardware for each simulation. All but the first two conditions are usually known accurately. Special measures must be taken to estimate these two initial conditions and these are discussed in the results section.

The Physical Description of the Apollo Single-Phase Oxygen System

Figure (3) shows a schematic of an Apollo single-phase oxygen storage and supply system. The oxygen storage container is essentially a thin wall pressure vessel covered by a super insulation system. The container is vented and filled through pipes which are imbedded inside the super insulation for some distance before penetrating either the inner or outer container shells. On leaving the container, these pipes pass to the space craft surface. They are only active during the preflight oxygen loading procedures and then are sealed off shortly before the flight. A third line is attached to the tank and supplies oxygen to the fuel cell regulator and the surge tank. The function of the surge tank is to separate the crew compartment from the low temperature cryogen and provide a large source of ambient gas ready for use at any time.

Inside the oxygen container are mounted two perforated tubes. One tube is a quantity gauge. The other tube is an extended surface for heat transfer. Several electrical resistance heater elements are helically wound around and welded to the heater tube. The control of the electrical power to the heating elements is accomplished by switches which are activated by fluid pressure. If the pressure falls below about 860 psia, the electrical power is engaged. If the pressure rises above about 900 psia, the electrical power is disengaged. Prior to Apollo 14, two fans were installed in the heater tube, one in each end. When operating, these fans draw oxygen through holes in the center of the heater tube assembly and ejected it radially at the ends, thereby stimulating circulating of the bulk of the stored cryogen. These fluid motions are potent enough to eliminate significant fluid temperature variations which are induced by heat transfer. As a result, the pressure history of the stored cryogen may be predicted by equations (A10) and A11). If the fans are not operated, the detail fluid motions in the container oxygen must be modelled in order to predict the pressure history. Successful modeling however, depends upon the prediction of the time variant "g" level, expulsion rate, and heat input. The method of determining each of these is now presented.

Reduction of Apollo Flight Data

It is the purpose of this discussion to provide some understanding of the considerations which are made in determining the "g" level, oxygen flow rate, and heat input histories as a function of the average stored oxygen density.

Figure (4a) shows a sketch of the space craft in relation to the roll, pitch and yaw axis and the earth. For simplicity the moon is not shown. Also shown in Figure (4b) is a cross section of the space craft perpendicular to the roll axis and through the two Apollo 12 oxygen tanks. The heater tube in each tank is parallel to the roll axis. The "g" level and direction is defined if the inertial space acceleration vector can be evaluated. The method of rigid body dynamics is used to calculate the history of this vector. The angular rotation rates are taken directly from the Digital Auto Pilot (DAP) data. The angular acceleration is obtained by numerical differentiation of the rotation rates. When DAP data are not available, rotation and acceleration vectors are obtained by successive differentiation of the gyroscopic gimbal angles. The calculations showed that the accelerations induced by the solar pressure and the solar wind are orders of magnitude less than the accelerations induced by the thrust of nozzles and rotations of the space craft about the three axes. (The Coriolis force is sometimes the same order of magnitude as the centripetal acceleration but for simplicity this component is neglected for the 1/2 box model simulation. Variations of the acceleration magnitude with position in the stored fluid is also neglected for simplicity in the 1/2 box model simulation.)

There are five predominate types of flight modes which each have a typical "g" level and direction. They include

1) engine burns

2) attitude control maneuvers

3) passive thermal control (PTC)

4) attitude hold in translunar or transearth orbit

5) attitude hold in lunar orbit

The acceleration vector is parallel to the heater tube for type 1) operation. For the last three types of operation, the acceleration vector is predominantly perpendicular to the heater tube. Typical "g" levels in the last three are respectively 3×10^{-6} "g", 7×10^{-8} "g", and 5×10^{-7} "g".

Abrupt increases in "g" level ("g" spikes) can accompany the use of the attitude control system. Then these "g" directions are not necessarily perpendicular or parallel to the heater tube.

The certainty with which the "g" level is known is estimated to be better than a factor of 2 at 7×10^{-8} "g" and better than a factor of 1.2 at 3×10^{-6} "g".

The energy input to the oxygen tank is composed of the heater power and insulation heat leak. The latter never exceeds about ten percent of the former. The estimation of the heat leak is no more accurate than the estimate of the oxygen flow rate but because it is a small fraction of the total energy input and because the heater power is known to about two percent, the overall energy input is believed to be known to better than three percent.

The average cryogen density is obtained from the quantity gauge and time integrals of the expulsion rate, initial density, and container volume. The quantity is believed to be known to about two percent.

The oxygen pressure is measured by a sensor whose output is digitized in four psi intervals at the rate of about one per second. The absolute value of pressure is known to about 20 psi at 900 psia. The differences in pressure are known to better than about four psi out of forty. A similar situation exists in the absolute pressure measurement of the surge tank.

If the difference of the container and surge tank pressure depended only on the difference in these absolute pressure measurements, considerable error would be possible. However, with normal crew compartment oxygen consumption rates and no use of surge tank gas for other purposes, the surge tank pressure must be the mean of the limit cycle values of the container.

Thus a reference value of pressure is known and the surge tank pressure gauge can be scaled accordingly. The flow through the restrictor depends upon the pressure differential between the container and the surge tank. Since there is a flow meter between the crew compartment and the surge tank, a flow calibration of the restrictor is possible. The only time that the measurement of the flow to the surge tank requires the use of the restrictor calculation is when the surge tank pressure is different than the mean of the limit cycle values for the container. The estimate of the flow measurement accuracy is about 30 percent for the restrictor calculations. The mass flow rate to the fuel cells is known to about three percent which frequently is over half of the flow demand. The precision of the flow measurements then can be anything between three and thirty percent accurate depending upon the steadiness of the pressure in the surge tank and the crew compartment consumption rate.

The only other way to predict the average flow to the surge tank is with equations (A10) and (A11). The heat input, cryogen density, and changes in cryogen pressure can be used to estimate the average flow rate to the surge tank. However this procedure only is adequate when the stored cryogen is very recently stirred by the fans so that it is spatially isothermal.

It is hoped that the previous comments give some idea of the difficulty in obtaining accurate data which may be used to make predictions with the 1/2 box model. In spite of this situation, the predicted oxygen tank pressure history agrees very favorably with the flight data. Because of the data uncertainty in some cases, good agreement may just be fortuitous. Some reduction of the ambiguity can be made by parametrically varying various of the data which are most suspect (e.g., "g" level and flow rate). The trends of such analysis can be used to gain confidence in the results and thus reduce the uncertainty.

The Comparison of Predictions and Flight Data

Two sets of data from the Apollo 12 flight have been reduced and summarized. Predictions for these cases have been made with the 1/2 box model. The comparisons are presented after some introductory discussion.

$\dot{P}_s/\dot{P}_e$ is defined as the ratio of the time derivative of the global pressure in cryogen which has a nonuniform and uniform time dependent temperature field respectively. For an ideal gas in which the compressibility and specific heats are constant, $\dot{P}_s/\dot{P}_e$ is unity whether or not temperature variations exist. In nonisothermal cryogen, at a density of about twice the critical, $\dot{P}_s/\dot{P}_e$ can approach a maximum value of about 16. As the density is reduced, $\dot{P}_s/\dot{P}_e$ approaches a value of unity. (Note that if $\dot{P}_s/\dot{P}_e$ is not unity, $\Delta\dot{P}|_{max}$ can acquire nonzero values.) The actual value that $\dot{P}_s/\dot{P}_e$ acquires in finite difference calculations depends upon the resolution of the thermal boundary layer. With increasing acceleration level, natural convective mass rates increase near the heater surface and the heater surface temperature decreases. $\dot{P}_s/\dot{P}_e$ tends to unity for such heater temperature variation irrespective of the density of the cryogen. Coarse grid calculations of a thermal boundary layer with the 1/2 box model provide less boundary layer temperature variation and thus $\dot{P}_s/\dot{P}_e$ tends to be less than if fine grid calculations are used. Accordingly, prediction of the pressure history is very sensitive to thermal boundary layer resolution where $\dot{P}_s/\dot{P}_e$ potentially can deviate from unity which is the situation near and above the critical density.

At cryogen densities below and above the critical density, the accuracy of the predicted pressure history is sensitive to thermal boundary layer resolution but for another reason. The heater tube has significant thermal capacitance. The coarse grid calculations always predict excessive heater surface temperatures and as a result of the heater thermal capacitance excessively long pressurization cycles are predicted. Convergence studies are employed to estimate the effects of coarse grid calculations. This means that the same problem is repeated for a number of different grid sizes.

For example, a 10 x 10, 20 x 10, 30 x 10, 40 x 10, 60 x 10, 80 x 10, 20 x 20 (the first and second integers are the number of computational cells in the x- and y- directions respectively), etc., grids may be used to predict a problem. By appropriately plotting the data, the convergence characteristics of some parameter of interest can be determined. If this procedure is used in a careful way beginning with the coarse grids first, estimates can be made as to how fine the grid must be to get the desired accuracy. This will be illustrated later.

The potential pressure decay ($\Delta P|_{max}$) may be defined as the amount the global pressure should decay when a cryogen is adiabatically restored to an isothermal state during which the fluid expulsion rate is zero. Truncation and conservation of energy errors can be delineated if the time integral of $\dot{P}_g$ is compared to the difference in the state of $\Delta P|_{max}$ for the boundary conditions of no boundary heating, no fluid expulsion, and no heater thermal capacitance. To illustrate such a comparison, two problems have been chosen and they differ only in the grid sizes which are a 6 x 6 and 12 x 12 and in the time step used after the "g" spike is initiated. The box has the dimensions of 2 x 2 x 1.187 feet for the height, width, and depth respectively. The initial density is about twice the critical density. Figure (5) shows the history of P_g and $\Delta P|_{max}$ of the 12 x 12 grid problem in which the fluid expulsion, wall heating, heater input, and acceleration level are nonzero for a period of time. The wall heating and heater input are chosen in order to generate an oscillating pressure history. The heater tube thermal capacitance is zero during the entire duration of the problem. The "g" level is chosen at 2×10^{-8} "g" so that the buoyantly driven mass rates are of the same order as the expulsion rate. At some later time, the "g" level is increased to 2×10^{-3} "g" in a time step and at the same time the expulsion rate and the boundary heating are set to zero. The "g" level increase causes a substantial increase in the buoyantly driven fluid velocity. As a result, the high energy fluid which is concentrated in a glob near the heater surface is rapidly stretched which substantially enlarges it's surface area. This in turn enhances the heat conduction and results in a rapid decrease in fluid temperature differences. The sharp reduction in nonuniform temperature field causes the global pressure to sharply decay. The pressure decay rate is an order of magnitude sharper than that which would have occurred had the "g" level been unchanged during the course of the problem. The time step is 30 seconds prior to the "g" spike and it is reduced by

$$\Delta t = 0.4 \sqrt{\frac{(\Delta x, \Delta y)_{MIN}}{g}}$$

when the "g" spike occurs which yields a $\Delta t = 0.6977$ seconds and $\Delta t = 0.4933$ seconds for the respective problems. The change in P_g of 41.0 and 49.3 corresponds to a change in $\Delta P|_{max}$ of 42.5 and 49.6 respectively for the 6 x 6 and 12 x 12 grid problems. This yields respective differences in the actual and ideal decay changes of 2.8 and 0.3 psi for the respective problems. The reduction in the error is entirely due to the time step reduction. Further reduction in the time step after the "g" spike will not significantly improve the result. This is due to the fact that there is a small time dependent nonconservative error in the energy convection terms. This error can be virtually eliminated in the manner outlined in reference (2).

Finally, the GEM has one other time related truncation error which for the problems considered is trivial. The algorithm exhibits a slight damping of kinetic energy and this error may be eliminated with a nontrivial increase in computer time. This consideration will be left to a future paper.

As a rule, the truncation errors in time are well controlled as the grid is refined. The significant errors for fine grid calculations reduce to the definition of the initial and boundary conditions. As has been mentioned previously the mass expulsion rate is probably the most inexactly known quantity. There are some other significant ones which are now discussed.

The elasticity factor (EF) for which a derivation is provided in the Appendix can be evaluated precisely except for term ($\rho_p V_p n / \rho_c V_c P$) which accounts for the external volume effect. Since there is no temperature sensor anywhere on the external plumbing, estimates of ρ_p and n (which is the reciprocal of the polytropic coefficient) must be made. (It is believed that ρ_p should be about 5 lb_m/ft^3 and n about 1.0. In this case, the magnitude of the effect of the external plumbing upon the elasticity factor is nearly negligible.) The elasticity factor is about one half at the high densities and rapidly approaches unity as the density is reduced to the critical value. It is unity for densities less than the critical value as well. Another difficulty in using the 1/2 box model arises in choosing the initial conditions for a given problem. As a rule, a uniform initial temperature field with a zero velocity field are the chosen initial conditions. The problems selected for analysis always have a fan cycle prior. Because the pressure response of the system appears to satisfy equations (A10) and (A11) of the Appendix, the isothermal assumptions appear to be warranted. But the zero velocity field prescription is certainly wrong except after the fluid motions from the fan cycle have decayed below those generated by the buoyant forces. Estimates of this decay time are made with fine grid calculations in which the initial field values of velocity are large. It has been found that less than about two hours are required to meet this condition at all fluid densities.

The treatment of the heater tube as a vertical flat plate in the 1/2 box model is believed to be wrong in one respect. Since the heater tube has only a few square inches of hole area through which high and low density fluid may flow, at low enough "g" levels some heated fluid can be trapped inside. This has the net effect of reducing the effective surface area for heat transfer. The "g" level at which the effective surface area is significantly reduced is at about 10^{-7} "g" or less.

The extremes of the surface area possible are

1) the total of the outside and the inside of the heater tube (about 1.1 ft^2)

2) the exterior of the portion of the tube which is wrapped with the heating elements (about 0.475 ft^2)

For the calculations presented, the value of 0.95 ft^2 is used and is twice the value of 2). This area certainly is a bit too large after some time period because of the restraint which the tube holes impose on the buoyantly driven flow and because the heater tube is not exactly isothermal along its length. (Evaluation of these two effects is currently under study.)

With these various reservations in mind, the two problems are now considered.

Two problems from Apollo 12 flight data were chosen for analysis because initial and boundary conditions could be reasonably assessed and because these problems exhibit the peculiar effects that the nonisothermal cryogen has upon the pressure history.

The 1/2 box model is assumed to be one foot wide, two feet high, and the depth is computed so that the volume is that of 1/2 of the oxygen tank which is 4.75 cubic feet.

The first flight problem of interest involves the prediction of the time required to raise the oxygen pressure about 33.5 psi in twelve minutes and forty seconds. The fan cycle occurred about eight hours prior to the time of interest. The pressure decayed steadily and the expulsion rate history could be found from equations (A10) and (A11). These values agreed well with those predicted from crew compartment and fuel cell flows. For this reason and since only heat leak was involved during the decay cycle, the system was believed to be essentially isothermal when the heater was activated, which is the beginning of the problem. The eight hour period was more than enough time for the fluid velocity field to decay adequately so that the zero field velocity prescription could be used at the beginning of the prediction with the 1/2 box model. The elasticity factor is about 0.97 so that the question of how to evaluate the external volume effect is trivial. Figure (6) shows the results of the 1/2 box model predictions as a function of the grid size with and without the heat tube capacitance of 0.07 BTU per degree Rankine. It may be noted that the 60 x 10 and the 80 x 10 grid results are nearly identical. Comparison of the velocity profiles show that the boundary layer is well resolved by the 80 x 10 grid.

It is curious that the resolution is only weakly dependent upon the number of cells in the y- direction. Figure (7) shows the asymtotic estimate of the 1/2 box model predictions. Figure (8) shows these asymtotic values replotted. The agreement of the prediction and the flight data is within about two percent which is better than would be expected in view of the probable errors of the various measurements. There are some interesting things to note about the predictions.

The cryogenic oxygen density is slightly less than the critical density. The average rate change of pressure is about 15 percent larger than that which would occur for isothermal cryogen. ($\dot{P}_s/\dot{P}_e$ is about 1.15 average value. As a result, the adiabatic potential pressure decay acquires a value of about 4 psi during the pressurization stroke.) Also, the heater tube thermal capacitance is shown to be a significant factor in the length of the pressurization stroke. Thus without accounting for the transient heater tube and thermal boundary layer interaction, the flight data could not well be predicted.

The 1/2 box model is used to simulate this problem again but it differs from that shown in Figure (6) only in the "g" level which is set at 4 x 10^{-7} "g". This lower "g" level results in lower buoyantly driven mass rates by the heater surface which results in a larger asymptotic heater surface temperature. The asymptotic temperature differences between the heater surface and the bulk fluid is 230° R and 340° R for the problems at 2×10^{-6} "g" and 4×10^{-7} "g" respectively. Had the $\dot{P}_s/\dot{P}_e$ ratio remained the same for each of these problems, the latter problem would have had a pressurization stroke about a minute longer than that found for the former problem. This time increase is due entirely to the increased energy requirement of the heater tube. However, since the average value of $\dot{P}_s/\dot{P}_e$ for the latter problem is 1.23, the time increase caused by the heater tube capacitance effect is almost exactly offset and the resultant stroke length is only a few seconds longer. Since the reduction of the heater surface area to about a value of 0.7 ft^2 in the former problem would result in about the same asymptotic heater surface temperature, the pressurization stroke length would be almost exactly the same as that found in the latter problem. But since the latter and former problems yield almost identical stroke lengths, this problem is not suited to determining with precision the effective heater tube area. After examining the various errors and their effect on the results of the simulation, it is concluded that the heat tube thermal capacitance and the differential pressure measurement during the stroke are the primary parameters upon which the accuracy of the simulation depends. Since the agreement is excellent between the flight data and the prediction, it is concluded that whatever errors there are in these two parameters, they must be compensatory.

The second flight problem of interest examined in detail involves a high density problem in which the initial density is about twice the critical density. The elasticity factor is between 0.58 and 0.35 depending upon how the external volume effect is accounted for. The latter value assumes that the entire external plumbing volume is filled with cryogen which is at the density of the average of that of the stored fluid. From thermal studies of this plumbing system, such a condition is unlikely and it is probably the case that the entire volume contains near ambient oxygen. Since the process in the plumbing during the pressure oscillations is probably isothermal, n is probably unity. With these assumptions the elastic factor is about 0.55 which means that the contribution from the external volume is only about five percent of the total.

The flow rate is time dependent and is modeled with the expression

$$\dot{m} = (0.755 + A + B)$$

where

$A = 0.1\ \mathrm{lb_m/hr}$ when the heater is on

$A = 0\ \mathrm{lb_m/hr}$ when the heater is off

$B = 0.17\ (P_g - P_{surge})^{0.488}$ if $(P_g - P_{surge}) > 0$

$B = 0$ if $(P_g - P_{surge}) \leq 0$

where B is the flow through the orifice which is upstream of the surge tank. B is zero if the pressure difference $(P_g - P_{surge})$ is negative because a check valve in the line prevents reverse flow. P_{surge} is the surge tank pressure. The "g" level is time dependent and the values used in the simulation are shown in Figures (9, 10, and 11). Actually there are many more "g" spikes than indicated but these were deemed insignificant compared to those shown. Figures (9, 10, and 11) also show the end points of the pressure strokes for the flight data. The fan cycle occurred at about a ground elapse time (GET) of 4 hours and 27 minutes so the residual velocities should have been gone at the most by the time GET = 6:27. However examination of the length of the strokes show that within about 40 minutes the predominate effects of the fan cycle had dissipated. Thus the stroke length is then relatively fixed and is modified predominantly by the "g" spikes. Note how sharp the pressure change is with the "g" spikes but that no substantial change in fluid pressure occurs until the "g" level increased to 10^{-3} "g". A dramatic decay of fluid pressure then ensues and an enlarged view of this event is shown in

Figure (11). The fans are turned on before the course of the "g" spike induced pressure decay stroke is run. It appears however from the slope of the decay curve prior to the fan cycle, that virtually all of the potential for pressure decay would have been absorbed. Thus properly interspersed "g" spikes of sufficient magnitude could be used to provide the same function as the fans, that of stirring the stored cryogen so that it's temperature field is for practical purposes isothermal.

Attempts to simulate the pressure history of this problem have begun but are not yet complete. As a consequence, only preliminary results from 1/2 box model studies are presented. Between GET = 4:29 and 4:41, the decay cycle as noted before, involves a cryogen whose temperature field is isothermal, but time dependent. The end points of this pressure cycle have been predicted to better than twenty seconds in eleven minutes with the 1/2 box model. The same result is obtained with the equations (A10 and A11). So that the remainder of the four hour simulation could be put on one plot, this decay stroke is omitted from any display. Figure (12) shows a pressure trace for a 60 x 10 grid in which the previously given flow rate equation was not employed. (The pressure trace for the included flow equation could not be prepared in time for this publication. With some exceptions the average flows are about the same and for discussion purposes it will serve to illustrate the important features of the simulation.) A convergence study shows that the 60 x 10 grid almost adequately resolves the thermal boundary layer during the periods between GET = 4:41 and 5:53 and between 6:40 and 8:33. During, and some time after the "g" spikes, the thermal boundary layer is not well resolved. It is estimated that about at least a 150 x 40 grid would be required during this period. (With existing computers, this degree of resolution is impractical. However, a variable mesh grid system is being developed which hopefully will permit resolution which is more nearly adequate.)

It should be noted that the length of the pressurization stroke in Figure (12) is short sooner than shown in Figure

(6). This is believed to be due to the difference in the initial conditions which has been already noted. At GET 5:41, the stroke lengths are about the same and this may be noted by examining Figure (13) which shows the plot of the pressurization stroke length versus the number of grid points. (The flight data is also shown.). The asymptotic value is believed to be almost attained with the 80 x 10 grid. (The variable mesh program may provide the tool necessary for the practical verification of this belief.) If so, the agreement between the simulation and the flight data is good.

The stroke length of the pressurization cycle shown in Figure (13) is about three times less than that predicted for a cryogen whose temperatire field is isothermal, but time dependent. If the heater tube thermal capacitance is zero in the 1/2 box model, the stroke length is about fifteen times less than that predicted for a cryogen whose temperature field is isothermal, but time dependent. The elasticity factor and expulsion mass rate inaccuracies can, at most, only affect the pressurization stroke length by about a factor of two. Thus accurate simulation of the transient thermal boundary layer and heater tube temperature are the most important considerations in predicting the pressurization stroke length.

With regard to the simulation of the "g" spikes, it may be noted that there are several qualitative and quantitative resemblences with the flight data. This is true of several of the small "g" spikes and the large "g" spike event which occurs at the end of the simulation. This latter event has been enlarged and displayed in Figure (14). The magnitude of the pressure decay is substantially attenuated by the heat which is derived from the rapid cooling of the heater tube. (Convergence studies are currently being performed for this "g" spike event in order to attempt to gain quantitative data on the grid sizes required for adequate resolution.) The obvious disagreements between the flight data and the simulation are believed to be due to

1) since simulated strokes are not in phase with flight

"g" data, the "g" spikes occur at different relative positions in the stroke than is shown for the flight data

2) the geometry of the heater tube probably plays some part

3) the grid is certainly too coarse

Further studies of this problem will hopefully provide the information which is necessary to delineate the importance of each of these considerations.

In spite of the preliminary nature of the data thus far acquired for this flight problem, the results to date are very encouraging, enough so that further work is warranted.

Conclusions

The methodology of the General Elliptic Method for the simulation of time dependent single-phase cryogenic flow has been presented. A brief description of the Apollo 12 single-phase oxygen storage system has been presented along with some discussion of the elements which are considered for the reduction of flight data. The 1/2 box model in which the boundary conditions used to simulate the cryogenic oxygen flow processes of the Apollo 12 oxygen tank has been presented. Mention has been made of some of the difficulties which have arisen in obtaining accurate quanitative data from the 1/2 box model and the flight data. In spite of these difficulties, the comparisons of the predictions and the flight data are shown to be good.

It is recommended that further application of the 1/2 box model be made to predict flight system response as the flight data becomes available. Assessment of the deficiencies and capabilities of the 1/2 box model would then be possible for a wide range of flight conditions. If the overall results are reasonably favorable, prediction of the oxygen tank pressure history for future missions could then be undertaken with a confidence well beyond that previously available.

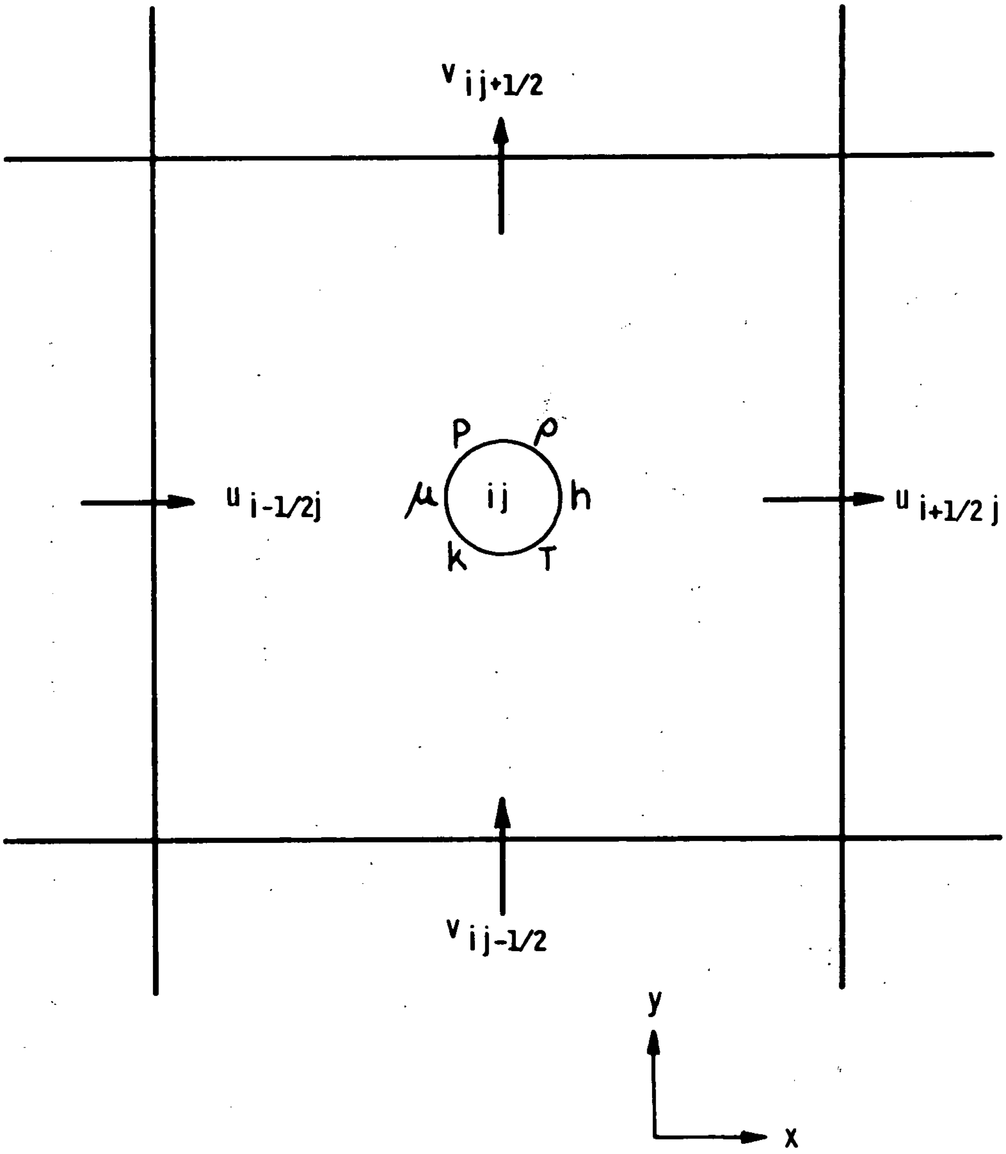

Figure 1. TYPICAL CROSS SECTION OF A COMPUTATIONAL CELL

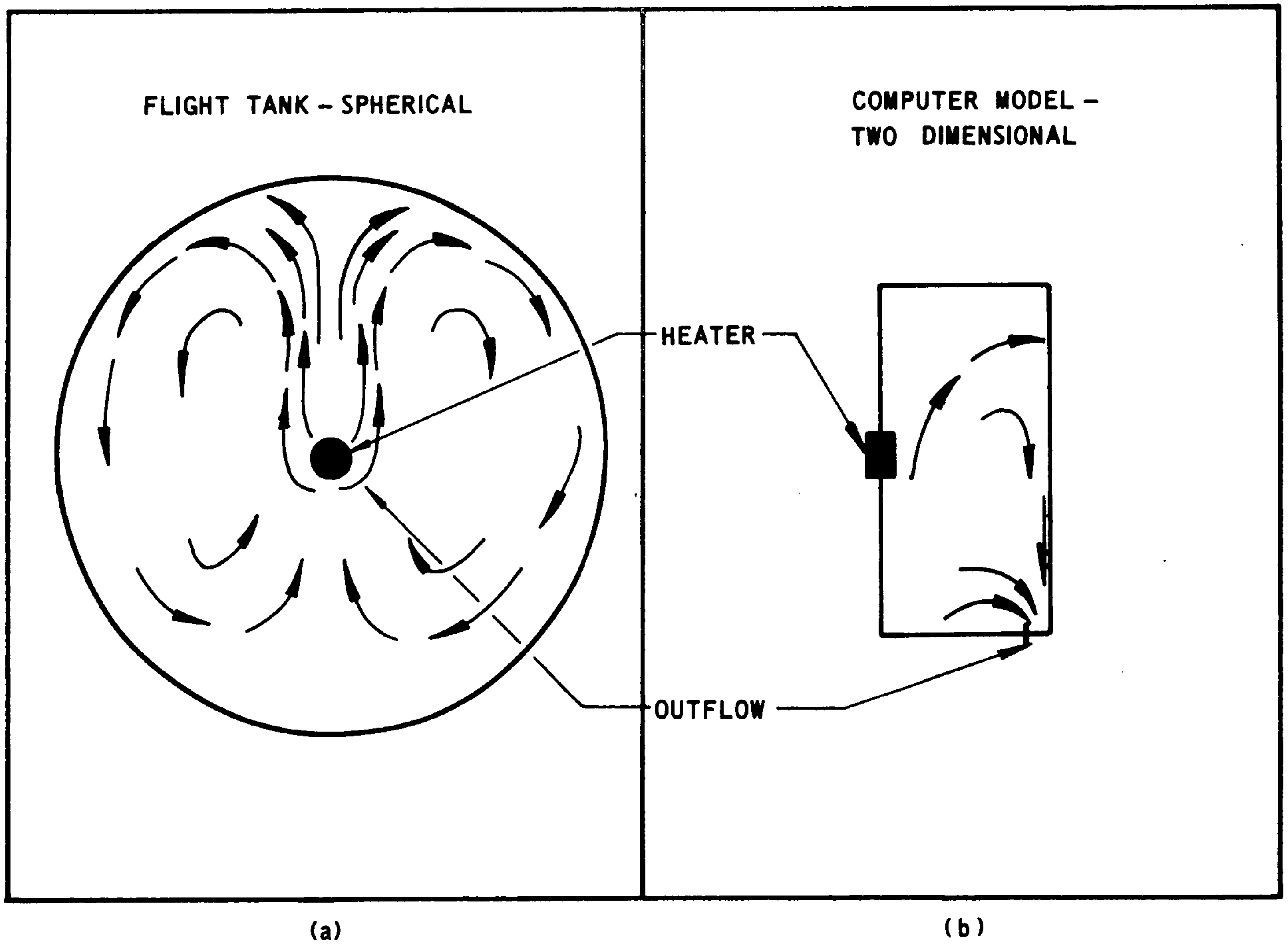

Figure 2. ANALYTICAL APPROACH

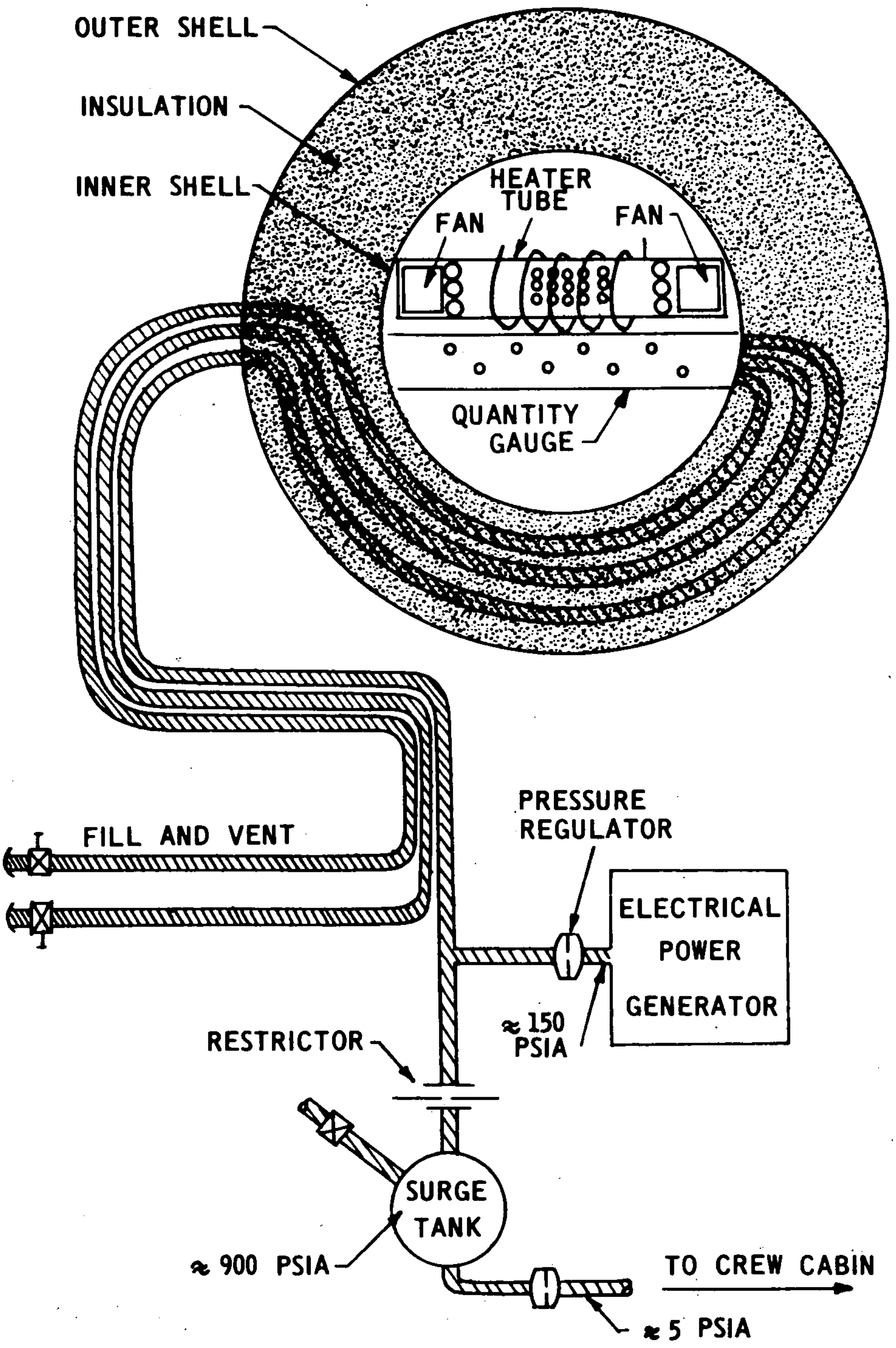

Figure 3. APOLLO 12 OXYGEN TANK AND SUPPLY SYSTEM SCHEMATIC

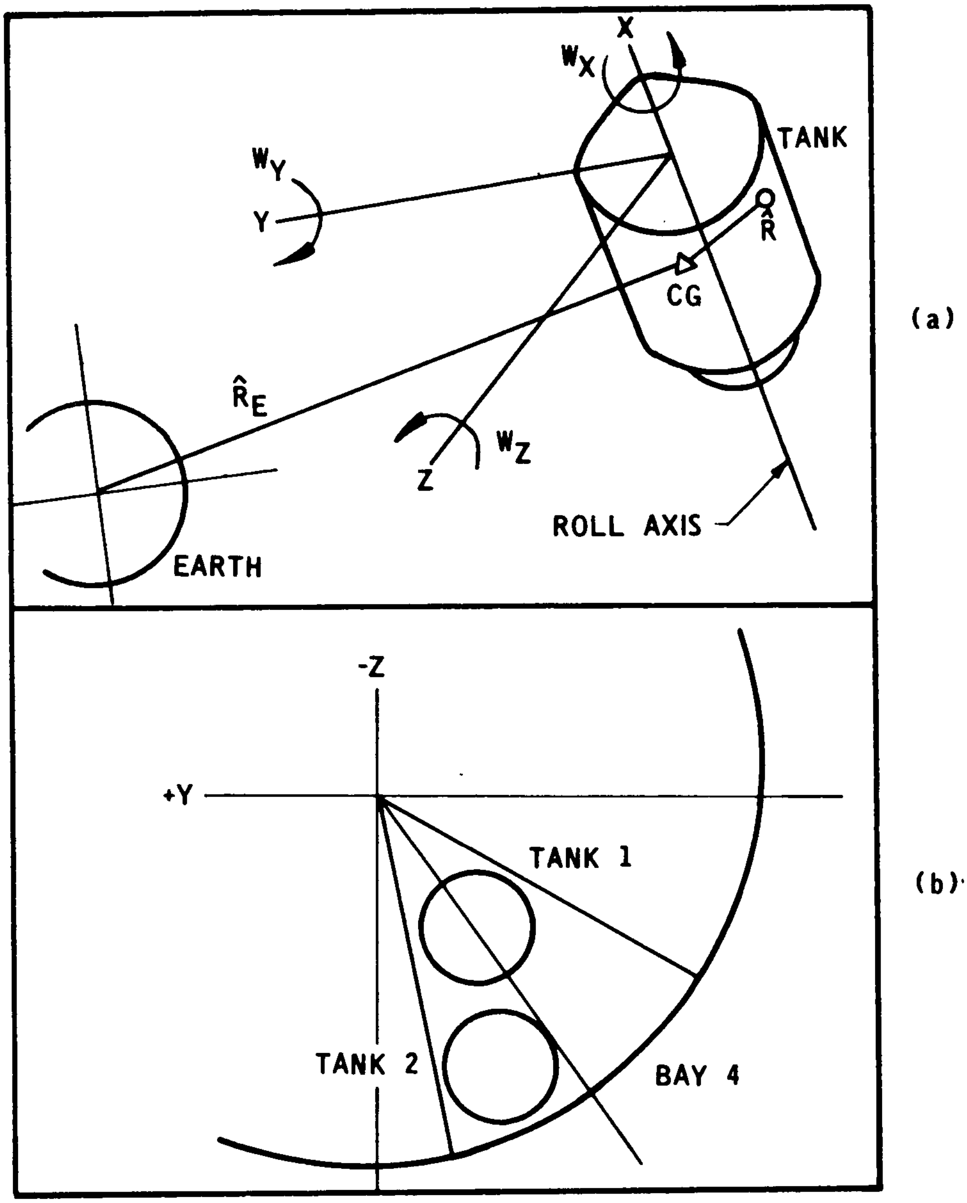

ACCELERATION DUE TO ROTATION:

$$A_{ROT} = (\dot{\hat{W}} \times \hat{R}) + (\hat{W} \times \hat{W} \times \hat{R})$$

ACCELERATION DUE TO GRAVITY GRADIENT:

$$A_{GG} = \frac{-2M_E G \; \hat{R}_E \cdot \hat{R}}{\hat{R}_E{}^4} \; \frac{\hat{R}_E}{|\hat{R}_E|} \qquad A_{TOTAL} = A_{ROT} + A_{GG}$$

SOLAR PRESSURE AND SOLAR WIND ARE NEGLECTED

Figure 4. O_2 TANK ACCELERATIONS

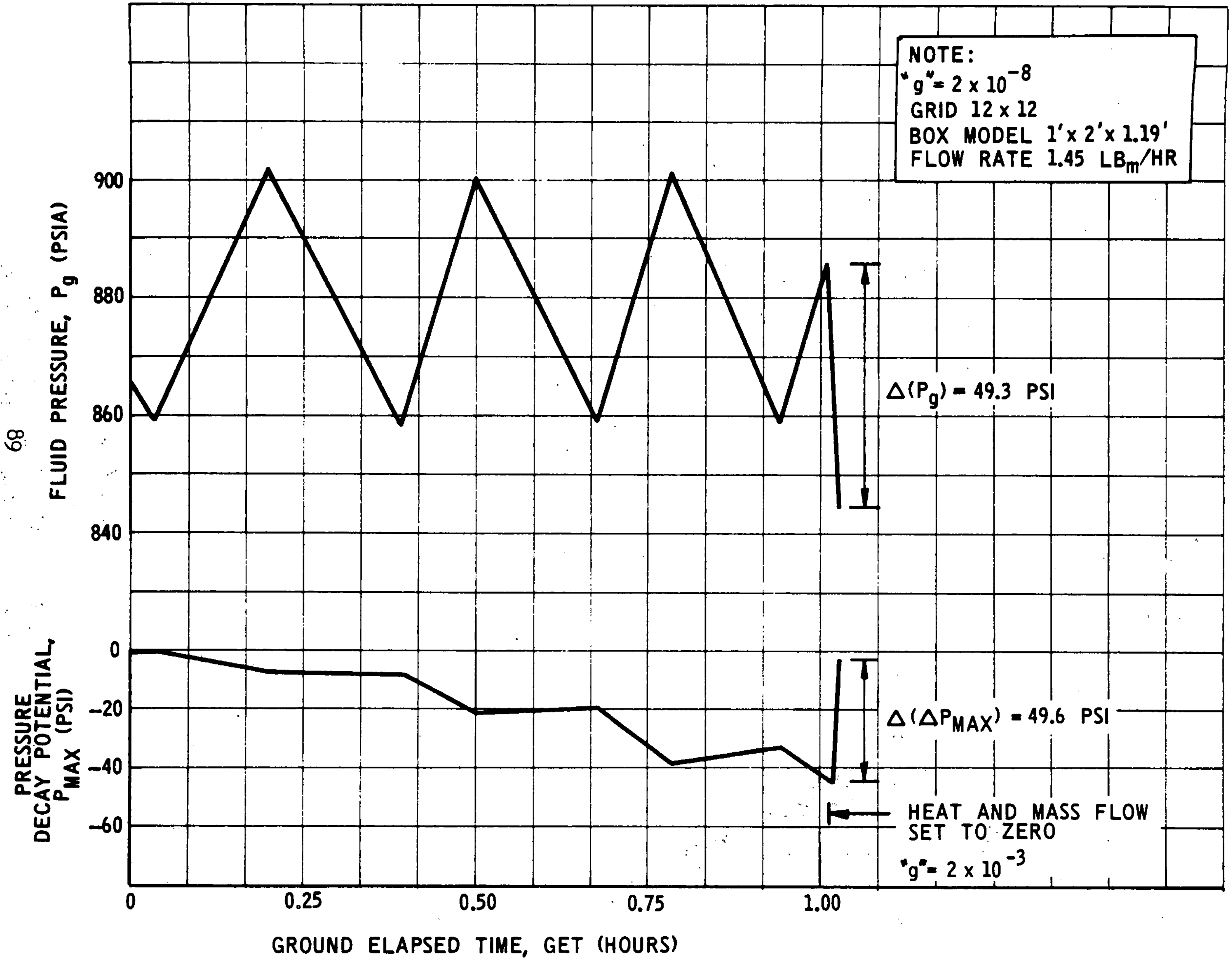

Figure 5. "g" SPIKE SIMULATION

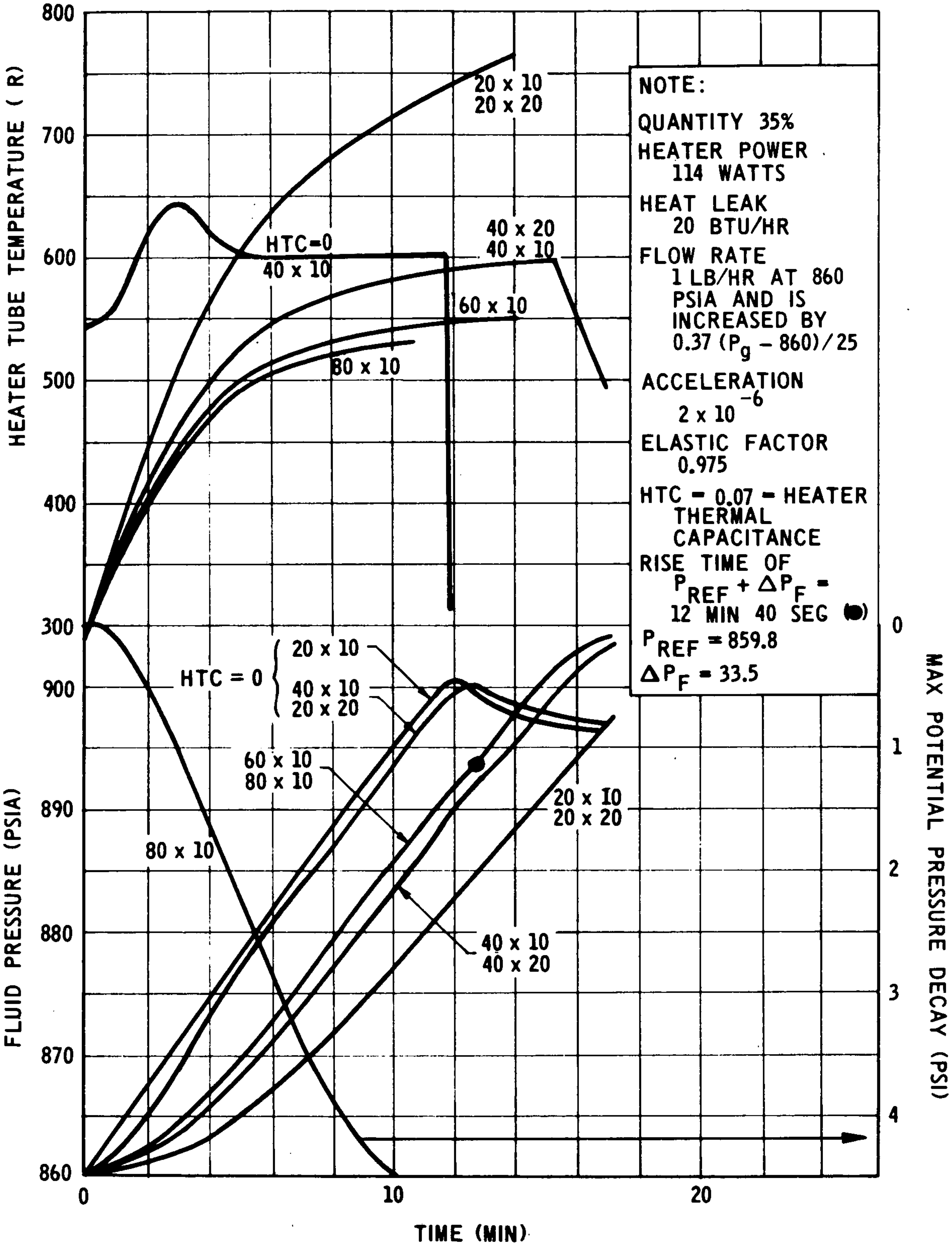

Figure 6. APOLLO 12 OXYGEN TANK No. 1
PASSIVE THERMAL CONTROL MODE

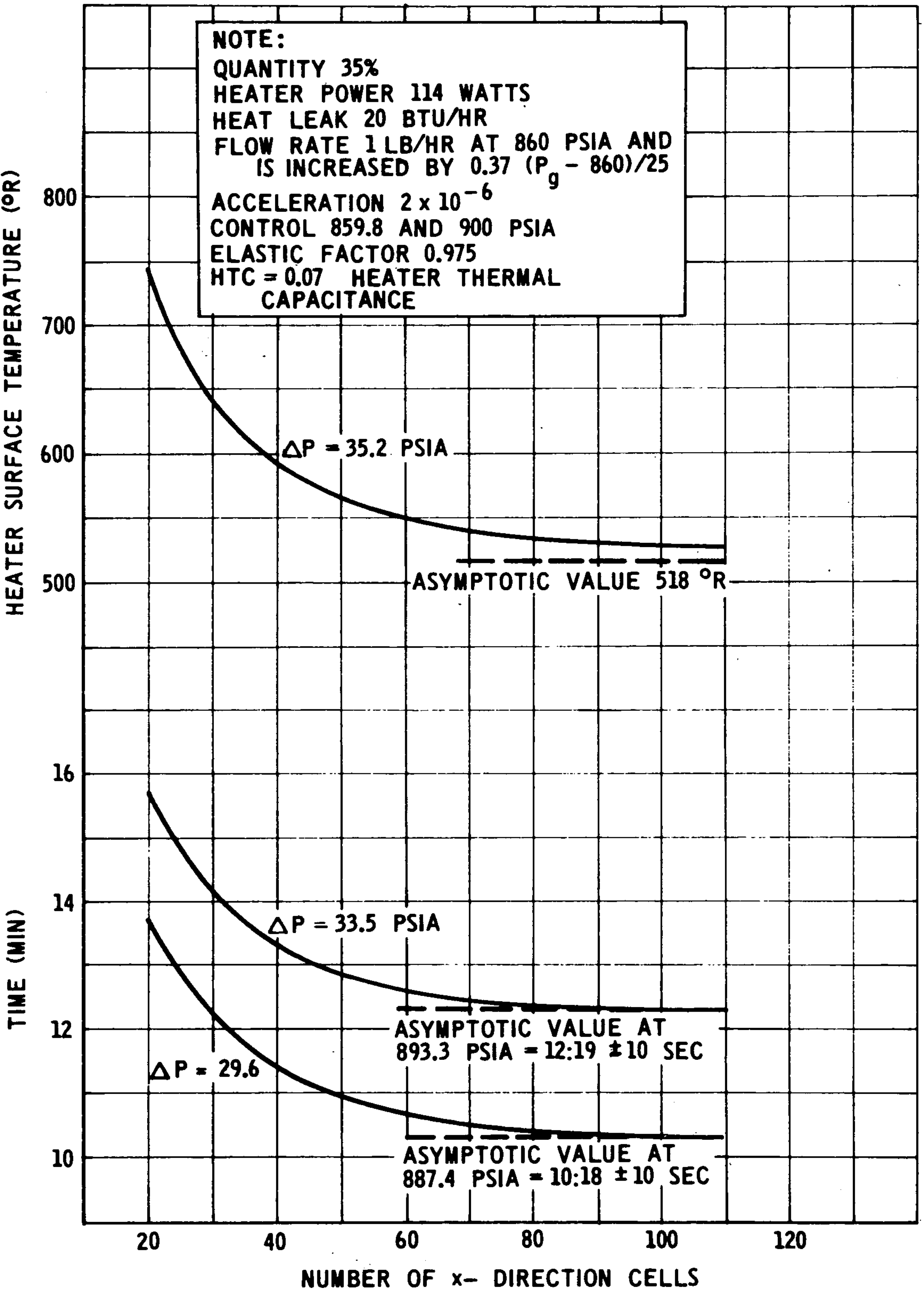

Figure 7. APOLLO 12 OXYGEN TANK No. 1
PASSIVE THERMAL CONTROL MODE

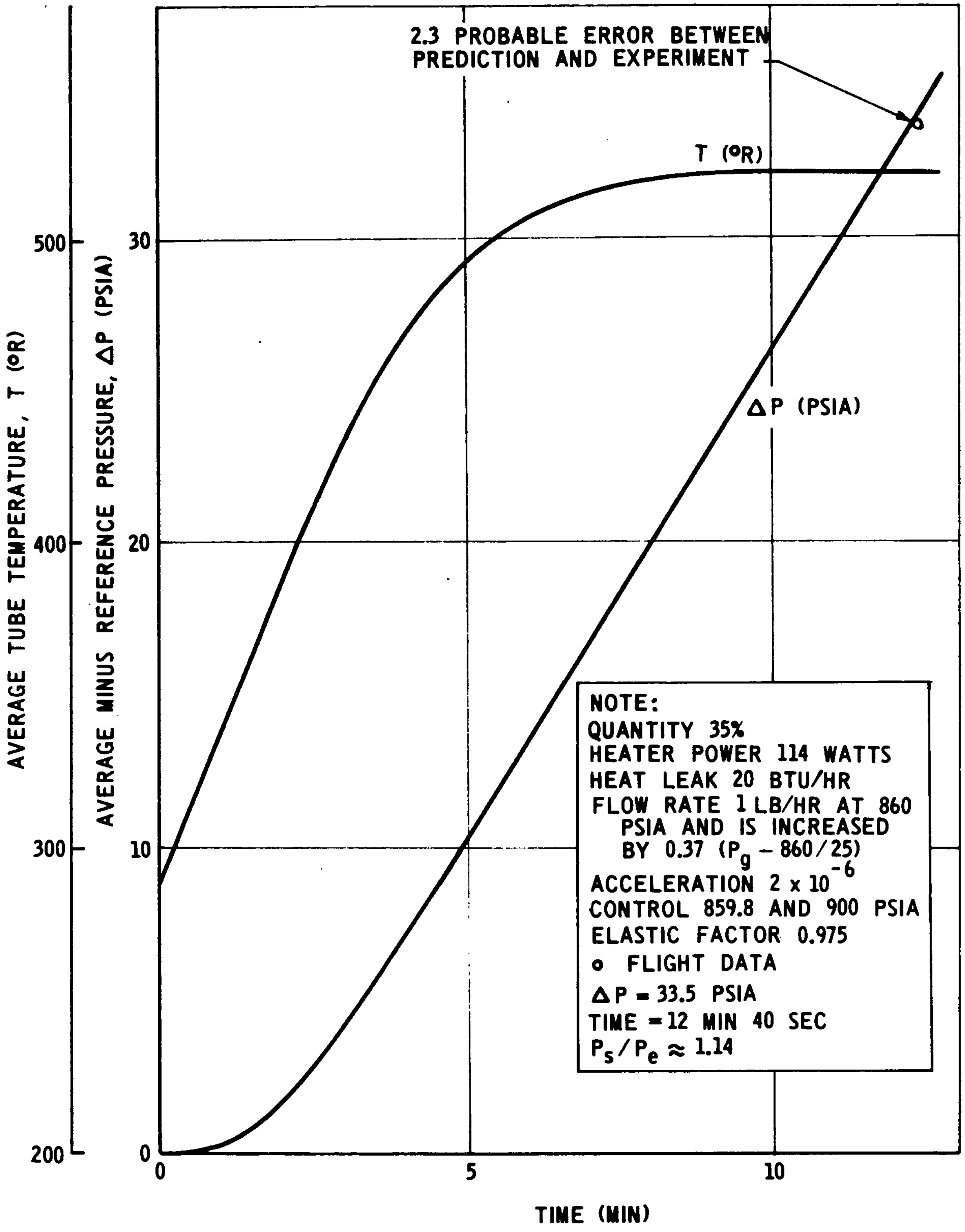

Figure 8. APOLLO 12 OXYGEN TANK No. 1
PASSIVE THERMAL CONTROL MODE

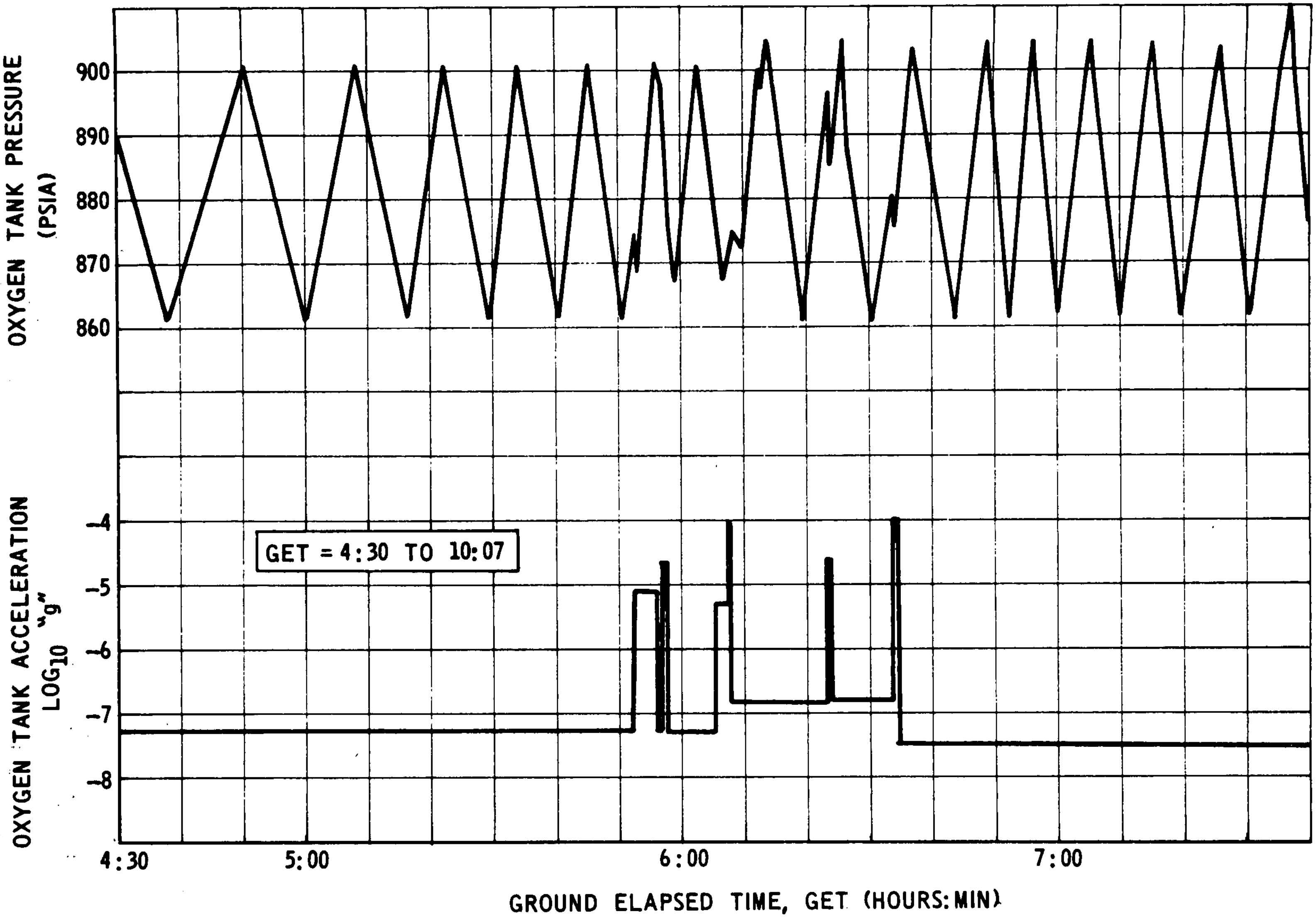

Figure 9. APOLLO 12 FLIGHT DATA – ATTITUDE HOLD

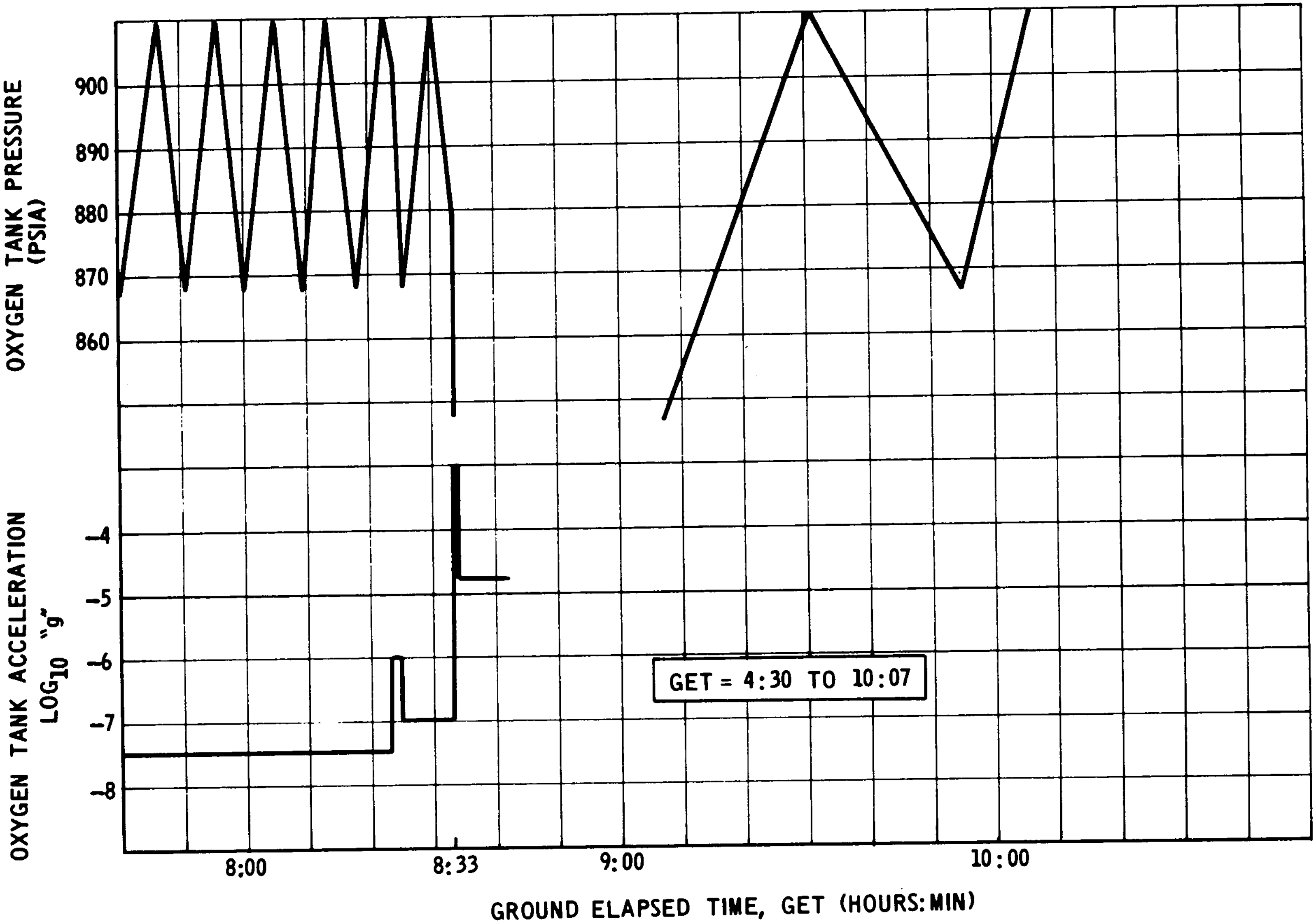

Figure 10. APOLLO 12 FLIGHT DATA – ATTITUDE HOLD

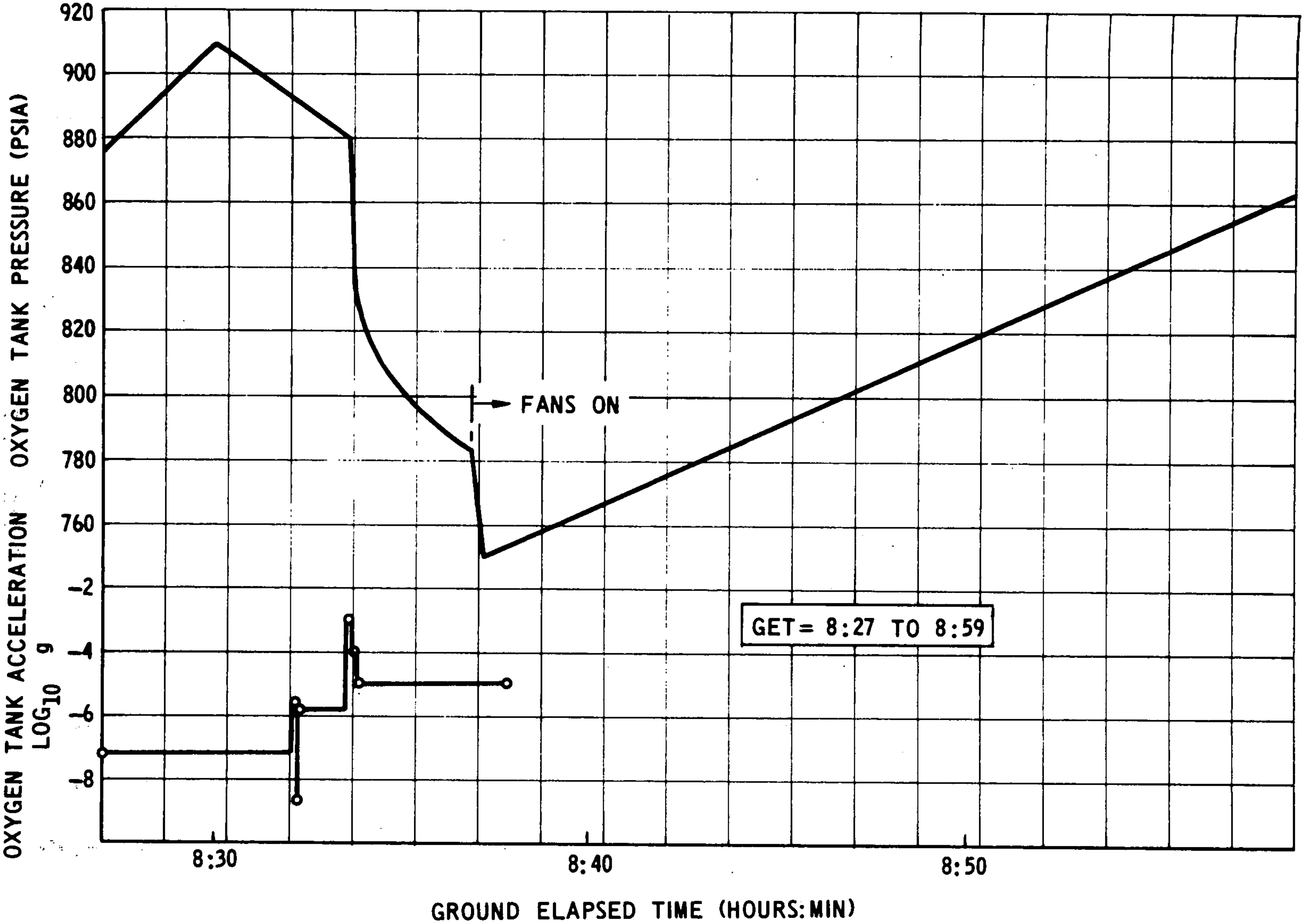

Figure 11. APOLLO 12 FLIGHT DATA – ATTITUDE HOLD

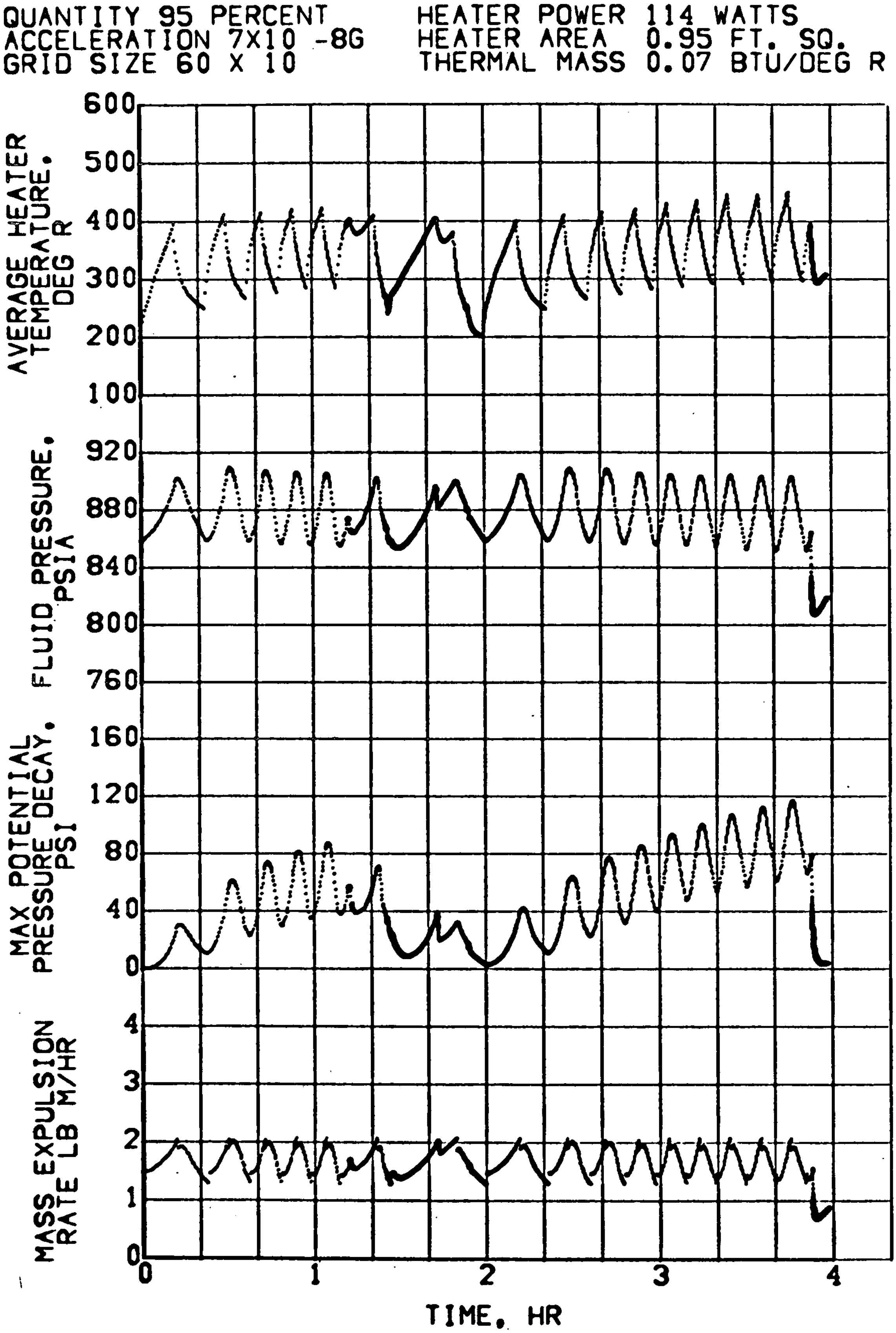

Figure 12. APOLLO 12 SIMULATION

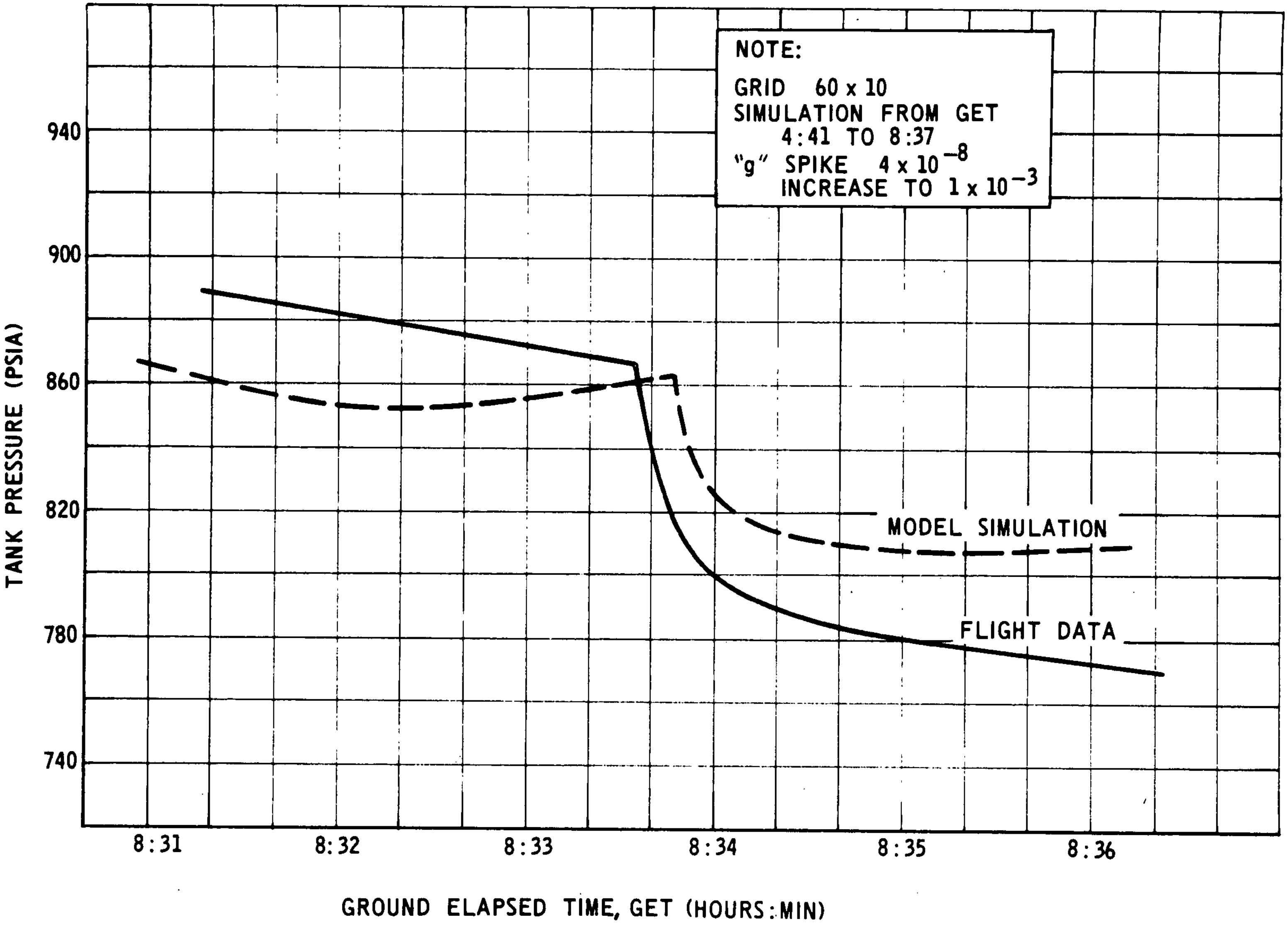

Figure 13. APOLLO 12 "g" SPIKE SIMULATION

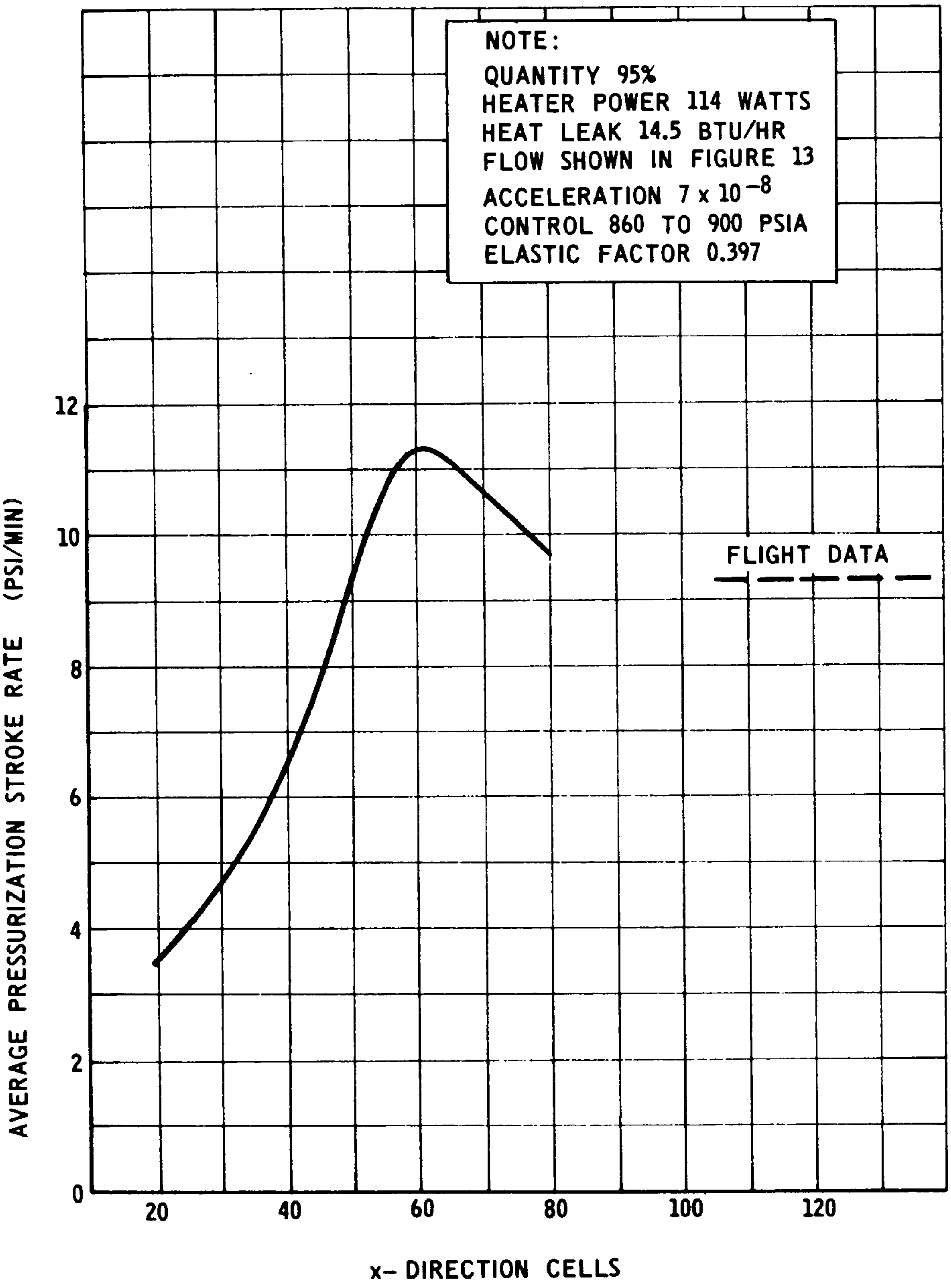

Figure 14. APOLLO PRESSURE STROKE RATE VS GRID SIZE

Appendix A

The Derivation of the Elastic Factor (EF) for the Spherical Container and the External Plumbing

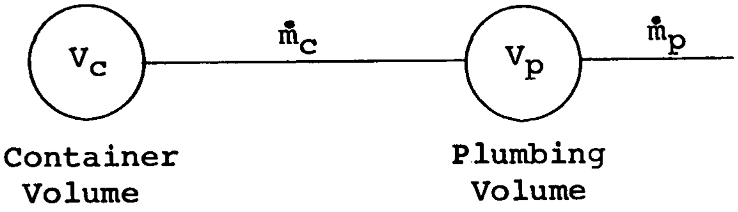

System Schematic

Assumptions:

1) The volume (V_c) is enclosed by a thin walled elastic spherical container with a response of
$$\left(\frac{1}{V_c}\right)\frac{dV}{dP}\bigg|_c = \frac{3r(1-\sigma)}{2bE}$$
where

r = container radius

σ = Poisson's ratio

b = container thickness

E = Young's modulus

2) The plumbing volumes (V_p) are rigid $(dV/dP)|_p = 0$ and contain a compressible gas with a response $P = Z \rho RT$ in which the rate change of compressibility (Z) with respect to the pressure (P) is zero ($dZ/dP = 0$).

3) The time (t) derivative of pressure is a constant for all the fluid in the system $(dP/dt)|_c = (dP/dt)/_p$.

4) The enthalpy and temperature properties are only functions of the pressure and the density for the stored fluid.

Now define

$$\theta \equiv -\rho \frac{\partial h}{\partial p}\Big|_{\rho} , \qquad \phi \equiv \frac{\partial P}{\partial(\rho e)}\Big|_{\rho} , \qquad h \equiv e + \frac{P}{\rho} ,$$

$$\frac{dM_C}{dt} \equiv -\dot{m}_C , \qquad \frac{dM_p}{dt} \equiv \dot{m}_C - \dot{m}_p , \qquad \frac{d\rho}{dt} \equiv \dot{\rho} ,$$

$$\frac{dP}{dt} \equiv \dot{P} , \qquad \rho_C \equiv \left(\frac{M}{V}\right)_C , \qquad \rho_p \equiv \left(\frac{M}{V}\right)_p$$

The result of time differentiation of ρ_c and ρ_p after invoking assumption 2) and some appropriation definitions are

$$\dot{\rho}_C = \frac{1}{V_C} \frac{dM}{dt}\Big|_C - \frac{M_C}{V_C^2} \frac{dV_C}{dt} = - \frac{\dot{m}_C}{V_C} - \frac{\rho_C}{V_C} \frac{dV_C}{dt} \tag{A1}$$

$$\dot{\rho}_p = \frac{\dot{m}_C - \dot{m}_p}{V_p} \tag{A2}$$

The energy balance for V_c is

$$\frac{d}{dt} (\rho e V)_c = \dot{Q}_C - \dot{m}_C h_C - p \frac{dV_C}{dt} \tag{A3}$$

The subscript c is now dropped from (A3) until some intermediate manipulations are complete. Since

$$\rho e = \rho e\,(P, \rho)$$

$$\frac{d(\rho e)}{dt} = \dot{\rho}\left[\frac{\partial(\rho e)}{\partial \rho}\bigg|_P\right] + \left[\frac{\partial(\rho e)}{\partial P}\bigg|_\rho\right]\dot{P}$$

$$= \dot{\rho}\left[\frac{\partial \rho\left(h - \frac{P}{\rho}\right)}{\partial \rho}\bigg|_P\right] + \frac{\dot{P}}{\Phi} = \dot{\rho}\,(h - \theta) + \frac{\dot{P}}{\Phi} \qquad \text{(A4)}$$

Now by substitution eliminate d (ρe)/dt from (A3) and (A4) and combine the result with (A1) and an appropriate definition to yield

$$\dot{P}\frac{V}{\Phi} + \frac{dV}{dt}\,(\rho\theta) = \dot{Q} - \dot{m}\,\theta \qquad \text{(A5)}$$

Now by the chain rule

$$\frac{dV}{dt} = \frac{dV}{dP}\,\frac{dP}{dt}$$

and combined with (A5) with the subscript c restored is

$$\dot{P}_c = \left(\frac{\Phi}{V}\right)_c\left(\dot{Q}_c - \dot{m}_c\,\theta_c\right)(EF) \qquad \text{(A6)}$$

where

$$(EF) \equiv \frac{1}{1 + (\rho\Phi\theta)_c\left(\frac{dV}{dP}\right)_c} \qquad \text{(A7)}$$

Invoking assumption (1), (A7) may be written as

$$(EF) = \frac{1}{1 + (\rho\phi\theta)_c \frac{3r(1-\sigma)}{2bE}} \qquad \text{(A8)}$$

The state equation $P = ZR\rho T$ with the appropriate definition may be written as

$$P = (ZRM\frac{T}{V})_P$$

and may be differentiated with respect to V_p and after some alegraic manipulation is

$$(V\frac{dV}{dP})_P = \left[-\frac{ZMRT}{VP^2} + \frac{MRT}{VP}\frac{dZ}{dP} + \frac{ZR}{VP}(T\frac{dM}{dt}\frac{dt}{dP} + M\frac{dT}{dP}) \right]_P$$

and after assumptions (3) and (4) and the definition of $d\rho_p/dt$ is employed, simplifies to

$$\dot{P}_p = \frac{(\dot{m}_c - \dot{m}_p) P_p}{(\rho V)_p} \qquad \text{(A9)}$$

(A6), (A8), and (A9) may be combined to yield

$$\dot{P}_c = (\frac{Q}{V})_c (\dot{Q}_c - \dot{m}_p \theta_c)(EF) \qquad \text{(A10)}$$

where

$$(EF) \equiv \frac{1}{1 + (\rho\phi\theta)_c \left[\frac{3r(1-\sigma)}{2bE} + \frac{(\rho V)_p (n)}{(\rho V)_c P)} \right]} \qquad \text{(A11)}$$

where $n = 1$

It can additionally be shown that for a polytropic heating $1 \geqslant n \geqslant C_v/C_p$ where n is unity for the isothermal case and C_v/C_p for the isentropic limit.

CORRELATION OF APOLLO OXYGEN TANK THERMODYNAMIC PERFORMANCE PREDICTIONS

H. W. Patterson
The Boeing Company
Space Division
Houston, Texas

ABSTRACT

Parameters necessary to analyze the stratified performance of the Apollo oxygen tanks include "g" levels, tank elasticity, flow rates and pressurized volumes. Methods for estimating "g" levels and flow rates from flight plans prior to flight, and from guidance and system data for use in the post flight analysis are described. Equilibrium thermodynamic equations are developed for the effects of tank elasticity and pressurized volumes on the tank pressure response and their relative magnitudes are discussed. Correlations of tank pressures and heater temperatures from flight data with the results of the stratification model developed by C. K. Forester are shown. Heater temperatures were also estimated with empirical heat transfer equations. Empirical equations were found to yield satisfactory agreement with flight data when fluid properties were averaged rather than evaluated at the mean film temperature.

NOMENCLATURE

Symbols

A	Area
b	Tank wall thickness
C_k	Constant in heater temperature sensor lag equation
C_p	Specific heat at constant pressure
C_s	Stefan Boltzman constant
C_{ra}	Constant in Rayleigh number heat transfer equation
D	Diameter
E	Young's modulus

Symbols

$\overline{F}$	Thrust vector
$\overline{g}$	Acceleration in Earth gravity units
GM	Product of gravitational constant and attracting body mass
h	Enthalpy
I	Vehicle inertia matrix
K	Thermal conductivity
L	Length
M	Mass
MC	Heater thermal mass
N	Polytropic exponent
P	Pressure
Q	Quantity of heat
$\overline{R}$	Position vector
R_a	Rayleigh number
r	Tank radius
T	Temperature
t	Time
U	Internal energy
V	Volume
$\overline{\alpha}$	Vehicle angular acceleration vector
β	Coefficient of thermal expansion
ε	Heater emissivity (0.2 assumed)
ρ	Density
ϕ	Thermodynamic property, $\frac{1}{\rho\frac{\partial U}{\partial P}}$
θ	Thermodynamic property, $-\rho\frac{\partial h}{\partial \rho}$
σ	Poisson's ratio
μ	Viscosity
$\overline{\omega}$	Vehicle angular velocity vector

Subscripts

b	Bulk fluid
cg	Center of gravity
d	Demand
f	Thrust
g	Attracting body (earth or moon)
h	Heater
L	Lines
o	Reference state or condition
t	Tank
s	Sensor

INTRODUCTION AND SUMMARY

Flight performance of single phase cryogenic tanks (pressure decays and heater temperatures) can be reasonably predicted by the techniques developed for the Apollo oxygen tanks. Very careful attention is necessary in the determination of flight operating conditions (accelerations and flow rates) to obtain accurate flight predictions.

The primary analysis tool used for the tank thermodynamic predictions was the numerical model* developed by C. K. Forester for a non-isothermal cryogen. It was evident that if this analysis method were to provide accurate flight predictions:

1. Acceleration must be accurately established to model the convection processes in the tank, and

2. Accurate flow rates are required to determine the pressure response to heat addition.

Procedures to calculate these accelerations and flow rates for Apollo 14 were developed. Early comparisons of the simulation results to flight data indicated that additional effects, such as heater thermal mass and tank elasticity, needed to be included in the basic solution. The basic method of solution did not require modifications. The resulting prediction techniques have been correlated to Apollo 14 flight data and show excellent agreement.

---

*Forester, C. K., "Pressurized Expulsion of Non-Isothermal Single Phase Cryogen", paper presented at the NASA-MSC Cryogenics Symposium, May 20-21, 1971.

Heater temperatures analyses were also made with an empirical Rayleigh number equation for convection. The fluid properties for this simplified analysis were averaged instead of evaluated using standard conventions. This approach resulted in good correlations with flight data and provides a convenient tool for heater temperature predictions.

SYSTEM DESCRIPTION

The oxygen flow distribution system is shown by Figure 1. The system includes check valves which are intended to prevent flow into the tanks during normal operation. The isolation valve between tanks 2 and 3 is normally open and for the Apollo 14 mission was closed only during the high flow test. The flow restrictors are capillary tubes which produce a pressure drop of approximately 800 psi at 3.5 lbs/hr flow rate. The restrictors are the only significant source of pressure drop in the system.

The data available from the system include fluid quantity and pressure, and heater temperature for each of the three cryogenic tanks. The surge tank is instrumented to provide pressure data only. The flow rate to the environmental control system is measured downstream of the surge tank and, therefore, includes contributions from all four of the tanks. The flow rate to the fuel cells is also measured, but can be more accurately determined from the electrical current.

FLOW RATES

The total flow from the three tanks during the Apollo 14 mission was determined from the fuel cell usage and the flow rate across the restrictors to the environmental control system (ECS). The fuel cell flow rate was computed using the fuel cell current, because the current data are more accurate than the fuel cell flow meters. The flow rate across the restrictors during high flow periods was based on the restrictor pressure drop calibrations. During low flow periods, the restrictor flows were obtained from the ECS flow rate (measured downstream of the restrictors) and the net change of mass in the surge tank during the period.

The flow rates from the individual cryogenic tanks were not measured, therefore, it was necessary to divide the total system flow among the three tanks. The individual tank flow rates were determined from the total system flow on the basis of equilibrium tank thermodynamics. The pressure differences between tanks were used to determine the check valves configuration and to constrain the thermodynamics calculations.

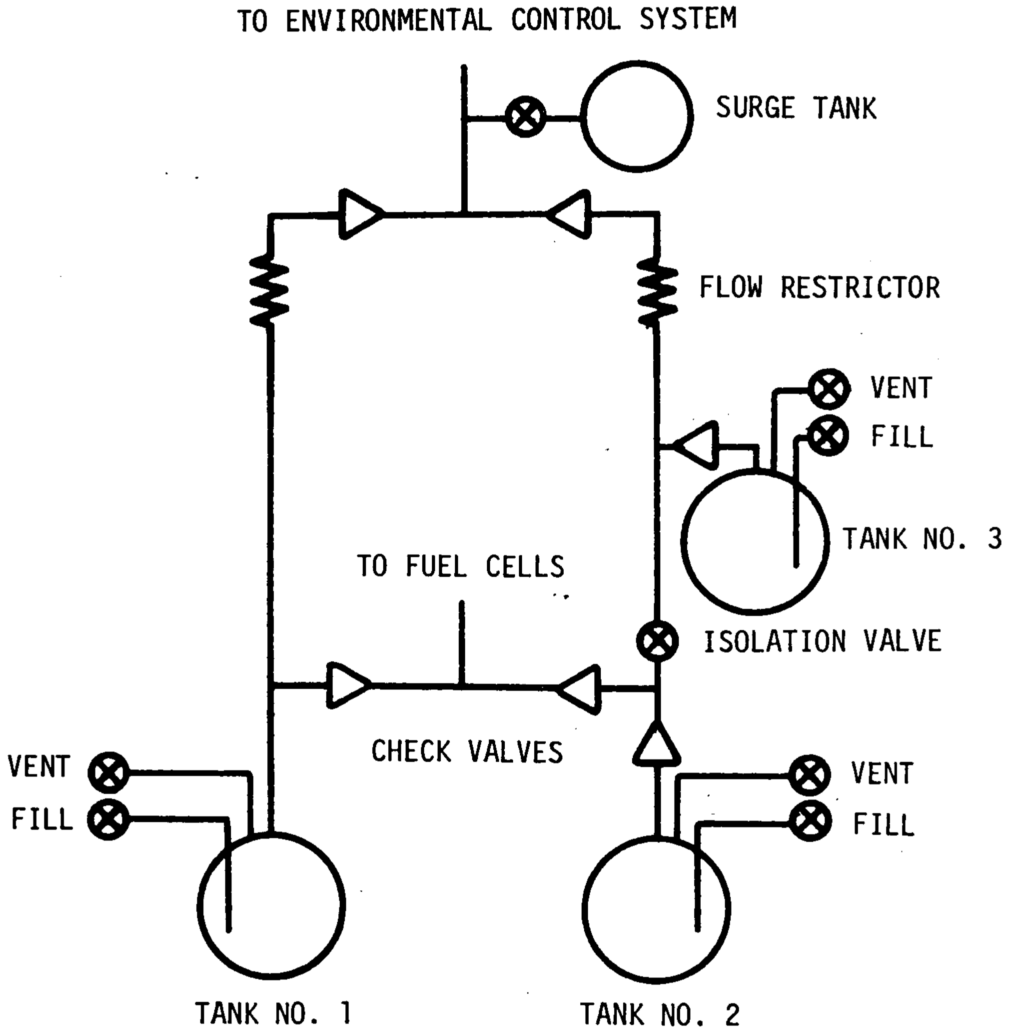

FIGURE 1 - APOLLO 14 OXYGEN SYSTEM FLOW SCHEMATIC

The flow distribution is affected by the heat input to the separate tanks, therefore, the heat leaks were estimated from flight data. The tank 1 and tank 3 heat leaks were found to be nominal at zero flow rate at 90% and 10% quantities, respectively. The tank 2 heat leak was not verified, but is believed to have been slightly greater than nominally expected. The tank 2 heat leak could not be determined for a zero flow condition because the check valve provided to isolate the tank leaked. The check valve permitted warm fluid to flow back into the tank causing warming of the insulation and increasing the heat leak.

The flow rate distributions were obtained by simultaneous solution of the pressure change equations (Appendix) for the tanks supplying the system flow. The calculations included the effects of tank elasticity, since the elasticity strongly affects the pressure change rate at high quantities (Figure 2). The simultaneous solution of equations A-19 for two tanks supplying the system demand relates the individual tank flow to the total flow. The total flow used for this calculation included the flow rate required to pressurize the external line volumes. These calculations are simplified if the pressure change rate is known and used with the nominal heat leak to determine the individual tank flows. The flow rates from this method are in the same ratio as those provided by simultaneous solution of the equations.

The tank 2 check valve leak required special consideration to determine the flow into the tank causing pressurization. The flow rate into the tank was determined from the volume change required to produce the observed pressure change. Using equation A-15 and considering the volume change due to a hot bubble as well as tank elasticity, the pressure change is:

$$\frac{dP}{dt} = \frac{\phi}{V}\left(\frac{dQ}{dt} + \theta\,\frac{dM_d}{dt}\right) - \frac{1}{V}\,\rho_t\theta\phi\left[\left(\frac{dV}{dt}\right)_t + \left(\frac{dV}{dt}\right)_L\right] \qquad (1)$$

where $\left(\frac{dV}{dt}\right)_L$ is the volume change due to a bubble of fluid at the line density.

During pressurization, the demand flow $\frac{dM_d}{dt}$ is zero. Substituting $-\frac{1}{\rho_L}\frac{dM}{dt}$ for $\left(\frac{dV}{dt}\right)_L$ and solving for $\frac{dM}{dt}$ we have:

$$\frac{dM}{dt} = \frac{\rho_L}{\rho_t}\,\frac{V}{\phi\theta}\left[\frac{dP}{dt} - \frac{\phi}{V}\,\frac{dQ}{dt} + \frac{1}{V}\,\rho_t\phi\theta\left(\frac{dV}{dt}\right)_t\right] \qquad (2)$$

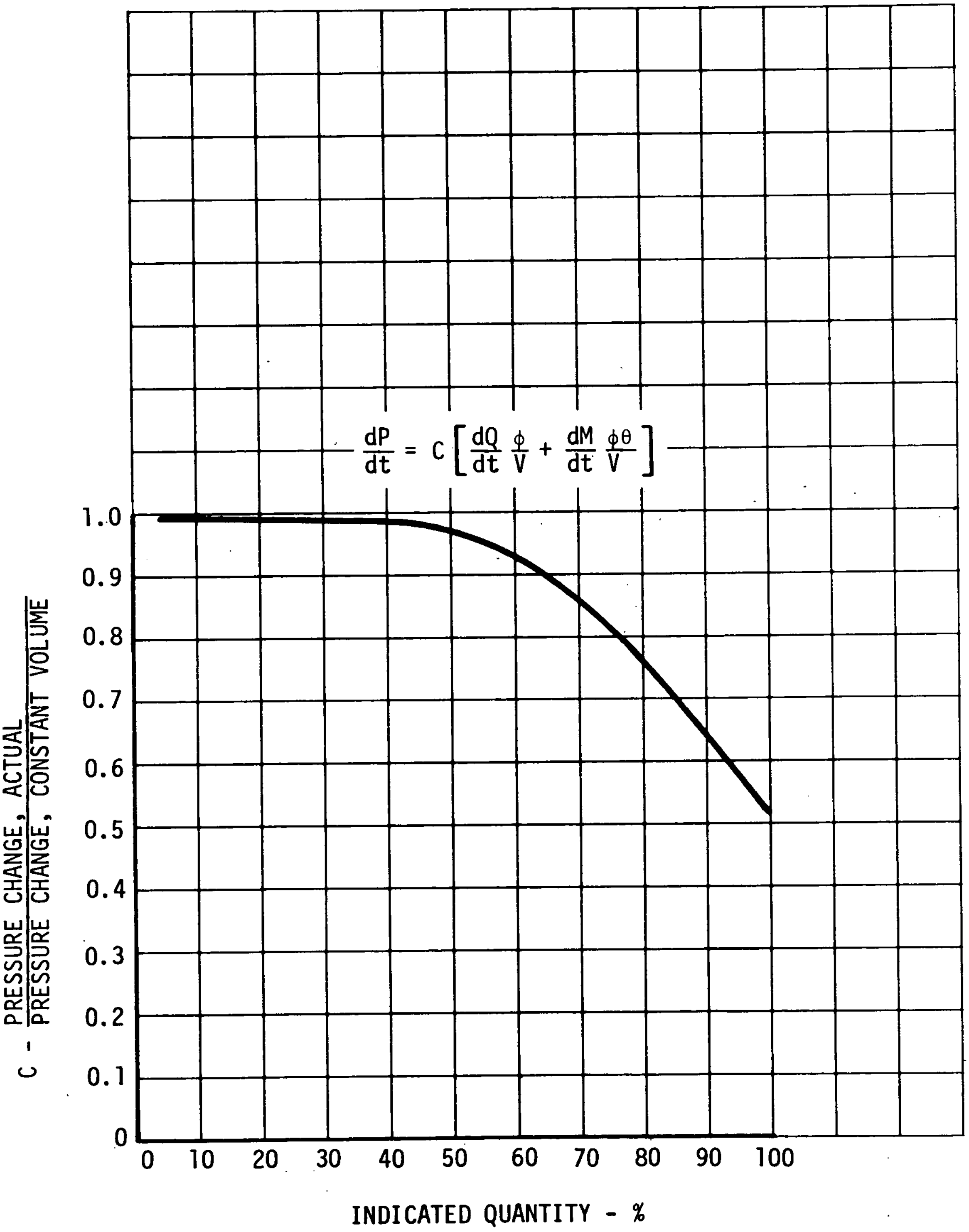

FIGURE 2 - OXYGEN TANK ELASTICITY EFFECT

This method of determining tank 2 inflow during the tank 3 heater cycle at 26 hours AET resulted in check valve leakage rates of approximately 0.05 lbs/hr which is believed to be realistic.

Thermodynamic analyses were not required to distribute the flows during the high flow test, since the isolation valve was closed. The tank 3 flow rates (Figure 3) during the tests were determined from the restrictor pressure drop while the surge tank valve was open. Flow rates were assumed constant while the surge tank valve was closed. The tank 1 flow rates (Figure 4) were also determined from the restrictor pressure drop, but included the fuel cell flow rate when the tank 1 pressure was greater than the tank 2 pressure.

TANK ACCELERATION ANALYSIS

The sources of accelerations in a space vehicle in drifting flight include vehicle rotations, thrusts caused by fluid venting, gravity gradients and solar pressure. The solar pressure is approximately 10^{-7} lbs/ft^2 and produces an acceleration of less than 5×10^{-9} "g" for the Apollo vehicle. The acceleration due to solar pressure was an order of magnitude smaller than the accelerations produced by vehicle rotations during a typical Apollo 12 attitude hold period and was, therefore, neglected.

The procedure for the analysis of accelerations during attitude hold conditions used rotation rates from guidance data directly for the centripetal acceleration. The rotation rates were numerically differentiated for the angular acceleration term. The total acceleration due to rotation is:

$$32.174\, \bar{g} = \bar{\omega} \times \bar{\omega} \times (\bar{R}_t - \bar{R}_{cg}) + \bar{\alpha} \times (\bar{R}_t - \bar{R}_{cg}) \qquad (3)$$

Telemetry data from the digital auto pilot used for the analysis includes the three components of the $\bar{\omega}$ vector and the calculation is, in principle, straightforward. Some difficulty does, however, arise due to the angular acceleration. The angular acceleration terms tends to dominate the centripetal term because the centripetal acceleration depends on the square of the rotation rate. The acceleration term also introduces questions of significance due to the short durations of application. Typically, the reaction control system jet firings cause angular accelerations greater than 2×10^{-4} radians/second^2, but the duration is of the order of 10 milliseconds. This acceleration results in a movement of the oxygen tank of about 10^{-7} inches during the time the acceleration is applied. This small displacement would appear to be negligible, however, the angular accelerations should

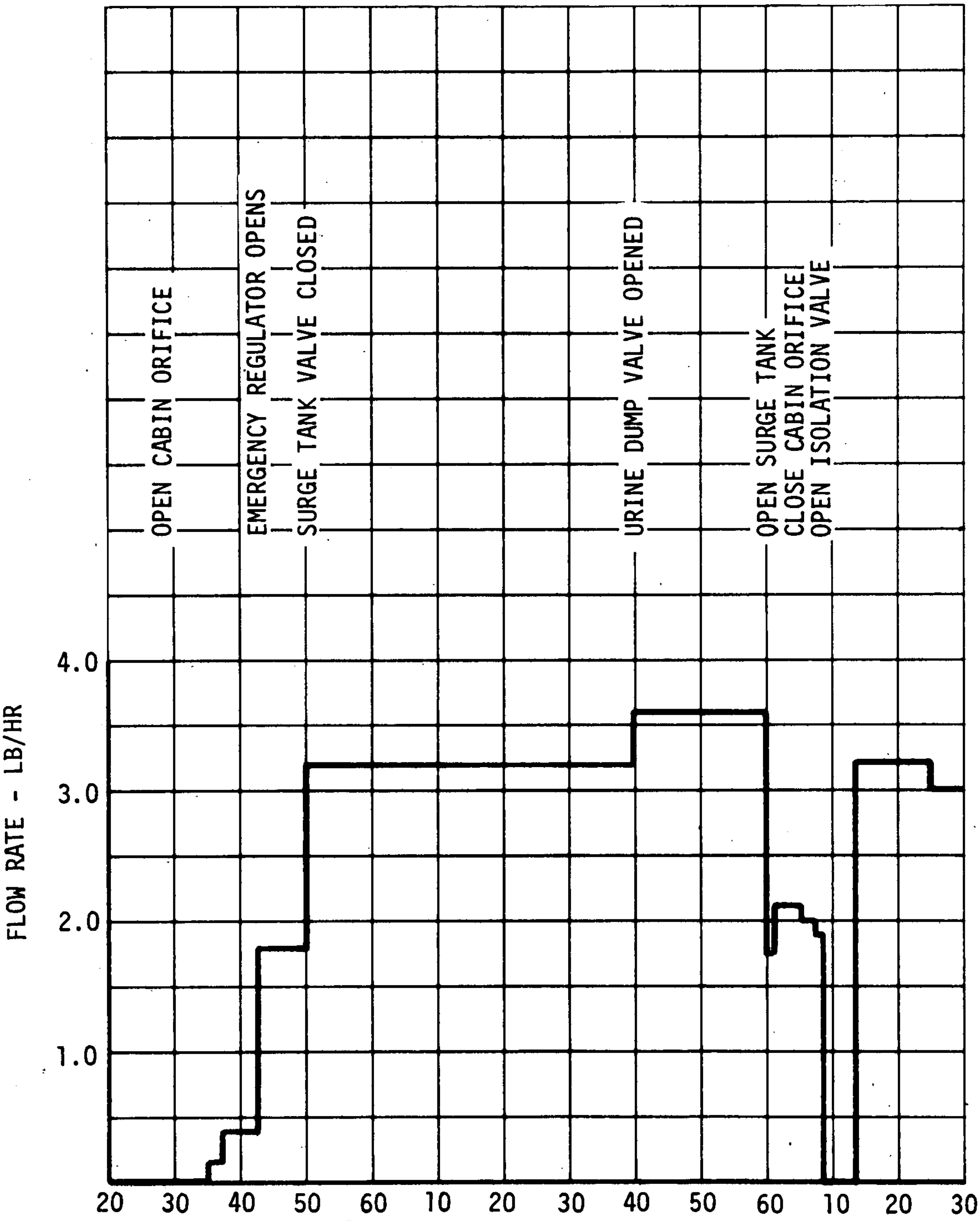

FIGURE 3 - TANK 3 TEST FLOW RATE

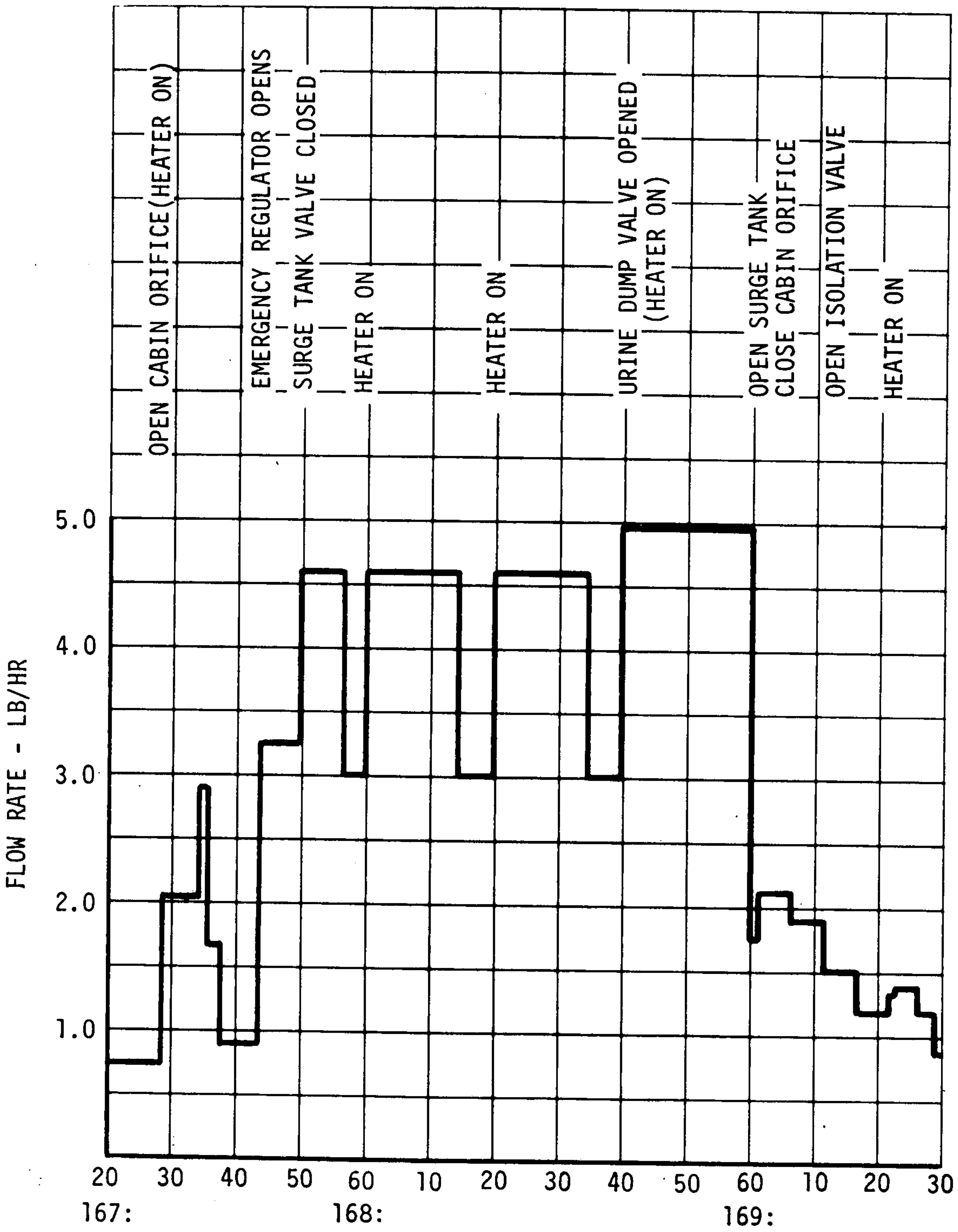

FIGURE 4 - TANK 1 TEST FLOW RATE

certainly not be entirely ignored. The approach used was to distribute the angular acceleration over time intervals of 10 seconds or greater by numerical differentiation of the observed angular rates at the end points of the time interval. The time intervals were selected on the basis of engineering judgement to adequately characterize the acceleration events. Although this procedure is arbitrary, the results appear to be satisfactory and a better method has not presented itself. Tank accelerations during an Apollo 12 attitude hold condition were typically 5 x 10^{-8} to 7 x 10^{-8} "g".

The tank accelerations during stable periods of passive thermal control (PTC) were calculated without consideration of angular accelerations. During PTC flight modes, the reaction control system is deactivated and the vehicle is essentially spin stabilized. For this condition, angular accelerations are generally negligible and the centripetal acceleration only is significant.

When the vehicle is in attitude hold in the near vicinity of the earth or moon, the gravity gradient acceleration is significant. This term, which must be added to the rotational accelerations, is:

$$32.174\ \bar{g} = \frac{2\ GM\ (\bar{R}_g \cdot \bar{R}_t)\ \bar{R}_g}{\bar{R}_g^{\ 4}\ \ |\bar{R}_g|} \tag{4}$$

The gravity gradient term is of the order of 10^{-7} "g" for a 100 mile altitude earth orbit. Since the magnitude of the gravity gradient is proportional to $1/|\bar{R}_g|^3$, the term becomes negligible at distances of 2-3 earth radii. The radius vector to the attracting body in the vehicle coordinate system is necessary to the gravity gradient calculation. This vector can only be determined from the vehicle trajectory and inertial platform data. A computer program for the calculation of the acceleration including the gravity gradient term derived from trajectory data has been developed by NASA-MSC for application to the Apollo 14 mission. The average tank acceleration in lunar orbit was 5 x 10^{-7} "g" for the Apollo 12 mission.

The tank accelerations for nominal flight conditions can reasonably be assumed to be the same as previous flights at similar conditions. The high flow oxygen tank tests during the Apollo 14 mission were not, however, in nominal flight "g" conditions due to overboard dumping of oxygen. The oxygen dumped overboard through a convergent nozzle in the command module entry hatch produced a significant thrust and vehicle acceleration.

The thrust of the 6.2 lbs/hr oxygen dumped overboard was calculated as the thrust from a choked convergent nozzle for a stagnation temperature of 60°F and a specific heat ratio of 1.4. The resulting thrust of 0.091 pounds is conservative, since no expansion downstream of the throat or plume effects were considered.

The 0.091 pounds thrust produced a linear "g" of 3.65×10^{-6} for the 24,985 pounds vehicle weight at the time of the test. The thrust vector was not through the vehicle center of mass, therefore, rotational accelerations were also produced. The equation for the angular accelerations is:

$$\bar{R}_f \times \bar{F} = I\,\bar{\alpha} \tag{5}$$

and solving for

$$\bar{\alpha} = I^{-1}\,(\bar{R}_f \times \bar{F}) \tag{6}$$

The moments of inertia obtained from pre-flight mass properties data were used with equation 6 to predict angular acceleration rates. The rotation rates were then calculated from the time required to rotate the vehicle through the 5° dead band. Finally, rotational tank accelerations were calculated from equation 3. The total tank 3 "g" was found to be 4.9×10^{-6} and for tank 1 a "g" of 4.7×10^{-6} was obtained. These accelerations neglected the effects of reaction control system firings as well as plume effects and therefore, may be somewhat lower than actually experienced. The pre-flight acceleration predictions have been used for the high flow test post flight analysis, since acceleration data reduction has not been completed.

ANALYSIS CORRELATIONS WITH FLIGHT DATA

Evaluations of the numerical model and empirical heater temperature equations were based on Apollo 14 flight data. The accelerations and flow rates required by the analyses were determined using the methods described earlier. Comparisons of simulations with Apollo 14 data showed good correlation with the flight pressures and temperatures.

THERMODYNAMIC SIMULATIONS

Detailed tank thermodynamic simulations were conducted with the numerical math model described in the paper* by C. K. Forester. This model uses a rectangular (x and y) grid of cells to approximate the flow fields in the tank. The simulations were accomplished for a range of grid sizes to permit extrapolations of variables to asymptotic limits. The effects of tank elasticity and heater temperature sensor lag were included.

---

*IBID, page 3.

The tank pressure and heater temperature results from a simulation of one PTC heater cycle are compared with flight data by Figure 5. This simulation was made with a heater area of 0.475 ft^2 which is the flat plate area equivalent to the 0.59 ft^2 outer surface of the cylindrical heater tube. Since the heater tube is perforated, flow through the tube could provide an effective flat plate heater area of 0.95 ft^2. Simulations were conducted for both heater areas to determine which provided the most accurate heater temperature. The results of the convergence analyses for the areas are shown by Figure 6. The asymptotic limit for the heater temperature with the 0.475 ft^2 area is within 9°F of the flight data. The asymptotic temperature with the larger heater area is not in good agreement with flight data. The asymptotic limit of the heater on time for the small heater is also in better agreement with flight data than the large heater. These results imply that the inside of the heater tube is not an effective heat transfer surface.

The simulation of the tank 3 high flow test is shown by Figure 7. The convergence study and the asymptotic limit for the heater temperature are shown by Figure 8. The asymptotic heater temperature with the 0.95 ft^2 heater area is 45°F below flight data. The PTC heater cycle simulation with this area resulted in a heater temperature 95°F below the flight data. Since the 0.475 ft^2 heater area provided good agreement for the PTC heater cycle, the 0.95 ft^2 area was expected to produce temperatures much lower than flight data. The heater temperature simulation results of the PTC heater cycle and the high flow test are contradictory. The contradiction may be due to the "g" level which was estimated as 4.9×10^{-7} "g" for the high flow test. A higher "g" level during the high flow test could bring the results into agreement. The discrepancy could also be due to residual fluid rotations caused by the prior PTC period. Resolution of this discrepancy must await more accurate determination of the "g" level from flight data.

EMPIRICAL HEAT TRANSFER EQUATIONS

Heater temperatures can be determined from the numerical math model, but the computer time requirements are excessive for the generation of parametric data and routine flight analyses. Empirical heat transfer equations were investigated to develop a more convenient tool for heater temperature studies.

The convective heat transfer from a horizontal cylinder is usually determined from a Rayleigh number equation.

$$\frac{dQ}{dt} = \pi \, L \, K \, \Delta T \, C_{ra} \, (R_a)^{1/4} \qquad (7)$$

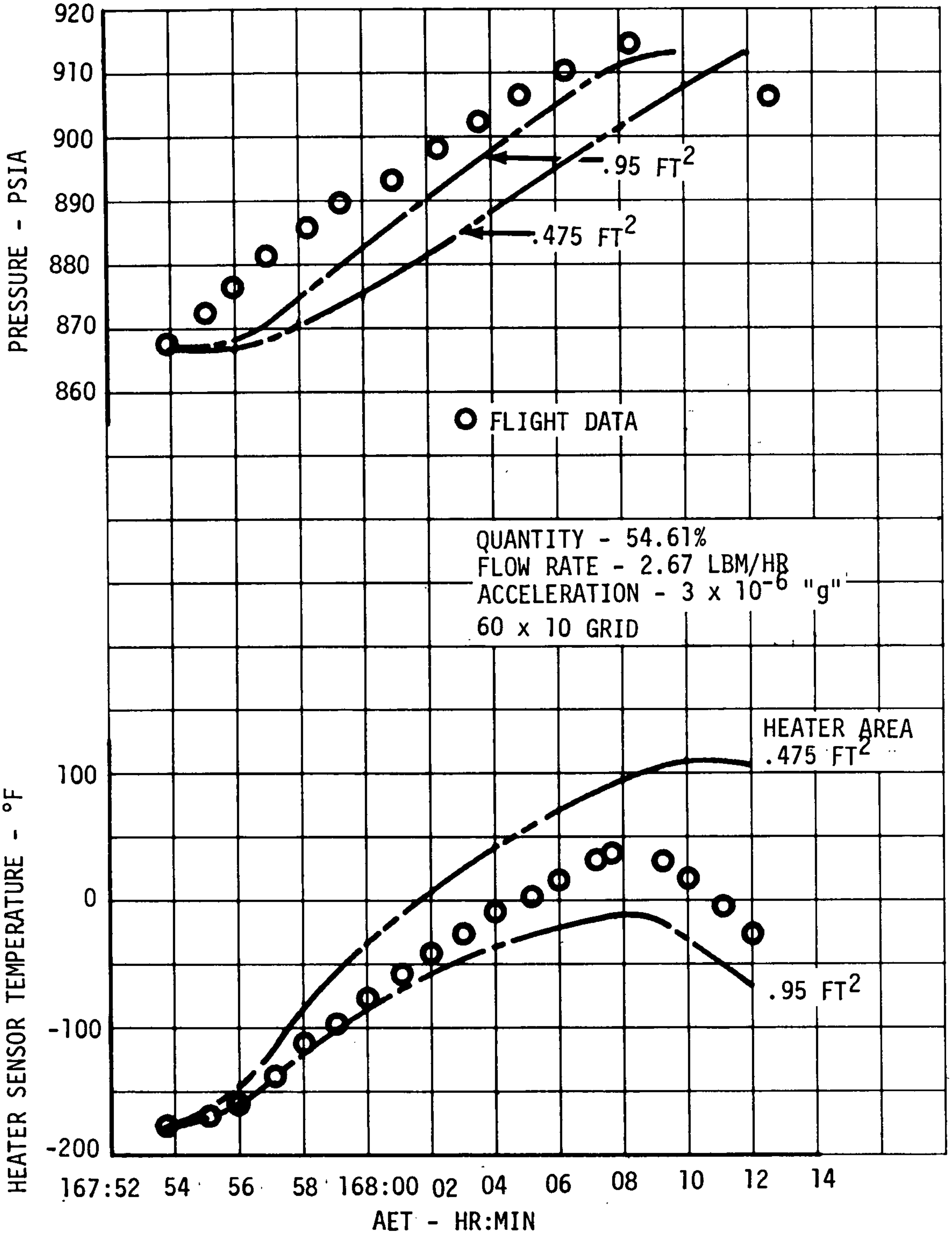

FIGURE 5 - PTC HEATER CYCLE SIMULATION

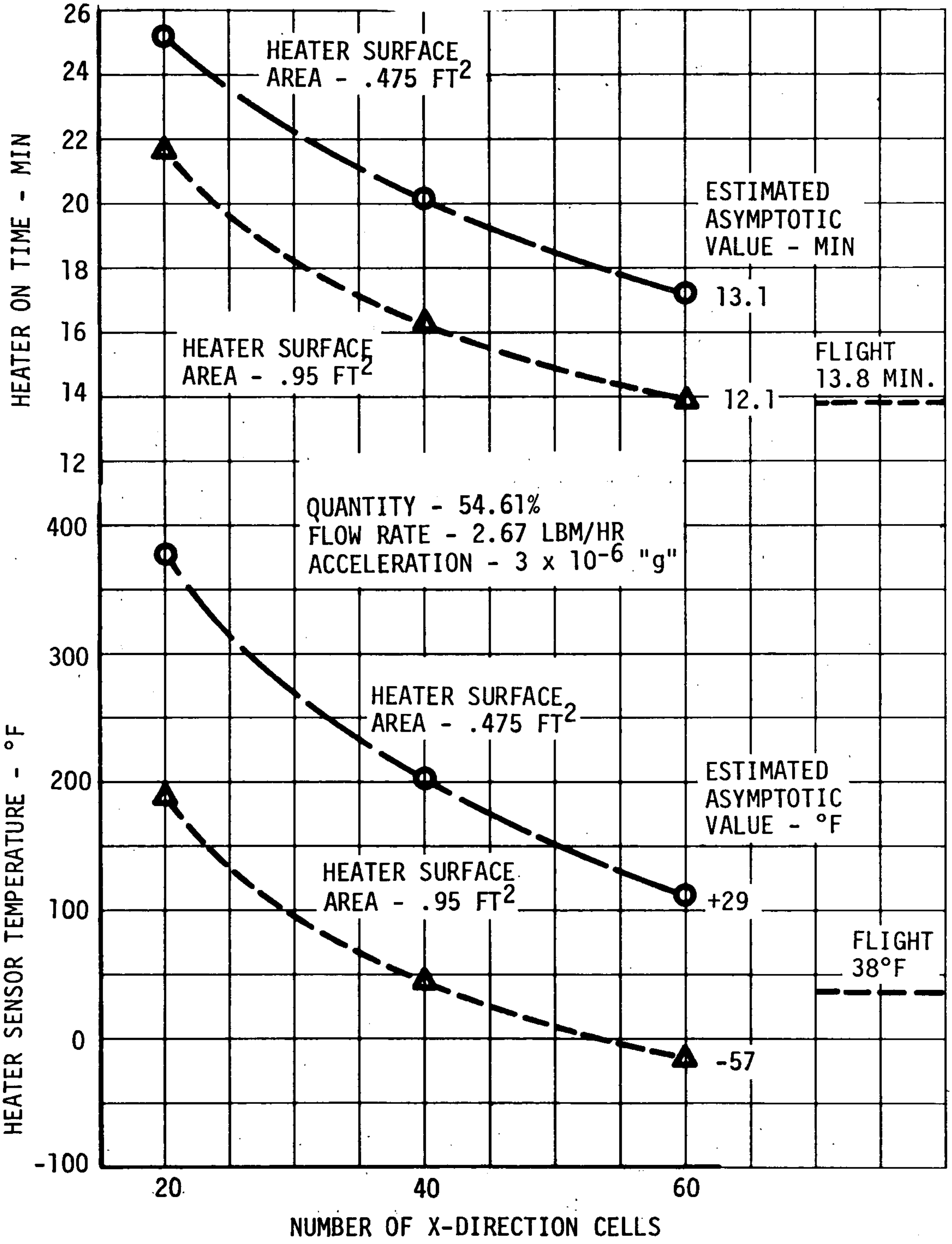

FIGURE 6 - PTC HEATER CYCLE CONVERGENCE

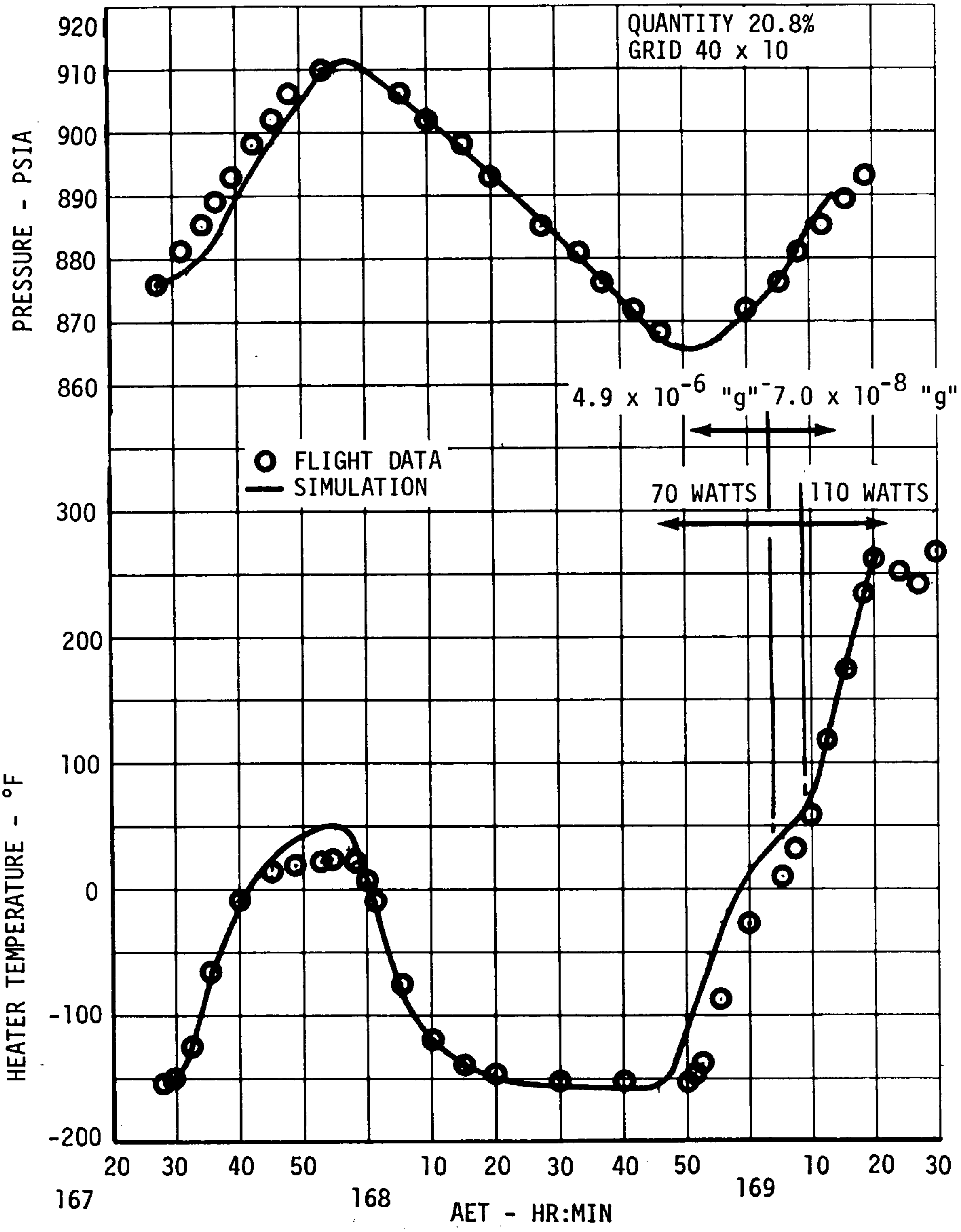

FIGURE 7 - TANK 3 TEST SIMULATION

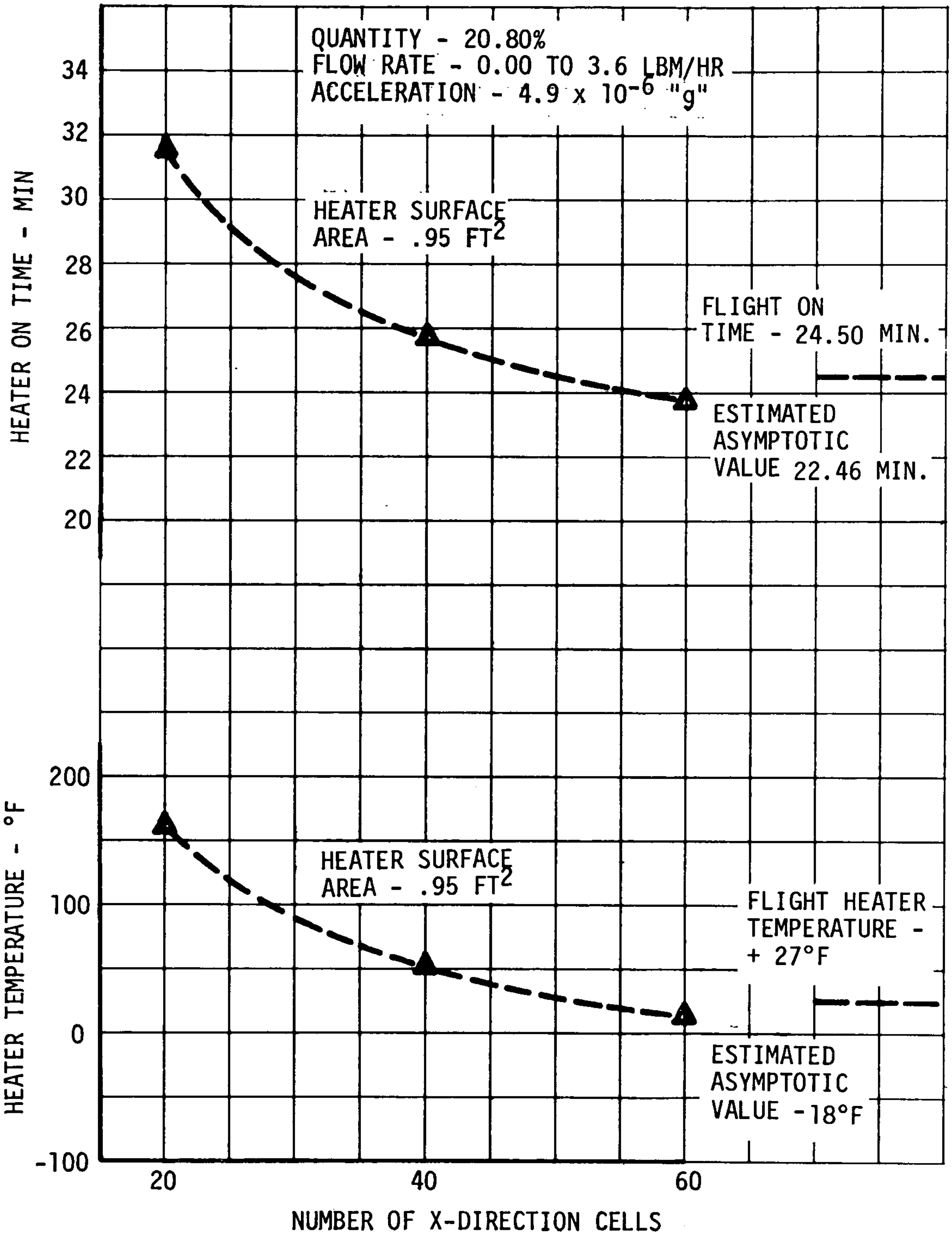

FIGURE 8 - TANK 3 TEST CONVERGENCE

The Rayleigh number is determined from:

$$R_a = \frac{D^3 \rho^2 \, 32.174 \, g \, \beta \, \Delta T \, C_p}{\mu K} \tag{8}$$

The fluid properties used to evaluate the Rayleigh number are usually taken at the mean film temperature. This convention is based on tests with simple fluids under 1 "g" conditions. Since the properties of supercritical oxygen may vary by an order of magnitude in the boundary layer, the properties in the Rayleigh number were averaged instead of taken at the mean film temperature. The viscosity, conductivity, and density were taken as the average of their values for the bulk temperature and the heater temperature. The specific heat was evaluated as the difference in the enthalpy at the heater and bulk temperatures divided by the temperature difference. The coefficient of expansion used was,

$$\beta = \frac{-1}{\rho_b} \frac{\rho_h - \rho_b}{T_h - T_b} \tag{9}$$

The radiation from the heater is also significant and was included in the complete heat transfer equation.

$$\frac{dQ}{dt} = \pi \, L \, K \, \Delta T \, C_{ra} \, (R_a)^{1/4} + \varepsilon \, C_s \, (T_h{}^4 - T_b{}^4) \, A \tag{10}$$

Heater temperatures were developed as a function of on time by numerical integration of the equation,

$$\frac{dT}{dt} = \frac{dQ}{dt} \left(\frac{1}{MC} \right) \tag{11}$$

where MC is the heater thermal mass of 0.1 BTU/°F. The heater temperature sensor lag was included in the integration to provide a means of comparison with flight data. The temperature sensor response was determined from:

$$\frac{dT_s}{dt} = C_k \, (T_h - T_s) \tag{12}$$

The temperature-time results of a simulation of one heater cycle using this simplified analysis (Figure 9) are in excellent agreement with flight data. Comparisons between actual and predicted heater temperatures (Figure 10) for several heater cycles indicates predictions within 50°F with the exception of the tank 3 heater cycle during the high flow test. As already mentioned, the "g" level assumed for this period is questionable.

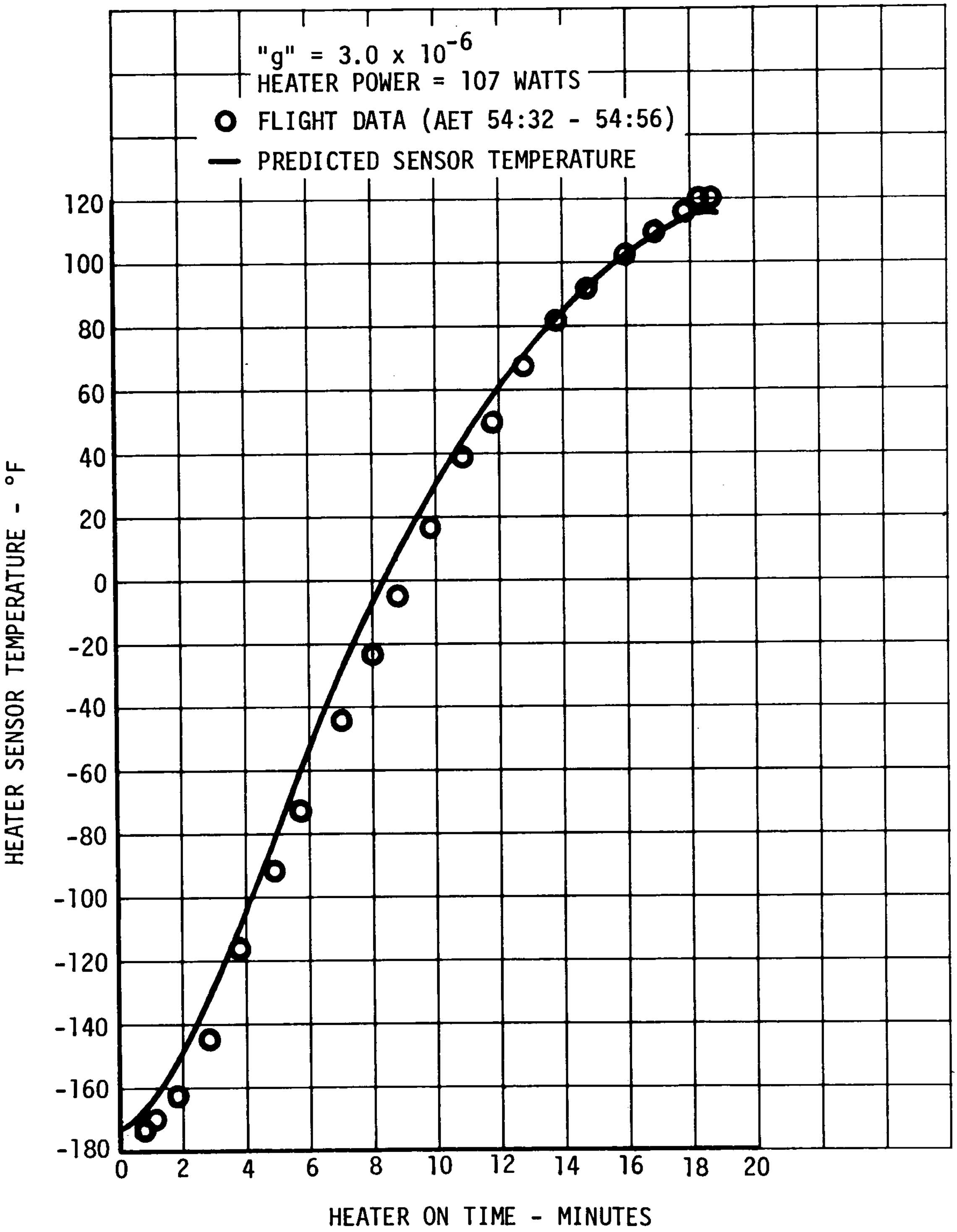

FIGURE 9 - EMPIRICAL HEATER RESPONSE

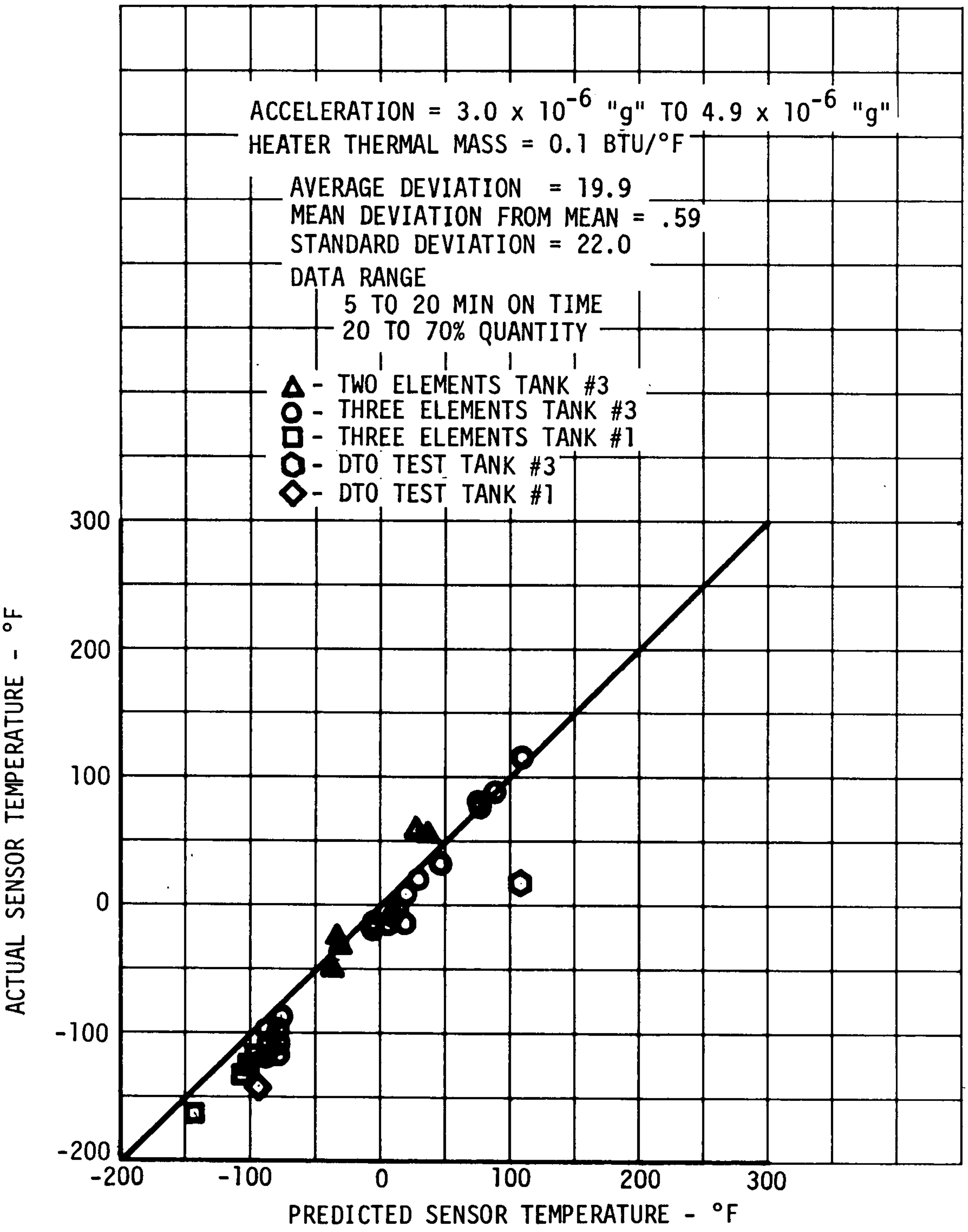

FIGURE 10 - TEMPERATURE COMPARISONS SUMMARY

Parametric heater temperatures (Figure 11) were generated for easy comparisons with flight data. The results of the comparisons made so far are promising, however, the full ranges of quantities and accelerations have not been investigated. A final determination of the empirical constants and the averaging method used for fluid properties can not be made, since attitude hold conditions have not been investigated.

CONCLUSIONS

Conclusions based on correlations with the Apollo 14 high flow tank tests and passive thermal control conditions are:

1. The flight performance of single phase cryogenic tanks can be reasonably predicted using the numerical model developed. Heat transfer and detailed thermodynamic processes (stratification) in the tanks are accurately modeled.

2. Heater temperatures can be predicted from empirical heat transfer equations if fluid properties are averaged instead of evaluated at the mean film temperature.

3. The accuracy of performance predictions is dependent on the ability to predict or control flight accelerations and flow rates.

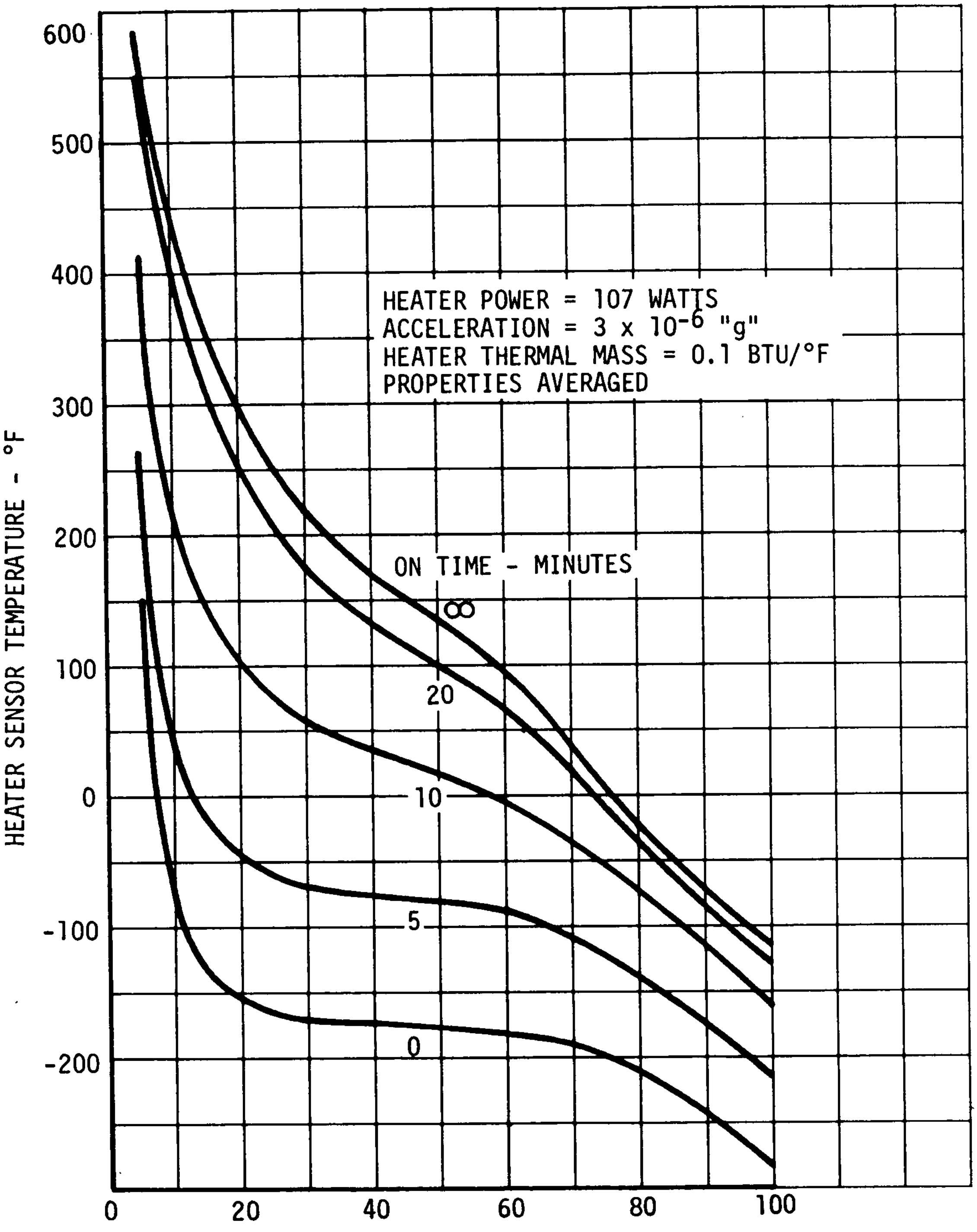

FIGURE 11 - PARAMETRIC HEATER TEMPERATURES

APPENDIX

THE PRESSURE CHANGE EQUATION FOR A CRYOGENIC TANK

The pressure changes in a cryogenic tank resulting from heat addition and mass extraction are usually calculated with the assumption that the tank is a constant volume container. This assumption causes large errors when the fluid is nearly incompressible and the pressure vessel is highly stressed. An error in the pressure change calculation is also caused by flows not usually measured that are required to pressurize plumbing system volumes at ambient temperature. In order to eliminate these errors, the pressure change equation for an equilibrium fluid in an elastic container has been derived and a method for including the external volume effects developed.

The thermodynamic system is bounded by the inside surface of the pressure vessel and is closed at the fluid outlet from the pressure vessel. The volume inside the thermodynamic boundary is not constant since the pressure vessel is elastic. The outflow velocity is assumed to be small enough that the kinetic energy and momentum of the outflow are negligible. The conservation equations for mass and energy, therefore, determine the system response to heat and mass flows.

The conservation of mass:

$$\frac{dM}{dt} = V\frac{d\rho}{dt} + \rho\frac{dV}{dt} \qquad \text{(A-1)}$$

The conservation of energy:

$$\frac{d}{dt}(\rho VU) = \frac{dQ}{dt} + h\frac{dM}{dt} - P\frac{dV}{dt} \qquad \text{(A-2)}$$

Expanding A-2 and using the definition of enthalpy

$$\rho V\frac{dU}{dt} + U\left(V\frac{d\rho}{dt} + \rho\frac{dV}{dt}\right) = \frac{dQ}{dt} + \frac{dM}{dt}\left(U + \frac{P}{\rho}\right) - P\frac{dV}{dt} \qquad \text{(A-3)}$$

Substituting A-1 in A-3 and simplifying

$$\rho V\frac{dU}{dt} = \frac{dQ}{dt} + \frac{P}{\rho}\frac{dM}{dt} - P\frac{dV}{dt} \qquad \text{(A-4)}$$

The internal energy is taken as a function of pressure and density

$$\frac{dU}{dt} = \frac{\partial U}{\partial P}\frac{dP}{dt} + \frac{\partial U}{\partial \rho}\frac{d\rho}{dt} \qquad \text{(A-5)}$$

Using A-1 and noting that $M = \rho V$

$$\frac{dU}{dt} = \frac{\partial U}{\partial P}\frac{dP}{dt} + \frac{\partial U}{\partial \rho}\left(\frac{1}{V}\frac{dM}{dt} - \frac{M}{V^2}\frac{dV}{dt}\right) \qquad \text{(A-6)}$$

Substituting A-6 in A-4

$$\rho V\left[\frac{\partial U}{\partial P}\frac{dP}{dt} + \frac{\partial U}{\partial \rho}\left(\frac{1}{V}\frac{dM}{dt} - \frac{M}{V^2}\frac{dV}{dt}\right)\right] = \frac{dQ}{dt} + \frac{P}{\rho}\frac{dM}{dt} - P\frac{dV}{dt} \qquad \text{(A-7)}$$

Solving for $\frac{dP}{dt}$ and rearranging

$$\frac{dP}{dt} = \frac{\frac{dQ}{dt} + \frac{P}{\rho}\frac{dM}{dt} - P\frac{dV}{dt} - \rho\frac{\partial U}{\partial \rho}\left(\frac{dM}{dt} - \frac{M}{V}\frac{dV}{dt}\right)}{\rho V\frac{\partial U}{\partial P}} \qquad \text{(A-8)}$$

Rearranging

$$\frac{dP}{dt} = \frac{\frac{dQ}{dt} + \frac{dM}{dt}\left(\frac{P}{\rho} - \rho\frac{\partial U}{\partial \rho}\right)}{\rho V\frac{\partial U}{\partial P}} + \frac{\rho\frac{\partial U}{\partial \rho}\frac{M}{V}\frac{dV}{dt} - P\frac{dV}{dt}}{\rho V\frac{\partial U}{\partial P}} \qquad \text{(A-9)}$$

and reducing the last term

$$\frac{dP}{dt} = \frac{\frac{dQ}{dt} + \frac{dM}{dt}\left(\frac{P}{\rho} - \rho\frac{\partial U}{\partial \rho}\right)}{\rho V\frac{\partial U}{\partial P}} + \frac{\rho^2\frac{dV}{dt}\left(\frac{\partial U}{\partial \rho} - \frac{P}{\rho^2}\right)}{\rho V\frac{\partial U}{\partial P}} \qquad \text{(A-10)}$$

Now define

$$\phi = \frac{1}{\rho\frac{\partial U}{\partial P}} \qquad \text{(A-11)}$$

and

$$\theta = -\rho\frac{\partial h}{\partial \rho} \equiv -\rho\left(\frac{\partial U}{\partial \rho} - \frac{P}{\rho^2}\right) \qquad \text{(A-12)}$$

Substituting A-11 and A-12 in A-10

$$\frac{dP}{dt} = \frac{\phi}{V}\left(\frac{dQ}{dt} + \theta\frac{dM}{dt}\right) - \frac{1}{V}\frac{dV}{dt}\rho\theta\phi \tag{A-13}$$

Equation A-13 provides a convenient method for calculating pressure response if the volume rate of change is known. The last term is zero for a constant volume system. If the container is elastic so that the volume change is related to the pressure change, some further reduction is possible.

$$\frac{dP}{dt} = \frac{\phi}{V}\left(\frac{dQ}{dt} + \theta\frac{dM}{dt}\right) - \frac{1}{V}\frac{dV}{dP}\frac{dP}{dt}\rho\theta\phi \tag{A-14}$$

Again solving for $\frac{dP}{dt}$

$$\frac{dP}{dt} = \frac{\frac{\phi}{V}\left(\frac{dQ}{dt} + \theta\frac{dM}{dt}\right)}{1 + \frac{1}{V}\frac{dV}{dP}\rho\theta\phi} \tag{A-15}$$

for a spherical tank

$$\frac{1}{V}\frac{dV}{dP} = \frac{3\ r\ (1-\sigma)}{2\ b\ E} \tag{A-16}$$

therefore

$$\frac{dP}{dt} = \frac{\frac{\phi}{V}\left(\frac{dQ}{dt} + \theta\frac{dM}{dt}\right)}{1 + \frac{3\ r\ (1-\sigma)}{2\ b\ E}\rho\theta\phi} \tag{A-17}$$

Now the outflow is measured at the end of the distribution lines which contain gas at the same pressure as the tank. The flow across the thermodynamic boundary must include the flow required to pressurize the lines. Two assumptions for determining the flow into the lines may be considered:

1. Fluid expelled from the tanks thermodynamic boundary maintains its density while compressing gas in the lines either adiabatically or isothermally.

2. Fluid expelled from the tank does not affect the temperature distribution from the thermodynamic boundary to the system outlet, but the density in the lines changes adiabatically or isothermally.

The phenomena of assumption 1 can be described by writing the polytropic relationship for the volume of gas in the lines.

$$\frac{V_L}{V_{L_o}} = \left(\frac{P}{P_o}\right)^{-\frac{1}{N}} \qquad \text{(A-18)}$$

Taking logarithms and differentiating we have:

$$\frac{dV_L}{V_L} = -\frac{1}{N}\frac{dP}{P} \qquad \text{(A-19)}$$

The flow rate into the tank thermodynamic boundary due to the lines is therefore:

$$\frac{dM_L}{dt} = -\rho_t \frac{V_L}{NP}\frac{dP}{dt} \qquad \text{(A-20)}$$

Where N=1 for isothermal compression and N=1.4 for adiabatic compression.

Now writing A-14 in terms of the demand and line flow rates.

$$\frac{dP}{dt} = \frac{\phi}{V}\frac{dQ}{dt} + \frac{\phi\theta}{V}\frac{dM_L}{dt} + \frac{\phi\theta}{V}\frac{dM_d}{dt} - \frac{1}{V}\frac{dV}{dP}\frac{dP}{dt}\rho\phi\theta \qquad \text{(A-21)}$$

Substituting A-20 in A-21 and again solving for $\frac{dP}{dt}$ we have:

$$\frac{dP}{dt} = \frac{\frac{\phi}{V}\left(\frac{dQ}{dt} + \theta\frac{dM_d}{dt}\right)}{1 + \frac{\rho\theta\phi}{V_t}\frac{dV}{dP} + \frac{\rho\theta\phi}{NP}\frac{V_L}{V_t}} \qquad \text{(A-22)}$$

The relationships for assumption 2 are developed by assuming that the fluid density in the lines is related to the pressure by the polytropic exponent.

$$\rho = \rho_o\left(\frac{P}{P_o}\right)^{\frac{1}{N}} \qquad \text{(A-23)}$$

Again taking logarithms and differentiating we have:

$$\frac{d\rho}{\rho} = \frac{1}{N}\frac{dP}{P} \qquad \text{(A-24)}$$

Therefore, the flow rate into the tank from the lines is:

$$\frac{dM_L}{dt} = - \frac{\rho_L Y_L}{NP} \frac{dP}{dt} \tag{A-25}$$

Substituting A-25 into A-14 and solving for $\frac{dP}{dt}$ as before we have:

$$\frac{dP}{dt} = \frac{\frac{\phi}{V}\left(\frac{dQ}{dt} + \theta \frac{dM_d}{dt}\right)}{1 + \frac{\rho_t \phi\theta}{V_t} \frac{dV_t}{dP} + \frac{\rho_L \phi\theta}{NP} \frac{V_L}{V_t}} \tag{A-26}$$

N72-23791

A NUMERICAL SOLUTION OF THE NAVIER-STOKES EQUATIONS FOR SUPERCRITICAL FLUID THERMODYNAMIC ANALYSIS

P. J. Heinmiller
TRW Systems Group
Houston, Texas

May 1971

ABSTRACT

An explicit numerical solution of the compressible Navier-Stokes equations is applied to the thermodynamic analysis of supercritical oxygen in the Apollo cryogenic storage system. The wave character is retained in the conservation equations which are written in the basic fluid variables for a two-dimensional Cartesian coordinate system. Control-volume cells are employed to simplify imposition of boundary conditions and to ensure strict observance of local and global conservation principles. Non-linear real-gas thermodynamic properties responsible for the pressure collapse phenomonon in supercritical fluids are represented by tabular and empirical functions relating pressure and temperature to density and internal energy. Wall boundary conditions are adjusted at one cell face to emit a prescribed mass flowrate. Electrical heater input is treated as localized internal heat generation, a fraction of which may be radiated to the walls where it is added to the prescribed boundary heat flux. The effect of "tank stretch" on dP/dt is included as out-of-plane fluid expansion. Scaling principles are invoked to achieve acceptable computer execution times for very low Mach number convection problems. Detailed simulations of thermal stratification and fluid mixing occurring under low acceleration in the Apollo 12 supercritical oxygen tank are presented which model the pressure decay associated with de-stratification induced by an ordinary vehicle maneuver and heater cycle operation.

ACKNOWLEDGMENT

The author wishes to express his appreciation to Dr. W. E. Simon of NASA-MSC who contributed a number of helpful suggestions and provided the necessary computing support.

TABLE OF CONTENTS

INTRODUCTION

Origin of Problem

Gaseous oxygen required for life-support and electrical power generation aboard the Apollo Command and Service Module is stored in super-insulated double-wall spherical tanks which are a portion of the storage and supply system. In these tanks, oxygen is maintained at cryogenic temperatures and at pressures somewhat above the critical pressure. (See Table 1 for system operating parameters.) Under these conditions, the oxygen is in the super-critical state which results in a high-density single-phase compressible fluid suitable for expulsion under zero-gravity conditions.

Storage tank pressure is maintained relatively constant during fluid withdrawal by increasing the fluid temperature using an internal filament-type electrical heater. Prior to and including Apollo 13, the energy supplied by this heater was dispersed throughout the fluid by means of internal mixing fans. However, following the failure of the oxygen system during the Apollo 13 mission, the mixing fans were removed from subsequent oxygen tanks to minimize the possible combustion hazard.

Numerical studies by Kamat and Abraham [2] have shown that a substantial decrease in pressure can result from fluid mixing if the heater input is not well distributed beforehand. The decrease in pressure can be of sufficient magnitude to cause the fluid to return to a two-phase condition. Since natural convection would have to be relied upon to limit the temperature concentrations, a considerable effort was initiated to refine the understanding of the thermodynamic and fluid dynamic behavior of locally-heated supercritical oxygen stored in a low acceleration environment.

Stratification and Pressure Collapse

Due to the low thermal conductivity of supercritical oxygen, electricial heaters generate local heat concentrations. Under low accelerations, these concentrations do not disperse rapidly. Without a mechanical means of mixing the heated fluid with the surrounding cold fluid, subsequent heater cycles result in increasingly severe heat concentrations, or "thermal stratification."

Thermophysical properties of oxygen in the vicinity of the critical point are strongly nonlinear and therefore deviate from the properties of an ideal gas. One of the ramifications of the specific heat nonlinearity is that the bulk fluid temperature is not equal to the equilibrium temperature which would exist if the fluid were mixed or otherwise brought to thermal equilibrium.

The equation of state is also nonlinear in this region and is sensitive to small changes in temperature. The result is that a modest drop in the bulk temperature brought about by fluid mixing from a stratified condition can cause a substantial decrease in pressure or "pressure collapse". Kamat and Abraham [2] have shown that the pressure decreases monotonically with mixing so that the final pressure is always below any intermediate pressure. It is possible for the collapse pressure to drop below the critical pressure in which case the fluid becomes sub-critical, a condition in which liquid and gaseous phases may co-exist. This condition must be avoided if a uniform single phase fluid expulsion is to be maintained.

This paper describes an explicit numerical solution of the compressible conservation equations that govern natural convection in compressible fluids. Real fluid thermodynamic relations are employed so that the pressure collapse phenomenon can be observed in super-critical fluids. A number of additional effects have been incorporated in the solution for engineering application including "tank stretch," heater thermal mass, and heater radiation.

Comparisons are made between the results of the present solution and Apollo 12 flight data occurring at 8 hours GET. Several other verification test cases also are presented to demonstrate the program capability.

Table 1 Cryogenic System Operational Parameters* - Oxygen

(Apollo 14 And Subsequent)

Stored Fluid Weight (100% indication)	330.1 lb
Usable Fluid Weight	323.5 lb
Tank Volume	4.75 ft^3
Normal Operating Pressure	900 ± 35 psi
Pressure Switch Deadband (Min)	30 psi
Total Heater Power (prior to Apollo 14)	434.8 B/hr (528.6)
Bulk Fluid Temperature	160 to 530 °R

* Data taken from Reference 1

APPROACH

Under low acceleration conditions, the potential pressure collapse depends primarily upon the amount of heat concentrated in the portion of fluid surrounding the heater. The heater cycle time, however, depends upon the actual pressure rise and decay rates which, in turn, are related to the processes taking place in the heater thermal boundary layer and to other effects such as tank stretch. At 95% of tank quantity, tank stretch decreases the magnitude of the pressure rate and therefore the cycle time by almost a factor of two[1].

A detailed knowledge of the temperature, density, and fluid velocity distributions is necessary in order to describe the heating and mixing processes and the resulting thermodynamic behavior of supercritical oxygen in the Apollo cryogenic storage tanks. This information can be obtained only by simultaneously solving the conservation equations of mass, momentum, and energy. These equations are coupled nonlinear partial differential equations which are not amenable to analytical solutions for any but the most restrictive of problems. However, finite-difference numerical techniques have been developed which allow these equations to be solved in their entirety.

The general solution procedure is to integrate numerically the conservation equations from a given set of initial conditions subject to the various boundary conditions imposed by the physical system. Although the fluid motion in the Apollo storage tanks is three-dimensional, a two-dimensional solution of the conservation equations is adequate to resolve the basic mechanisms which produce stratification and mixing.

The basic model consists of a two-dimensional fluid slab of unit depth to which the conservation equations are applied. The momentum equations include the gravitational body force terms so that natural convection may develop. The basic provisions necessary to model the Apollo storage tank are: two acceleration components, a localized internal heat source, external heat leak, and a fluid outlet port. Non-linear thermodynamics require that real-gas properties be used. To adequately describe the actual pressure rise rate for engineering purposes, a number of refinements to the idealized model were required which include accounting for the thermal mass of the heater, heater radiation to the tank wall, and tank stretch.

Acceleration Components

In general, two acceleration components are required to describe the body forces acting on the fluid. Stratification develops under a uniform low-level acceleration in a constant relative direction. Such an acceleration arises from the centripetal acceleration $(\vec{\omega} \times \vec{\omega} \times \vec{r})$ associated with the three revolutions per hour roll rate used for passive thermal control (PTC).

Maximum mixing resulting from a G-spike, (e.g., RCS thruster firing) occurs when the direction of the G-spike is normal to the density gradient. A tangential acceleration $(\dot{\vec{\omega}} \times \vec{r})$ results from a change in the roll rate during spin-up to or de-spin from the PTC mode. The effects of coriolis acceleration, non-constant radius vector, and planetary gravity gradient are insignificant compared to the acceleration forces discussed above and are not considered in this analysis.

Internal Heater

The heater element is simulated as an internal energy source at an appropriate location in the fluid volume. No velocity boundary conditions are attempted at these "heater cells" due to the computational difficulty in resolving the flow boundary layer. The heater does not represent the heater cylinder itself but rather the heated fluid sheath surrounding the heater cylinder. The number of heater cells is selected such that the combined volume is equal to the "effective boundary layer volume". This effective volume has been postulated in order to explain observed pressure rise rates, since the grid spacing of the numerical solution is too coarse to resolve the actual thermal boundary layer. The effective boundary layer volume was derived on the basis of empirical flight data.

Heater Thermal Mass Effect

Heater-on operation is modeled as a prescribed heat generation rate within the heater cells. When steady-state heating conditions are approached, a power balance at the heater implies that the impressed electrical power is converted directly to a heating rate of the fluid sheath surrounding the heater. The heater thermal mass absorbs heater power until heat conduction into the fluid reaches steady-state. For the present purposes, this build-up rate is approximated as an equivalent linear ramp up to the steady-state rate which occurs during the interval T_{lag}. (See Nomenclature.) Defining C_{lag} as a ramp function, the internal heat generation rate then is given by:

$$\dot{Q} = C_{lag} \dot{Q}_{heater} \tag{1}$$

After the heater is turned off, the heater cylinder rejects the heat stored in its thermal mass. Assuming that the heater temperature returns to the previous low temperature, the inverse linear ramp was used for flux decay. The internal heat generation rate during the heater-off ramp then becomes

$$\dot{Q} = (1 - C_{lag}) \dot{Q}_{heater} \tag{2}$$

Heater Radiation

During the latter portions of the Apollo mission, the heater temperature rises high enough that thermal radiation plays an important heat transfer role. At a specified time in the mission, the energy radiated from the heater may be represented as a constant fraction of the heater power not absorbed by the thermal mass:

$$\dot{Q}_{rad} = C_{rad} (C_{lag} \dot{Q}_{heater}) \tag{3}$$

and the rate of heat entering the fluid becomes:

$$\dot{Q} = (1 - C_{rad}) C_{lag} \dot{Q}_{heater} \tag{4}$$

Outlet Port

A fluid outlet port is modeled at the periphery of the fluid volume by specifying a fluid velocity at a location on the boundary such that the prescribed mass withdrawal rate occurs. This same velocity is used to convect momentum and energy from the system.

It was necessary to relocate the outlet port from its actual position to a position lying in the plane of the model. The flow distortion introduced by this relocation appears to be negligible for the flowrates presently being considered.

Heat Leak

Heat entering the fluid after passing through the super-insulation surrounding the storage tank is called heat leak and for the Apollo oxygen tank has a nominal value of about 25 BTU/hr. The quantity entering the fluid model is proportioned according to the volume ratio C_{vol}. Heat leak is imposed as a uniformly distributed heat flux over the exposed fluid boundary. The decision to specify the heat flux at the boundary as opposed to specifying the boundary temperature was based upon the fact that the rate of heat leak into the fluid is more accurately known than the wall temperature of the inner tank. Global conservation principles also are more easily satisfied. Since oxygen is primarily transparent in the region, the energy radiated from the heater cylinder is not absorbed until it reaches the tank wall from which it enters the fluid by conduction.

Tank Stretch/Line Compression

The elasticity of the thin-wall tank permits a volume expansion with pressure (dV/dP) of about 3.6×10^{-5} ft^3/psi at the normal operating pressure. At high tank quantities (80%-100%) fluid pressure is very sensitive to density, and variations in tank volume have a significant effect on the pressure rise rate [1, p3-16] decreasing the magnitude of dP/dt by over 40% at 95% quantity. Tank stretch is modeled as an out-of-plane fluid expansion by permitting the unit z dimension to vary with pressure according to dV/dP.

Seto[3] derived an expression for the effect on dP/dt of fluid compression in the external plumbing. Tests with the equilibrium tank model described in this reference show that this effect is of the same order as the effect of tank stretch. For the present purpose, line compression is represented as an increase in the tank stretch factor dV/dP.

GOVERNING EQUATIONS

General Discussion

The equations governing the conservation of mass, momentum, and energy in a fluid system may be formulated in either Eulerian or Lagrangian coordinates. The Lagrangian formulation fixes the coordinate system in the fluid mass and is convenient for problems involving a free surface. However, accuracy is seriously impared with time as the coordinates deform and move with fluid convection.[4] In the Eulerian formulation, the coordinate system is fixed in the fluid volume so that the fluid moves through the coordinate system. For this reason, the Eulerian formulation is generally superior for complex convection problems and is used for the present analysis.

Richtmyer and Morton [4] and others recommend the use of conservation equations in the "conservative" or "divergence" form which preserves the conservation principles when solved at a finite number of discrete points. If the conservative form is not used, computational sources and sinks can appear as fluid is convected from one cell to the next, their origin being the non-constant coefficients appearing in front of the derivatives. For example, the mass leaving a cell through one of its faces does not necessarily appear in total in the adjacent cell. Although these errors are small, they occur at each cell interface at each time step and can accumulate with time. The propagation of these errors eventually can lead to computational instability. Computationally non-conservative equations are derived by performing flux balances on an infinitesimal control volume[5]. These equations can be converted to conservative form by adding the continuity equation to each of the other three conservation equations. The divergence form is developed directly from surface and volume integrals of flux vectors employing the Gauss Divergence Theorem[6].

A very clean form of the general conservation equations was obtained with minor modification from Goodrich[7]. These equations are in conservative form and are written in terms of the basic fluid variables for a two-dimensional Cartesian coordinate system. The non-dimensional form was not used because of the difficulty in assigning characteristic reference values for non-linear real fluid thermodynamic properties.

The general equations governing a compressible viscous fluid with body forces and internal heat source are:

Mass Continuity

$$\frac{\partial\rho}{\partial t} + \frac{\partial(\rho u)}{\partial x} + \frac{\partial(\rho v)}{\partial y} = 0 \tag{5}$$

X-Component Momentum

$$\frac{\partial(\rho u)}{\partial t} + \frac{\partial}{\partial x}(\rho uu + P + \tau_{xx}) + \frac{\partial}{\partial y}(\rho uv + \tau_{xy}) = \rho g_x \tag{6}$$

Y-Component Momentum

$$\frac{\partial(\rho v)}{\partial t} + \frac{\partial}{\partial x}(\rho vu + \tau_{xy}) + \frac{\partial}{\partial y}(\rho vv + P + \tau_{yy}) = \rho g_y \tag{7}$$

Energy

$$\begin{aligned}\frac{\partial(\rho E)}{\partial t} &+ \frac{\partial}{\partial x}[(\rho E + P)u + q_x + u\tau_{xx} + v\tau_{xy}] \\ &+ \frac{\partial}{\partial y}[(\rho E + P)v + q_y + v\tau_{yy} + u\tau_{xy}] = \dot{Q}_v\end{aligned} \tag{8}$$

where:

$$E = e + \tfrac{1}{2}(u^2 + v^2) \tag{9}$$

$$P = P(\rho, e) \tag{10}$$

$$T = T(\rho, e) \tag{11}$$

$$\begin{aligned} q_x &= -k\frac{\partial T}{\partial x} \\ q_y &= -k\frac{\partial T}{\partial y} \end{aligned} \tag{12}$$

$$\begin{aligned} \tau_{xx} &= -\frac{2}{3}\mu\left(2\frac{\partial u}{\partial x} - \frac{\partial v}{\partial y}\right) \\ \tau_{yy} &= -\frac{2}{3}\mu\left(2\frac{\partial v}{\partial y} - \frac{\partial u}{\partial x}\right) \\ \tau_{xy} &= -\mu\left(\frac{\partial u}{\partial y} + \frac{\partial v}{\partial x}\right) \end{aligned} \tag{13}$$

The form of the energy equation in which temperature is the integrated variable [5, Ch XIV] is not appropriate for supercritical fluid analysis since this form assumes a constant specific heat (C_v).

Program Formulation

The above equations are more general than necessary for the present analysis so that a number of non-critical terms were eliminated to improve computational speed.

An advantage in using the internal energy form of the energy equation is that the fluid temperature is almost entirely dependent upon the specific internal energy and only slightly dependent upon density. Therefore, over a relatively wide range of pressures, the relation $T=T(\rho,e)$ was replaced by the computationally simpler function involving only a one-dimensional table interpolation:

$$T = T\ (e) \tag{14}$$

Figure 1 shows this function (obtained from Weber's [8] data) plotted at 55, 60 and 65 atmospheres to indicate the error incurred by neglecting pressure variation in the vicinity of the critical point.

The form of the equation of state shown by eqn. (10) was not available, so that it was necessary to use the equivalent (though for this application computationally less desirable) relation

$$P = P\ (\rho,\ T) \tag{15}$$

which was available in Stewart's equation of state [9]. The relations selected for pressure and temperature are acceptable in that an iterative procedure is not required. However, if pressure is to be computed from temperature, the above approximation to the temperature-energy function may be more critical than if temperature is used only for heat conduction.

The general governing equations assume only that Stokes hypothesis regarding the viscosity coefficients holds, and that thermal radiation/absorbtion effects are insignificant. For the present application, a number of simplifications to these equations are made. First, the velocities developed in the low acceleration environment are so small that the kinetic energy terms in the energy equation may be neglected. Second, the low velocities coupled with the low viscosity of oxygen make the viscous terms in the energy equation negligible. For computational simplicity thermal conductivity and viscosity are assumed constant. The remaining viscous terms are further simplified by assuming that the fluid is incompressible as far as viscous dissipation is concerned.

Incorporating these simplifications in the general equations and rearranging, the governing equations used in this analysis are written.

Continuity

$$\frac{\partial \rho}{\partial t} = -\frac{\partial(\rho u)}{\partial x} - \frac{\partial(\rho v)}{\partial y} \tag{16}$$

X-Component Momentum

$$\frac{\partial(\rho u)}{\partial t} = -\frac{\partial(\rho uu)}{\partial x} - \frac{\partial(\rho uv)}{\partial y} - \frac{\partial P}{\partial x} + \rho g_x + \mu\left(\frac{\partial^2 u}{\partial x^2} + \frac{\partial^2 u}{\partial y^2}\right) \tag{17}$$

Y-Component Momentum

$$\frac{\partial(\rho v)}{\partial t} = -\frac{\partial(\rho vu)}{\partial x} - \frac{\partial(\rho vv)}{\partial y} - \frac{\partial P}{\partial y} + \rho g_y + \mu\left(\frac{\partial^2 v}{\partial x^2} + \frac{\partial^2 v}{\partial y^2}\right) \tag{18}$$

Energy

$$\frac{\partial(\rho e)}{\partial t} = -\frac{\partial(\rho e+P)}{\partial x} - \frac{\partial(\rho e+P)}{\partial y} + k\left(\frac{\partial^2 T}{\partial x^2} + \frac{\partial^2 T}{\partial y^2}\right) + \dot{Q}_v \tag{19}$$

Thermodynamic Relation

$$T = T(e) \tag{20}$$

Equation of State

$$P = P(\rho,T) \tag{21}$$

Typical initial conditions are:

$$\begin{aligned} u(x,y,o) &= 0 \\ v(x,y,o) &= 0 \\ P(x,y,o) &= P_o(x,y) \text{ (specified to balance body forces)} \\ T(x,y,o) &= T_o \\ \rho(x,y,o) &= \rho_o(P,T_o) \\ e(x,y,o) &= e_o(T_o) \end{aligned} \tag{22}$$

Boundary conditions for a closed tank take the form:

$$\begin{aligned} u(w,y,t) &= u(x,w,t) = 0 \\ v(w,y,t) &= v(x,w,t) = 0 \\ \frac{\partial T}{\partial x}(w,y,t) &= \frac{\partial T}{\partial y}(x,w,t) = -\frac{q(t)}{k} \text{ (heat leak)} \end{aligned} \tag{23}$$

where w indicates a value of x or y at any wall.

The addition of boundary conditions defining a heater and an outlet port is discussed more thoroughly in a following section. Basically, however, the heater is a region of fluid in which internal heat generation is specified, and the outlet port is defined by a normal velocity at a section of the tank wall such that a prescribed mass withdrawal rate occurs. This exit velocity convects mass, momentum, and energy from the system.

FINITE DIFFERENCE FORMULATION

Discussion of Numerical Techniques

A wide variety of finite-difference schemes are available for evaluating the governing equations, and Richtmyer and Morton [4] provides a good source reference. The AIAA reprint series [10] contains an extensive bibliography and a collection of the more interesting recent papers relating primarily to high-speed flow. Numerical methods discussed in Ralston and Wilfe[11], and Cheng[12] summarizes the fundamental principles relating to the numerical solution of the Navier-Stokes equations.

The numerical integration of the governing equations is performed at a finite number of discrete points located throughout the fluid volume. The difference equations are obtained by replacing the partial derivatives with suitable finite-difference approximations typically derived by Taylor-series expansions in space and time. Alternately, the difference equations can be derived directly from fundamental conservation principles applied to a fluid control volume [12]. This method avoids taking the limit as $\Delta V \to 0$ to form the differential equations followed by the reverse process of discretization. The two methods are basically equivalent; however, the latter is quite useful for visualizing and formulating conservative-form difference equations particularly in curvilinear coordinate systems and parameter spaces.

The time variable is discretized and is given by $t^n = n\,\Delta t$. The fluid state is advanced from the (n) time plane to the (n+1) time plane by integration. When the time derivative is approximated by a forward difference, all information used to advance the state to (n+1) Δt is available at the n^{th} time plane. This is the explicit formulation and is equivalent to a step integration procedure. The two-step Lax-Wendroff [4] scheme generates provisional values at $(n + \frac{1}{2})\,\Delta t$ which are used to advance to the (n+1) time plane. This procedure centers the time difference which gives second order accuracy in time.

Various other numerical schemes are available which use weighted averages of data obtained from several time planes (n-1), (n), and (n+1) to obtain the updated value at (n+1). Schemes which require data at the (n+1) time plane to advance the time to (n+1) Δt are implicit and require the simultaneous solution of high-order systems of equations. Efficient relaxation techniques make the implicit formulation quite powerful for certain types of problems.

Most implicit schemes are unconditionally stable for any time step, whereas, explicit schemes are stable only when rather stringent stability conditions are observed. However, explicit schemes are straight forward and require the least computation per time step. The advantage of one scheme over the other depends upon the rate at which the fluid properties are changing. Explicit schemes are preferred for time-dependent problems in high-speed flow and for problems in which wave propagation is important. Implicit schemes are effective for problems in low speed flow and certain steady-state problems. The use of scaling principles to transform the low speed flow problem into one in which the transport mechanisms occur very much faster than in real time appears to be effective in broadening the class of problems which may be solved efficiently using the explicit formulation.

Problems can arise in achieving stability in the explicity-formulated conservation equations. Lax and Wendroff[4] used second-order accurate centered time differences. Rusanov[13] added numerical damping terms to the space differences. Goodrich[14] has shown that the numerical damping terms of Rusanov can be represented by a weighted biasing of the convective difference terms; a method which is similar to the upstream differencing technique used below. Richtmyer[4] has suggested adding pseudo-viscosity terms of the form $a \frac{\partial u}{\partial x} \left| \frac{\partial u}{\partial x} \right|$ to stabilize the momentum equations.

Technique Employed

The technique employed in this analysis is patterned after the method of Courant, Fredricks, and Lewy (1929) for the wave equation[4, p 292]. In this method, the momentum equations are advanced to the (n+1) time plane first, and the updated velocities u^{n+1}, v^{n+1} are then used to advance the continuity and energy equations. By performing the integration in two steps, the continuity and energy equations appear to be semi-implicit, although they are effectively explicit since the necessary information is available from previous calculation. However, when this method is used with centered space differences, physically unrealistic temperature profiles result as fluid convection takes place. Richtmyer [4, p 292] credits the cure for this problem to Lelevier. This solution replaces the centered space differences used for the convective terms by forward or backward space differences as the sign of the convecting velocity is negative or positive. This procedure is quite common and goes by a number of names including upwind or upstream differencing and donor-cell differencing. These differences, however, are only of first order accuracy.

As applied to the grid system used in this analysis, upstream differencing has the effect of defining the values of the convected properties at the control-volume interface as being the values of the upstream cell. Central differencing implies averages of the adjacent cell values at the interface.

Grid System

Grid points are uniformly spaced in the x and y directions at constant intervals $\Delta x = \Delta y = L$. It is convenient to visualize an elemental control volume $\Delta V = \Delta x \ \Delta y \ \Delta z = L^3$, referred to as a cell, surrounding each grid point. According to Cheng [12], "The fluxes must be evaluated on the cell boundary while the conserved quantities are determined only as averages over the cell."

The two-dimensional fluid volume is characterized by several hundred of these cubic cells arranged in a plane. The circular configuration of the oxygen tank crosssection is approximated in a stepwise fashion by removing cells from corners of the rectangular cell grid. For example see Figure 9.

Individual cells are identified by the indicies (i,j) in the x- and y- direction as shown in Figure 2 so that the physical position of the center of cell (i,j) is located at

$$(x_i, y_j) = (i-\tfrac{1}{2})\Delta x, \ (j-\tfrac{1}{2})\Delta y \qquad (24)$$

The integrated fluid properties ρ, ρu, ρv, and ρe are identified with each cell center and represent the average properties over the cell volume. The value of a property at the center of cell (i,j) is designated for example as

$$P_{ij} = P(x_i, y_j) \qquad (25)$$

For mathematical consistency, the velocities and the thermodynamic properties of the fluid in the cell also are defined at the cell center so that the following relationships can be used:

$$u_{ij} = \rho u_{ij} / \rho_{ij}$$

$$v_{ij} = \rho v_{ij}/\rho_{ij} \qquad (26)$$

$$T_{ij} = T\ (\rho e_{ij}/\rho_{ij})$$

$$P_{ij} = P\ (\rho_{ij}, T_{ij})$$

It is convenient to define properties, certain gradients, and convection velocities at the cell walls which lie midway between grid points, and which are indicated by half-subscripts. Convection velocities at these faces are evaluated by linear interpolation:

$$u_{i-\frac{1}{2},j} = \tfrac{1}{2}(u_{i-1,j} + u_{ij})$$

$$v_{i,j-\frac{1}{2}} = \tfrac{1}{2}(v_{i,j-1} + v_{ij}) \qquad (27)$$

To achieve upstream differencing for the convection terms, the value of a convected property is defined as the value existing in the upstream cell as determined by the sign of the convecting velocity at the cell interface. Convected properties evaluated in this manner are $\rho, \rho u, \rho v$, and $(\rho e + P)$. The result is that the upstream property is convected across the interface at the average velocity. A typical flux at the left face of cell (i,j) is illustrated as

$$\rho_{i-\frac{1}{2},j}\ u_{i-\frac{1}{2},j} \qquad (28)$$

The difference in mass flux across cell (i,j) in the x-direction becomes

$$\delta_x(\rho u)_{ij} = \rho_{i+\frac{1}{2},j}u_{i+\frac{1}{2},j} - \rho_{i-\frac{1}{2},j}\ u_{i-\frac{1}{2},j} \qquad (29)$$

Since the quantities at cell walls are invarient during calculations at the upstream and downstream cells, local conservation principles are observed identically. Whatever quantity leaves one cell across a cell wall must enter the adjacent cell.

An attempt was made to describe the transition of fluid properties from one cell to the next as a parabola which was biased in the upstream direction.[15] While this scheme was numerically stable, it did not eliminate temperature decreases in cells surrounding the high temperature heater cell.

The pressure gradient across the node is represented by a centered space difference. To accomplish this in the present formulation, the cell wall pressure is defined as an average:

$$P_{i-\frac{1}{2},j} = \tfrac{1}{2}(P_{i-1,j} + P_{i,j}) \tag{30}$$

The resulting pressure difference at cell (i,j),

$$\delta_x P_{ij} = P_{i+\frac{1}{2},\,j} - P_{i-\frac{1}{2},\,j} \tag{31}$$

is identical to the centered pressure difference taken across two cell intervals.

The diffusion terms such as $\frac{\partial^2 T}{\partial x^2}$ and $\frac{\partial^2 u}{\partial x^2}$ are not influenced by fluid convection and usual centered differences are used:

$$\delta_x{}^2\, T_{ij} = T_{i-1,j} - 2T_{ij} + T_{i+1,j} \tag{32}$$

While not employed here due to time limitation, it would be convenient to express the first temperature differences at the cell walls and obtain the second differences as

$$\delta_x{}^2\, T_{ij} = \delta_x\, T_{i+\frac{1}{2},j} - \delta_x\, T_{i-\frac{1}{2},j} \tag{33}$$

A temperature-dependent conductivity could be added by a simple extension as:

$$\delta_x(k\,\delta_x\, T)_{ij} = (k\,\delta_x\, T)_{i+\frac{1}{2},j} - (k\,\delta_x\, T)_{i-\frac{1}{2},j} \tag{34}$$

The difference forms of the governing equations employed are shown below along with the necessary supporting equations and definitions. Unless otherwise indicated, data is taken at the n^{th} time plane.

$$\begin{aligned}
\rho u_{ij}^{n+1} &= \rho u_{ij}^{n} + \frac{\Delta t}{\Delta x}\left[-\delta_x \rho uu_{ij} - \delta_y \rho uv_{ij} - \delta_x P_{ij} - \rho_{ij} g_x + \frac{\mu}{\bar{\rho}\Delta x}(\delta_x^2 \rho u_{ij} + \delta_y^2 \rho v_{ij})\right] \\
\rho v_{ij}^{n+1} &= \rho v_{ij}^{n} + \frac{\Delta t}{\Delta x}\left[-\delta_x \rho vu_{ij} - \delta_y \rho vv_{ij} - \delta_x P_{ij} - \rho_{ij} g_x + \frac{\mu}{\bar{\rho}\Delta x}(\delta_x^2 \rho v_{ij} + \delta_y^2 \rho v_{ij})\right] \\
\rho_{ij}^{n+1} &= \rho_{ij}^{n} + \frac{\Delta t}{\Delta x}(-\delta_x \rho u_{ij} - \delta_y \rho v_{ij}) \\
\rho e_{ij}^{n+1} &= \rho e_{ij}^{n} + \frac{\Delta t}{\Delta x}\left[-\delta_x \rho hu_{ij} - \delta_y \rho hv_{ij} + \frac{k}{\Delta x}(\delta_x^2\, T + \delta_y^2\, T)\right]
\end{aligned} \quad . \tag{35}$$

Typical quantities used in the above equations are illustrated below in the x-direction. Quantities relating to the y-direction are analogous.

$$\rho h_{ij} = \rho e_{ij} + P_{ij} \tag{36}$$

$$\delta_x \rho u_{ij} = \rho_{i+\frac{1}{2},j} u^{n+1}_{i+\frac{1}{2},j} - \rho_{i-\frac{1}{2},j} u^{n+1}_{i-\frac{1}{2},j}$$

$$\delta_x \rho uu_{ij} = \rho u_{i+\frac{1}{2},j} u_{i+\frac{1}{2},j} - \rho u_{i-\frac{1}{2},j} u_{i-\frac{1}{2},j} \tag{37}$$

$$\delta_x \rho vu_{ij} = \rho v_{i+\frac{1}{2},j} u_{i+\frac{1}{2},j} - \rho v_{i-\frac{1}{2},j} u_{i-\frac{1}{2},j}$$

$$\delta_x \rho hu_{ij} = (\rho e_{i+\frac{1}{2},j} + P_{i+\frac{1}{2},j})\, u^{n+1}_{i+\frac{1}{2},j} - (\rho e_{i-\frac{1}{2},j} + P_{i-\frac{1}{2},j})\, u^{n+1}_{i-\frac{1}{2},j}$$

$$\delta_x^2 \rho u_{ij} = \rho u_{i-1,j} - 2\rho u_{ij} + \rho u_{i+1,j}$$

$$(38)$$

$$\delta_x^2 \rho v_{ij} = \rho v_{i-1,j} - 2\rho v_{ij} + \rho v_{i+1,j}$$

$$u^{n+1}_{i+\frac{1}{2},j} = \frac{1}{2}\left(\frac{\rho u^{n+1}_{i+1,j}}{\rho^{n}_{i+1,j}} + \frac{\rho u^{n+1}_{ij}}{\rho^{n}_{ij}}\right) \tag{39}$$

$$P_{i+\frac{1}{2},j} = \frac{1}{2}(P_{ij} + P_{i+1,j}) \tag{40}$$

If $u_{i+\frac{1}{2},j} > 0$	If $u_{i+\frac{1}{2}} < 0$ (41)
$\rho_{i+\frac{1}{2},j} = \rho_{ij}$	$\rho_{i+\frac{1}{2},j} = \rho_{i+1,j}$
$\rho u_{i+\frac{1}{2},j} = \rho u_{ij}$	$\rho u_{i+\frac{1}{2},j} = \rho u_{i+1,j}$
$\rho v_{i+\frac{1}{2},j} = \rho v_{ij}$	$\rho v_{i+\frac{1}{2},j} = \rho v_{i+1,j}$
$\rho e_{i+\frac{1}{2},j} = \rho e_{ij}$	$\rho e_{i+\frac{1}{2},j} = \rho e_{i+1,j}$
$P_{i+\frac{1}{2},j} = P_{ij}$ (work terms)	$P_{i+\frac{1}{2},j} = P_{i+1,j}$

Stability Conditions

Stability of finite-difference equations is discussed in detail in Richtmyer and Morton.[4] The basic requirements for a stable differencing scheme is that the difference equations converge to the differential equations in the limit as $\Delta x \to 0$, $\Delta t \to 0$ which implies that disturbances in the solution decay with time. Stability constraints limit the maximum time increment (Δt) permissible.

The difference analogs of the Navier-Stokes equations are too complex to be fully analyzed with current stability analysis methods. The standard procedure is to evaluate the stability of the hyperbolic and the parabolic terms separately and to use the more restrictive of the two stability constraints.

In the explicit formulation of the Navier-Stokes equations, the hyperbolic limit is usually the most restrictive and results in the stability condition

$$(|u| + c) \frac{\Delta t}{\Delta x} \leq 1 \tag{42}$$

where u is the fluid velocity and c is the local adiabatic speed of sound. If $u << c$, the condition may be interpreted as limiting the propagation of a pressure wave to the distance of one space increment during a time step Δt.

For a two-dimensional problem, the stability condition becomes

$$(|\vec{u}| + c) \frac{\Delta t}{\Delta x} \leq \frac{1}{\sqrt{2}} \tag{43}$$

In the present problem, under the conditions being considered, the speed of sound is about 2500 ft/sec. With a grid spacing of Δx=.1 ft. the theoretical stability limit gives $\Delta t = .283 \times 10^{-4}$ sec.

Modification For Tank Stretch

Tank stretch affects the fluid state primarily by changing the density of the fluid properties. The work done on the boundaries changes the internal energy and also must be included.

During a tank expansion, the mass residing in an arbitrary volume becomes distributed throughout a larger volume. In the present Eulerian formulation, it is very difficult to adjust the x-y fluid boundaries to achieve this volume increase. The change was taken up in the z direction by permitting the unit depth to increase. Since no fluid crosses a node boundary during such an expansion, the mass (m) in the volume is unchanged.

Multiplying through by the node volume, $V=L^2L_z$, the continuity equation on a mass basis becomes:

$$\frac{\partial m}{\partial t} \equiv \frac{\partial \rho V}{\partial t} = -V\left(\frac{\partial \rho u}{\partial x} + \frac{\partial \rho v}{\partial y}\right) \qquad (44)$$

Upon discretizing the time variable and introducing the forward time difference, the equation becomes:

$$\frac{m^{n+1}-m^n}{\Delta t} \equiv \frac{\rho^{n+1}V^{n+1}-\rho^n V^n}{\Delta t} = -V^n \left(\frac{\partial \rho u}{\partial x} + \frac{\partial \rho v}{\partial y}\right) \qquad (45)$$

Finally, dividing by $\frac{V^{n+1}}{\Delta t}$ and rearranging,

$$\rho^{n+1} = \frac{V^n}{V^{n+1}} \left[\rho^n + \Delta t \left(\frac{\partial \rho u}{\partial x} + \frac{\partial \rho v}{\partial y}\right)\right] \qquad (46)$$

The above volume ratio is represented as

$$C_{str} = \frac{V^n}{V^{n+1}} = \frac{V^n}{V^n + \Delta V} \qquad (47)$$

where

$$\Delta V = \frac{dV}{dP} \Delta\bar{P} \qquad (48)$$

$\Delta\bar{P}$ = change in average tank pressure during Δt.

The same argument can be used to develop the expressions for the momentum and energy equations. However, the rate of work done on the boundary during an expansion must be included in the energy equation.

$$\frac{dW}{dt} = PL^2 \frac{dL_z}{dt} = P\frac{dV}{dt} \qquad (49)$$

Upon discretization

$$\frac{\Delta W}{\Delta t} = P \frac{\Delta V}{\Delta t} \tag{50}$$

Next, dividing by $\frac{V^{n+1}}{\Delta t}$ as before, the work done per unit volume during Δt becomes:

$$\frac{\Delta W}{V^{n+1}} = \frac{P \Delta V}{V^{n+1}} = P \frac{V^{n+1} - V^{n}}{V^{n+1}} \tag{51}$$

or

$$\frac{\Delta W}{V^{n+1}} = P \left(1 - \frac{V^{n}}{V^{n+1}}\right) \tag{52}$$

and finally,

$$\frac{\Delta W}{V^{n+1}} = P (1 - C_{str}) \tag{53}$$

Since this is the work done on the boundary by the fluid, it must be subtracted from the available internal energy in the cell.

The conservation equations modified for tank stretch are collected together below in a form showing just the time differences:

$$\begin{aligned} \rho^{n+1} &= C_{str} \left[\rho^{n} + \Delta t \left(\frac{\partial \rho u}{\partial x} + \frac{\partial \rho v}{\partial y}\right)\right] \\ \rho u^{n+1} &= C_{str} \left[\rho u^{n} + \Delta t \left(\ldots \quad\right)\right] \\ \rho v^{n+1} &= C_{str} \left[\rho v^{n} + \Delta t \left(\ldots \quad\right)\right] \\ \rho e^{n+1} &= C_{str} \left[\rho e^{n} + \Delta t (\ldots)\right] - \bar{P} (1 - C_{str}) \end{aligned} \tag{54}$$

where the average tank pressure $\bar{P}$ is used for the work term.

For computational reasons, C_{str} lags by one time step the above calculations so that in reality it is defined as:

$$C_{str} = \frac{V^{n-1}}{V^{n}} \tag{55}$$

NUMERICAL BOUNDARY CONDITIONS

Boundary Location

Consistent with the control-volume concept, solid boundaries were located at the outward-looking faces of the boundary cells. This location has distinct advantages in simplifying the definition and imposition of boundary conditions.

The alternative to this formulation (i.e. placing boundary mesh points at the wall surface) creates problems in evaluating the fluid properties at the wall, and global conservation may not be observed computationally. In this context, Roache and Mueller[16] cited the difficulty of imposing adiabatic (and therefore any chosen heat flux) conditions at the wall. They also observed that non-conservative methods used to define the wall density led to slow but continuous mass loss in a flow problem over a backstep.

The procedure of defining flux quantities and convection velocities at cell faces further simplifies the imposition of boundary conditions, and permits a unified application of the conservation equations to both interior and boundary cells. This procedure also avoids the use of imaginary grid points located outside the fluid boundary defined by reflection principles. The present method is considerably simpler to apply when flow obstructions or wall irregularities are considered.

Boundary Values

Convection velocities are set to zero at boundary surfaces thus assuring strict global conservation for convective terms. Pressure at the wall, which is necessary only for the momentum equations, is obtained by linear extrapolation from the first two normal interior grid points. Thermal boundary conditions take advantage of the fact that the heat leak is more accurately known than the temperature of the inner tank wall. When calculated at a boundary cell, temperature difference equations are employed which make use of the relations

$$\left.\frac{\partial T}{\partial x}\right|_{\text{wall}} = -\frac{q_{x\ \text{leak}}}{k}$$
$$\left.\frac{\partial T}{\partial y}\right|_{\text{wall}} = -\frac{q_{y\ \text{leak}}}{k} \tag{56}$$

where $q_{x\ \text{leak}}$ and $q_{y\ \text{leak}}$ are the boundary heat fluxes obtained by distributing the known heat leak rate $\dot{Q}_{\text{leak}}$ uniformly over the exposed surface area. This formulation identically satisfied the global energy balance and avoids the difficulty in defining the thermal boundary condition discussed by Roach and Mueller.[16]

Separate equations are used at boundary cells to evaluate the viscous dissipation terms in the momentum equations. For example, instead of the centered second difference terms used at interior cells which have the form:

$$(\delta_x^2\ \rho u)_{ij} = (\rho u_{i-1,j} - 2\rho u_{ij} + \rho u_{i+1,j}) \tag{57}$$

forward and backward second differences are employed which make use of the zero velocity conditions at the wall:

$$\begin{aligned} (\delta_x^2\ \rho u)_{ij} &= (-3\ \rho u_{ij} + \rho u_{i+1,j}) \text{ at left wall} \\ (\delta_x^2\ \rho u)_{ij} &= (\rho u_{i-1,j} - 3\rho u_{ij}) \text{ at right wall} \end{aligned} \tag{58}$$

Boundary conditions are imposed at the exterior face of cell (20, 10) such that the prescribed mass withdrawal rate occurs. Since the sign of the convection velocity $u_{20\frac{1}{2},10}$ must be positive, the necessary quantities at the cell wall (P, ρ, ρu, ρv, and ρe) are obtained by linear extrapolation of the form

$$\rho_{i+\frac{1}{2},j} = \tfrac{1}{2}(-\rho_{i-1,j} + 3\rho_{ij}) \tag{59}$$

The necessary convection velocity is obtained from the mass flow relation $\dot{m} = \rho A u$ as

$$u_{20\frac{1}{2},10} = \frac{\dot{m}}{\rho_{20\frac{1}{2},10} L^2} \tag{60}$$

With the cell wall quantities thus defined, the difference equations are applied at the outlet port cell as at any other cell. The convection of mass, x- and y- momentum, and enthalpy from the system takes place automatically.

SCALING PRINCIPLES

Computational stability considerations place stringent requirements on the permissible size of the time step (Δt) required to integrate the governing equations in the explicit formulation. The time step is determined by the time interval required for a pressure wave to propagate the distance of one cell. Time steps of this order are required for problems in high-speed flow or for problems in which pressure wave propagation contributes significantly to the solution. In the present problem, wave propagation may be of importance if fluid oscillations following a G-spike are of sufficient magnitude to destroy thermal gradients generated by heater operation under a low-g environment.

However, fluid heating and stratification occur on a time scale very much larger than that of wave motion, and the resulting computer time required to simulate an appropriate duration of flight is excessive. For this reason it was necessary to introduce scaling principles to transform the original problem into an equivalent scaled problem in which certain mechanisms of importance occur in the scaled time very much faster than in real time. Since non-linear real gas properties are used to describe the fluid temperature and pressure, the thermodynamic state cannot be scaled easily. Therefore, the conditions governing thermal stratification and fluid mixing are adjusted so that these mechanisms operate in scaled time. The desired rates of heating, fluid withdrawal, and fluid motion are increased such that the resulting pressures and temperatures remain unaltered at corresponding times in the scaled and unscaled systems.

The specific heat (C_v), pressure (P), temperature (T), and density (ρ) are not altered. However, the transport constants, thermal conductivity (k) and absolute viscosity (μ), are adjusted as required. Since the values of μ and k for supercritical oxygen are small and do not dominate the stratification and mixing mechanisms, these parameters are considered constant. Therefore, the following principles have been applied. The scale factor is designated by s, and the subscript s represents a value appearing in the scaled system such that the real time t is given by

$$t = st_s \tag{61}$$

The following constraints have been placed upon the scaled system:

$$\begin{aligned} \rho_s &= \rho \qquad \text{(density)} \\ T_s &= T \qquad \text{(temperature)} \end{aligned} \tag{62}$$

$(C_p)_s = C_p$ (specific heat)

$L_s = L$ (characteristic length)

Since it is desired that the flow processes occur more rapidly,

$$\begin{array}{lll} u_s = su & \text{(x velocity)} & \\ v_s = sv & \text{(y velocity)} & (63) \\ q_s = sq & \text{(heat flux)} & \\ \dot{m}_s = s\dot{m} \text{ mass flow rate} & \text{(mass flow rate)} & \end{array}$$

The similarity parameters which apply are:

Reynolds Number $R_e = \dfrac{\rho VL}{\mu} = \dfrac{\text{inertial forces}}{\text{viscous forces}}$

Prandtl Number $P_r = \dfrac{C_p\mu}{k} = \dfrac{\text{heat generation}}{\text{heat conduction}}$

Nusselt Number $N_u = \dfrac{qL}{k\Delta T} = \dfrac{\text{total heat transfer}}{\text{conductive heat transfer}}$

Grashof Number $G_r = \dfrac{\rho^2 g\beta\Delta T\ L^3}{\mu^2} = \dfrac{\text{bouyant forces}}{\text{viscous forces}}$

To maintain similarity of R_e, μ is scaled as:

$$\mu_s = s\mu. \qquad (64)$$

Similarity of both P_r and N_u require that:

$$k_s = sk. \qquad (65)$$

Recognizing that the heat diffusion rate must be scaled, the requirement placed upon k can be obtained directly from the definition of the thermal diffusivity.

$$\alpha_s = s\alpha = s\left(\frac{k}{\rho C_p}\right). \qquad (66)$$

Since the compressibility (β) remains unchanged by the initial constraints, to maintain Grashof number similarity, the acceleration must be scaled as:

$$g_s = s^2 g. \tag{67}$$

It should be emphasized that this scaling procedure speeds up the physical processes occurring in the fluid without disturbing the thermodynamic properties of the fluid itself. To accomplish this, it is necessary to adjust only the transport properties μ and k. In particular, the properties which determine the sonic velocity in the fluid have been preserved. The basic purpose for scaling is to increase the ratio of the fluid velocity to the sonic velocity (Mach number) because the sonic velocity of the explicit numerical solution limits the size of the permissible computation time steps.

Verification of this scaling procedure was performed by comparing temperature and velocity profiles taken at corresponding times from computer runs in which differing scale factors are used. In addition, good results were obtained for the Apollo 12 pressure collapse and heater cycle simulations in which scale factors of 2400 and 6000 were employed.

The increase in acceleration required to maintain the Grashof number in the scaled solution affects the required hydrostatic pressure distribution and, therefore, the distribution of the fluid mass. However, for problems involving a low-G environment, a scale factor which permits a reasonable simulation time gives rise to a negligibly small fictitious pressure gradient.

It appears that the maximum valid scale factor is restricted by the magnitude of the acceleration. Figure 3 shows the relative increase in hydrostatic pressure from the center of the tank to the tank wall necessary to counteract the scaled gravitational body forces. At a given G-level, experimentation indicates that a scale factor that produces a 1% pressure increase does not alter the convection or thermodynamic behavior observed in the Apollo 12 simulation. It should be cautioned that scaling amplifies fluid-dynamic start-up transients resulting from imprecisely known initial conditions (eg. the velocity profile around the outlet port), so that additional scaling restrictions must be considered.

In addition, it should be noted that stability conditions relate permissible time steps to thermal conductivity and to fluid viscosity. However, these constraints are less restrictive of the scale factor than the G-constraint for the present problem.

NUMERICAL RESULTS

Natural Convection in a Rectangular Enclosure

A test case in natural convection was run and the results are compared with an incompressible solution of a similar problem obtained by Wilkes and Churchill.[17]

A two-dimensional rectangular enclosure containing an incompressible fluid is oriented in a vertical plane with respect to the gravity vector. The left wall is held at a constant temperature T_1, and the right wall is held at a higher temperature T_2 also assumed constant. The other two walls are insulated. Initially, the fluid is at rest and at a temperature equal to the average of the boundary wall temperatures. The problem is to find the fluid velocity components and temperature at points throughout the fluid as steady-state conditions are approached.

As heat conduction takes place, a negative horizontal density gradient develops. The resulting unbalanced vertical buoyant forces cause two vortices to form with a net counter-clockwise rotation of the fluid. As the flow continues, the density gradient deforms and the two vortices eventually merge into one due to the viscous dissipation of momentum. As steady-state conditions are approached, the moment produced by the viscous forces acting at the walls balances the net buoyant moment.

Wilkes and Churchill introduced the vorticity and stream functions into the non-dimensionalized equations of motion. A linear density dependence upon temperature was used to produce the essential density gradients for natural convection. An implicit alternating direction technique was used to advance the time-dependent solution toward steady state. Figures presented[17] show the stream function and isotherms at several times including steady state. The dimensionless conditions associated with these figures are: $P_r = .733$, $G_r = 20,000$, $N_n = 2.874$.

The formulation used in the present solution necessitated two modifications to the problem. First, fluid compressibility was introduced in order to compute pressure explicity in terms of temperature and density. The ideal gas relation was assumed for this purpose. Second, the constant-temperature boundary conditions were changed to constant-heat-flux boundary conditions to be compatible with the model capability developed for simulation of heat leak into the Apollo oxygen tank.

The compressibility modification had a negligible effect on the solution since the vertical pressure differential was kept small with respect to the bulk fluid pressure. The second modification resulted in observable differences in the temperature profiles near the vertical walls. However, the basic character of the temperature profile away from these walls is preserved, and the resulting velocity profiles are similar to those obtained by Wilkes and Churchill.

The fluid properties, heating rate, and acceleration were adjusted so that the proper boundary temperatures were approached at steady-state. The final dimensionless quantities achieved were: Pr = .611, Gr = 21,000, and Nu = 3.88 which are in reasonable agreement with the Wilkes and Churchill values and yielded similar results. These values were computed using the average extrapolated wall temperatures.

A 10 x 10 cell grid was used to describe the fluid volume. Dimensions of the square enclosure, the bulk density, and the compressibility of the fluid were selected to yield a problem in which heating and fluid motion took place rapidly in real time in order to minimize computer time. Problem conditions are shown in Figure 4.

Figure 5a is a computer-generated velocity vector plot which shows the two initial counter-clockwise rotating vortices after 1/2 second of flow development. Figures 5b and 5c show the two vortices merging into one and the development of circularized flow. Figure 5d shows the essentially steady velocities at 4.95 seconds. Figure 6 shows the same vector plot at 4.95 seconds on which the dimensionless stream function obtained from the Wilkes and Churchill solution has been superimposed. Steady-state temperature profiles at ten horizontal cross-sections and fluid isotherms are shown in Figures 7 and 8. The general shape of the isotherms is in good agreement with the dimensionless isotherms of Wilkes and Churchill.

It is important to note the difference in the thermal boundary conditions. Isotherms cannot intersect the constant temperature walls used by Wilkes and Churchill. However, to maintain a uniform heat flux at the wall as assumed in the present solution, the wall temperature must vary in the vertical direction and isotherms intersect these walls as shown. Although the present results cannot be compared directly with those of Wilkes and Churchill, the general character of the solutions appears to be in reasonable agreement.

It is interesting to note that starting from zero, the fluid rotation rate passes through a maximum before approaching the steady-state rate. This phenomenon is the result of the inertial lag in responding to a change in heat flux at the walls (as occurs at t = 0). During this lag, high temperature and low temperature fluid masses accumulate near the respective walls, resulting in an over-acceleration of the fluid. The bulk rotation rate then builds up to a maximum and carries the heated and cooled fluid elements across the vertical centerline. At this point, a net counter-acting moment develops which retards the bulk rotation, and the steady-state rate is approached asymptotically.

Apollo 12 Pressure Collapse Simulation

The program was operated for flight conditions to demonstrate capability to simulate the stratification and mixing of supercritical oxygen which takes place under a flight-type acceleration environment. These conditions are shown in Figure 9 and are approximately those of the Apollo 12 mission at 7:30 GET. The density corresponds to the 95% tank quantity.

The heat added to the fluid cross section was input at cell (12,10) as shown in Figure 9. This single heater cell represents a heater boundary layer volume of 1.73 cubic inches. The rate of oxygen withdrawal was 1.4 lbm/hr. The outlet port was the exterior face of cell (20,10). The pressure limits for the heater switch were set at 860 and 900 psi so that the heater cycled automatically keeping the bulk pressure within a 40 psi dead band. A constant acceleration of $2\text{x}10^{-8}$ G's was applied in the -Y direction. At a simulation time of 70.5 minutes, an acceleration step to 10^{-4} G's was applied in the -X direction and the heater was turned off. The scale factor of 2400 was used in this simulation to achieve a computer time to simulation time ratio of 5/1 using a program time step of $.5 \times 10^{-4}$ seconds.

Figure 10 shows the stratified tank pressure (upper curve) and the equilibrium pressure (lower curve) as functions of time. The simulation started from equilibrium conditions. The equilibrium pressure rise rate was 3.7 psi/minute and the decay rate was -3.8 psi/minute. After 70 minutes of stratification, the minimum potential pressure collapse developed was 80 psi. The general divergence of the two curves shows that a quasi-steady state pressure collapse potential had not been reached after 70 minutes of stratification. The time required for the first complete heater cycle is about 12 minutes. The cycle time for succeeding cycles decreased to about 3 minutes per cycle which is about one-third the time required for a flight heater cycle under similar conditions. The inclusion of tank stretch would about double this cycle time. The maximum temperature reached in this simulation was 287°R at the heater node. Negligible fluid convection occurred in the vertical direction.

Figure 11 shows the tank pressure decaying toward the equilibrium pressure in response to the G-step to 10^{-4} G's at 70.5 minutes simulation time. Fluid oscillations in the tank caused by the G-step and accentuated by scaling have been smoothed. The pressure decay observed in the Apollo 12 data at 8:36 GET also is shown for comparison.

Apollo 12 Heater Cycle Simulation

Following the relatively successful initial simulation which demonstrated thermal stratification with ensuing pressure collapse, it was decided to incorporate refinements to the idealized model in an effort to more accurately predict the heater cycle times. These refinements included the effects of tank stretch, line compression, heater thermal mass, and heater radiation to the tank wall.

Under similar environment and initial conditions but with somewhat more rigorously defined heating and mass flowrates, a second Apollo 12 simulation was undertaken which incorporated the above refinements. The time step of $.25 \times 10^{-4}$ seconds as indicated by stability conditions was observed even though a time step twice as large did not appear to alter the numerical stability. The problem was scaled by a factor of 6000 so that 60 minutes of simulation time was covered by 0.6 seconds of solution time. The associated computer time was three hours resulting a computer time/real time ratio of 3/1 on the 1108 system at the NASA-MSC computing center. Considering the change in scale factor and the smaller time steps taken, revisions made to the program allow it to run two times faster than it did for the first Apollo 12 simulation.

Figure 12 shows the resulting computed tank pressure history. Pressure switch limits were set at 860 and 900 psi. The run was performed in a number of segments using the program re-start capability. At the beginning of the second and third segments at 13.5 and 23 minutes the heater switch was inadvertently reset to the "on" position which accounts for the fact that the pressure does not decay to the lower pressure limit at the end of the first two cycles.

The fact that the tank stretch and other refinements do indeed lengthen the heater cycle times may be seen by comparing Figures 10 and 12. The heater cycle time appears to be around 12 minutes which agrees well with the 13 minute cycle time predicted from Figure 3.4.10 of the Apollo Handbook.[1]

The effect of heater thermal mass is observed to cause pressure excusions beyond the pressure limits and a rounding of the pressure peaks. The developed shape of the pressure decay from the peak is due to the decay of the local high temperature at the heater node followed by the more gradual decay resulting from the general fluid expansion caused by mass withdrawal. The highest temperature reached by the fluid in the heater node was 293°R.

In this problem, fluid convection was virtually non-existent. After one hour of simulation, the only apparent migration of the fluid was toward the outlet port which is located perpendicular to the acceleration vector. Therefore, under 2×10^{-8} G's these results indicate that conduction is the primary heat transfer mechanism.

Acceleration Effects

The above Apollo 12 simulation was repeated but under an acceleration of -2×10^{-5} G's - two orders of magnitude higher - to illustrate the effects of acceleration on convection velocities. Employing a scale factor of 2400, the simulation was run to 11.5 minutes by which time a maximum convection velocity of $.35\times10^{-3}$ ft/sec had developed at the heater node. Figure 13 shows a velocity vector plot of the convection pattern developed by time. Density and temperature data indicate that the heated fluid migrated a distance of about 1-1/2 cells or 1.8 inches which corresponds to an average velocity of about $.2\times10^{-3}$ ft/sec.

Scaling Verification

It was tacitly assumed in the discussion of scaling procedures that all the transport process would in fact take place in scaled time. Also assumed was that the pressure and temperature distributions would not be altered by the scaling procedure.

The Apollo 12 convection problem just described was repeated using a scale factor of 4800 instead of 2400. Comparisons of the data from the two cases indicate that the temperature profiles and pressure rise rates are preserved. At a scaled time of 5 minutes for both cases the tank pressures agreed within 1 psi and the heater cell temperatures agree within 1°R after rising 53°R during heater operation. Scaled fluid velocities in the second case (scale factor = 4800) are just double the scale velocities of the first case (scale factor = 2400) as required. Upon descaling, the actual fluid velocities obtained from the two scaled systems are the same, and the scaling procedure is verified.

Evidence supporting the scaling procedure also can be inferred from the quality of the Apollo 12 simulations which were scaled between 3 and 4 orders of magnitude.

High Heat Leak and Boundary Roughness

The circular cross sectional geometry of the Apollo oxygen tank was approximated in a step-wise fashion. A test case was performed to investigate the affect of such a boundary on the flow pattern. In this case, high heat leak of 2000 BTU/hr was imposed at the fluid boundary. This rate corresponds to the limiting heat leak that would occur if the annulus vacuum were lost.[3] An acceleration level of 10^{-5} G's was imposed in the -y direction, and the scale factor of 4800 was used.

The velocity vector plots in Figure 14 show the natural convection after 10, 20, and 32.5 minutes of simulation. The maximum velocity indicated is 10^{-5} ft/sec. Figure 14c shows that local flow distortions are introduced at the protruding corners. This surface roughness probably makes this approach unsuitable for investigations involving tank rotation.

SUMMARY

The conservation equations governing the motion of a compressible viscous fluid were solved in two dimensions using an explicit finite-difference technique. The difference equations were formulated in terms of control-volume grid cells which simplified the imposition of heat flux boundary conditions and assured computational observance of local and global conservation principles. This system also permitted the unified application of the difference equations to both interior and boundary cells without resorting to exterior cells and reflection principles. Real-fluid properties describing the thermodynamic behavior of supercritical oxygen were used so that the pressure collapse phenomenon could be observed in the Apollo oxygen Cryogenic Storage System operating under low - G conditions.

The numerical procedure was applied to the simulation of thermal stratification and fluid mixing in the Apollo oxygen storage tank.

The convex tank geometry was approximated by removing the corner cells of a rectangular cell grid. Wall boundary conditions were adjusted at one cell face to emit a prescribed mass flowrate. Electrical heater input was treated as local internal heat generation. The effects of heater thermal mass and radiation to the tank were included. The effect of tank stretch and line compression on dP/dt was modeled as an out-of-plane fluid expansion. Scaling principles were invoked to achieve acceptable computer execution times for reasonable flight durations.

A verification test case was performed involving heat transfer and natural convection in a vertically-oriented rectangular volume. The convection pattern and isotherms are in good agreement with another numerical solution.

A simulation of stratification and mixing occurring around 7:30 GET in the Apollo 12 mission was presented. Natural convection under 2×10^{-8} G's acceleration was shown to be negligible. The pressure collapse of about 75 psi following a simulated vehicle maneuver is compared with flight data with good results.

Modifications in the heater characterization along with tank stretch effects were shown to significantly improve the simulation of heater cycle operation. A number of additional cases were presented to show the effects of higher acceleration on convection velocities to verify the scaling techniques employed and to evaluate the effects of boundary roughness on convection patterns.

The results obtained for these initial test cases indicate the general capability of this analysis. Unfortunately, time limitations prevented the refinement of certain empirical considerations which would further improve the accuracy of the Apollo simulations.

Future Developments

It has been observed that the finite-difference solution of partial differential equations is limited more by currently available theoretical understanding than by computer capability.[4] However present computers, which perform all operations serially, are not particularly well adapted to computing finite-difference solutions which proceed in a series-parallel fashion. It seems reasonable that the multi-processing capability of present machines will be extended to parallel processing within the same computer program. Such is the thrust of the new multi-computing system at the University of Illinois.[18] This system, called ILLIAC IV, consists of 64 independent processors which operate in unison. By using parallel processing, computer run time can be reduced by a factor of 64. Thus it appears certain that next generation computers of this type will significantly increase the capability of finite difference solutions in multiple space dimensions.

NOMENCLATURE

Symbol	Description
C_{lag}	heater on/off ramps $(0 \leq C_{lag} \leq 1)$
C_{rad}	heater radiation factor $(0 \leq C_{rad} \leq 1)$
C_{str}	tank stretch factor $(= V^{n-1}/V^{n})$
C_{vol}	model/actual volume ratio (Apollo 12 = .075)
e	internal energy per unit mass
E	total energy per unit mass $(= e + \frac{1}{2}(u^2 + v^2))$
g	gravitational acceleration
k	thermal conductivity
P	pressure
q	heat flux
$\dot{Q}$	internal heat generation rate
$\dot{Q}_{leak}$	boundary heat leak rate
$\dot{Q}_v$	internal heat generation rate per unit volume
$t, \Delta t$	time, time increment
T	temperature
u	velocity, x-component
v	velocity, y-component
V	tank volume
μ	absolute viscosity
ρ	density
ρe	internal energy per unit volume
ρu	momentum, x-component
ρv	momentum, y-component
Δx, Δy, L	node dimensions
τ	shear stress
Subscript	
i	x-direction index
j	y-direction index
x	x-component
y	y-component
Superscript	
n	time step index

Figure 1 Oxygen Temperature - Energy Relation

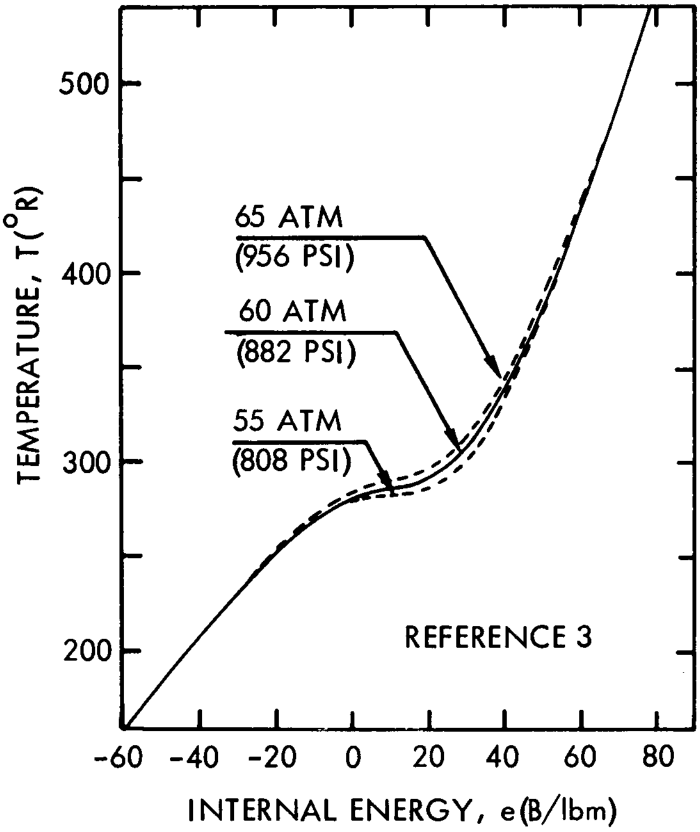

Figure 2 Grid System and Indexing Procedure

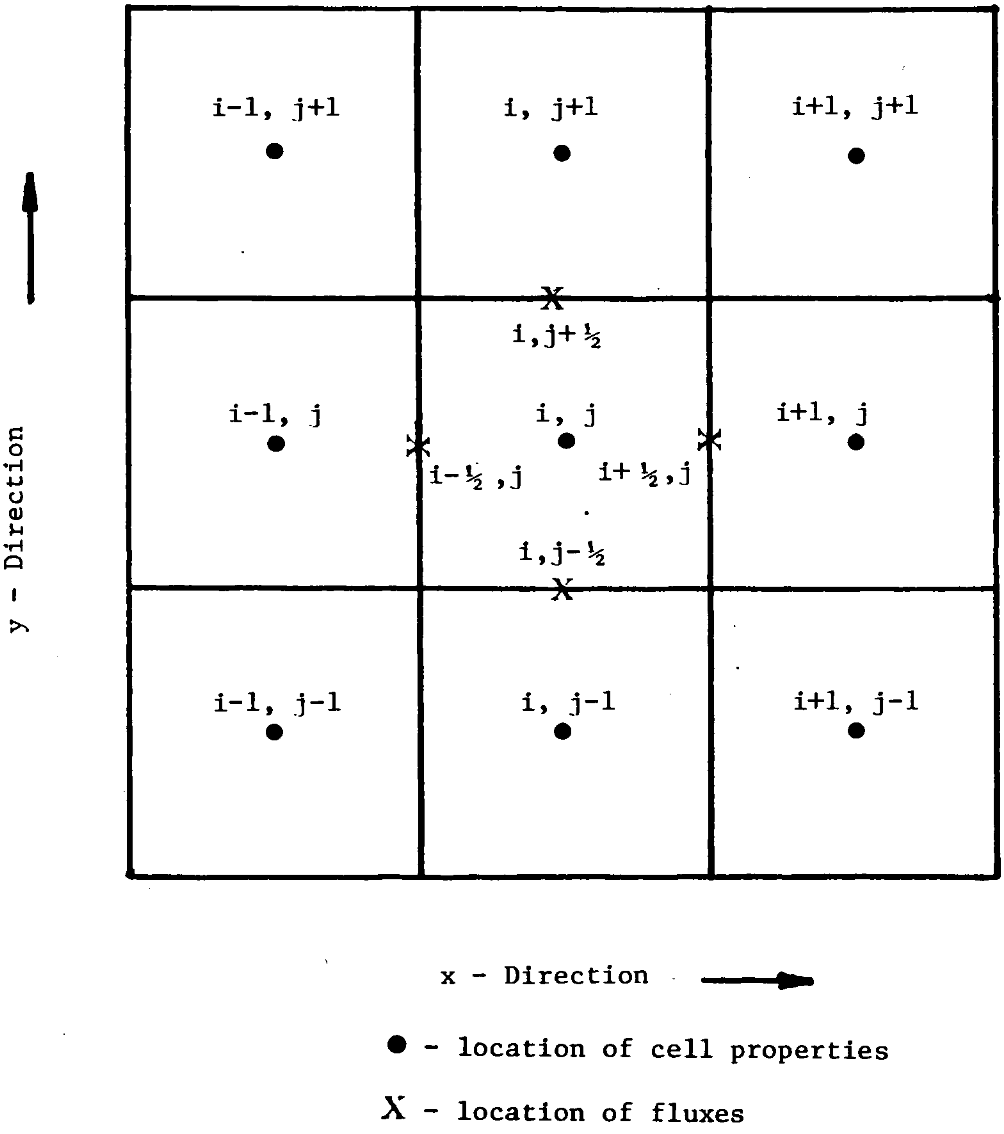

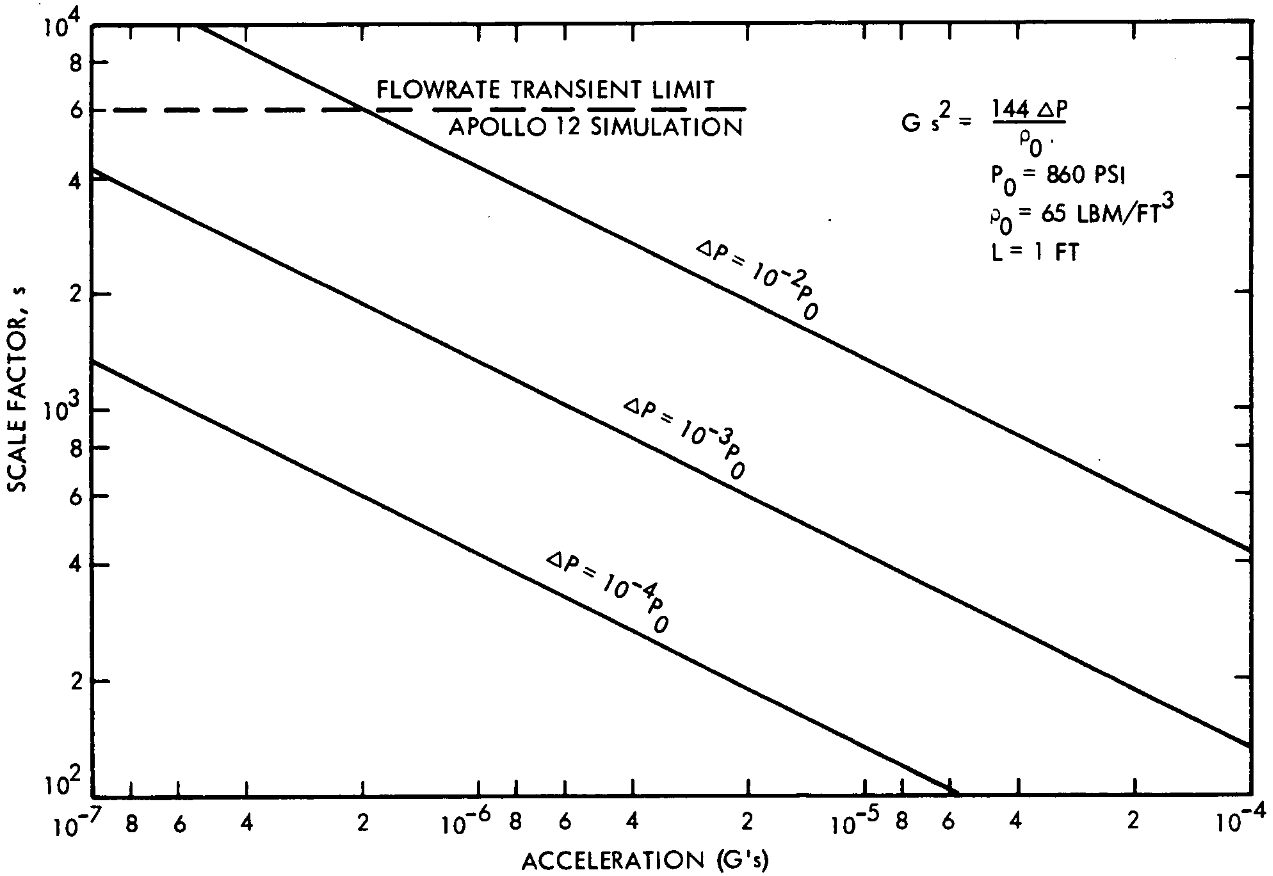

Figure 3 Scale Factor vs Acceleration

Figure 4 . Natural Convection Conditions

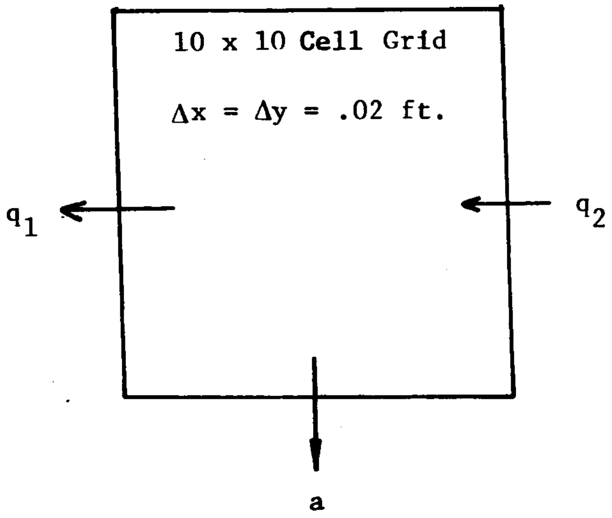

Initial Conditions

$u = v = 0$

$T_o = 100\ ^oR$

$P_o = 500$ psi

$\rho_o = 49.71\ lbm/ft^3$

$z = .3$

MW = 32. lbm/lbm-mole

$C_v = .2\ B/lbm\text{-}^oR$

$\mu = .45$ Poise

$k = 39\ B/ft\text{-}hr\text{-}^oR$

Boundary Conditions

$q_1 = q_2 = .3\ B/ft^2\text{-}sec$

$u_{wall} = v_{wall} = 0$

a = 8 G's

Figure 5 Natural Convection

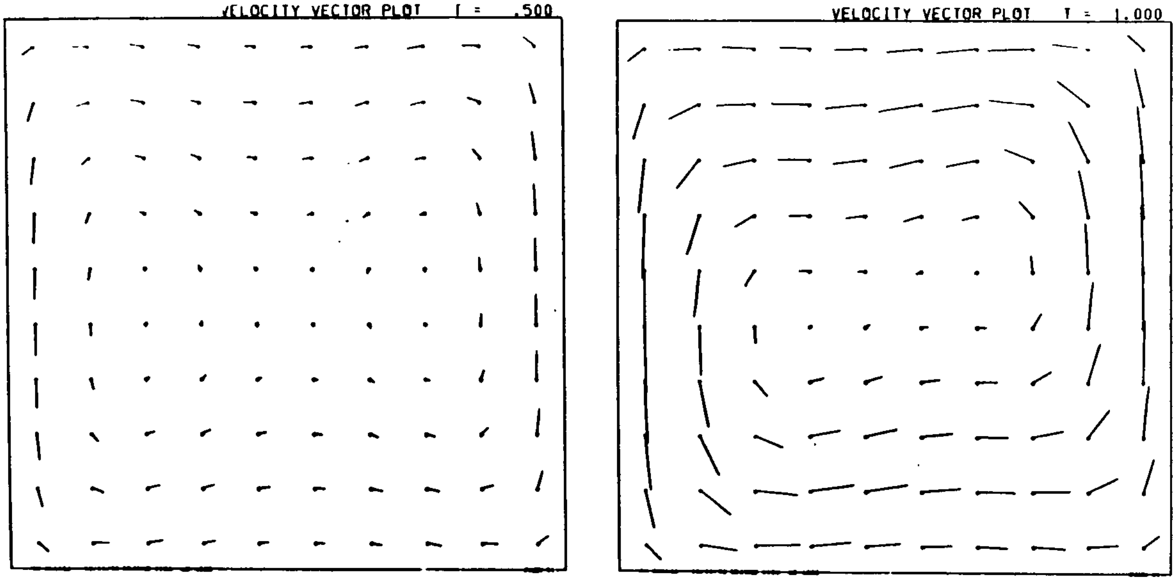

a. Initial Vorticies

b. Vorticies Merging

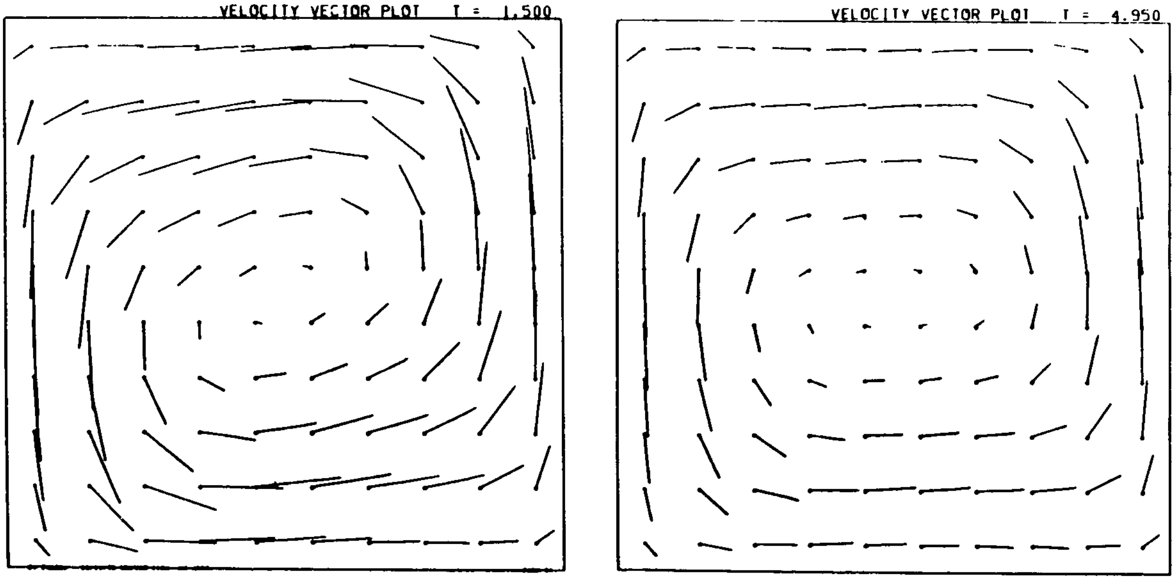

c. Circularized Flow

d. Steady State

Figure 6 Comparison With Wilkes and Churchill

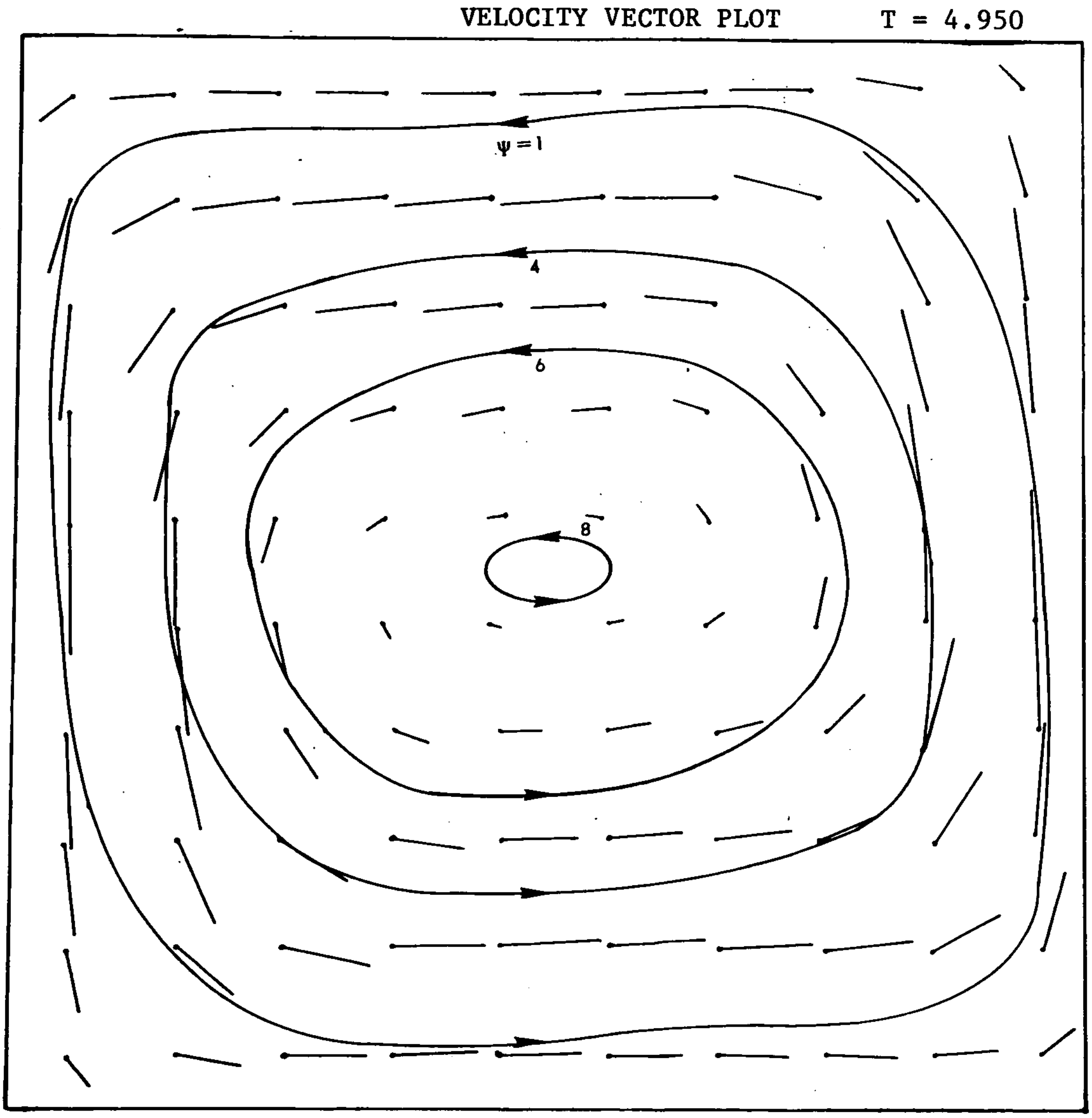

VELOCITY VECTOR PLOT T = 4.950

Figure 7 Steady-State Temperature Profiles

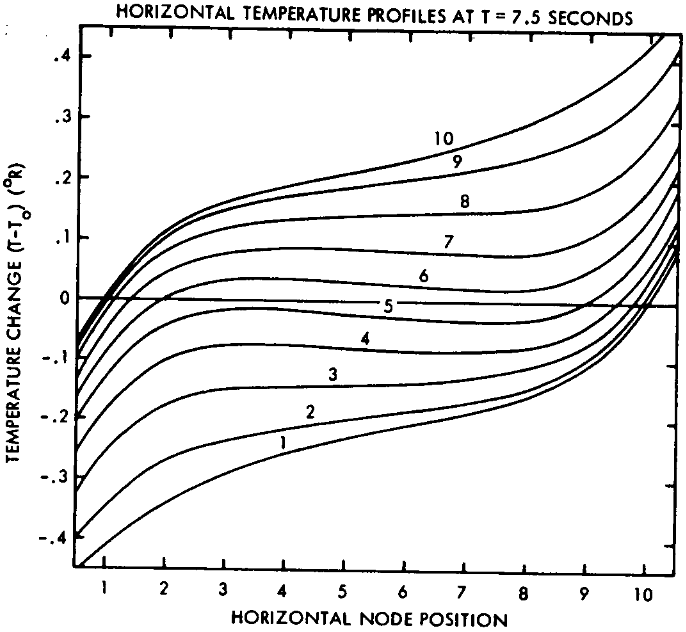

Figure 8 Steady-State Isotherms

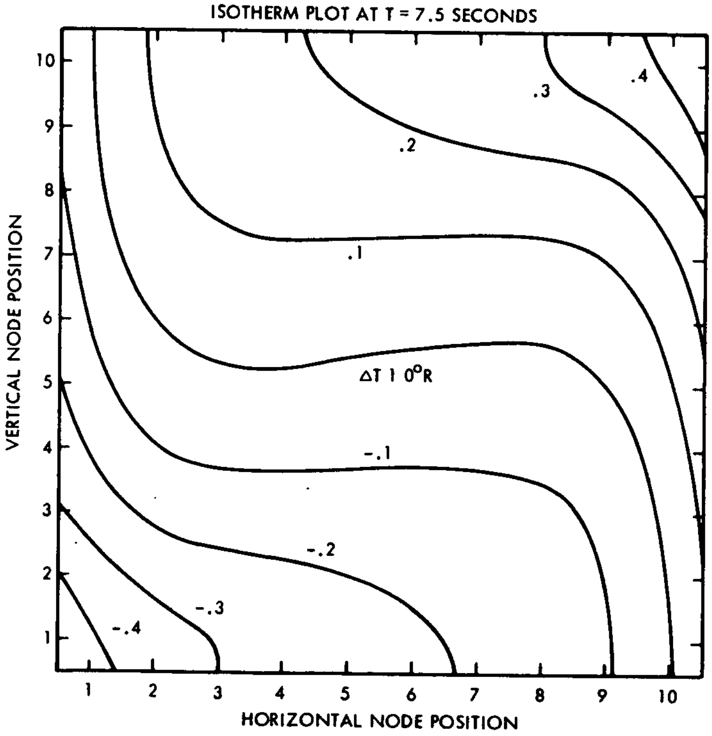

Figure 9 Apollo 12 Simulation Conditions

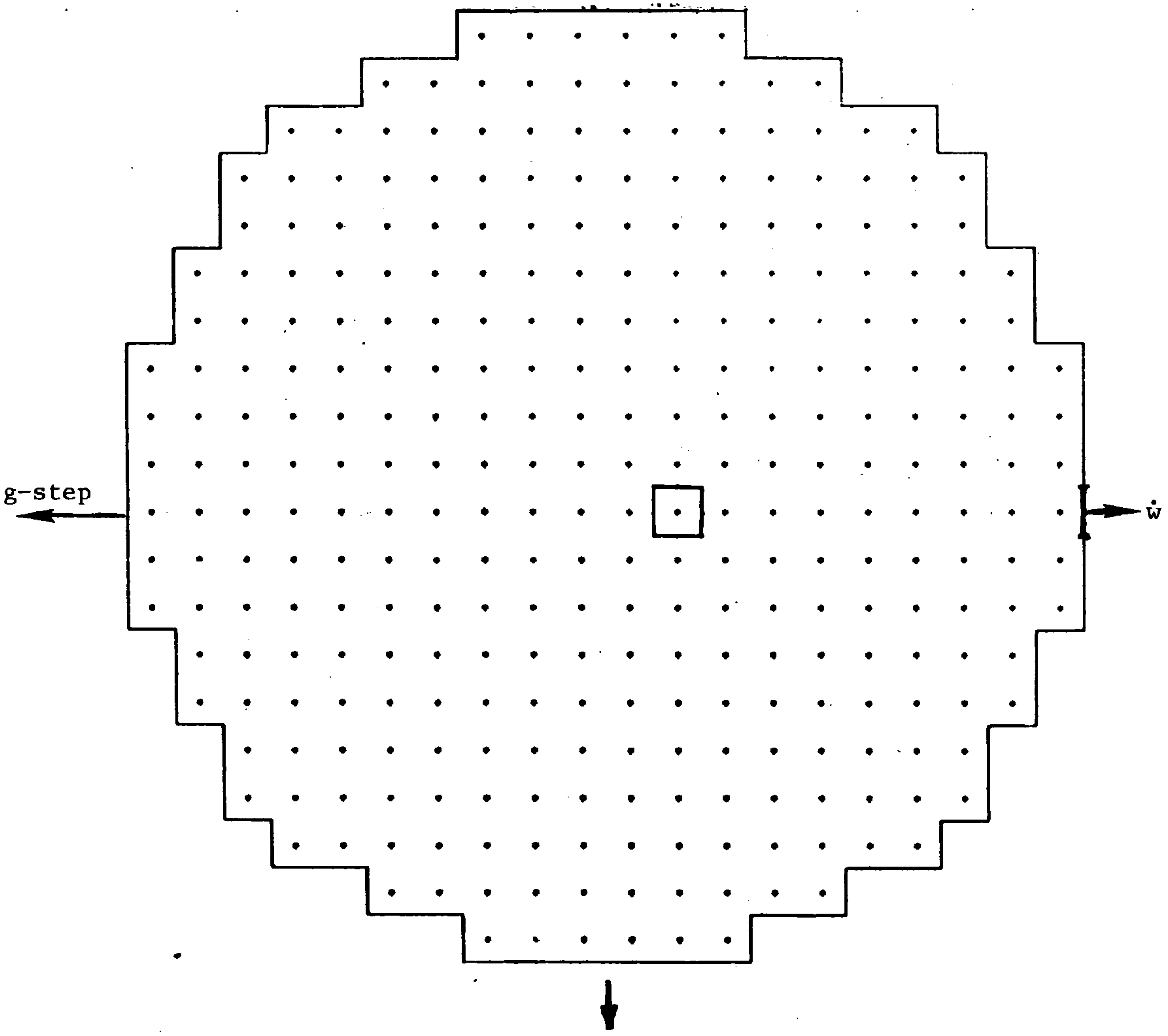

ACCELERATION, a

Conditions

P_o = 867.7 psi

T_o = 200 °R

ρ_o = 65.45 lbm/ft^3

a = $-2. \times 10^{-8}$ G's

Heater = 1 node

$\dot{q}$ = 528.6x(1/17) B/hr

$\dot{w}$ = 1.4x(3/40) lbm/hr

Scale = 2400

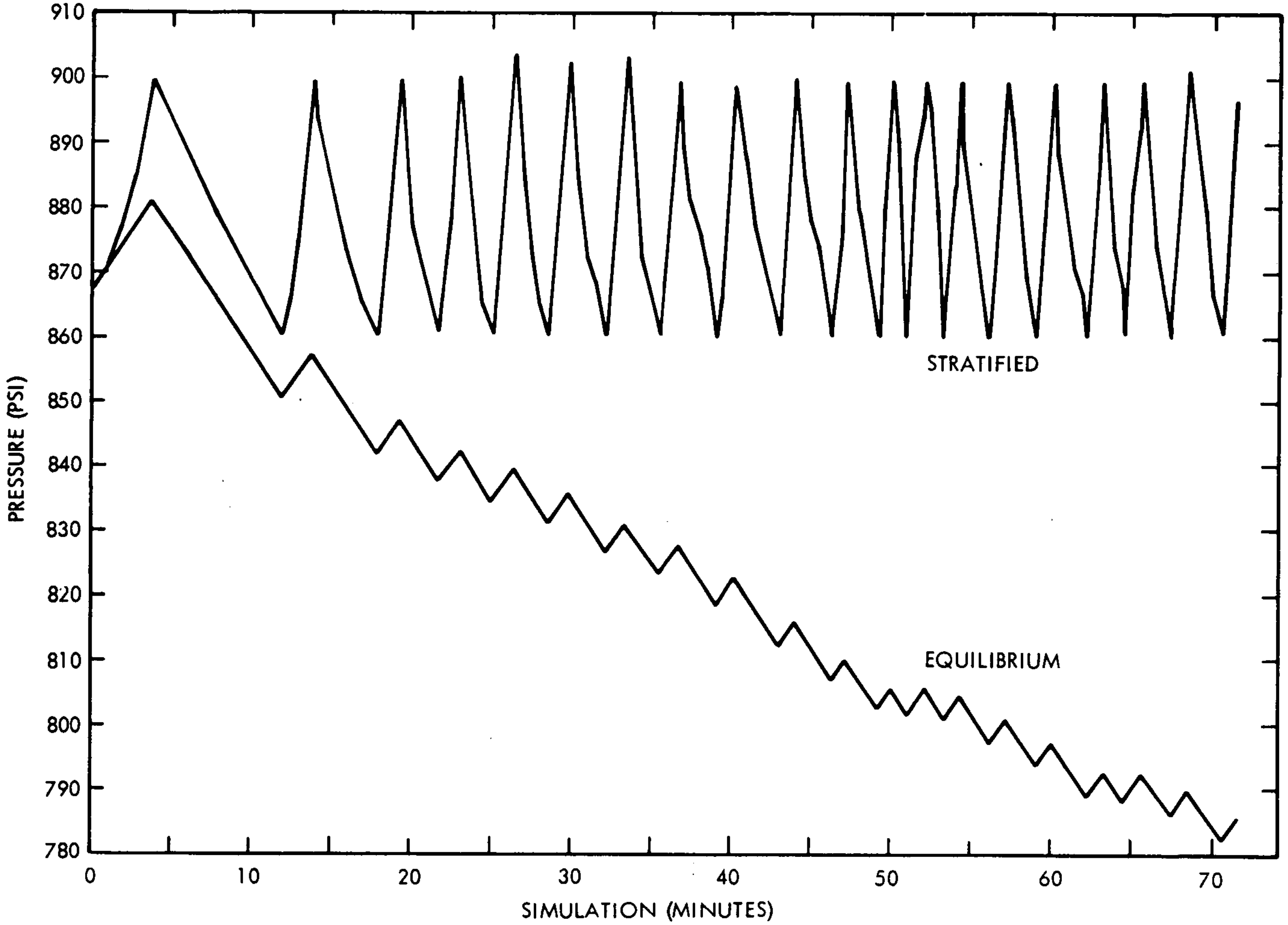

Figure 10 Apollo 12 Stratified and Equilibrium Pressures

Figure 11 Apollo 12 Pressure Collapse

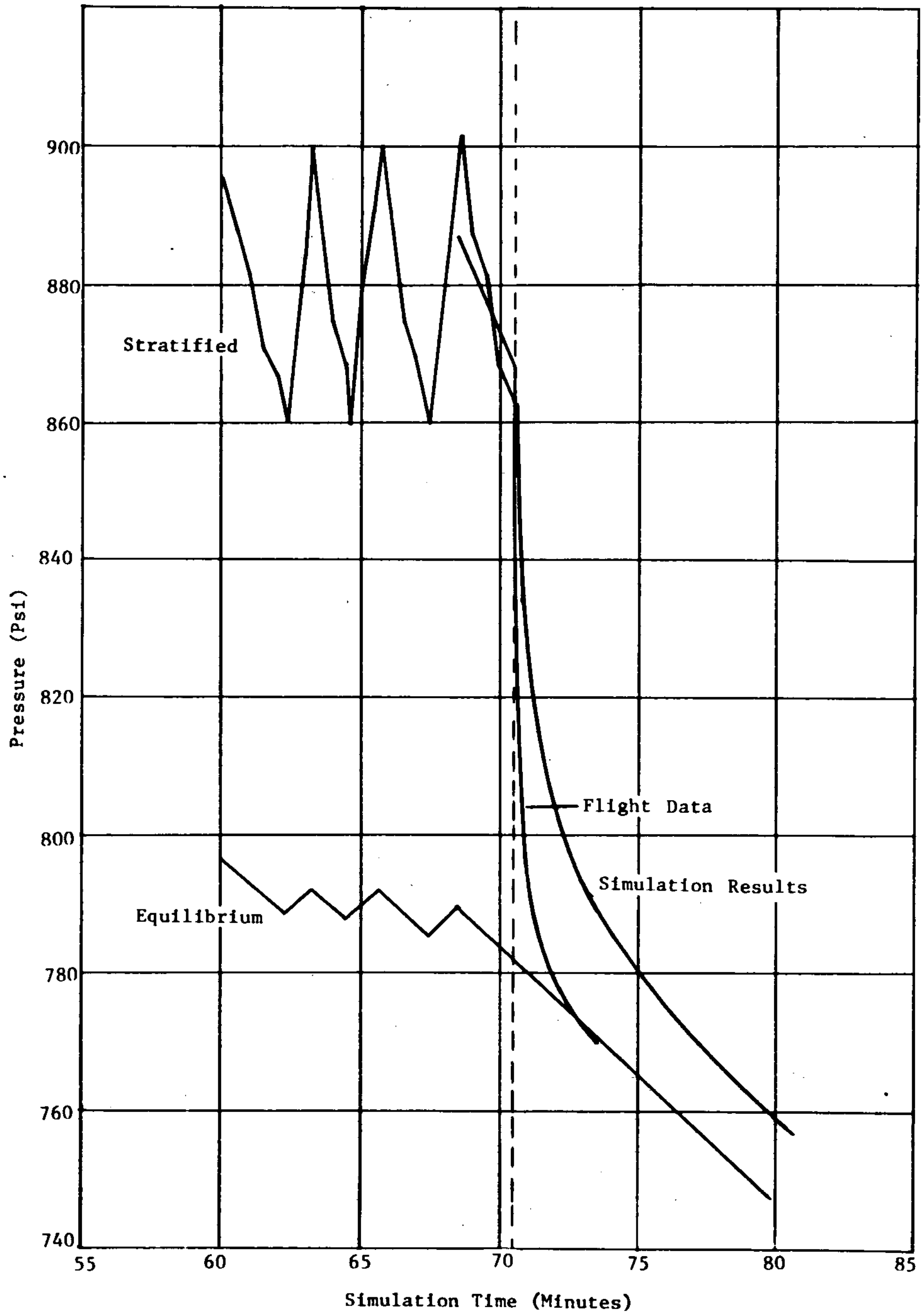

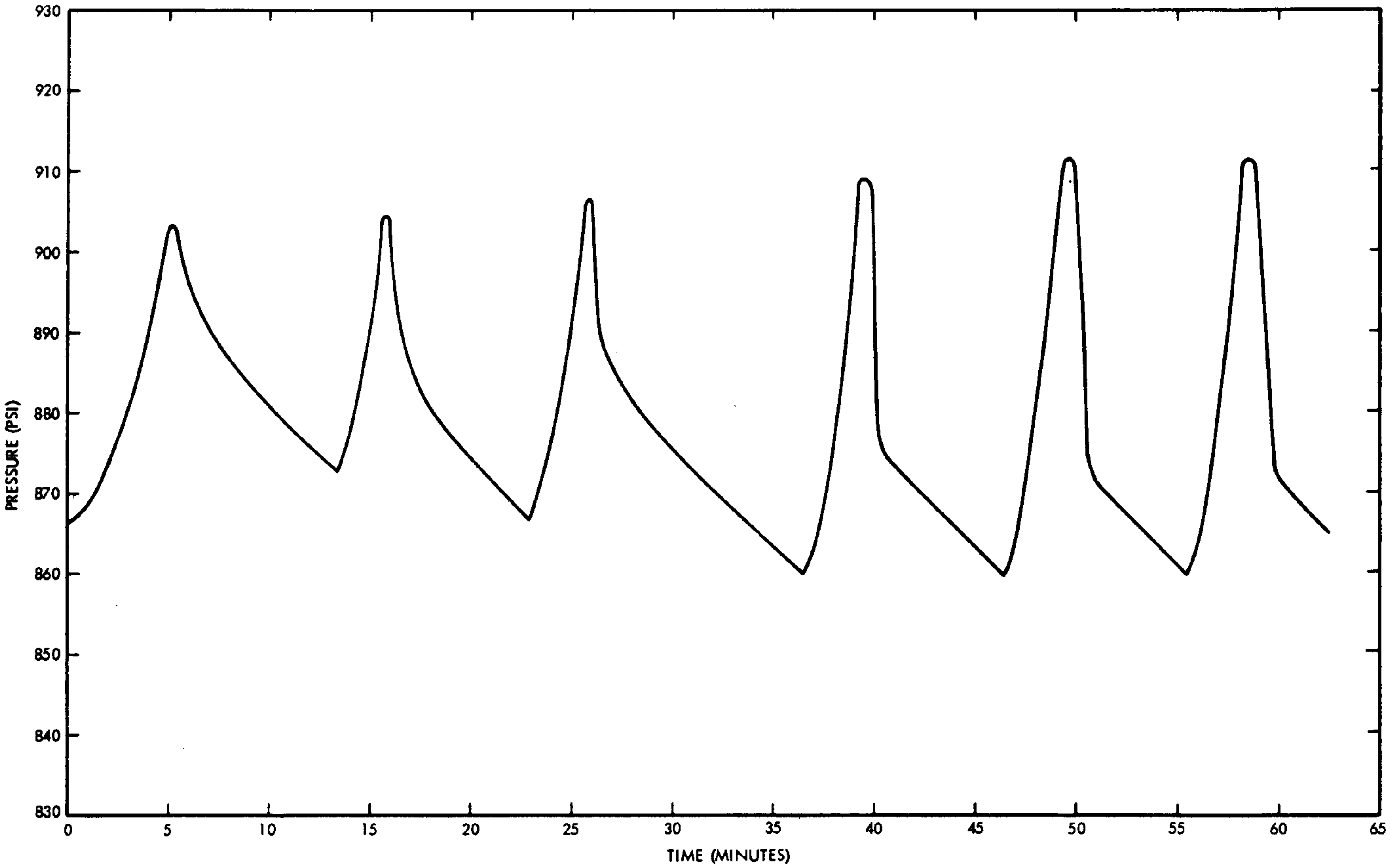

Figure 12 Apollo 12 Stratified Pressure - Including Refinements

Figure 13 Apollo Convection at 2×10^{-5} G's

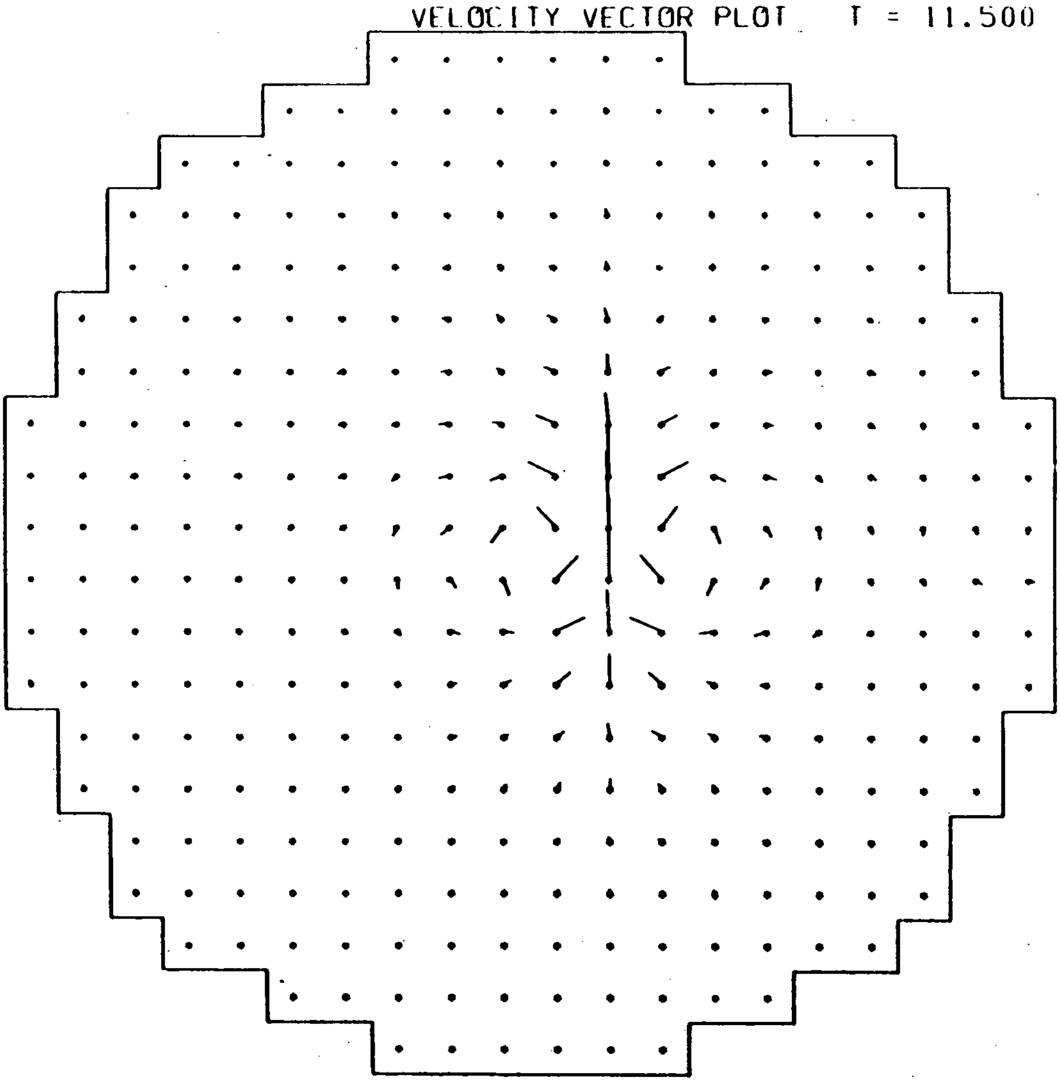

Figure 14 Surface Effects Under High Boundary Heat

a.

Test Conditions

P_o = 850 psi
T_o = 200 °R
L = .1 ft
$g_y = -2 \times 10^{-5}$ G's
$\dot{Q}_{leak}$ = 2000 B/hr
dV/dP = 0
$\dot{Q}_{heater}$ = 0
$\dot{W}_{outlet}$ = 0
Scale = 4800
$\Delta t = .25 \times 10^{-4}$

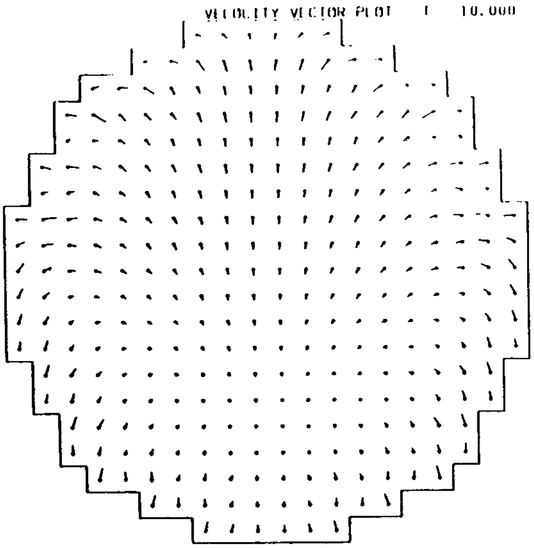

b.

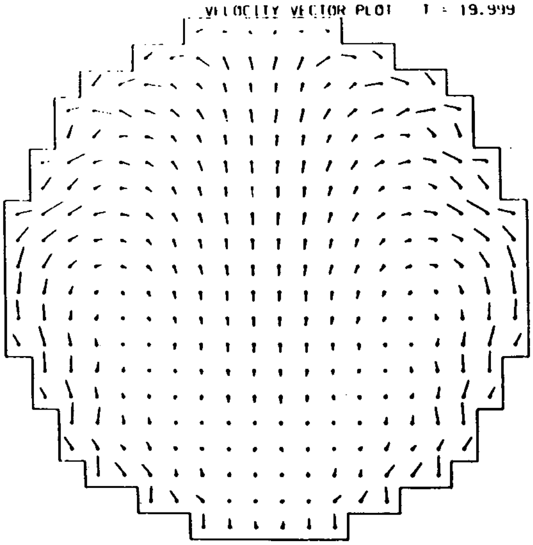

c.

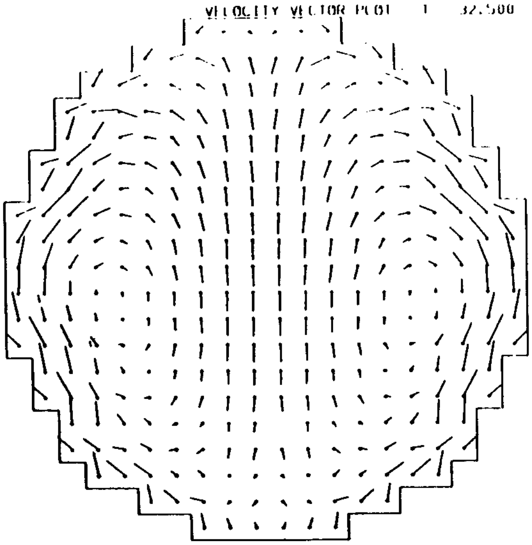

REFERENCES

1. Owens, S., "Apollo Fuel Cell and Cryogenic Gas Storage System Flight Support Handbook," NASA, MSC.
2. Kamat, D. V. and Abraham, W. H., "Pressure Collapse in Oxygen Storage Under Zero-g," Journal of Spacecraft & Rockets, Vol 5, No 2, Feb, 1968, ppg. 184-188.
3. Seto, R. K. M., et al, "Apollo Cryogenic Systems Programs," TRW Project Technical Report 17618-H090-R0-00, December 1970.
4. Richtmyer, R. D. and Morton, K. W., Difference Methods for Initial Value Problems, Interscience, New York, 2nd ed., 1967.
5. Schlichting, H., Boundary Layer Theory, McGraw-Hill, New York, 4th Ed., 1960.
6. Liepmann, H. W., and Roshko, A., Elements of Gasdynamics, Wiley, New York, 1957.
7. Goodrich, W. D., "A Numerical Solution for Problems in Laminar Gas Dynamics," PhD Dissertation, University of Texas at Austin, May, 1969.
8. Weber, L. A., "Thermodynamic and Related Properties of Oxygen from the Triple Point to 300 K at Pressures to 330 Atmospheres Supplement A (British Units)," National Bureau of Standards Report 9710 A, August 29, 1968.
9. Stewart, R. B., "The Thermodynamic Properties of Oxygen," PhD Thesis, University of Iowa, June 1966.
10. Chu, C. K., Editor, "Computational Fluid Dynamics," AIAA Selected Reprint Series, Vol 4, July 1968.
11. Ralston, A., and Wilf, H. S., Mathematical Methods for Digital Computers, Wiley, Vol. 1, 1960.
12. Cheng, S. I., "Numerical Integration of Navier-Stokes Equations," AIAA Journal, Vol. 8, No. 12, December 1970.
13. Rusanov, V. V., "The Calculation of the Interaction of Non-Stationary Shock Waves and Obstacles", National Research Council of Canada Library, Ottawa, Canada, Tech. Translation by D. A. Sinclair, 1962. Translated from: Zhurnal Vychislitelnoi Fiziki, Akademiya Nauk, SSSR 1, Vol. 1, No. 2, 1961, pp. 267 - 279.

14. Goodrich, W. D., Personal Communication, March 1971.

15. Heinmiller, P. J., "A Numerical Solution For The Prediction of Pressure Collapse in Supercritical Oxygen," TRW Project Technical Report 17618-H080-R0-00, December, 1970.

16. Roache, P. J., and Mueller, T. J., "Numerical Solutions of Compressible and Incompressible Laminar Separated Flows," AIAA Paper No. 68-741.

17. Wilkes, O. J. and Churchill, S. W., "The Finite-Difference Computation of Natural Convection in a Rectangular Enclosure," AIChE Journal, Vol. 12, No. 1, January 1966.

18. Slotnick, D. L., "The Fastest Computer," Scientific American Vol. 224, No. 2, February 1971.

N72-23792

HEAT TRANSFER AND THERMAL STRATIFICATION IN THE APOLLO 14 CRYOGENIC OXYGEN TANKS

By

S. S. Fineblum, A. S. Haron, J. A. Saxton
Bellcomm
Washington, D. C.

INTRODUCTION

Two significant facets of Apollo oxygen tank operation are the occurrence of thermal stratification at high fluid densities and the tendency toward high heater temperatures at low fluid densities. Some insight into the nature of these phenomena can be gained, respectively, by consideration of a two fluid stratification model and a conductive heat transfer model. The alternative of convective blowdown tank operation at low densities is briefly examined.

STRATIFICATION

Thermal stratification is significant in the Apollo oxygen tanks because of the greatly reduced mixing in the low gravity field and the low thermal conductivity of the oxygen. In the stratified tank adjacent phases of different temperature coexist stably. The less dense phase exerts a pressurizing influence on the relatively incompressible dense phase. The effects of stratification are for the most part limited to high density conditions; for example, pressure decays have not been observed on Apollo flights for densities of less than ∿42 lb/ft^3 (60% tank quantity). The phenomena of pressure decay relates to the fact that at the higher densities the energy input necessary to achieve a given pressure rise is measurably less with stratification than without. Hence the tank can maintain operating pressure despite a small energy deficit;

induced mixing, as caused by a vehicle maneuver, then results in a sudden pressure drop or decay.

By conservation of energy the relation between energy input, mass outflow, and pressure rise rate for a homogeneous fluid is:

$$\frac{dp}{dt} = \frac{C\phi}{V} (Q - \omega\Theta) \tag{1}$$

where

$$\phi \equiv \frac{1}{\rho} \left(\frac{\partial p}{\partial u}\right)_{\rho} \tag{2}$$

$$\Theta \equiv -\rho \left(\frac{\partial h}{\partial \rho}\right)_{p} \tag{3}$$

$$C = \left(1 + \frac{\rho\Theta\phi}{V} \frac{dV}{dp}\right)^{-1} \tag{4}$$

and Q, ω, V, p, u, and h are the heat input, mass outflow, volume, pressure, internal energy, and enthalpy, respectively. The coefficient C accounts for the change in tank volume with increasing pressure. Equations (1) - (4) yield the pressure rise rate when heat is added uniformly, that is, stratification does not occur.

Over the entire pressure cycle the energy input is related solely to the fluid's enthalpy-density relationship Θ and the rate of mass outflow from the tank ω. That is, there is no net pressure change so Equation (1) becomes

$$Q = \omega\Theta \tag{5}$$

Figure 1 shows the energy input data for Apollo 14. The solid curves were computed by Equation (5) for a mean tank pressure of 900 psi using the average flow rates and heat leaks indicated. Tank quantity rather than density is used as the abscissa, with 100% quantity equal to 69.5 lb/ft^3. The spread in the data reflects the variation of the flow rates about the mean value.

The time to pressurize the tank within its operating band offers a direct measure of the stratification occurring. Figure 2 portrays this data for Apollos 12 and 14. The spread of the data points below 60% for the two missions is traceable to two effects.* Firstly, because of the tank arrangement on Apollo 14, Tank 3 mass outflow during its heater operation was substantially increased by leakage of the Tank 2 check valve. In effect Tank 3 pressurized Tank 2 during each cycle. Secondly, for thermal reasons only two of the three Tank 3 heater elements were employed below 41% (with two exceptions). With this in mind the pressurization times for Apollos 12 and 14 are essentially identical even though Apollo 12 utilized fans for periodic mixing (twice daily). That is, the fan operations did not appear to noticeably reduce stratification effects on pressurization.

In Figure 3 the Apollo 14 data are plotted with the pressurization time predicted by Equations (1) - (4) indicated by the solid lines. The flowrates employed are given in Figure 4. The flow values are taken from the quantity guage readings, corrected in the case of Tank 3 for the flow necessary to pressurize Tank 2. As expected, the agreement between data and prediction is relatively good below 60%, but not above.

---

*Note: On Apollo 14 all data above 60% is from Tanks 1 and 2 and below 60% is from Tank 3; whereas on Apollo 12 Tanks 1 and 2 were operated concurrently throughout (there was no third tank).

The basic elements of the effect of stratification on pressurization are the localized storage of energy in the vicinity of the heater and the nature of the enthalpy-density relationship as reflected in Θ. Following heater activation the fluid adjacent to the heater increases in temperature, and hence expands. This expansion mechanically pressurizes the remainder of the fluid. The pressurization of the bulk fluid by the hot "bubble" is given by

$$\Delta p = \left(\frac{\partial p}{\partial h}\right)_{\rho} \Delta h + \left(\frac{\partial p}{\partial \rho}\right)_{h} \Delta p = - \left(\frac{C\rho\phi\Theta}{V}\right)_{B} \Delta V_B \qquad (6)$$

where the tank heat leak and outflow have been neglected. The bulk's volume change is equal and opposite to that of the bubble, whose mass is assumed constant:

$$\Delta V_B = -\Delta V_s = \left(\frac{V}{\rho\phi\Theta}\right)_{S} \Delta p - \left(\frac{1}{\rho\Theta}\right)_{S} \Delta Q \qquad (7)$$

The stratified pressure response of the system, Δp, to a localized heat input, ΔQ, is therefore given by:

$$\Delta p = \frac{\dfrac{\rho_B\Theta_B}{\rho_s\Theta_s}\,\dfrac{C\phi_B}{V_B}\,\Delta Q}{1 + \dfrac{\rho_B\Theta_B\phi_B}{\rho_s\Theta_s\phi_s}\,\dfrac{V_s}{V_B}\,C} \qquad (8)$$

with subscripts s and B referring to the stratified bubble and bulk fluid, respectively. The Θ curve passes through a minimum at a density of ~ 26 lb/ft^3. If the bulk density is greater than this, the Θ and ρ variations accompanying the creation of a less dense phase (film) adjacent to the heater combine to cause a larger pressure rise for a given heat input. Below ∿42 lb/ft^3 density (60%) the Θ decrease with expansion falls off and below 26 lb/ft^3 the Θ variation counteracts the effect of density decrease on pressure rise.

A rough indication of the extent of the stratification process can be gained by a two fluid calculation. The model is schematically depicted in Figure 5. Initially all heater energy Q_{HTR} is assumed confined to the stratified volume adjacent to the heater. The energy is accommodated by fluid outflow $\dot{m}_1$ from this volume. The bulk fluid receives this stratified outflow as well as heat leak Q_{HLK} from the environment and supplies tank outflow $\dot{m}_o$ to the spacecraft systems. Equations (1) - (4) describe the pressure rise in each phase. When the stratified fluid density has diminished to that point where its Θ value has passed through the minimum and risen to the bulk value, the heater energy is assumed to be transferred uniformly to the bulk phase. Of course, other phenomena take place, such as stratified volume growth, mass transfer from the bulk, and energy sharing with the bulk. Nevertheless, the simplified model exhibits the basic attributes of the observed pressure behavior as shown by the dashed line in Figure 3. The calculation results are for a stratified volume of 0.0119 ft^3 (1/4% of tank volume) or a radial distance of 1/8 inch. This is on the order of boundary layer dimensions, and explains the insensitivity of pressurization times to overall tank flow condition as evidenced by the close grouping of Apollo 12 and 14 data for a variety of spacecraft inertial conditions.

Some interesting aspects of stratification are shown in Figure 6. Here fan activation causes the expected pressure decay. The divergence from uniform heating conditions of the pressure profile prior to fan operation reflects stratification. The pressure behavior during the heater cycle following fan operation is significant, though. As expected, in the well mixed tank the pressure behavior follows a uniform heating path. However, the recovery from the low pressure point occurs at a rate identical to the pressure rise rate prior to fan operation. Hence, even in this clearly active fluid motion environment some stratification of the same type as that observed in the quiescent period prior to fan operation occurs.

CONDUCTIVE HEAT TRANSFER MODEL

Since the gravitational forces exerted on the vehicle during steady flight are quite small, ranging from roughly 7 x 10^{-8}g in attitude hold to 3 x 10^{-6}g during 3 rph passive thermal control, the buoyant motion of the fluid during heat transfer periods is correspondingly reduced. In the limit, heat is transferred into the fluid solely by conduction. This constitutes a worst case in terms of maintaining a low heater temperature while transferring the heat required to sustain tank operating pressure. Therefore, a conduction model was developed to predict worst case (zero gravity) heater temperatures (Reference 1).

The simplified model is schematically depicted in Figure 7. It assumes spherical symmetry (as the tank) and adapts the cylindrical heater parameters to this configuration. The spherical heater area is set equal to its cylindrical counterpart, while its internal volume is adjusted to match the true cylindrical volume. Twelve fluid nodes of equal thickness are dispersed between the heater and tank wall; the fluid within the heater is represented by one node; and the heater, tank wall and SM environment are represented by one node each.

The CINDA-3G numerical heat transfer program was employed. The logic of this program is shown in Figure 8 via its electrical analogue where each node with its own capacitance is linked to adjacent nodes by resistive circuits. The radiative transfer between the heater and the tank wall is included as is the heat leak to the tank from the surrounding environment. Tank pressure is held constant throughout each calculation, and the nodal mass, specific heat, and thermal conductivity are adjusted at each time step in accord with the nodal temperatures resulting from the conductive heat transfer. The oxygen properties as correlated by R. B. Stewart (Reference 2) are employed for density and specific heat, while the thermal conductivity is taken from a North American Rockwell report (Reference 3).

The model is admittedly crude. It does, however, furnish some interesting results. Firstly, the predicted temperatures agree well with those for steady attitude hold heater cycles. Figure 9 illustrates this. Here the temperature profile and maximum temperature indicated by the heater temperature sensor are closely matched by the model. (One qualification to be made is that the model assumes a uniform heater temperature while the data is from a thermocouple linked to one point on the heater. The excellent correlation between the two is taken to mean that the temperature sensor reflects an effective mean heater temperature from a heat transfer standpoint.) It appears that some mixing occurred at the beginning of the heating cycle but after this delay the temperature rise and fall off after heater deactivation are as predicted. Thus, the g forces exerted during attitude hold seem to produce little convective mixing, although the more rapid return of the heater to its original temperature indicates some convection.

It is interesting to look next at the ability of spacecraft rotation to enhance heat transfer. Figures 10 and 11 show the heater temperature profiles for rotation rates of 1 rph and 3 rph respectively. The ratio of the maximum temperature rise achieved in each case to the maximum temperature rise predicted by the conductive model offers a rough measure of the convective heat transfer coefficient. The increased rate of rotation clearly produces improved heat transfer.

Another form of convective motion is shown in Figure 12. Here the spacecraft has been brought to rest from a 3 rph passive thermal control rotation. The low temperatures indicate substantial fluid motion. By comparison, Figure 9 for attitude hold eight hours after the cessation of 1 rph rotation shows little evidence of fluid motion.

From the foregoing we conclude that a simplified conductive model closely models attitude hold conditions and can serve as a useful real time indicator of the level of convective motion in the tanks.

CONVECTIVE BLOWDOWN

The energy input required to maintain tank operating pressures of 900 psi increases sharply as low tank quantities are approached, and the dilute gas offers a diminished energy sink for the heater. Thus high heater temperatures may be encountered. An alternative operational mode is to take advantage of the pressurization energy and operate the tank as a compressed gas source. A constraint is that tank pressure be maintained at greater than 150 psi for proper flow to the fuel cells. One way of satisfying this requirement is to add sufficient energy to follow an isothermal path once past the apex of the two phase region, for example the -160° F isotherm in Figure 13. The energy required for total evacuation from 20% (71.3 lb) via such an isothermal blowdown is given in Figure 14 as a function of tank outflow rate. A portion of the needed heat is provided by heat leak from the surrounding environment. In fact, the heat leak supplies all necessary energy for evacuation at an outflow rate of 0.5 lb/hr, and the heater duty cycles for 1.0 and 1.5 lb/hr flows are minimal (<10%).

CONCLUSIONS

Two simplified models have been found to yield useful insights into the oxygen tank thermal behavior. The two fluid stratification model indicates that stratification of less than 1% of the fluid will lead to the observed pressure response times. The involvement of such a small fluid volume explains the insensitivity of the pressurization times to overall tank fluid motion and the rapid pressure recovery following fan operation. The conductive/radiative heat transfer model furnishes a worst case heater temperature prediction and can serve as an indication of the extent of convective mixing. It is seen that the g-force exerted during attitude hold is insignificant in terms of enhanced heat transfer, but that $\sim$3 rph passive thermal control has a noticeable effect.

ACKNOWLEDGMENT

The significant contribution of M. V. Drickman in adapting R. B. Stewart's programs for the thermodynamic properties of oxygen to the Bellcomm computer and developing a number of related subprograms is gratefully acknowledged.

REFERENCES

1. Haron, A. S., "Transient Analysis of Heat Transfer in a Simplified Model of the Apollo Oxygen Tank", Bellcomm Memorandum for File, B70 12076, December 30, 1970.

2. Stewart, R. B., "The Thermodynamic Properties of Oxygen", PhD Thesis, University of Iowa, 1966.

3. Moses, R. E., "Internal Communication", Rocketdyne, Space Division of North American Rockwell, Inc., April 1964.

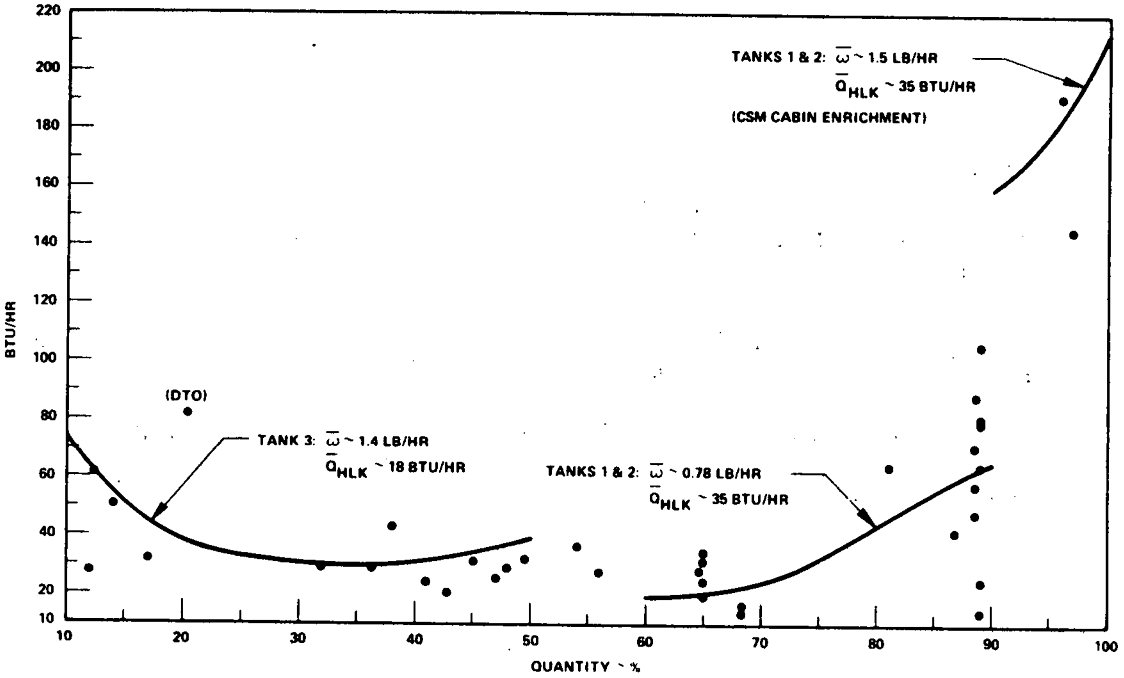

FIGURE 1 - ENERGY INPUT RATE AS FUNCTION OF QUANTITY AND FLOW RATE

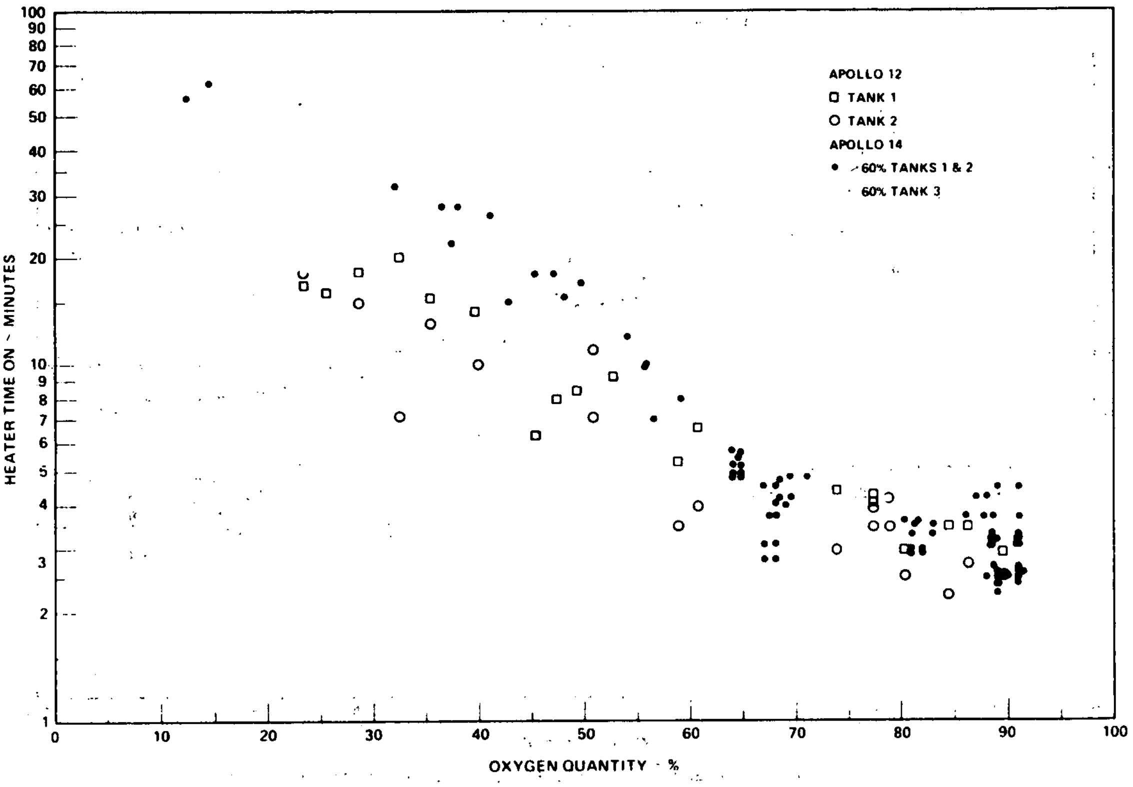

FIGURE 2 APOLLOS 12/14 PRESSURIZATION TIMES

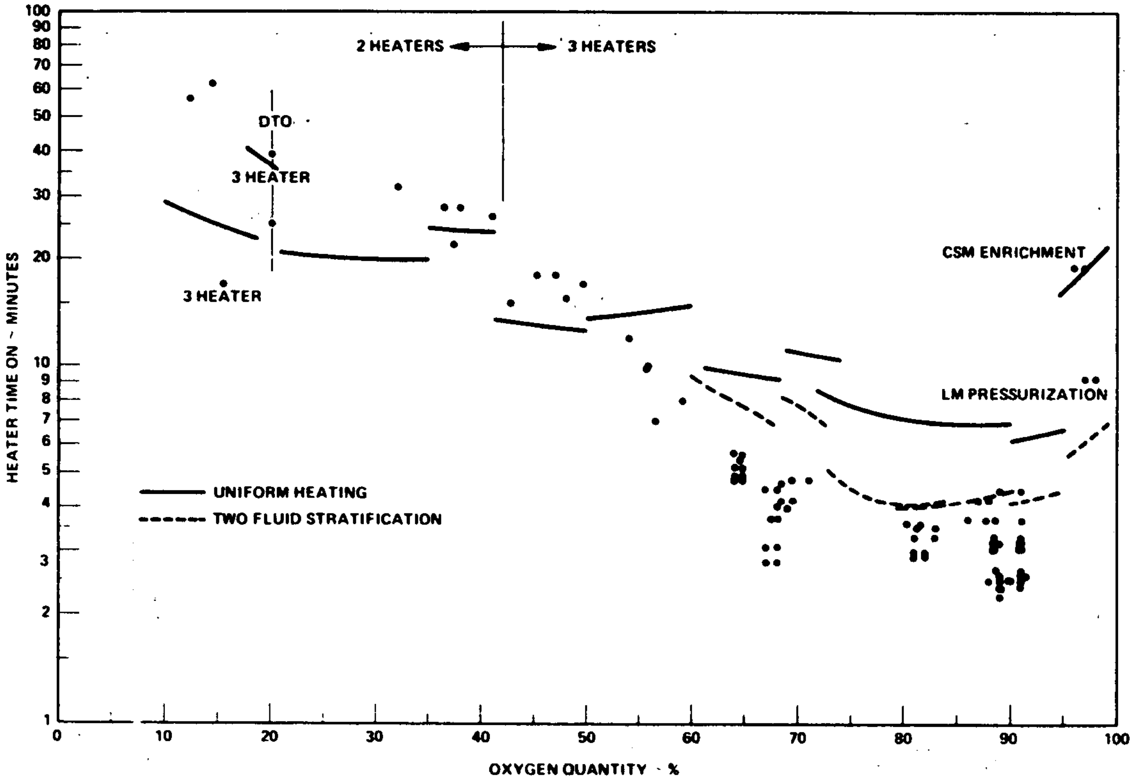

FIGURE 3 APOLLO 14 PRESSURIZATION TIMES DEPICTING EFFECT OF STRATIFICATION

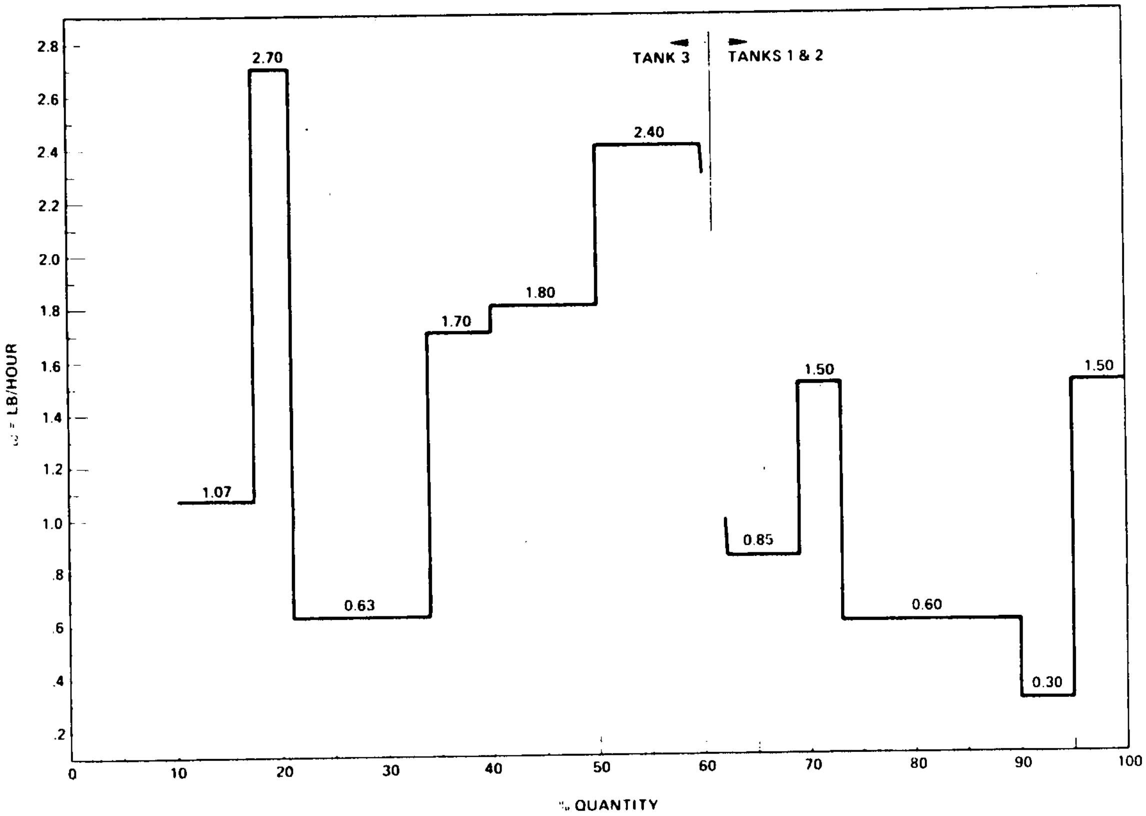

FIGURE 4 APOLLO 14 AVERAGE O_2 FLOW RATES DURING HEATING OPERATION

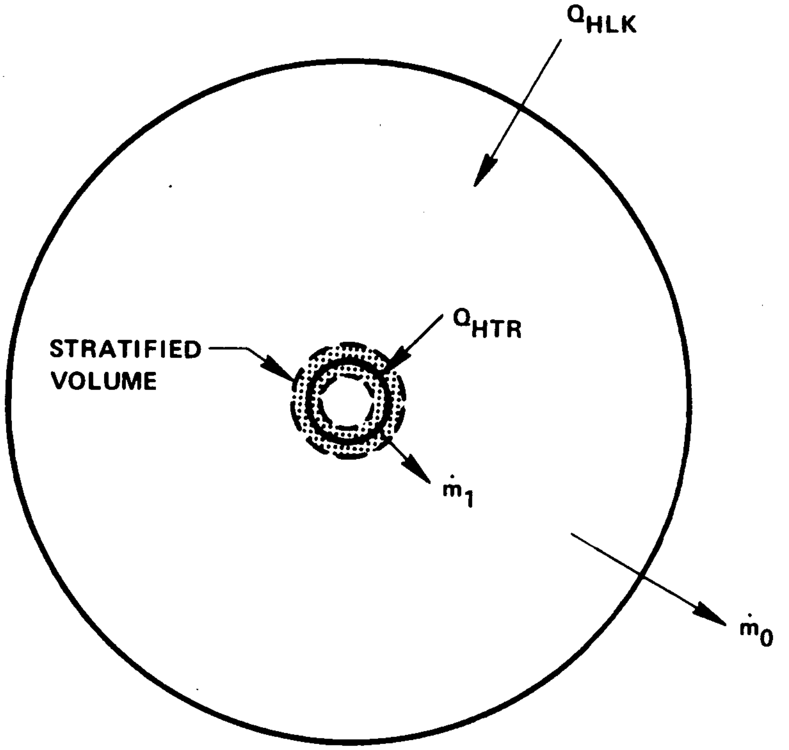

FIGURE 5 - SCHEMATIC OF TWO FLUID MODEL

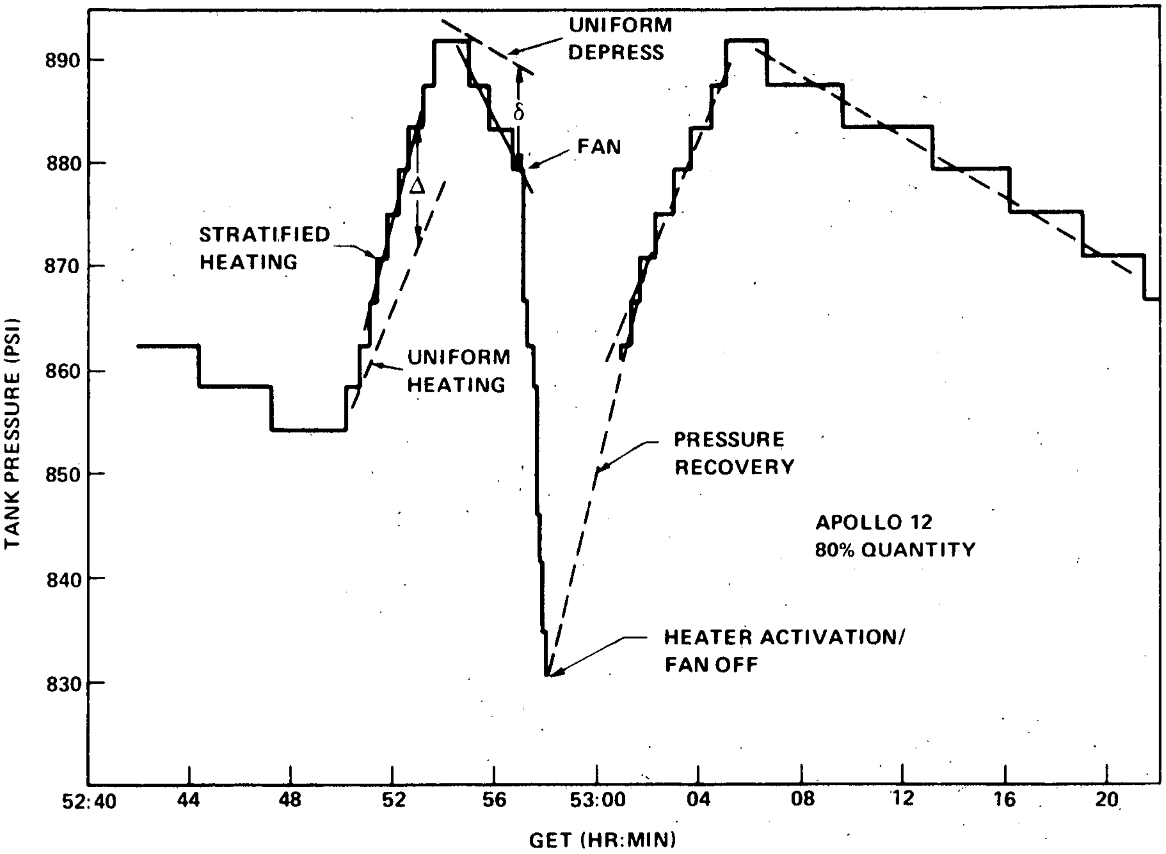

FIGURE 6 - PRESSURE CYCLES BEFORE/AFTER FAN CYCLE

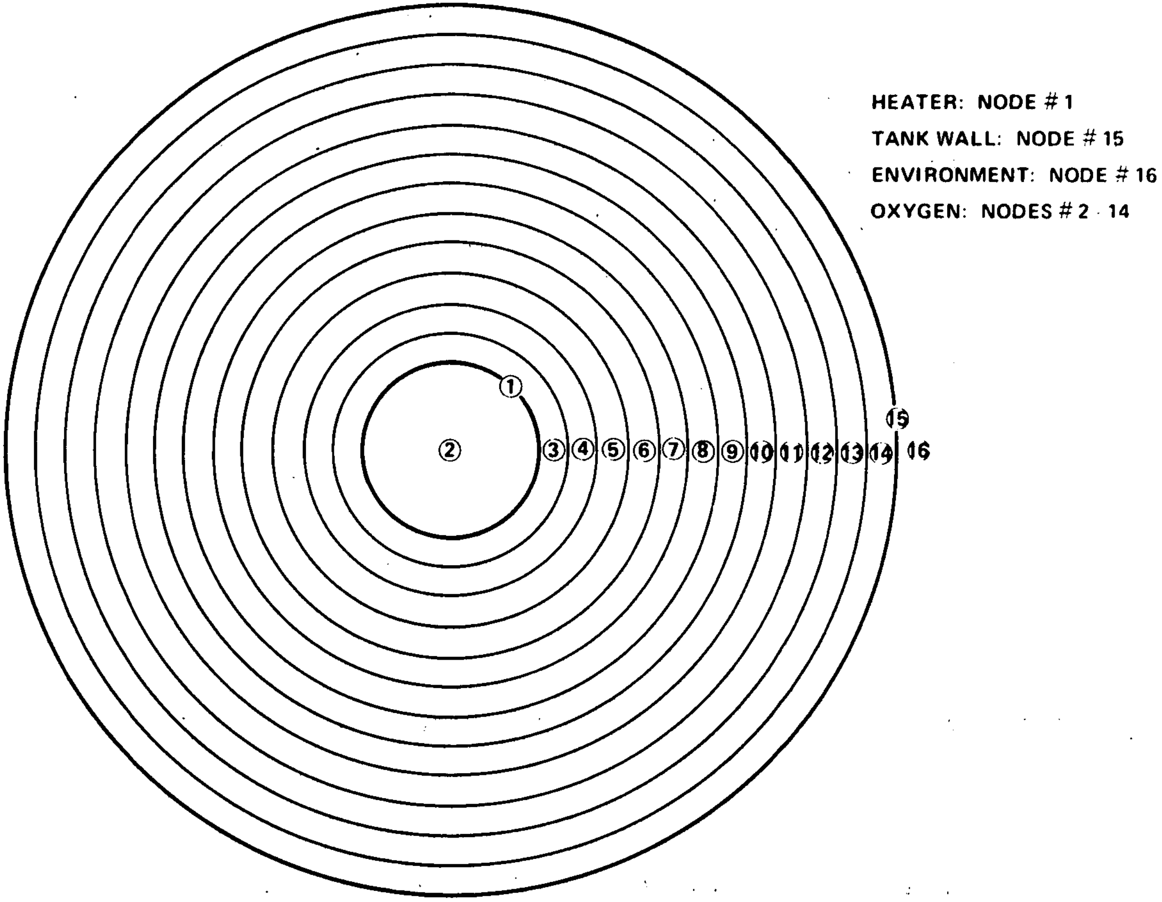

FIGURE 7 - OXYGEN TANK PHYSICAL MODEL

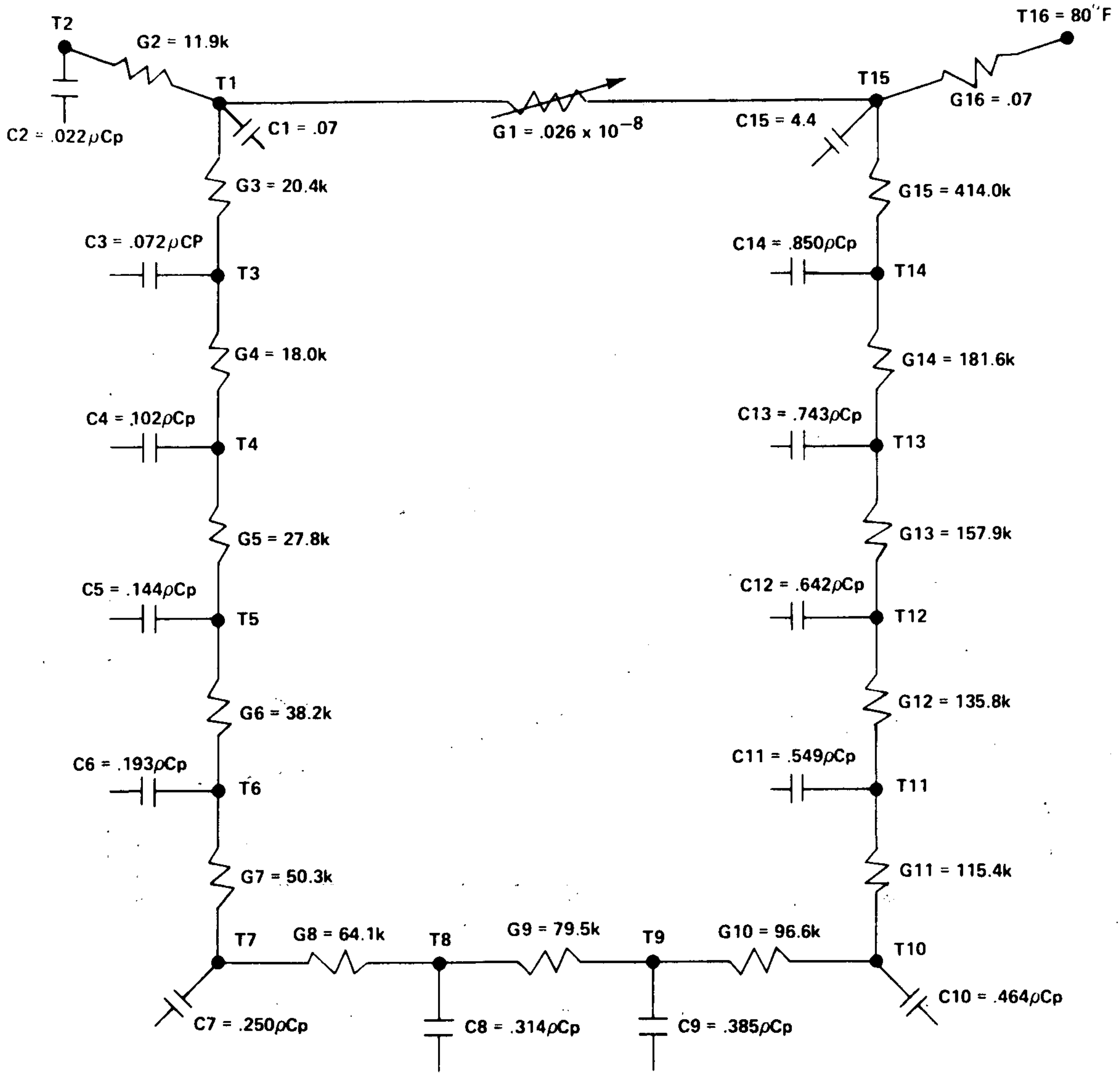

TX = TEMPERATURE OF NODE "X"
CX = MASS X SPECIFIC HEAT OF NODE "X" IN BTU/°F $\equiv$ (VOLUME) (ρCp)
GX = EFFECTIVE CONDUCTANCE BETWEEN ADJACENT NODES IN BTU/HR °F $\equiv kA/\chi$
G1 = EFFECTIVE RADIANCE BETWEEN NODES (1) AND (15) IN BTU/HR $^\circ F^4 \equiv A\epsilon\sigma$

FIGURE 8 - NETWORK DIAGRAM OF OXYGEN TANK THERMAL MODEL

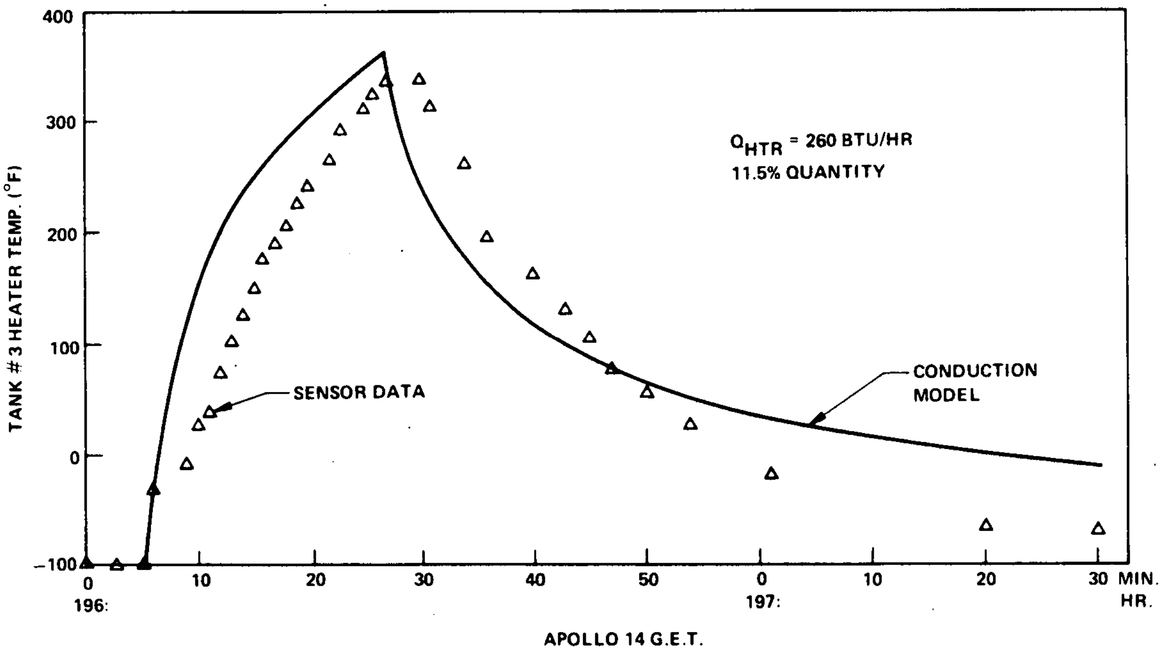

FIGURE 9 - HEATER TEMPERATURE PROFILE DURING ATTITUDE HOLD

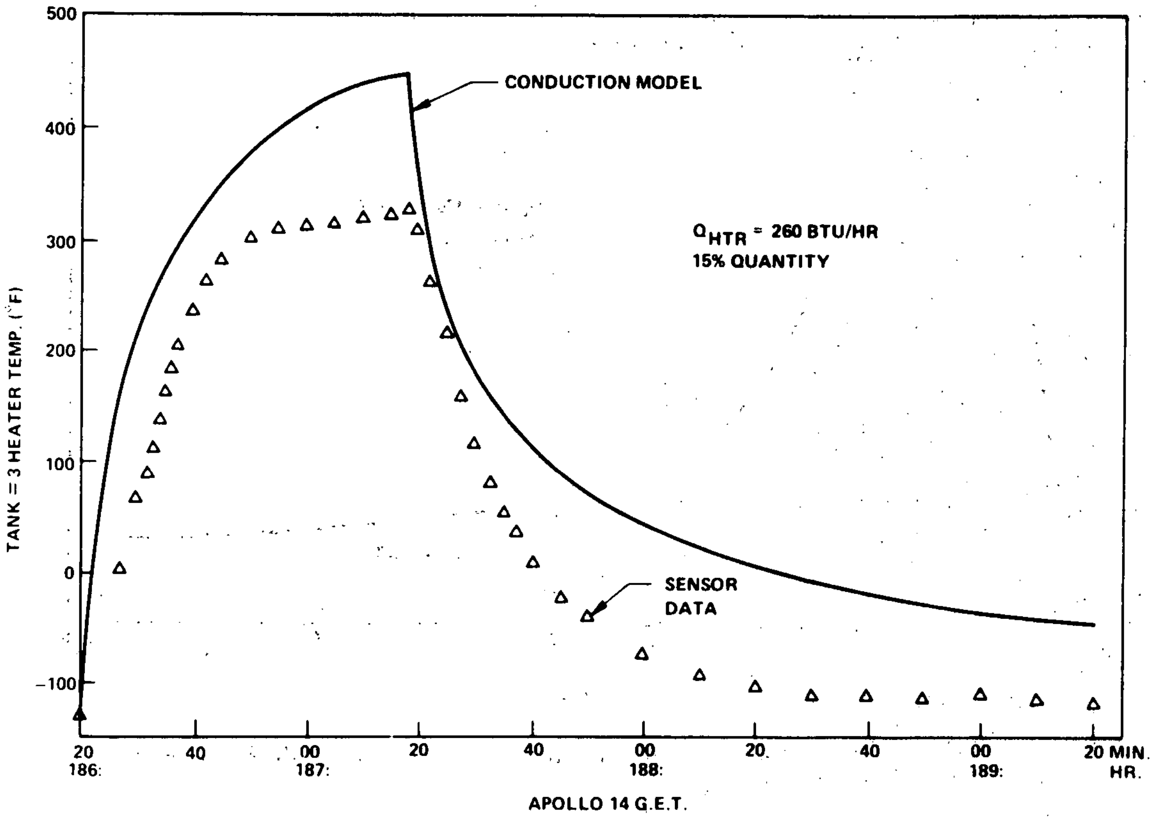

FIGURE 10 - HEATER TEMPERATURE PROFILE DURING ~ 1 RPH SPACECRAFT ROTATION

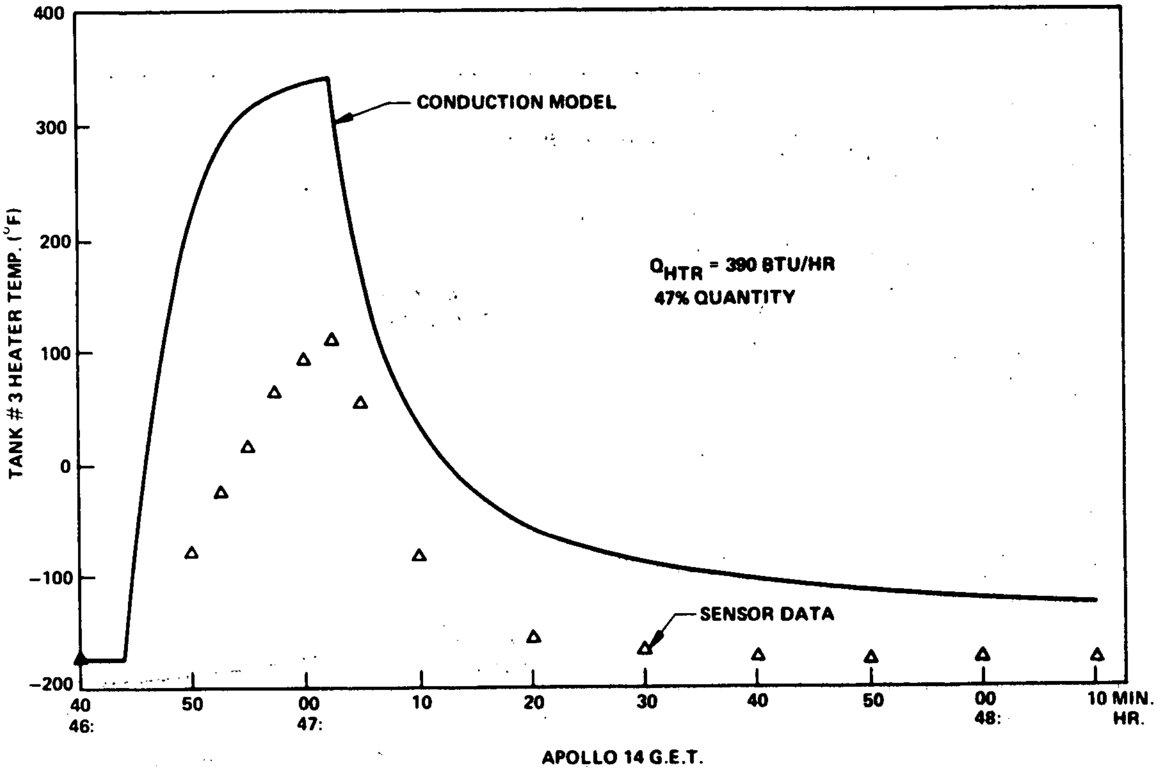

FIGURE 11 - HEATER TEMPERATURE PROFILE DURING ~ 3 RPH SPACECRAFT ROTATION

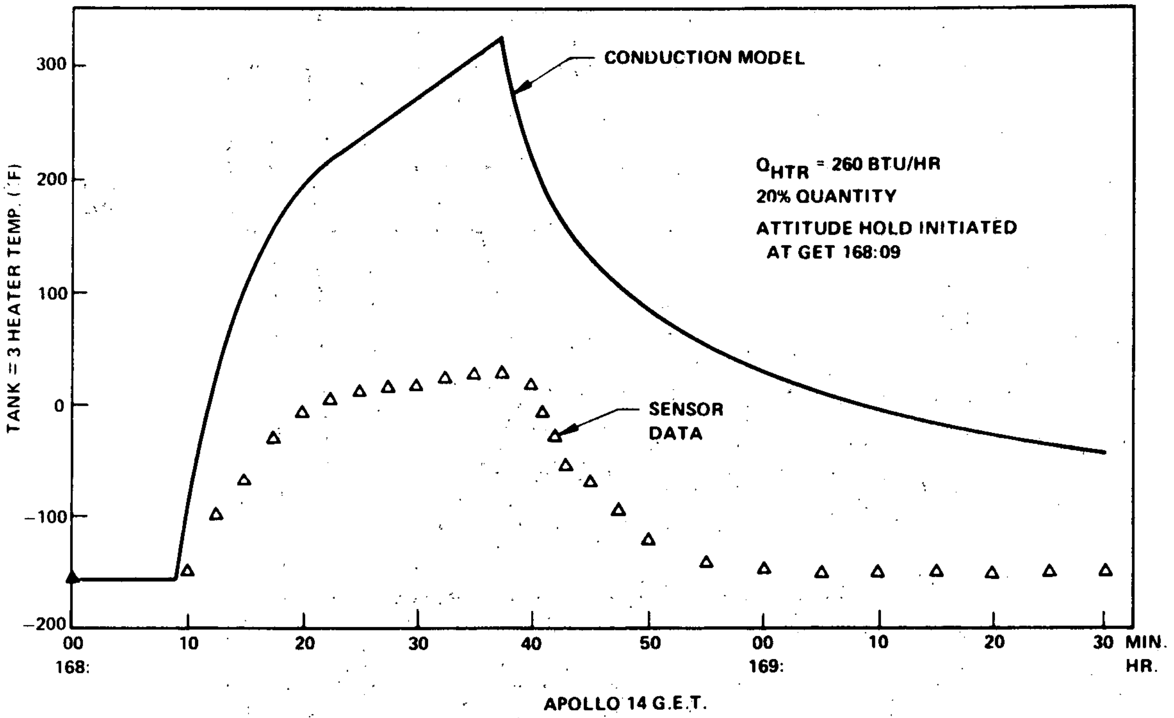

FIGURE 12 - HEATER TEMPERATURE PROFILE FOLLOWING SPACECRAFT ROTATIONAL MANEUVER

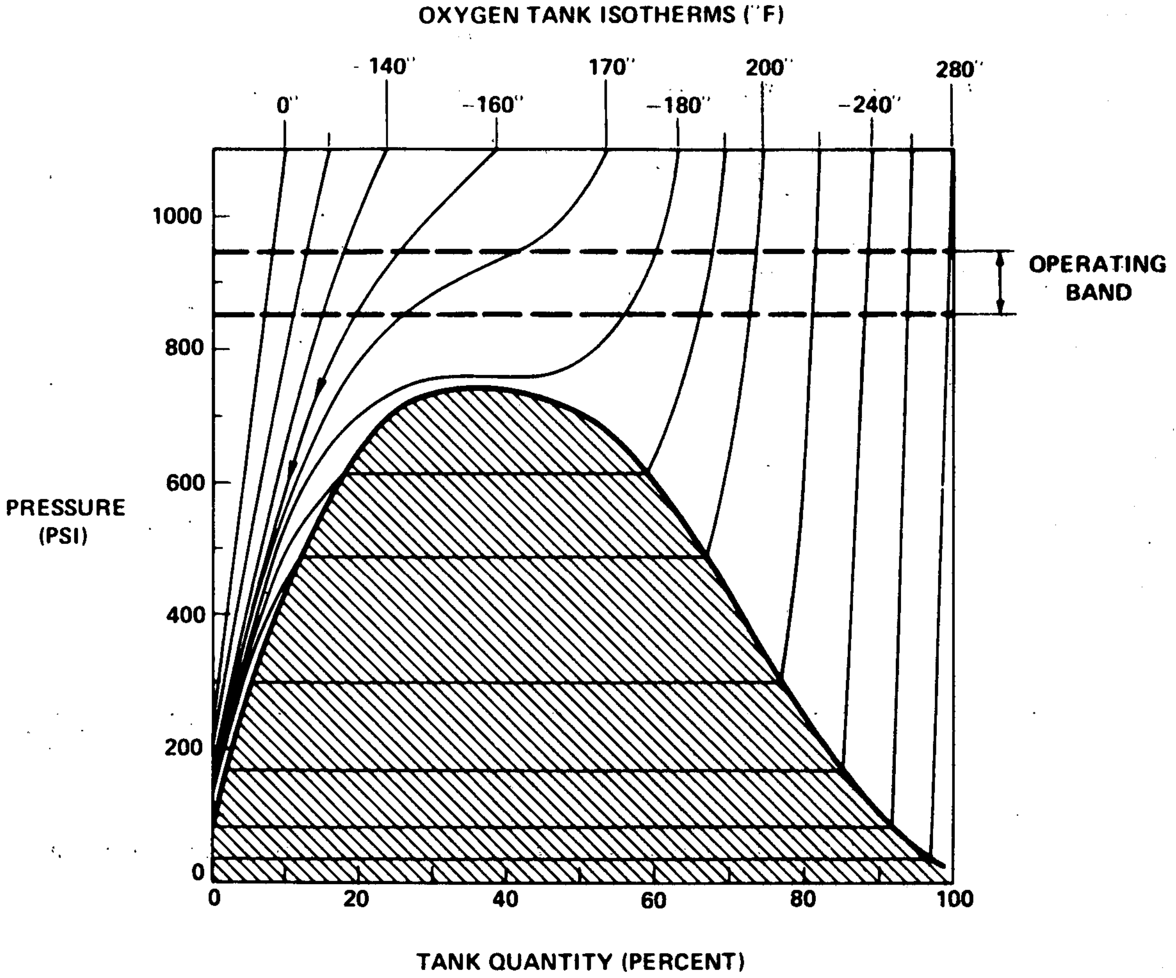

FIGURE 13 - OXYGEN SUPPLY PRESSURE VERSUS TANK QUANTITY

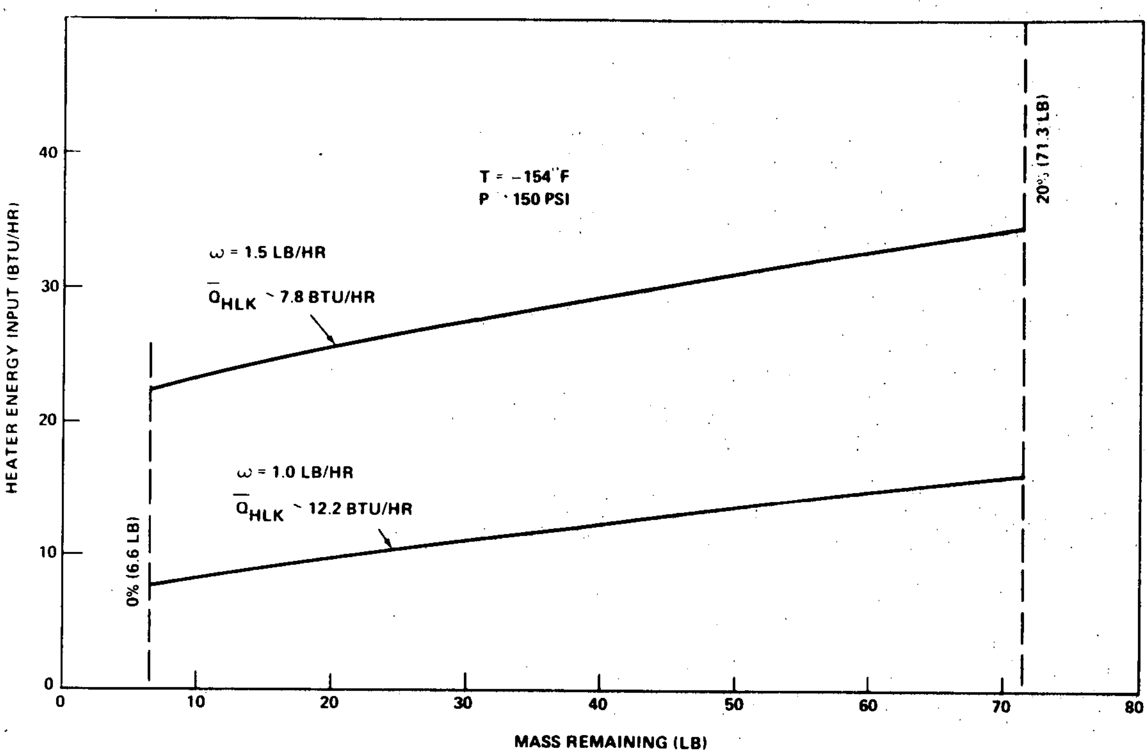

FIGURE 14 - HEATER ENERGY INPUT FOR ISOTHERMAL BLOWDOWN FROM 20% QUANTITY

N72-23793

MIXING EFFECTIVENESS IN THE APOLLO OXYGEN TANKS OF SPIN-UP AND ROTATION-REVERSAL MANEUVERS

By Barrett Baldwin, E. Dale Martin, Walter A. Reinhardt,
and Yvonne Sheaffer

Ames Research Center, NASA, Moffett Field, Calif. 94035

Abstract

Two-dimensional simulations of stratified flows in the Apollo oxygen tanks have been used to estimate the mixing effectiveness of spin-up and rotation-reversal maneuvers. Calculations have been made for square and circular cylindrical tank geometries. Differences arising from heater position on the tank wall or near the center of the tank have been investigated. In the event of a prolonged period without normal maneuvers, our investigations show that the potential pressure decay (drop in pressure that would result from adiabatic mixing) can be suppressed by more than a factor of two through the use of spin-up and rotation-reversal maneuvers. Changes in rotation rate of order three revolutions per hour or greater are sufficient for this purpose.

Introduction

Analyses of Apollo 12 data by several investigators (ref. 1) indicated that no serious stratification problems were to be expected from operation of the Apollo oxygen tanks with the mixing fans removed. This expectation was reinforced by the successful Apollo 14 flight during which additional information was secured. The view might be adopted that further investigation of a working system is not necessary. Yet in view of the serious consequences that could result from an undisclosed weakness it seems worthwhile to understand the operation of all parts of the system as thoroughly as possible.

Theoretical investigations of the degree of stratification to be expected in the absence of convection have indicated that potential pressure decays amounting to several hundred psi could develop (refs. 2 and 3). The pressure drops that would result from sudden mixing according to these predictions would not interfere with the operation directly. But a two-phase mixture could be produced in the oxygen tanks with possible damaging consequences elsewhere in the system. On the other hand, stratification analyses, which account for convection as well as conduction, indicate that excessive buildup of the potential pressure decay is averted by the mixing that results from normal vehicle maneuvering (refs. 4 and 5). Much as in the case of an earthquake, it is better to undergo numerous small maneuvers rather than a prolonged period of quiet followed by a big one.

Pressure and temperature data from past Apollo flights is useful for understanding the relationship between maneuvers and conditions in the oxygen tanks. However, direct measurements of velocity and temperature distributions in the tanks have not been made. At present the best information on detailed conditions in the tanks is based on two-dimensional computational simulations of the stratified flows resulting from maneuvers.

In this paper results are presented from a series of such calculations utilizing the methods described in references 5 through 10. Preliminary results based on the van der Waals equations of state were presented at meetings on the Apollo oxygen system held at the Manned

Spacecraft Center prior to the Apollo 14 flight. It was concluded by participants at the meetings that normal vehicle maneuvering could be relied upon to produce the necessary mixing. Nevertheless, several investigations were made of emergency procedures that could be used if the performance fell below the predicted level. Two-dimensional numerical simulations of stratified oxygen flows indicated that vehicle maneuvering leading to acceleration fields of order 10^{-3} g lasting for several seconds would produce effective mixing (ref. 4). The question was also raised whether reversal of the rotation rate starting at 3 revolutions/hour would provide useful mixing action in the oxygen tanks. From our preliminary results based on the van der Waals equations it was concluded that this latter maneuver would indeed provide an effective backup means for mixing the oxygen if normally occurring maneuvers proved insufficient. That conclusion is of continuing interest for future Apollo flights in which vehicle maneuvering is relied upon to produce the necessary mixing in the oxygen tanks.

In this paper we present results from calculations based on the accurate thermodynamic relations described in reference 8. The preliminary conclusions are verified and put on a firmer basis by these results. The effect of changes in rate of rotation on additional types of stratification are investigated. Preliminary calculations showing the rate of buildup of potential pressure decay during heater cycling are described.

Analytical Method

A two-dimensional square tank geometry similar to that of references 4 and 5 is utilized for the numerical simulation. The integration procedure used for the results in this paper is described in references 6 and 9. The equations expressing conservation of mass, momentum, and energy are cast in a form in which the primary dependent variables are the vorticity and temperature distributions. A pair of coupled differential equations results. A predictor-corrector method is used in the numerical differencing procedure. A time-dependent temperature distribution is determined from the integration. Several approximations are employed. Although pressure gradients must be considered in the momentum equations, it can be shown that for the low-velocity cryogenic oxygen flows under consideration, pressure gradients can be neglected in the energy equation. Likewise, the variations in pressure with time have only a cumulative effect in the energy equation that does not affect the motion of the gas directly. The most important coupling between the momentum and energy equations is through temperature gradients and convection of temperature variations. As a result, for the purpose of finding the motion of the gas, the density can be considered a function of temperature with pressure as a slowly varying parameter. If the temperature variations are sufficiently mild, the density and enthalpy can be approximated by the first several terms of series expansions in temperature with coefficients that vary slowly in time due to cumulative changes in pressure and temperature level. The derivation in reference 6 shows that to lowest order the flow equations can be cast in a form that is then independent of pressure and density variations. The corresponding integration procedure described in reference 9 requires as input a mean density $\bar{\rho}$ and thermal expansion coefficient β, each of which can be time dependent to allow for cumulative changes in pressure and temperature level. A time-dependent temperature distribution results from the integration procedure. The purpose of this section is to indicate how such output can be interpreted to determine the attendant slowly varying pressure as well as other thermodynamic variables such as the density distribution and the potential pressure decay that would result from adiabatic mixing.

As far as the thermodynamic state of the gas is concerned, pressure gradients are negligible at the low velocities that occur in a cryogenic oxygen storage tank in a near-zero gravitational environment. The pressure can therefore be considered uniform in the tank. The kinetic energy associated with the motion of the gas is also negligible compared to changes in the internal energy of interest. Thus the problem to which we shall address ourselves here is that of evaluating the time-dependent thermodynamic state of a stationary stratified gas from a knowledge of the time-dependent mean density and temperature distribution. The degree of rigor brought to bear is independent of the means used to arrive at the input information on mean density and temperature distribution. The methods developed for this purpose would, therefore, be applicable to the results from more accurate three-dimensional analyses of the convection and conduction processes within the tank. We have considered the problem at two levels of rigor. In preliminary work (ref. 5), the van der Waals equations of state were employed and in this paper we include results based on the accurate thermodynamic relations developed in reference 8.

Approximate Procedure Based on van der Waals Equations

As discussed above, the problem at hand is to find the pressure and other thermodynamic quantities when the mean density and temperature variation in the tank are known. The mean density $\bar{\rho}$ is known in terms of the total mass of oxygen M from the relation

$$\bar{\rho} = M/V_T \tag{1}$$

where V_T is the tank volume. A method for including the effect of tank stretch on the rate of pressure rise, not included in this description, is given in reference 7. The rate of change of mean density is found by differentiation

$$\frac{d\bar{\rho}}{dt} = \frac{(dM/dt)}{V_T} \tag{2}$$

where dM/dt is the rate of gas removal (typically, 0 to 3 lbm/hr). Values of $\overline{\rho}$ are computed at each time step from the relation

$$\overline{\rho}_{t+\Delta t} = \overline{\rho}_t + \Delta t \frac{(dM/dt)}{V_T} \tag{3}$$

using input values of dM/dt and V_T which are held constant during the integration.

At each time step the values of temperature T_{jk} at the computational grid points are determined from the integration procedure. The corresponding densities ρ_{jk} are computed to lowest order from the relation

$$\rho = \overline{\rho}[1 - \beta(T - \overline{T})] \tag{4}$$

where $\overline{T}$ is the volume average of the temperature variation T_{jk} and $\beta = -(1/\rho)(\partial\rho/\partial T)_p$ is the coefficient of thermal expansion corresponding to the state $\overline{\rho}$, $\overline{T}$. The van der Waals equation for pressure p is

$$p = \frac{RT\rho}{1 - b\rho} - a\rho^2 \tag{5}$$

Differentiation leads to the relation

$$\beta = \frac{R(1 - b\rho)}{RT - 2a\rho(1 - b\rho)} \tag{6}$$

for the coefficient of thermal expansion. In our preliminary results a constant value of β evaluated at the initial values of $\overline{\rho}$ and $\overline{T}$ was used.

Since a uniform spacing of computational grid points is employed in the integration procedure, the volume average $\overline{T}$ can be computed according to the relation

$$\overline{T} = \frac{\sum_{j,k} T_{j,k} W_{j,k}}{\sum_{j,k} W_{j,k}} \tag{7}$$

where $W_{j,k}$ is a weighting function that is taken equal to 1.0 at interior points, 0.5 at boundary points except in the corners, and 0 in the corners. The corners are excluded (zero weight) because, in the integration procedure described in reference 9, temperatures at the corners are not used and are not computed.

Substitution of T_{jk} and ρ_{jk} into equation (5) would lead to pressures p_{jk} that are not all equal. Since the pressure should be uniform in the tank, it is expedient to evaluate an average pressure according to the relation

$$\overline{(p + a\rho^2)(1 - b\rho)} = R\overline{T\rho}$$

where the bar indicates a volume average of the same type as in equation (7). Substitution of equation (4) into this relation, use of the fact that $\overline{(T - \overline{T})} = 0$, and omission of $\overline{(T - \overline{T})^3}$ terms lead to the approximate expression

$$p = \frac{R\overline{T}\overline{\rho}}{1 - b\overline{\rho}} - a(\overline{\rho})^2 + \frac{[a(\overline{\rho})^2(3b\overline{\rho} - 1)\beta^2 - R\overline{\rho}\beta]\overline{(T - \overline{T})^2}}{1 - b\overline{\rho}} \tag{8}$$

for the pressure in terms of average density, average temperature, and mean squared deviation of the temperature from the average value. The latter quantity is computed at each time step as in equation (7) according to the relation

$$\overline{(T - \overline{T})^2} = \frac{\sum\limits_{j,k} (T_{jk} - \overline{T})^2 W_{jk}}{\sum\limits_{j,k} W_{jk}} \tag{9}$$

In addition to the pressure, the potential pressure decay that would result from complete adiabatic mixing is of interest. In general, the procedure for evaluation of this quantity is as follows:

$M = \overline{\rho}V_T$	total mass
$E = \overline{e\rho}V_T$	total internal energy
$e_c = E/M$	specific internal energy of collapsed state resulting from complete adiabatic mixing
$\rho_c = \rho/(1 - K_S)$	density of collapsed state
$T_c = T(e_c, \rho_c)$	temperature of collapsed state
$p_c = p(T_c, \rho_c)$	collapse pressure
$p - p_c$	potential pressure decay

where e is the specific internal energy and $\overline{e\rho}$ is a volume average. The factor $(1 - K_S)$ allows for shrinkage of the tank volume due to a drop in pressure and can be evaluated from the relation (ref. 4)

$$K_S = \frac{3r(1 - \sigma)(p - p_c)}{2b_1 E_y}$$

where

r/b_1 = ratio of spherical tank radius to wall thickness

σ = Poisson's ratio for tank wall material

E_y = Young's modulus for tank wall material

Evaluation of the tank stretch effect requires iterative solution for K_S and $p - p_c$. Recently, we have made calculations in which this procedure is included.

The above procedure for determination of the potential pressure decay can be carried out using approximate equations of state or the more exact relations of reference 8. Our preliminary results were based on the van der Waals equations of state, equation (5), and (ref. 11)

$$e = c_1 + c_v T - a\rho \tag{10}$$

Substitution of equation (5) into (10) to eliminate the temperature and use of the fact that the pressure is uniform in the initial stratified state yield the formula

$$p - p_c = \frac{ab[\overline{\rho^3} - (\overline{\rho})^3] - a[1 - (R/c_v)][\overline{\rho^2} - (\overline{\rho})^2]}{1 - b\overline{\rho}}$$

where $\overline{\rho^2}$ and $\overline{\rho^3}$ indicate volume averages. Substitution of the first-order density relation, equation (4), rearrangement, and omission of $(T - \overline{T})^3$ terms lead to the approximation

$$p - p_c = \frac{a(\overline{\rho})^2[3b\overline{\rho} - 1 + (R/c_v)]\beta^2\overline{(T - \overline{T})^2}}{1 - b\overline{\rho}} \tag{11}$$

which expresses the potential pressure decay in terms of the average density and mean squared deviation of temperature from the average value.

The specific heat at constant pressure is needed in the integration procedure described in references 6 and 9. The van der Waals equations of state (eqs. (5) and (10)) can be used to derive the relation

$$c_p = c_v + \frac{R}{1 - 2a\rho(1 - b\rho)^2/RT} \tag{12}$$

In our preliminary results a constant value of c_p was used, evaluated at the initial values of $\bar{\rho}$ and $\bar{T}$. The values of the constants R, b, a, c_v used in the van der Waals equations were chosen such that the critical pressure, temperature, and density are matched exactly according to relations given by Hirschfelder, Curtiss, and Bird (ref. 11).

Procedure Based on Exact Thermodynamics

In this section an exact method is described for finding the pressure and other thermodynamic quantities when the mean density and temperature distribution in the tank are known. For this purpose it was found expedient to determine a temperature distribution function $F_T(N)$ of the type developed in reference 8 rather than to consider thermodynamic quantities at each computational grid point. The function $F_T(N)$ is defined to be a weighted number of computational grid points with temperatures between $T_N - \Delta T$ and $T_N + \Delta T$ where the T_N are a fixed array of temperatures with uniform spacing equal to ΔT. The weighting employed is proportional to the volume associated with each computational grid point. Interior points are given a weight $w_{jk} = 1.0$, for boundary points $w_{jk} = 0.5$ and the corner points are given zero weight since their temperatures are not computed in the integration procedure. For each value of j and k, w_{jk} is assigned to the two $F_T(N)$ between which its temperature lies in proportion to its proximity to each; that is, if $T_N < T_{jk} < T_{N+1}$, $F_T(N)$ is increased by an amount $w_{jk}(T_{N+1} - T_{jk})/\Delta T$ and $F_T(N+1)$ is increased by an amount $w_{jk}(T_{jk} - T_N)/\Delta T$. Thus the sum

$$\sum_{N=1}^{N_{MAX}} F_T(N)$$

is equal to the total number of interior computational grid points plus half the number of boundary points, not counting corners. The quantity $F_T(N)$ is essentially equal to the total number of computational grid points with temperature between $T_N - (1/2)\Delta T$ and $T_N + (1/2)\Delta T$ except for a small readjustment corresponding to a linear interpolation. Figure 1 shows an example of a temperature distribution $F_T(N)$ plotted versus T_N. Additional examples and further discussion of the meaning of this distribution function are contained in references 7, 8, and 10.

An array of temperatures T_N is associated with the temperature distribution function $F_T(N)$. At a given tank pressure p, associated arrays of density ρ_N and internal energy e_N can be computed according to the relations

$$\rho_N = \rho(p, T_N) \tag{13}$$

$$e_N = e(\rho_N, T_N) \tag{14}$$

The computation of the functions $\rho(p, T_N)$ and $e(\rho_N, T_N)$ is described in reference 8. Since the $F_T(N)$ are proportional to the volume of gas in the temperature range $T_N - (1/2)\Delta T$ to $T_N + (1/2)\Delta T$, the volume averages $\overline{\rho}$ and $\overline{\rho e}$ can be computed according to

$$\overline{\rho} = \frac{\sum_{N=1}^{N_{MAX}} F_T(N)\rho_N}{\sum_{N=1}^{N_{MAX}} F_T(N)} \tag{15}$$

$$\overline{\rho e} = \frac{\sum_{N=1}^{N_{MAX}} F_T(N)\rho_N e_N}{\sum_{N=1}^{N_{MAX}} F_T(N)} \tag{16}$$

Values of gas density and the transport properties at the computational grid points are found by linear interpolation of values computed at the conditions ρ_N, T_N.

At the beginning of an integration for the time-dependent temperature distribution, a tank pressure p and values of temperature T_{jk} at the computational grid points are specified. The distribution function $F_T(N)$ is computed and the above relations are used to determine the initial values of $\overline{\rho}$ and $\overline{\rho e}$. In the subsequent integration the variation of $\overline{\rho}$ is computed from equations (3) and depends on the specified constant rate of gas removal dM/dt. The values of T_{jk} resulting from the integration are used to compute $F_T(N)$ at the end of each time step. The problem then arises of computing the change in pressure p in each time step. By differentiation it can be seen that changes in the ρ_N are related to changes in pressure according to

$$\Delta\rho_N = \frac{\Delta p}{(\partial p/\partial\rho_N)_{T_N}} \tag{17}$$

since the values of T_N are held fixed throughout the integration. Substitution of this in the relation

$$(\rho_N)_{n+1} = (\rho_N)_n + \Delta\rho_N \tag{18}$$

yields

$$(\rho_N)_{n+1} = (\rho_N)_n + \frac{\Delta p}{(\partial p/\partial\rho_N)_{T_N}} \tag{19}$$

where the subscript n refers to the time step in the integration. Multiplication of the last equation by $F_T(N)_{n+1}$, summation over N, and substitution of

$$\sum_{N=1}^{N_{MAX}} F_T(N)_{n+1}(\rho_N)_{n+1} = \bar{\rho}_{n+1} \sum_{N=1}^{N_{MAX}} F_T(N)_{n+1} \tag{20}$$

yield

$$\bar{\rho}_{n+1} \sum_{N=1}^{N_{MAX}} F_T(N)_{n+1} = \sum_{N=1}^{N_{MAX}} F_T(N)_{n+1}(\rho_N)_n + \Delta p \sum_{N=1}^{N_{MAX}} \frac{F_T(N)_{n+1}}{(\partial p/\partial\rho_N)_{T_N}} \tag{21}$$

Since $\bar{\rho}_{n+1}$ and $F_T(N)_{n+1}$ are known at the end of the (n+1)st time step, this equation can be used to compute the change in pressure Δp associated with the time step. Once Δp is known, equation (19) can be used to compute the updated values of density $(\rho_N)_{n+1}$. As a check, $\bar{\rho}_{n+1}$ can be computed using equation (20) for comparison with the imposed value of $\bar{\rho}_{n+1}$ from equation (3). Finally, the updated pressure is computed according to

$$p_{n+1} = p_n + \Delta p \tag{22}$$

The structure of equation (21) is such that the value of $\bar{\rho}_{n+1}$ computed from equation (20) will always be driven toward the imposed value from equation (3) so that cumulative drifts cannot occur. Cumulative drifts of the individual $(\rho_N)_{n+1}$ computed from equation (19) can take place, however. To avoid this, at every tenth time step, the ρ_N are recomputed according to equation (13). It has been found that the foregoing procedure is quite stable and, for the sizes of time step imposed by stability criteria of the integration procedure, is quite accurate with a 1° K spacing of the temperature elements T_N. It can be noted that the foregoing procedure could not be applied at the computational grid points since equation (19) is valid only for an array of constant temperatures T_N.

Once the pressure is determined the potential pressure decay can be computed by the procedure described in reference 8 that utilizes the distribution function $F_T(N)$. As a check, the potential pressure decay can also be computed by the alternative method of reference 8 for which the pressure p and temperatures at computational grid points are utilized. Figure 2 shows a comparison of potential pressure decays computed by the two methods for a linear temperature distribution. The dashed lines indicate the potential pressure decay for each case computed exactly by evaluation of the thermodynamic quantities at all computational grid points. The symbols indicate values of the potential pressure decay computed using the distribution function $F_T(N)$ for various values of the temperature array spacing ΔT. It can be seen from the results in figure 2 that the temperature array spacing $\Delta T = 1°$ K provides adequate accuracy for all of the cases considered.

Method for Simulating Heater

An internal heater is used in the Apollo oxygen tanks to increase the pressure when it falls below 870 psia due to gas removal. In reference 4 a segment of the wall is used to simulate such a heater. It was found that the boundary-layer flow in the neighborhood of the heater cannot be adequately resolved with a uniform grid spacing when the acceleration field is of order 10^{-6} g or greater. Methods can nevertheless be found that lead to physically reasonable and qualitatively correct results if attention is confined to energy conservation, and accurate values of heater temperature are not required.

The energy balance will be properly maintained if at the beginning of each time step the heater element temperatures are increased by an amount ΔT_H corresponding to a specified heater power dQ/dt added to the total gas volume V_{HT} associated with the heater element computational grid points; that is,

$$\Delta T_H = \frac{(dQ/dt)\ \Delta t}{\rho C_p V_{HT}} \qquad \text{(before integration step)} \qquad (23)$$

The gas volume associated with each interior computational grid point is

$$V_H = \frac{V_T \, \Delta x \, \Delta y}{\ell_x \ell_y} \tag{24}$$

where Δx and Δy are the distances between grid points and ℓ_x, ℓ_y, the tank dimensions.

If the heater element computational grid points are interior points, the total heater gas volume V_{HT} is the number of heater elements times V_H. But heater volume elements on the boundary are half the value given in equation (24) since the boundary passes through the grid points. When the heater elements are in the interior their temperatures will rise until a balance is reached between the temperature increase from equation (23) and the decrease due to convection and conduction computed in the integration procedure. When the heater elements are on the boundary, however, the integration procedure does not modify their values. In that case, it is necessary to allow for a decrease in temperature at the *end* of each time step according to the amount of heat transferred to the interior grid points from the heater elements. The appropriate change in wall heater element temperatures is

$$\Delta T_H = - \frac{2K(T_H - T_{\text{interior}}) \, \Delta t}{C_p \rho (\Delta x)^2} \qquad \text{(after integration step)} \tag{25}$$

If the heater is on a wall, the ΔT_H computed in equation (25) corresponds to an insulated wall boundary condition except for a small (physically correct) lag due to the heat capacity of the gas adjacent to the wall.

The same type of computation as that in equations (23) and (25) can be used at all boundary points to simulate the heat leak from the exterior of the tank. In that case dQ/dt in equation (23) is replaced by the heat leak power dQ_L/dt.

The power radiated from the heater can be allowed for by means of the relation

$$\frac{dQ}{dt} = \frac{d\tilde{Q}}{dt} - Q_{RAD} \tag{26}$$

where $d\tilde{Q}/dt$ is the specified input heater power and

$$Q_{RAD} = \varepsilon \sigma_R [T_H^4 - (\bar{T})^4] A_H \tag{27}$$

where ε is the emissivity (typically, 0.32), σ_R the Stefan-Boltzmann constant, and A_H the heater area. According to reference 12, less than 10 percent of the radiated power is absorbed in the oxygen (usually much less depending on the heater temperature). Therefore, most of the radiation is absorbed in the tank wall and Q_{RAD} should be added to the heat leak power dQ_L/dt. In reference 7, methods for including the effects of tank stretch are described.

Results

Mixing Effectiveness of Rotation Reversal

Calculations were made in which the vehicle was taken to be rotating initially at 3 revolutions/hour. A series of initial stratified states were imposed with the temperature varying linearly across the tank. The hot gas was placed in the stable position toward the center of rotation outside the tank. Such stratification can be expected to develop after many heater cycles while operating with a steady vehicle rotation rate, although no heater was actually used in this first type of calculation. In the absence of other vehicle maneuvering and with the heater turned off, the calculations show a very slow decrease in potential pressure decay and no motion of the gas. The decrease in potential pressure decay in this case is due to conduction arising from the mild temperature gradient. When the direction of rotation is abruptly reversed, however, a swirling motion of the gas ensues and leads to mixing and enhanced temperature gradients. Figure 3 depicts the velocity field in the flow that results. Photographs are shown of a cathode ray display tube on which were plotted the velocity vectors at the computational grid points. The upper left photograph shows the velocities immediately after rotation reversal. The magnitude of the velocity near the tank boundaries is about 0.02 ft $\sec^{-1}$. The clockwise swirling motion results in part from the rotational inertia of the gas which tends to retain the motion it possessed before the rotation reversal of the vehicle. A lateral linear acceleration, present during the reversal, acts differentially on the stratified layers to give an additional kick to the swirling motion. The other photographs in figure 3 show the velocity vectors at later times. The off-center swirl that develops because of the stratification present moves continuously in the clockwise direction which is also the direction of motion of the gas. The center of rotation is about 1-1/2 tank diameters below the center of the tank.

In addition to velocity vectors, several other features are visible in the photographs in figure 3. The arrow midway up on the right indicates the direction of the sun. The graph at the bottom is a running plot of the potential pressure decay versus time. The scale is automatically decreased when the plot becomes overextended. In the lower right photograph the time scale has been decreased by a factor of 2 relative to that in the other photographs. The numerical values visible on the right represent the following quantities:

OMEG	vehicle rotation rate, radian sec^{-1}
DQDT	heater power, W
RHOB	mean density, g cm^{-3}
TB	mean temperature, °K
TH	heater temperature, °K
P	pressure, psia
DPC	potential pressure decay (method 1, ref. 8), psi
PPD	potential pressure decay (method 2, ref. 8), psi
COUNT	number of time steps in the integration

Method 1 of reference 8 utilizes a temperature distribution function, while method 2 uses temperatures at the computational grid points.

Figure 4 contains photographs showing the evolution of temperature distribution in the tank. For temperatures greater than the average, the deviations from the mean temperature are represented by vertical lines. As an aid to visualization, for temperatures less than average the deviations from the mean are shown as horizontal lines. In either case, the length of the lines indicates the magnitude of the temperature deviation from the mean at each computational grid point. The upper left photograph in figure 4 shows the initial assumed linear temperature distribution. The hot gas is toward the center of rotation, which is 1-1/2 tank diameters below the center of the tank. The remaining photographs show temperature distributions at later times after mixing has resulted from the swirling motion.

Figure 5 contains plots of the thermodynamic state of the gas without regard to position in the tank (see ref. 8). This is the number of computational grid points within 1° K temperature intervals. The unfilled histogram represents the initial linear temperature distribution. The shaded histogram shows the distribution 40 minutes after rotation reversal when considerable mixing has taken place and the steep temperature gradients have reduced the temperature deviations from the average temperature.

The variation of potential pressure decay with time for two cases is shown in figure 6. The curve labeled Stewart was computed using the accurate thermodynamic functions described in reference 8. The curve labeled van der Waals is from our preliminary report (ref. 5). The preliminary results compare favorably with those from the present more accurate calculations. In these runs no provision was made for heater cycling and the pressure dropped to about 700 psia as a result of the mixing. The mean density was held fixed corresponding to a zero rate of gas removal. The mean temperature remained constant at about 150° K.

The close agreement between the preliminary results based on the van der Waals equations and the present calculations is somewhat fortuitous. Figure 7 contains plots of potential pressure decay versus the magnitude of linear temperature variations for several tank pressures according to the van der Waals equations. Figure 8 shows results for the same conditions based on the accurate thermodynamics of reference 8. It is not necessary to superimpose figures 7 and 8 to see that the van der Waals results disagree grossly with those based on Stewart's equations when the pressure is held constant. However, for the rotation-reversal computations in which the pressure was allowed to decrease, the results in figure 6 show much smaller differences than would be expected from comparison of figures 7 and 8. The preliminary conclusions on the mixing effectiveness of the rotation-reversal maneuver, although not changed, have been put on a firmer basis by the calculations utilizing accurate thermodynamics in this paper.

The sharp bends in the curves contained in figure 8 are of interest. The flattening out takes place when a level of stratification is reached for which the collapsed state contains a two-phase mixture of liquid and vapor. Many other interesting aspects of the behavior of cryogenic oxygen are illustrated in the thermodynamic property plots presented in reference 8.

Figure 9 contains results based on accurate thermodynamics for several cases with less severe initial stratification. Decreases in potential pressure decay by a factor of 2 or more result from rotation reversal in these cases also. Most of the calculations in this paper were made with a value of 0.8 for the Courant number as defined in reference 9. Case I in figure 9 was also computed with a Courant number of 0.4. It can be seen that there is little difference. Appreciable variations in the flow variables extend over several computational grid points except in the boundary layer at the wall. Changes taking place in the boundary layer do not significantly affect the evolution of the potential pressure decay in the rotation-reversal problem. For this reason, as discussed in reference 5, the results are insensitive to a change in grid spacing from a 17 × 17 matrix to a 33 × 33 matrix.

Mixing Effectiveness of Spin-Up After Attitude Hold

In the previous section, initial stratified states were considered that would be expected to result after many heater cycles with the vehicle in the PTC mode (rotation at a steady rate). Another case of interest is the type of stratification that would result after many heater cycles in the attitude hold mode. In the absence of vehicle maneuvering no convection currents would develop and the heat from the heater can spread into the gas only by conduction. A localized hot spot around the heater somewhat diffused by conduction is to be expected in this case with essentially zero gas velocity. It is of interest to determine the mixing effectiveness on such an initial stratified state of a vehicle spin-up to the PTC mode. In the coordinate system fixed with respect to the tank used in this paper changes in rotation rate cause a rotating motion of the gas. The velocity field that occurs as a result of spin-up is similar to that shown in figure 3. Figure 10 illustrates the effect of spin-up on the temperature distribution. The upper left photograph shows the initial assumed distribution. Subsequent distortions and dissipation resulting from the swirling motion are shown in the remaining photographs.

Figure 11 is a plot of potential pressure decay versus time after spin-up. For comparison, a plot is included showing the very slow decrease in potential pressure decay that occurs as a result of conduction when the attitude hold condition is maintained. Again it is found that a change in vehicle rotation rate provides effective mixing action.

Flows and Stratified States Produced by Heater Cycles

Figure 12 shows the velocity fields that develop after several heater cycles for different tank geometries and heater positions. The flow field in the photograph on the upper left was generated with elements on the left wall acting as a heater. The plot at the bottom of the upper left frame is the potential pressure decay versus time from the beginning of the calculation. The potential pressure decay rises when the heater is on and subsides when the heater is off. It can be seen that about 6-1/2 heater cycles have taken place since the beginning of the calculation at the time of the photograph. A vehicle rotation rate of 0.4 revolution/hour was imposed in all of the cases shown in figure 12 corresponding to about 5×10^{-8} g at the center of the tank. Additional information on these runs is presented in subsequent figures. The meanings of the numerical values on the right of each frame was explained earlier in this paper in connection with figure 3.

In the upper right photograph of figure 12 the velocity field is shown for a calculation in which the heater is located near the center of the tank. The lower left frame contains similar results for a circular cylindrical tank geometry with an off-center internal heater position. The lower right frame shows the temperature distribution in the tank corresponding to the same calculation. For times of order 2 hours with small vehicle rotation rates, only a small volume of gas near the heater is heated appreciably.

Figure 13 shows the pressure cycles and potential pressure decay versus time corresponding to the upper left frame of figure 12. The next two figures contain similar results corresponding to the other frames of figure 12. Comparison of these results indicates that the heater cycle durations and magnitudes of potential pressure decay are insensitive to the tank geometry and heater positions used in the calculations. However, the results do depend on the total volume associated with the computational grid points assigned as heater elements. The results in figures 13 to 15 correspond to a heater area of approximately 0.5 ft^2.

Figure 16 shows the effect of vehicle spin-up on the pressure cycle and the potential pressure decay. In this calculation a circular cylindrical tank geometry with off-center internal heater was employed. A smaller heater volume was used corresponding to a heater area of about 0.3 ft^2. During the initial buildup of potential pressure decay, the vehicle was not rotating. The spin-up was started at 127 minutes after the start of the calculation and was completed in about 5 minutes. The rotation rate was held constant at 3 revolutions/hour thereafter. After a delay of about 10 minutes the swirling motion of the gas introduced by the vehicle spin-up had a large effect on the pressure cycle. The potential pressure decay dropped off precipitously, causing a drop in pressure as well. Thus, even though the heater was turned on at 149 minutes when the pressure fell below 870 psia, the pressure continued to drop and was down to 810 psia at the end of the calculation. Thus the same conclusion on the mixing effectiveness of a change in vehicle rotation rate has been arrived at from a calculation in which the stratification was produced by heater cycling. Additional calculations have been made for tank quantities between 65 and 90 percent with similar results.

Conclusions

The foregoing results show that appreciable mixing can be achieved in a short time by changing the vehicle rotation rate by modest amounts. No significant differences were found in the calculations for square or circular cylindrical tank geometries. Results from calculations in which the heater was located on the wall did not differ grossly from those in which the heater position was near the center of the tank. Earlier predictions based on the van der Waals equations of state have been verified by the use of accurate thermodynamic relations.

It appears that changes in the vehicle rate of rotation by several revolutions per hour or greater could be used in the same way that the mixing fans were used in earlier Apollo flights for which fans were installed in the oxygen tanks. Namely, such a maneuver could be initiated if there is reason to believe that the level of stratification is high. Time lags of order 20 minutes to an hour are to be expected before effective mixing will occur after the maneuver is initiated. A spin-up followed by a spin-down in less than 20 minutes would be less effective than if the new rotational state were maintained for a longer period.

References

1. Anon.: Minutes of the Third Apollo Cryogenic Oxygen Tank Analysis Meeting. NASA MSC, Houston, Texas, Jan. 1971.
2. Kamat, D. V.; and Abraham, W. H.: Pressure Collapse in Oxygen Storage under Zero-g. J. Spacecraft, 5, 184, 1968.
3. Haron, A. S.: Transient Analysis of Heat Transfer in a Simplified Model of the Apollo Oxygen Tank-Case 320. Memorandum for file. Included in Minutes of Third Apollo Cyrogenic Oxygen Tank Analysis Meeting, NASA MSC, Houston, Texas, Jan. 1971.
4. **Forester**, C. K.; Rule, D. D.; and Patterson, H. W.: Apollo Oxygen Tank Stratification Analysis. Boeing Document No. D2-118357-1, Nov. 1970.
5. Baldwin, B.; and Sheaffer, Y.: Mixing Effectiveness of Vehicle Rotation Reversal in Apollo Oxygen Tanks. Included in Minutes of Third Apollo Cyrogenic Oxygen Tank Analysis Meeting, NASA MSC, Houston, Texas, Jan. 1971.
6. Martin, E. D.; and Baldwin, B. S.: Flow Equations Governing Combined Forced and Natural Convection in a Rotating Tank. Proposed NASA TR.
7. Baldwin, B.; Reinhardt, W. A.; and Sheaffer, Y.: Thermodynamic Interpretation of Incompressible Flow Simulation of Gas Motion in the Apollo Oxygen Tanks. Proposed NASA TR.
8. Reinhardt, W. A.: Calculation of Thermodynamic Properties of Oxygen Near the Critical Point. Proposed NASA TR.
9. Lomax, H.; and Bailey, F. R.: Computational Method for Calculating Convection in a Rotating Square Tank. Proposed NASA TR.
10. Baldwin, B. S.; Reinhardt, W. A.; and Sheaffer, Y.: Results from Numerical Computations Simulating Flows in an Apollo Oxygen Tank. Proposed NASA TR.
11. Hirschfelder, J. O.; Curtiss, C. F.; and Bird, R. B.: Molecular Theory of Gases and Liquids. John Wiley & Sons, New York, 1954, pp. 237, 250-252.
12. Borucki, W. J.: Absorption of Infrared Radiation by High Density Oxygen. To be published in AIAA Journal, May or June 1971.
13. Anon.: Apollo Fuel Cell and Cryogenic Gas Storage System Flight Support Handbook. Prepared by Propulsion and Power Division, NASA MSC, Houston, Texas, Feb. 1970.

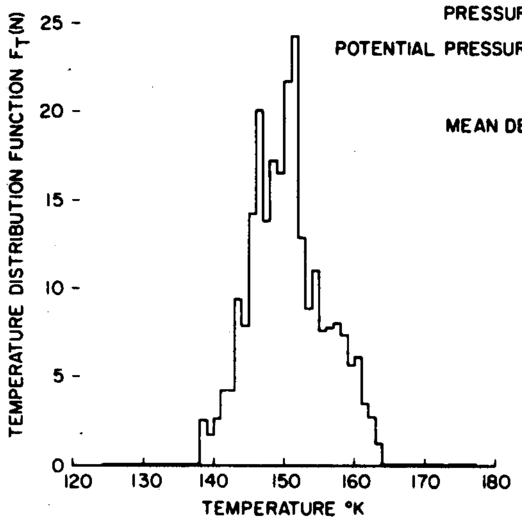

Figure 1. Typical temperature distribution function.

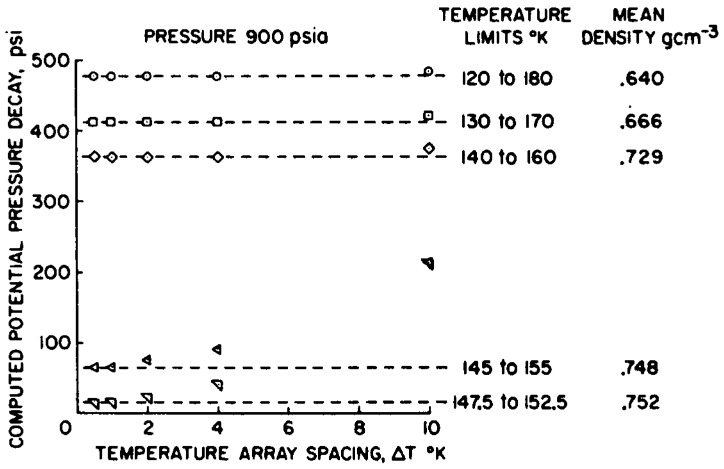

Figure 2. Effect of temperature array spacing on computed potential pressure decay.

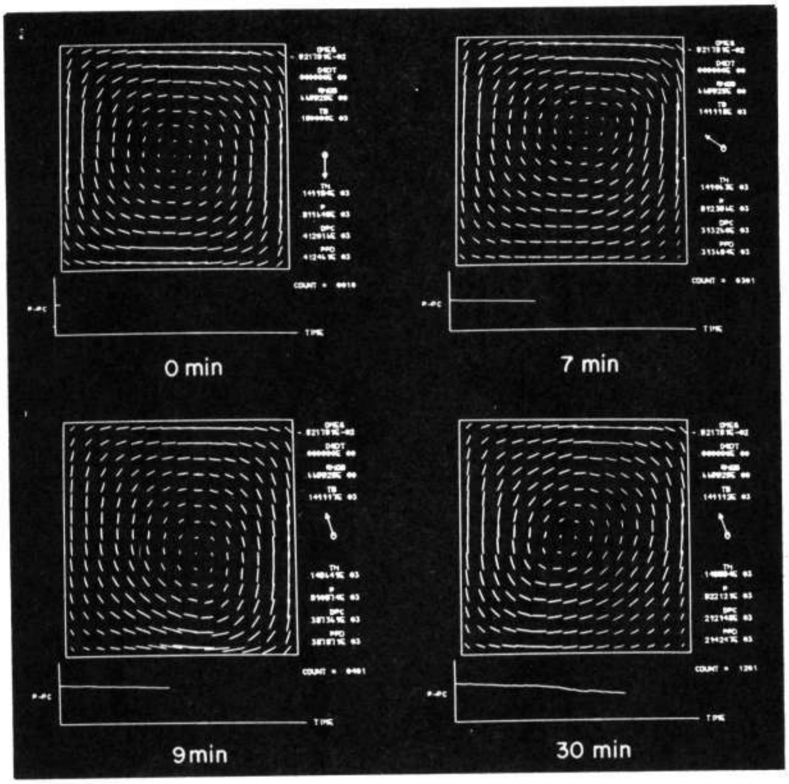

Figure 3. Velocity vectors after rotation reversal.

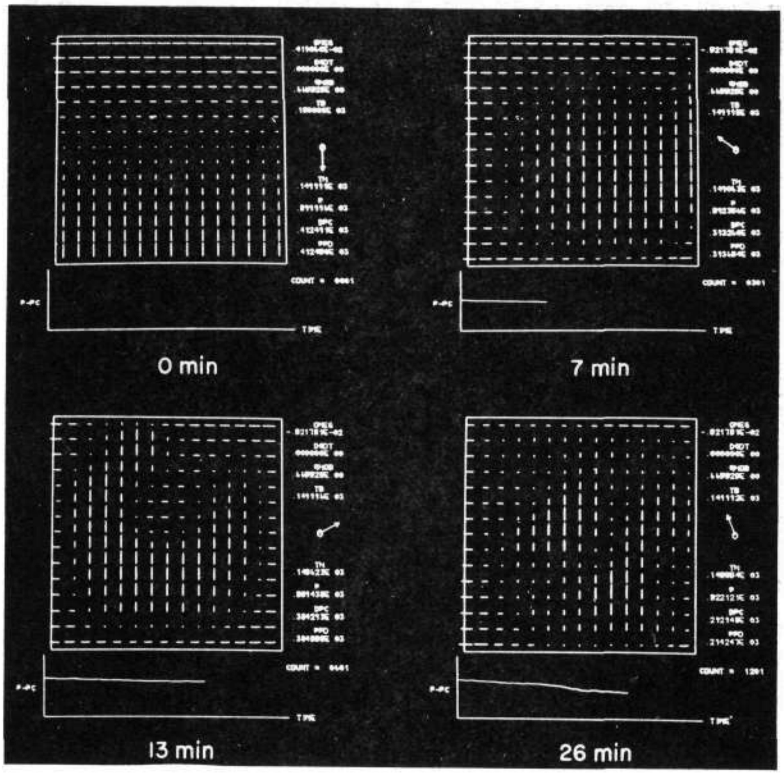

Figure 4. Temperature distributions after rotation reversal.

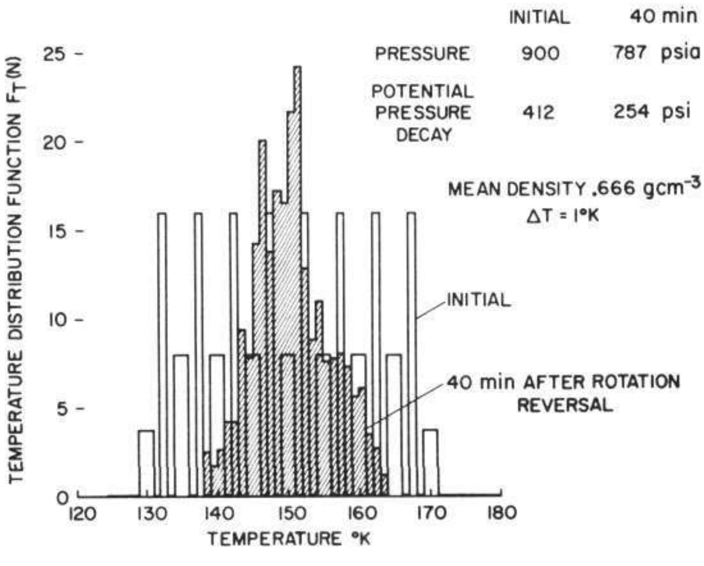

Figure 5. Temperature distribution functions.

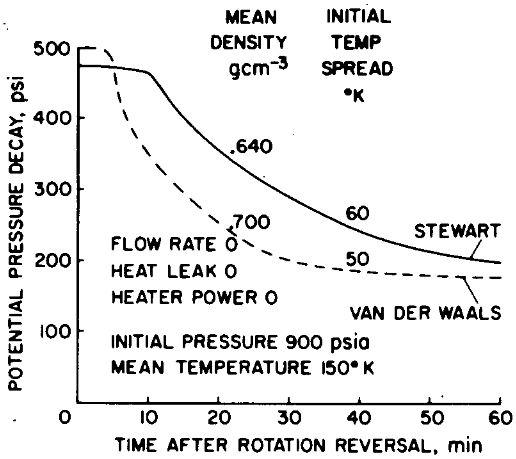

Figure 6. Comparison of potential pressure decay for van der Waals and exact thermodynamics.

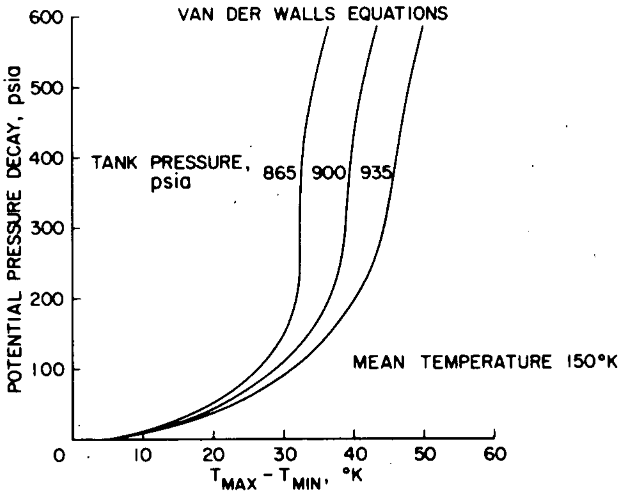

Figure 7. Potential pressure decay for linear temperature variations; van der Waals equations.

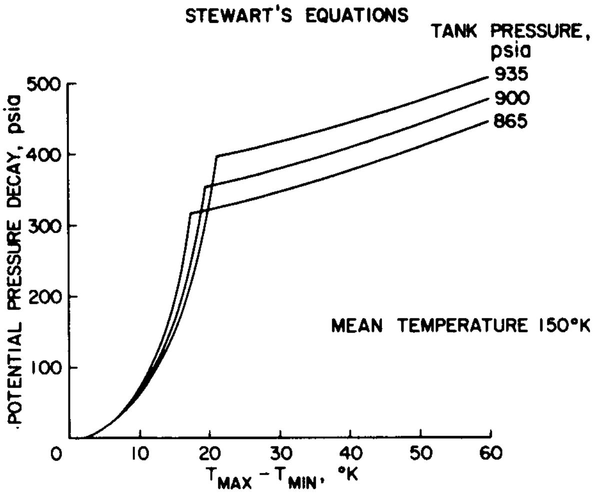

Figure 8. Potential pressure decay for linear temperature variations; Stewart's equations.

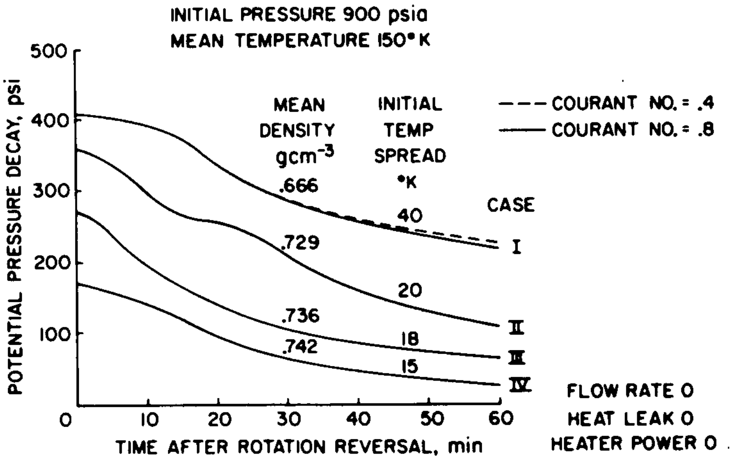

Figure 9. Potential pressure decay after rotation reversal.

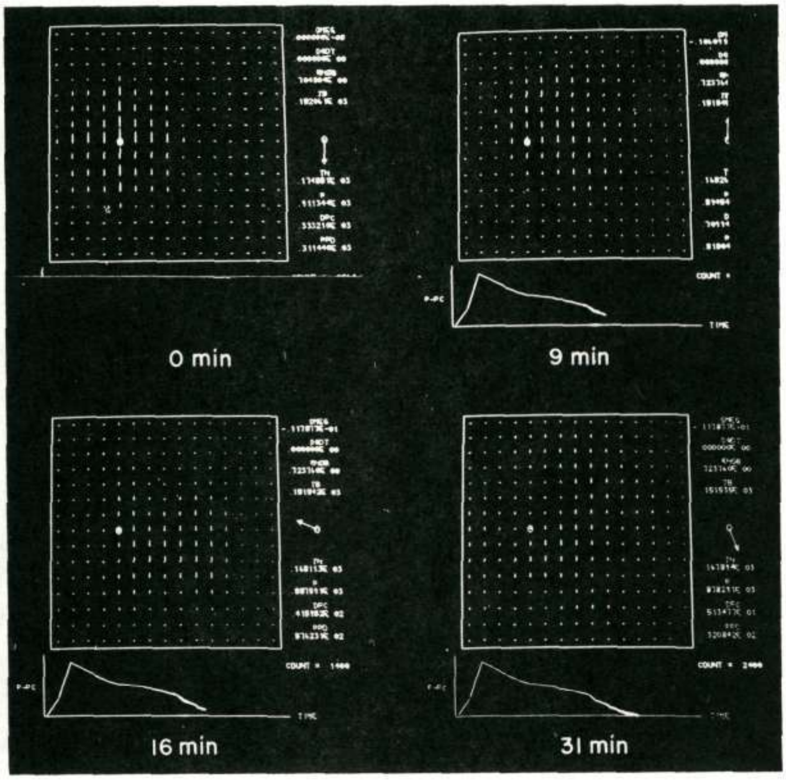

Figure 10. Temperature distributions after spin-up.

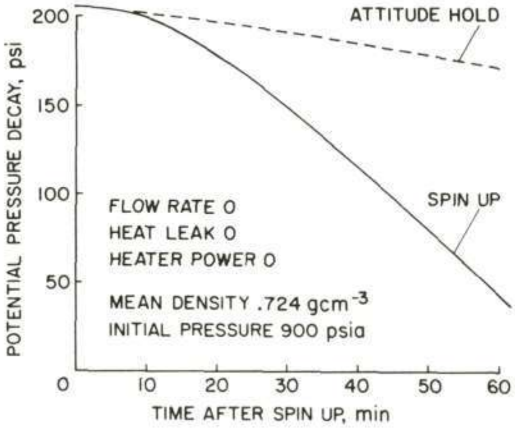

Figure 11. Reduction in potential pressure decay due to spin-up.

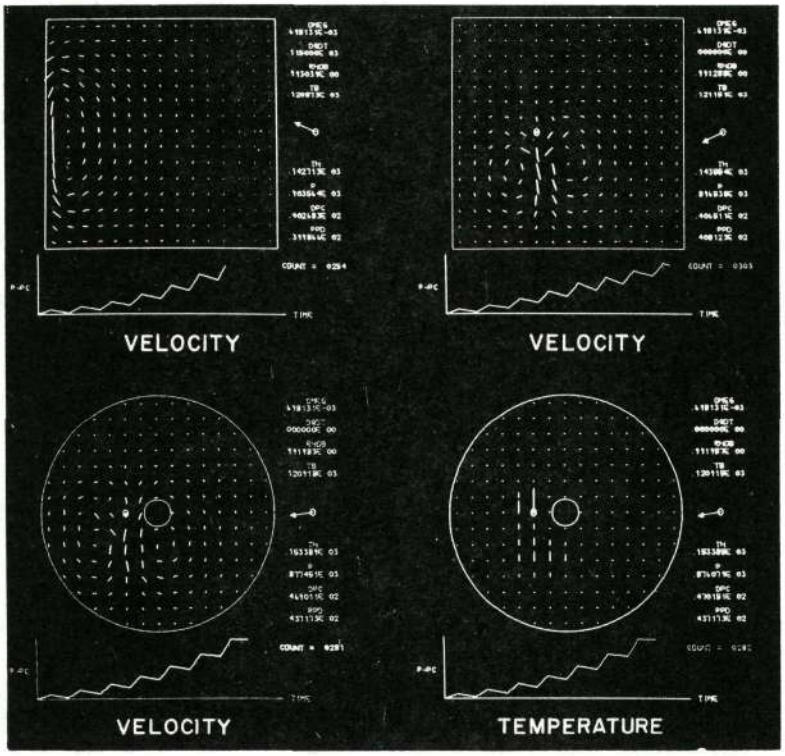

Figure 12. Velocity and temperature distributions resulting from heater operation.

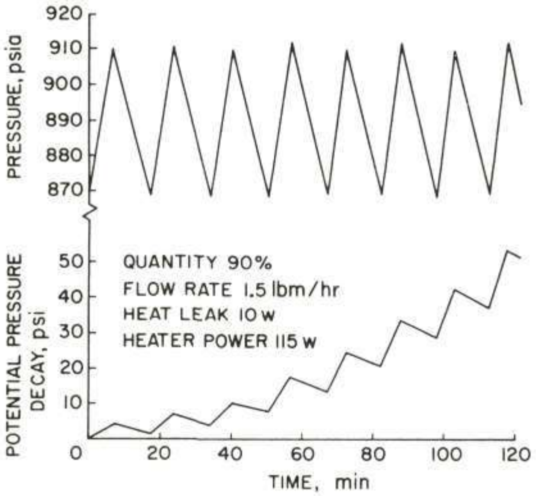

Figure 13. Pressure cycles for square tank with wall heater.

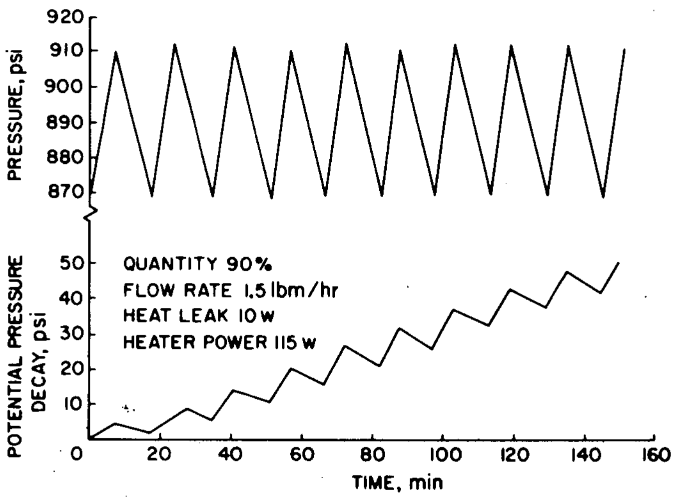

Figure 14. Pressure cycles for square tank with off-center heater.

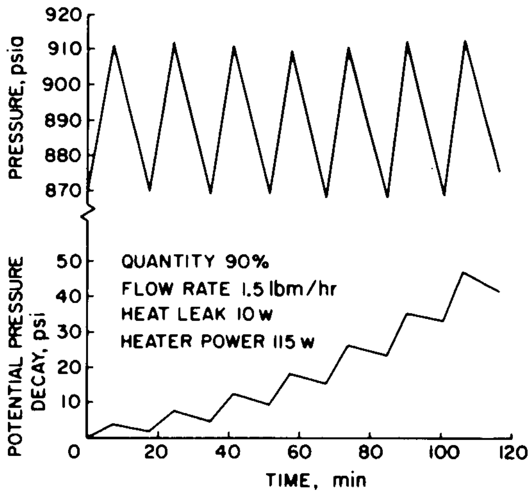

Figure 15. Pressure cycles for circular cylindrical tank.

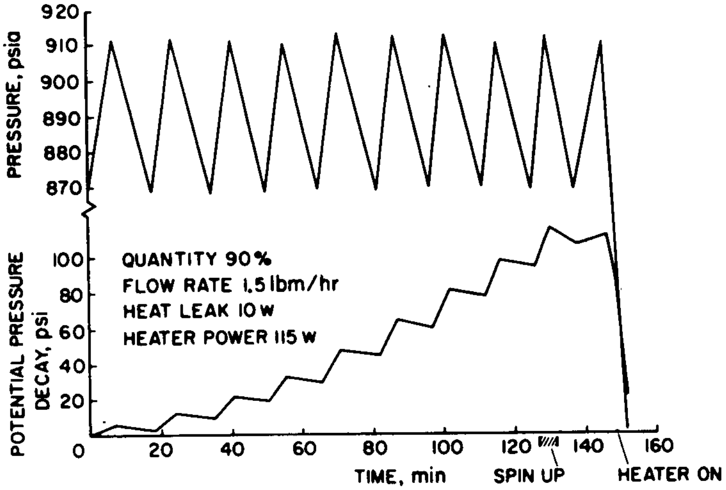

Figure 16. Effect of spin-up on pressure cycle (circular cylindrical tank).

N72-23794

STRATIFICATION CALCULATIONS IN A HEATED CYROGENIC OXYGEN STORAGE TANK AT ZERO GRAVITY

By John T. Suttles and G. Louis Smith

NASA Langley Research Center
Hampton, Virginia 23365

Abstract

A cylindrical one-dimensional model of the Apollo cyrogenic oxygen storage tank has been developed to study the effect of stratification in the tank. Zero gravity is assumed, and only the thermally induced motions are considered. The governing equations are derived from conservation laws and solved on a digital computer. Realistic thermodynamic and transport properties are used. Calculations were made for a wide range of conditions. The results show the fluid behavior to be dependent on the quantity in the tank or equivalently the bulk fluid temperature. For high quantities (low temperatures) the tank pressure rises rapidly with heat addition, the heater temperature remains low, and significant pressure drop potentials accrue (over 100 psia in 2 hours). For low quantities the tank pressure rises more slowly with heat addition and the heater temperature becomes high (as much as 500° K (440° F)). A high degree of stratification resulted for all conditions; however, the stratified region extended appreciably into the tank only for the lowest tank quantity. The calculations also indicate a significant flux of mass from the heater tube for high tank quantities. The results have been compared with Apollo 14 flight data. For attitude hold conditions (i.e. no spacecraft motions) the calculations are in good agreement with the data.

Introduction

The removal of the mixing fans from the supercritical oxygen storage tanks in the Apollo spacecraft introduces the possibility that the fluid in the tank can become stratified. Stratification, which results from the temperature gradients surrounding the heating element used for pressurization of the tank, can have several possibly serious effects. First it can cause erroneous quantity probe measurements with the potential for precipitating a mission abort. Second, if the low density fluid from the stratified layer enters the oxygen supply lines, the potential exists for fuel cell shutdown. Finally, if the stratified layer becomes too extensive, a perturbing force of even extremely low magnitude can cause depressurization with the potential for the existence of two phase fluid in the tank.

The purpose of this paper is to examine the extent of the stratification and the potential for depressurization which might exist in the supercritical oxygen storage tank. The worst case of no natural convection, has been assumed for the stratification calculations. The depressurization calculations are based on uniform (completely mixed) conditions in the tank. Zero gravity has been assumed throughout the analysis.

The approach which has been taken is to use a simple mathematical model which facilitiates a solution but retains the essential features of the actual cryogenic storage tank. For this purpose a one-dimensional cylindrical tank model is used. The governing equations are derived from the conservation laws and solved numerically on a digital computer. Realistic thermodynamic properties based on information from the National Bureau of Standards (ref. 1) and transport properties from ref. 2 are used throughout the analysis.

Symbols

A	area, m^2
C_p	specific heat, $j/kg\text{-}^oK$
k	thermal conductivity, $j/m\text{-}sec\text{-}^oK$
K	arbitrary constant
L	length, m
m	mass of fluid, kg
M	mass of heater tube, kg
$\vec{n}$	unit normal to tank surface
p	pressure, N/m^2 or psia
q	heat flux, $watts/cm^2$
Q	heat rate, watts
Q_{leak}	heat rate due to heat leak at tank wall, watts
Q_{input}	heat rate input to heater tube, watts
Q_{stored}	heat stored by heater tube, watts
Q_{net}	net heat rate to fluid (see equation 26), watts
r	radius of point in tank, m
t	time, sec.
T	temperature, ^oK or ^oF
v	radial velocity of fluid in tank, m/sec.
V	volume of tank, m^3
$\vec{V}$	velocity vector of fluid in tank, m/sec.
α	arbitrary function of time and space

∇	del operator
ε	emissivity
η	non-dimensional Lagrange space-coordinate
ϕ	function defined by equation (27)
ρ	fluid density, kg/m^3
σ	Stephan-Boltzmann constant, 5.6697×10^{-8} watts/ m^2-$^oK^4$
θ	function defined by equation (28)

Subscripts

o	initial value
w	value at tank wall
HTR	value at heater
COND	result of conductivity
RAD	result of radiation
b	value at a boundary
$(\dot{\ })$	$\frac{d(\ )}{dt}$
$\frac{D(\ )}{Dt}$	substantive derivative of ( )
$\Delta(\ )$	increment in ( )

Analysis

Model and Basic Equations

A simplified tank model which includes the essential features of an actual storage tank is illustrated in figure 1. A cylindrical tank with a radius of .305 meters (1 foot) is assumed with variations in properties in the radial direction only (i.e., the model is one-dimensional). To provide a specified heat input for maintaining tank pressure a cylindrical heater tube with a radius of .025 meters (1 inch) is centered in the tank. A uniform heat leak is assumed to exist over the wall of the tank since cyrogenic storage tanks always experience such a heat leak. In order to retain the simplicity of the model the effect of fluid withdrawal is included by assuming a uniform mass flux through the tank wall.

For the model shown in figure 1 fluid exists inside the heater tube as it does in the actual tank. The heater tube in the actual tank is provided with numerous holes so that fluid may move in or out the tube. In the model two approaches were used to calculate the thermally induced flow in and out the heater tube. In one approach the tube was considered to be a separate tank. By assuming that the pressure in the tube is the same as that in the main tank, the mass flux from the heater tube can be calculated directly. In this approach no attempt was made to include the effect of the fluid leaving or entering the tube on the behavior of the fluid in the tank. In the other approach the tube and tank were considered to be one system. Since the heater tube mass flux can not be calculated directly in this method, the mass of fluid in the tube was computed at each time by integrating the fluid density over the volume of the tube. The mass flux for the tube was then calculated by differentiating the mass of fluid with time.

In this analysis a one-dimensional model of a supercritical cyrogenic oxygen storage tank in zero gravity is considered. For a zero gravity environment fluid velocities are generated only by thermal expansion and mass removal effects and thus are expected to be small. Therefore, viscous effects and inertial forces are neglected. An examination of the thermodynamic data for cyrogenic oxygen in reference 1 shows that for the pressure (700-900 psia) and temperatures (100-300^{o}K) of interest the speed of sound varies from approximately 150 to approximately 900 meters per second. The speed of sound is therefore considerably larger than any expected fluid velocities. Thus pressure variations across the tank are negligible with respect to the mean pressure. The analysis is therefore based on the equations which follow:

continuity: $$\frac{D\rho}{Dt} + \rho\nabla\cdot\vec{V} = 0 \qquad (1)$$

momentum: $$\nabla p = 0 \qquad (2)$$

energy : $$\rho C_p \frac{DT}{Dt} = -\left(\frac{\partial\rho}{\partial T}\right)_p \frac{DP}{Dt} + \nabla\cdot(k\nabla T) - \nabla\cdot q_{RAD} \qquad (3)$$

If pressure gradients are retained then the equations are hyperbolic and describe sound waves so that small characteristic times result. Neglecting the pressure gradients reduces the system to parabolic equations with considerably larger characteristic times and consequent savings in computer time.

To obtain a solution to the basic equations (1)-(3) an equation of state (i.e., $\rho = f(p,T)$), various thermodynamic properties $\left(C_p, \left(\frac{\partial\rho}{\partial T}\right)_p, \left(\frac{\partial\rho}{\partial p}\right)_T\right)$ and transport properties (k) are required. For this work the equation of state and required thermodynamic properties were obtained from the data in reference 1. The thermal conductivities were obtained from the data in reference 2. The data from the references has been arranged in the form of a table from which desired values are found using a table look-up scheme with first order interpolation.

The radiation transport term has been included in the energy equation since the work of reference 3 has indicated the possible importance of this mechanism. The absorption coefficient data used in that work however, is questionable. At the present time work is being done at the National Bureau of Standards, Boulder, Colorado to generate more meaningful data. When that data is available the effect of radiation energy transport can be evaluated with more confidence. The radiation effect has not been included in this analysis.

Stratified Tank Analysis

Development of equation. - As previously mentioned the tank characteristics of primary interest in this study are the tank pressure fluctuations and thermal stratification resulting from withdrawing fluid and cycling a heater to maintain the pressure in a specified range. The basic equations will therefore be utilized to develop an equation giving the tank pressure as a function of time and an equation giving the temperatures in the tank as a function of space and time. With pressure and temperatures the density as a function of space and time can then be computed from the equation of state (data of ref. 1).

In the development of the pressure and temperature equations the use of the momentum equation is avoided by using a Lagrangian viewpoint for the substantive derivatives. That is, the substantive derivative is written as

$$\frac{D(\ )}{Dt} = \left[\frac{\partial(\ )}{\partial t}\right]_{\text{particle}} \tag{4}$$

so that particles (small volume elements) are followed in the solution. In the one-dimensional analysis being used the particles or small volume elements can be followed by using the condition that the particle mass is constant. Thus

$$\rho_o dV_o = \rho dV$$

where the subscript "o" denotes values at the initial time and the unsubscripted quantities are values at a subsequent time. For one-dimensional cylindrical coordinates

$$\rho_o r_o dr_o = \rho r dr \tag{5}$$

where r_o and r represent the initial and subsequent position of a particle. The simplicity of using the Lagrangian viewpoint is obtained by transforming to the initial (r_o) coordinates for the computation and transforming back to the actual coordinates (r) to analyse the results.

One possible complication does arise with the use of the Lagrangian viewpoint because with mass removal occurring particles are leaving the system. At each time the initial coordinate of the particle at the tank wall must be determined and particles with larger initial coordinates must be considered to have left the system. To avoid the problem resulting from this continuous change in the coordinate system, a set of non-dimensional initial coordinates can be defined. The non-dimensional coordinates are given by

$$\eta = \frac{r_o}{r_{o,w}} \tag{6}$$

where $r_{o,w}$ is a function of time and can be obtained by considering the loss of mass from the system in time dt

$$\dot{r}_{o,w} = \frac{dr_{o,w}}{dt} = \frac{\dot{m}}{2\pi L\rho_w r_{o,w}} \tag{7}$$

$$r_{o,w} = \int_o^t \dot{r}_{o,w} dt \tag{8}$$

To transform partial differential equations from r_o,t coordinates to η,t coordinates the required relations are

$$\left[\frac{\partial(\ )}{\partial r_o}\right]_t = \frac{1}{r_{o,w}}\left[\frac{\partial(\ )}{\partial \eta}\right]_t \tag{9}$$

$$\left[\frac{\partial(\ )}{\partial t}\right]_{r_o} = \left[\frac{\partial(\ )}{\partial t}\right]_\eta - \eta\,\frac{\dot{r}_{o,w}}{r_{o,w}}\,\frac{\partial(\ )}{\partial \eta} \tag{10}$$

The pressure equation development is begun by dividing the continuity equation (equation 1) by ρ and integrating over the tank volume

$$\int_V \frac{1}{\rho}\frac{D\rho}{Dt}\,dV + \int_V \nabla\cdot\vec{V}dV = o \tag{11}$$

The Gauss Theorem can be applied to the second integral to obtain

$$\int_V \frac{1}{\rho}\frac{D\rho}{Dt}\,dV + \int_A \vec{V}\cdot\vec{n}\,dA = o$$

Since uniform mass flux over the tank surface has been assumed then

$$\int_A \vec{V}\cdot\vec{n}dA = v_w A_w = - \frac{\dot{m}}{\rho_w}$$

where the convention is taken that a positive velocity will produce a negative mass flux. Thus,

$$\int_V \frac{1}{\rho}\frac{D\rho}{Dt}\,dV = \frac{\dot{m}}{\rho_w} \tag{12}$$

If the density is considered to be a function of pressure and temperature then

$$\frac{D\rho}{Dt} = \left(\frac{\partial\rho}{\partial P}\right)_T \frac{Dp}{Dt} + \left(\frac{\partial\rho}{\partial T}\right)_p \frac{DT}{Dt}$$

and since $\nabla p = o$ then $\frac{Dp}{Dt} = \frac{\partial p}{\partial t}$ which is uniform in the volume. Using these conditions in equation (12) it follows that

$$\frac{\partial p}{\partial t} = \frac{\frac{\dot{m}}{\rho_w} - \int_V \frac{1}{\rho}\left(\frac{\partial\rho}{\partial T}\right)_p \frac{DT}{Dt}\,dV}{\int_V \frac{1}{\rho}\left(\frac{\partial\rho}{\partial p}\right)_T dV} \tag{13}$$

is the equation governing the pressure changes. Equation (13) and the energy equation (equation (3) without the radiation term) both contain $\frac{\partial p}{\partial t}$ and $\frac{DT}{Dt}$ so they are solved simultaneously to give

$$\frac{\partial p}{\partial t} = \frac{\frac{\dot{m}}{\rho_w} - \int_V \left\{ \frac{1}{\rho^2 C_p} \left(\frac{\partial \rho}{\partial T}\right)_p \nabla\cdot(k\nabla T) \right\} dV}{\int_V \frac{1}{\rho} \left\{ \left(\frac{\partial \rho}{\partial p}\right)_T - \frac{T}{\rho^2 C_p} \left[\left(\frac{\partial \rho}{\partial T}\right)_p\right]^2 \right\} dV} \tag{14}$$

and

$$\frac{DT}{Dt} = -\left(\frac{\partial \rho}{\partial T}\right)_p \frac{T}{\rho^2 C_p} \left(\frac{\partial p}{\partial t}\right) + \frac{1}{\rho C_p} \nabla\cdot(k\nabla T) \tag{15}$$

where equation (14) can be used first to obtain $\frac{\partial p}{\partial t}$ which appears in equation (15).

For one-dimensional cylindrical coordinates

$$dV = 2\pi L r dr$$

where L is an arbitrary length chosen to produce a desired tank volume and

$$\nabla\cdot(k\nabla T) = \frac{1}{r} \frac{\partial}{\partial r} \left(kr \frac{\partial T}{\partial r} \right)$$

Since it is desired to work in the Lagrangian viewpoint the transformations defined by equations (5-10) are used so that equations (14) and (15) become

$$\frac{\partial p}{\partial t} = \frac{\frac{\dot{m}}{2\pi L \rho_w} - \int_{\eta_1}^{1} \frac{1}{r_{o,w}\rho_o \rho^2 C_p} \left(\frac{\partial \rho}{\partial T}\right)_p \frac{\partial}{\partial \eta} \left(k \frac{r^2}{r_{o,w} r_o} \rho \frac{\partial T}{\partial \eta} \right) d\eta}{\int_{\eta_1}^{1} \frac{\rho_o r_o r_{o,w}}{\rho^2} \left\{ \left(\frac{\partial \rho}{\partial p}\right)_T - \frac{T}{\rho^2 C_p} \left[\left(\frac{\partial \rho}{\partial T}\right)_p\right]^2 \right\} d\eta} \tag{16}$$

$$\left(\frac{\partial T}{\partial t}\right)_{\text{particle}} = - \left(\frac{\partial \rho}{\partial T}\right)_p \frac{T}{\rho^2 C_p} \frac{\partial p}{\partial t} + \frac{1}{\rho_o{}^2 C_p \, r_o r_{o,w}} \frac{\partial}{\partial \eta} \left(\frac{k r^2 \rho}{r_{o,w} \, r_o} \frac{\partial T}{\partial \eta} \right)$$

$$- \eta \frac{\dot{r}_{o,w}}{r_{o,w}} \frac{\partial T}{\partial \eta} \qquad (17)$$

where $\eta, r_{o,w}$ and $\dot{r}_{o,w}$ are defined by equations (6), (7), and (8) respectively. To find the location of particles equation (5) is used to obtain

$$\left[\frac{r^2}{2}\right]_{r_1}^{r} = \int_{r_{o,1}}^{r_o} \frac{\rho_o}{\rho} \, r_o dr_o \qquad (18)$$

Boundary conditions.- Since equation (17) is a second order partial differential equation, two boundary conditions are required. For the fluid in the heater tube a symmetry condition is applied at the center of the tube

$$\left(\frac{\partial T}{\partial r}\right)_{r=o} = 0 \qquad (19)$$

and the temperature of the fluid at the heater tube wall is equated with the heater temperature.

$$T = T_{HTR} \qquad (20)$$

For the fluid outside the heater tube, the temperature of the fluid at the heater tube wall is equated to the heater temperature

$$T = T_{HTR} \qquad (21)$$

and at the tank wall a heat flux (heat leak is imposed)

$$Q_{leak} = - \left(k \frac{\partial T}{\partial r}\right)_w A_w \qquad (22)$$

For two of the boundary conditions the heater temperature is required. To determine its temperature the heater tube is considered to be a lumped mass and a heat balance is computed. The elements shown on figure 1, are considered to obtain

$$Q_{stored} = Q_{input} - \Sigma\, Q_{COND} - \Sigma\, Q_{RAD}$$

$$M_{HTR} C_{p,HTR} \frac{\partial T_{HTR}}{\partial t} = Q_{INPUT} - \left[\left(k \frac{\partial T}{\partial r} \right)_{\substack{\text{inside} \\ \text{HTR WALL}}} - \left(k \frac{\partial T}{\partial r} \right)_{\substack{\text{outside} \\ \text{HTR WALL}}} \right] \times$$

$$A_{HTR} - \varepsilon_{HTR}\, \sigma \left(T_{HTR}^4 - T_w^4 \right) A_{HTR} \tag{23}$$

which is the equation used to find the heater temperature.

Uniform Tank Analysis

For a uniform tank the temperature and density are constant over the tank volume. Equations (14) and (15) can be simplified for this case by performing the volume integrals in equation (14) and by integrating equation (15) over the tank volume. The results are

$$\frac{\partial p}{\partial t} = \frac{\dot{m} - \frac{1}{\rho C_p} \left(\frac{\partial \rho}{\partial T} \right)_p Q_{net}}{\left\{ \left(\frac{\partial \rho}{\partial p} \right)_T - \frac{T}{\rho^2 C_p} \left[\left(\frac{\partial \rho}{\partial T} \right)_p \right]^2 \right\} V} \tag{24}$$

and

$$\frac{\partial T}{\partial t} = -\left(\frac{\partial \rho}{\partial T} \right)_p \frac{T}{\rho^2 C_p} \frac{\partial p}{\partial t} + \frac{1}{\rho C_p} \frac{Q_{net}}{V} \tag{25}$$

where the Gauss Theorem has been used to write

$$\int_V \nabla \cdot (k \nabla T)\, dV = \int_A (k \nabla T) \cdot \vec{n}\, dA \tag{26}$$

$$= \Sigma\, Q_{COND} + \Sigma\, Q_{RAD} = Q_{net}$$

If one defines

$$\phi = \frac{1}{\left\{\left(\frac{\partial\rho}{\partial p}\right)_T - \frac{T}{\rho^2 C_p}\left[\left(\frac{\partial\rho}{\partial T}\right)_p\right]^2\right\}} \qquad (27)$$

and

$$\theta = -\frac{1}{\rho C_p}\left(\frac{\partial\rho}{\partial T}\right)_p \qquad (28)$$

then (25) and (26) can be written in the simpler form

$$\frac{\partial p}{\partial t} = \frac{\phi}{V}\,\dot{m} + \frac{\phi\theta}{V}\,Q_{net} \qquad (29)$$

$$\frac{\partial T}{\partial t} = \frac{\theta T}{\rho}\,\frac{\partial P}{\partial t} + \frac{Q_{net}}{\rho C_p V} \qquad (30)$$

Numerical Method

The stratified tank calculations are performed by solving the partial differential equations given by (16) and (17) with boundary conditions given by equations (19) - (23). Equations (6) - (8) and (18) are used to convert the normalized Lagrangian space coordinate η to the physical coordinates r. For the uniform tank calculations the ordinary differential equations given by (29) and (30) are solved. The numerical method employed is to replace the derivaties in each equation by appropriate finite difference approximations and advance the solution in time. The integrals in equation (16) are evaluated using the trapezoidal rule.

Finite difference expressions. - For purposes of illustration an arbitrary function of time and space $\alpha(t,r)$ is considered. The difference expressions are:

$$\frac{\partial\alpha}{\partial t} = \frac{\alpha(t+\Delta t,r) - \alpha(t,r)}{\Delta t} \qquad (31)$$

$$\frac{\partial\alpha}{\partial r} = \frac{\alpha(t,r + \Delta r) - \alpha(t,r - \Delta r)}{2\Delta r} \qquad (32)$$

$$\frac{\partial^2\alpha}{\partial r^2} = \frac{\alpha(t,r + \Delta r) - 2\alpha(t,r) + \alpha(t,r - \Delta r)}{\Delta r^2} \qquad (33)$$

For functions of time only an expression like equation (31) is used. At the boundary points the difference expression used for $\frac{\partial\alpha}{\partial r}$ is

$$\left(\frac{\partial\alpha}{\partial r}\right)_b = \frac{\alpha(t,r_b) - \alpha(t,r_b \pm \Delta r)}{\mp\Delta r} \qquad (34)$$

where the signs (±) are selected depending on whether the boundary is a right hand or left hand boundary.

If a boundary condition of the form

$$\left(\frac{\partial\alpha}{\partial r}\right)_b = K \qquad (35)$$

is specified then $\left(\frac{\partial^2\alpha}{\partial r^2}\right)_b$ is written as

$$\left(\frac{\partial^2\alpha}{\partial r^2}\right)_b = \frac{K - \left[\frac{\alpha(t,r_b) - \alpha(t,r_b \pm \Delta r)}{\mp\Delta r}\right]}{\Delta r} \qquad (36)$$

Stability. - In a finite difference approach such as that used the stability of the computing scheme must be considered. The equations of interest as far as stability is concerned are equations (16) and (17). A linear stability analysis applied to equation (17) yields

$$\Delta t < \frac{1}{\left[\frac{2kr^2\rho}{r_o{}^2\rho_o{}^2C_p(\Delta r)^2} + \frac{1}{\rho^2C_p}\left(\frac{\partial\rho}{\partial T}\right)_p \frac{\partial p}{\partial t}\right]} \qquad (37)$$

as a restriction on the time step size. However, the integral nature of equation (16) precludes any simple stability analysis of that equation. Therefore it was decided to use equation (37) to define the time steps for both equations. Because of the uncertainty with regard to the stability of equation (16) the results must be checked by making calculations for a range of time step sizes and noting the changes in the solutions. The results of such a procedure are discussed in the section which follows:

Results and Discussion

Calculated Results

Calculations for a uniform tank have been made and the results are presented in figure 2. The calculations give the time rate of change of pressure as a function of temperature for a range of mass flux rates both for heat addition (Q_{net} = 125 watts) and for no heat addition. The results indicate that for temperatures up to near critical values (i.e., near critical temperatures are between 155 and 165°K) the magnitude of the pressure derivative is relatively high and varies significantly with temperature whereas at higher temperatures the magnitude is relatively low and the variations are only slight. The unusual variations in the pressure derivative in the near-critical region reflects the rapid changes in thermodynamic properties in this region. These results also show that the mass flux rate has a strong influence at temperatures below the near critical region but has only a weak influence at higher temperatures.

Stratified tank calculations for four typical tank operating conditions have been made. The tank and heater physical properties which were used for all the computations are given in Table I. Input values for each of the four cases computed are given in Table II. Because of the questionable stability of equation (16) each of the cases was calculated with the time step size determined by 1/3 of the expression in equation (37) and for values successively smaller until the solution became stationary with respect to step size changes. The time step sizes determined for stability of cases 1 and 2 were about an order of magnitude lower than the initially computed values whereas the initially computed values were found to be adequate for cases 3 and 4. The results for cases 1-4 are presented in figures 3-14. The quantities shown are the time histories of heater temperature, tank pressure, and heater tube mass flux and profiles of temperature and density across the tank for pertinent simulated times. The pressure change potentials are indicated in the results by the differences between the stratified tank pressure and the associated uniform tank pressure. The degree and extent of stratification in the tank is assessed by examining the temperature and density profiles.

The time histories in figure 3 show that cases 1 and 2 have the same characteristic feature, that is many heater cycles occurred during the two-hour simulated time of the calculations. In contrast less than one heater cycle was obtained for cases 3 and 4. This difference in characteristic behavior is probably due to the fact that the initial temperatures of cases 1 and 2 are in the sensitive range below the near critical region whereas the initial temperature of case 3 is in the near critical region and that for case 4 is considerably higher. It should be noted that the relative insensitivity of the tank pressure to heat input for the lowest density cases (cases 3 and 4) causes the heater temperature to reach quite high values ($T_{HTR} > 500^oK$ for case 4). The very high frequency heater cycling for case 1 apparently results when the heater temperature becomes stationary ("locked" or "trapped") in the near critical temperature region. In this regard it is noted that when the heater temperature for case 2 is in the near critical region the heater cycles at a relatively high rate but the rate diminishes as the heater temperature rises above the near critical region.

Results for the possibility of a pressure change caused by mixing indicate significant pressure drop potentials for cases 1 and 2 (100 and 120 psia respectively at $t = 120$ min), initially a pressure drop potential and later a pressure rise potential for case 3, and significant pressure rise potentials for case 4 (60 psia at $t = 120$ min). These pressure rise potentials are in disagreement with analyses of other investigators (see for example reference 4) and require further study.

The heater mass flux rates obtained are presented in figure 4. The results presented are for the separate heater tube and tank model only. These results show that the heater mass flux rates for cases 1 and 2 are relatively high compared to the mass flux rate of the tank whereas the rates for cases 3 and 4 are relatively low. The calculations indicate that fluid leaves the heater tube when the heater is on and enters the tube when the heater is off. Thus for some tank operating conditions this mechanism may be important as far as inducing convective motions of the fluid.

Heater mass flux rate results considering the tank as one system are not available because of excessive computer time required. In this approach the heater location moves from node to node because of the Lagrangian coordinate system used. As a consequence a fine nodal spacing and hence very large computational times were required to avoid numerical difficulties. However, a limited number of calculations using this approach have been made. They indicate that the heater tube mass fluxes may be as much as a factor of 2 lower than those calculated by the separate heater tube approach. The gross tank behavior however is not significantly effected.

Profiles of temperature and density in the tank are presented in figure 5 for simulated times which were judged to be pertinent as far as illustrating the stratifications obtained. It is seen that the degree of stratification is significant in all the cases. For example, the density in the area next to the heater is 1/2 to 1/4 of the density in the outer portion of the tank. However, except for case 4, the extent of the stratification is confined to a region very close (within about .025 m (1 in.)) to the heater. For case 4 the density (and temperature) stratification is significant and extends far into the tank. For cases 3 and 4 the increase in density in the unstratified portion of the tank over the initial value is a result of the work done on that portion of the fluid by the expansion of the stratified fluid near the heater.

Comparison With Flight Data.

The calculations just described have been compared with Apollo 14 flight data. The comparisons are of the heater temperature and tank pressure and are presented in figures 6-9. Cases 1 and 2 are high quantity cases (95% and 75% respectively) for times when the spacecraft is in an attitude hold condition. Cases 3 and 4 are moderate to low quantity cases (52% and 12% respectively) for times when the spacecraft is spinning for passive thermal control (PTC). Since the calculation method presented here considers only thermally induced motions, then it should be expected that a better agreement between calculated and flight data would be obtained for cases 1 and 2 than for cases 3 and 4. An examination of figures 6-9 shows this to be true.

For cases 1 and 2 the calculations correctly predict the general characteristics of the heater cycling and the maximum heater temperature. The flight data in figure 6 show the existance of the condition previously discussed in the calculated data where the heater temperature becomes nearly stationary in the near-critical region and the heater begins cycling at a high frequency. The comparison in figure 7 indicates that for early simulation times the calculations do not agree well with the flight data. For latter simulation times when stratifications have accrued the calculations agree well with the data.

For cases 3 and 4 the calculations are seen to over predict both the time for the heater cycle and the maximum heater temperature.

In figure 8 note that after the heater is shut-off the pressure does not decay as rapidly in the calculations as in the data. Also the heater temperature is higher in the calculation than in the data for the entire heater cycle. These differences are attributed to the fact that the present calculation method neglects the convective transport mechanisms resulting from the spacecraft motions. The differences in the pressure cycle in figure 9 are not adequately understood. However the differences in the heater temperature again indicate an effect due to convective energy transport.

Conclusions

Calculations have been made of the behavior of supercritical oxygen in a storage tank in zero gravity while fluid is withdrawn and a heater is cycled to maintain the tank pressure in the range of 5.9295×10^6 N/m^2 (860 psia) to 6.2116×10^6 N/m^2 (900 psia). A one-dimensional model was used and the thermally induced movemoment of the fluid was the only motion considered. Four cases representing a wide range of tank operating conditions were considered. Based on the results obtained the following general conclusions are made:

1. For initial temperatures below near-critical, the tank pressure oscillates at a relatively high rate and the heater temperature remains low whereas for initial temperatures above near critical the tank pressure changes slowly and high heater temperatures result.

2. The results for pressure change potentials have indicated that for initial temperatures below near-critical,significant pressure drop potentials accrue (over 100 psia in 2 hours).

3. For initial conditions below the near-critical values the flux of fluid mass into and out of the heater tube is significant and may be important as far as inducing convective motion of the fluid.

4. A high degree of stratification was obtained for all cases considered however the stratified region extended appreciably into the tank only for the case with highest initial temperature, 194^{o}K.

5. A comparison of the calculations with Apollo 14 flight data has indicated that for attitude hold conditions the calculations are in good agreement with the flight data but for conditions when the spacecraft is spinning the calculations over predict the heater temperature and the time for a heater cycle.

References

1. Weber, L. A.: "Thermodynamic and Related Properties of Oxygen from the Triple Point to 300 K at Pressures to 330 Atmospheres," NBS Report 9710, June 20, 1968.

2. Stiel, L. I., and Thodos, George: "The Prediction of the Transport Properties of Pure Gaseous and Liquid Substances," Progress in International Research on Thermodynamic and Transport Properties. ASME, New York, 1962, p. 352.

3. Sollami, B. J., and Abraham, W. H.: "Heat-Transfer Characteristics of a Supercritical Cryogenic Storage System in Space," Bendix Technical Journal, Vol. 3, Spring 1970, p. 34-40.

4. Kamat, D. V., and Abraham, W. H.: "Pressure Collapse in Oxygen Storage Under Zero-g," Journal of Spacecraft and Rockets, Vol. 5, No. 2, Feb. 1968, pp. 184-188.

TABLE I

Physical Properties Used in Calculations

Tank Radius = 0.305 m (1.0 ft)

Tank Length = 0.463 m (1.52 ft)

Tank Volume = 0.135 m^3 (4.75 ft^3)

Heater on Pressure = 5.9295 x 10^6 N/m^2 (860 psia)

Heater off Pressure = 6.2116 x 10^6 N/m^2 (900 psia)

Heater Radius = 0.025 m (1. in.)

Heater Mass = 1.13 kg (2.5 lbm)

Heater Specific Heat = 460. j/kg-°K (0.11 Btu/lbm-°F)

Heater Emissivity = 0.3

Computing Nodes inside Heater Tube = 6

Computing Nodes in Main Tank = 57

TABLE II

Input Conditions for Stratified Tank Calculations

Case 1 - Attitude hold, approximately 95% quantity

T_o = 110°K (198°R)

P_o = 5.9295×10^6 N/m^2 (860 psia)

ρ_o = 1054.5 kg/m^3 (65.83 lbm/ft^3)

Q_{input} = 123.03 watts (419.82 Btu/hr)

Q_{leak} = 8.06 watts (27.5 Btu/hr)

$\dot{m}$ = -0.00011 kg/sec (0.87 lb/hr)

Case 2 - Attitude hold, approximately 75% quantity

T_o = 142°K (255°R)

P_o = 5.9295×10^6 N/m^2 (860 psia)

ρ_o = 837.76 kg/m^3 (52.30 lbm/ft^3)

Q_{input} = 123.24 watts (420.53 Btu/hr)

Q_{leak} = 6.45 watts (22.0 Btu/hr)

$\dot{m}$ = -0.000116 kg/sec (0.92 lb/hr)

TABLE II (concluded)

Case 3 - Passive thermal control (PTC)-approximately
52% quantity

T_o = 157°K (283°R)

P_o = 5.925×10^6 N/m^2 (860 psia)

ρ_o = 536.4 kg/m^3 (33.49 lbm/ft^3)

Q_{input} = 111.45 watts (380.30 Btu/hr)

Q_{leak} = 4.55 watts (15.5 Btu/hr)

$\dot{m}$ = -.000155 kg/sec (1.23 lb/hr)

Case 4 - Passive thermal control, approximately 12% quantity

T_o = 194°K (350°R)

P_o = 5.9295×10^6 N/m^2 (860 psia)

ρ_o = 148.73 kg/m^3 (9.28 lbm/ft^3)

Q_{input} = 111.45 watts (380.30 Btu/hr)

Q_{leak} = 4.25 watts (14.5 Btu/hr)

$\dot{m}$ = -.000107 kg/sec (0.85 lb/hr)

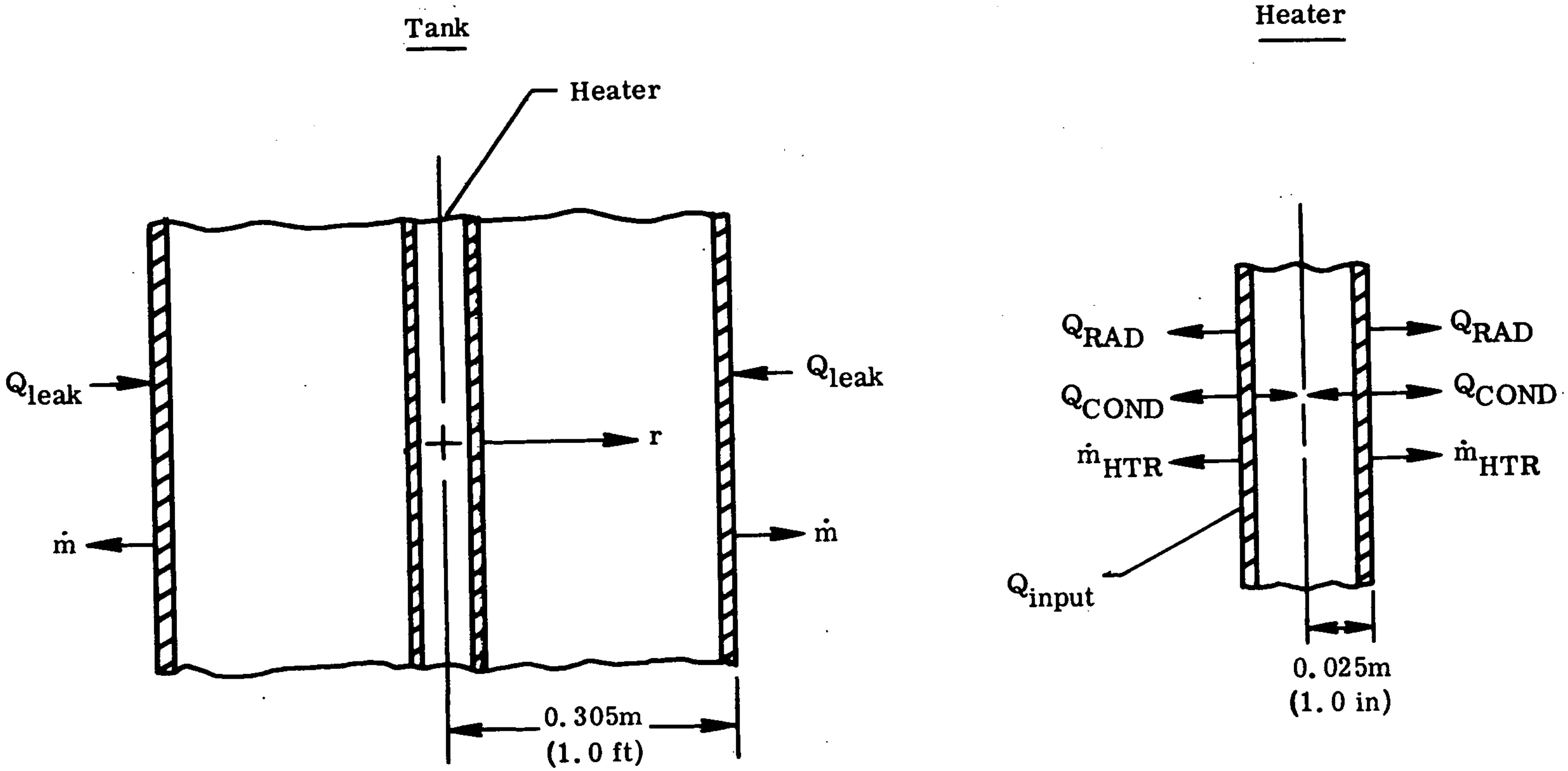

Figure 1. - Sketch of tank and heater showing essential features of model.

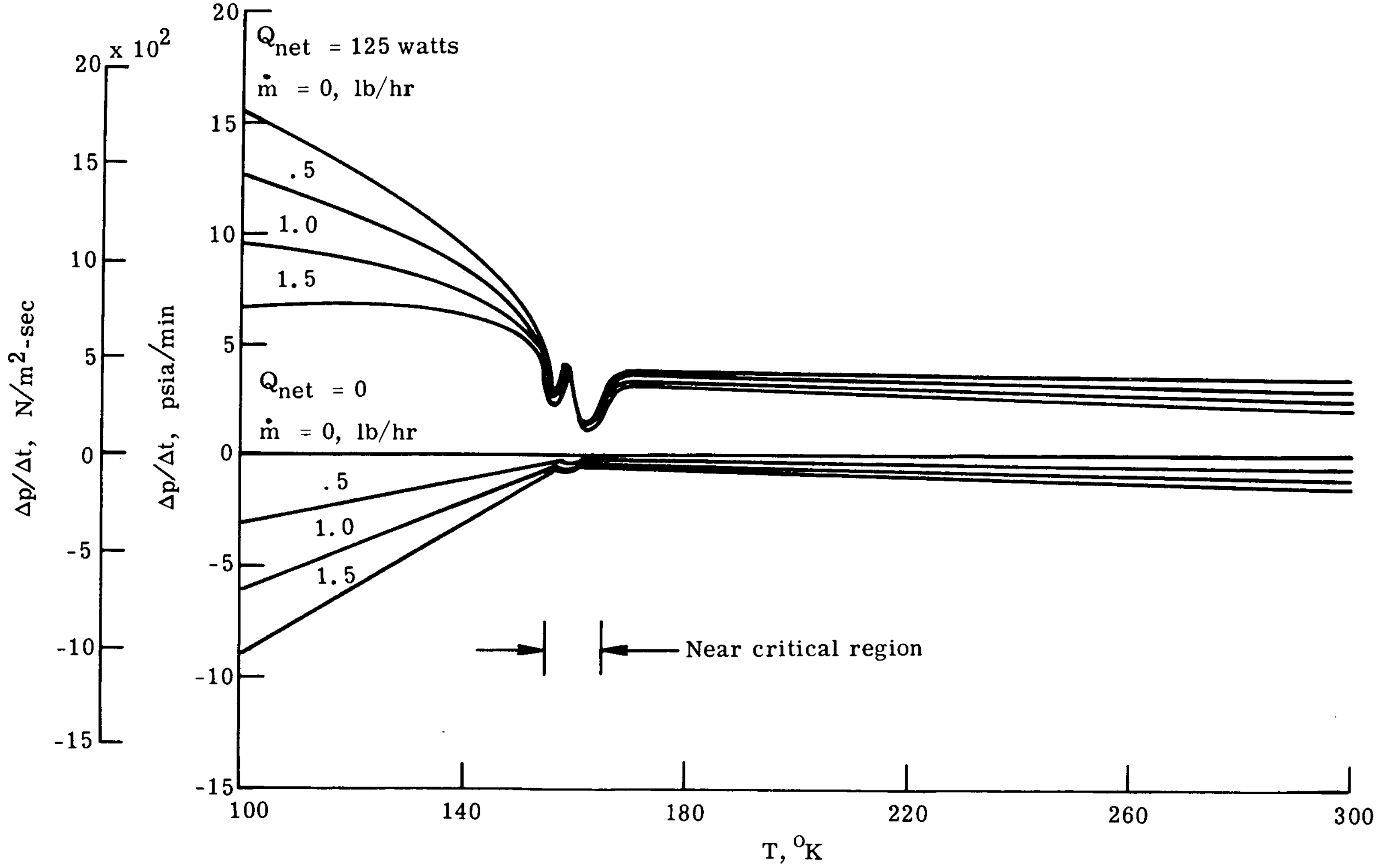

Figure 2. - Time rate of change of pressure in a uniform tank. $p = 5.9295 \times 10^6$ N/m^2 (860 psia), $V = 0.135$ m^3 (4.75 ft^3).

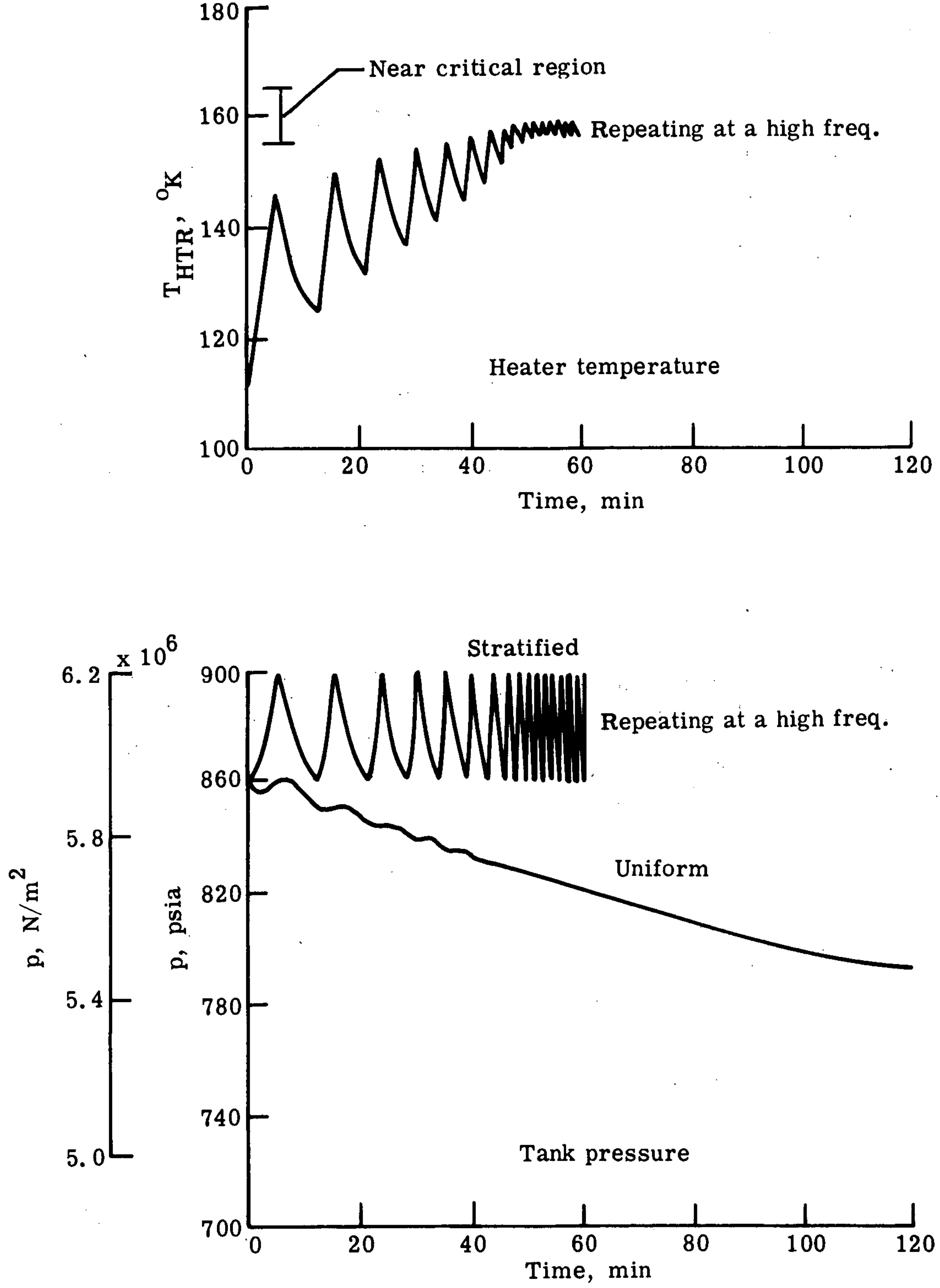

(a) Case 1.

Figure 3. - Time histories of heater temperature and tank pressure for cases 1-4.

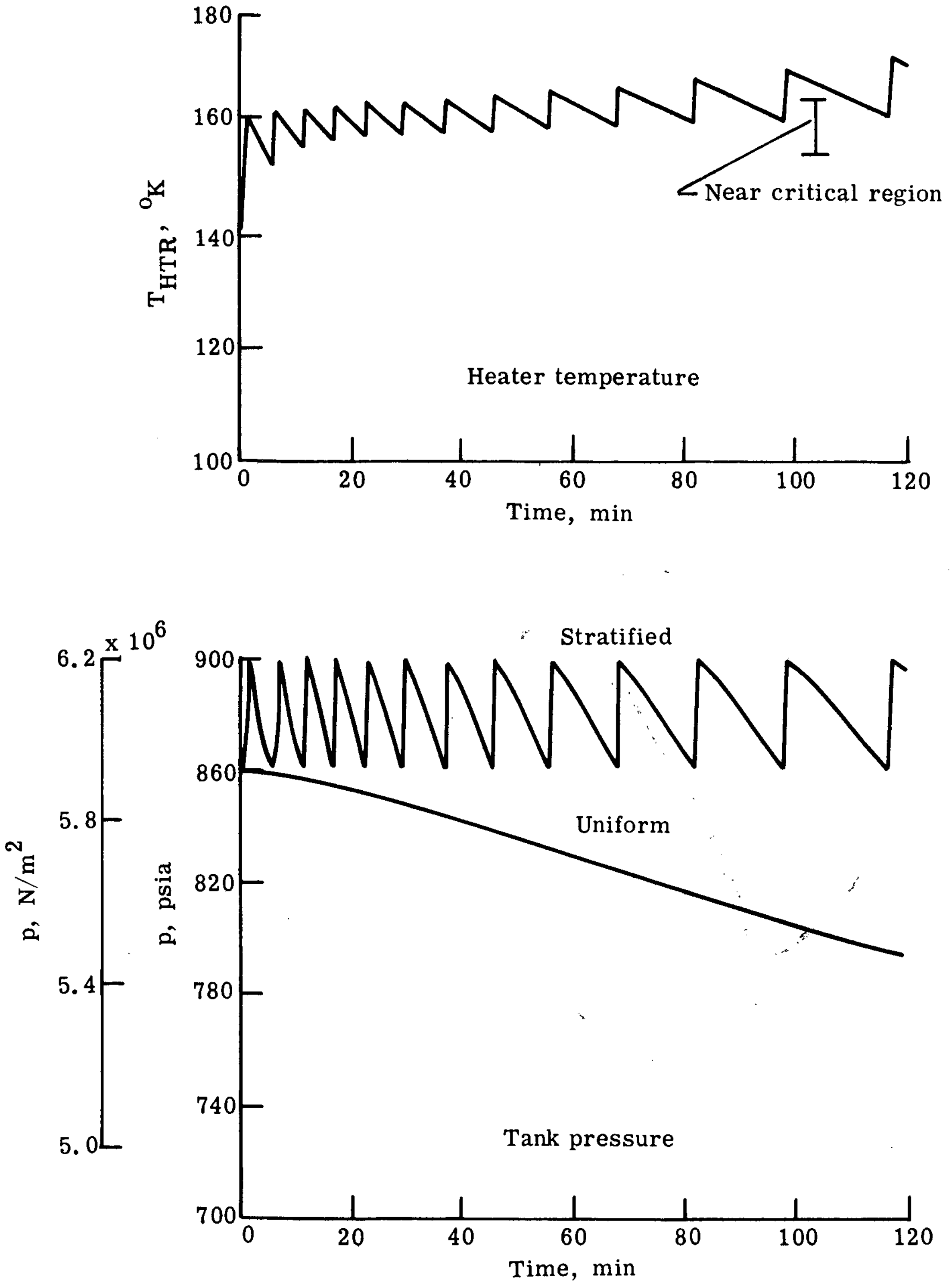

(b) Case 2.

Figure 3. - Continued.

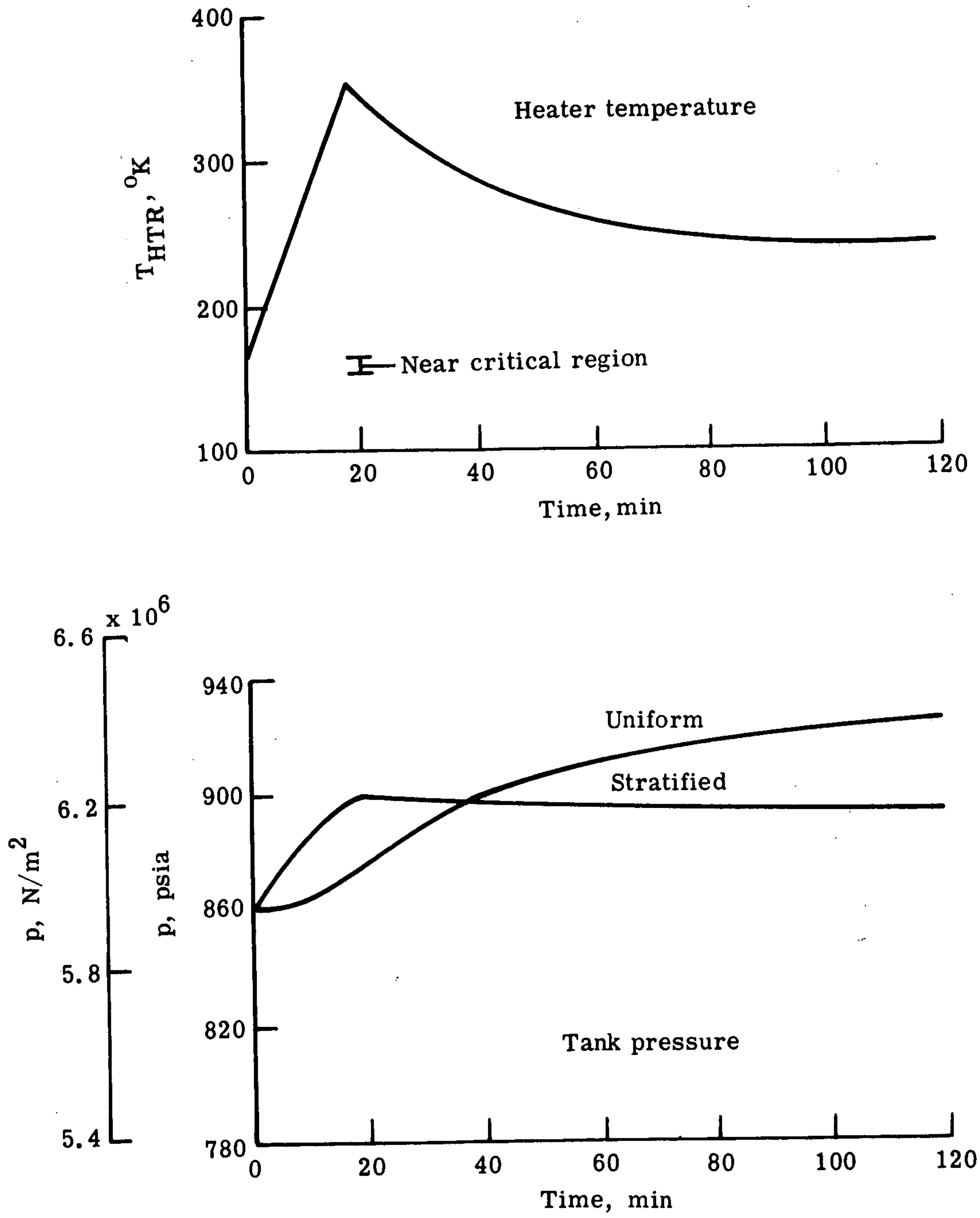

(c) Case 3.

Figure 3. - Continued.

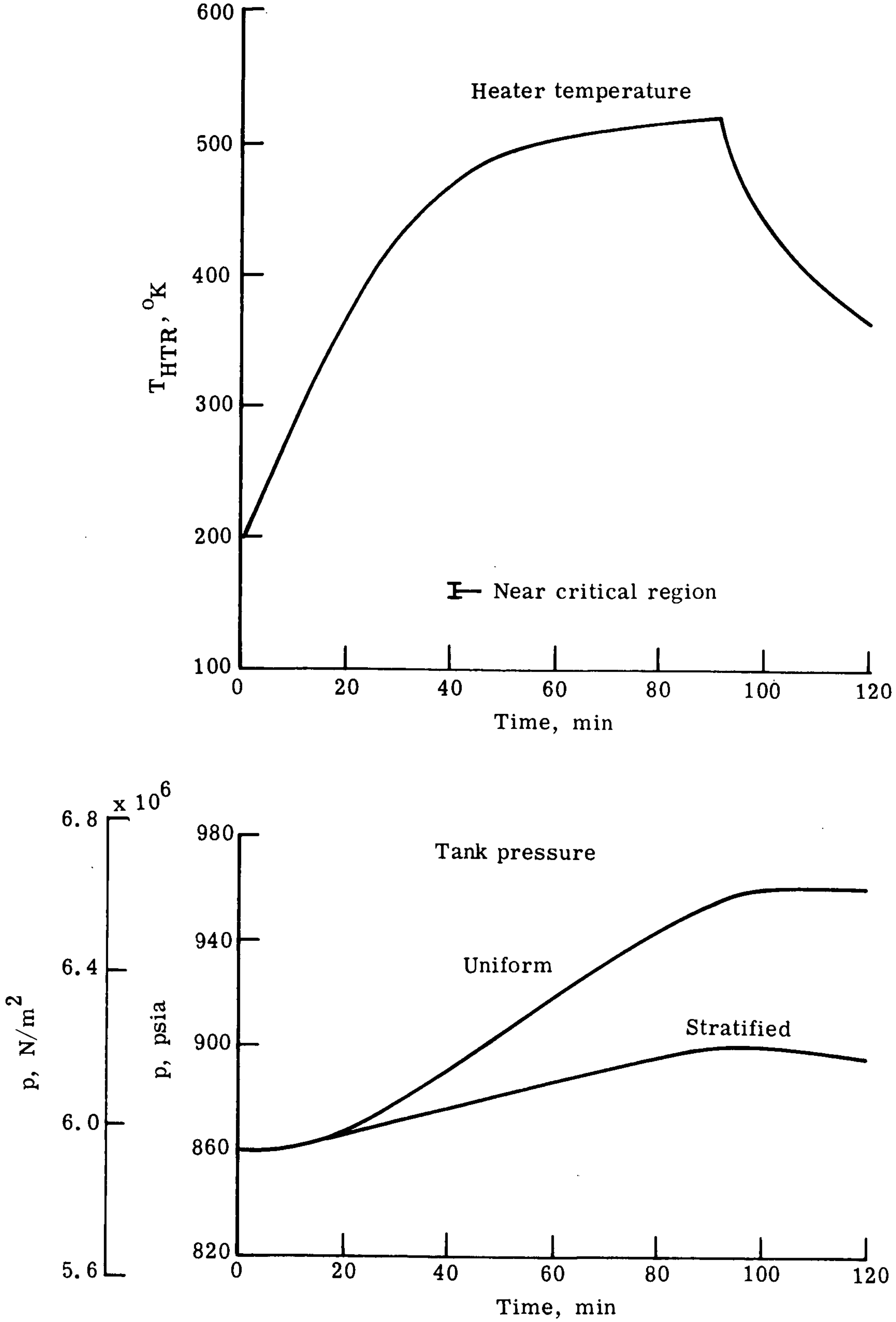

(d) Case 4.

Figure 3. - Concluded.

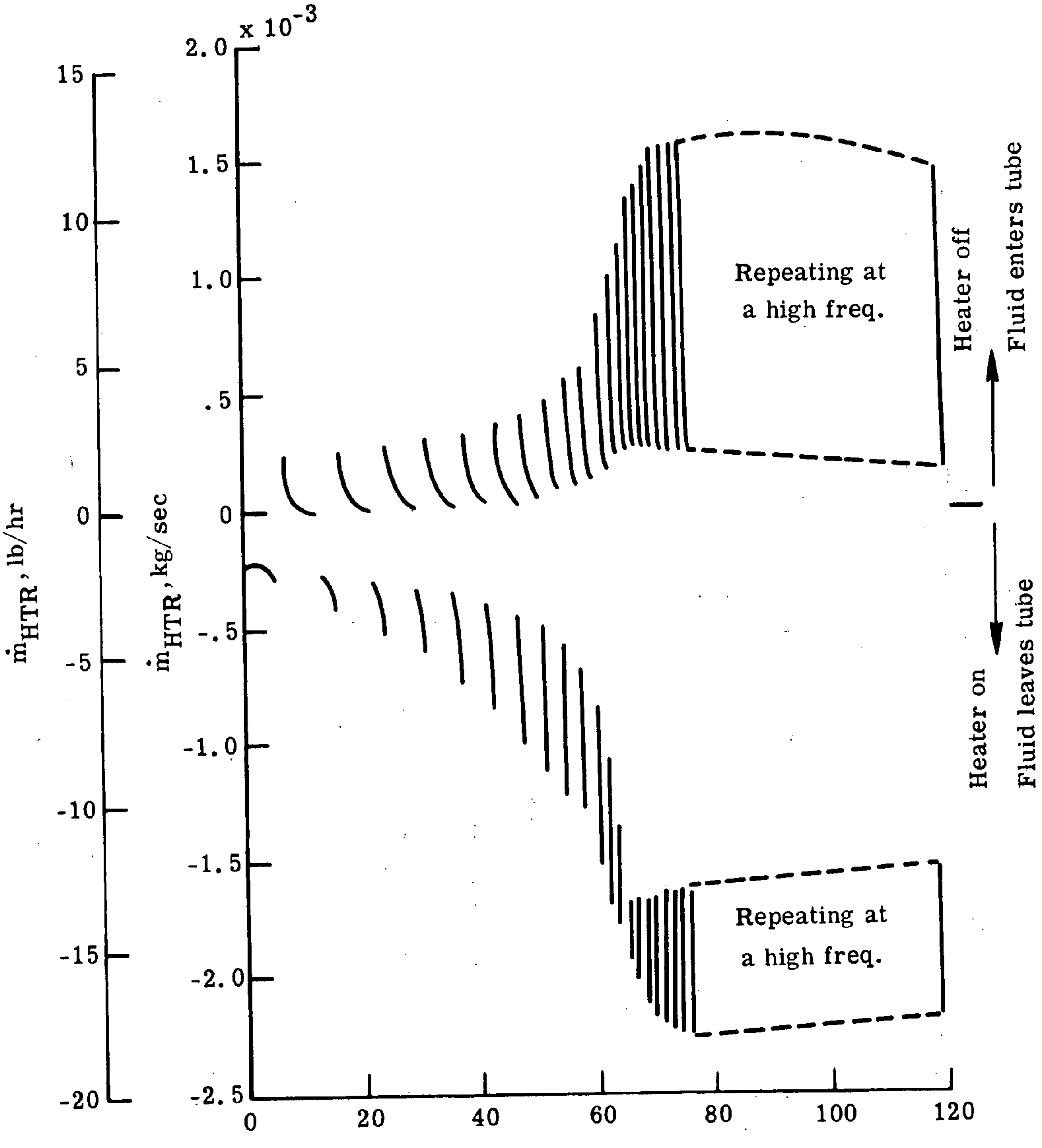

(a) Case 1.

Figure 4. - Time history of heater mass flux.

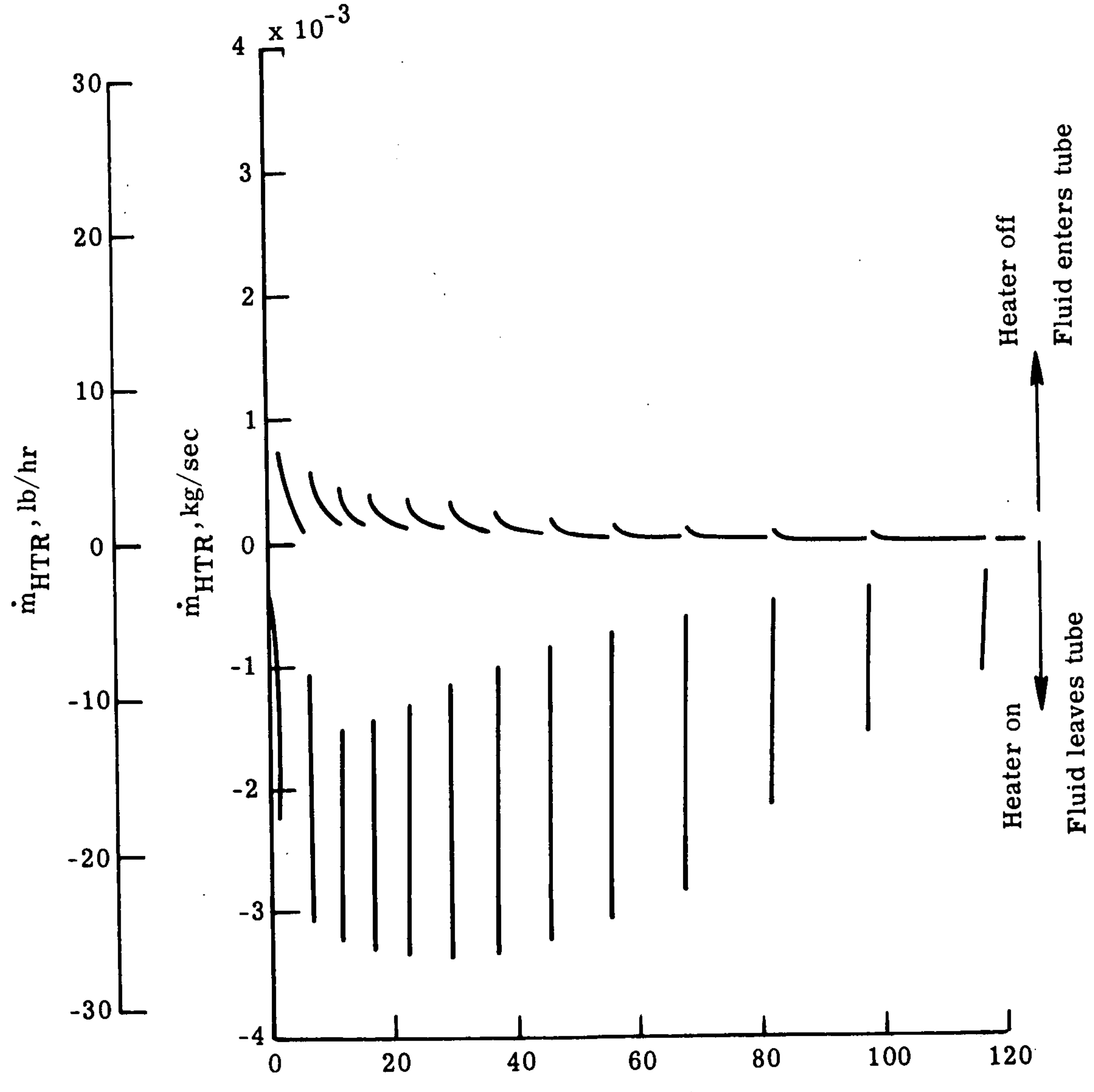

(b) Case 2.

Figure 4. - Continued.

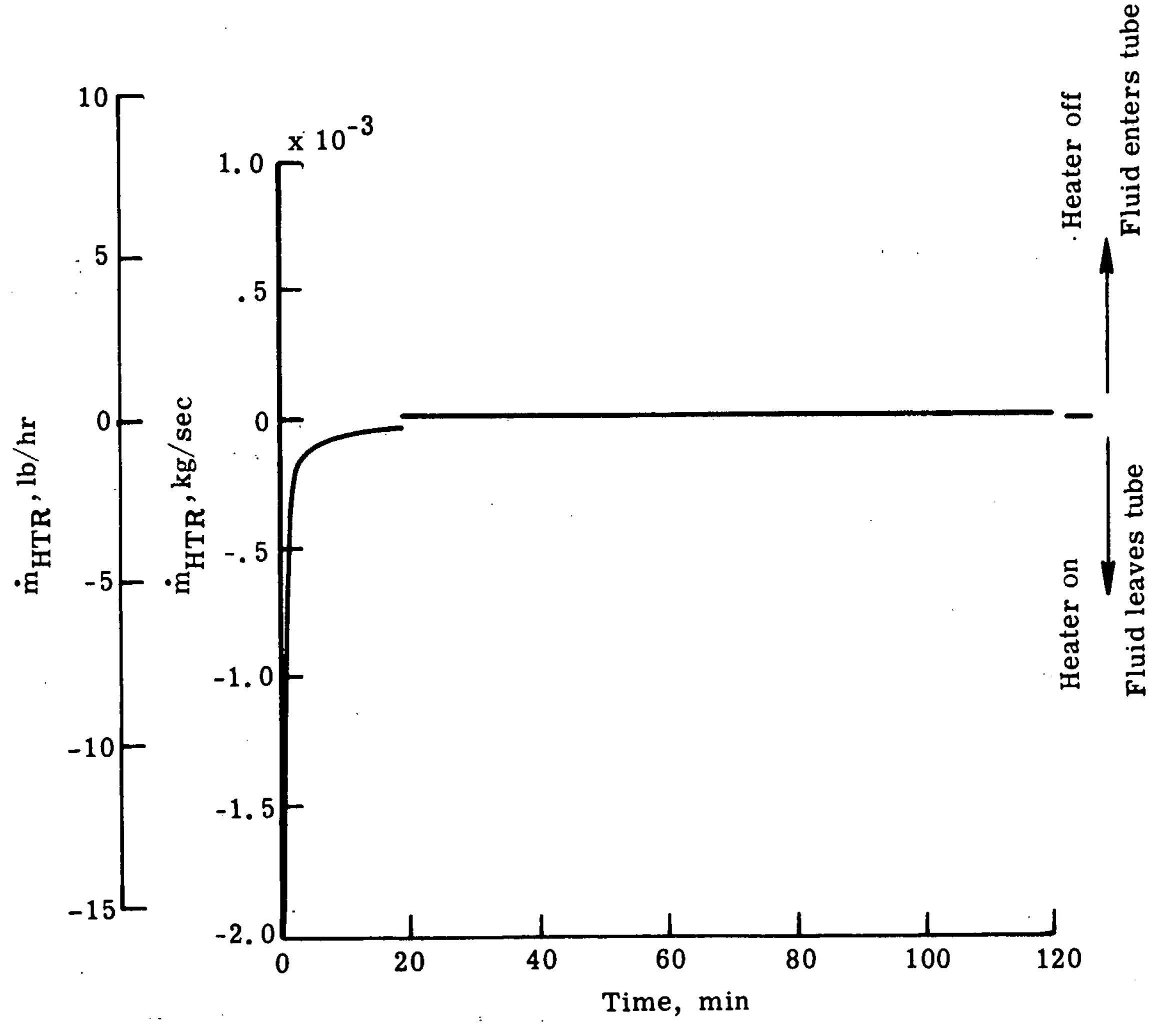

(c) Case 3.

Figure 4. - Continued.

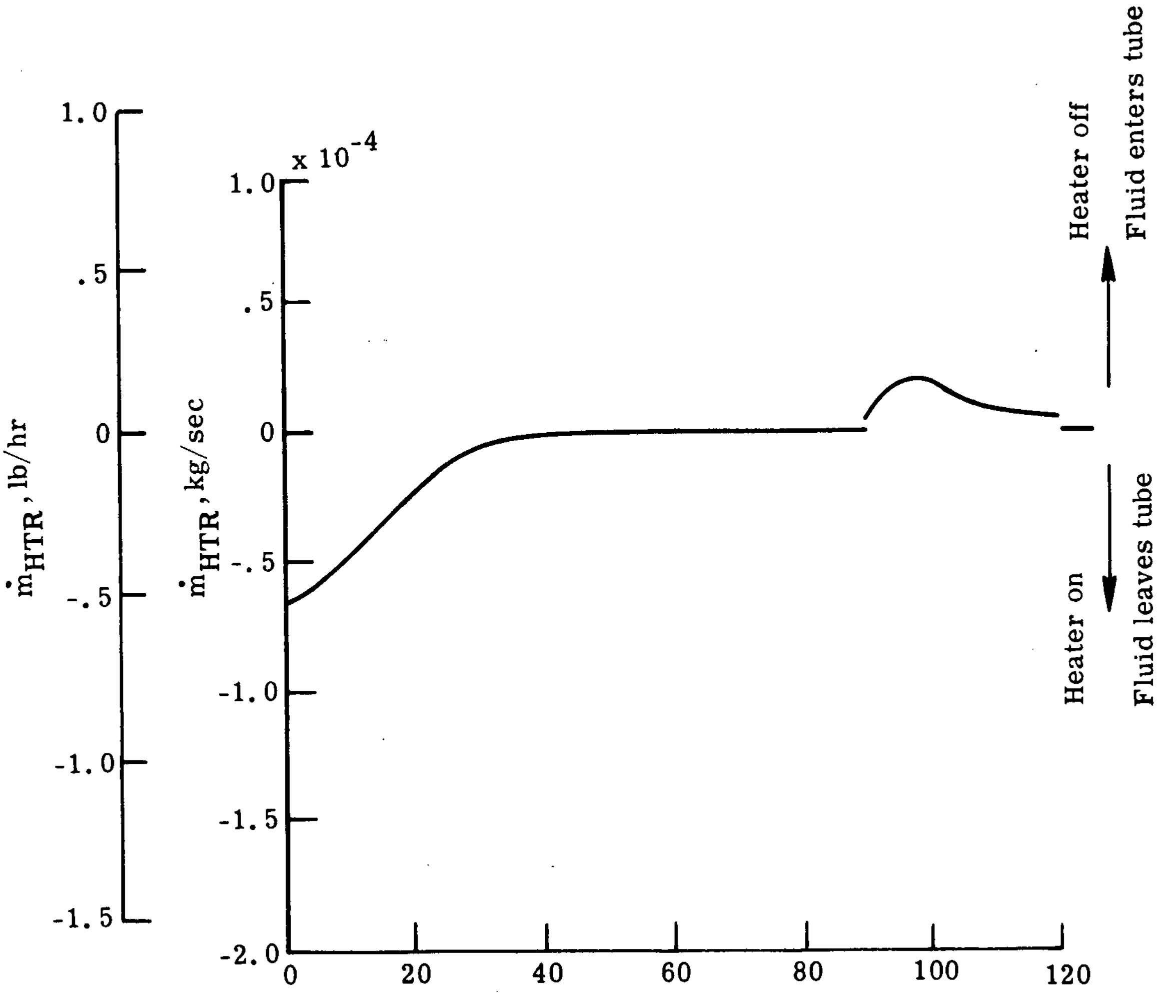

(d) Case 4.

Figure 4. - Concluded.

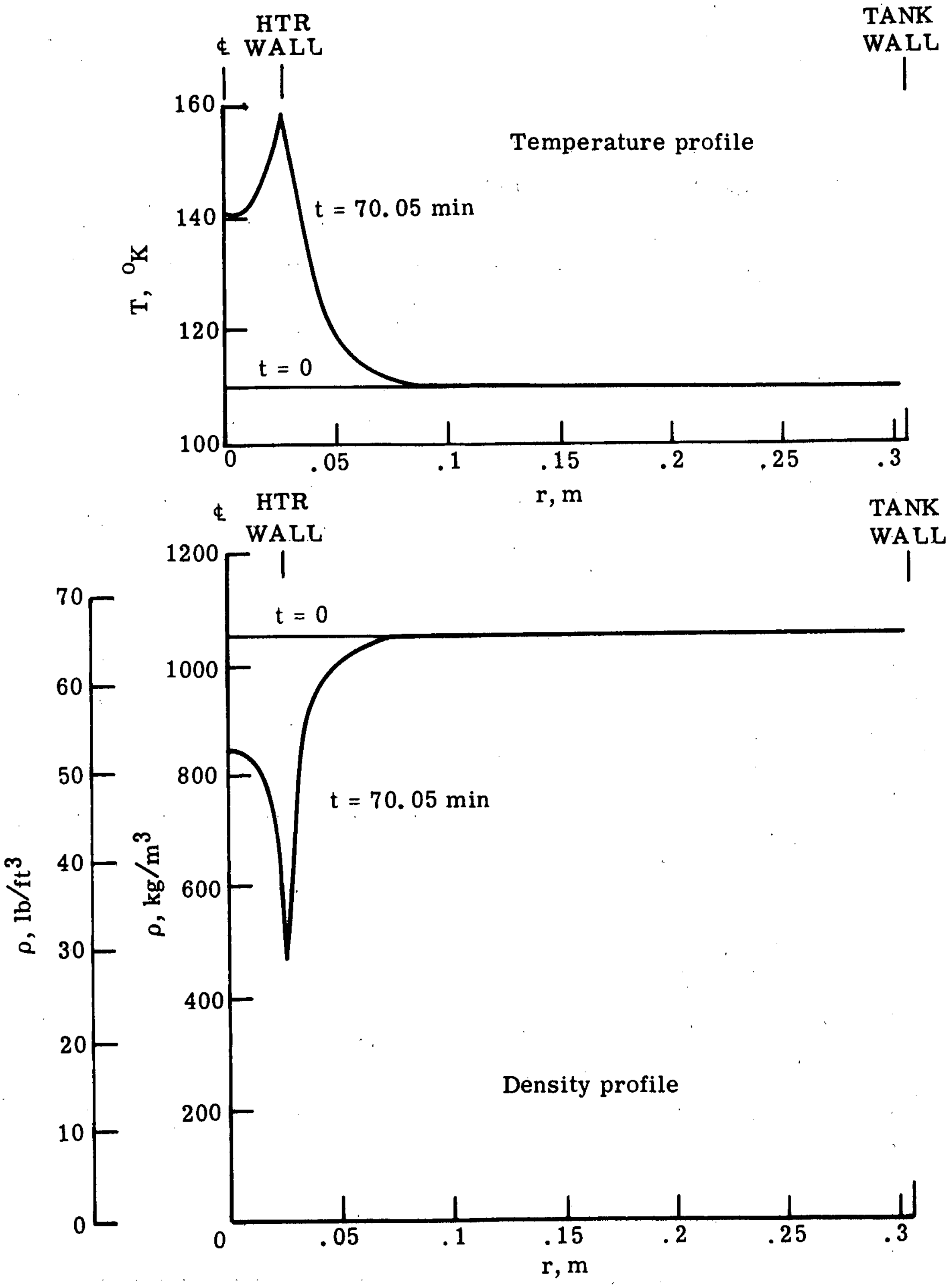

(a) Case 1.

Figure 5. - Profiles of temperature and density in tank for cases 1-4.

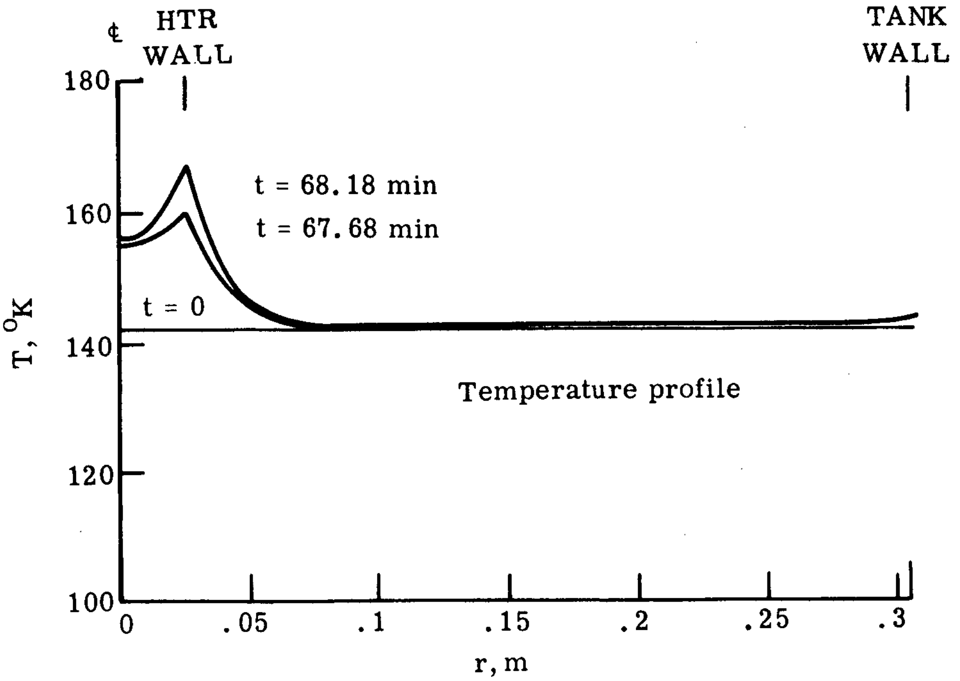

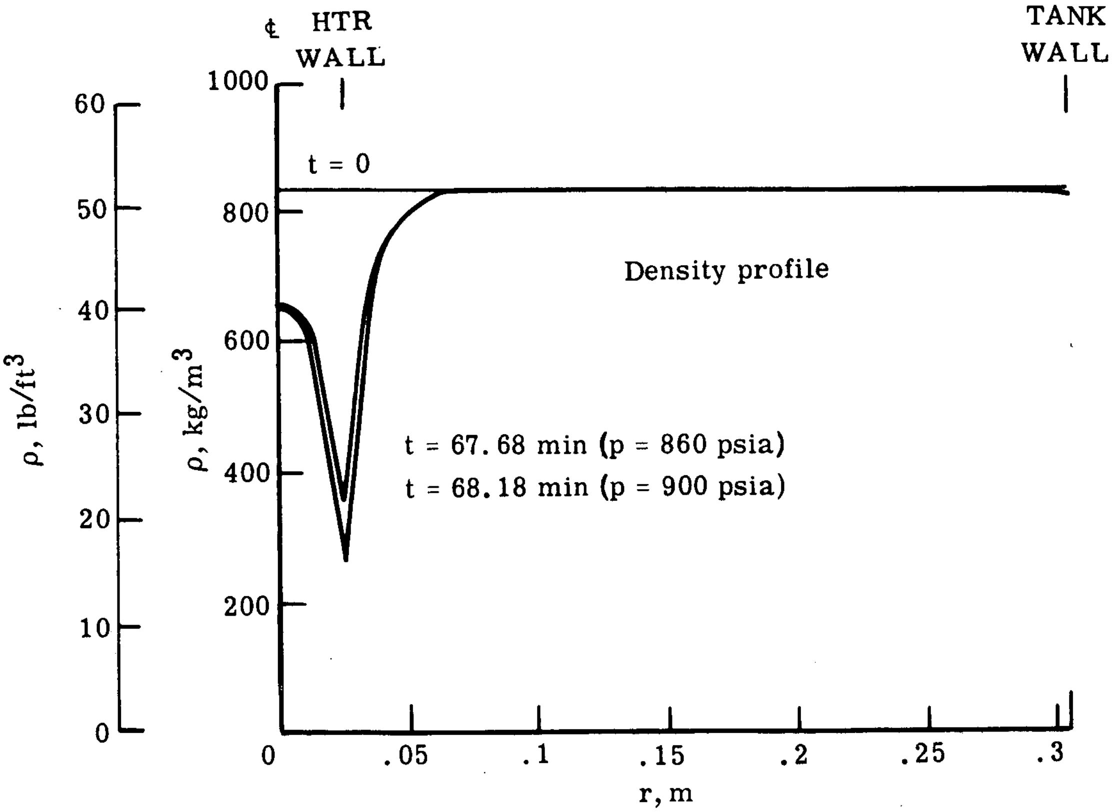

(b) Case 2.

Figure 5. - Continued.

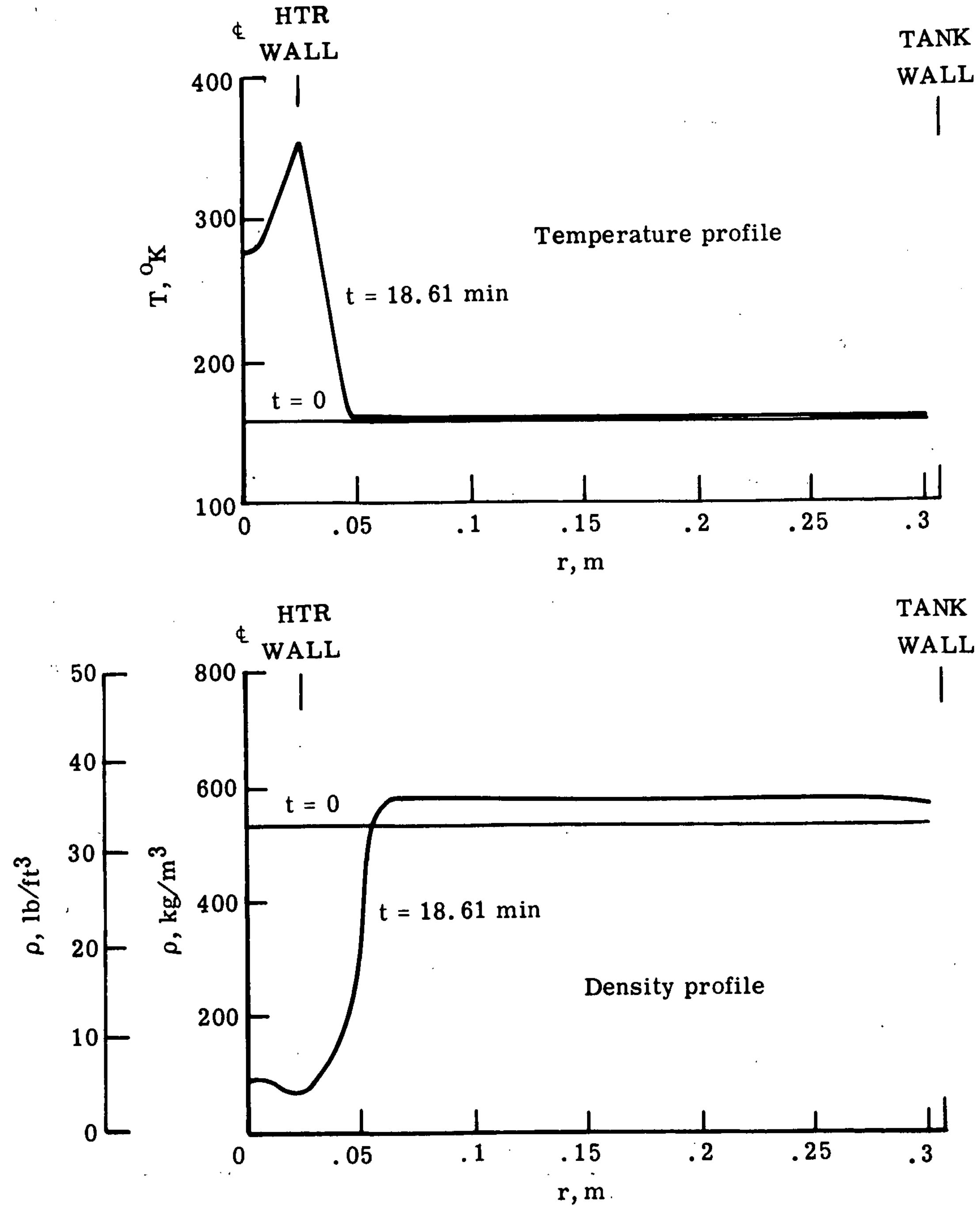

(c) Case 3.

Figure 5. - Continued.

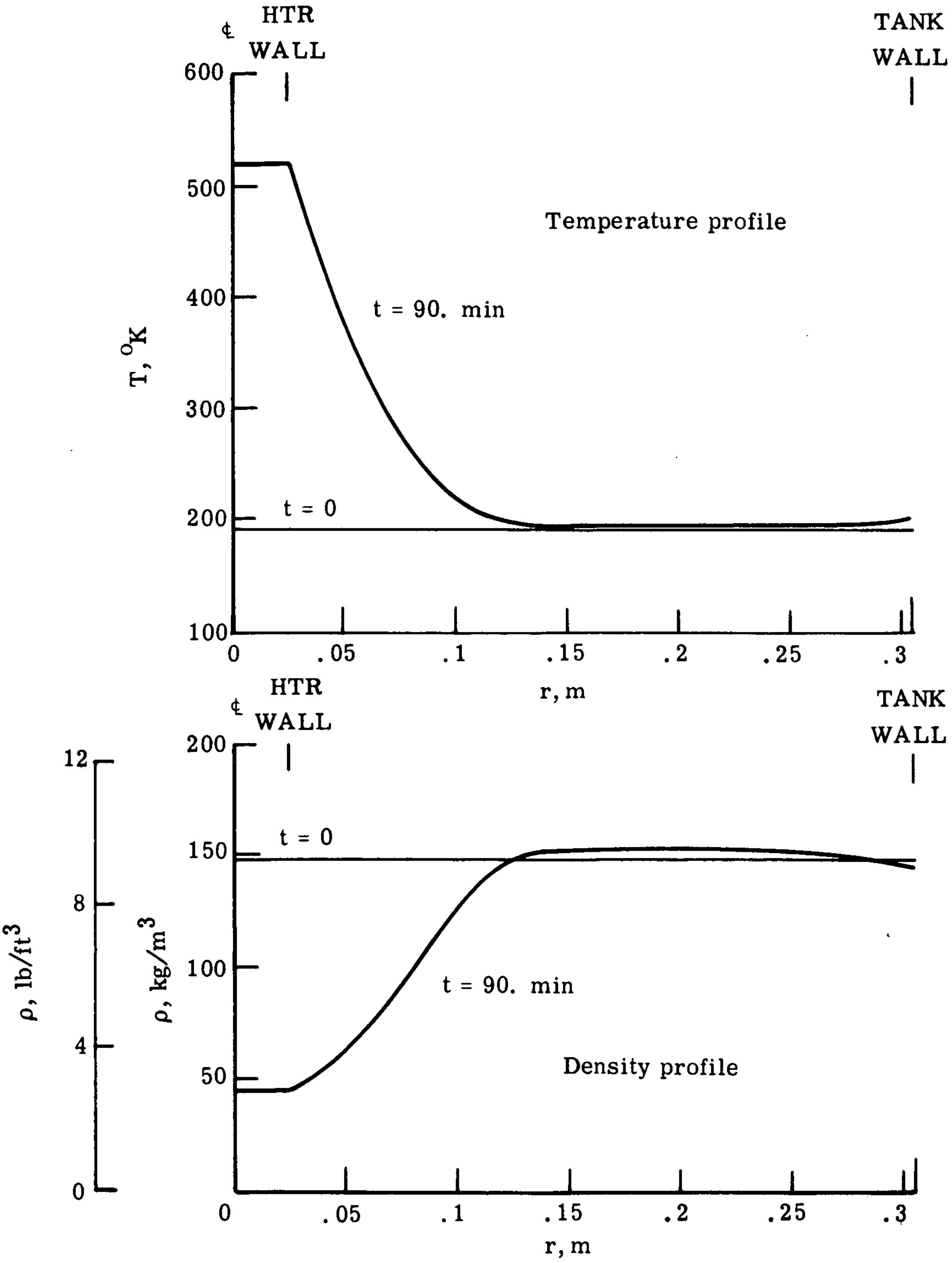

(d) Case 4.

Figure 5. - Concluded.

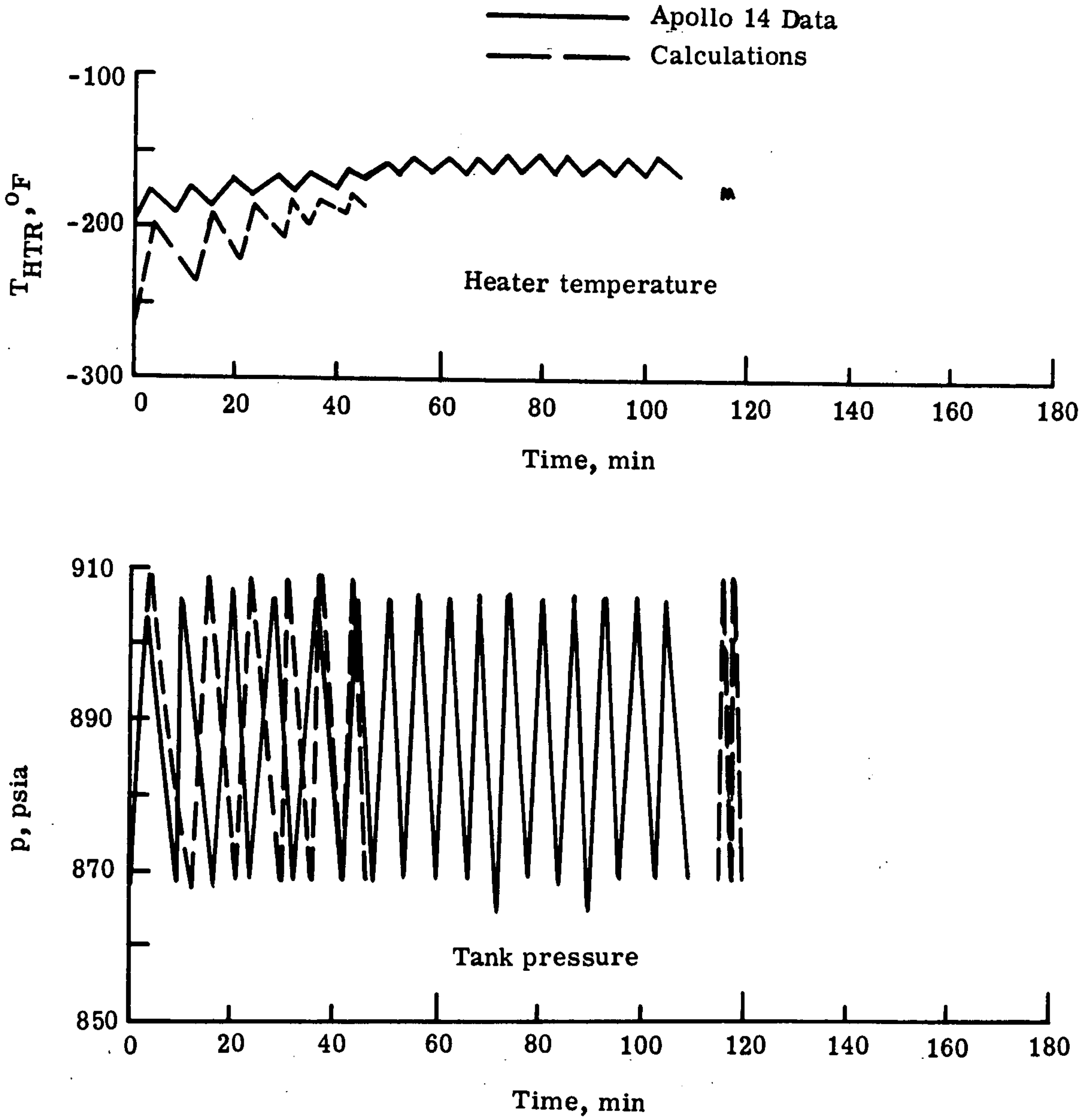

Figure 6.- Comparison of calculations for Case 1 with Apollo 14 flight data. Flight data begins at 10 hours 25 min. GET.

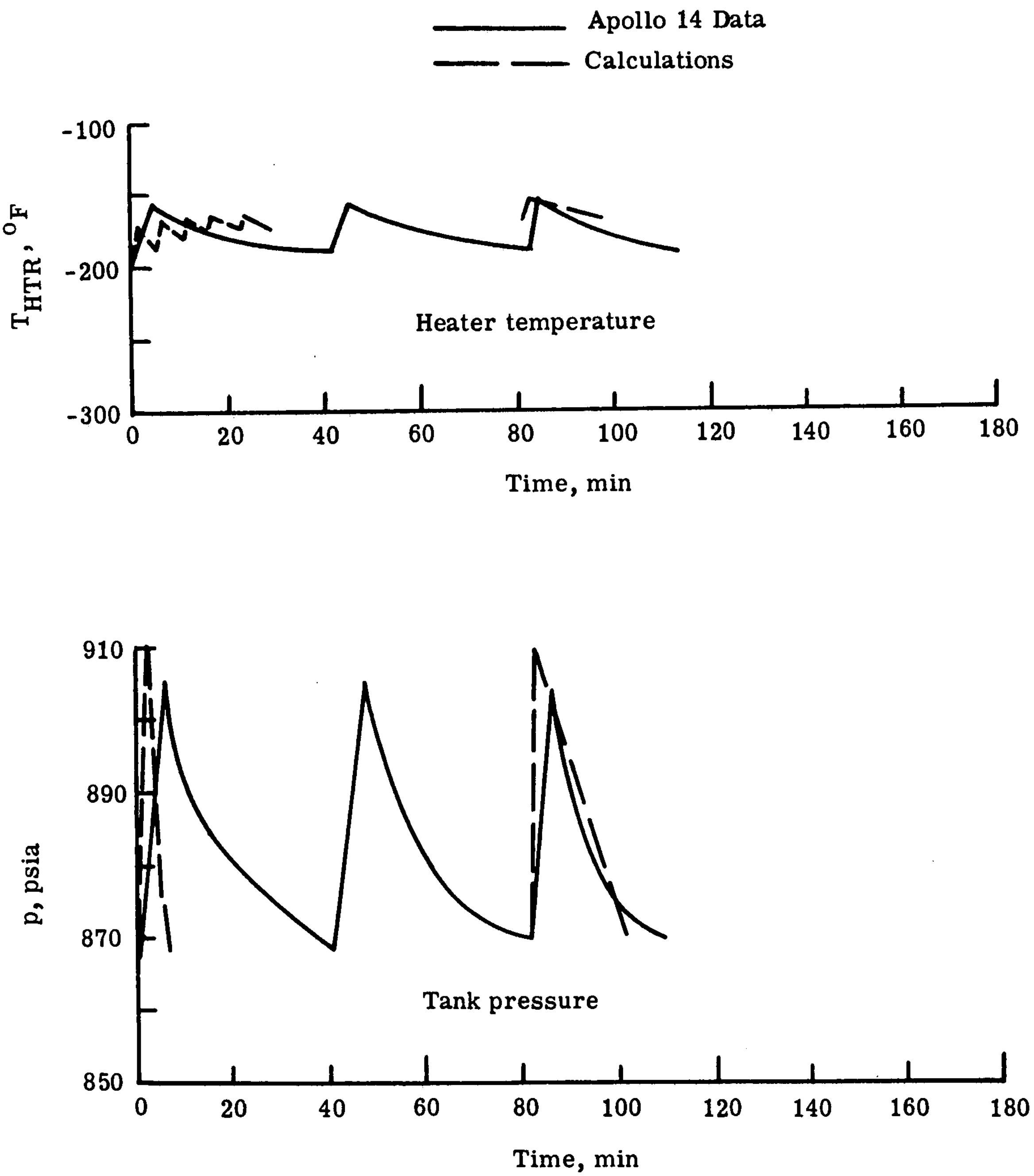

Figure 7.- Comparison of calculations for Case 2 with Apollo 14 flight data. Flight data begins at 151 hours GET.

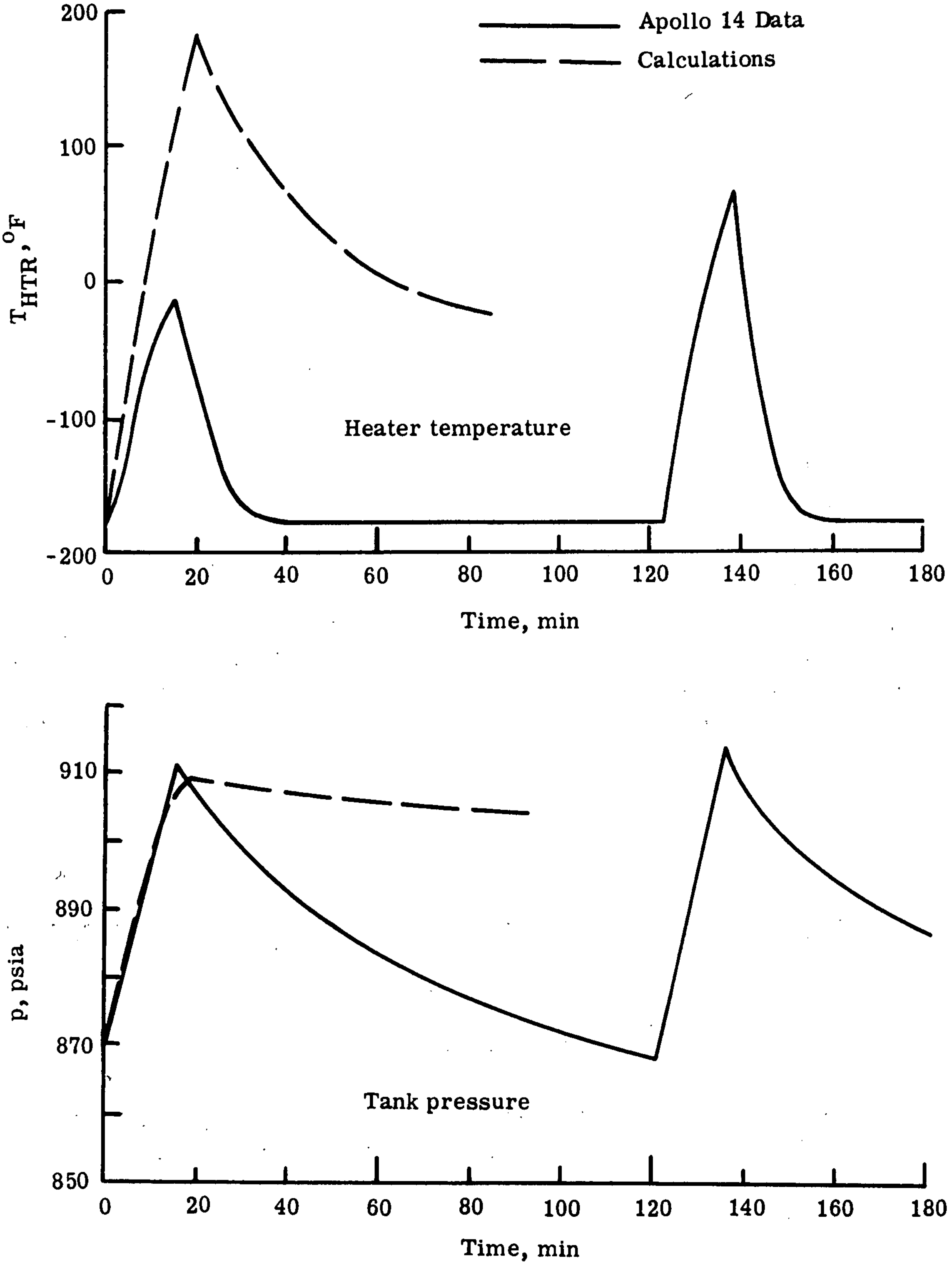

Figure 8.- Comparison of calculations for Case 3 with Apollo 14 flight data. Flight data begins at 30 hours 10 min. GET.

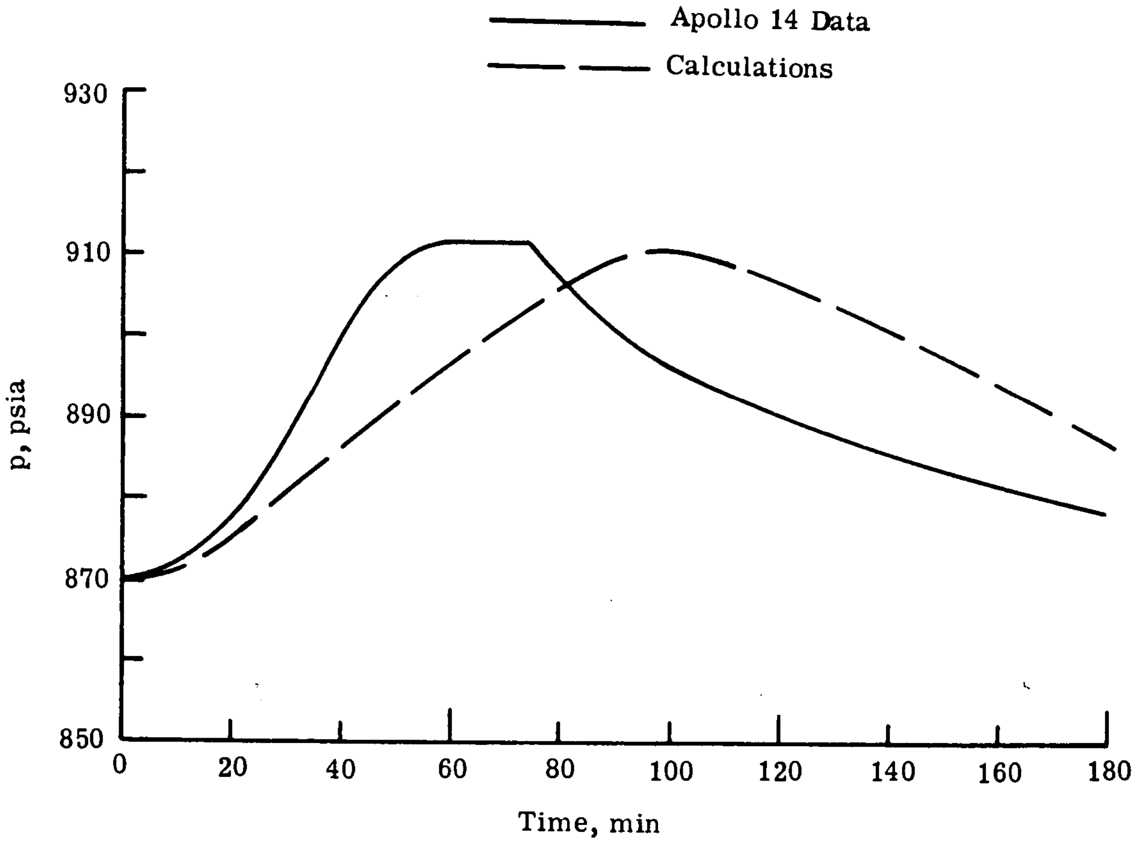

(a) Tank pressure.

Figure 9.- Comparison of calculations for Case 4 with Apollo 14 flight data. Flight data begins at 192 hours 20 min. GET.

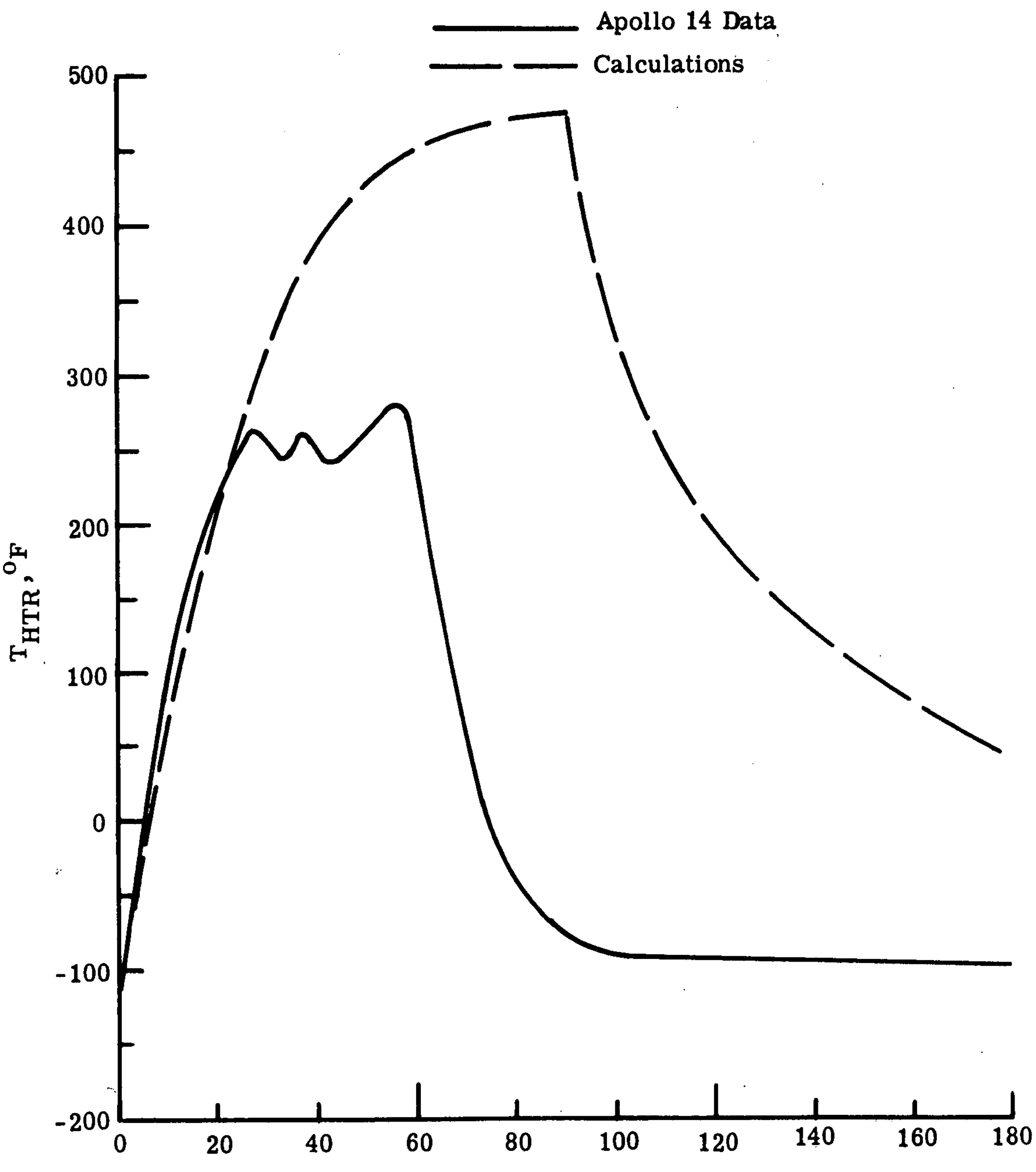

(b) Heater temperature.

Figure 9.- Concluded.

N72-23795

PREDICTION OF THE EFFECTS OF THERMAL STRATIFICATION ON PRESSURE AND TEMPERATURE RESPONSE OF THE APOLLO SUPERCRITICAL OXYGEN TANK

I. M. Chen and R. E. Anderson

North American Rockwell Corporation
Space Division, Downey, California

A semi-empirical design-oriented model has been developed for the prediction of the effects of thermal stratification on tank pressure and heater temperature response for the Apollo supercritical oxygen tank. The heat transfer formulation describes laminar free convection at low-g and takes into account the radiation and conduction processes occurring in the tank. The non-equilibrium thermodynamic behavior of the system due to localized heating of the stored fluid is represented by the characteristics of a discrete number of fluid regions and thermal nodes. Solutions to the time dependent variable fluid property problem are obtained through the use of a reference temperature procedure. A criterion which establishes the reference temperature as a function of the fluid density ratio, ρ/ρ_{cr} is derived. The analytical results are compared with the flight data.

I. Introduction

As a result of the use of supercritical cryogenic systems for space missions, considerable interest has been directed to the phenomenon of thermal stratification at low-gravity and its effects on the storage and expulsion performance of the system. The need for a better understanding of the problem is further emphasized due to the design support requirements for the present configuration of the Apollo cryogenic oxygen storage system (CSS). Of basic concern to the CSS is the degree of stratification due to local heating of the stored medium by the tank heating element. The effects on the heater temperature and the tank pressure response, and potential pressure decay, are expected to be significantly accentuated by the extremely low acceleration flight environment.

In view of the difficulty associated with obtaining analytic solutions to the non-equilibrium thermodynamic phenomenon for a geometrically complex system, a semi-empirical approach, based on subdividing the system into an arbitrary number of regions and thermal nodes, was selected for modeling the system.

The model was correlated initially with experimental data derived from a series of one-g, heat transfer tests. Owing to the exact geometric similarity of the test article to the flight hardware, these tests provided basic characteristic data and system constants essential for determining the radiative and conductive transport properties of the system. Free convective heat transfer characteristics of the CSS heater in low Rayleigh number regime were investigated through scaling tests. The results served as a basis for checking the adequacy of the model.

Using the refined model, pre-flight prediction of the Apollo 14 CSS performance was generated. Results showed good agreement with the flight data, especially in the low fluid density range. Post-flight data analysis provided a broad spectrum of system information for further model correlation and refinement.

Of significance in the model verification is the correlation of the free convection heat transfer process in the supercritical temperature region where the fluid properties exhibit the most severe variations. A simple solution to the variable fluid property problem was obtained through the use of a reference temperature procedure.

To provide perspective on the capabilities of the simulation model, computer results were compared with Apollo 14 flight data over a range of fluid densities, acceleration, and heater input power levels.

II. Description of the Model

The model of the Apollo cryogenic oxygen storage system was formulated on the basis of its design configuration and flight operational characteristics. The model describes the laminar free convection at low-gravity and takes into account the radiation and conduction phenomena occurring in the tank. The non-equilibrium thermodynamic behavior of the system due to localized heating of the stored fluid in a low acceleration environment is represented by three arbitrary cells as shown in Figure 1. The acceleration vector due to the rotation of the spacecraft is assumed to be normal to the heater axis. The first cell is formed by the accumulation of the rising boundary layer flow generated by the thermal energy released from the external surface of the heater. The growth of this (external) cell is governed by the rate at which the boundary layer flow is developed. The second cell is formed within the hollow structure of the heating element. The relatively confined fluid in this cell expands and contracts as its temperature fluctuates. The change of the fluid density in this(internal) cell causes part of the fluid mass to flow in or out of this region. The third cell comprises the main (bulk) region which slowly gains in temperature responding to heat transfer from the tank shell and the associated tank internal structures.

Specific system hardware included in the model are the heater, fluid quantity probe, and the attendent tank shell structures. The thermal capacitance effects of these components are lumped by using a discrete number of thermal nodes. The paths by which energy is transported and the interrelationships of the nodal masses or the fluid cells are depicted in Figure 2. The thermal energy generated from the electrical heater is transmitted predominantly by radiation and conduction to the hardware components and by convection to the external and internal cell fluids. The radiant energy absorbed by the shell structure is transmitted, in turn, through convection to the bulk cell fluid. The heat and mass transport process between the three cells are evaluated by the total enthalpies associated with the fluid flows crossing the cell boundaries. Since the kinetic energy associated with the free laminar boundary layer flow is rather small in the low-g field, the convective transport of momentum from the external cell to the bulk cell is considered to be insignificant. Heat transfer due to fluid mixing effects and cell temperature gradient is estimated by an idealized conduction analogy for a stable thermal layer with an arbitrary cell interface.

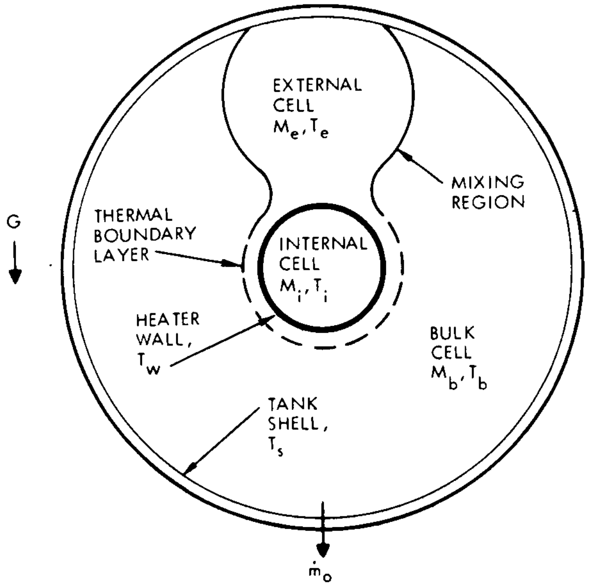

Fig. 1 Analytical Model

Test data derived from a series of one-g scaling tests were used to establish the basic system characteristics related to heat transfer. In order to evaluate the constants appearing in the analysis, radiative and conductive heat fluxes were measured with an actual full scale evacuated tank in which the surface emission and reflective characteristics, and the geometry of the tank components were duplicated. Data related to the convective heat transfer process at low-g was obtained from experiments using oxygen at reduced pressure as the test fluid based on Rayleigh number scaling techniques. Due to the inherent limitations associated with scaling and selection of a fluid with suitable thermal physical properties, only a limited Rayleigh number regime, encompassing a few equivalent acceleration levels and fluid density data points, was evaluated.

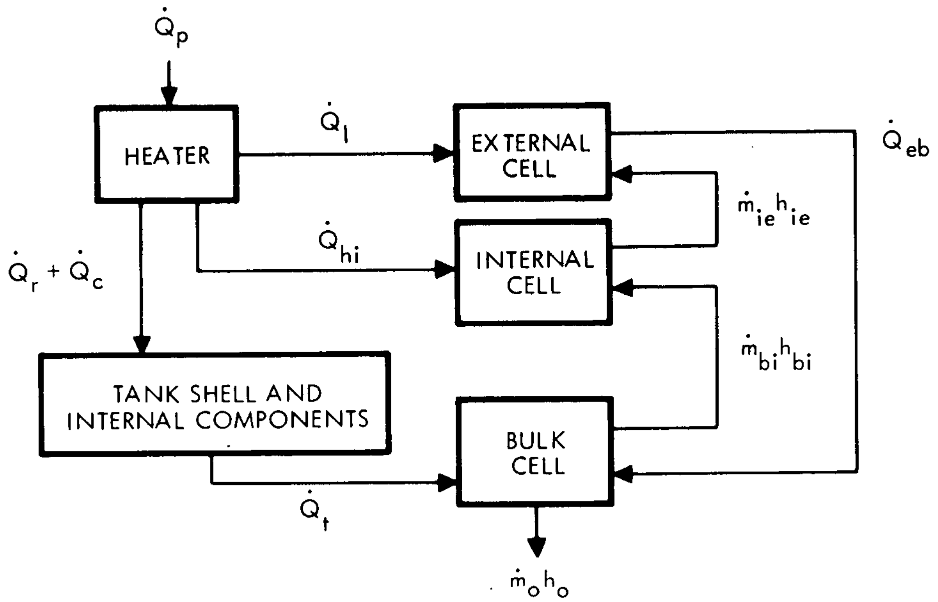

Fig. 2 Model Energy Flow Diagram

In the following sections, the equations essential to the description of the heat transfer and thermodynamic characteristics of each of the three lumped cells will be presented and the coupling of the equations to form the system dynamic simulation model will be discussed.

III. System Equations

Heat Transfer Formulation

The description of the thermal radiation and conductive processes between the various nodal masses assumed for the model are based on Stefan-Boltzmann and Fourier law equations. The net radiant energy interchange rates between interaction surfaces of the heater and the tank internal components are expressed as

$$q_{r,net} = \sum_{k=1}^{m} \sigma \mathcal{F}_{w,k} (T_w^4 - T_k^4) \qquad (1)$$

where $\mathcal{F}_{w,k}$ is the node-to-node interchange factor, the values of which, for the CSS, were established by experiments.

The conductive flux at a nodal point is represented by

$$q_{c,j} = \sum_{j=1}^{n} \frac{k_j}{x_j} (T_w - T_j) \tag{2}$$

where k_j is the effective thermal conductance and x_j is the penetration thickness.

The formulation, describing the convective energy transport process from the heater to the external, internal, and bulk cells, is separately summarized as follows.

External Cell. The heat energy transferred to the fluid external to the heater is assumed to be absorbed completely by the boundary layer which forms a part of the external cell. The temperature of the external cell fluid is assumed to be uniform; as the rising boundary flow is added to the cell, it is assumed to mix instantaneously with all of the external cell fluid. Detailed analysis of the free laminar boundary layer heat transfer has been extensively treated in the literature (References 1, 2, 3).

Estimates of the heat transfer rates from the horizontal cylindrical heater surface are derived from a basic vertical flat plate analogy which gives the result that heat transfer from a vertical flat plate and a horizontal circular cylinder are identical when the height of the plate is 2.5 times the cylinder diameter.

The integral forms of the momentum and energy equations for steady state boundary layer flow on a vertical flat plate are:

$$\frac{d}{dX} \int_0^{\delta} u^2 dy = g\beta \int_0^{\delta} (T - T_b)\, dy - \nu \left[\frac{du}{dy}\right]_w \tag{3}$$

$$\frac{d}{dX} \int_0^{\delta} u\,(T - T_b)\, dy = \frac{-k}{\rho c_p} \left[\frac{dT}{dy}\right]_w \tag{4}$$

Using the conventional approximations for the velocity and temperature profiles for the boundary layer flow, Eqs. (3) and (4) can be reduced into a set of simultaneous ordinary differential equations, the solution of which leads to the determination of $\delta(x)$ and $u\,(x)$, (Reference 3).

A dimensionless representation of the boundary layer heat transfer, the local Nusselt number, is then obtained by relating the local heat transfer coefficient to the boundary layer thickness and thermal conductivity.

$$Nu_x = \frac{h_x x}{k} = \frac{q}{(T_w - T_b)} \frac{x}{k} = 2 \left(\frac{x}{\delta} \right) \qquad (5)$$

The average heat flux for a vertical flat plate based upon the integrated local heat transfer coefficient can be expressed as

$$\bar{q} = \frac{8}{3} \frac{k}{\delta} (T_w - T_b) \qquad (6)$$

The average convective heat flux for the horizontal cylindrical heater is estimated based on the average heat flux computed for a flat plate, Eq. (6), with an equivalent characteristic dimensional height (Reference 3).

The growth of the external cell reflecting the increase of its mass, m_e, is determined by integrating the boundary layer flow.

$$m_e = \int_0^t \dot{m}_\ell \, dt \qquad (7)$$

where

$$\dot{m}_\ell = \rho \, \bar{v} \, (x,t) \, \delta (x,t) \, L \qquad (8)$$

The variables ρ , $\bar{v}$, and δ are respectively the instantaneous fluid density, mean boundary layer velocity, and thickness of the boundary layer flow when it mixes with the external cell fluids, i.e., at the top of the equivalent plate.

The shape of the external cell is arbitrary. The transfer of energy at the hypothetical cell boundary to the bulk fluids due to mixing in this model is approximated by the Fourier conduction law equations with an arbitrary scale length.

Internal Cell. The estimates of heat transfer from the interior surface of the heater to the cell fluid in an enclosed space is complicated and empirical results must also be used. Theoretical analyses dealing with laminar steady convective flows and heat transfer specifically for a horizontal tube with circular cross-section have been examined by Martini and Churchill (Reference 4) and Weinberg (Reference 5). Solutions of partial differential equations describing the conservation of mass and energy for the system have yielded reasonable predictions of temperature fields for specific cases of interest. These results are in good agreement with experimental measurements. Estimates of the average heat transfer coefficient for free convection inside a horizontal cylinder can generally be obtained using the following correlation, (Reference 6)

$$\frac{\overline{Nu}}{Gr^{1/4}} = c_1 \left[\frac{Pr^2}{1+Pr}\right]^{1/4} \tag{9}$$

For the ranges of Prandtl and Grashof numbers considered for the internal cell, $c_1 = 0.35$ is assumed.

To account for the effects of the expansion and contraction of the internal cell fluid as its temperature fluctuates during a heating cycle, the change of the fluid mass in the internal cell is given by

$$\dot{m}_i = V_i \, \dot{\rho}_i \tag{10}$$

where V_i is the internal physical volume of the heater tube and the rate of change in the cell fluid density is

$$\dot{\rho}_i = -\left|\beta \rho \dot{T}\right|_i \tag{11}$$

The fluid mass expelled due to the internal cell temperature rise ($\dot{T}_i$ is positive) is assumed to be mixed with the external cell. Since the enthalpy of the expelled fluid element greatly exceeds its kinetic energy, the momentum transfer is neglected. For the case where the cell temperature decreases ($\dot{T}_i$ is negative), the fluid from the bulk region is assumed to be drawn into the internal cell compensating for the fluid density change.

Bulk Cell. It is assumed that the temperature of the bulk cell is uniform but varies with time. During a heater cycle, the tank shell temperature increases due to radiative and conductive heat flux from the heater. The convective heat transfer, due to the temperature gradient developed between the tank shell and the bulk fluid, contributes to the bulk fluid temperature rise.

The laminar free convective heat transfer from the spherical tank shell to the bulk fluid is approximated by a dimensionless heat transfer parameter correlation, similar to that used for the cylindrical internal cell.

$$\frac{\overline{Nu}}{Gr^{1/4}} = c_2 \left[\frac{Pr^2}{1+Pr}\right]^{1/4} \tag{12}$$

On the basis of scaling test data correlation, $c_2 = 0.45$ is assumed.

The effective heat transfer surface area for the tank shell is estimated on the basis of the geometric volume equivalence of a cylindrical container.

Thermodynamic Formulation

The development of the equation describing the thermodynamic behavior of the supercritical cryogenic storage system is based on the statement of the First Law. Each cell of the model is assumed to be a totally enclosed thermodynamic system with arbitrary moving boundaries. Letting Q be the total heat input in the system, the basic equation relating the total internal energy and thermodynamic variables of the system is

$$dU = \sum_{j=1}^{n} h_j dm_j + dQ - pdV \tag{13}$$

where h_j represents the specific enthalpies associated with the masses, m_j, added and/or removed from the system.

Treating p and ρ as the independent thermodynamic state variables, Eq. (13) may be expressed as

$$\rho V \left[\left(\frac{\partial u}{\partial p}\right)_\rho dp + \left(\frac{\partial u}{\partial \rho}\right)_p d\rho \right] + ud(\rho V) =$$

$$\sum_{j=1}^{n} h_j dm_j + dQ - pdV \qquad (14)$$

By letting

$$\phi = \frac{1}{\rho} \left(\frac{\partial p}{\partial u}\right)_\rho$$

and

$$\psi = \rho \left(\frac{\partial u}{\partial \rho}\right)_p$$

and treating the system variables as functions of time, the above equation for an adiabatic cell can be transformed to a characteristic equation relating the cell volume, V, to the system pressure, p, as

$$\frac{dV}{dp} = \frac{1}{(\rho\psi - p)} \left\{ \frac{V}{\phi} - \left[\sum_{j=1}^{n} h_j \dot{m}_j - (u + \psi)\, \dot{m} \right] \frac{1}{\dot{p}} \right\} \qquad (15)$$

Let η be the energy rate parameter representing the sum of the heat and mass rates of addition or removal from the cell. Then,

$$\frac{dV}{dp} = \frac{1}{(\rho\psi - p)} \left[\frac{V}{\phi} - \frac{\eta - (u + \psi)\dot{m}}{\dot{p}} \right] \qquad (16)$$

where

$$\eta = \sum_{j=1}^{n} h_j \dot{m}_j$$

It is convenient to define additional parameters as

$$\Omega = \frac{\eta - (u + \psi)\,\dot{m}}{(\rho\psi - p)}$$

and

$$\Gamma = \frac{V}{\phi\,(\rho\psi - p)}$$

Eq. (16) for the three cells can be rewritten in a generalized form as

$$\left(\frac{dV}{dp}\right)_j = \Gamma_j - \frac{\Omega_j}{\dot{p}} \qquad (17)$$

Based upon the assumptions made relating the heat and mass transfer across the specific cell boundaries, the energy rate parameters, η_e, η_i, and η_b, for the external, internal, and bulk cells, respectively, are expressed as follows.

First,

$$\eta_e = h_\ell \dot{m}_\ell + h_i \dot{m}_i - \dot{Q}_{eb}$$

The first two terms on the right hand side of the equation represent the enthalpies associated with the boundary layer flow generated by the external surface of the heater and that associated with the flow expelled from the internal cell during the heat up process. Q_{eb} is the interfacial heat transfer rate from the external to bulk cell.

Similarly,

$$\eta_i = h_b \dot{m}_b - h_i \dot{m}_i + \dot{Q}_{hi}$$

The first two terms on the right hand side of the equation represent the enthalpies associated with flow replenished from the bulk cell during cooling and the flow expelled from the internal cell during heating of the cell fluid. $\dot{Q}_{hi}$ is the heat transfer rate from the heater interior surface to the internal cell.

And finally,

$$\eta_b = \dot{Q}_{eb} + \dot{Q}_b - h_b \dot{m}_t$$

where $\dot{Q}_b$ is the sum of all radiative and convective heat transfer rate from the tank shell and interior components, and $\dot{m}_t$ is the mass flow rate transferred from the bulk cell to the adjacent cells and includes that which is withdrawn from the tank.

Coupling of the Cells

Based upon the cell volume relationships, the total tank internal volume, V_t, may be expressed as

$$V_t = V_e + V_i + V_b \tag{18}$$

By differentiating Eq. (18) with respect to the tank pressure, assuming the tank to be elastic, and letting

$$\frac{dV_t}{dp} = \epsilon \tag{19}$$

an expression which establishes the dynamic coupling effects of the individual cells is obtained.

$$\frac{dV_e}{dp} + \frac{dV_i}{dp} + \frac{dV_b}{dp} = \epsilon \tag{20}$$

Replacing the three derivative terms in Eq. (20) by the respective characteristic equation defined in Eq. (17) and solving the resulting equation in terms of $\dot{p}$, one obtains

$$\dot{p} = \frac{\sum_{j=1}^{3} \Omega_j}{\sum_{j=1}^{3} \Gamma_j - \epsilon} \tag{21}$$

In this equation, the index, j = 1,2,3, designates the parameters for the external, internal, and bulk cells, respectively.

Eq. (21) can be integrated to obtain the tank pressure as a function of time reflecting the non-equilibrium thermodynamic effects of the transient heat and mass transfer processes occurring during a heating and expulsion cycle of a single phase supercritical cryogenic tank.

Pressure Decay Potential

The non-equilibrium thermodynamic state in the tank is inherently unstable. Any external perturbation will cause the tank pressure to decay because of the natural tendency of the system to establish thermal equilibrium. The pressure decay potential of such a system may be computed by an approximate heat deficiency equation based on the difference between the average heat content of the system and that of the sum of the stratified cells. The equation is

$$\Delta Q = (\bar{\rho}\bar{u})\, V - \sum_{j=1}^{3} (\rho u V)_j \tag{22}$$

where ΔQ stands for heat deficiency, the bar denotes average parameter values, and the summation is extended over the three cells into which the thermodynamic system has been subdivided.

The instantaneous pressure decay potential can then be determined by

$$\Delta p_{max} = \frac{\bar{\phi}}{V} \Delta Q$$

Using ΔQ defined in Eq. (20) and taking into account the elastic effects of the tank, the maximum pressure collapse potential of the stratified system can be expressed as:

$$\Delta p_{max} = \frac{\bar{\phi}(\bar{\rho}\bar{u})V - \sum_{j=1}^{3}(\rho u V)_j}{V - \epsilon \bar{\phi}\bar{\rho}\bar{\theta}} \qquad (23)$$

The pressure dependencies of u, θ, and ϕ are considered and evaluated by solving the above equation through an iterative procedure.

IV. Comparison of Analytical and Flight Data

Numerical solutions to the time dependent model equations were obtained in terms of heater temperature and tank pressure for a wide range of parametric system conditions. Major system and operational parameters considered in the study include heater input power, local acceleration level, and fluid expulsion flow rate. In the following sections, significant results and observations which are critical to the system design evaluation and flight performance predictions are discussed. Comparisons of these results with Apollo 14 flight data are presented.

Peak Heater Temperature

During an expulsion process, the supercritical tank pressure is maintained within a prescribed band by controlling the heater input power through a pressure switch. In the course of a tank pressure cycle and at a given heater input power level, the heater temperature reaches its maximum value either when the tank pressure reaches the maximum pressure switch setting and the heater power is cut off, or when the thermal equilibrium is approached and the heater is saturated. The peak temperature and its variability due to bulk fluid density change is of particular concern to the system designers.

Predicted values of peak heater temperatures plotted as a function of bulk density showing its dependencies on local acceleration level and heater input power are illustrated in Figures 3 and 4, respectively. The dominance of convective heat transfer in the high density region ($\rho > 50$ lb/cu ft) is evidenced by the fact that the heater saturates at relatively low temperatures (approximately -150°F). The average heat transfer coefficient is of the order of 5 Btu/hr-sq ft-R. The peak heater temperature exhibits a weak dependence on gravity. A temperature difference of approximately 20 degrees is observed as the local acceleration level changes by two orders of magnitude.

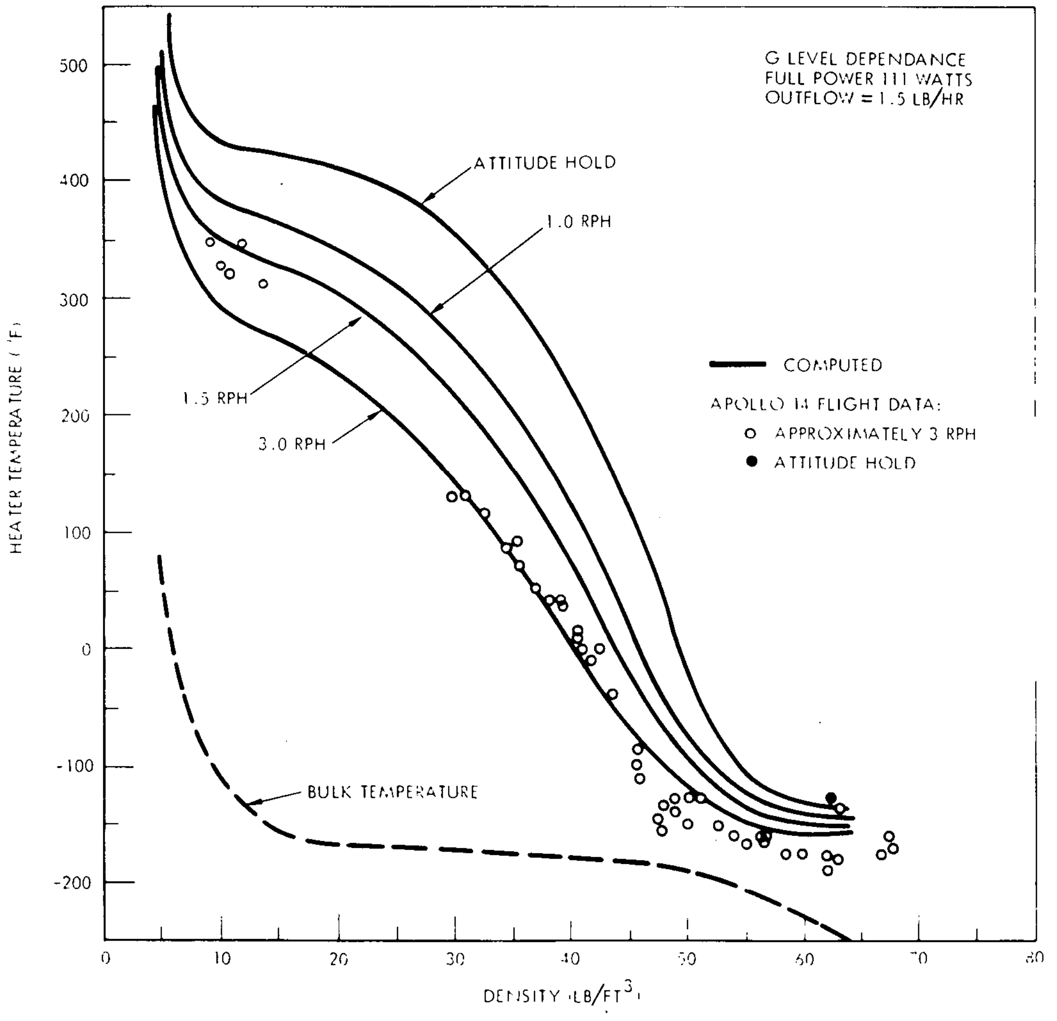

Fig. 3 Peak Heater Temperature Vs. Fluid Bulk Density for Selected Acceleration Levels

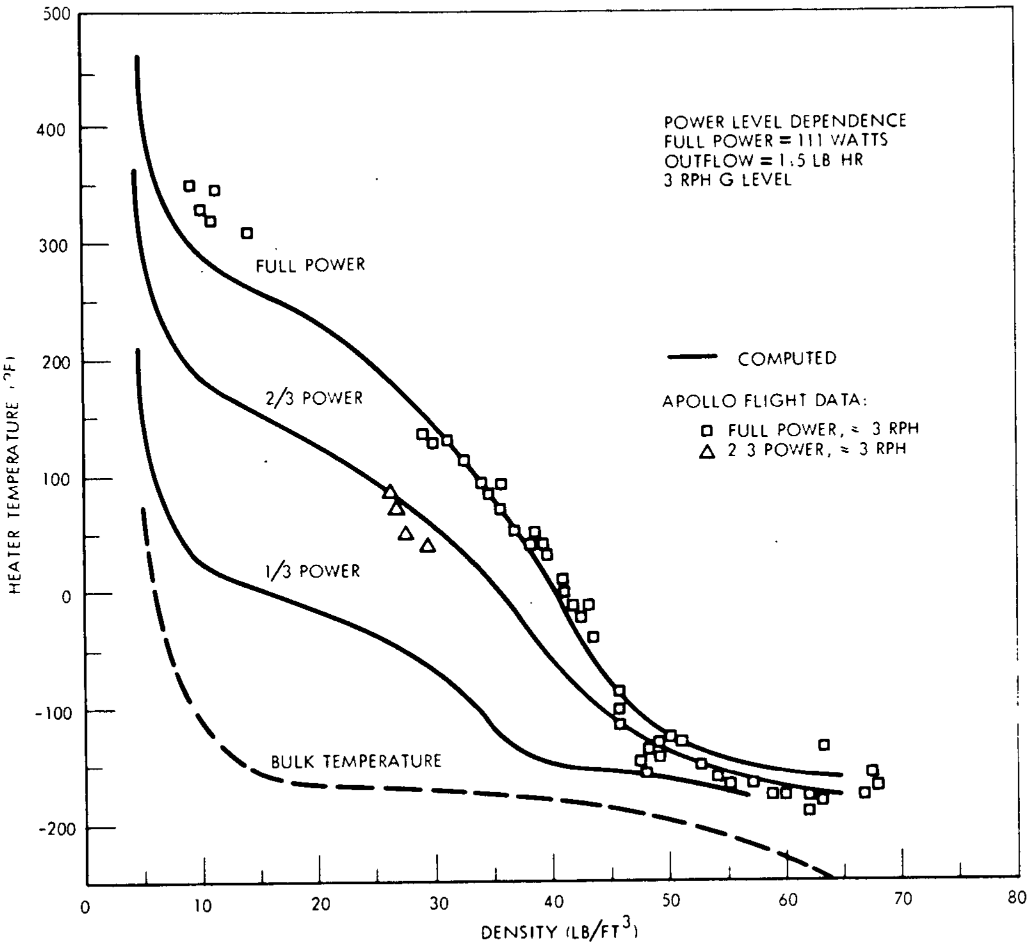

Fig. 4 Peak Heater Temperature Vs. Fluid Bulk Density for Selected Heater Input Power Levels

In the intermediate density range ($10 < \rho < 50$ lb/cu ft), the influence of g-level on the peak heater temperature is pronounced. The temperature shows a wide divergence as the fluid density decreases. For the g-level limits shown in the graph, as much as 200 degrees temperature difference exists over most of the density range.

At densities below 10 lb/cu ft, the peak heater temperatures at the noted g condition begin to converge showing the sharply reduced convective heat transfer rate. The average heat transfer coefficient in this range is approximately 0.5 Btu/hr-sq ft-R. Below a bulk density of 5 lb/cu ft, the heater temperature saturates, as the radiation mode of heat transfer becomes dominant, and shows insignificant g dependencies.

The heater input power has a marked influence on the peak heater temperature when the tank fluid density drops below 45 lb/cu ft as shown in Figure 4. At a constant expulsion rate and g level, the reduction of heater input power has a gradually more pronounced effect on lowering the peak heater temperature as the fluid density decreases. The magnitude of the peak temperature reduction reflects the lower heater temperature response rates at lower input power level while the convective heat transfer rates remain relatively constant. In view of this characteristic behavior, heater power management in the lower density range appears to be an effective means for constraining the peak heater temperature within allowable limits. However, it should be noted that there is a minimum heater power that must be provided to maintain tank pressurization for a given expulsion flow rate.

Heat Transfer Near the Critical Temperature

The comparison of analytical and flight data in the critical region, i.e., pressure greater than the critical pressure and temperature in the region of the critical temperature, affirmed that the convective heat transfer rate differs significantly from that in other thermodynamic regions. This is evidenced by the fact that dramatically lower peak heater temperatures were observed when the bulk fluid density was greater than 48 lb/cu ft. This apparent increase in heat transfer near the critical temperature regime resulting in lower heater temperature is attributed to the abrupt changes in the fluid thermal transport properties (Reference 7). Early studies showed that conventional methods for correlating the convective heat transfer data were unable to account for the effects exhibited by supercritical fluids in this temperature region (References 8 and 9). For supercritical fluids, some investigations have been performed to evaluate the heat transfer in the forced convection regime. However, there is a lack of experimental work related to the free laminar convection region, especially at low Rayleigh numbers. A method which has been applied with reasonable success in correlating heat transfer data in the critical temperature regime involves the use of a well established variable fluid property scheme. Extending this procedure to the present analysis, a variable reference temperature method, similar to that suggested by Eckert (Reference 10) was chosen. In this method, fluid properties are evaluated at a reference temperature, T_{ref}, where $T_{ref} = T_w - \alpha(T_w - T_b)$. The dimensionless parameter, α, is assumed to be a unique function of ρ_b/ρ_{cr}, where ρ_{cr} is the fluid density at the critical temperature. Based upon the Apollo 14 flight data, a criterion relating the dimensionless temperature ratio, $(T_w - T_{ref})/(T_w - T_b)$, to the density ratio, ρ_b/ρ_{cr} was established as shown in Figure 5.

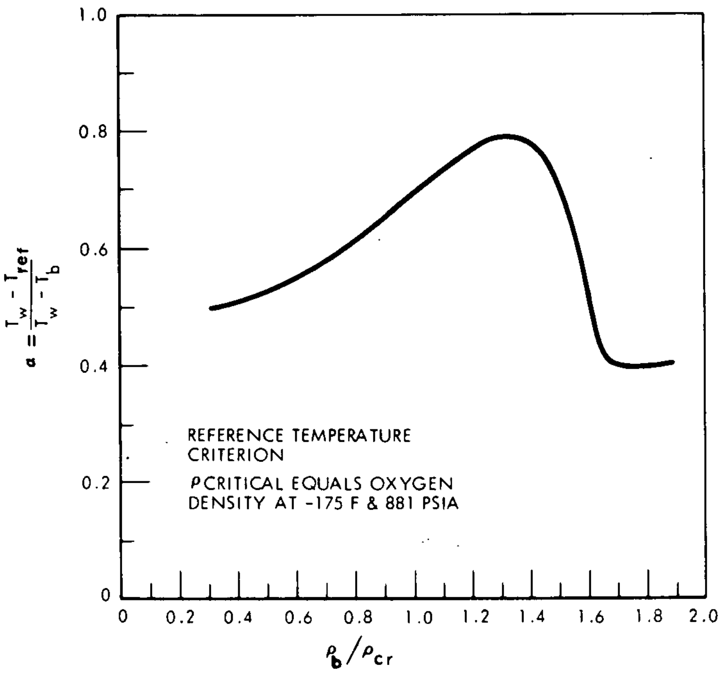

Fig. 5 Dimensionless Temperature Ratio Vs. Critical Density Ratio

Tank Pressure Response

The pressure rise and decay times associated with a heater cycle (pressure cycle period) are affected by the expulsion flow rate at a given heater input power level and fluid density. The pressure cycle frequency as a function of bulk fluid density is shown in Figure 6 for a range of expulsion flow rate conditions. In the high fluid density region, ($\rho > 55$ lb/cu ft), the expulsion flow rate has the greatest influence on the cycle frequency. In this region, the cycle frequency for a given flow rate is nearly constant. As the density is decreased, the cycle frequency is sharply reduced because of the rapid changes of the fluid thermal transport properties and resultant reduction in convective heat transfer rates. In addition, the characteristic variation in the thermodynamic function θ also contributes to the characteristic shift in frequency. It is of interest to note that the pressure cycle frequency becomes less sensitive to flow rate variability at lower fluid densities.

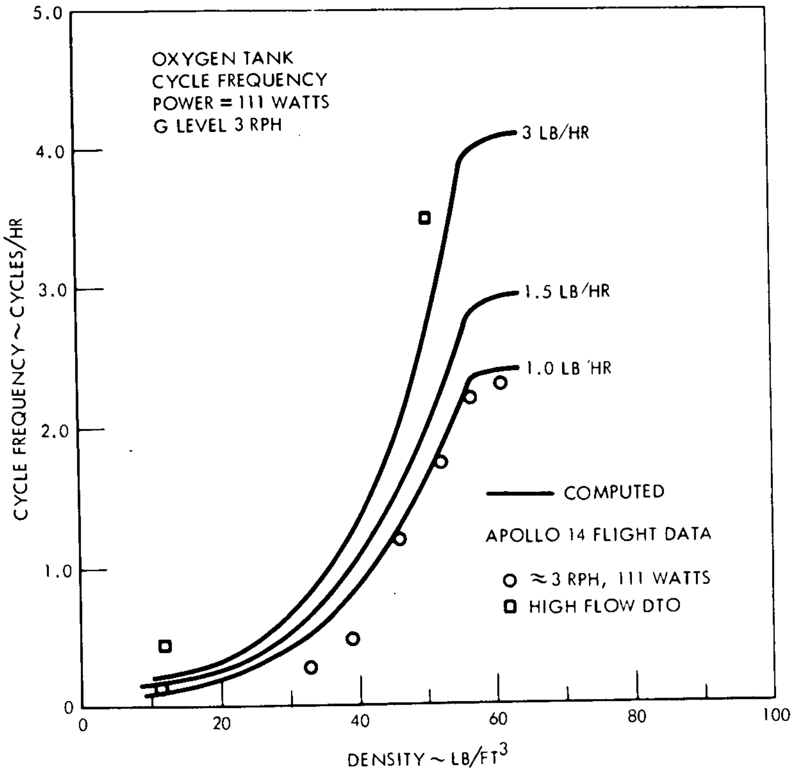

Fig. 6 Tank Pressure Cycle Frequency Vs. Fluid Bulk Density for Selected Expulsion Rates

Flight Data Correlation

Figures 7 and 8 compare the analytical predicted heater temperature and pressure response at two selected bulk fluid density conditions with the Apollo 14 flight data. The flight and analytical values of the peak heater temperature and the pressure rise rate are found to be in good agreement. The model shows a slightly higher initial heater temperature response rate. This is partially due to the quasi-steady state approximation of the heat transfer transients and the inaccuracies associated with the lumped parameter approach used for the model.

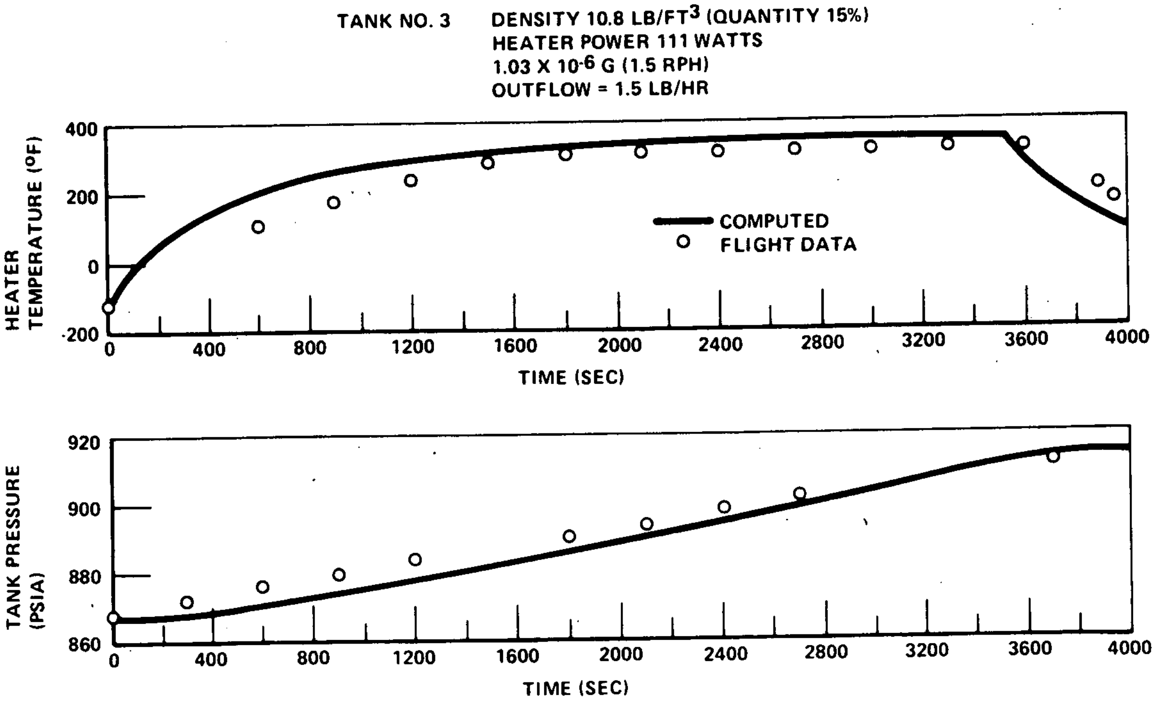

Fig. 7 Heater Temperature and Tank Pressure Vs. Time at O_2 Quantity 15%

Figure 9 compares the model predictions with the flight data for a case at relatively high bulk density conditions and high expulsion flow rate. The system characteristics associated with repeated cycling of the heater are illustrated. The comparison of the temperature and pressure response data showed close agreement for the initial cycles. The slight deviation that appears for the remaining cycles is due to changes in outflow and g-level occurring in flight which are not accounted for in the simulation. It is of interest to note that there is only a small net heater temperature gain (0.5 degrees) after each successive heater cycle.

Figure 10 shows the time characteristic changes in the temperatures of the three hypothetical cells of the model. The accumulative increase in the magnitude of the maximum pressure decay potential reflecting the progressively increased degree of stratification in the system is also illustrated. Among the three cells, the most significant gain in fluid temperature is noted in the internal cell due to the lack of cooling during the heater-off periods. This phenomenon contributes appreciably to the rise of the maximum decay potential. To minimize the problems associated with the potential tank pressure collapse, particularly at high fluid bulk density conditions, a passive means which can facilitate cooling of the internal cell fluids would be highly effective.

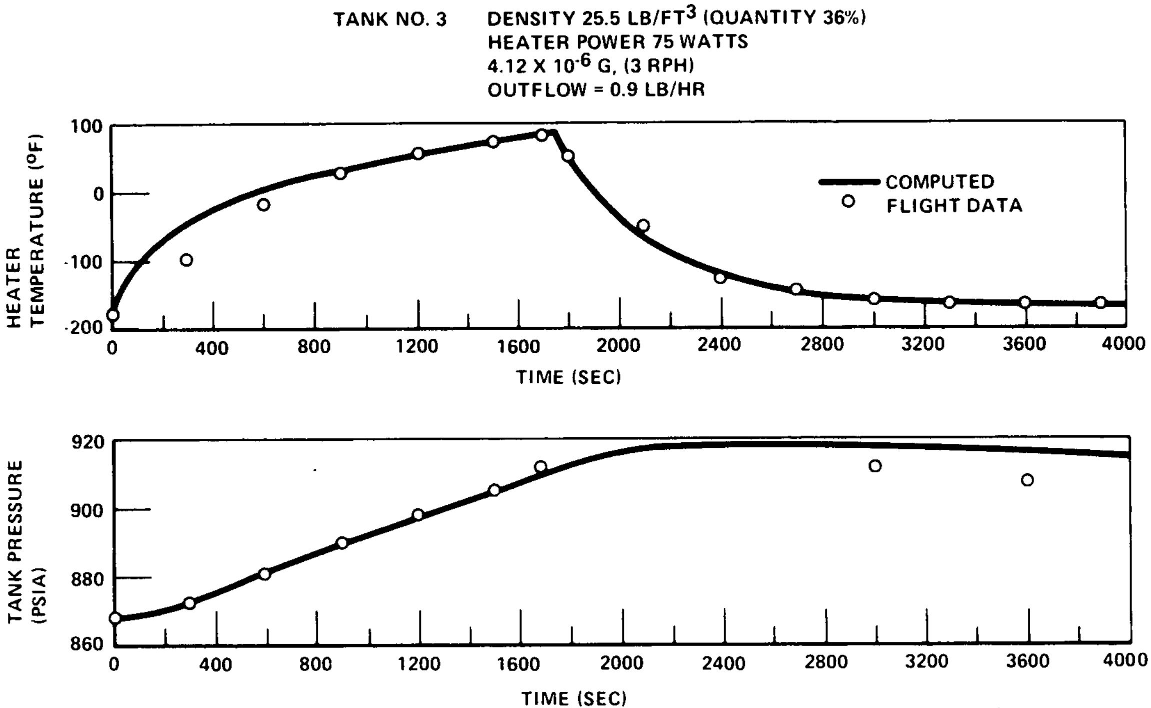

Fig. 8 Heater Temperature and Tank Pressure Vs. Time at O_2 Quantity 36%

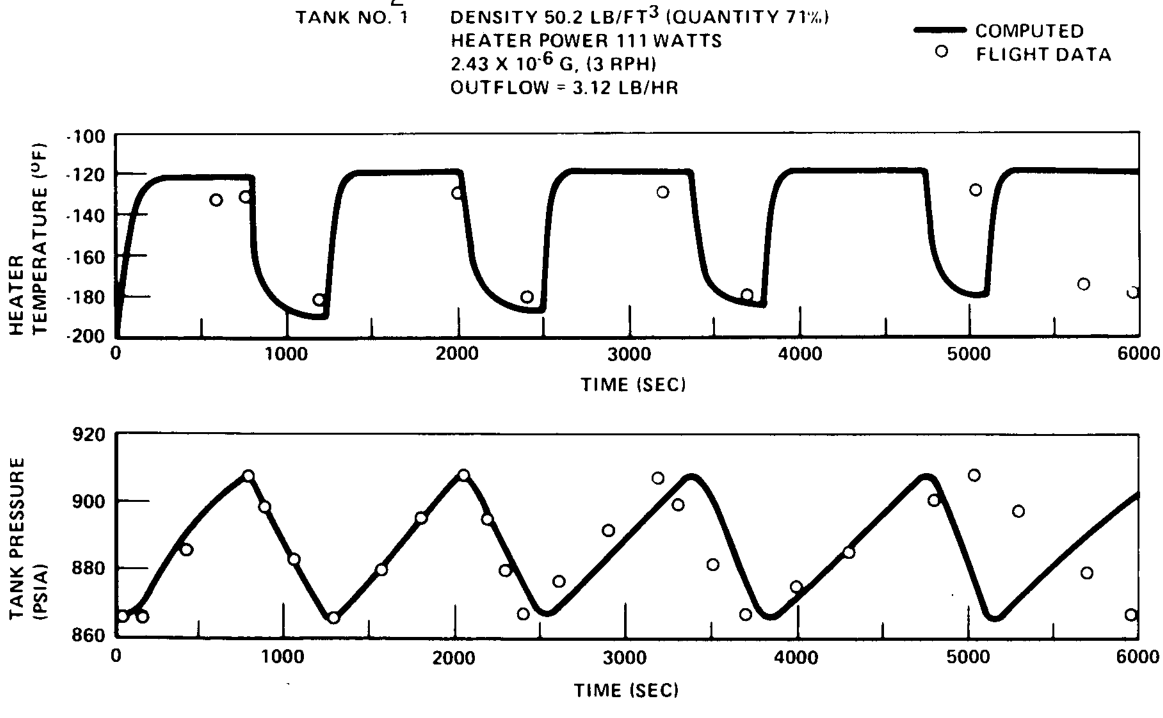

Fig. 9 Heater Temperature and Tank Pressure Vs. Time at O_2 Quantity 71%

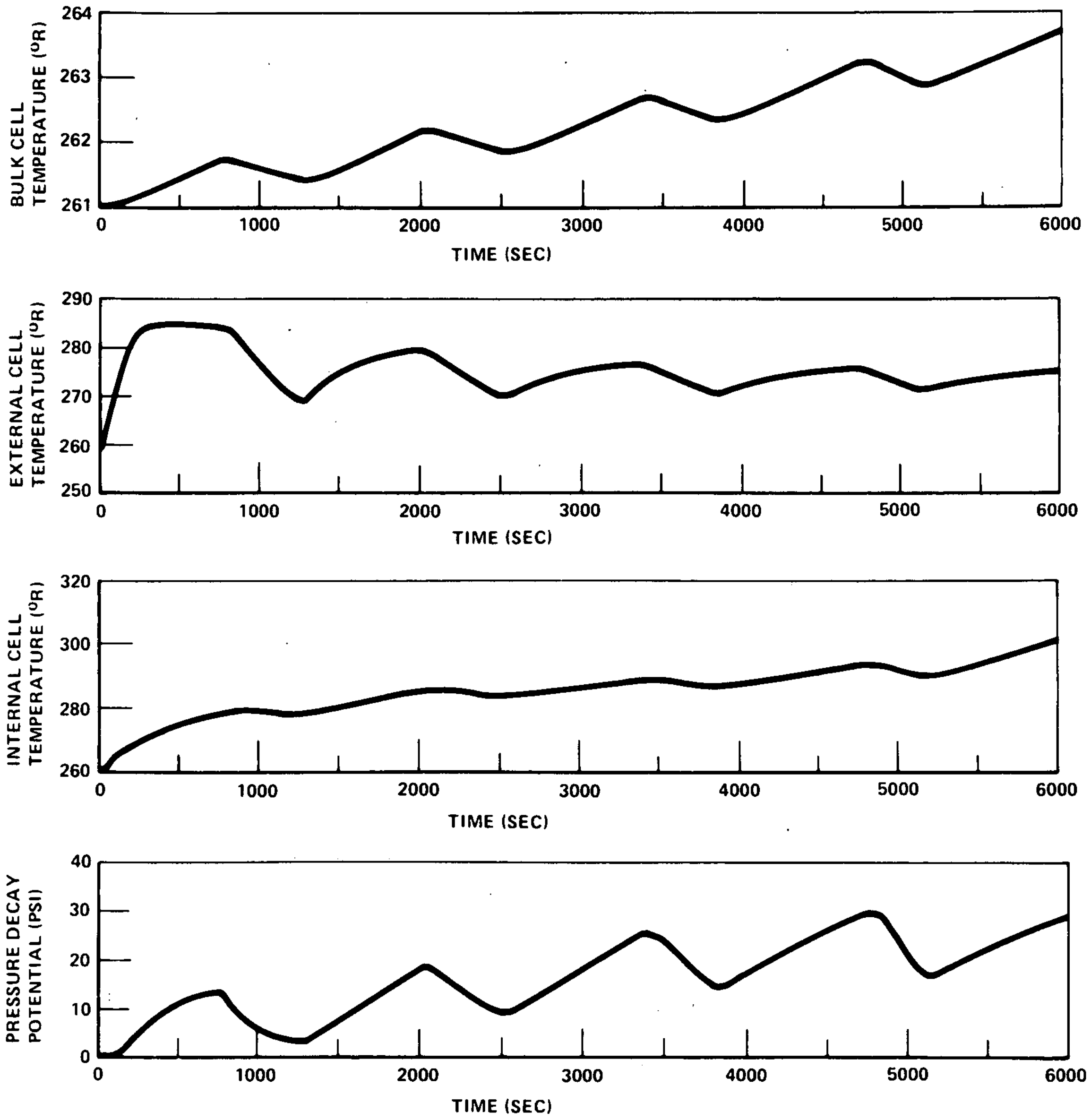

Fig. 10 Fluid Cell Temperature and Pressure Decay Potential Vs. Time at O_2 Quantity 71%

V. Concluding Remarks

Although the Apollo 14 flight data provided a limited number of applicable measurement points pertaining to the CSS, development of the analytical model and correlation of available data have provided insight and understanding of the low-g free convective heat transfer and non-equilibrium behavior of the supercritical cryogenic storage system. On the basis of the analysis of the flight data and parametric evaluation results of the model, the following concluding remarks are presented.

1. When the mean boundary layer temperature is near the critical temperature regime, the heater saturates at relatively low temperatures due to significantly high convective heat transfer associated with large fluid thermal transport property changes. The peak heater temperature shows a noticeable dependence on the magnitude of the heater input power and is influenced to a lesser degree by the acceleration level.

2. When the fluid bulk density drops below 10 lb/cu ft, the convective heat transfer rate is sharply reduced. At a bulk density below 5 lb/cu ft, the radiation mode of heat transfer becomes dominant. The heater temperature then saturates as the radiative heat transfer rate approaches an asymptotic level for a given heater input power.

3. The tank pressure decay potential is significant at high fluid density conditions. When the system is undisturbed, the pressure decay potential becomes progressively higher as a result of rapid successive heater cycles.

4. Satisfactory solutions to the variable fluid property, low-g heat transfer problem, throughout the fluid density range can be obtained through the use of a reference temperature procedure.

5. The semi-empirical approach to the model formulation does yield reasonably accurate predictions of the supercritical cryogenic system behavior and provide data well suited for design applications.

Nomenclature

c_p	Specific heat at constant pressure, Btu/lb-R
d	Diameter of heater, outside, ft
$\mathcal{F}_{w,k}$	Node-to-node interchange factor
g	Acceleration, ft/hr^2
Gr	Grashof Number - $g\beta\Delta Tx^3/\nu^2$
h	Enthalpy, Btu/lb
h_x	Heat transfer coefficient, Btu/hr-sq ft-R
j,k	indices
k	Thermal conductivity, Btu/hr-ft-R
L	Length of equivalent plate, ft
m	Mass, lb
$\dot{m}$	Mass rate, lb/hr
$\dot{m}_o$	Expulsion rate, lb/hr
$\dot{m}_t$	Total mass rate, includes expulsion rate, lb/hr
Nu_x	Nusselt number - $h_x x/k$
p	Pressure, lb/sq ft
Pr	Prandtl number - $c_p\mu/k$
q	Heat flux, Btu/hr-sq ft
Q	Heat, Btu
$\dot{Q}$	Heat rate, Btu/hr
$\dot{Q}_{eb}$	Interfacial heat transfer rate from external to bulk cell, Btu/hr

Nomenclature (Continued)

$\dot{Q}_{hi}$	Heat transfer rate from the heater interior surface to internal cell, Btu/hr
t	Time, hr
T	Temperature, R
T_{ref}	Reference temperature, R
T_w	Wall temperature, R
u	Internal energy, Btu/lb
u	Velocity in the x direction, ft/hr
U	Energy, Btu
v	Velocity in the y direction, ft/hr
V	Volume, cu ft
V_t	Total volume, cu ft
x	Distance in the x direction, ft

<u>Greek</u>

α	Temperature ratio, $(T_w - T_{ref})/(T_w - T_b)$, dimensionless
β	Expansion coefficient, $\frac{1}{\rho}\left(\frac{\partial\rho}{\partial T}\right)_p$, 1/R
Γ	Transfer parameter, $V/\left[\phi(\rho\psi - p)\right]$, ft^5/lb
δ	Boundary layer thickness, ft
ϵ	dV/dt, ft^5/lb
η	Energy rate parameter, Btu/hr
θ	Transfer parameter, $-\rho\left(\frac{\partial h}{\partial \rho}\right)_p$, Btu/lb

Nomenclature (Continued)

Greek (Continued)

ν	Kinematic viscosity, ft^2/hr
ρ	Density, lb/cu ft
ρ_{cr}	Density at critical temperature, lb/cu ft
σ	Stefan-Boltzman constant, Btu/hr-sq $ft\text{-}R^4$
ϕ	Transfer parameter, $1/\rho\ (\partial p/\partial u)_\rho$, dimensionless
ψ	Transfer parameter, $\rho(\partial u/\partial \rho)_p$, Btu/lb
Ω	Transfer parameter, $[\eta + (u + \psi)\ \dot{m}]/\ (\rho\psi - p)$, cu ft/hr

Subscripts

b	Bulk
c	Conduction
e	External
i	Internal
k	Inlet
ℓ	Boundary layer
r	Radiation

References

1. Ostrach, S., "An Analysis of Laminar Free-Convection Flow and Heat Transfer About a Flat Plate Parallel to the Direction of the Generating Body Force," NACA TR 1111, (1953).

2. Sparrow, E. M. and Gregg, J. L., "The Variable Fluid-Property Problem in Free Convection," Trans. ASME, 80, 879, (1958).

3. Eckert, E. R. G., and Drake, R. M., "Heat and Mass Transfer," McGraw-Hill, 2nd Edition, (1959).

4. Martini, W. R. and Churchill, S. W., "Natural Convection Inside a Horizontal Cylinder," A.I.Ch.E. Journal, 6, 251, (1960).

5. Weinbaum, S., "Natural Convection in a Horizontal Circular Cylinder," J. of Fluid Mech., 18, (1964).

6. Shaidvrov, G. F., "Convective Heat Transfer in Horizontal Cylinder," Int. J. Heat Mass Transfer, 2, 280, (1960).

7. Weber, L. A., "Thermodynamic and Related Properties of Oxygen from the Triple Point to 300 K at Pressures to 330 Atmospheres Supplement A (British Units)," NBS Report 9710 A, (August 1968).

8. Hess, H. L. and Kunz, H. R., "A Study of Forced Convection Heat Transfer to Supercritical Hydrogen," Trans ASME, 87, 41, (1965).

9. Hendricks, R. C. and Simoneau, R. J., "Survey of Heat Transfer to Near Critical Fluids," NASA TM X-52612, (June 1969).

10. Deissler, R. G., "Heat Transfer and Fluid Friction for Fully Developed Turbulent Flow of Air and Supercritical Water with Variable Fluid Properties," Trans. ASME, 56, 73, (1954).

N72-23796

THE CRYOGENICS ANALYSIS PROGRAM FOR APOLLO MISSION PLANNING AND ANALYSIS

By Walter Scott
NASA Manned Spacecraft Center, Houston, Texas

and

Jack Williams
Lockheed Electronics Company, Houston, Texas

Abstract

The Cryogenics Analysis Program was developed as a simplified tool for use in premission planning operations for the Apollo command-service module. Through a dynamic development effort, the program has been extended to include real-time and postflight analysis capabilities with nominal and contingency planning features. The technical aspects of the program and a comparison of ground-test and mission data with data generated by using the Cryogenics Analysis Program are presented.

By using the electrical power and environmental control systems requirements, computation of the thermodynamic state variables is provided by the program for each of the cryogenic storage tanks of the spacecraft. These calculations are accomplished by combining computations of the equilibrium state variables with a simplified model of the delivery system, including models for heat leak, environmental control system restrictors, and surge tank, check valves, isolation valves, relief valves, and heater/fan pressure-switch logic. Modifications that will permit heater-element temperature computations and will allow for check-valve failures are being incorporated.

The results of the Cryogenics Analysis Program capability to predict flight requirements also are presented. Comparisons of data from the program with data from flight results, from a tank-qualification program, and from various system anomalies that have been encountered are discussed.

Future plans and additional considerations for the program also are included. Among these plans are a three-tank management scheme for hydrogen, venting-profile generation for Skylab, and a capability for

handling two-gas atmospheres. The plan for two-gas atmospheres will involve the addition of the capability to handle nitrogen as well as oxygen and hydrogen.

Introduction

The Cryogenics Analysis Program (CAP) was designed to provide a flexible mission-planning tool in which a fast execution time could be achieved without undue loss of computational accuracy. The CAP can be used for the analysis of the cryogenic oxygen and cryogenic hydrogen systems in any of the configurations proposed for the Apollo command-service module (CSM) by selecting the number of oxygen (O_2) tanks and hydrogen (H_2) tanks in any combination up to a maximum of three each. For systems analyses, tank conditions are computed as a function of time, systems parameters, and environmental control system (ECS) and electrical power system (EPS) flow-rate requirements. In addition to systems analyses, various parametric studies can be performed for individual cryogen tanks operating at specified tank pressures.

The general program philosophy is described in this report, and pertinent mathematical expressions are given. No program is complete until a thorough checkout has been performed. Fortunately, test data were available that provided good information for program verification before the Apollo 14 mission. Postflight data provided a second check on the program.

A dynamic program such as the CAP will undergo continual changes as spacecraft hardware changes are made. These changes and future plans for the program are discussed in the final section of this report.

Program Description

The current CAP is based on the Apollo 14 configuration. A schematic diagram of the system model, which incorporates all system components included in the CAP, is shown in figure 1. A simplified flow diagram of the program logic is presented in figure 2.

Flow Sharing

The CAP uses a simplified flow-sharing model in which pressure drops in the lines, except for the ECS restrictors, are considered to be negligible. The effect of the ECS surge tank on the system flow rate may be either considered or ignored.

Environmental Control System Flow Rate

The pressure drop (in psi) across the ECS restrictors is represented by the cubic equation

$$\Delta P = 51.475\left(\dot{M}_r\right) - 9.911\left(\dot{M}_r\right)^2 + 12.40\left(\dot{M}_r\right)^3 \qquad (1)$$

where

$\dot{M}_r = (3.833/\dot{M}_c)\dot{M}_{ECS}$, lb/hr
$\dot{M}_c$ = flow rate for a 750-psi pressure drop, lb/hr
$\dot{M}_{ECS}$ = actual flow rate, lb/hr

If the surge-tank isolation valve is closed, the equations for the two restrictors are solved simultaneously for flow rates so that (1) the sum of the restrictor flow rates is the demanded ECS flow rate, and (2) the restrictor pressure drops lead to the same value for pressure at the downstream junction of the restrictors.

If the surge tank isolation valve is open, the pressure drop across each restrictor is computed by subtracting the surge-tank pressure from the storage-tank pressure. Equation (1) is used to compute the required ECS flow rate for each restrictor. If the total restrictor flow is less than the demanded ECS rate, the oxygen flow from the surge tank is used to make up the difference. If the combined restrictor flow exceeds the ECS usage rate, the excess flow is stored in the surge tank. Thus, the surge tank operates as a buffer for smoothing the ECS flow demands placed on the supply system.

Surge-Tank Model

The surge tank is treated as a pressure vessel in which the pressure, temperature, and density are related by the ideal-gas equation. For constant temperature, the pressure in the surge tank P_s is given by

$$P_s = \frac{900M_s}{M_n} \qquad (2)$$

where M_s is the surge tank oxygen mass and M_n is the mass in the surge tank when $P_s = 900$ psi.

Equal-Pressure-Rate Equations

The pressure-change rate is given by the equation

$$\dot{P}_i = A_i\dot{M}_i + B_i\dot{Q}_i \tag{3}$$

where

$\dot{P}_i$ = pressure change rate for the ith tank
$\dot{M}_i$ = mass flow rate for the ith tank
$\dot{Q}_i$ = heat input rate for the ith tank
A_i = density-dependent parameter $\phi\theta/V$ for the ith tank
B_i = density-dependent parameter ϕ/V for the ith tank
ϕ, θ = density-dependent parameters
V = volume

If program logic dictates that the total flow rate M_T must be provided from only one tank, the flow-rate division will be

$$\dot{M}_i = \dot{M}_T = \dot{M}_{EPS} + \dot{M}_{ECS} \tag{4}$$

and

$$\dot{M}_j = \dot{M}_k = 0 \tag{5}$$

where i, j, and k separately assume the values 1, 2, and 3. If tanks i and j are to share the flow (that is, a two-tank operation), the equations become

$$\dot{M}_i = \frac{A_j\dot{M}_T + B_j\dot{Q}_j - B_i\dot{Q}_i}{A_i + A_j} \tag{6}$$

$$\dot{M}_j = \dot{M}_T - \dot{M}_i \tag{7}$$

$$\dot{M}_k = 0 \tag{8}$$

When all three tanks participate, the equations become

$$\dot{M}_i = \frac{A_j A_k \dot{M}_T + A_j\left(B_k \dot{Q}_k - B_i \dot{Q}_i\right) + A_k\left(B_j \dot{Q}_j - B_i \dot{Q}_i\right)}{A_i + A_j + A_k} \tag{9}$$

where $\dot{M}_j$ and $\dot{M}_k$ are given by perturbations of the indices or by using the basic equation (3) to compute the pressure rate for tank i. Then, with this pressure rate for tank i, the flow rates for tanks j and k are computed. In any case,

$$\dot{M}_i + \dot{M}_j + \dot{M}_k = \dot{M}_T \tag{10}$$

for the three-tank flow-sharing situation.

Combined Flow-Sharing Logic

The EPS flow-rate demand is computed from the electrical load imposed on the fuel cells. The ECS usage rates are input data. When the surge tank is isolated from the system, the ECS flow-rate demand is the same as the usage rate. When the surge tank is not isolated, the ECS demand placed on the storage tanks is computed as described previously. Then, the system pressures are tested against check-valve pressure dead bands to determine which check valves are permitting flow. When the number of tanks supplying flow has been determined, the total flow rate (EPS demand plus ECS demand) is used in the equal-pressure change-rate flow-sharing equations to compute the anticipated flow rates from each tank. Next, the ECS flow rate required by each restrictor is computed. If the anticipated tank flow rates can meet the ECS demand, these flow rates become the flow rates for the individual tanks. However, the ECS flows must be provided through the restrictors so that pressure considerations are satisfied. If the anticipated flow rates are insufficient to supply the required restrictor flows, the restrictor-flow requirements are met, and the minimum possible adjustment in the anticipated flow from each tank is made. For example, a certain case may call for a 1.5-lb/hr EPS flow rate and a 6.5-lb/hr ECS flow rate or a total flow rate of 8.0 lb/hr. The flow-sharing computations are performed (with the total flow provided from tanks 1 and 3), and anticipated flows of 3.0 lb/hr from tank 1 and 5.0 lb/hr from tank 3 are obtained. The restrictor calculations dictate that the ECS flow must be shared equally by the two tanks; that is, each tank must supply 3.25 lb/hr to the ECS system. The anticipated flow for tank 3 will meet this requirement, but the anticipated flow for tank 1 is insufficient. Thus, the minimum adjustment is made by increasing the flow from tank 1 by 0.25 lb/hr and decreasing the flow from tank 3 by the same amount. Thus, tank 1 will supply 3.25 lb/hr to the ECS system, and the EPS system will receive none. Tank 3 will supply 3.25 lb/hr to the ECS system and the total requirement of 1.5 lb/hr to the EPS system. Instead of having equal pressure rates, the tank 3 pressure will increase relative to the tank 1 pressure. If a 2.9-lb/hr flow was required by restrictor 1 and if a 3.6-lb/hr flow was required by restrictor 2, the anticipated flow rates would be sufficient; each tank would supply the flow to the EPS and the ECS; and the tank pressures would rise or fall together.

Relief-Valve Model

The characteristics of the oxygen and hydrogen overpressure (or vent valves), relief valves supplied by the Propulsion and Power Division of the Manned Spacecraft Center (MSC), are shown in figure 3. Each valve has two distinct modes of operation. The particular parametric values assigned to the various transition points are shown in table I for both the oxygen and the hydrogen valves.

Establishing a model of this relief valve requires a combination of equation (3), which sets forth the pressure rate in terms of flow rate, and the relationships of pressure to flow rate shown in figure 3. The vent-flow rate $\dot{M}_V$ is expressed mathematically by

$$\dot{M}_V = S\left(P - P_R\right) + \dot{M}_R \tag{11}$$

where P is the operating pressure, P_R is the reference pressure, and S is a slope computed according to the particular region of the characteristic curve and depending on whether the pressure is increasing or decreasing. One of the pressures defined by points B, C, D, or E will be P_R; $\dot{M}_R$ is the flow rate corresponding to P_R. This procedure dictates that the pressure increase or decrease will always be directed toward one of the points B, C, D, or E. To make the pressure and average-mass-flow computations independent of step size, an integration of the pressure-rate equation was performed by considering the vent characteristics, and the resulting equations (12) and (13) were programed.

$$P(t) = P(t_o) + \dot{P}(t_o)(AS)^{-1}[\exp(AS\ \Delta t) - 1] \tag{12}$$

$$\Delta M = \dot{M}_T(t_o)\Delta t + \dot{P}(t_o)A^{-2}S^{-1}[\exp(AS\ \Delta t) - AS\ \Delta t - 1] \tag{13}$$

where

t_o = time at beginning of time step
t = time at end of time step
$\Delta t = t - t_o$
$P(t)$ = pressure at time t
$P(t_o)$ = pressure at time t_o
$\dot{P}(t_o)$ = pressure rate at time t_o
A = density-dependent parameter $\phi\theta/V$
S = slope of relief valve characteristic
ΔM = total mass lost during time step
$\dot{M}_T(t_o)$ = total flow rate $(\dot{M}_{ECS} + \dot{M}_{EPS} + \dot{M}_V)$ at time t_o

The vent flow rate is used to compute a vent thrust using

$$\text{thrust} = \dot{M}_V\sqrt{\frac{RT_e}{Mg}}\,\frac{(\gamma + 1)}{\sqrt{\gamma}} \tag{14}$$

where

$\dot{M}_V$ = vent flow rate
R = gas constant
T_e = temperature at the exit nozzle
M = molecular weight
g = gravitational acceleration
γ = specific-heat ratio

This equation was derived assuming sonic flow at the exit nozzle.

Heat Leak

Heat-leak calculations are based on the following assumptions.

1. The heat leak into the tank is given by the product of a tank thermal conductivity C_T and the temperature difference between the external temperature T_a and the internal temperature T_T.

2. The C_T is assumed to be constant with temperature.

3. The vapor-cooled-shield effect produces a linear reduction in C_T up to some maximum flow rate.

Standard heat-leak information is built into the program. These data consist of heat-leak values corresponding to minimum and maximum flow rates for a tank temperature TT_R and an ambient temperature TA_R. The reference values may be adjusted for a particular mission by supplying the experimental heat leak $\dot{Q}_{in}$ at minimum dQ/dM tank conditions.

The necessary steps for heat-leak computation are outlined as follows:

1. Compute the flow rate at which the observed heat leak was measured.

2. Compute the reference heat leak corresponding to the computed flow rate, the minimum dQ/dM tank conditions, and the environmental temperature TA_{in}.

3. Take the ratio of $\dot{Q}_{in}$ to the heat leak computed in step 2.

4. Update the value of the tank thermal conductivity by using the ratio in step 3.

The heat leak can be computed by using the updated thermal conductivity and the mission values of tank temperature, environmental temperature, and flow rate.

A detailed discussion of the particular equations involved is considered to be too cumbersome for this discussion. The formal program documentation, scheduled for publication in August 1971, will provide a complete discussion of these equations.

Equations of State

Oxygen

The equation of state used in the CAP is based on R. B. Stewart's dissertation of 1966 (ref. 1). The equation of state and its first-order partials, defined in reference 1, have been coded and have been used in the CAP. Later work by Weber (ref. 2) also was programed, and the results were compared with Stewart's results. The two methods compared very closely for the regions and parameters of interest in the present program. However, Stewart's equation of state is more readily adaptable to computer application at a very slight sacrifice in accuracy.

Hydrogen

At present, no equation of state for hydrogen is used in the CAP. The current basis for the computation of the hydrogen thermodynamic properties is the National Bureau of Standards (NBS) program described in reference 3. The subprogram achieves high speed and a good degree of accuracy by using linear interpolation in a grid of selected data points that define the surface of the returned property. The data used in the program were recorded from laboratory tests performed at the NBS in Boulder, Colorado. The property routines generated by using these data were inserted into the predecessors of the CAP and have been retained during the program development.

Computation of the Program Time Interval

The variable time step used for the program is governed by events that lead to a reconfiguration of the instantaneous cryogen system or by maximum changes that are specified for certain parameters considered by the program. Current calculations limit the time interval to the minimum value of the times required to reach the following events.

1. Hydrogen fan cycling
2. Violation of a pressure-switch limit
3. Violation of the vent-pressure limit
4. Fuel-cell purging
5. Intersection of pressures of two or more tanks
6. Surge-tank pressure-change limit

7. Time for the program-summary print

8. System redefinition (restart or new flow requirement)

The largest time step allowed is 0.5 hour; the smallest time step is 0.03 hour.

Updating the Cryogen States

The cryogen state for each tank is updated at the end of each time interval by computing new masses and new pressures according to system operating parameters. The equations of state are used to compute new temperatures. The mass lost from a tank is computed as the product of the tank flow rate and the current time interval. By using the constant tank volume, the density is updated. A new pressure for each tank is computed by using equation (3) with computed flow rates and heat-input rates that are the sums of the heat-leak rate and the heater/fan heat-input rates. Once these values of density and pressure are available, the equations of state are solved to determine the tank temperatures.

Heater-Element Temperature Computations

Heater-element temperature computations are performed by combining parametric data provided by the MSC Structures and Mechanics Division with heater data computed with the CAP. The parametric data consist of node temperature compared with time for various heater-on/heater-off time intervals. Parameters include tank quantities, local g level, and the heat rate supplied by the heaters. The heater on/off times are supplied by the CAP, and an efficient interpolation scheme is used to generate the nodal temperatures for selected nodes.

Analysis is in progress that will permit the previously described parametric data to be used in refined heater calculations that account for heat stored by and released by the heater elements during the appropriate phases of the heater cycles.

Program Checkout

The first exercise performed with the previously described program was that of defining an oxygen-tank-management scheme. Figure 4 shows a simplified schematic of the Apollo 14 oxygen delivery system. The first attempt to manage the system was to use all three tanks during the high-flow periods. It was here that the program first proved to be of value. Results of each computer run indicated a pressure collapse in oxygen tank 1 (fig. 5). First impressions were that an error existed in the program; however, during further analysis, the program was shown to be correct. The spacecraft heater (pressure-switch) logic specifies that the pressure valve of oxygen tanks 1 and 2 must be below approximately 865 psia before the heaters will come on. Oxygen tank 3 operates independently. While tanks 2 and 3 were feeding one restrictor, the tank 2 pressure decay was only one-half as fast as that in tank 1. The heater logic also implies that only one tank (either tank 1 or 2) must be at the cut-off pressure of approximately 925 psia. Thus, with the large pressure drop in tank 1 and only one-half as much pressure drop in tank 2, it is apparent that the tank 1 pressure can never recover in the heater cycle. In fact, the pressure drops lower with each cycle. The solution is to use only oxygen tanks 1 and 2 for the high-flow period and to inhibit the heater in tank 3. This problem was later confirmed by independent investigations.

Manufacturer's Test Study

The next task was to verify the program by attempting to simulate the laboratory tests performed by the tank manufacturer. Set test data and system performance for each tank were provided by the manufacturer. Input parameters such as ambient temperature, flow rates, and tank-management (heater-switching) times were input to the CAP. Tank pressures, temperatures, and quantities were calculated in the program and compared with the test data of the manufacturer. The quantity profiles are shown in figure 6. Note that the correlation is excellent.

The tank management scheme shown in table II was specified in the test procedures. However, analysis of the test data indicated that the actual management scheme was that shown in table III. At two discrete test points (noted in table III with a single asterisk), a quantity balance appeared to have been attempted between oxygen tanks 1 and 2. The test procedure specified an ECS flow of 3.35 lb/hr from 40:55 to 46:36 g.e.t. This specification was determined to be a procedural error because a pressure collapse occurred in tank 1. The CAP simulated this effect. This anomaly, while undesirable in the test, did confirm the CAP prediction that a pressure collapse would happen under similar conditions.

In addition, heater control, as described by the Apollo 14 flight plan, was specified in the test procedures. This specification was based on a heat-leak characteristic similar to that found in the service module (that is, a bay temperature of approximately 70° F). The test by the manufacturer was run at an ambient temperature of 140° F. Because the heater switching is a function of quantity levels and mission time, it became apparent that the increased heat leak, caused by the high ambient temperatures, would force earlier switching times. Again, an accurate calculation of the increased heat-leak function was obtained with the CAP. The results of this detailed comparison study gave a much higher degree of confidence in the overall program and in the capability of the program to support the Apollo 14 mission.

Apollo 14 Premission Analysis

Once the program had simulated the manufacturer's test satisfactorily, production of several profiles for support of the Apollo 14 flight was required. Simulator data for crewmember training, spacecraft consumables analysis, and crew charts for monitoring onboard systems are among the most important support profiles. The crew chart for hydrogen, which was the constraining gas for this mission, is shown in figure 7. Shown on the chart, also, is the hydrogen redline, which is the minimum return quantity based on a tank failure at the critical point in the flight. Critical point is defined as the point at which no return to the primary landing area can be accomplished before the planned nominal time. This point usually is determined by the limitations of the main propulsion system. However, because the Apollo 14 spacecraft was to begin the return to earth as soon as possible after the docking of the lunar module (LM) and the CSM, the critical point occurred during the second lunar surface extravehicular activity. The oxygen crew chart is shown in figure 8. The desired management scheme is reflected by the chart, and the tank-failure capability is retained. For the first time, a cryogen tank for a manned space flight was off-loaded before lift-off. This was required for the demonstration of low-density tank performance, because the Skylab Program will require depleting the tanks.

During the Apollo 14 premission analysis, parametric studies, including the important tank-blowdown analysis, were conducted. The blowdown analysis was performed to verify the capability of the tank 3 enhancement mode. A failure similar to the failure that occurred during the Apollo 13 flight (but without the LM) was assumed for this mode. With the isolation valve closed, no heaters operating in tank 3, and a heat leak approaching zero, proof was required that sufficient oxygen remained to provide ECS oxygen for a return from lunar orbit. Basically, when the heat leak is zero, the cryogen tanks function as high-pressure gas-storage bottles. The tanks will store, without loss, an oxygen quantity at 900 psia that is a function of the ambient temperature. This capability is shown in figure 9. Later tests performed at MSC verified a no-heater blowdown mode capability from a 20-percent quantity level. These tests demonstrated a flow rate equal to (1) an emergency return of a 40-ampere load on the fuel cell plus the ECS requirements and (2) an ECS pressure decay flow.

Flight Support

During the Apollo 14 flight, several profile updates were scheduled to adjust for lift-off values; later, profile updates were to be performed to adjust for heat-leak and pressure-switch shifts. However, early in the flight, it became apparent that a check valve on oxygen tank 2 was not functioning. An analysis was required to determine the effect the failure would have during the rest of the mission. Figure 10 shows the predicted profile based on this failure. The total use, a function of system demands, was not affected, but flow sharing between the tanks was changed. This difference can be observed by comparing the oxygen crew chart to figure 10. The check valve failure significantly impaired the capability to recalculate the heat-leak function; consequently, no further quantity predictions were made.

However, another problem occurred. For Apollo 14 prelaunch and flight operations, the redline on the oxygen tank heater element was set at 200° F. Preliminary analysis had indicated that the peak temperature on oxygen tank 3 (the lowest in density) would exceed the redline only slightly. However, it became obvious that the knowledge of stratification and low-g effects caused by passive thermal control was limited, because the redline was violated before the spacecraft entered lunar orbit. After a new set of thermal tapes had been provided, the heater-on times were recalculated. By processing the thermal tapes, computation of new heater-element temperature limits was possible. This analysis was more realistic than the prelaunch predictions and became the guideline for the balance of the mission.

From the preliminary postflight mission analysis, it is apparent that the predictions made for the Apollo 14 mission were extremely accurate. The results of the preliminary postflight analysis are shown in table IV. Although flow sharing between the tanks deviated slightly from the premission prediction, good correlation existed with the inflight revision. The depletion profile for the Apollo 14 oxygen tank 3 is shown in figure 11. The effect for tanks 1 and 2 is similar to that of tank 3.

Future Plans

Inasmuch as changes are made to the spacecraft, the cryogenic gas storage system, and the delivery system, the CAP must be considered to be changing dynamically as well. Because the program is modular in concept, modification is relatively easy. It has been pointed out previously that any desired tank configuration can be defined, but plumbing changes must be implemented.

In addition to the spacecraft hardware changes, the following items are under investigation.

1. An improvement in the oxygen equation of state

2. Development of an equation of state for hydrogen

3. Addition of the thermodynamic properties of nitrogen for future evaluation of a two-gas atmosphere

The CAP, while certainly not designed for the space shuttle, will provide the basic thermodynamic properties required for the analytical requirements of the shuttle program.

References

1. Stewart, R. B.: The Thermodynamic Properties of Oxygen. Ph. D. Dissertation, Univ. of Iowa, 1966.

2. Weber, L. A.: P-V-T, Thermodynamic and Related Properties of Oxygen from Triple Point to 300 K at Pressures to 33 MN/m^2. J. Res. NBS, vol. 74A, no. 1, Jan.-Feb. 1970, pp. 93-129.

3. Hall, W. J.; McCarty, R. D.; and Roder, H. M.: Computer Programs for Thermodynamic and Transport Properties of Hydrogen. Nat'l. Bureau of Standards Tech. Rept. 9288, Aug. 1967.

TABLE I.- CHARACTERISTIC VALUES FOR THE PRESSURE-RELIEF VALVE

(a) Pressure values

Point	Oxygen pressure, psi	Hydrogen pressure, psi
E	965.0	268.0
D	974.0	270.5
A	983.0	273.0
B	989.8	282.8
C	1010.0	283.0

(b) Flow-rate values

Cryogen	Flow rate, point B, lb/hr	Flow rate, point C, lb/hr
Oxygen	3.0	26.0
Hydrogen	.69	6.0

TABLE II.- HEATER CONTROL ACCORDING TO TEST PROCEDURES

g.e.t., hr:min	Heater control		
	Tank 1	Tank 2	Tank 3
00:00	Automatic	Automatic	Off
11:10	Off	Off	Automatic
59:30	Automatic	Automatic	Off
65:10	Off	Off	Automatic
81:20	Automatic	Automatic	Off
162:10	Automatic	Off	Off
*168:10	Automatic	Off	Automatic
171:40	Off	Off	Automatic
**200:12	Automatic	Automatic	Off
216:12	Off	Off	Off

*Isolation valve to be closed from 168:10 to 171:40 g.e.t.

**This switchover is to occur when tank 3 quantity is 6 percent or less.

TABLE III.- HEATER CONTROL ACCORDING TO TEST DATA

g.e.t., hr:min	Heater control		
	Tank 1	Tank 2	Tank 3
00:00	Automatic	Automatic	Off
11:10	Off	Off	Automatic
59:10	Automatic	Automatic	Off
65:10	Off	Off	Automatic
81:20	Automatic	Automatic	Off
*115:30	Off	Automatic	Off
**133:00	Automatic	Off	Automatic
136:30	Off	Off	Automatic
*149:30	Off	Automatic	Off
181:30	Automatic	Automatic	Off
216:12	Off	Off	Off

*Started tank 1 and 2 quantity balance.

**Isolation valve closed at 133:00 and opened at 136:30 g.e.t.

TABLE IV.- PRELIMINARY POSTMISSION ANALYSIS OF HYDROGEN AND OXYGEN

Cryogen	Premission prediction, lb	Actual remaining, lb
Oxygen	[a]433.1 (1.2)	438.1
Hydrogen	[a]14.8 (3.0)	15.25

[a]Percent deviation, $\frac{P - A}{P}$.

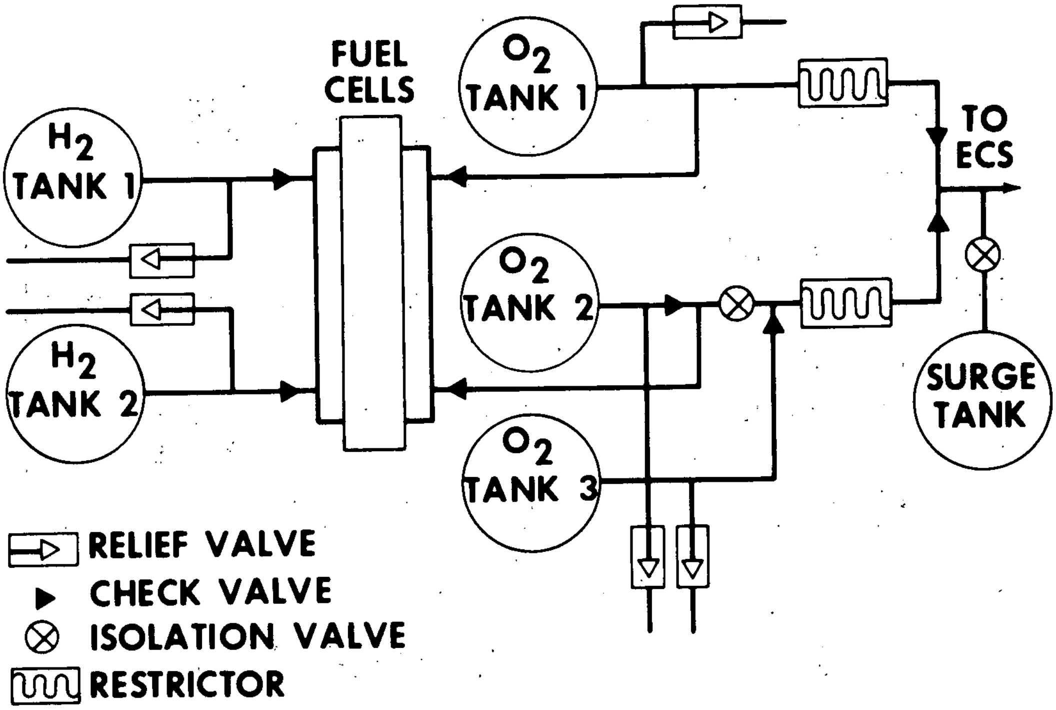

Figure 1.- Apollo 14 storage and delivery system.

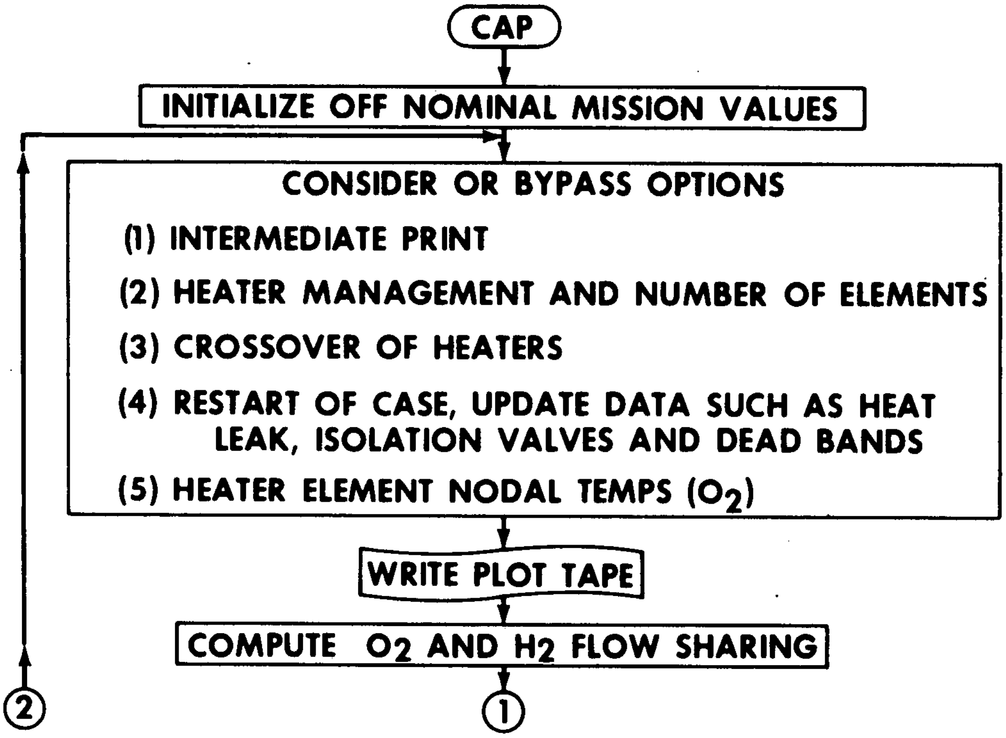

Figure 2.- Simplified flow diagram of the CAP logic.

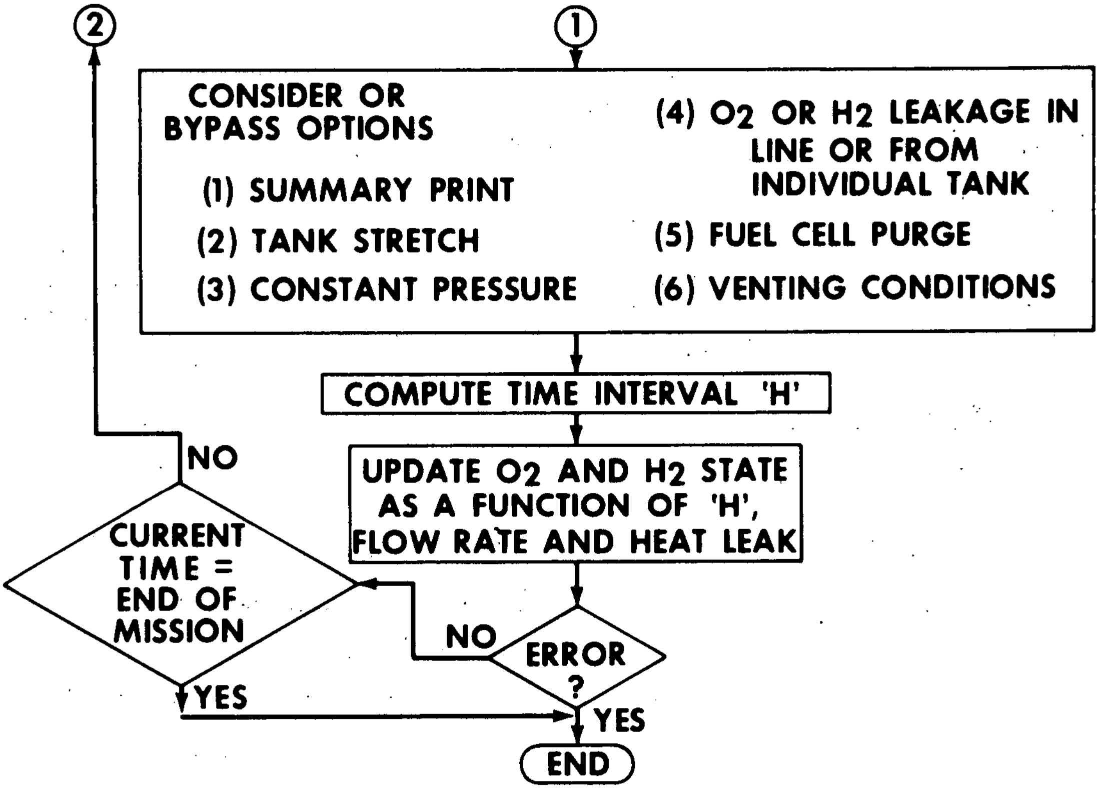

Figure 2.- Concluded.

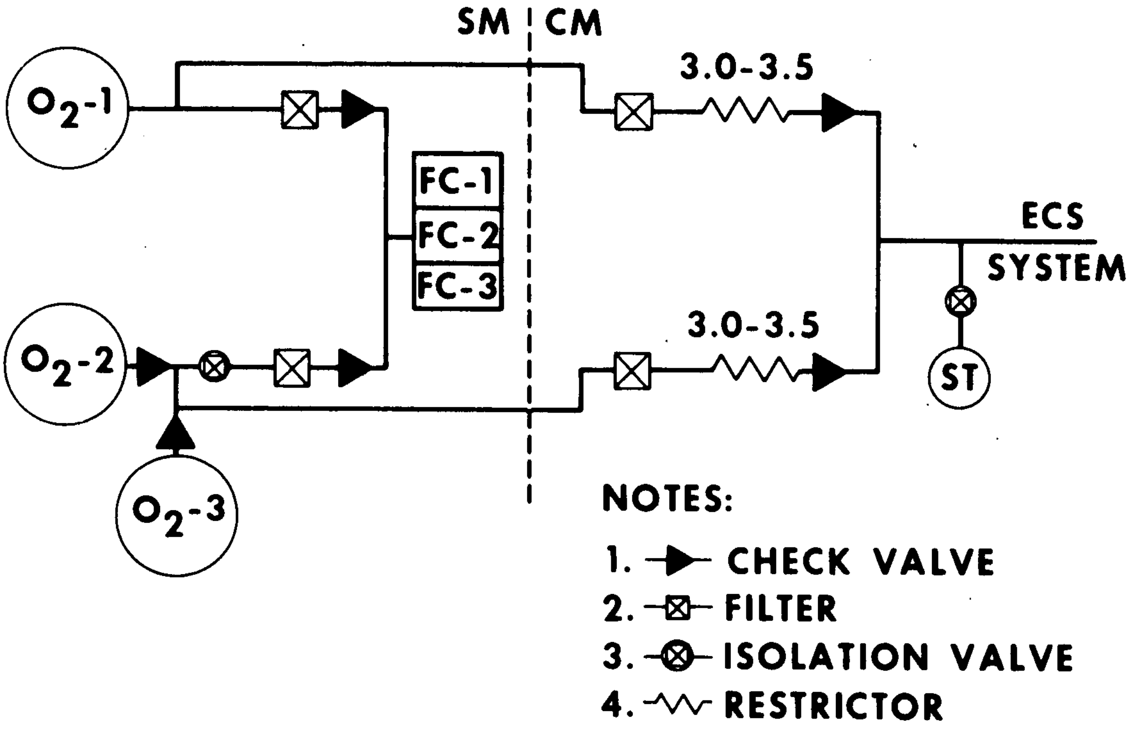

Figure 3.- Simplified oxygen delivery system.

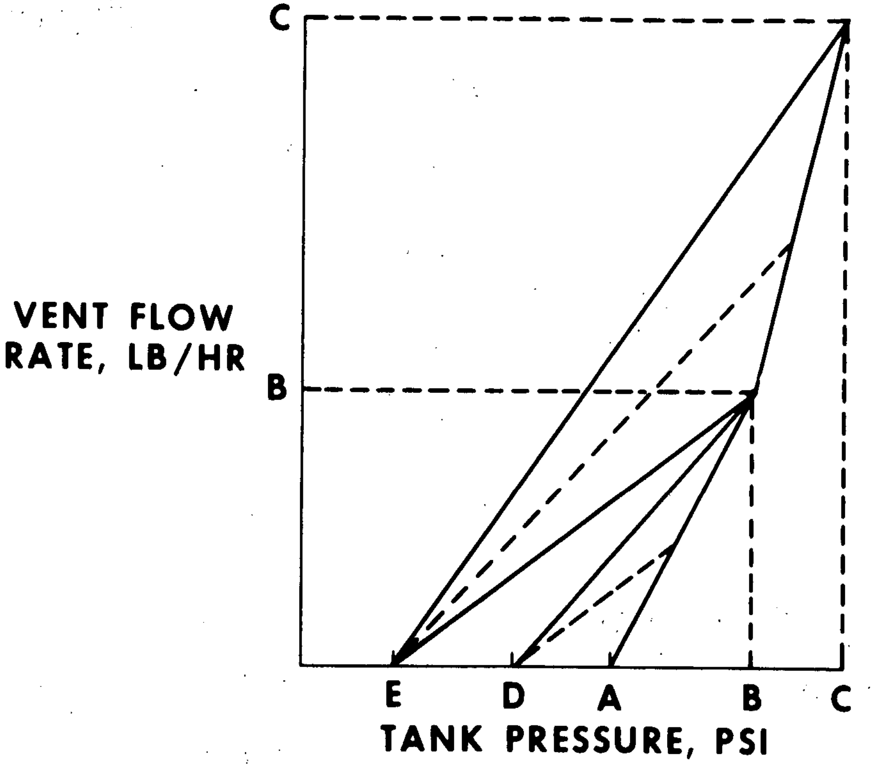

Figure 4.- Apollo CSM vent-valve characteristics.

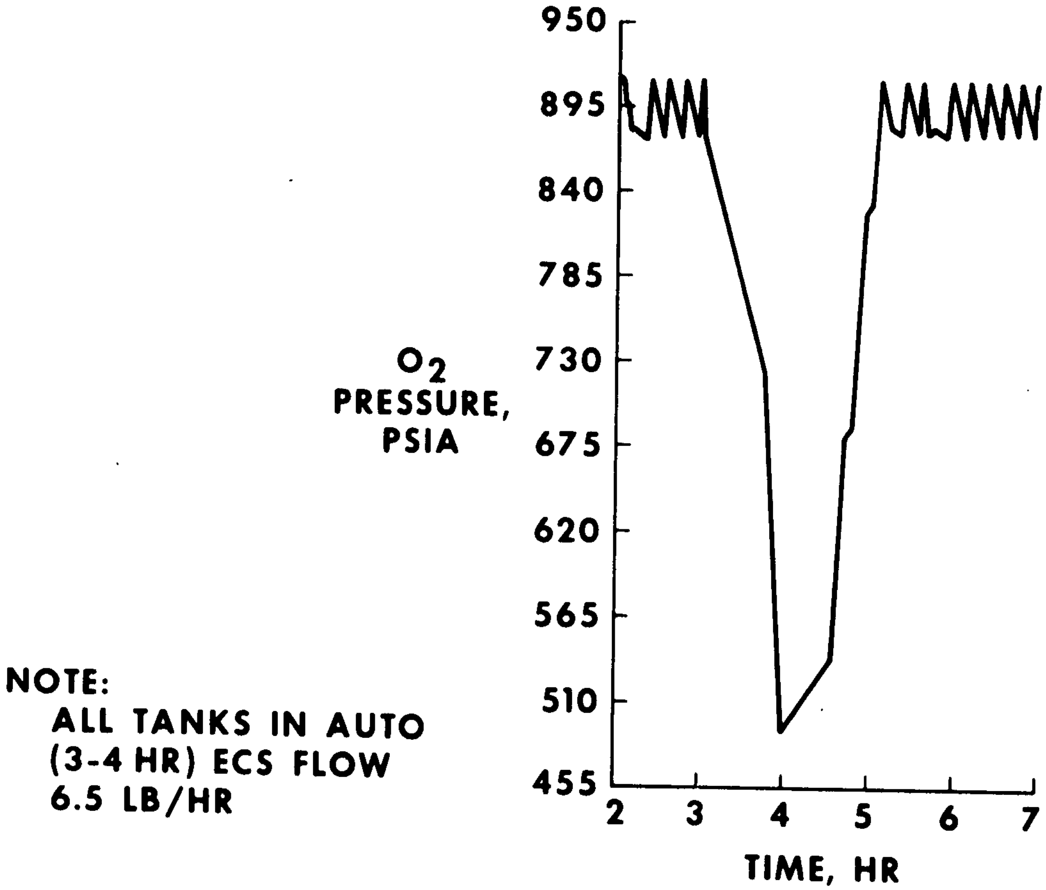

Figure 5.- Oxygen tank 1 pressure collapse.

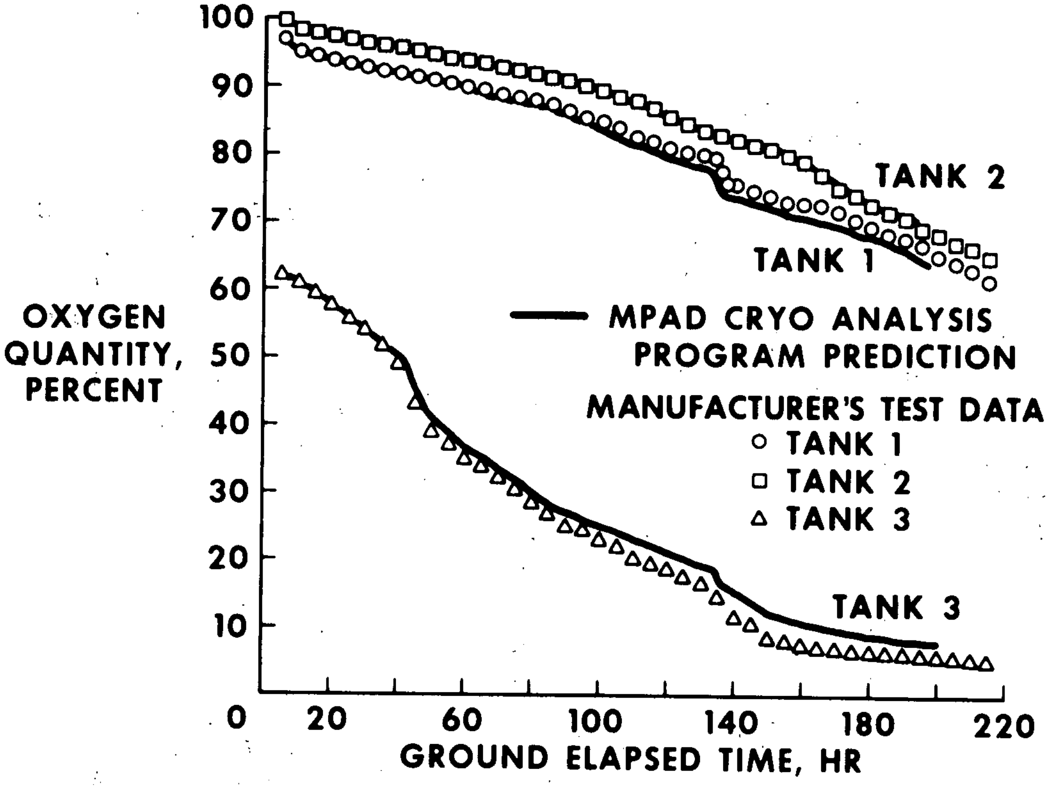

Figure 6.- Comparison of manufacturer test data to the CAP computer prediction model.

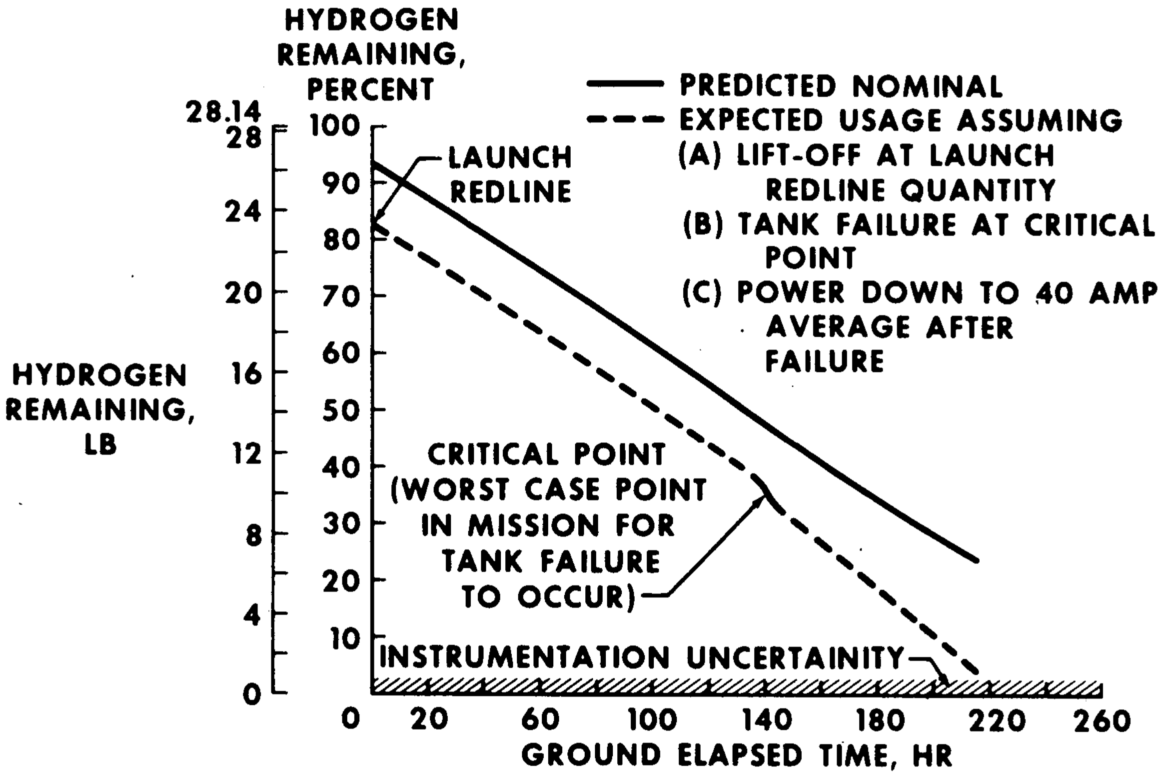

Figure 7.- Hydrogen remaining in one tank of the CSM.

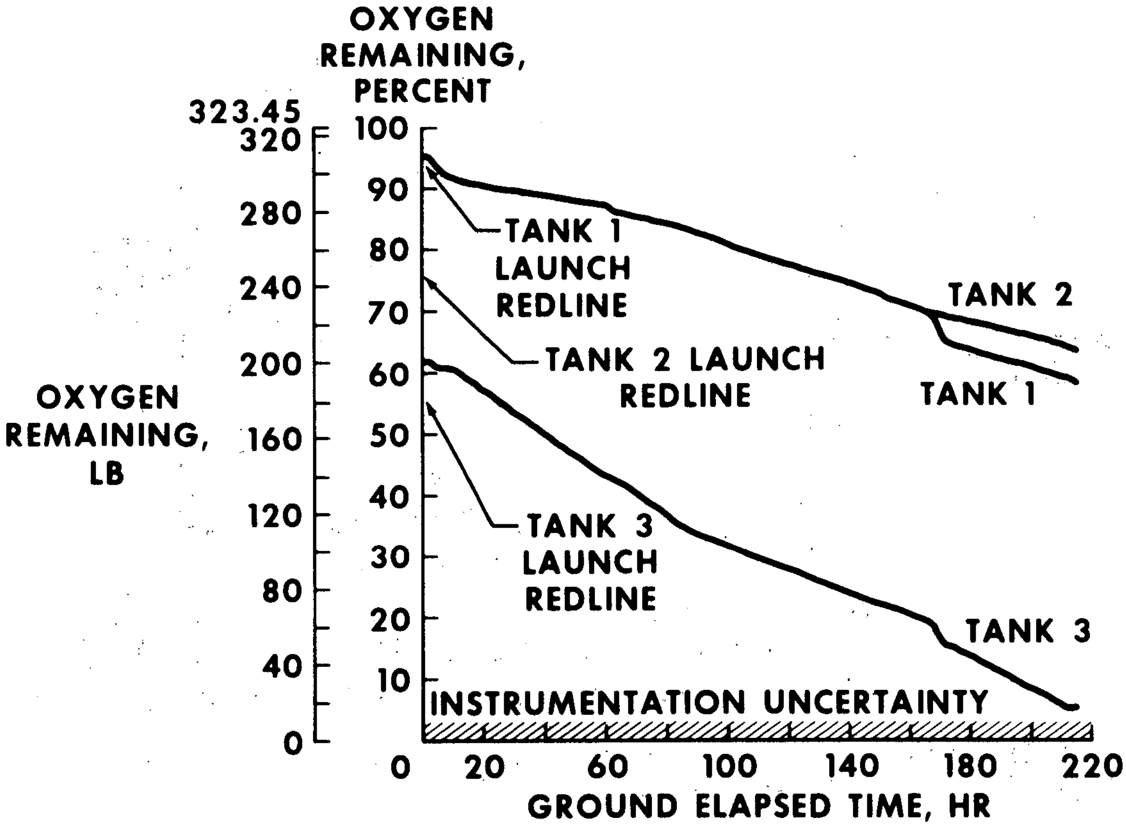

Figure 8.- Oxygen remaining in the CSM.

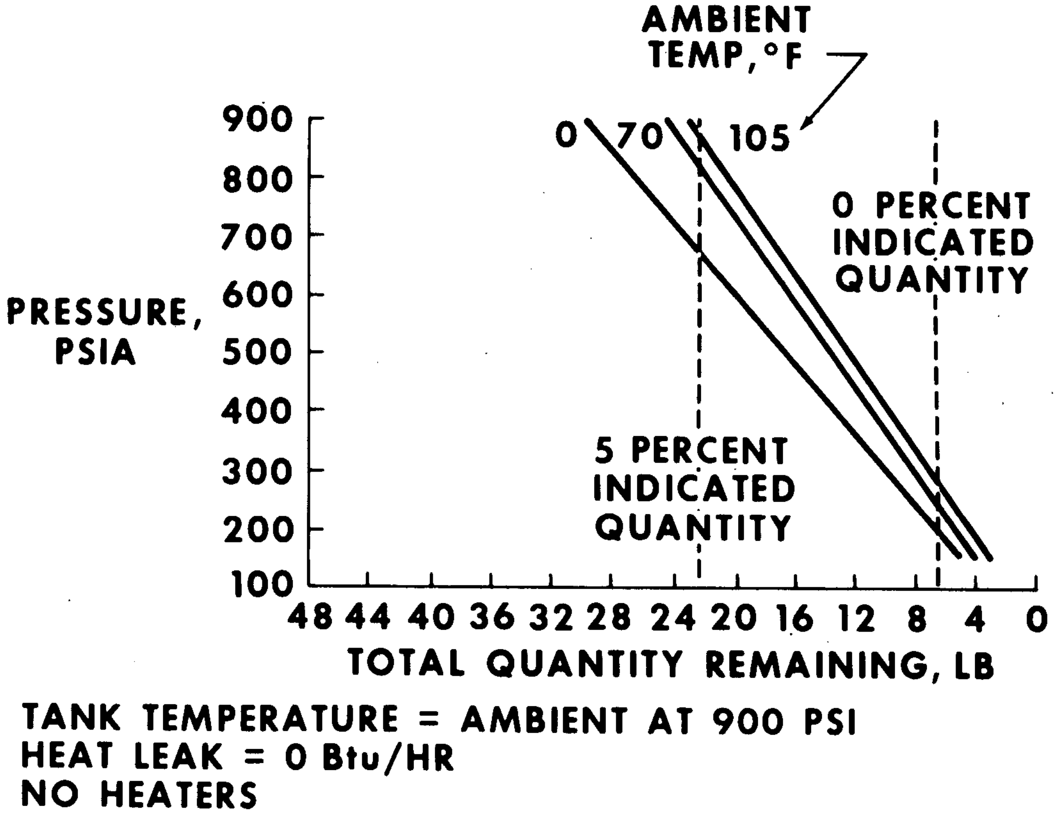

Figure 9.- Oxygen blowdown capability.

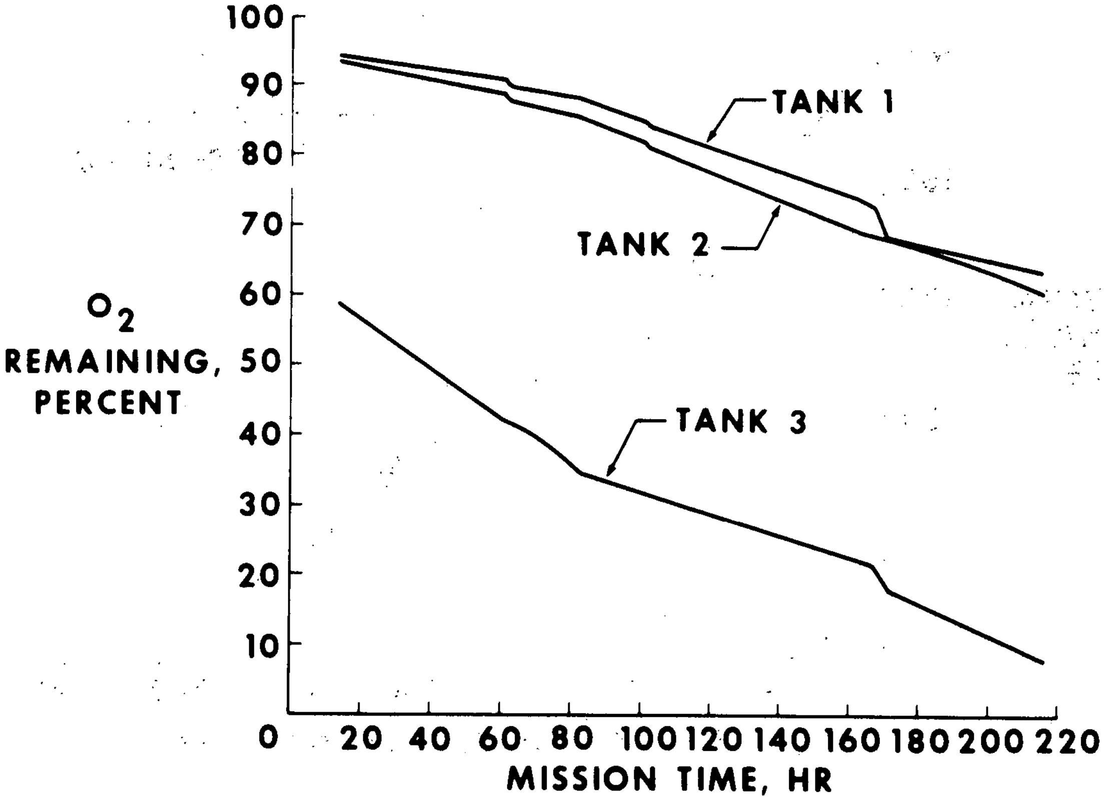

Figure 10.- Oxygen remaining in tanks 1, 2, and 3 of the Apollo 14 spacecraft.

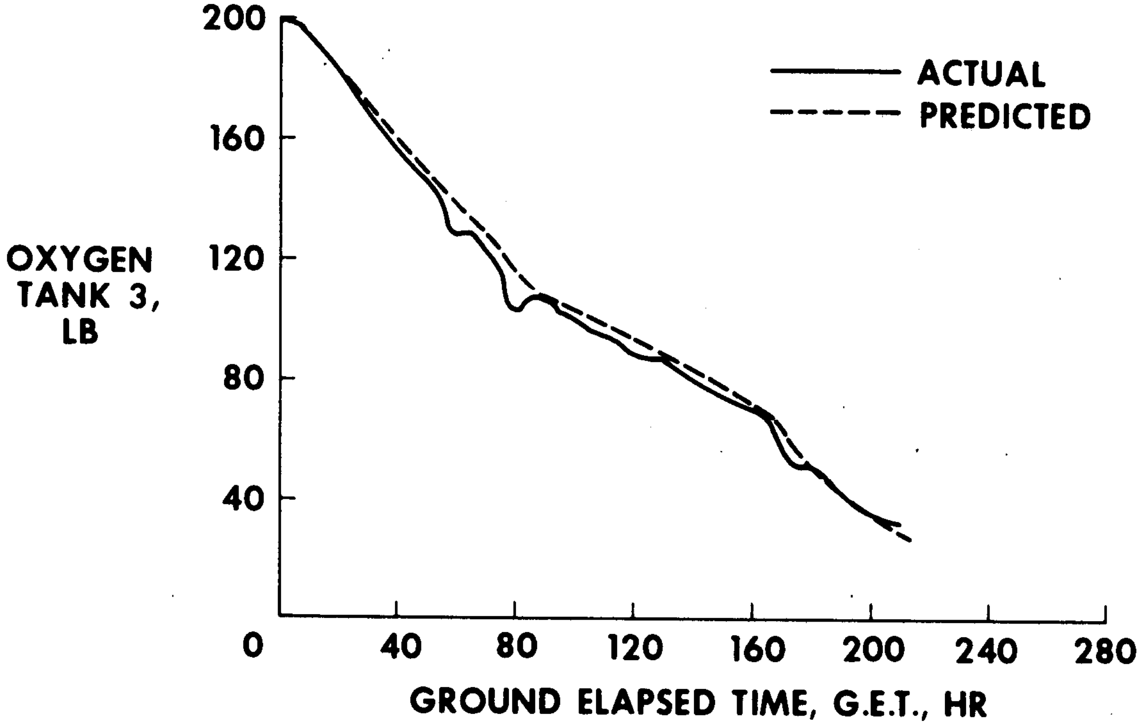

Figure 11.- Depletion profile for Apollo 14 oxygen tank 3.

N72-23797

APOLLO CRYOGENIC INTEGRATED SYSTEMS PROGRAM

R. K. M. Seto

J. E. Cunningham

TRW SYSTEMS GROUP

HOUSTON, TEXAS

ACKNOWLEDGEMENTS

The development of the Apollo Cryogenic Storage System Integrated Systems Program was the result of the combined efforts of several individuals. The contributions of these individuals are acknowledged.

The tankage model was developed by C. E. Barton. J. G. Torian and R. A. Cailleteau developed the components and lines model. The vehicle thermal model was derived by P. J. Knowles, while the oxygen and hydrogen thermophysical routines were adapted by E. Joseph. Programmers for the effort were J. G. Lindsey, J. I. Prewitt and A. Rios.

ABSTRACT

The Integrated Systems Program is capable of simulating both nominal and anomalous operation of the Apollo Cryogenics Storage System (CSS). Two versions of the program exist; one for the Apollo 14 configuration and the other for "J" Type Mission configurations. The program consists of two mathematical models which are dynamically coupled. A model of the CSS components and lines determines the oxygen and hydrogen flowrate from each storage tank given the tank pressures and temperatures, and the Electrical Power Subsystem (EPS) and Environmental Control Subsystem (ECS) flow demands. Temperatures and pressures throughout the components and lines are also determined. A model of the CSS tankage determines the pressure and temperatures in the tanks given the flowrate from each tank and the thermal environment. The model accounts for tank stretch and includes simplified oxygen tank heater and stratification routines. Supporting subroutines are used to calculate thermophysical properties from National Bureau of Standards (NBS) data and to calculate the CSS thermal environment during various mission phases. Anomalous conditions such as a fan and/or heater failure, degraded tank vacuum annulus performance, failed check values, and leaking lines can be simulated. The program is currently operational on the Univac 1108 computer.

CONTENTS

TABLES

CONTENTS (Continued)

FIGURES

INTRODUCTION

The Integrated Systems Program is a mathematical representation of the Apollo Cryogenic Storage System (CSS) and is capable of simulating both nominal and anomalous operation of the system. The program is modular in structure and consists of a storage tank model, a components and lines model and auxiliary routines. Two versions of the program exist; one for the Apollo 14 spacecraft configuration and the other for the "J" Type Mission configuration. The "J" configuration differs from the Apollo 14 configuration primarily by the addition of a hydrogen storage tank and several other components.

The tankage model is capable of simulating the thermodynamic performance of the CSS hydrogen and oxygen tanks. The model accounts for the effects of heat leakage, heater and/or fan operation, duty cycles, and control equipment as well as all significant thermal, elastic, thermoelastic and thermodynamic effects which influence tank performance. Capability to predict the effects of thermal stratification on the oxygen tank performance and to define oxygen tank heater temperatures are included.

The components and lines model determines the oxygen and hydrogen flowrate from each storage tank based on the pressures and temperatures of the individual tanks and the flow demands of the Electrical Power Subsystem (EPS) and the Environmental Control Subsystem (ECS). A transient analysis is performed to determine the pressures and temperatures at each junction and the flowrates in each leg of the system. These values are used to determine the instantaneous steady state pressure drop across all components in each leg.

Anomalous operation of the tanks, such as heater and/or fan failures, degraded tank vacuum annulus performance, and loss of tanks, may be simulated. In addition, line leaks and anomalous operation of any component may be simulated for the oxygen and/or hydrogen distribution systems.

The auxiliary routines describe the thermal environment of the CSS and provide oxygen and hydrogen thermophysical data. The vehicle thermal model computes the outer wall temperatures of the storage tanks as well as spacecraft bay wall and shelf temperatures for various mission phases including translunar coast, transearth coast, attitude holds, and lunar orbit. The thermophysical data routine contains data for both oxygen and hydrogen obtained from the National Bureau of Standards (NBS) over the expected system operating range.

Input to the Integrated Systems program includes the initial state and quantities of the cryogens in the tanks, EPS and ECS flowrate demands, component characteristics, inertial accelerations and the mission mode.

The program, written in Fortran V, is operational on the Univac 1108 computer.

SYSTEM DESCRIPTION

The Apollo CSS supplies oxygen and hydrogen on a demand basis to the EPS and the ECS. The cryogenic fluids are stored in their supercritical states in tanks located in the Service Module (SM). Each tank is equipped with individual components for filling; venting; quantity, temperature, and pressure measurements; pressure control and relief; and the accompanying displays and controls. For all missions through Apollo 13, the storage system was comprised of two hydrogen tanks and two oxygen tanks. The arrangement of these tanks in Sector IV of the SM is shown in Figure 1. For the Apollo 14 Mission the storage system consisted of an additional oxygen tank located in Sector I of the SM making a total of three oxygen tanks and two hydrogen tanks. Subsequent missions will have three hydrogen tanks as well as three oxygen tanks. The additional hydrogen tank will also be located in Sector I of the SM. Figure 2 presents the tankage arrangement in Sector I.

During nominal operation, the storage system is maintained at a relatively constant pressure with fluid temperature increasing during the mission. Pressure is maintained above the critical pressure in the tanks by the application, either manually or automatically, of electrical heater power. Prior to the Apollo 14 Mission, electrical heat was supplied to the storage tanks in conjunction with destratification fans. However, subsequent to the Apollo 13 oxygen system failure, the system was redesigned to eliminate the fans in the oxygen tanks, although fans are still used in the hydrogen tanks.

The nominal operating pressure of the storage tanks is 245 ± 15 psia and 900 ± 35 psia for the hydrogen and oxygen tanks, respectively.

The fluid flow rate is controlled on a demand basis by the ECS and EPS regardless of the storage system's pressure or operating mode. Under nominal operating conditions there are 29.3 pounds of hydrogen and 330.1 pounds of oxygen loaded into each of the storage tanks. Of these amounts, there are 28.2 pounds of usable hydrogen and 323.5 pounds of usable oxygen. Other pertinent storage system operational parameters are presented in Table 1.

Cryogenic Storage Tanks

A major difference between the oxygen and hydrogen tanks is in the material used in their fabrication. These materials are listed in Table 1 and were obtained from Reference 1. In the broad sense, the physical configuration for both tanks is similar in nature and they can be described as a typical unit.

Each tank consists of two concentric spherical shells with thermal insulation in the annular space between the shells. In the oxygen tanks, the insulation supports the pressure vessel. The annulus of each tank is equipped with a vac-ion pump to maintain the low pressure required for adequate vacuum insulation, although in flight the oxygen pumps are the only pumps which may be operated. In addition, the pressure vessel supports (hydrogen tank only), fluid lines, and the electrical conduit are located within the evacuated annulus. The exit fluid line is routed through the annulus before exiting from the tank to provide vapor cooling.

Prior to Apollo 13, each tank was equipped with a two element heater and two destratification fans. However, following the Apollo 13 oxygen system failure, the two element heater and destratification fans in the oxygen tanks were removed and replaced with a three element heater. In addition, the heater thermostat for protection against high heater temperatures was removed and replaced with a temperature sensor. The new sensor is located on the heater tube. Another temperature sensor is located above the capacitance probe and measures the bulk fluid temperature. Electrical lines leading into the redesigned oxygen tank have also been sheathed to reduce the fire hazard.

Cryogenic System Components and Lines

Figures 3 and 4 are schematics of the component and line configurations for the Apollo 14 oxygen and hydrogen systems, respectively, showing the relative locations of the components which make up the system. Figures 5 and 6 present similar schematics for the "J" Type Mission system. In general, the system is composed of lines, valve modules, flow filters and flow restrictors. For missions prior to Apollo 14, the system valve modules for both the hydrogen and oxygen systems each contained two relief valves, two pressure transducers, two pressure switches and one check valve. For Apollo 14, a half valve module was added for oxygen tank 3 and contains one relief valve, one pressure switch, and a check valve. A solenoid operated shutoff valve was also added between oxygen tanks 2 and 3.

The relief valves in these modules are a gradual opening differential pressure poppet type which assures the lowest possible leakage with virtually zero delta pressure between crack and full flow. These valves are designed to be unaffected by back pressure in the downstream plumbing and are temperature compensated over the full range of fluid temperatures which may occur.

The pressure transducers are absolute pressure devices which utilize bonded strain gauges to produce millivolt signals to the signal conditioner. The signal conditioner is integral to the transducer with a 0 to 5 VDC output linearly proportioned to tank pressure. The transducers can operate at environmental temperatures as low as -80°F and are capable of supplying a continuous readout of pressure over the specified range with a maximum error of ± 2-1/2 percent of full scale.

The pressure switches are single-throw, single pole absolute pressure devices which may be used to control the motor switches which activate the destratification motors and/or tank heaters. These switches have been used successfully in an environment of -400°F.

The check valve is a spring loaded poppet type and is designed to open at a differential pressure of approximately 1 psi. The valve seat has a large area to prevent chattering during flow in the normal direction and to help obtain a positive seal if pressurized in the reverse direction.

The fuel cell valve module for the hydrogen system consists of two check valves and three solenoid operated valves in one valve body. The check valves are a dual seat type which allow the main passage to be full open and the auxiliary passage barely cracked at low flows. At high flows, both the main and auxiliary passages are completely open. The solenoid valves are poppet latch type and are actuated by a magnetic armature suspended on a Bellville spring. Opening and closing coils on both sides of the armature actuate the valve. The valves open against pressure and pressure helps to seal the valve against leakage when closed to flow in the normal flow direction.

For the oxygen system, the fuel cell valve module contains check valves similar to those in the hydrogen fuel cell valve module. However, subsequent to Apollo 13, the solenoid valves have been taken out of the module and mounted externally and upstream of the flow transducers to the fuel cells.

The oxygen and hydrogen inline filters consist of several chemically etched discs stacked in a cartridge. They are rated at 5 microns nominally and 12 microns absolute with a capacity to contain .25 grams contaminant.

Several components have been added to the CSS for missions subsequent to the Apollo 14 ("J" type missions). A half valve module containing a relief valve, a pressure switch, and a check valve has been added for the third hydrogen tank. There are three oxygen restrictors in the ECS for "J" type missions versus two for other Apollo missions. The third restrictor line is a branch of the oxygen tank 2 ECS supply line and reconnects downstream of the junction of the other two restrictor lines. This restrictor line includes a filter and check valve.

ANALYTICAL FORMULATION

The Integrated Systems Program was developed as a tool to aid in the preflight planning and the postflight analysis of the Apollo Cryogenic Storage System. Modular in structure, the program is comprised of a tankage model, a components and line model and several auxiliary subroutines. All significant effects which influence system performance, such as thermal environment and mission mode, are included.

Given the component characteristics, the initial state of the cryogens in the tanks, the EPS and ECS flow requirements and the mission mode, the program is capable of simulating the nominal performance of the CSS. Figure 7 presents a flow diagram of the program. Output includes the temperature, pressure and flowrates at various points in the system as well as the remaining quantities and state of the cryogens in the tanks.

In addition to nominal performance, the program is capable of simulating the operation of the CSS under anomalous conditions. The effects of degraded performance of the tank vacuum annulus caused by the presence of air or the cryogen in the jacket may be determined. Abnormal environmental temperatures or tank fan and heater failures may be simulated. Anomalous operation of the check valves, filters, relief valves or flow restrictors may be investigated. Oxygen or hydrogen line leaks may be modeled nearly anywhere in the system.

Two versions of the program were developed. One version is capable of simulating the CSS up to and including the Apollo 14 configuration. The other is capable of simulating the "J" Type Mission configuration. The primary difference in these programs is in the components and lines model. Only the "J" Type configuration will be discussed in this document.

The following sections discuss the analytical formulation of the major models and supporting subroutines which comprise the Integrated Systems Program.

Storage Tank Model

The storage tank model was developed to simulate the thermodynamic performance of the Apollo CSS oxygen and hydrogen tanks. Given the initial conditions and flow demands, the model simultaneously updates the thermodynamic state in each storage tank based on control equipment operation, tank characteristics and heat leak. A flow diagram of the model is presented in Figure 8.

The model may be divided into two sections. The first section determines the maximum time increment over which all tanks may be simulated. The second section uses this time increment to update the state of the fluid in each tank corresponding with the conditions which prevail at the end of the time increment.

The time increment depends on the rate of change of pressure and the operation of the pressure switches in each tank. The time for the tank pressure to reach a specified excursion (currently 15 psi) from its initial state is compared to the time required to reach the pressure control limit. The shorter of these two time intervals is defined as the maximum dynamic simulation time increment for a given tank. Dynamic simulation time increments for all tanks are compared and the smallest one is chosen as the total tank system dynamic simulation time increment. This value is then compared with a user specified increment and the lesser is selected as the time increment for use in updating the state of all cryogenic tanks.

Upon the determination of the time increment, the thermodynamic state of the fluid in each tank is updated. The average pressure for the time interval is determined from the initial tank pressure, the initial pressure rise (or decay) rate, and the length of the time interval. The average density for the time increment is determined from the tank volume, the initial weight of cryogen in the tank, and the flowrate. Using these averaged thermodynamic properties, the average pressure change rate is recomputed for each tank. The average pressure change rate and flowrate are then used to update the pressure and density at the end of the time interval. Finally, fluid temperatures are obtained using the thermophysical routines.

In addition to updating the state of each storage tank, the additional flowrates required by the fuel cells to provide power for all electrical equipment operating during the time interval are determined and added to the EPS flow demand. The time required for a complete pressure cycle and heater cycle is also computed for each tank.

One of the basic functions of the model is the determination of the rate of change of tank pressure with respect to time. The method of determining this derivative differs for the two cryogens since the effects of thermal stratification are considered significant in the oxygen tanks, but not in the hydrogen tanks.

Oxygen Tank. The thermal stratification, resulting from non-uniform heating of the cryogen, significantly affects the operation of the oxygen tanks. The non-uniform heating leads to higher pressurization rates than that which would result from uniform heating. Furthermore, at high densities, thermally stratified oxygen can experience rapid pressure decay upon mixing due to the thermodynamic properties of the oxygen.

In order to determine the pressure derivative, the oxygen tank is represented by three nodes or volumes. One node (V_1) is associated with the fluid within the tank heater column. A second node (V_2) represents the fluid immediately surrounding the heater column. The final node (V_3) represents the remaining fluid in the tank. The nodal representation of the tank is shown in Figure 9.

The oxygen which flows from the tank is withdrawn from V_3. Mass interchange is permitted between V_1 and V_2, but not between V_2 and V_3. A result of this constraint is that V_2 continuously increases during a mission due to fluid withdrawal from V_3. The effects of tank stretch and the compression of the fluid in the fill and vent lines (see Appendix II) on the pressure derivative are accounted for in V_3.

The cylindrical heater is described by a heat source of a specified temperature with a specified heat flux into the two adjacent oxygen nodes. The heater temperature data used in the model were obtained from Apollo 14 flight data and computer simulations of heater operation. The heat flux to the surrounding nodes is calculated from the electrical energy input to the heater, the heater configuration, and the time history of the heater temperature. Heat input is apportioned between the nodes adjacent to the heater by a simple conduction analogy which satisfies a total energy balance for the heater column. Heat conduction is permitted between V_2 and V_3, but not directly between V_1 and V_2. The thermal energy exchange between V_1 and V_2 must pass through the heater tube. All external heat leak is applied to V_3. Heat leak radiant energy transfer is assumed to be negligible.

Mass and energy balance relationships were developed for the fluid in each of the tank nodes. The energy balance equations are:

$$\frac{dp}{dt} = \frac{\phi_1}{V_1} \left\{ q_1 + \dot{m}_1 \left[H(\dot{m}_1)h_2 + H(-\dot{m}_1)h_1 \right] - \dot{m}_1 (h_1 - \theta_1) \right\} \tag{1}$$

$$\frac{dp}{dt} = \frac{\phi_2}{V_2} \left\{ q_2 + \dot{m}_2 \left[H(\dot{m}_2)h_1 + H(-\dot{m}_2)h_2 \right] - \rho_2 \Theta_2 \frac{dV_2}{dt} - \dot{m}_2 (h_2 - \theta_2) \right\} \tag{2}$$

and

$$\frac{dp}{dt} = \frac{\phi 3}{V_3} \left\{ q_3 - \rho_3 \, \Theta_3 \, \frac{dV_3}{dt} + \dot{m}_3 \, \Theta_3 \right\} \qquad (3)$$

where:

$$H(x) = \begin{cases} 0 & x < 0 \\ 1 & x \geq 0 \end{cases}$$

$$\frac{dV_3}{dt} = \frac{dV_{tank}}{dp} \, \frac{dp}{dt} - \frac{dV_2}{dt} - \frac{dV_L}{dt}.$$

The mass balance equations are:

$$\dot{m}_1 = \dot{m}_2$$

$$\dot{m}_3 = \dot{m}_{withdrawal}$$

The Nomenclature used in these equations is defined in Appendix I.

The mass balance relations may be substituted into Equations (1), (2) and (3) to yield a set of three non-linear equations in the three variables $\frac{dp}{dt}$, $\dot{m}$, and $\frac{dV_2}{dt}$ which may be solved iteratively. The resulting pressure derivative is then applied as described above.

The pressure collapse potential is defined as the difference between the instantaneous value of pressure and the value that would result from sudden complete mixing of the fluid. Using the individual values of enthalpy for the three volumes, a mean enthalpy is determined for each tank. The mean density of the fluid in each tank is then determined from the known weight of the remaining oxygen and tank volume. The tank pressure for this mixed condition is obtained from the thermophysical routines. Finally, the pressure collapse potential is computed using this pressure and the pressure under stratified conditions.

Hydrogen Tank. During the Apollo 7 Mission, flight tests were performed which demonstrated that thermal stratification did not significantly affect the performance of the hydrogen tanks. It was therefore assumed that thermodynamic equilibrium existed in the hydrogen tanks at all times. The equation which determines the rate of change of pressure with respect to time for the hydrogen tanks is:

$$\frac{dp}{dt} = \frac{\frac{\Theta\phi}{V}\,\dot{m}\left[1 - \frac{3\alpha\rho\,\frac{\partial T}{\partial p}}{V\,(1+3\alpha\rho\,\frac{\partial T}{\partial p})}\right] + \frac{\Phi q}{V}}{\frac{\Theta\phi\rho}{1+3\alpha\rho}\,\frac{\partial T}{\partial \rho}\left[\frac{V_L}{VNp} + \frac{3r}{2\beta Y}\,(1-\upsilon) + 3\alpha\,\frac{\partial T}{\partial p}\right]} \qquad (4)$$

Equation (4) is derived in Appendix II and accounts for variations in tank volume due to fluid pressure and temperature excursions as well as the compression of fluid in the fill and vent lines. All terms of Equation (4) may be determined from the CSS system and fluid thermodynamic properties.

Components and Lines Model

The components and lines model simulates the operation of the Apollo CSS from the tanks to the user subsystems. Given the EPS and ECS flow demands, and the tank conditions, the pressures, temperatures and flowrates are determined at various points in the system. A flow diagram of the model is shown in Figure 10.

The model is divided into two parts which are called, for convenience, the matrix and nodal models. The matrix model is a mathematical representation of the oxygen and hydrogen systems based on the linearized electrical analogs shown in Figures 11 and 12, respectively. A transient, compressible flow analysis of each system is performed to determine the flow rate in each leg and the pressure at each matrix node. The nodal model then uses this information to perform a steady-state, incompressible flow analysis of each leg to determine the pressure at selected locations along that leg and to update the non-linear characteristics of the individual components and line segment resistances. The nodal model also performs a transient thermal analysis of the lines and components. Detailed electrical analogs of the oxygen and hydrogen systems are shown in Figures 13 and 14, respectively.

Matrix Model. The conservation of mass principle is used to determine the matrix node pressures. For any node i, this may be written (see Appendix III)

$$\Sigma I_i = C_i \frac{dE_i}{dt} - I_{R_i} \qquad (5)$$

where

$$C_i = \frac{V_i}{2RT_i\sqrt{E_i}} \tag{6}$$

and

$$I_{R_i} = \frac{V_i\sqrt{E_i}}{RT_i^2}\,\frac{dT_i}{dt} \tag{7}$$

The matrix model solves this set of simultaneous equations for each system by an implicit backward differencing technique. The flow rate in each leg is then evaluated using the conductances in the characteristic matrix.

The program can simulate up to two leaks in each system at any location except downstream of relief valves. Adding a leak is equivalent to adding a matrix node. These are included in the characteristic matrix as floating columns and rows. The flow at leaks is assumed to be choked and is evaluated in the same manner as overboard vents which are discussed below.

Nodal Model. The nodal model performs a steady state analysis of each leg using the matrix model node pressures and temperatures as boundary conditions. The individual components and line segments are analyzed as follows:

Lines and Fittings. The pressure drop in a line segment from inlet i to outlet j is calculated by (see Appendix III):

$$P_i^2 - P_j^2 = \left[\frac{128\ L\mu R}{g_c\ \pi D^4}\ (T_i + T_j)\right]\dot{m} \tag{8}$$

where

$$T_j = T_k\left[1-e^{-\left(\frac{UA}{\dot{m}c_p}\right)}\right]+T_i e^{-\left(\frac{UA}{\dot{m}c_p}\right)} \tag{9}$$

Since fluid velocities are small, it is assumed in the derivation of Equation (8) that the flow is laminar and incompressible. The conservation of energy principle is used to determine the line temperatures. It is assumed that conduction through the stand-off brackets and along the lines is negligible. Then, for any node, k,

$$(mc_p)_k \frac{dT_k}{dt} = \sigma A_k \varepsilon_k \left(T_s^4 - T_k^4\right) - UA\,\Delta T_{LM} \qquad (10)$$

Fittings have an equivalent L/D of approximately 3. Bends are included by an equivalent L/D which is a function of the bend angle (Figure 15). Clogged lines are simulated by incorporating an increased equivalent length into Equation (8).

Filters, Check Valves, Relief Valves, and Shutoff Valves. The pressure drops across filters and all open valves are evaluated from Equations (8) and (9). An equivalent L/D of 100 is assumed for filters, open check valves, and open relief valves. The equivalent L/D for open shutoff valves is assumed to be 10. The pressure drop across all closed valves is calculated from:

$$p_i^2 - p_j^2 = \frac{1}{G}\dot{m} \qquad (11)$$

where the conductance G, is assumed to be 10^{-7} for check valves and 10^{-10} for relief valves. Check valve and relief valve hysteresis is modeled as shown in Figures 16 and 17, respectively. Clogged filters and valves are simulated by incorporating an equivalent L/D that is larger than the nominal value. Failed check valves and relief valves are simulated by incorporating a cracking and/or reseat pressure that will hold the valve open or closed as desired.

The temperature of filters and individual valves are determined from

$$(mc_p)_k \frac{dT}{dt} = -\,UA\,\Delta T_{LM}, \qquad (12)$$

while the temperatures of valves contained in a valve module housing are determined from

$$(mc_p)_k \frac{dT_k}{dt} = \left(\frac{kA}{\Delta L}\right)_k (T_1 - T_k) - UA\,\Delta T_{LM} \qquad (13)$$

Restrictors. The pressure drop across the oxygen system flow restrictors is evaluated using the data in Figure 18. It is assumed that the process is isothermal.

Overboard Vents. For compressible flow such as overboard venting, the flow is choked. The pressure is evaluated by:

$$p_i = \frac{\sqrt{T_i}}{A_i K} \dot{m} \quad . \tag{14}$$

The nodal model also checks the solution for convergence. The updated resistance of each component and line segment is compared to the resistance used to calculate the flow rates. If the difference in resistor values is within the convergence criteria, the program proceeds to the next time step; if not, the flow rates are re-evaluated based on the updated resistances. Iteration of the characteristic matrix proceeds in this manner until the solution converges (normally within two iterations).

Auxiliary Routines

In order to adequately simulate the operation of the Cryogenic Storage System, it was necessary to develop several auxiliary routines. Two of the most important routines will be discussed in this section. They are the vehicle thermal model and the thermophysical properties routine.

Vehicle Thermal Model. The vehicle thermal model was developed to compute the Cryogenic Storage System environmental temperatures and to determine the heat leak of the oxygen and hydrogen tanks under normal conditions or under conditions of loss of vacuum in the insulation annulus. The heat leak into the storage tanks is primarily a function of the flowrate through the vapor cooled shroud (VCS) and the temperature in the bay. The bay temperature depends to a large extent upon whether the vehicle is in an inertial hold mode or a passive thermal control mode. The effect of vacuum loss in the jacket is to increase the heat leak into the tank.

Oxygen Tank Heat Leak. The heat leak into the oxygen tanks during nominal operating conditions is computed in the thermal model using empirical data correlations developed by the Beech Aircraft Company (Reference 2). These correlations relate the heat transfer into the oxygen tank with the temperature of the oxygen in storage, the oxygen expulsion rate and the tank outer wall temperature. These correlations are given by the following equations:

$$Q_r = AL1 \; (T_1^{2.5} - T_{vcs}^{2.5}) - \dot{m} \; (h_{vcs} - h) \tag{15}$$

$$Q_r = AL2\ (T_{vcs}^{2.5} - T_2^{2.5}) \qquad (16)$$

$$q = AL3\ (T_1 - T_2) + .9Q_r \qquad (17)$$

The value of the constants which apply to Equations (15), (16), and (17) are as follows:

Redesigned Tank: $AL1 = .9205 \times 10^{-5}$ BTU/HR°R$^{2.5}$

$AL2 = .7278 \times 10^{-5}$ BTU/HR°R$^{2.5}$

$AL3 = .03775$ BTU/HR°R

The amount and temperature of the oxygen in storage is computed in the tankage model of the Integrated Systems Program and is input to the thermal subroutine.

The outer wall tank temperature is computed within the thermal subroutine through a series of data curve fit correlations. The data for these correlations were obtained using the Thermal Mathematical Model (TMM) of the Apollo Service Module. This program is composed of over 800 lumped parameters that constitute a thermal network specifically formated for solution with the SINDA Multi-Option computer program. Using TMM, a set of parametric computer runs was performed varying the mission mode (inertial hold, passive thermal control or lunar orbit), the quantity of the cryogen in the tanks, and the flowrates from the tanks. A uniform internal tank temperature was assumed in determining the temperature of each oxygen and hydrogen tank surface.

For use in the thermal subroutine, the temperatures computed for the surface of the oxygen tanks by the TMM were averaged for each tank and curve fit as a function of time. The form of the resulting curve fit equations is:

$$T = a_o + a_1x + a_2x^2 + a_3x^3 \qquad (18)$$

where x is the time argument. The coefficients for the polynomial curve fit equations are shown in Table 2. Using these equations, the tank outer wall temperatures are first estimated as a function of mission mode, time in mode and quantity. These values are then adjusted for the sun look angle. The temperature of the fluid in the VCS is then computed from the temperature of the fluid in storage and the outer wall temperature using an iteration scheme. Once the temperature of the VCS fluid has been determined, the heat flux is computed using Equations (15), (16), and (17).

Hydrogen Tank Heat Leak. The heat leak to the hydrogen tank under nominal operating conditions is computed in the thermal model using data taken from the Apollo Flight Support Handbook (Reference 1). This data, presented in Figure 19, is a correlation of estimated heat flux as a function of the fluid expulsion rate and the quantity of fluid remaining in the tank. This data, however, does not include the effect of temperature in the bay on the heat flux. Since the outer wall temperature is not taken into account, the mission mode cannot be considered in the calculation for the hydrogen tank heat leak. In addition, the discontinuity occurring in the curves at a flow rate of 0.25 lbm/hr does not appear reasonable. Although the correlations presented in Figure 19 do not appear to adequately define the heat leak into the hydrogen tanks, it is the only data currently available. However, if additional data becomes available, the hydrogen tank heat leak correlations used in this portion of the program may be updated easily.

Vacuum Annulus Failure. The nominal pressure in the tank annulus under the design vacuum condition is approximately 2×10^{-9} psia (10^{-7} mm Hg). Depending upon the type of failure, the annulus pressure in the failed condition will be somewhere between the nominal pressure and the annulus burst disc pressure. Burst disc pressures for the oxygen and hydrogen tanks are approximately 75 and 80 psia, respectively. Within these pressure bounds, gas in the annulus may exist in either rarefied or continuum regimes. The criteria for determining the gas regime is based primarily on the ratio of the molecular mean free path to the amount of space available for molecular motion. This ratio is defined as the Knudsen number (K_n). For values of $K_n < 0.01$ the gas is normally treated as continuum flow, while for values of $K_n > 1.0$ the gas is assumed to be in the rarefied regime. For the CSS tanks, an annulus pressure on the order of 10^{-3} psia represents the transition between the two regimes.

The type of analysis used to compute the amount of heat transferred across the annulus depends upon the flow regime. For the rarefied regime the equation for determining the heat flux per unit area is given by Reference 3 as:

$$\dot{q} = A_c \left(\frac{n+1}{n-1}\right) \frac{\sqrt{R}}{8\Pi} \frac{p}{\sqrt{MT}} (T_2-T_1) \tag{19}$$

For continuum flow regimes, the heat flux per unit area is given by Reference 4 as:

$$\dot{q} = -k\frac{(T_2-T_1)}{(R_2-R_1)} \tag{20}$$

An analysis was performed for the Apollo cryogenic storage tanks (Reference 5) assuming residual gas in the annulus consisted of air or the appropriate cryogen. The analysis showed that for an annulus pressure of less than approximately 10^{-7} psia, heat conduction by the residual gas was essentially negligible. However, heat conduction increased rapidly with increasing annulus pressure. The total heat transfer to the tanks as a function of the annulus pressure is shown in graphical form in Figures 20 and 21. These curves have been incorporated into the thermal model such that when the thermal subroutine encounters a failed tank flag, the data presented in the figures is used to determine the heat flux to the tank based upon the vacuum jacket pressure. This pressure is an input to the program.

Components and Line Environmental Temperatures. The environmental temperatures used to determine the state of the fluid in the components and lines were obtained in a manner identical to the tank environmental temperatures. The Thermal Mathematical Model of the Apollo Service Module was used to obtain data at several locations as given in Table 3. These data were incorporated into the Integrated Systems Program as a series of curve fit correlations. The form of the resulting equation is the same as Equation (18). The coefficients for the curve fit equations are presented in Table 2.

The TMM did not model the Command Module (CM) cabin, the CM Reaction Control System Tank Annulus, or the ECS umbilical. The temperature at these locations was assumed to be 70°F.

Thermophysical Properties for Oxygen and Hydrogen. Computer subroutines for computing the thermophysical properties for oxygen and hydrogen were developed and included into the Integrated Systems Program. The majority of the data used in these subroutines was recommended by the National Bureau of Standards (NBS). That data not available from the NBS was taken from Reference 6 (Stewart). In general these subroutines determine pressure (p), temperature (T), density (ρ), enthalpy (h), the specific heat at constant pressure (c_p), the specific heat at constant volume (c_v), viscosity (μ), thermal conductivity (k), isotherm and isochor derivatives and the functions ϕ and Θ, providing sufficient information concerning the fluid state is known. The data is included in the subroutines both in equation and table form. A routine is also included in the subroutines for interpolating between values from the tables.

Oxygen Properties. Data contained in the subroutines for computing the thermophysical properties of oxygen were taken from References 6, 7, and 8. Reference 6 presents an equation of state for oxygen determined by R. B. Stewart. The isotherm and isochor derivatives were derived from this equation. While Reference 7 (Weber) also presents data for the isotherm and isochor derivatives, the results derived from Reference 6 are valid for a greater range. Both sets of data were included in the thermophysical subroutines to provide greater flexibility since the derivatives derived from Reference 6 may be determined with known values of temperature and density, while the data from Reference 7 uses either pressure and temperature or pressure and density.

The equation of state provided by Reference 6 may be used to compute pressure from known values of density and temperature. This equation is valid for temperatures between 117 and 540°R and for pressures to 5000 psia. The equation of state is as follows:

$$
\begin{aligned}
p = \rho R T \; & + (n_1 T + n_2 + n_3/T^2 + n_4/T^4 + n_5/T^6)\rho^2 \\
& + (n_6 T^2 + n_7 T + n_8 + n_9/T + n_{10}/T^2)\rho^3 \\
& + (n_{11} T + n_{12})\rho^4 + (n_{13} + n_{14} T)\rho^5 \\
& + \rho^3 (n_{15}/T^2 + n_{16}/T^3 + n_{17}/T^4) \exp(n_{25}\rho^2) \\
& + \rho^5 (n_{18}/T^2 + n_{19}/T^3 + n_{20}/T^4) \exp(n_{25}\rho^2) \\
& + \rho^7 (n_{21}/T^2 + n_{22}/T^3 + n_{23}/T^4) \exp(n_{25}\rho^2) \\
+ n_{24}\rho^{(n_{28}+1)} & (\rho^{n_{28}} - \rho_c^{n_{28}}) \exp\left[n_{26}(\rho^{n_{28}} - \rho_c^{n_{28}})^2 + n_{27}(T - T_c)^2\right] \qquad (21)
\end{aligned}
$$

where: ρ_c = 13.333 gmol/liter, critical density

T_c = 154.77 °K, critical temperature

In this expression, p is in atmospheres, T is in °K, and ρ is in gmol/liter. The constants for this equation are given in Table 4. The subroutine in which Equation (21) is programmed converts the units of density from lbm/cu-ft to gmol/liter and temperature from °R to °K prior to use. The output pressure is in psia.

The isotherm derivative, $\left.\frac{\partial p}{\partial \rho}\right|_T$, is the partial derivative of Equation (21) with respect to the density at constant temperature and is given by:

$$\left.\frac{\partial p}{\partial \rho}\right|_T = R\,T + \sum_{i=1}^{24} n_i X_i \qquad (22)$$

Values for the variables in this equation are presented in Table 5.

The coefficients n_i are the same as those for Equation (21). The subroutine which computes the isotherm derivative converts density from lbm/cu-ft to gmol/liter and temperature from °R to °K prior to its use in Equation (22). The output derivative is in units of psia-ft^3/lbm.

The isochor derivative $\left.\frac{\partial p}{\partial T}\right|_\rho$, is the partial derivative of Equation (21) with respect to temperature at constant density and is given by:

$$\left.\frac{\partial p}{\partial T}\right|_\rho = \rho R + \sum_{i=1}^{24} n_i X_i \qquad (23)$$

where the coefficients n_i are the same as those listed for Equation (21). The variables in this equation are shown in Table 6. The conversion from one set of units to the other is performed the same as for Equations (21) and (22). The output derivative is in units of psia/°R.

In addition to providing data for the isotherm derivative and the isochor derivative, Reference 7 presents data for density, enthalpy, specific heats (at constant pressure and volume) and the functions Θ and ϕ. All are in tabular form. Further flexibility was provided by permitting these properties to be determined from known values of pressure and temperature or from pressure and density. These tables are valid for temperatures from 100 to 540°R at 5 degree increments and for pressures ranging from 367 to 1250 psia at increments of 73.5 psi. Table 7 lists the thermophysical parameters which are available.

Data from Reference 8 is also in the form of tables and provides viscosity and thermal conductivity as functions of pressure and temperature. This data is valid for temperatures ranging from 180 to 540°R at increments of 18 degrees and for pressures from 367 to 1250 psia at increments of 73.5 psi.

Hydrogen Properties. The thermophysical properties used in the hydrogen subroutine are based upon computer programs developed by the NBS (Reference 9). These properties are valid for pressures from 1 to 5000 psia and for temperatures ranging from 25 to 5000 °R. In the NBS programs all thermophysical properties are determined from known values of pressure and temperature and include enthalpy, density, specific heats for both constant pressure and constant volume, viscosity and thermal conductivity. However, in the subroutine developed for the Integrated System Program, provision was made to compute the pressure and temperature from other known properties as described below. The pressure, density and temperature are in units of psia, lbm/ft^3, and °R, respectively.

The NBS program expresses hydrogen density as a polynominal equation in terms of pressure and temperature, $\rho = \rho\ (p,T)$. The equation has been programmed such that pressure may be determined from this equation as a function of density and temperature using a Newton-Raphson iteration method. An a priori value of pressure is required to initiate the iteration and should be estimated as closely as possible to the actual value. Temperature is computed in a manner similar to that of pressure from this same expression.

The available parameters are listed in Table 7.

REFERENCES

1. NASA Document, "Apollo Fuel Cell and Cryogenic Gas Storage System Flight Support Handbook," Manned Spacecraft Center, Houston, Texas, 18 February 1970.
2. Analysis of Oxygen Tank Heat Leak, obtained informally from Beech Aircraft Co., Boulder, Colorado.
3. Corruccini, R. J., "Gaseous Heat Conduction at Low Pressures and Temperatures," Vacuum, Vol. VII and VIII, April, 1959.
4. McAdams, W. H., "Heat Transmission," McGraw-Hill Cook Company, 3rd Edition, 1954.
5. TRW IOC 70.4354.3-104, "Effect of CSS Tank Vacuum Annulus Leakage on Heat Transfer Rates," P. J. Knowles, 23 November 1970.
6. Stewart, R. B., "The Thermodynamic Properties of Oxygen," PhD Thesis, University of Iowa, June, 1966.
7. Weber, L. A., "Thermodynamic and Related Properties of Oxygen from the Triple Point to 300°K at Pressures to 330 Atmospheres," NBS Report 9710A, 29 August 1968.
8. Roder, H. M., "Viscosity and Thermal Conductivity of Oxygen," NBS letter 275.02 to J. Smithson, EP5, NASA/MSC, September 24, 1970.
9. Hall, W. J., R. D. McCarty, and H. M. Roder, "Computer Programs for Thermodynamic and Transport Properties of Hydrogen," NBS Report #9288, (NASA-CR88086), August, 1967.

TABLE 1

CRYOGENIC SYSTEM OPERATIONAL PARAMETERS

	Hydrogen	Oxygen
TANK MATERIAL	5 Al-2.5 Sn ELI tl	Inconel 718
TANK WEIGHT (PER TANK)		
Empty (Approx)	80.00 lb.	90.82 lb.
Usable Fluid	28.15 lb.	323.45 lb.
Stored Fluid (100% indication)	29.31 lb.	330.1 lb.
Residual	4%	2%
Maximum Fill Quantity	30.03 lb.	337.9 lb.
TANK VOLUME (PER TANK)	6.80 ft^3	4.75 ft^3
TANK PRESSURIZATION		
Heaters elements per tank	2	3
Flight Resistance	78.4 ohms per element	18.45 ohms per element
Nominal Voltage	28 V DC	28 V DC
Power	10 watts per element*	42.5 watts per element*
Total Heater Heat Input Per tank	68.2 BTU/Hr	434.8 BTU/Hr
Ground Resistance	78.4 ohms per element	18.45 ohms per element
Voltage	28 V DC	28 V DC
Power	10 watts per element*	42.5 watts per element*
Total Heater Heat Input Per Tank	68.2 BTU/Hr	434.8 BTU/Hr

TABLE 1 (Continued)

	Hydrogen	Oxygen
Pressure Switch		
Open Pressure Max.	260 psia	935 psia
Close Pressure Min.	225 psia	865 psia
Deadband Min.	10 psia	30 psia
Destratification Motors (2 Motors Per Tank)		
Voltage	115/200 V 400 cps	None
Power - Average	3.5 watts per motor*	None
Total Average Motor Heat Input Per Tank	23.8 BTU/Hr	None
SYSTEM PRESSURES		
Normal Operating	245 ± 15 psia	900 ± 35 psia
Spec Min. Dead Band of Pressure Switches	10 psi	30 psi
Relief Valve Note:	Relief Valves are referenced to environmental pressure, therefore pressure at sea level (psig) will be the same value in vacuum (psia)	
Crack Min.	273 psig	938 psig
Full Flow Max.	285 psig	1010 psig
Reseat Min.	268 psig	865 psig
Outer Tank Shell Burst Disc		
Nominal Burst Pressure	90 $^{+10}_{-20}$ psid	75 ± 7.5 psid
SYSTEM TEMPERATURES		
Stored Fluid	-425 to 80°F	-300 to 80°F

*Conversion Factor: 1 watt = 3.41 BTU/Hr

TABLE 2

CURVE FIT COEFFICIENTS REPRESENTATIVE OF THE CSS THERMAL ENVIRONMENT

Mission Mode	Node	a_o (°F)	a_1 (°F/Hr)	a_2 (°F/Hr^2)	a_3 (°F/Hr^3)	T_{inf} °F	Time Argument	
							t+3 (Hrs)	$\frac{1}{t+3}$ (Hrs)$^{-1}$
PTC	Tanks 1 & 2	46.152	35.715	105.97	-38.106			X
PTC	Tank 3	25.164	73.761	202.92	-112.08			X
Hot Soak	Tanks 1 & 3	60.0	4.44	.0	0.0		X	
Hot Soak	Tank 2	58.523	31.715	-3.57	0.1277		X	
Cold Soak	Tanks 1 & 3	-15.824	368.40	-485.5	232.26			X
Cold Soak	Tank 2	-61.812	549.39	-650.84	283.34			X
PTC	150	66.0	0.0	0.0	0.0	66.0		X
PTC	151	85.3	-64.0	0.0	0.0	80.0		X
PTC	152	47.0	0.0	0.0	0.0	47.0		X
PTC	153	49.5	28.6	0.0	0.0	57.0		X
PTC	154	42.5	46.5	0.0	0.0	48.0		X
PTC	155	117.3	-130.0	0.0	0.0	101.0		X
PTC	156	132.4	-145.3	0.0	0.0	118.0		X
PTC	157	91.8	-77.3	0.0	0.0	86.0		X
PTC	158	70.0	0.0	0.0	0.0	70.0		X
PTC	159	48.4	18.2	0.0	0.0	49.0		X
PTC	163	47.0	0.0	0.0	0.0	47.0		X
Cold Soak	150	80.0	-3.9	0.27	0.0	56.0		X

TABLE 2 (Cont'd)

CURVE FIT COEFFICIENTS REPRESENTATIVE OF THE CSS THERMAL ENVIRONMENT

Mission Mode	Node	a_o (°F)	a_1 (°F/Hr)	a_2 (°F/Hr^2)	a_3 (°F/Hr^3)	T_{inf} °F	Time Argument t+3 (Hrs)	Time Argument $\frac{1}{t+3}$ (Hrs)$^{-1}$
Cold Soak	151	115.2	-18.6	1.4	-0.036	31.0		X
Cold Soak	152	109.3	-22.3	1.7	-0.041	5.0		X
Cold Soak	153	88.7	-10.2	0.45	-0.0074	7.0		X
Cold Soak	154	107.5	-18.3	1.2	-0.03	6.0		X
Cold Soak	155	60.7	-0.25	0.046	-0.0021	58.0		X
Cold Soak	156	51.3	7.65	-0.42	0.0067	96.0		X
Cold Soak	157	99.6	-12.6	1.07	-0.029	50.0		X
Cold Soak	158	50.0	5.8	-0.26	0.0039	96.0		X
Cold Soak	159	111.6	-20.1	1.42	-0.035	5.0		X
Cold Soak	163	32.1	12.2	-0.70	-0.013	109.0		X
Hot Soak	150	103.3	-10.2	0.812	-0.002	50.0		X
Hot Soak	151	47.7	8.73	-0.443	0.00071	103.0		X
Hot Soak	152	32.1	12.2	-0.7	0.013	109.0		X
Hot Soak	153	105.2	75.8	-882.4	396.6	105.0		X
Hot Soak	154	97.2	62.1	-870.3	395.0	99.0		X
Hot Soak	155	120.7	40.4	-975.4	450.0	122.0		X
Hot Soak	156	24.6	17.9	-0.892	0.013	136.0		X
Hot Soak	157	17.0	17.6	-1.2	0.028	105.0		X

TABLE 2 (Cont'd)

CURVE FIT COEFFICIENTS REPRESENTATIVE OF THE CSS THERMAL ENVIRONMENT

Mission Mode	Node	a_o (°F)	a_1 (°F/Hr)	a_2 (°F/Hr^2)	a_3 (°F/Hr^3)	T_{inf} °F	Time Argument	
							t+3 (Hrs)	$\frac{1}{t+3}$ (Hrs)$^{-1}$
Hot Soak	158	86.1	-6.2	0.2	-0.0021	25.0		X
Hot Soak	159	102.2	63.1	-885.9	401.9	10.0		X
Hot Soak	163	109.3	-22.3	1.7	-0.041	5.0		X
Lunar Orbit	150	53.5	5.5	0.0	0.0	114.0	X	
Lunar Orbit	151	74.6	-1.52	0.0	0.0	54.0	X	
Lunar Orbit	152	45.0	0.0	0.0	0.0	45.0	X	
Lunar Orbit	153	79.0	0.0	0.0	0.0	79.0	X	
Lunar Orbit	154	58.0	0.0	0.0	0.0	58.0	X	
Lunar Orbit	155	51.1	2.63	0.0	0.0	84.0	X	
Lunar Orbit	156	58.9	3.89	0.0	0.0	107.0	X	
Lunar Orbit	157	69.0	0.0	0.0	0.0	69.0	X	
Lunar Orbit	158	76.72	-2.24	0.0	0.0	42.0	X	
Lunar Orbit	159	57.0	0.0	0.0	0.0	57.0	X	
Lunar Orbit	163	45.0	0.0	0.0	0.0	45.0	X	

$T = a_o + a_1X + a_2X^2 + a_3X^3$ where X = time argument

TABLE 3

ENVIRONMENTAL TEMPERATURE LOCATIONS

SINK INDEX	LOCATION
150	TUNNEL
151	Bay 4
152	Bay 4
153	Forward Bulkhead
154	Bay 4
155	Bay 4
156	Bay 4
157	Bay 4
158	Forward Bulkhead
159	Forward Bulkhead
160	Umbilical
161	CM RCS Tank Annulus
162	CM Cabin
163	Bay 1

TABLE 4

CONSTANTS FOR STEWART'S EQUATION OF STATE

$R = 0.0820535$
$n_1 = 3.38759078 \times 10^{-3}$
$n_2 = -1.31606223$
$n_3 = 1.92049067 \times 10^{3}$
$n_4 = 1.92049067 \times 10^{7}$
$n_5 = -2.90260005 \times 10^{10}$
$n_6 = -5.70101162 \times 10^{-8}$
$n_7 = 7.96822375 \times 10^{-5}$
$n_8 = 6.07022502 \times 10^{-3}$
$n_9 = -2.71019658$
$n_{10} = -3.59419602 \times 10$
$n_{11} = 1.02209557 \times 10^{-6}$
$n_{12} = 1.90454505 \times 10^{-4}$
$n_{13} = 1.21708394 \times 10^{-5}$
$n_{14} = 2.44255945 \times 10^{-3}$

$n_{15} = 1.73655508 \times 10^{2}$
$n_{16} = 3.01752841 \times 10^{5}$
$n_{17} = -3.49528517 \times 10^{7}$
$n_{18} = 8.86724004 \times 10^{-1}$
$n_{19} = -2.67817667 \times 10^{2}$
$n_{20} = 1.05670904 \times 10^{5}$
$n_{21} = 5.63771075 \times 10^{-3}$
$n_{22} = -1.12012813$
$n_{23} = 1.46829491 \times 10^{2}$
$n_{24} = 9.98868924 \times 10^{-4}$
$n_{25} = -0.00560$
$n_{26} = -0.157$
$n_{27} = -0.350$
$n_{28} = 0.90$

TABLE 5 - VARIABLES FOR COMPUTING ISOTHERM DERIVATIVES

$X_1 = 2\rho T$

$X_2 = 2\rho$

$X_3 = 2\rho/T^2$

$X_4 = 2\rho/T^4$

$X_5 = 2\rho/T^6$

$X_6 = 3\rho^2T^2$

$X_7 = 3\rho^2T$

$X_8 = 3\rho^2$

$X_9 = 3\rho^2/T$

$X_{10} = 3\rho^2/T^2$

$X_{11} = 4\rho^3T$

$X_{12} = 4\rho^3$

$X_{13} = 5\rho^4$

$X_{14} = 5\rho^4/T$

$X_{15} = f_6/T^2$

$X_{16} = f_6/T^3$

$X_{17} = f_6/T^4$

$X_{18} = f_7/T^2$

$X_{19} = f_7/T^3$

$X_{20} = f_7/T^4$

$X_{21} = f_8/T^2$

$X_{22} = f_8/T^3$

$X_{23} = f_8/T^4$

$X_{24} = f_9f_2f_3 + \rho^{(n_{28+1})}f_{10}f_3 + \rho^{(n_{28+1})}f_2f_{11}$

$f_1 = \exp\,(n_{25}\rho^2)$

$f_2 = \rho^{n_{28}} - \rho_{c_2}^{n_{28}}$

$f_3 = \exp\left[n_{26}f_2 + n_{27}(T-T_c)^2\right]$

$f_4 = 2n_{27}(T-T_c)f_3$

$f_5 = 2f_1\rho\, n_{25}$

$f_6 = 3f_1\rho^2 + f_5\rho^3$

$f_7 = 5f_1\rho^4 + f_5\rho^5$

$f_8 = 7f_1\rho^6 + f_5\rho^7$

$f_9 = (n_{28+1})\,\rho^{n_{28}}$

$f_{10} = n_{28}\rho^{(n_{28-1})}$

$f_{11} = 2f_2n_{26}f_3f_{10}$

TABLE 6

VARIABLES FOR COMPUTING ISOCHOR DERIVATIVE

$X_1 = \rho^2$

$X_2 = 0$

$X_3 = -2\rho^2/T^3$

$X_4 = -4\rho^2/T^5$

$X_5 = -6\rho^2/T^7$

$X_6 = 2T\rho^3$

$X_7 = \rho^3$

$X_8 = 0$

$X_9 = -\rho^3/T^2$

$X_{10} = -2\rho^3/T^3$

$X_{11} = \rho^4$

$X_{12} = 0$

$X_{13} = 0$

$X_{14} = -\rho^5/T^2$

$X_{15} = -2\rho^3 f_1/T^3$

$X_{16} = -3\rho^3 f_1/T^4$

$X_{17} = -4\rho f_1/T^5$

$X_{18} = -2\rho^5 f_1/T^3$

$X_{19} = -3\rho^5$

$X_{20} = -4\rho^5 f_1/T^5$

$X_{21} = -2\rho^7 f_1/T^3$

$X_{22} = -3\rho^7 f_1/T^4$

$X_{23} = -4\rho^7 f_1/T^5$

$X_{24} = \rho^{(n_{28}+1)} f_2 f_4$

where: $f_1 = \exp(n_{28}\rho^2)$

$f_2 = \rho^{n_{28}} - \rho_c^{n_{28}}$

TABLE 7

THERMOPHYSICAL PROPERTIES SUBROUTINES

PROPERTY	UNITS	INPUT VARIABLES	REFERENCE
OXYGEN			
Density	lbm/ft^3	P&T	7
Enthalpy	btu/lbm	P&T	7
Enthalpy	btu/lbm	P&ρ	7
Function Θ	btu/lbm	P&T	7
Function ϕ	psia-ft^3/btu	P&T	7
Isochor	psia/°R	T&ρ	6
Isochor	psia/°R	P&T	7
Isochor	psia/°R	P&ρ	7
Isotherm	psia-ft^3/btu	T&ρ	6
Isotherm	psia-ft^3/btu	P&T	7
Isotherm	psia-ft^3/btu	P&ρ	7
Pressure	Psia	T&ρ	6
Specific Heat, C_P	btu/lbm-°R	P&T	7
Specific Heat, C_P	btu/lbm-°R	P&ρ	7
Specific Heat, C_v	btu/lbm-°R	P&T	7

TABLE 7 (CONT'D)

THERMOPHYSICAL PROPERTIES SUBROUTINES

PROPERTY	UNITS	INPUT VARIABLES	REFERENCE
OXYGEN			
Specific Heat, C_v	btu/lbm-°R	P&ρ	7
Thermal Conductivity	btu(ft/hr)/ ft^2/°R	P&T	8
Temperature	°R	P&ρ	7
Viscosity	lbf-hr/ft^2	P&T	8
HYDROGEN			
Density	lbm/ft^3	P&T	9
Enthalpy	btu/lbm	P&T	9
Function Θ	btu/lbm	P&T	9
Function ϕ	psia-ft^3/btu	P&T	9
Isochor	psia/°R	P&T	9
Isotherm	psia-ft^3/btu	P&T	9
Pressure	Psia	T&ρ	9
Specific Heat, C_p	btu/lbm-°R	P&T	9
Specific Heat, C_v	btu/lbm-°R	P&T	9
Thermal Conductivity	btu(ft/hr)/ ft^2/°R	P&T	9
Temperature	°R	P&ρ	9
Viscosity	lbf-hr/ft^2	P&T	9

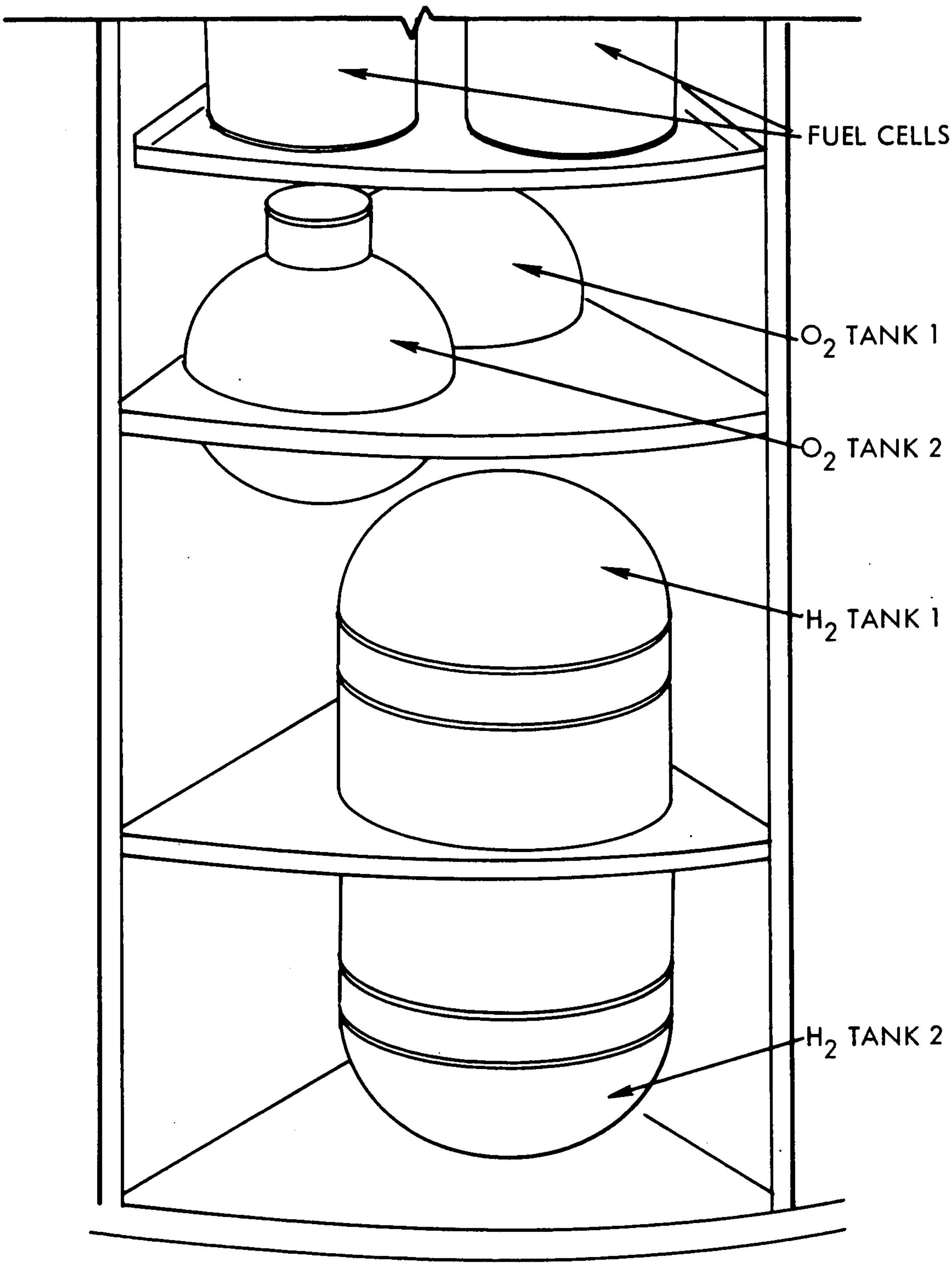

FIGURE 1. SM SECTOR IV CSS TANKAGE ARRANGEMENT

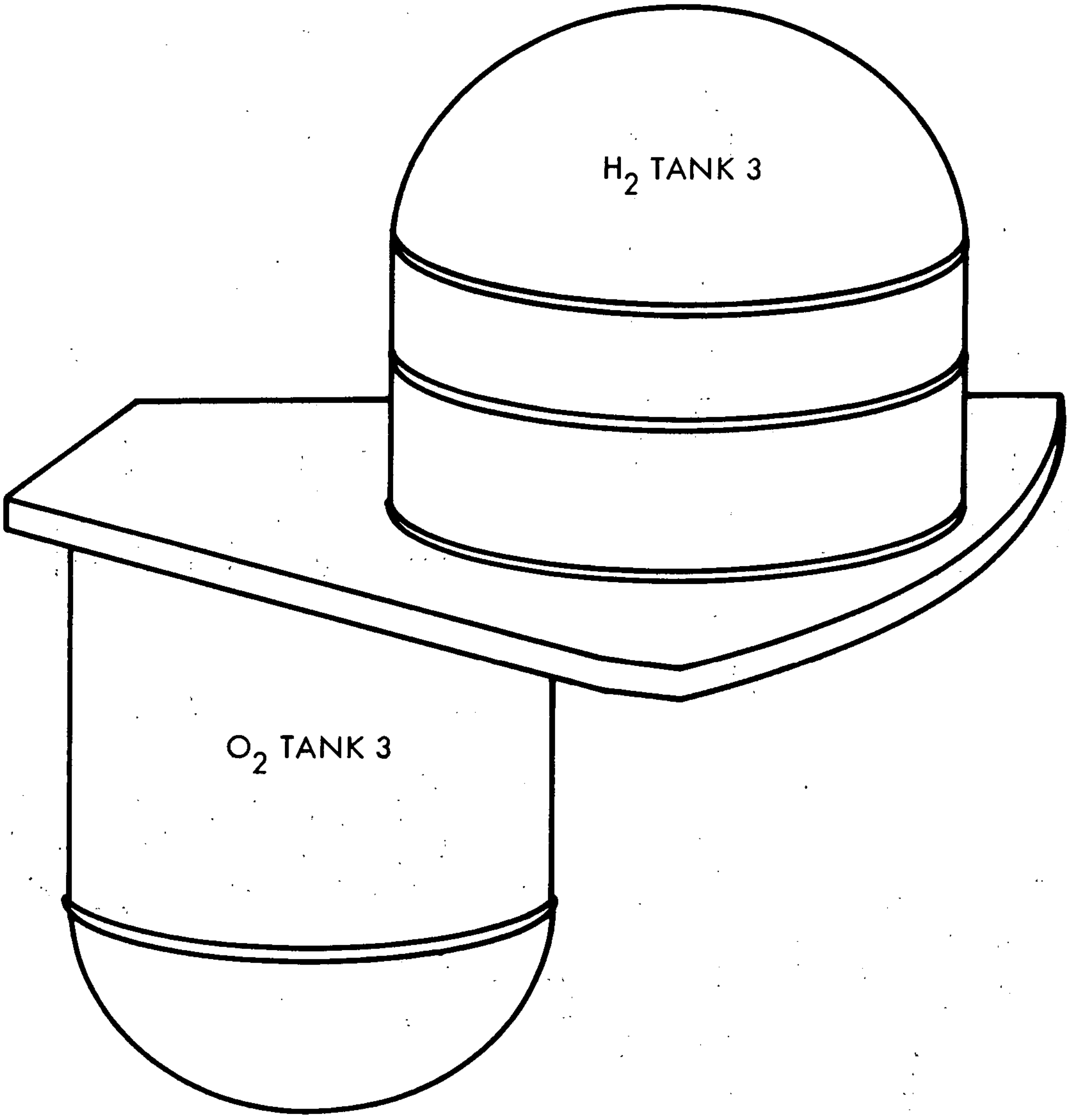

FIGURE 2. SM SECTOR I CSS TANKAGE ARRANGEMENT

FIGURE 3

APOLLO 14 CRYOGENIC STORAGE SYSTEM

OXYGEN SCHEMATIC

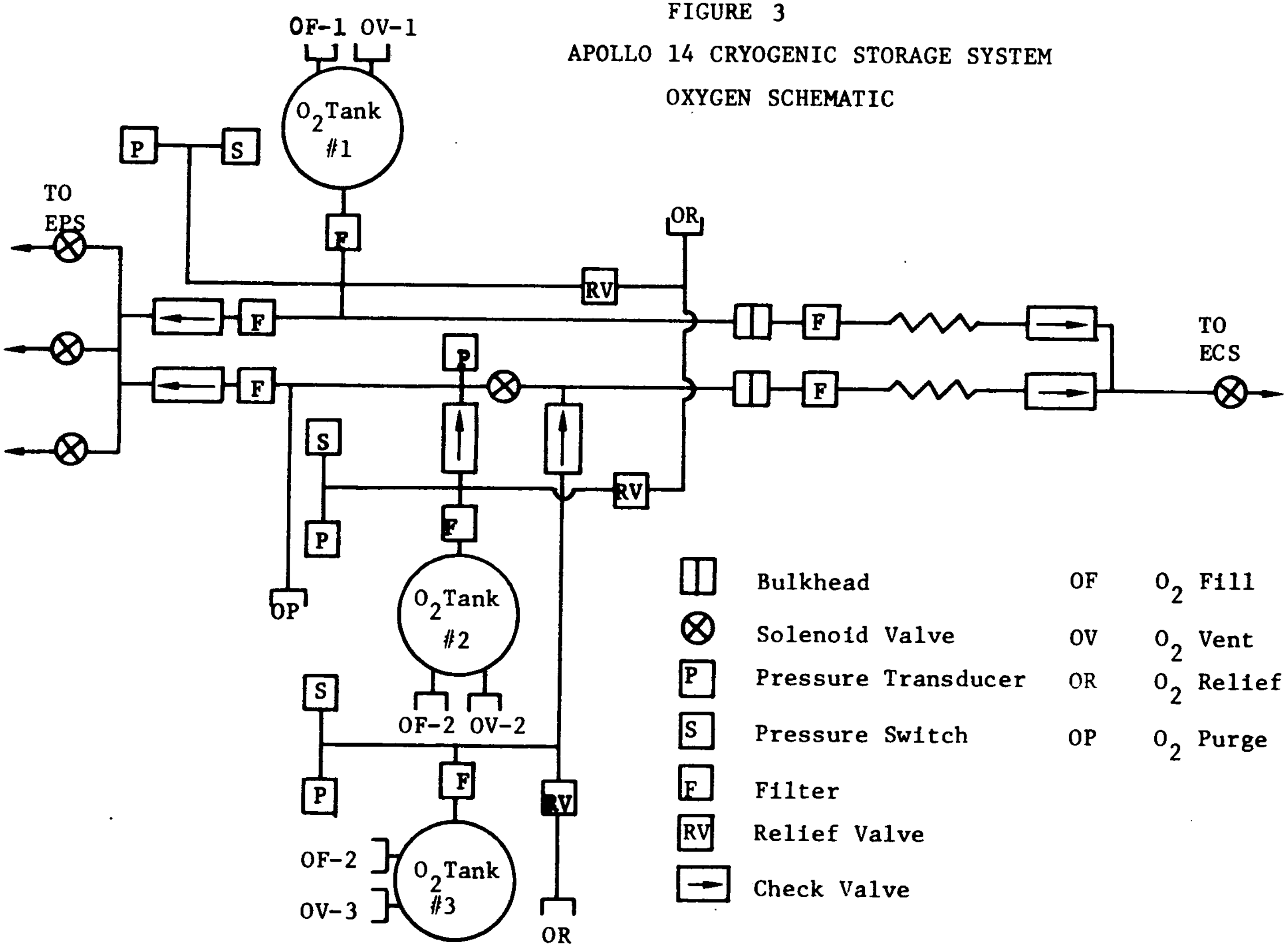

FIGURE 4
APOLLO 14 CRYOGENIC STORAGE SYSTEM
HYDROGEN SCHEMATIC

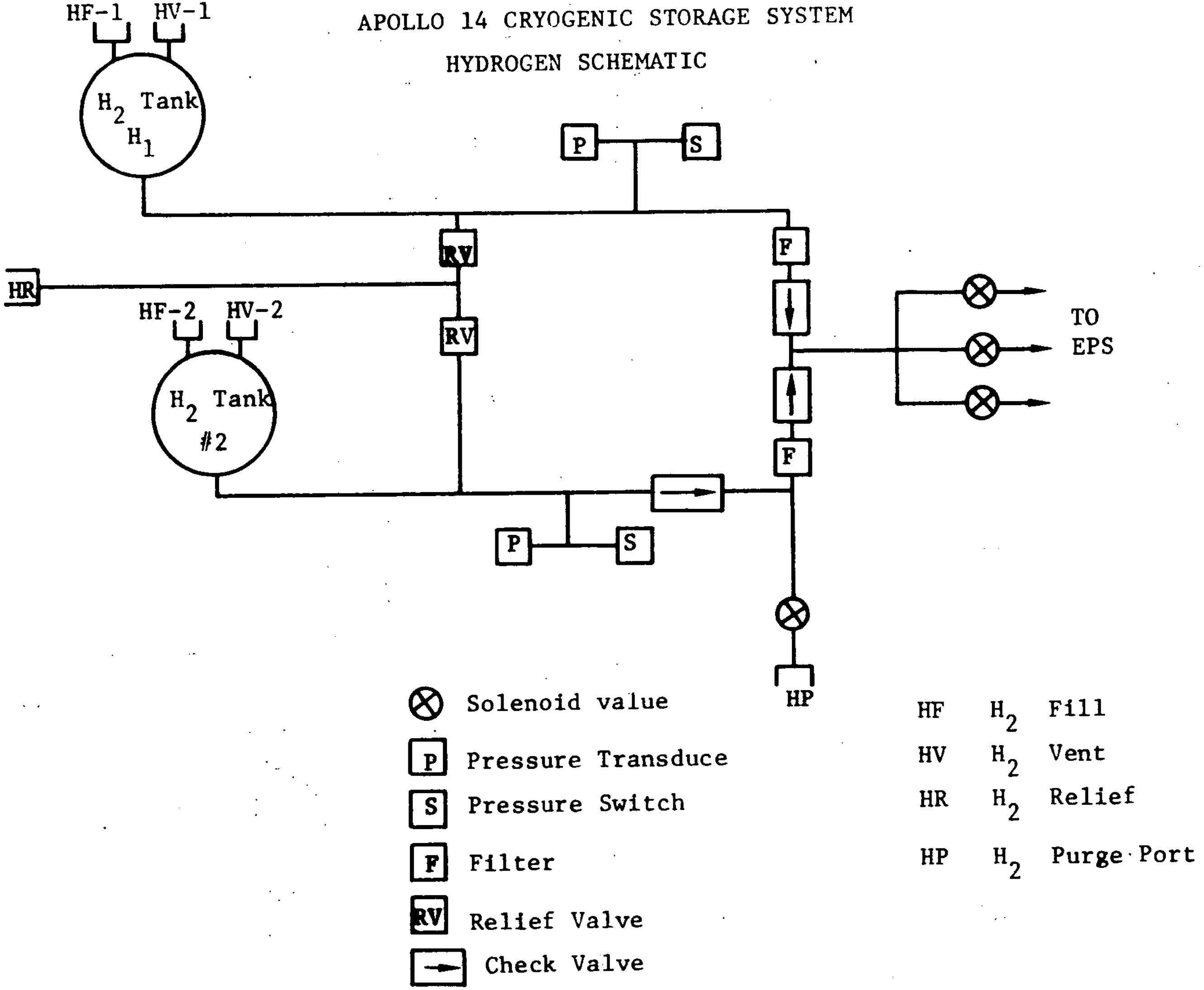

FIGURE 5

APOLLO J TYPE CRYOGENIC STORAGE SYSTEM

OXYGEN SCHEMATIC

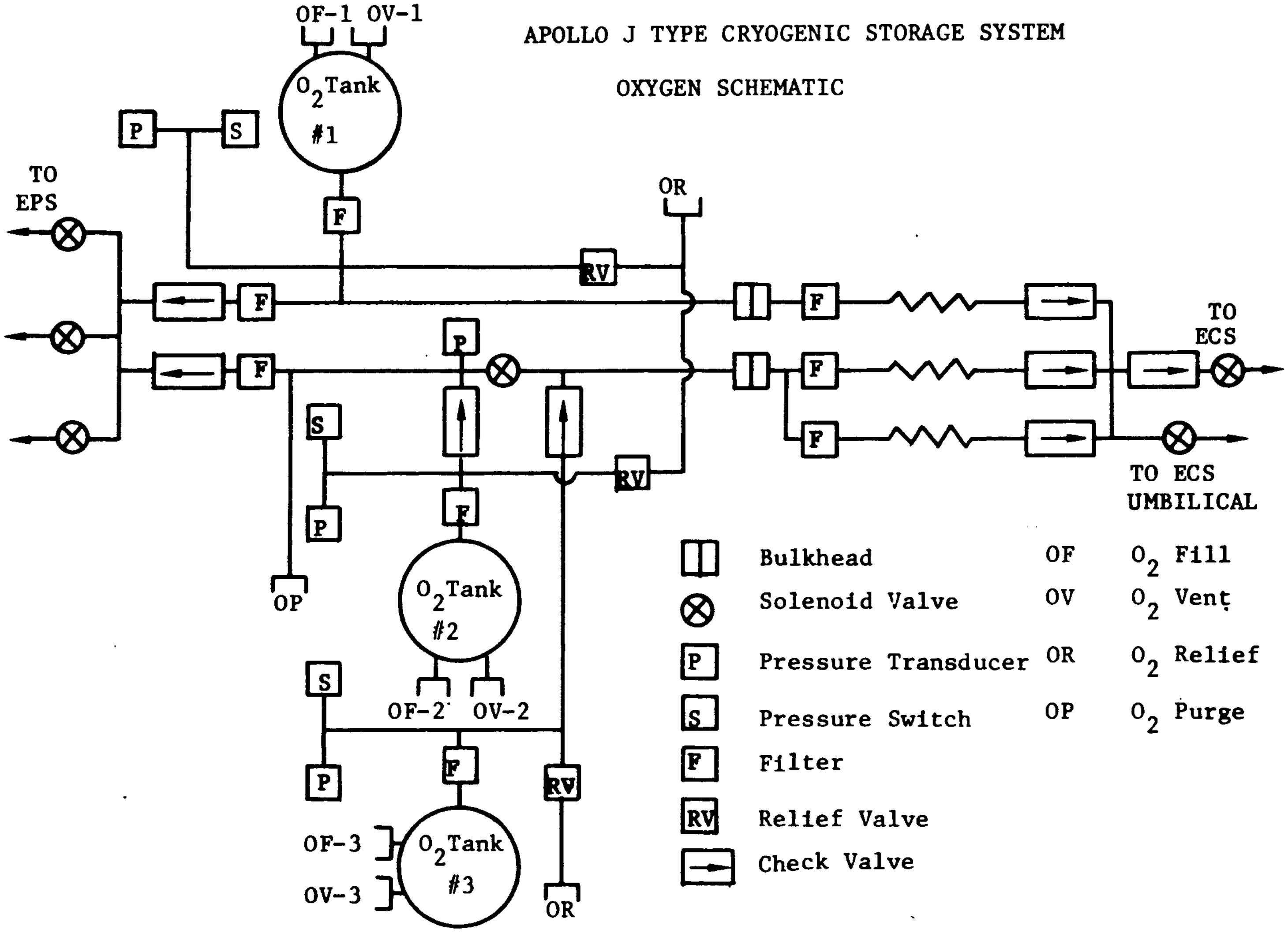

FIGURE 6
APOLLO J TYPE CRYOGENIC STORAGE SYSTEM
HYDROGEN SCHEMATIC

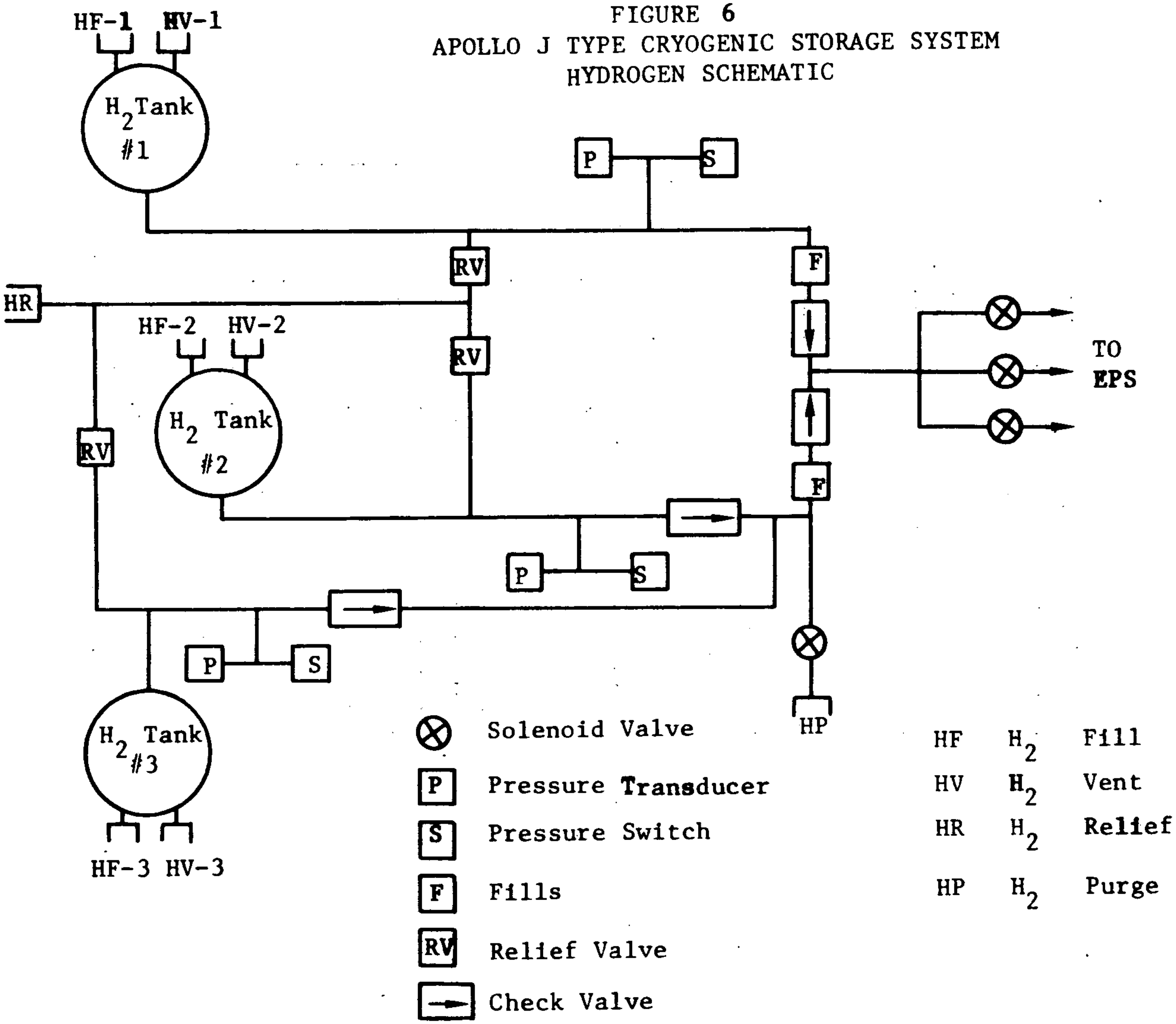

FIGURE 7

INTEGRATED SYSTEMS PROGRAM
FLOW DIAGRAM

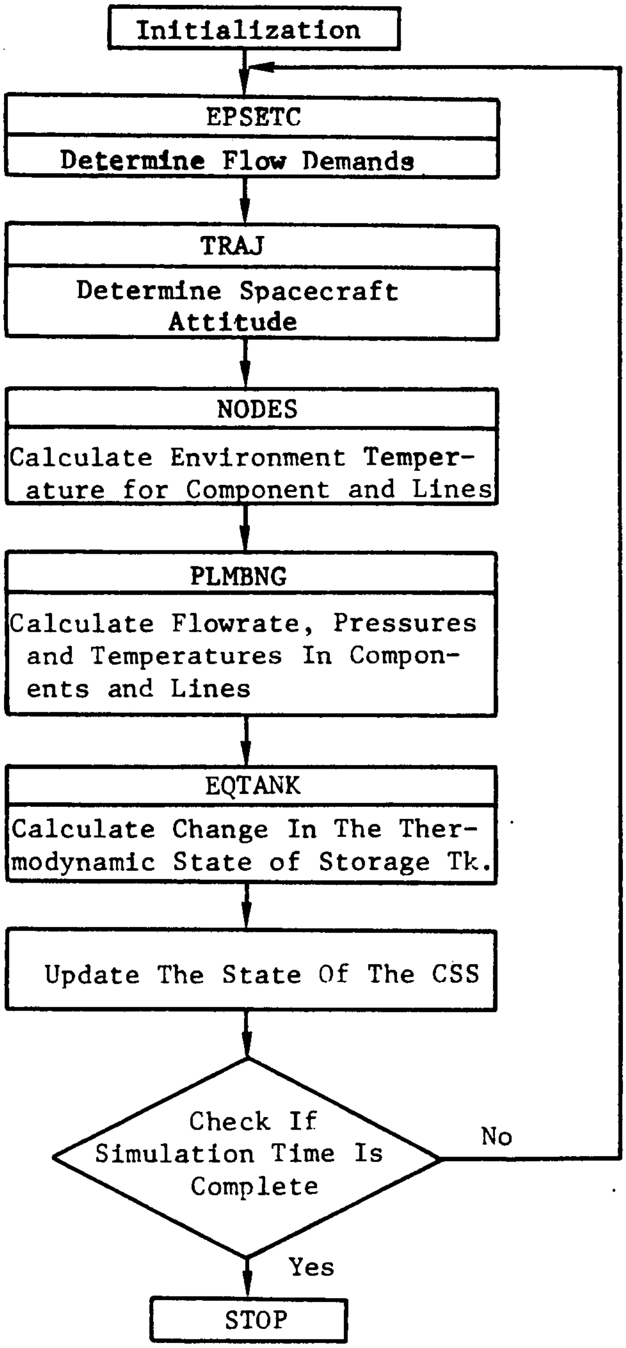

FIGURE 8

STORAGE TANK MODEL

FLOW DIAGRAM

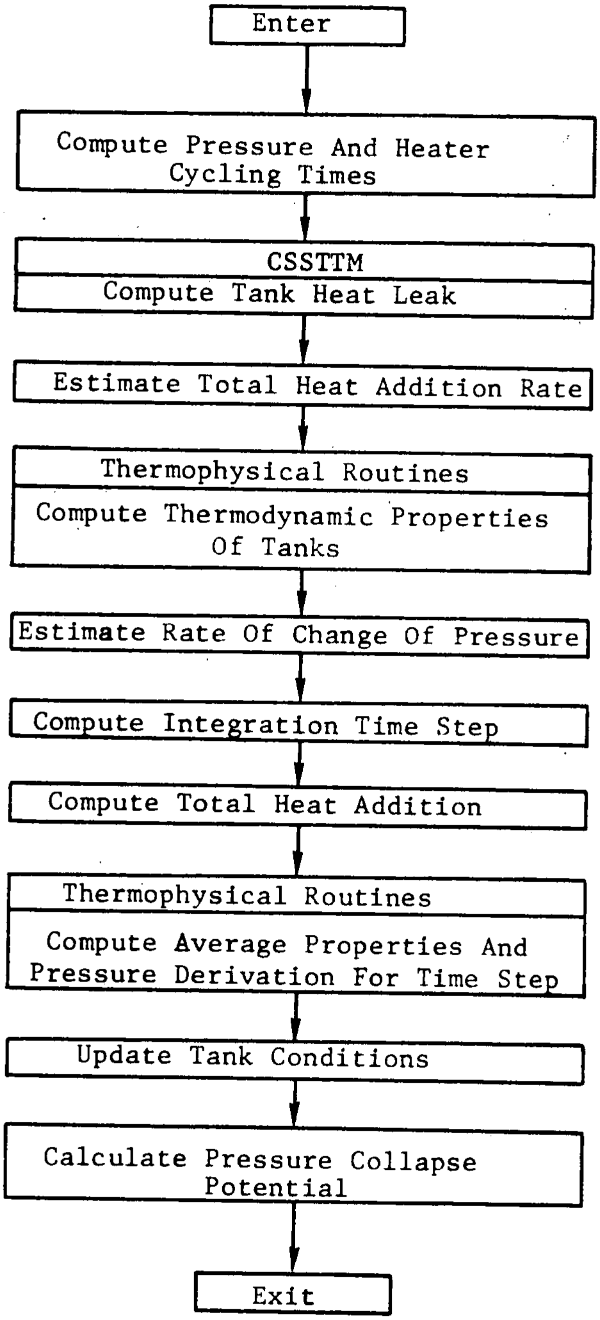

FIGURE 9

OXYGEN TANK NODAL MODEL

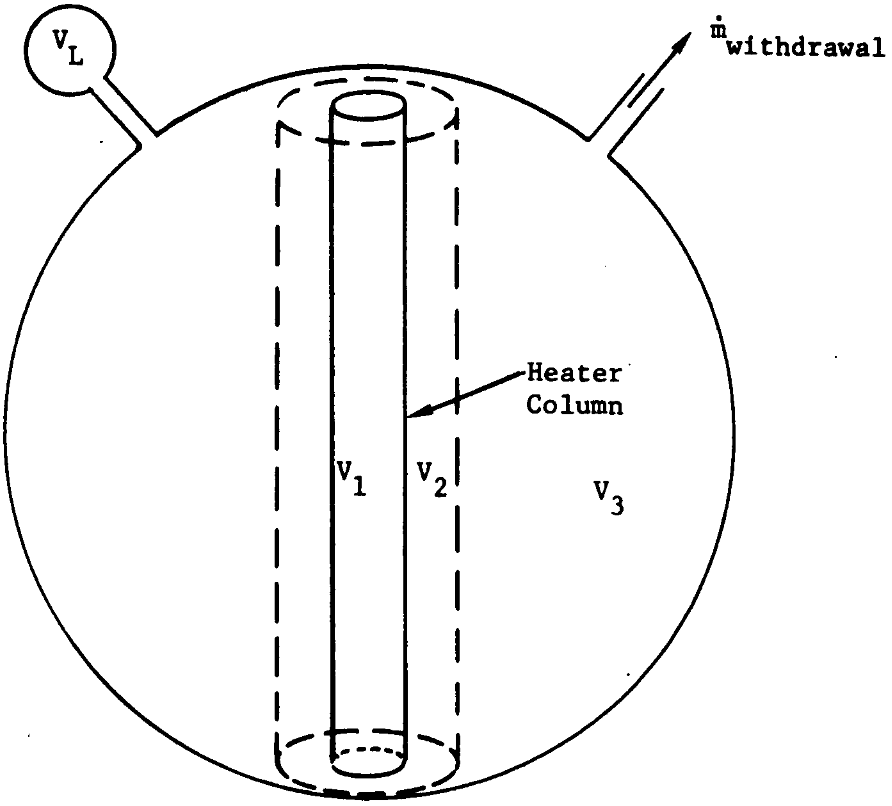

FIGURE 10

J TYPE COMPONENT AND LINES

MODEL FLOW DIAGRAM

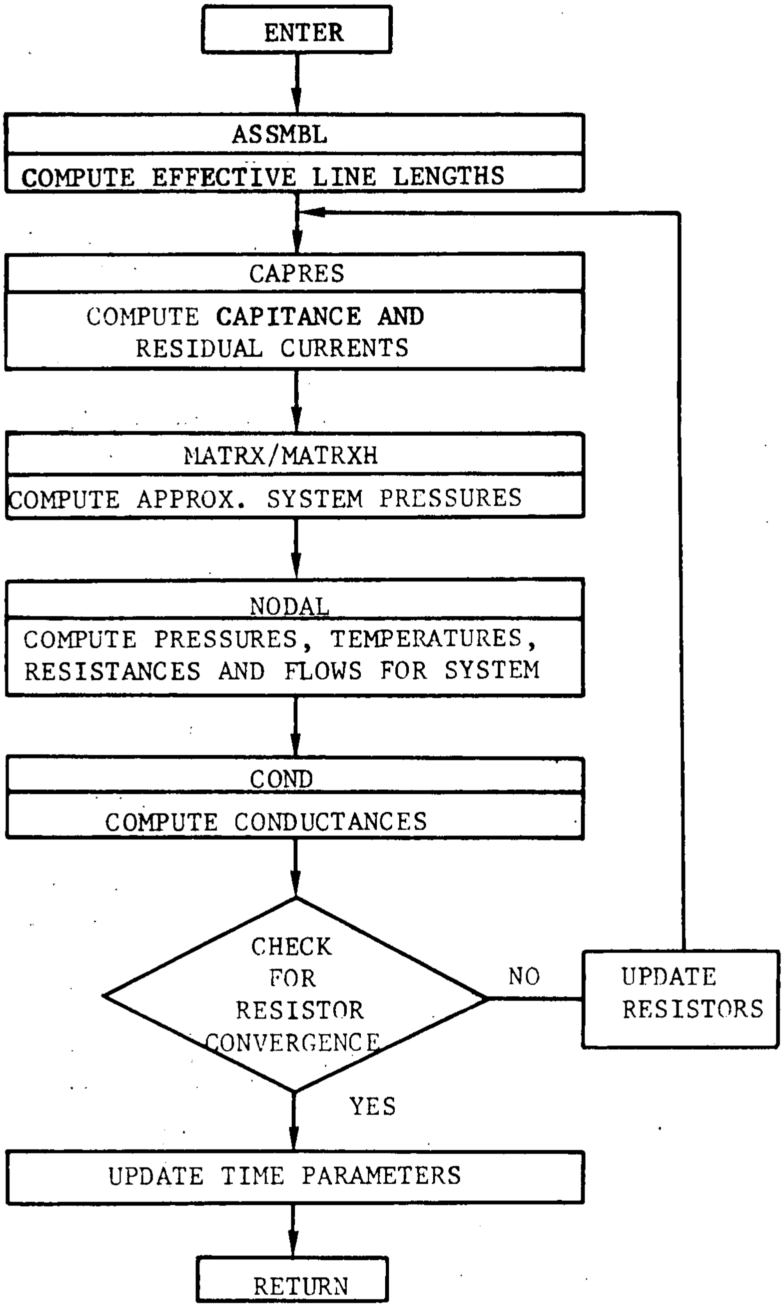

FIGURE 11

ELECTRICAL ANALOG OF THE OXYGEN SYSTEM
FOR THE MATRIX MODEL

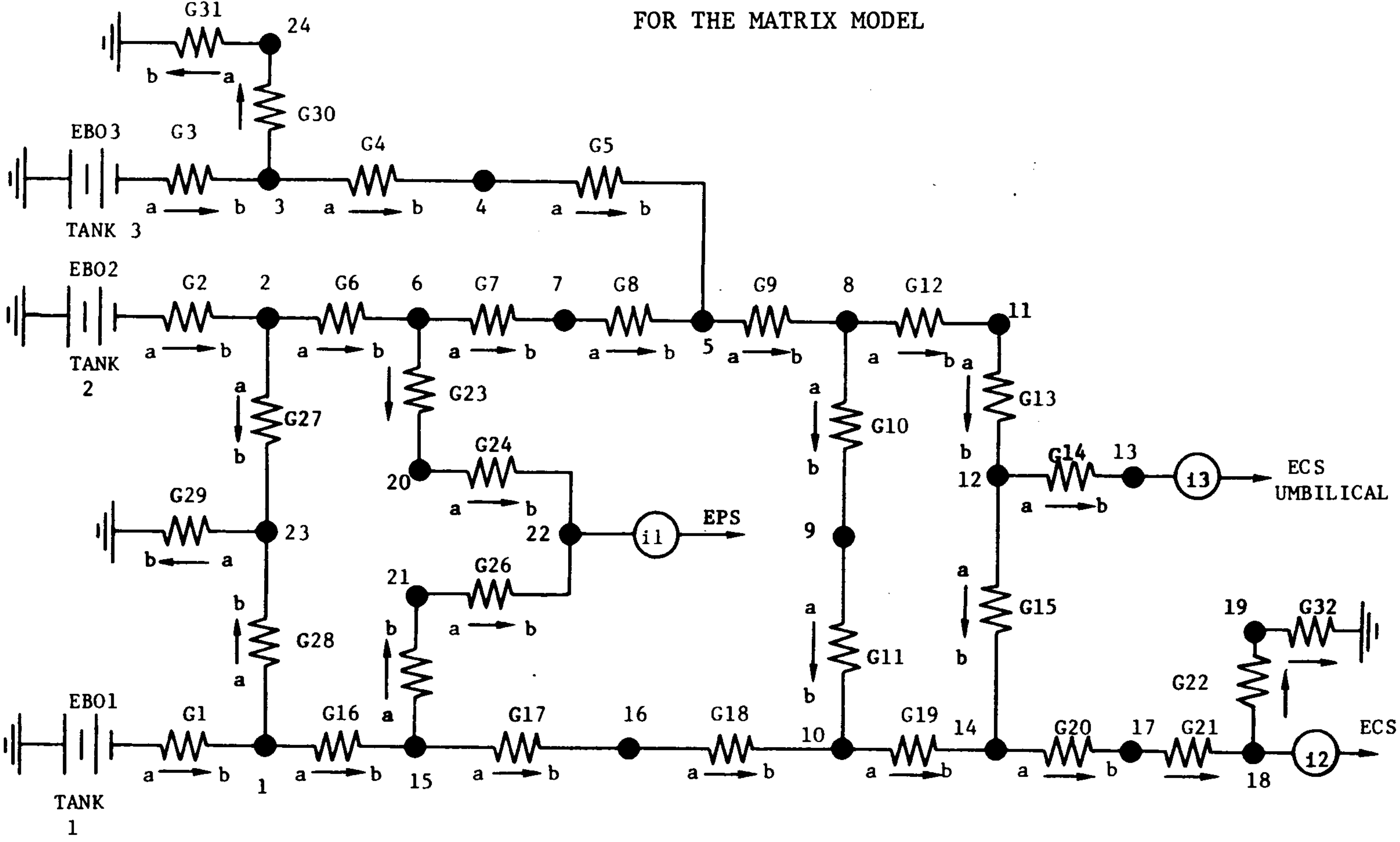

a	Upstream
b	Downstream
EBOx	Electrical Potential Analog in tanks
Gx	Conductance analog
(ix)	Flow Demand
●	Matrix Nodes

FIGURE 12

ELECTRICAL ANALOG OF THE HYDROGEN SYSTEM
FOR THE MATRIX MODEL

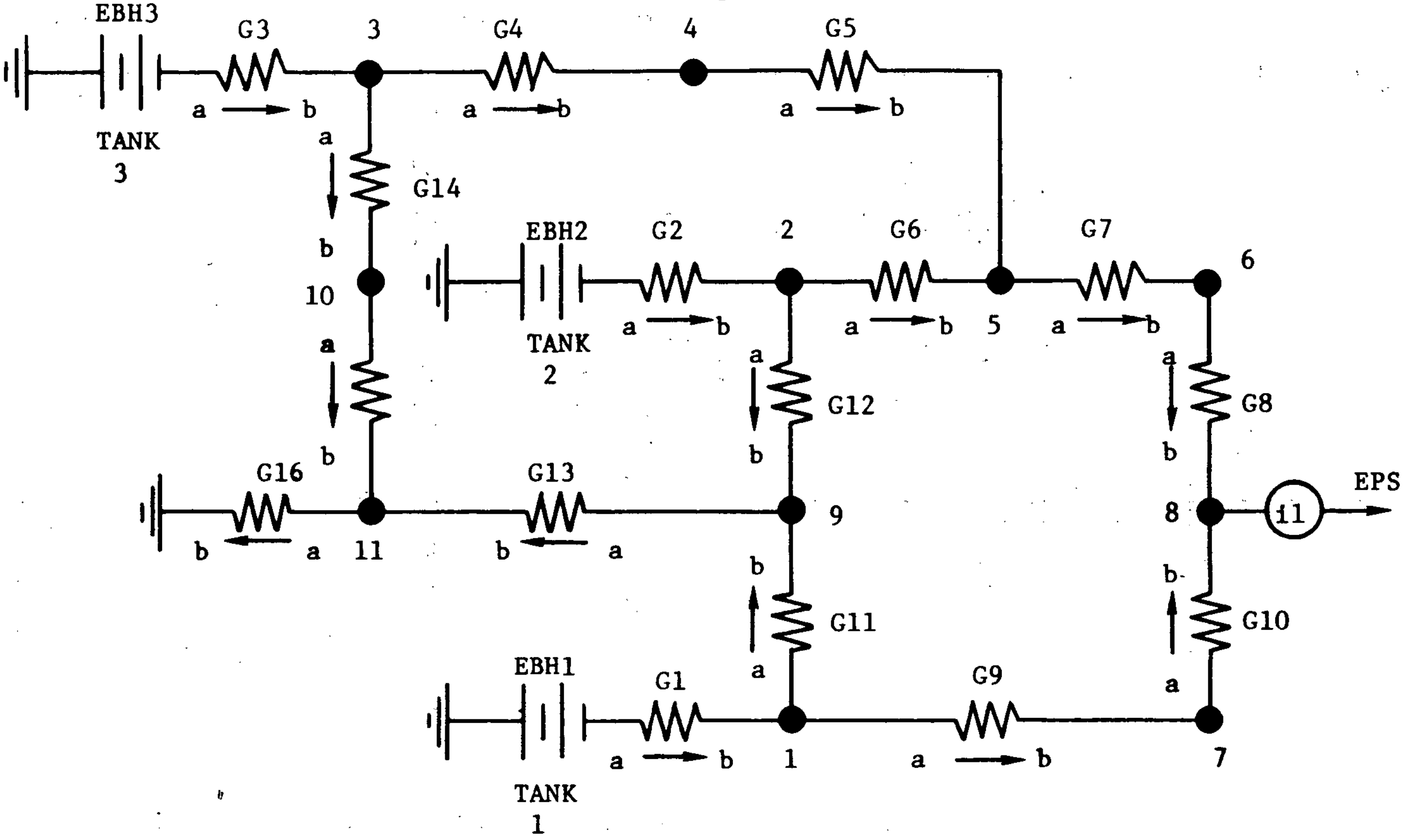

a Upstream

b Downstream

EBH2 Electrical Potential analog for tanks

Gx Conductance Analog

ⓘⓧ Flow Demand

● Matrix Nodes

FIGURE 13
ELECTRICAL ANALOG OF THE OXYGEN SYSTEM FOR THE NODAL MODEL

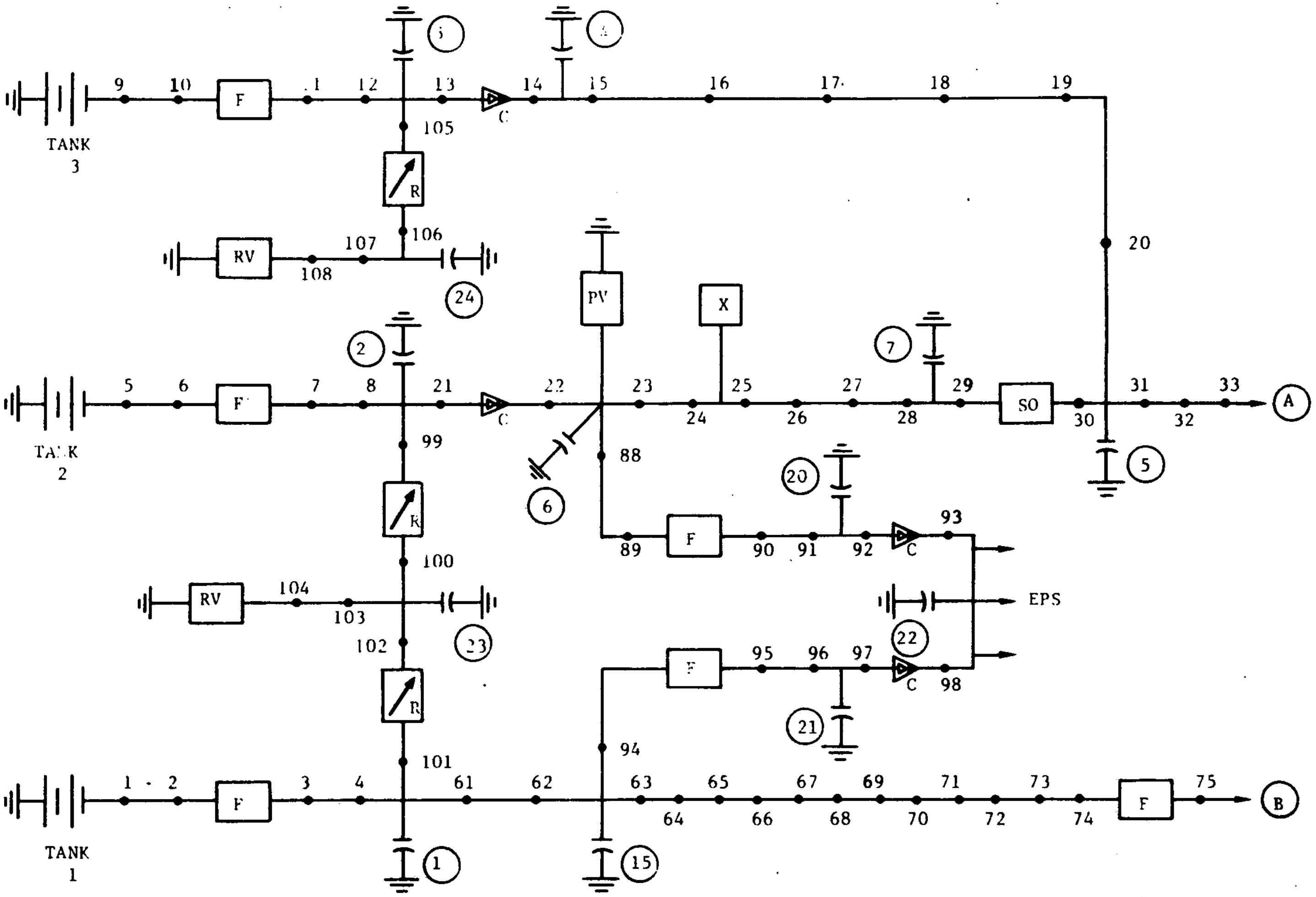

C - Check Valve
F - Filter
R - Relief Valve
RV - Relief Vent
PV - Purge Vent
X - Purge Port
SO - Shutoff Valve
○ - Matrix Nodes

FIGURE 13 (Cont'd)

ELECTRICAL ANALOG OF THE OXYGEN SYSTEM FOR THE NODAL MODEL

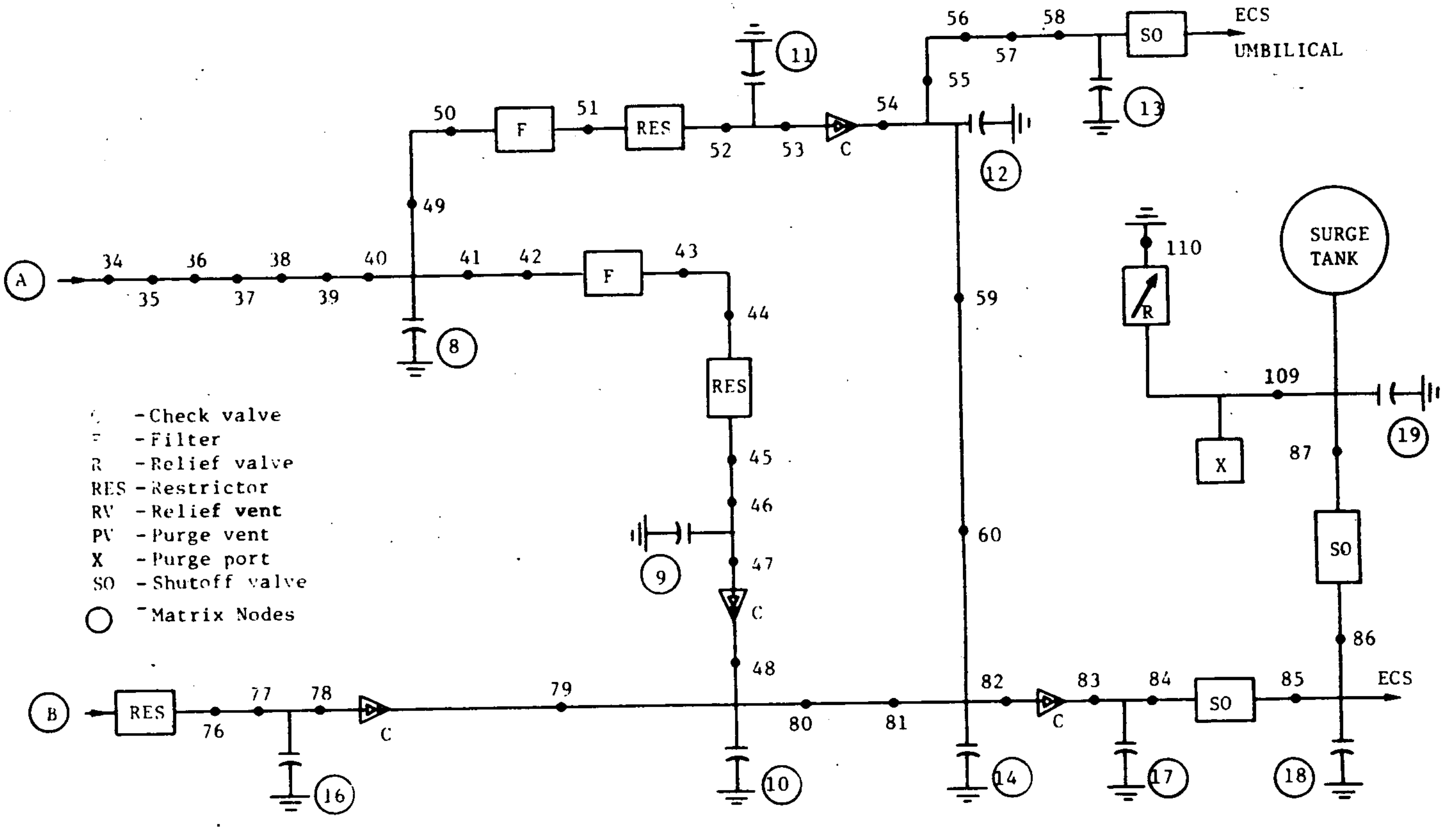

FIGURE 14

ELECTRICAL ANALOG OF THE HYDROGEN SYSTEM FOR THE NODAL MODEL

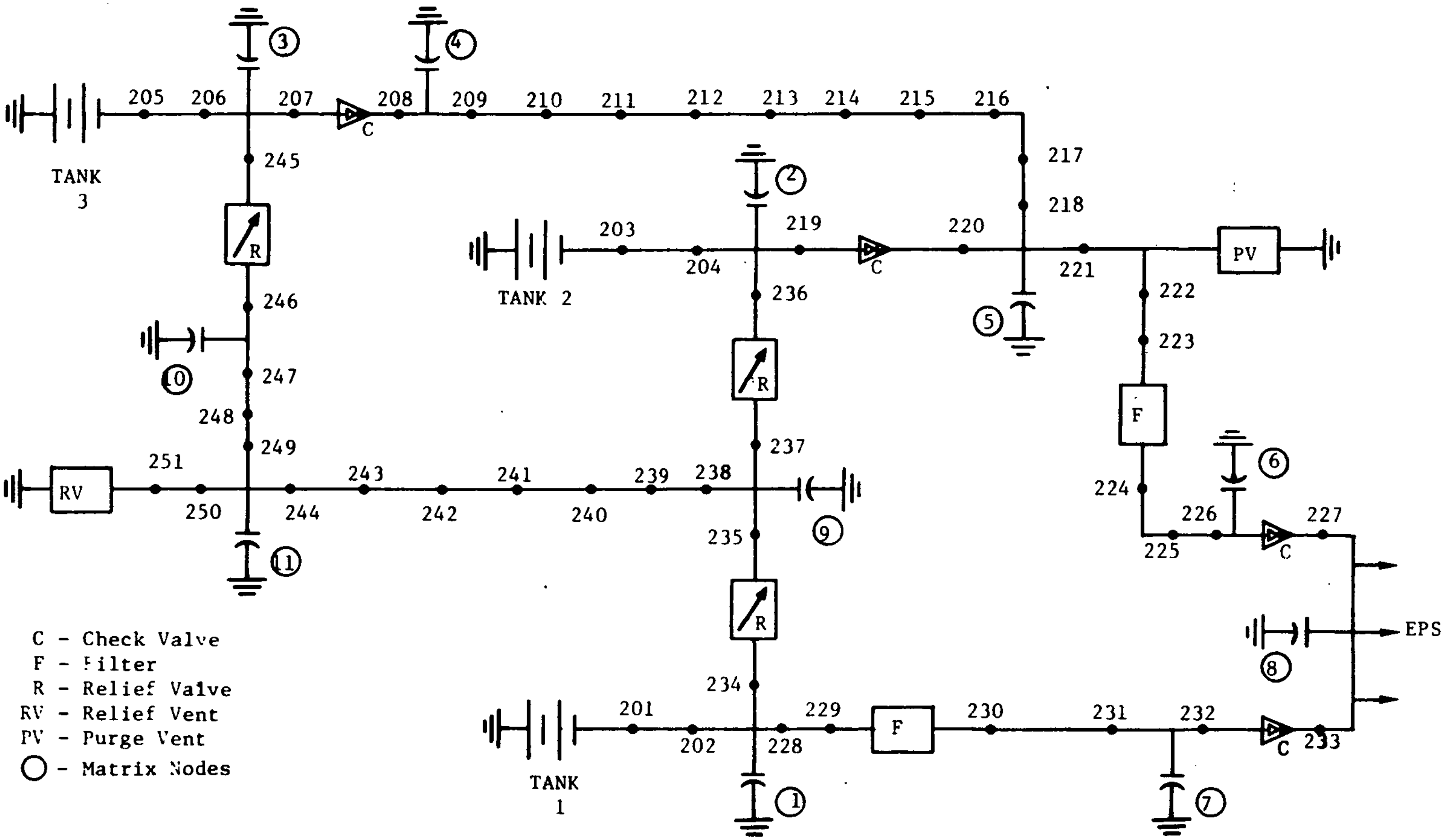

FIGURE 15
EQUIVALENT L/D FOR BEND LOSSES*

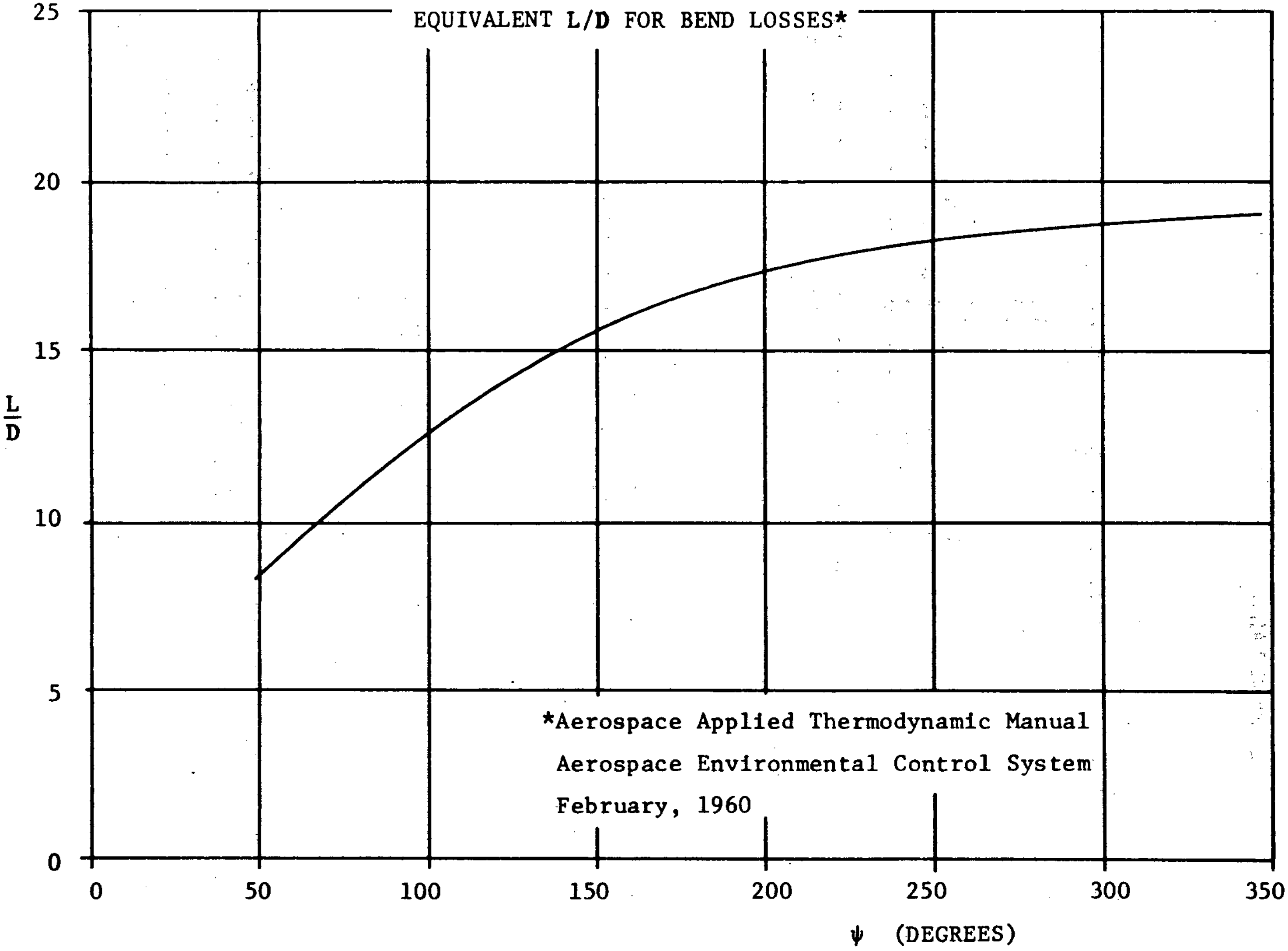

*Aerospace Applied Thermodynamic Manual
Aerospace Environmental Control System
February, 1960

FIGURE 16

CHECK VALVE RESISTANCE CHARACTERISTICS

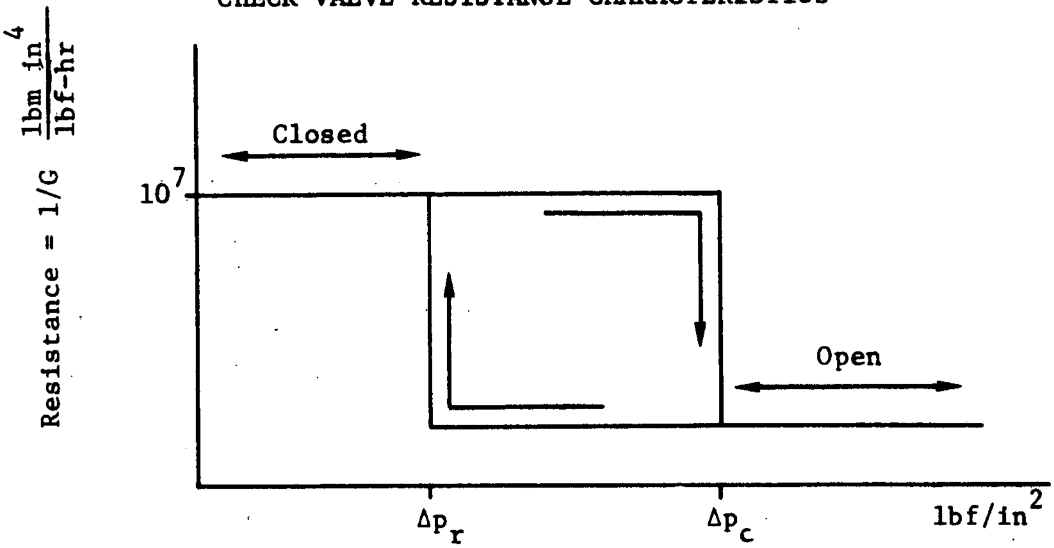

FIGURE 17

RELIEF VALVE RESISTANCE CHARACTERISTICS

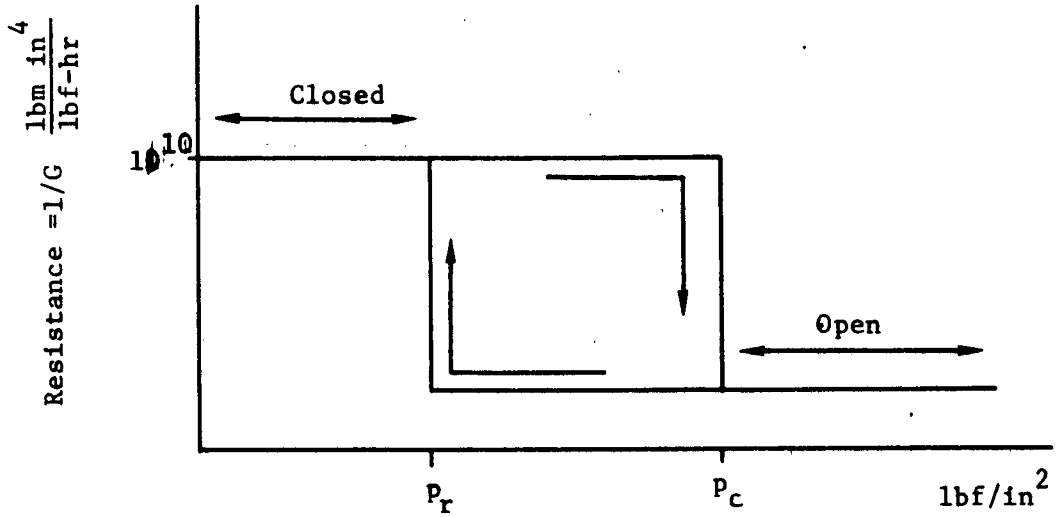

FIGURE 18

RESTRICTOR PRESSURE DROP*

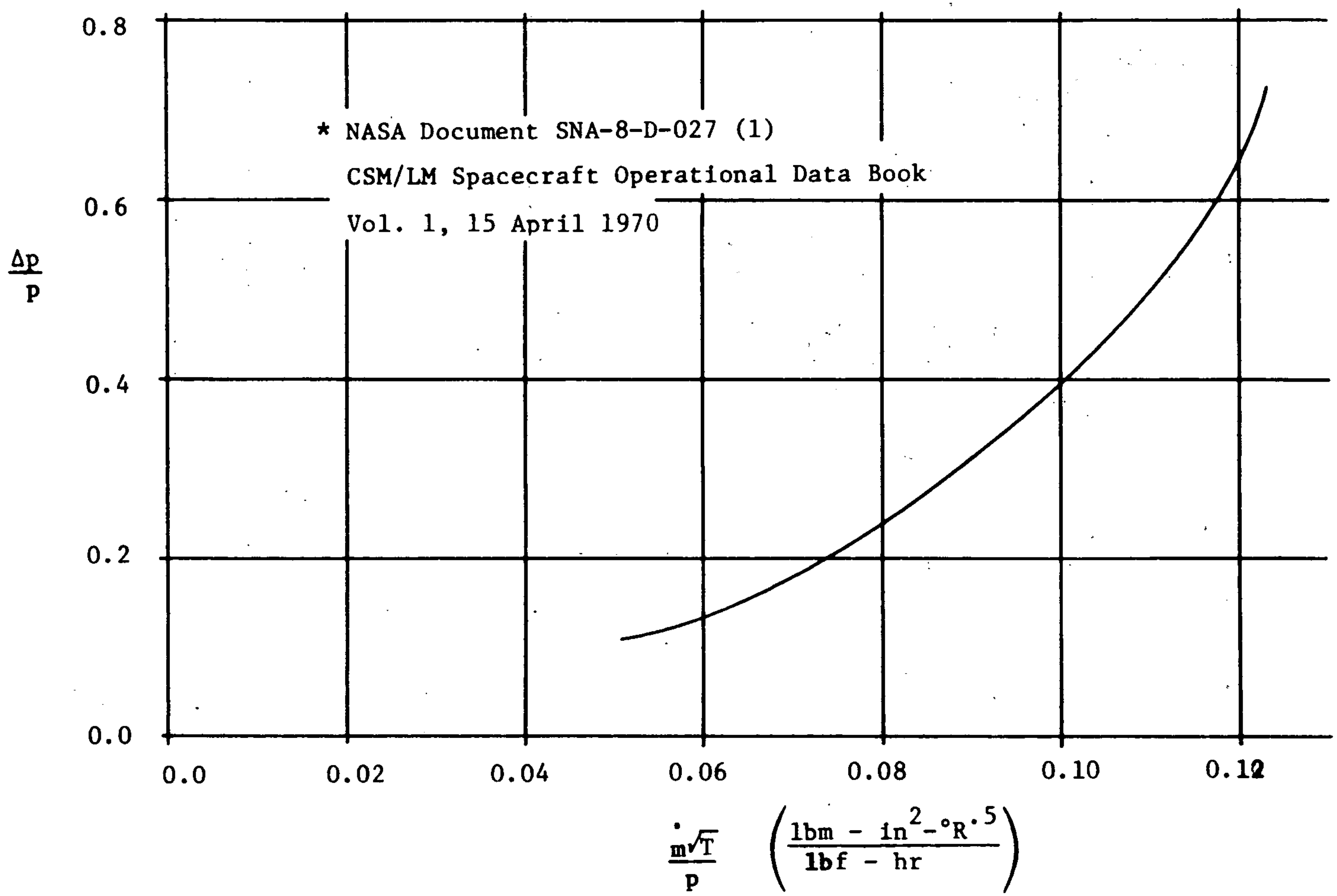

* NASA Document SNA-8-D-027 (1)
CSM/LM Spacecraft Operational Data Book
Vol. 1, 15 April 1970

FIGURE 19

HYDROGEN TANK HEAT LEAK

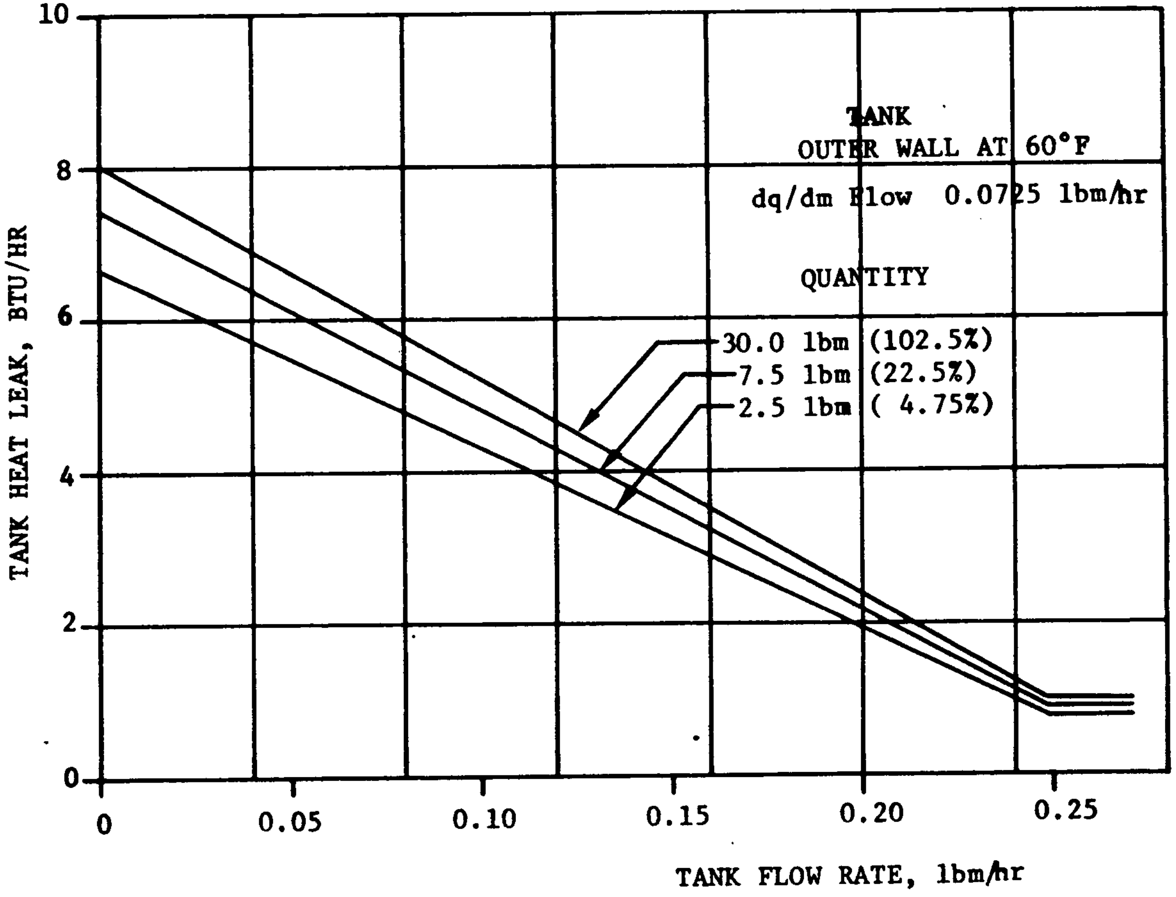

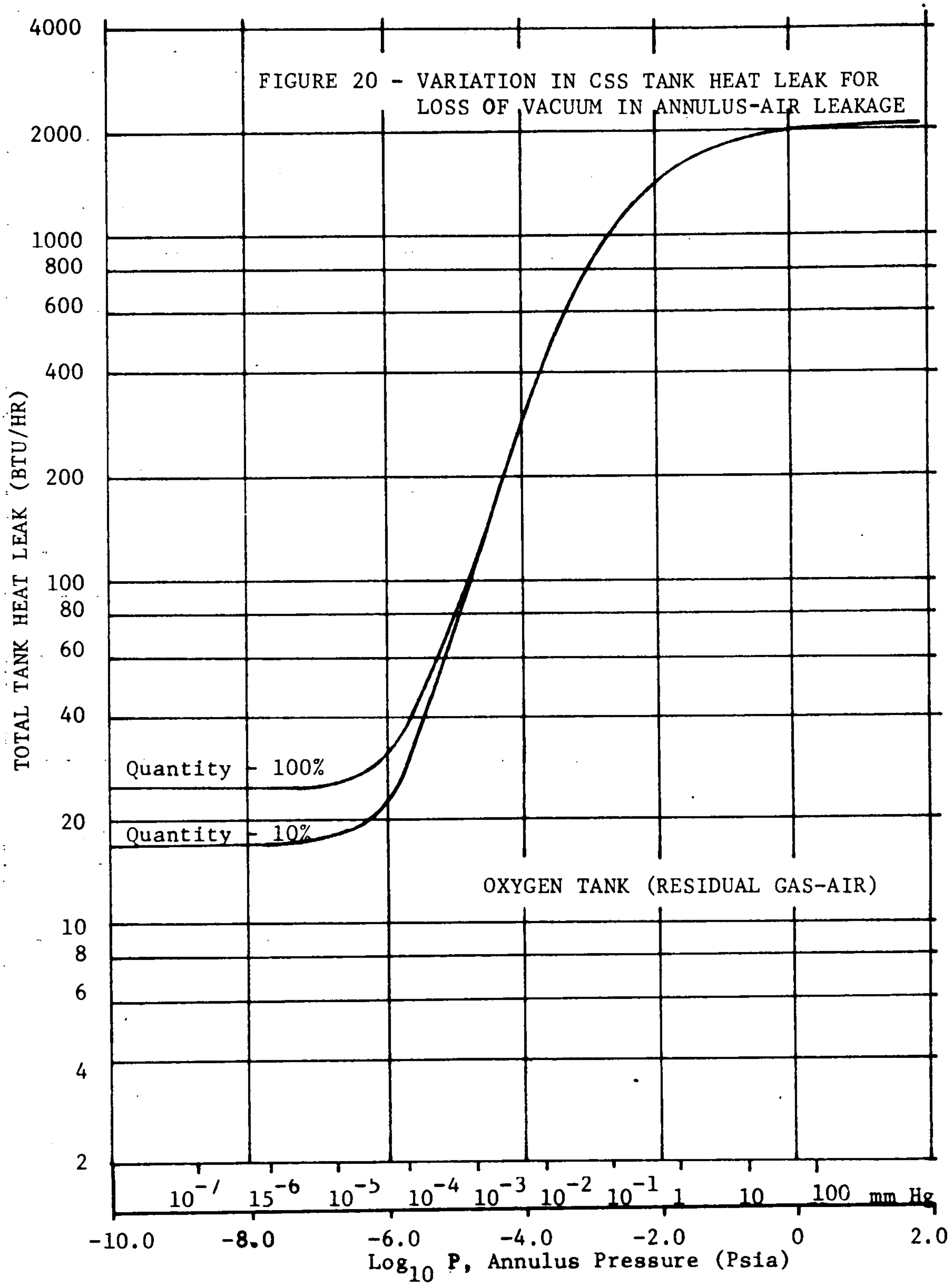
FIGURE 20 - VARIATION IN CSS TANK HEAT LEAK FOR LOSS OF VACUUM IN ANNULUS-AIR LEAKAGE

FIGURE 21- Variation of CSS Tank Heat Leak for Loss of Annulus Vacuum - Hydrogen or Oxygen Leakage

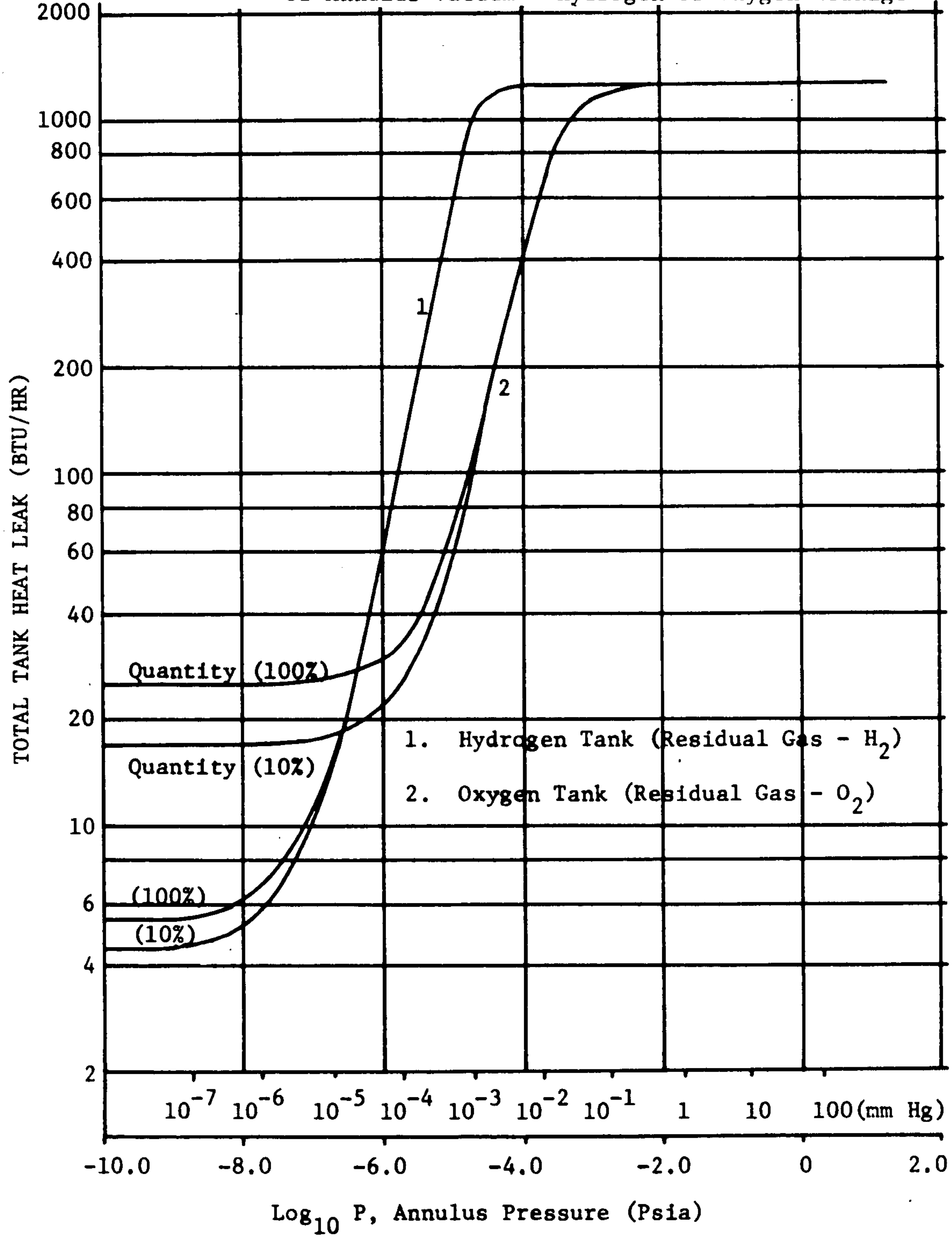

APPENDIX I

NOMENCLATURE

A	Area, in^2.
A_c	Accommodation coefficient, equal to 1.0.
C	Capacitance analog, $C = \frac{V}{2RTp}$, lbm - in^4/lbf^2
c_p	Specific heat of fluid at constant pressure, btu/(lbm-°R).
c_v	Specific heat of fluid at constant volume, btu/(lbm - °R).
d	Wall thickness, in.
D	Line diameter, in.
E	Electrical potential analog, $E = p^2$, lbf^2/in^4.
En	Energy of system
f	Friction factor, dimensionless.
G	Conductance analog lbf^2-hr/(lbm-in^4)
g_c	Gravity constant lbm-in/(lbf-hr^2)
h	Enthalpy of stored fluid, btu/lbm
h'	Enthalpy at initial state, btu/lbm
h_{vcs}	Enthalpy of fluid in vapor cooled shroud, btu/lbm.
I	Current analog, $I = \dot{m}$, lbm/hr.
I_R	Residual current analog, $I_R = \frac{pV}{RT^2} = \frac{dT}{dt}$, lbm/hr.
k	Thermal conductivity, btu/(hr-ft-°R).
K	Constant, $K = \left(\frac{g_c n}{R}\right)^{1/2} \left(\frac{n+1}{2}\right)^{-\frac{n+1}{2(n-1)}}$, lbm-°R$^{1/2}$/(lbf-hr).
K_n	Knudsen number, λ/l, dimensionless.
l	Characteristic length, ft.

L	Length, in.
M	Gas molecular weight, lbm/(lb-mole)
m	Mass, lbm.
$\dot{m}$	Mass flowrate, lbm/hr.
n	Ratio of specific heats, c_p/c_v, dimensionless.
N	Polytropic exponent for gas lines attached to tank, dimensionless.
N_{RE}	Reynolds number, $\frac{\rho V D}{\mu}$, dimensionless.
P,p	Pressure, psia
q	Total heat input rate, btu/hr.
$\dot{q}$	Heat leak flux, btu/(hr-ft^2)
Q_r	Radiation heat leak, btu/hr.
r	Mean pressure vessel radius, in.
R	Universal gas constant.
R_1	Inner tank wall radius, ft.
R_2	Outer tank wall radius, ft.
s	Fluid velocity, in/hr.
t	Time, hr.
T	Temperature, ^oR.
T_1	Temperature of tank outer wall, ^oR.
T_2	Temperature of tank inner wall, °R.
T_{vcs}	Average temperature of fluid in vapor cooled shroud, °R.
u	Internal energy of fluid, btu/lbm.

U	Overall heat transfer coefficient, btu/(hr-in^2-°R).
v	Specific volume, ft^3/lbm.
V	Tank Volume, ft^3.
V_L	Volume of lines attached to tank, ft^3.
Y	Young's modulus for tank material, psi.
α	Tank material thermal expansion coefficient, 1/°R.
β	Tank thickness, in.
Δ	Difference, dimensionless
ε	Emissivity, dimensionless
θ	Thermodynamic function, $-\rho \frac{\partial H}{\partial \rho}\Big\vert_p$, btu/lbm.
λ	Mean free path, ft.
μ	Viscosity, lbm/ (in-hr).
ρ	Fluid density, lbm/ft^3.
σ	Stephan-Boltzman constant, $= 1.1\text{x}10^{-11}$, btu/(hr-in^2-°R^4).
ν	Poisson's ratio for tank material, dimensionless.
ϕ	Thermodynamic function, $\frac{1}{\rho} \frac{\partial p}{\partial u}\Big\vert_\rho$ psia-ft^3/btu.
ψ	Line bend angle, degrees.

Subscripts

c	Cracking
i	Inlet
j	Outlet
k	Arbitrary Line or node
l	Arbitrary line or node
LM	Logarithmic mean
r	Reseat
R	Residual
s	Sink

APPENDIX II

DERIVATION OF dp/dt FOR VARIABLE VOLUME TANKS DUE TO PRESSURE AND TEMPERATURE CHANGES

Introduction.

An expression for the rate of change of pressure for the cryogenic storage tanks has been developed for a constant volume (Reference A-1) and for a variable volume caused by tank stretch due to pressure changes (Reference A-2). The latter expression is:

$$\frac{dp}{dt} = \frac{\frac{\phi\Theta}{V}\dot{m} + \frac{\phi}{V}\; q}{1 + \frac{3\Theta\phi\rho r}{2dY}\;(1-\upsilon)} \qquad \text{(AII-1)}$$

where:

$$\Theta = -\rho \left(\frac{\partial h}{\partial \rho}\right)_p \qquad \text{(AII-2)}$$

$$\phi = \frac{1}{\rho}\left(\frac{\partial p}{\partial u}\right)_\rho \qquad \text{(AII-3)}$$

If Young's Modulus, Y, is taken as infinity (no tank stretch), Equation (AII-1) reduces to the expression for dp/dt as presented in Reference A-1.

The expression for dp/dt considering variable volume resulting from tank stretch due to both pressure and temperature changes is developed in this Appendix. For completeness, a portion of the derivation from Reference A-2 is also presented.

Derivation.

The First Law of Thermodynamics may be written:

$$\frac{dEn}{dt} = q + \dot{m}\, h' - p\,\frac{dV}{dt}$$

If it is assumed that the system is at uniform pressure, p, and that kinetic and potential energy may be neglected, then

$$En = mu = \rho V u$$

and

$$\frac{d(\rho Vu)}{dt} = q + \dot{m}\,h' - p\frac{dV}{dt}$$

$$\frac{ud(\rho V)}{dt} + \rho V\frac{du}{dt} = q + \dot{m}\,h' - p\frac{d(mv)}{dt}$$

Now

$$u = h - pv.$$

Then

$$\frac{udm}{dt} + \rho V\frac{d(h-pv)}{dt} = q + \dot{m}\,h' - \frac{pmdv}{dt} - \frac{pvdm}{dt}$$

$$u\dot{m} + \rho V\,\frac{dh}{dt} - \rho V\,\frac{d(pv)}{dt} = q + \dot{m}\,h' - pm\,\frac{dv}{dt} - p\,v\,\dot{m}$$

$$\dot{m}\,(u + pv) + \rho V\,\frac{dh}{dt} - \rho Vp\,\frac{dv}{dt} - \rho Vv\,\frac{dp}{dt} = q + \dot{m}\,h' - pm\,\frac{dv}{dt}$$

$$\dot{m}\,h + \rho V\,\frac{dh}{dt} - m\,\cancel{p\,\frac{dv}{dt}} - V\,\frac{dp}{dt} = q + \dot{m}\,h' - p\,\cancel{m\,\frac{dv}{dt}}$$

$$V\,\frac{dp}{dt} = \rho\,V\,\frac{dh}{dt} - q + \dot{m}\,(h - h')$$

$$\frac{dp}{dt} = \rho\,\frac{dh}{dt} - \frac{q}{V} + \frac{\dot{m}}{V}\,(h - h').$$

Since $h \approx h'$, the last term is negligible.

Thus, $\frac{dp}{dt} = \rho\frac{dh}{dt} - \frac{q}{V}$ (AII-4)

Assume that

$$h = h(p,\rho).$$

then

$$dh = \left.\frac{\partial h}{\partial p}\right|_{\rho} dp + \left.\frac{\partial h}{\partial \rho}\right|_{p} d\rho$$

$$\frac{dh}{dt} = \left.\frac{\partial h}{\partial p}\right|_{\rho} \frac{dp}{dt} + \left.\frac{\partial h}{\partial \rho}\right|_{p} \frac{d\rho}{dt} .$$

Now,

$$V = \frac{m}{\rho}$$

and $$\frac{d\rho}{dt} = \frac{d\left(\frac{m}{V}\right)}{dt} = \frac{1}{V}\frac{dm}{dt} - \frac{m}{V^2}\frac{dV}{dt} = \frac{\rho}{m}\frac{dm}{dt} - \frac{\rho}{V}\frac{dV}{dt} .$$

So,

$$\frac{dh}{dt} = \left.\frac{\partial h}{\partial p}\right|_{\rho} \frac{dp}{dt} + \left.\frac{\partial h}{\partial \rho}\right|_{p} \left[\frac{\rho}{m}\frac{dm}{dt} - \frac{\rho}{V}\frac{dV}{dt}\right].$$

Substituting for Θ from Equation (AII-2)

$$\frac{dh}{dt} = \left.\frac{\partial h}{\partial p}\right|_{\rho} \frac{dp}{dt} - \frac{\Theta}{m}\dot{m} + \frac{\Theta}{V}\frac{dV}{dt}$$

Since $h = u + pv = u + \frac{p}{\rho}$,

then $$\left.\frac{\partial h}{\partial p}\right|_{\rho} = \left.\frac{\partial u}{\partial p}\right|_{\rho} + \left.\frac{\partial\left(\frac{p}{\rho}\right)}{\partial p}\right|_{\rho}$$

$$\left.\frac{\partial h}{\partial p}\right|_{\rho} = \left.\frac{\partial u}{\partial p}\right|_{\rho} + \frac{1}{\rho}$$

So,

$$\frac{dh}{dt} = \left[\left.\frac{\partial u}{\partial p}\right|_{\rho} + \frac{1}{\rho}\right]\frac{dp}{dt} - \frac{\Theta}{m}\dot{m} + \frac{\Theta}{V}\frac{dV}{dt} .$$

Substituting for Θ from Equation (AII-3)

$$\frac{dh}{dt} = \left[\frac{1}{\rho\phi} + \frac{1}{\rho}\right]\frac{dp}{dt} - \frac{\Theta}{m}\dot{m} + \frac{\Theta}{V}\frac{dV}{dt} . \qquad \text{(AII-5)}$$

It is at this point that the assumption is made that tank stretch is a function of both pressure, p, and temperature, T.

$$\frac{dV}{dt} = \frac{\partial V}{\partial p}\bigg|_T \frac{dp}{dt} + \frac{\partial V}{\partial T}\bigg|_p \frac{dT}{dt} \,. \qquad \text{(AII-6)}$$

It is necessary to determine dT/dt

$$\frac{dT}{dt} = \frac{\partial T}{\partial p}\bigg|_\rho \frac{dp}{dt} + \frac{\partial T}{\partial \rho}\bigg|_p \frac{d\rho}{dt} \,. \qquad \text{(AII-7)}$$

Now, $m = \rho V$

$$\frac{dm}{dt} = \frac{d\rho}{dt} V + \rho \frac{dV}{dt}$$

So, $$\frac{d\rho}{dt} = \frac{\dot{m}}{V} - \frac{\rho}{V}\frac{dV}{dt} \qquad \text{(AII-8)}$$

Substituting Equations (AII-8) into Equation (AII-7), and substituting Equation (AII-7) into Equation (AII-6) results in:

$$\frac{dV}{dt} = \frac{\partial V}{\partial p}\bigg|_T \frac{dp}{dt} + \frac{\partial V}{\partial T}\bigg|_\rho \left[\frac{\partial T}{\partial p}\bigg|_\rho \frac{dp}{dt} + \frac{\partial T}{\partial \rho}\bigg|_p \left(\frac{\dot{m}}{V} - \frac{\rho}{V}\frac{dV}{dt}\right)\right]$$

For convenience, the following substitutions have been made:

$$A = \frac{\partial V}{\partial p}\bigg|_T \qquad B = \frac{\partial V}{\partial T}\bigg|_p$$

$$C = \frac{\partial T}{\partial p}\bigg|_\rho \qquad D = \frac{\partial T}{\partial \rho}\bigg|_p$$

Then,

$$\frac{dV}{dt} = A\frac{dp}{dt} + B\left[C\frac{dp}{dt} + D\left(\frac{\dot{m}}{V} - \frac{\rho}{V}\frac{dV}{dt}\right)\right]$$

$$\frac{dV}{dt} = (A + BC)\frac{dp}{dt} + BD\frac{\dot{m}}{V} - \frac{BD\rho}{V}\frac{dV}{dt}$$

$$\left(1 + \frac{BD\rho}{V}\right) \frac{dV}{dt} = (A + BC) \frac{dp}{dt} + \frac{BD\dot{m}}{V}$$

$$\frac{dV}{dt} = \frac{(A + BC)\dfrac{dp}{dt} + \dfrac{BD\dot{m}}{V}}{1 + \dfrac{BD\rho}{V}} \qquad \text{(AII-9)}$$

Substituting Equation (AII-9) into Equation (AII-5).

$$\frac{dh}{dt} = \left[\frac{1}{\rho\phi} + \frac{1}{\rho}\right] \frac{dp}{dt} - \frac{\Theta}{m}\dot{m} + \frac{\Theta}{V}\left[\frac{(A + BC)\dfrac{dp}{dt} + BD\dfrac{\dot{m}}{V}}{1 + \dfrac{BD\rho}{V}}\right]$$

$$\frac{dh}{dt} = \left[\frac{1}{\rho\phi} + \frac{1}{\rho} + \frac{\Theta(A + BC)}{V+BD\rho}\right] \frac{dp}{dt} - \frac{\Theta\dot{m}}{m} + \frac{\Theta BD\dot{m}}{V(V+BD\rho)} \quad .$$

But from Equation (AII-4)

$$\frac{dh}{dt} = \frac{1}{\rho}\frac{dp}{dt} + \frac{q}{\rho V} \quad .$$

Therefore,

$$\cancel{\frac{1}{\rho}\frac{dp}{dt}} + \frac{q}{\rho V} = \left[\frac{1}{\rho\phi} + \cancel{\frac{1}{\rho}} + \frac{\Theta(A+BC)}{V+BD\rho}\right] \frac{dp}{dt} - \frac{\Theta\dot{m}}{m} + \frac{\Theta BD\dot{m}}{V(V+BD\rho)}$$

and,

$$\left[\frac{1}{\rho\phi} + \frac{\Theta(A+BC)}{V+BD\rho}\right] \frac{dp}{dt} = \frac{\Theta\dot{m}}{m} - \frac{\Theta BD\dot{m}}{V(V+BD\rho)} + \frac{q}{\rho V}$$

resulting in:

$$\frac{dp}{dt} = \frac{\dfrac{\Theta\dot{m}}{\rho V} + \dfrac{q}{\rho V} - \dfrac{\Theta BD\dot{m}}{V(V+BD\rho)}}{\dfrac{1}{\rho\phi} + \Theta\dfrac{(A+BC)}{V+BD\rho}}$$

or,

$$\frac{dp}{dt} = \frac{\frac{\Theta\dot{m}\phi}{V} + \frac{\phi q}{V} - \frac{\Theta\phi BD\dot{m}\rho}{V(V+BD\rho)}}{1 + \frac{\phi\Theta\rho(A+BC)}{V+BD\rho}}$$

Substituting for A, B, C and D

$$\frac{dp}{dt} = \frac{\frac{\Theta\dot{m}\phi}{V} + \frac{\phi q}{V} - \frac{\Theta\phi\dot{m}\rho\,\frac{\partial V}{\partial T}\Big|_p\frac{\partial T}{\partial \rho}\Big|_p}{V(V+\rho\,\frac{\partial V}{\partial T}\Big|_p\,\frac{\partial T}{\partial \rho}\Big|_p)}}{1 + \frac{\Theta\phi\rho(\frac{\partial V}{\partial p}\Big|_T + \frac{\partial V}{\partial T}\Big|_p\,\frac{\partial T}{\partial p}\Big|_\rho)}{V + \rho\frac{\partial V}{\partial T}\Big|_p\,\frac{\partial T}{\partial \rho}\Big|_p}} \qquad \text{(AII-10)}$$

Reference A-2 presents the derivation for change in volume with respect to pressure at constant temperature as:

$$\frac{\partial V}{\partial p}\Big|_T = \frac{3rV}{2dY}(1-\upsilon) \quad . \qquad \text{(AII-11)}$$

The change in volume with respect to temperature may be obtained as follows:

$$\frac{\partial V}{\partial T}\Big|_p = \frac{\partial V}{\partial r}\Big|_p\,\frac{\partial r}{\partial T}\Big|_p$$

$$\frac{\partial V}{\partial r} = \frac{\partial}{\partial r}\left(\frac{4}{3}\pi r^3\right) = 4\pi r^2 = \frac{3V}{r} \quad .$$

For small changes in temperature, then

$$\frac{\partial V}{\partial T}\Big|_p \frac{3V}{r}\,\frac{\Delta r}{\Delta T} = 3\alpha V \qquad \text{(AII-12)}$$

Substituting these expressions into Equation (AII-10) results in:

$$\frac{dp}{dt} = \frac{\dfrac{\Theta\dot{m}\phi}{V} + \dfrac{\phi q}{V} - \dfrac{\Theta\phi\dot{m} \quad 3\alpha\rho \left.\dfrac{\partial T}{\partial \rho}\right|_p}{V\ (1+\rho 3\alpha \left.\dfrac{\partial T}{\partial \rho}\right|_p)}}{\dfrac{1 + \Theta\phi\rho(\dfrac{3r}{2dY}\ (1 - \upsilon) + 3\alpha\left.\dfrac{\partial T}{\partial p}\right|_\rho\ )}{1 + 3\alpha\rho \left.\dfrac{\partial T}{\partial \rho}\right|_p}} \qquad \text{(AII-13)}$$

It is necessary to account for one additional effect which results in a variation in the change in volume with respect to pressure. This effect is the compression of the fluid in the fill and vent lines of the tank. These lines extend from the pressure vessel to the warm environment. The fluid at the cold ends is relatively incompressible as compared to the near ideal gas conditions at the other ends. When pressure increases, the fluid in the lines is compressed by the expanding stored fluid which move up the lines. To account for this effect, it was assumed that the lines will be filled with an ideal gas at ambient temperature and that no mixing between the tanked cryogen and the perfect gas would take place. Then:

$$pV_L^n = \text{constant.}$$

Thus,

$$V_L^n \frac{dp}{dt} + npV_L^{n-1} \frac{dV_L}{dt} = 0$$

or

$$\frac{dV_L}{dt} = \frac{-V_L}{np} \frac{dp}{dt} \qquad \text{(AII-14)}$$

The mass flow, $\dot{m}$, is the total flow from the tank:

$$\dot{m} = \dot{m}_o + \dot{m}_2 \qquad \text{(AII-15)}$$

where: $\dot{m}_o$ = flow to EPS and ECS subsystems, lbm/hr.

$\dot{m}_2 = \rho\dfrac{dV_L}{dt}$ = flow from fill and vent lines, lbm/hr

Note: Flow out of the tank is negative in sign.

Substituting Equation (AII-14) into Equation (AII-15) yields:

$$\dot{m} = \dot{m}_o - \rho \frac{V_L}{np} \frac{dp}{dt}$$

When this equation is substituted into equation (AII-13) and rearranged, the resulting expression is:

$$\frac{dp}{dt} = \frac{\frac{\Theta\phi}{V} \dot{m}_o + \frac{\phi}{V} q - \frac{\Theta\phi}{V} \frac{\dot{m}_o \, 3\alpha\rho \frac{\partial T}{\partial \rho}\Big|_p}{(1 + \rho \, 3\alpha \frac{\partial T}{\partial \rho}\Big|_p)}}{1 + \frac{\Theta\phi}{V} \frac{\rho V_L}{np} - \frac{\Theta\phi}{V} \frac{V_L \, 3\alpha\rho^2 \frac{\partial T}{\partial \rho}\Big|_p}{np \, (1 + 3\alpha\rho \frac{\partial T}{\partial \rho}\Big|_p)} + F} \qquad \text{(AII-16)}$$

where:

$$F = \frac{\Theta\phi\rho \left(\frac{3r}{2dY} (1-\upsilon) + 3\alpha \frac{\partial T}{\partial p}\Big|_\rho\right)}{1 + 3\alpha\rho \frac{\partial T}{\partial \rho}\Big|_p}$$

Thus, Equation (AII-16) describes the rate of change of pressure for a variable tank volume considering both pressure and temperature changes. Note that if the coefficient of thermal expansion, α, is equal to zero and if the plumbing fluid compression volume, V_L, is zero, Equation (AII-1) is obtained. Table A-1 presents the constants used for both the oxygen and hydrogen tanks. The partial derivatives are obtained by differentiating the equation of state. Since the Integrated Systems Program uses an equation of state that is a function of temperature and density, it is desirable to obtain $\partial T/\partial \rho$ in the following form:

$$\frac{\partial T}{\partial \rho}\Big|_p \frac{\partial \rho}{\partial p}\Big|_T \frac{\partial p}{\partial T}\Big|_\rho = -1$$

This relation was taken from Reference A-4, page 32, Equation (3-11).

Then

$$\left.\frac{\partial T}{\partial \rho}\right|_p = \frac{1}{-\left.\frac{\partial \rho}{\partial p}\right|_T \left.\frac{\partial p}{\partial T}\right|_\rho} = -\left.\frac{\partial p}{\partial \rho}\right|_T \left.\frac{\partial T}{\partial p}\right|_\rho$$

Thus, this partial derivative may also be obtained from the equation of state.

TABLE A-1
CRYOGENIC TANK PROPERTIES

OXYGEN

Material	Inconel 718
Volume, V, ft^3	4.75
Inside Radius, r, in	12.513
Young's Modulus, Y, psi	30×10^6
Poisson's Ratio, υ, dimensionless	0.29
Wall Thickness, d, in	0.059
Coefficient of Thermal Expansion, α, /°R	5.93×10^{-6}

HYDROGEN

Material	Titanium-5AL-2.5SN ELI
Volume, V, ft^3	6.80
Inside Radius, r, in	14.103
Young's Modulus, Y, psi	17×10^6
Poisson's Ratio, υ, dimensionless	0.30
Wall Thickness, d, in	0.044
Coefficient of Thermal Expansion, α, /°R	1.23×10^{-6}

Note: Values for α were derived from Reference A-3, Table 7.3.4, page 7-59.

APPENDIX II REFERENCES

A-1. TRW IOC 70.4354.3-84, "Thermodynamics Relations for the Quasi-Static Flow of Single Phase Fluids," C. E. Barton, 17 August 1970.

A-2. TRW IOC 70.4354.36-2, "Derivation of the Cryogenic Pressure Rise/Decay Rates," C. W. Wurst, 26 October 1970.

A-3. "Apollo Fuel Cell and Cryogenic Gas Storage System Flight Support Handbook," NASA/MSC, 18 February 1970.

A-4. Thermodynamics, the Kinetic Theory of Gases, and Statistical Mechanics, F. W. Sears, Addison-Wesley Publishing, 1953.

APPENDIX III

DERIVATION OF EQUATIONS USED IN THE COMPONENT AND LINE MODEL

MATRIX MODEL

The matrix model determines the pressures for each of the oxygen and hydrogen system nodes shown in Figures 11 and 12, respectively.

The conservation of mass principle may be written:

$$\sum \dot{m} = V\frac{d\rho}{dt} . \tag{AIII-1}$$

For a perfect gas,

$$p = \rho RT. \tag{AIII-2}$$

Combining Equations (AIII-1) and (AIII-2) and performing the differentiation results in:

$$\sum \dot{m} = \frac{V}{RT^2} (T\frac{dp}{dt} - p\frac{dt}{dt}). \tag{AIII-3}$$

To set up an electrical analogy, let

$$E \equiv p^2 \tag{AIII-4}$$

for an equivalent driving function, and

$$I \equiv \dot{m} \tag{AIII-5}$$

for the current.

In terms of the transforms variables, Equation (AIII-3) becomes:

$$\sum I = \frac{V}{2RT\sqrt{E}} \frac{dE}{dt} - \frac{V\sqrt{E}}{RT^2} \frac{dT}{dt} \tag{AIII-6}$$

or

$$\sum I = C\frac{dE}{dt} - I_R \tag{AIII-7}$$

where

$$C = \frac{V}{2RT\sqrt{E}} \tag{AIII-8}$$

is an equivalent capacitance, and

$$I_R = \frac{V\sqrt{E}}{RT^2} \frac{dT}{dt} \qquad \text{(AIII-9)}$$

is an equivalent residual current.

NODAL MODEL

The nodal model determines the pressures of the oxygen and hydrogen along each leg of the oxygen and hydrogen, Figures 13 and 14, respectively.

The instantaneous pressure drop for incompressible flow through a line with inlet i and outlet j is given by the Darsy-Weisbach equation,

$$p_i - p_j = \left(\frac{4fL}{D}\right)_{ij} \frac{\rho s^2}{2g_c} . \qquad \text{(AIII-10)}$$

For incompressible flow in a circular tube,

$$\dot{m} = \rho A s = \frac{\pi D^2 \rho s}{4} . \qquad \text{(AIII-11)}$$

Combining Equations (AIII-10) and (AIII-11) and simplifying results in:

$$p_i - p_j = \left(\frac{4fL}{D}\right)_{ij} \frac{8\dot{m}^2}{g_c \pi^2 D^4 \rho} . \qquad \text{(AIII-12)}$$

Let the mean density between i and j be based on the average pressure and temperature. Then,

$$\rho_{ij} = \frac{1}{R} \frac{p_i + p_j}{T_i + T_j} . \qquad \text{(AIII-13)}$$

Substituting Equation (AIII-13) into Equation (AIII-12) and simplifying yields:

$$p_i^2 - p_j^2 = \left[\frac{8R(T_i + T_j)}{g_c \pi^2 D^4} \left(\frac{4fL}{D}\right)_{ij} \right] \dot{m}^2 . \qquad \text{(AIII-14)}$$

For laminar, incompressible flow in a circular tube,

$$f = \frac{16}{N_{RE}} = \frac{4\pi\mu D}{\dot{m}} . \qquad \text{(AIII-15)}$$

Combining Equations (AIII-14) and (AIII-15) and simplifying results in:

$$P_i^2 - P_j^2 = \left[\frac{128 L \mu R}{g_c \pi D^4} \quad (T_i + T_j) \right] \quad \dot{m} \qquad \text{(AIII-16)}$$

In terms of the electrical analog variables, Equation (AIII-16) becomes:

$$E_i - E_j = \frac{I}{G} \quad . \qquad \text{(AIII-17)}$$

where

$$G = \left[\frac{128 L \mu R}{g_c \pi D^4} \quad (T_i + T_j) \right]^{-1} . \qquad \text{(AIII-18)}$$

An instantaneous heat balance through a line with inlet i and outlet j is:

$$UA \ \Delta T_{LM} = \dot{m} \ c_p \ (T_j - T_i) \ . \qquad \text{(AIII-19)}$$

where

$$\Delta T_{LM} = \frac{(T_k - T_i) - (T_k - T_j)}{\ln \left(\dfrac{T_k - T_i}{T_k - T_j} \right)} \quad . \qquad \text{(AIII-20)}$$

Combining Equations (AIII-19) and (AIII-20) and simplifying yields:

$$T_j = \left[1 - e^{-\left(\frac{UA}{\dot{m} c_p} \right)} \right] T_k + e^{-\left(\frac{UA}{\dot{m} c_p} \right)} \ T_i . \qquad \text{(AIII-21)}$$

N72-23798

ZERO-GRAVITY TRANSIENT THERMAL MIXING SIMULATION

by

Jack F. Lands, Jr.

Aircraft Mechanisms Section

and

Robert C. Ried, Jr.

Head, Aerothermodynamics Section

Structures and Mechanics Division

NASA - Manned Spacecraft Center

Houston, Texas

I. ABSTRACT

The experimental program described in this paper is an outgrowth of independent investigations into alternate redesign concepts for the Apollo SM cryogenic oxygen storage system. The experiments were continued, after the redesign was established, to provide physical insight into transient thermal mixing in zero-gravity and to aid in the characterization of the system performance in flight.

Zero-gravity heat transfer and fluid mixing were simulated experimentally through an analogy between unsteady heat conduction and species diffusion. The forced convection and transient fluid mixing associated with initiation, reversal or termination of spacecraft passive thermal control (PTC) motions have been studied through geometric and Reynolds number similarity and by the use of a dye diffusing into water. Motion pictures of the simulation have been made and radial measurements of the time for the fluid to come to equilibrium with the tank motion were taken. The results indicate that there should be a negligible potential for pressure collapse in the oxygen tanks for a significant period of time after a change in PTC. These times vary with the mass of oxygen in the tank, however, they are on the order of from 3 to 10 hours. Unfortunately, experimental simulation of the heat transfer at the heater-fluid interface was not adequate for quantitative assessment of overall energy transport, however, in principle the potential for this simulation does exist.

To further support numerical analyses of the cryogenic oxygen storage system, the experimental investigation was extended to include a cubical tank geometry, representative of existing numerical models. In general, the transient flow patterns in the cubical tank are far more complex than those of the spherical tank and the extent of fluid mixing is significantly greater but less repeatable.

II. INTRODUCTION

The experimental program reported herein is an outgrowth of independent investigations into alternate redesign concepts for the Apollo SM cryogenic oxygen storage system. These experiments were continued, after the redesign was established, to aid in the characterization of the system performance in flight.

8

The basic objective of these experiments has been to provide information on energy transport and fluid mixing in a zero-gravity environment. Since it is impossible to produce a zero-gravity environment on the earth for an extensive period of time, an analogy was drawn between thermal diffusion and constant density species diffusion. This enabled an experimental simulation of the transient flow and mixing associated with initiation, termination or reversal of spacecraft passive thermal control (PTC) roll motion. Following is a discussion of the analogy, experimental apparatus, tests conducted, and test results.

III. THEORETICAL BASIS

Consideration of energy addition and distribution processes in the Apollo cryogenic oxygen system involves a matrix of phenomena and motions as shown in figure 1. In the case of zero motion, and in the absence of gravity, energy transfer is accomplished through conduction and secondary flows created by thermal expansion. Although conduction is readily calculated secondary flow processes require a numerical flow description. When the spacecraft is undergoing PTC the oxygen tanks experience a radial acceleration which in turn allows for a dominant free convection heat transfer and associated fluid mixing. Although free convection heat transfer can be calculated readily through semi-empirical film heat transfer coefficients, the associated fluid mixing requires either numerical or experimental simulation.

After initiation or reversal of PTC, the extensive transient motion involves all of the phenomenon shown in figure 1. The transient motion associated with termination of PTC involves all but free convection heat transfer. The specification of all simultaneous phenomenon requires numerical computation or flight experimentation. The forced convection and mixing associated with the transient motion can be obtained by a Reynolds number simulation of PTC coupled with a concentration diffusion simulation of thermal conduction.

The first order behavior of both unsteady thermal conduction and the diffusion of a dye into water can both be described by the diffusion equation:

$$\frac{\partial \theta}{\partial t} = \alpha^2 \nabla^2 \theta \qquad 0 \leq \theta \leq 1$$

Where for thermal conduction,

$$\theta = \frac{T - T_\infty}{T_{source} - T_\infty}$$

$$\alpha^2 = D_T = \frac{k}{\rho C_v} = \text{mean thermal diffusivity}$$

T_∞ = bulk fluid temperature

T_{source} = effective source temperature

And for the diffusion of dye into water,

$$\theta = \frac{\text{dye concentration}}{\text{source dye concentration}}$$

α^2 = diffusion constant, dye/water, D_{12}

To compare absolute times for the two physical processes the:

$$\text{Characteristic time for thermal diffusion} = \frac{D_{12}}{D_T} \times \text{Characteristics time for dye diffusion}$$

The dye diffusion constant in these experiments was measured to be on the order of 10^{-1} of the calculated thermal diffusivity of the oxygen at significant conditions.

The flight oxygen tank Reynolds number based on tank radius and PTC rotation rate (Ω = 3 revolutions per hour) is shown in figure 2 as a function of the oxygen mass remaining in the tank. The circled points indicate the test simulation conditions with water at approximately 30 revolutions per hour (.5 RPM). The model flow times relative to the flight oxygen tank flow times can be scaled inversely with kinematic viscosity. Therefore, the model or test flow occurs ten times faster than in the flight case. In these tests the dye diffusion proceeded at a rate of 10^{-2} relative to the flight thermal conduction. Although this does not provide a good simulation, it does provide a conservative model for the extent of mixing in the tank. Due to this diffusion time difficulty and due to the difficulty associated with simulating the precise energy transport at the heater surface, the main results of these tests are characteristic motion times and the physical insight gained concerning zero-gravity phenomenon.

IV. EXPERIMENTAL APPARATUS

Two experimental investigations were conducted. The first was a simulation of the Apollo SM cryogenic oxygen storage system including the use of a simulated spherical tank. To support numerical analysis efforts the experimental investigation was extended to a second program which included a cubical tank having the same volume as the previous and actual tank.

Simulated Tank - As shown in figure 3, the first experimental apparatus consisted of the following: a counter-balanced, reversible rotating beam of sufficient length to represent the location of the inner O_2 tank of the SM, a plexiglas mock-up of the O_2 tank, a metal/wood mock-up of the heater and quantity probe assembly, a dye injection system, motion picture cameras, and a radial dye injection system. The radial dye injector was not used while motion pictures were being obtained. A cloth tent was fabricated to diffuse the available indoor lighting thereby reducing unwanted reflections which would degrade the motion pictures.

To obtain a condition representative of a "hot" heater, a high concentration of dye around the heater mock-up was desired. Through trial and error the following combination was found to give acceptable results. A 3/16-inch copper tube was spirally wrapped around the heater mock-up with a pitch of approximately 7/8 inches. At 90 degree intervals the tubing was perforated by a .010-inch drill at two locations, one directed upward and one downward. The tubing was not terminated at the lower end of the heater mock-up, but rather was routed vertically to the tank exterior. Such a configuration allowed dye to be injected at either the upper or lower end of the heater assembly.

The area representing the heater surface was wrapped with cheese cloth which was subsequently wrapped with a fiber napkin, similar to a paper dinner napkin. The upper and lower regions were taped and the lap joint was sealed with a silicon rubber compound. A series of cord bindings were then added at each tubing spiral for the purpose of attempting to create small dye sources. A beaker of concentrated methonal blue was elevated above the tank to provide the dye source to the simulated heater tubing.

After initial tests were conducted, a tube was extended along a tank radius in a horizontal plane as shown in figure 4. Small holes were drilled in the tube at one inch intervals to provide twelve radial locations at which flows could be observed. The tube was extended up the exterior of the capacity probe to the tank exterior and the dye reservoir. Holes in the radial tube were located to oppose the relative fluid (simulated O_2) motion. Therefore, when no stagnation and reverse flow of dye occurred, a station could safely be assumed at equilibrium conditions. Because of the small quantities of dye injected during the radial equilibrium experiments, no photographic equipment was used in these experiments.

Cubic Tank - The experimental apparatus was identical to that used in the spherical tank tests with the following exceptions: the test tank was a plexiglas cube (volume of approximately 4.75 ft^3), the simulated heater and quantity probe assembly was necessarily shorter, consisting of a wooden dowel of the proper diameter simulating the heater and a metal tube with a diameter equal to that of the center portion of the quantity probe. The simulated heater extended to within one-half inch of the top and bottom surfaces of the tank. For tests that would correspond to previous radial tube tests, two configurations were examined: in one, the tube was extended from the quantity probe to a corner with the heater positioned such that the flow just prior to the heater was measured. The second configuration consisted of a tube extending from the quantity probe to a wall so that the tube was perpendicular to the wall. Again, the heater was oriented so that the tube measured flow that would logically have contacted the heater surface.

For the motion pictures studies, the apparatus was identical with that used in the spherical tank tests except that the top view was changed to provide a view through the top surface of the tank, although not at a normal orientation. When motion pictures were obtained, the complete dye injection system used with the spherical tank was utilized.

V. SIMULATION CONDITIONS AND TEST PROCEDURES

Three S/M roll conditions were evaluated: the starting transient, the stopping transient, and the combination of these, the roll reversal.

Where the simulated heater-dye injector system was used the procedure was as follows. The heater probe assembly was inserted in the spherical tank of water and was undisturbed for two hours. Dye (at near the tank water temperature) was slowly fed into the upper and lower regions of the heater assembly. As the dye penetrated the cheesecloth/napkin wrapper, a reasonably uniform cylinder of dye could be formed. If the dye injection was successful at this time, motion picture cameras were activated and rotation of the tank begun. Filming was continued for approximately 45 minutes. At the end of this time, while fluid motion still existed, inadequate contrast between stream lines had greatly reduced the value of photography.

For the radial tube experiments during the starting transient essentially the same procedure was used until the initiation of rotation. At 7-1/2 minute intervals, dye was injected along the tube in a direction opposing the tank fluid flow. Visual observations were made of each location and recorded. When the dye no longer stagnated and returned beyond the tube, flow was considered to have ceased.

Stopping transients were similarly investigated. The wrapped heater assembly was inserted and the tank rotation begun. After rotating for two hours, an attempt was made to uniformly inject dye through the heater tubes to form a cylinder of dye around the heater assembly. If this condition was satisfactory, cameras were started and rotation terminated.

The radial tube tests were similar. After rotation was ceased, dye was injected at 7-1/2 minute intervals through the radial tube and observations were made.

Roll reversal tests were like the stopping transient tests except that the rotation was reversed rather than stopped.

VI. TEST RESULTS

Test results are presented in the form of motion pictures as tabulated in Tables I and II and plotted flow relaxation time data for starting, stopping, and roll reversal transient conditions. Note that motion pictures were obtained at approximately four frames per second, and, therefore, if viewed at 16 frames per second events are occurring 40 times faster than in the flight O_2 tank.

Simulated Tank - To illustrate the flow and mixing simulation obtained in the experiments figure 5 shows five time sequences of a starting transient flow. Motion was initiated immediately following the first view of essentially stagnant injected dye. Considerable mixing occurs with the initial motion as shown in the second view at one minute of model time. The mixing decays as shown until in the last view at nine minutes model time the dye distribution rate is governed primarily by diffusion.

With the radial tube injection device the radial distribution of flow relaxation times were measured as shown in figures 6 and 7. The repeatability of the relaxation times for the spherical tank are as illustrated in figure 6 for two independent tests of the starting transient. The character of the flow relaxation is significantly different for the starting, stopping, and roll reversal as shown in figure 7. The radial relaxation patterns are consistent with the observed mixing in that the starting and roll reversal provided significantly better mixing than the stopping transient. As shown in figure 7, the flow came to rest around the heater sooner for the stopping transient and thereby produces less mixing of the dye or simulated hot fluid.

Except for the stopping transient, some flow was noted for almost any test duration. This flow was not significant near the heater assembly, but was noted primarily near the tank wall. A flow reversal and oscillation was noted in the wall boundary layer in several starting transient tests. This occurred at approximately 20 SC hours and was most prolonged in the case of roll reversal.

All test observations indicate some small radial flow toward the capacity probe.

All tests also indicated, as would be expected, that longer flow durations are obtainable at a tank radius of five to six inches.

The observed test times for relaxation of the relative motion about the heater element have been transposed to real flight times as shown in figure 8. Again the stopping transient is a characteristically different flow from the starting or reversal and as such relaxes in less than half the time as shown in figure 8.

Cubic Tank - In the cubical tank tests the fluid was essentially stagnant in the tank corners with the primary flow resembling that which would be expected in a cylindrical tank. The tank geometry, however, does significantly effect the flow patterns as can be determined by comparing the spherical and cubical tank data for identical test conditions. In general, the cubical tank data were not as repeatable or as uniform as that obtainable with the spherical tank. Although there is a similarity of a portion of the data for the two tanks, the flow patterns were observed to be substantially different. For example, with the cubical tank flow at several "radial" stations ceased at essentially the same time rather than uniformly decaying as was generally observed in the spherical tank. With the spherical tank, the primary flow under investigation was dominant and secondary flows, while present, did not significantly alter the flow patterns. With the cubical tank, primary and secondary flows can equally influence the overall flow patterns and mixing. In the cubical tank, flows perpendicular to a "radius" were observed at times to be in three alternate directions, a condition which could later change to one or two directional flow. In tests, where secondary flows were less dominant, the cubical tank flow patterns more nearly resembled those observed in the spherical tank.

Figure 9 presents data from two starting transient tests of the same configuration. In one test, the flow uniformly relaxes, while in the other the flow abruptly ceased between 3 and 6 inches radius. Figure 10 presents data for the same configuration obtained in a simulated roll reversal. As with the spherical tank, relaxation times for roll termination with the cubical tank were extensive and were generally not recorded to their completion. The flow, while present, was observed to be very slow and at a location not under investigation. Figure 11 illustrates typical roll termination data obtained with the cubical tank. No abrupt ceasing of flow was observed during any of the roll termination tests. Figure 12 presents a summary of data obtained with the "radial" tube injector orientated perpendicular to a tank wall. The relaxation times are for a station at the outer heater surface. The cubical tank data does not define a distinct difference between the test conditions as was obtained with the spherical tank.

Figure 13 illustrates data obtained from three transient tests with the "radial" dye injector tube extending from the probe to a tank corner. Although not shown in this figure, fluid flow was also observed to abruptly cease at several radial stations at the same time with this configuration. The stopping and reversal transients provide the longest period of fluid motion past the heater surface.

Figure 14 is a summary of all data obtained for the probe-to-corner tube configuration. A comparison between figures 12 and 14 indicates that the heater orientation in the cubical tank does not significantly affect the relaxation times. However, neither figure indicates significantly different relaxation times for the stopping transient as obtained with the spherical tank.

Motion picture data provides a more complete illustration of the flow patterns and presents one case (S71-079) where secondary flows significantly influence the flow field. Under this condition, mixing is enhanced and exceeds that obtained with the spherical tank.

VII. CONCLUDING REMARKS

The forced convection and transient mixing associated with changes in spacecraft PTC provide a significant mode of energy distribution within the cryogenic oxygen tanks. The transient effects last for a period of up to six to nine hours from termination of PTC and up to fourteen to twenty-three hours from initiation or reversal of PTC. The associated mixing during these times should provide for negligible potential for pressure collapse. The transient motion from initiation or reversal of PTC should also provide a significant enhancement of the free convection and otherwise steady flow and mixing processes.

The forced convection and transient mixing in a cubical tank does not provide a good simulation of conditions to be expected with a spherical tank. In general, the overall flow in the cubical tank is far more complex, less repeatable, and can provide significantly greater mixing than in the spherical tank. Portions of the flow field in the cubical tank, particularly near the heater can at various times provide characteristics similar to the simulated tank flow.

The significant differences in the flow and mixing between the two tanks indicates that fluid mixing could be enhanced considerably through irregular geometry or protuberances.

MSC MOTION PICTURE FILE NUMBERS FOR O_2 MIXING STUDIES*

TABLE 1 - SIMULATED TANK

STARTING TRANSIENT	
Dye injected before initiation of rotation	S-70-310
Dye injected after rotating 1 hour (lab time)	S-70-337
STOPPING TRANSIENT	
Dye injected before termination of rotation	S-70-333 S-70-338
REVERSAL TRANSIENT	
Dye injected after rotating 2 lab hours and before reversing rotational direction	S-70-343

TABLE II - CUBICAL TANK

STARTING TRANSIENT	
Dye injected before initiation of rotation	S-71-075
Dye injected after rotating 1 hour (lab time)	S-71-106
STOPPING TRANSIENT	
Dye injected before termination of rotation	S-71-079
REVERSAL TRANSIENT	
Dye injected after rotating 2 lab hours and before reversing rotational direction	S-71-116

* Each film reel contains two camera views, one above, one below.

NASA-S-71-1429-X

ENERGY ADDITION AND DISTRIBUTION MECHANISMS

		RELATIVE MOTION			
PHENOMENON	CONTROLLING PARAMETERS	ZERO	STEADY ROLL (PTC)	TRANSIENT	
				START OR REVERSE PTC	STOP PTC
CONDUCTION	$D_T = \frac{k}{\rho C_v}$, ∇T	√ a,s,n	√ n	√ s	√ s
CONVECTION: FREE	ACCELERATION FIELD, $\nabla \rho$	--	√ n,a	√	
FORCED	VELOCITY FIELD, ∇T	--	--	√ s	√ s
MIXING: FLUID	VEOCITY, $\nabla \vec{v}$	--	√ n	√ s	√ s
THERMAL	$\frac{\partial \rho}{\partial t}$, ∇T	√	√	√	√

s - SIMULATION BY CURRENT EXPERIMENTS
a - READILY ANALYZED
n - NUMERICAL DESCRIPTION AVAILABLE

NOTE: THERMAL RADIATION IS SIGNIFICANT ONLY FOR ENERGY EXCHANGE BETWEEN SURFACES

Figure 1.

NASA-S-71-1439-X

REYNOLD'S NUMBER VS TANK QUANTITY

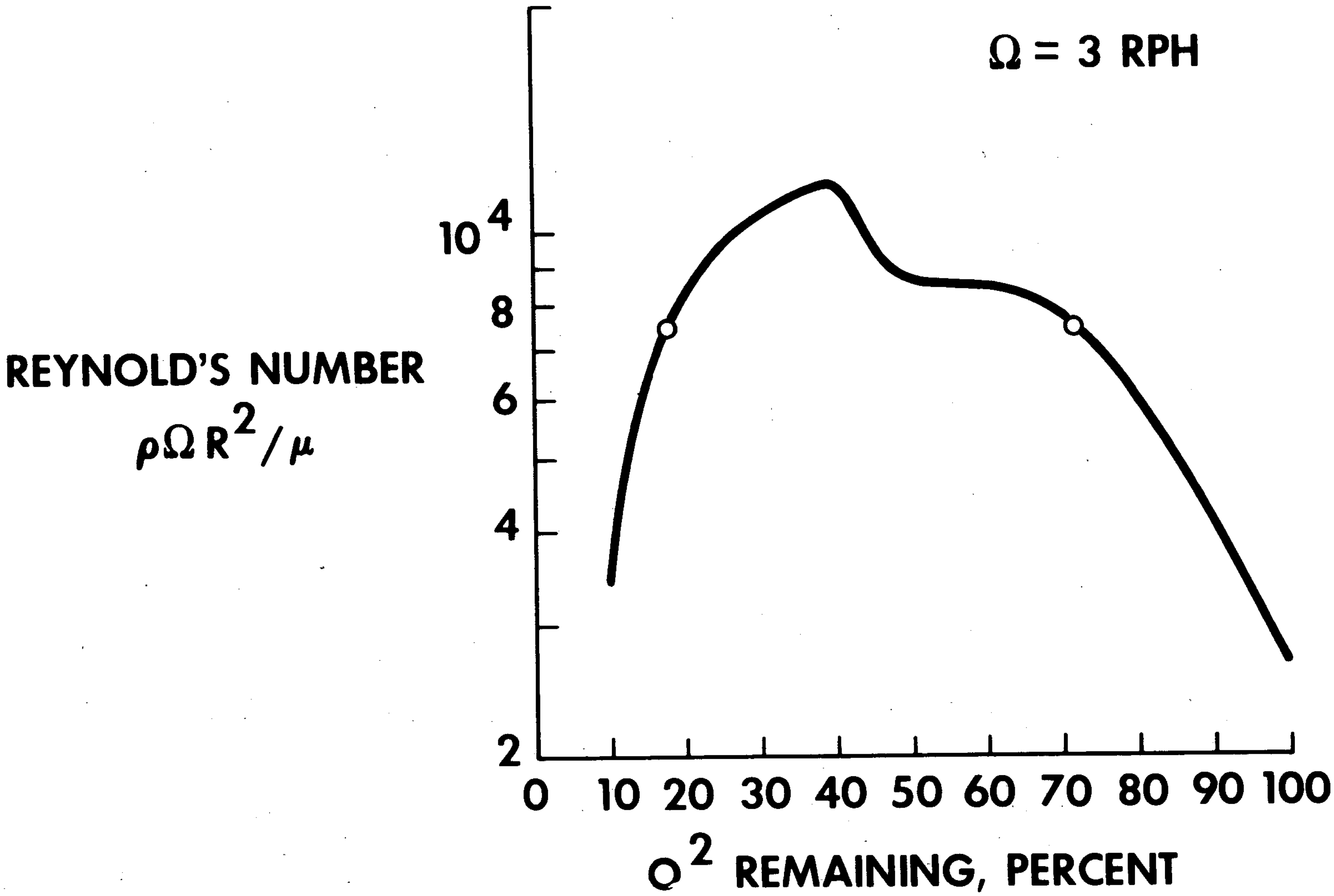

Figure 2.

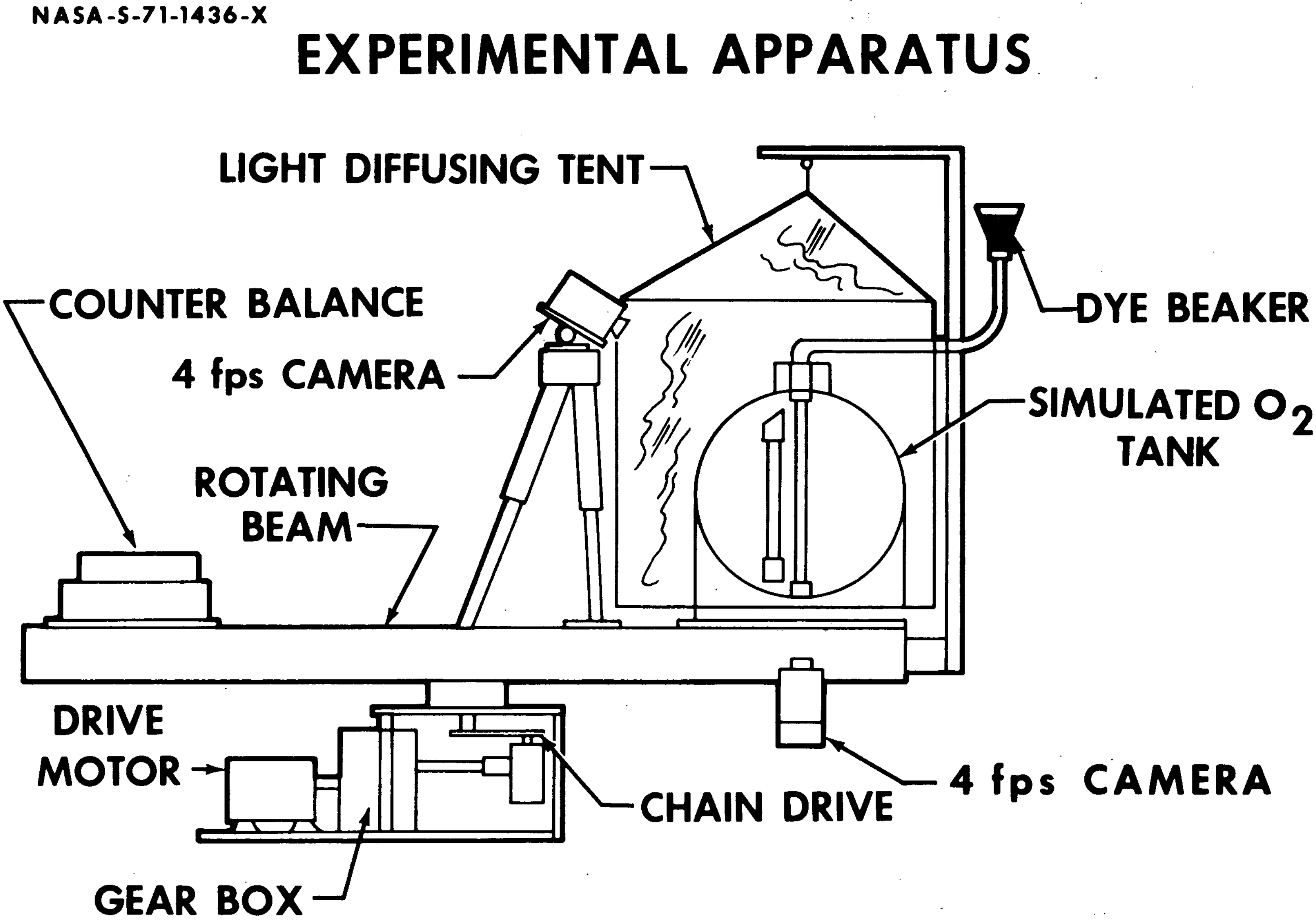
NASA-S-71-1436-X
EXPERIMENTAL APPARATUS
LIGHT DIFFUSING TENT
COUNTER BALANCE
DYE BEAKER
4 fps CAMERA
SIMULATED O_2 TANK
ROTATING BEAM
DRIVE MOTOR
CHAIN DRIVE
4 fps CAMERA
GEAR BOX

Figure 3.

NASA-S-71-1441-X

EXPERIMENTAL APPARATUS

RADIAL TUBE TEST

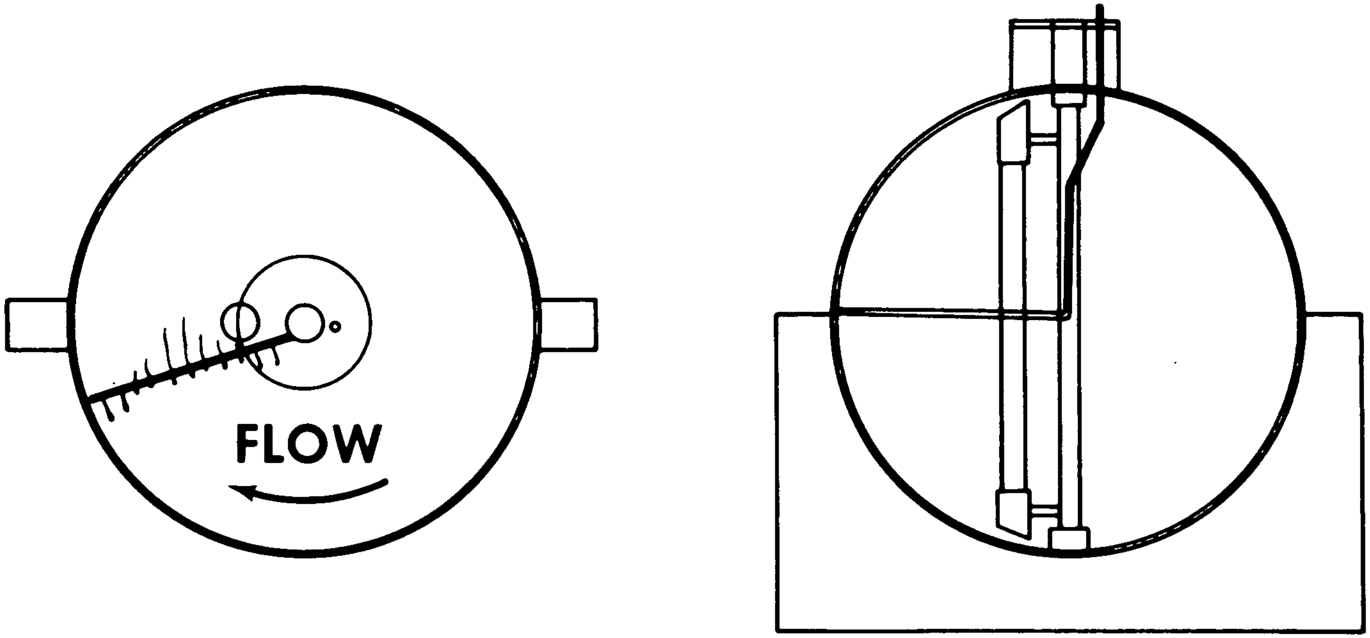

Figure 4.

NOT REPRODUCIBLE

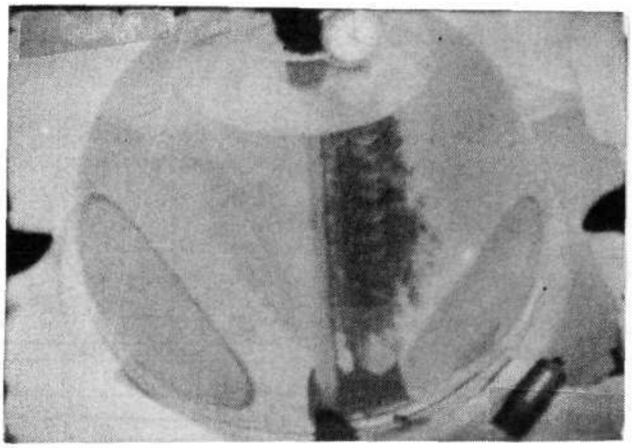

t = 0

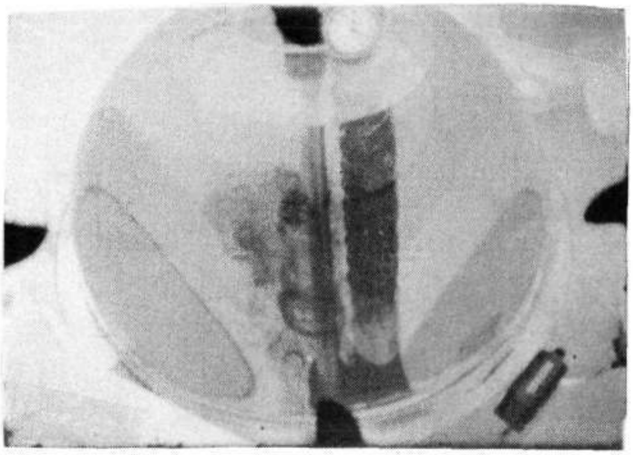

t = 1 min.

FIGURE 5 - STARTING TRANSIENT TIME SEQUENCE
(MODEL TIMES)

NOT REPRODUCIBLE

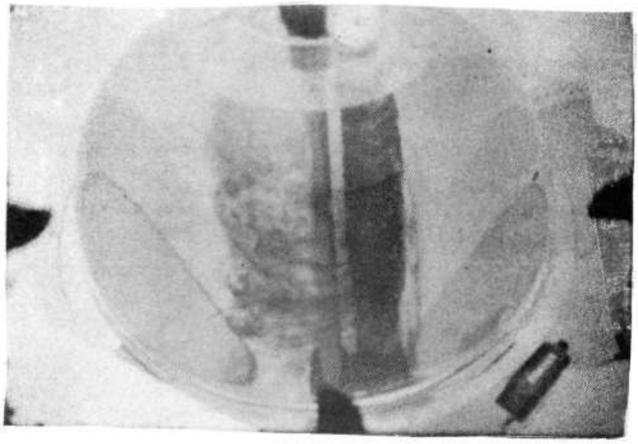

t = 3 min.

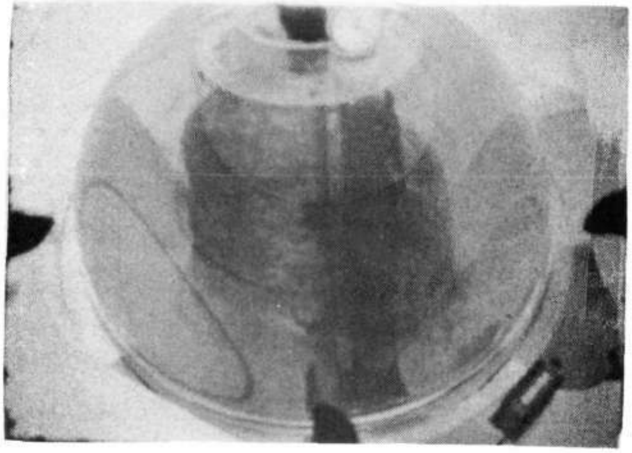

t = 6 min.

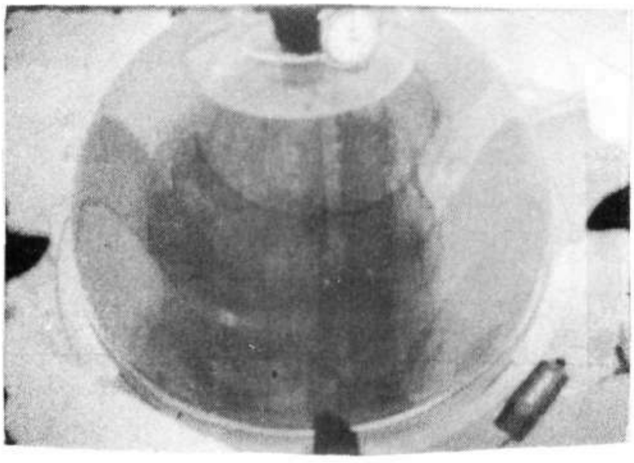

t = 9 min.

NASA-S-71-1433-X

TIME TO STEADY STATE STARTING TRANSIENT

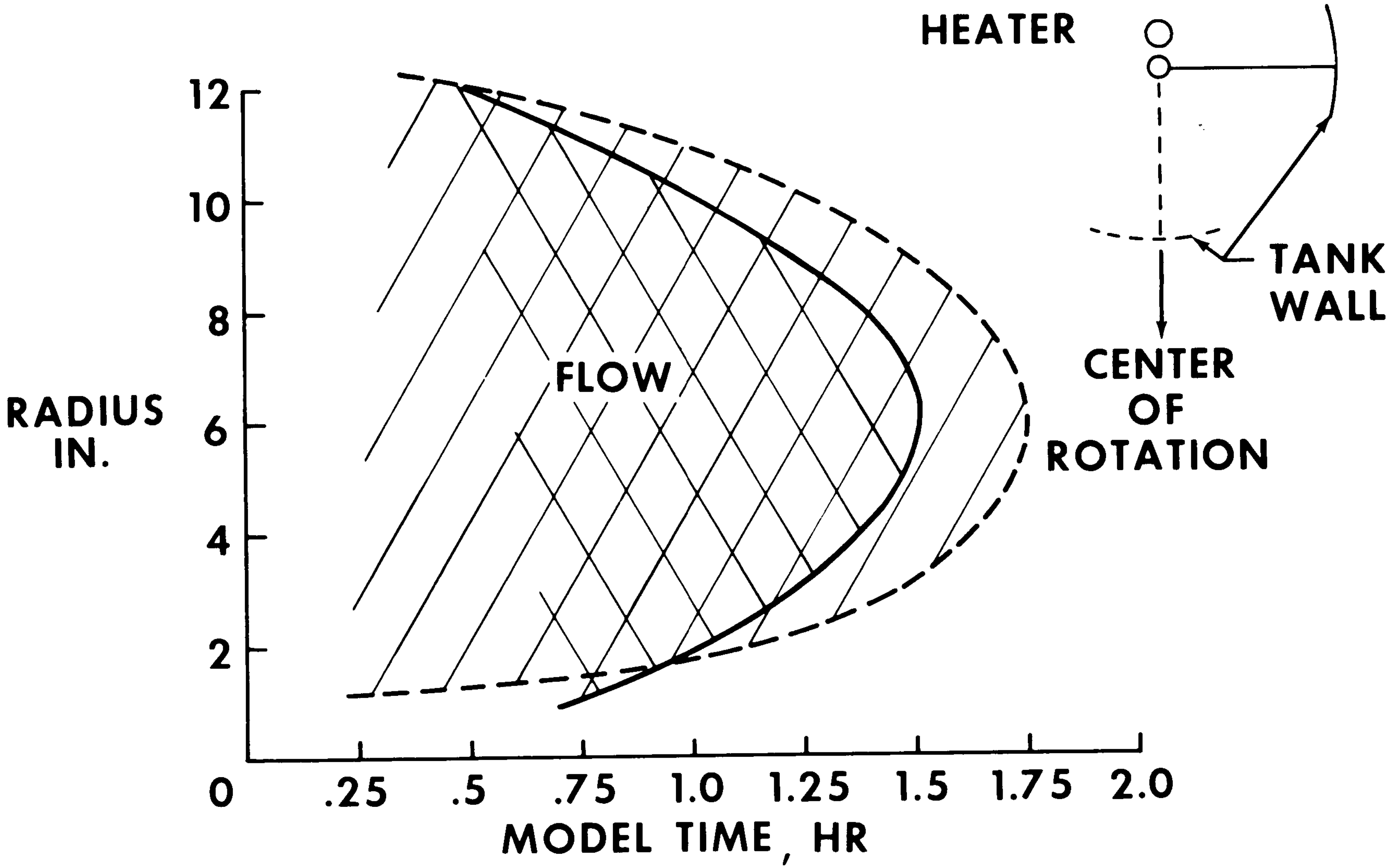

Figure 6.

NASA-S-71-1434-X

TIME TO STEADY STATE

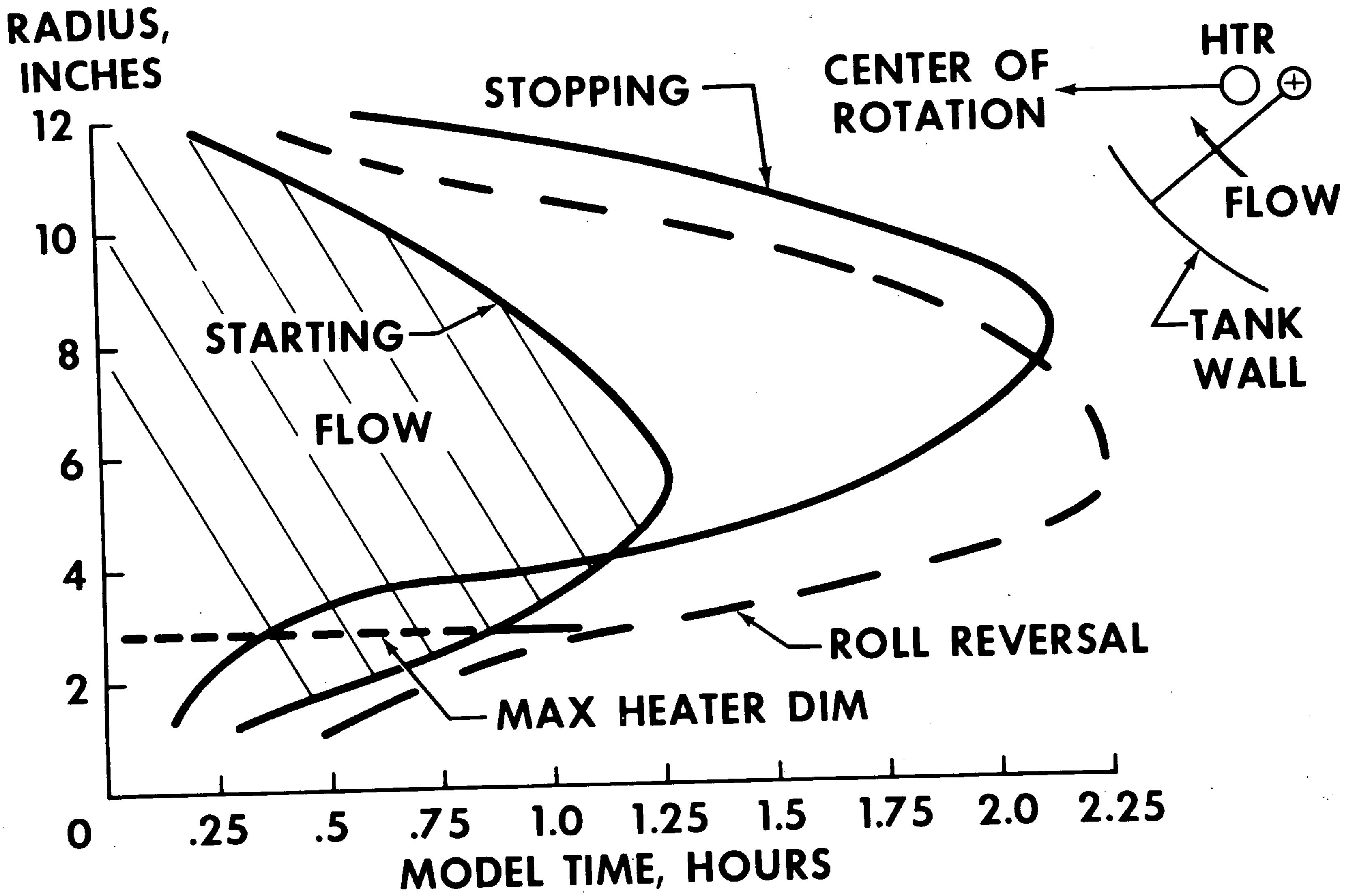

Figure 7.

NASA-S-X-71-1430-X

TIME FOR O_2 TO COME TO REST ABOUT THE HEATER VS MASS FRACTION OF OXYGEN REMAINING IN TANK

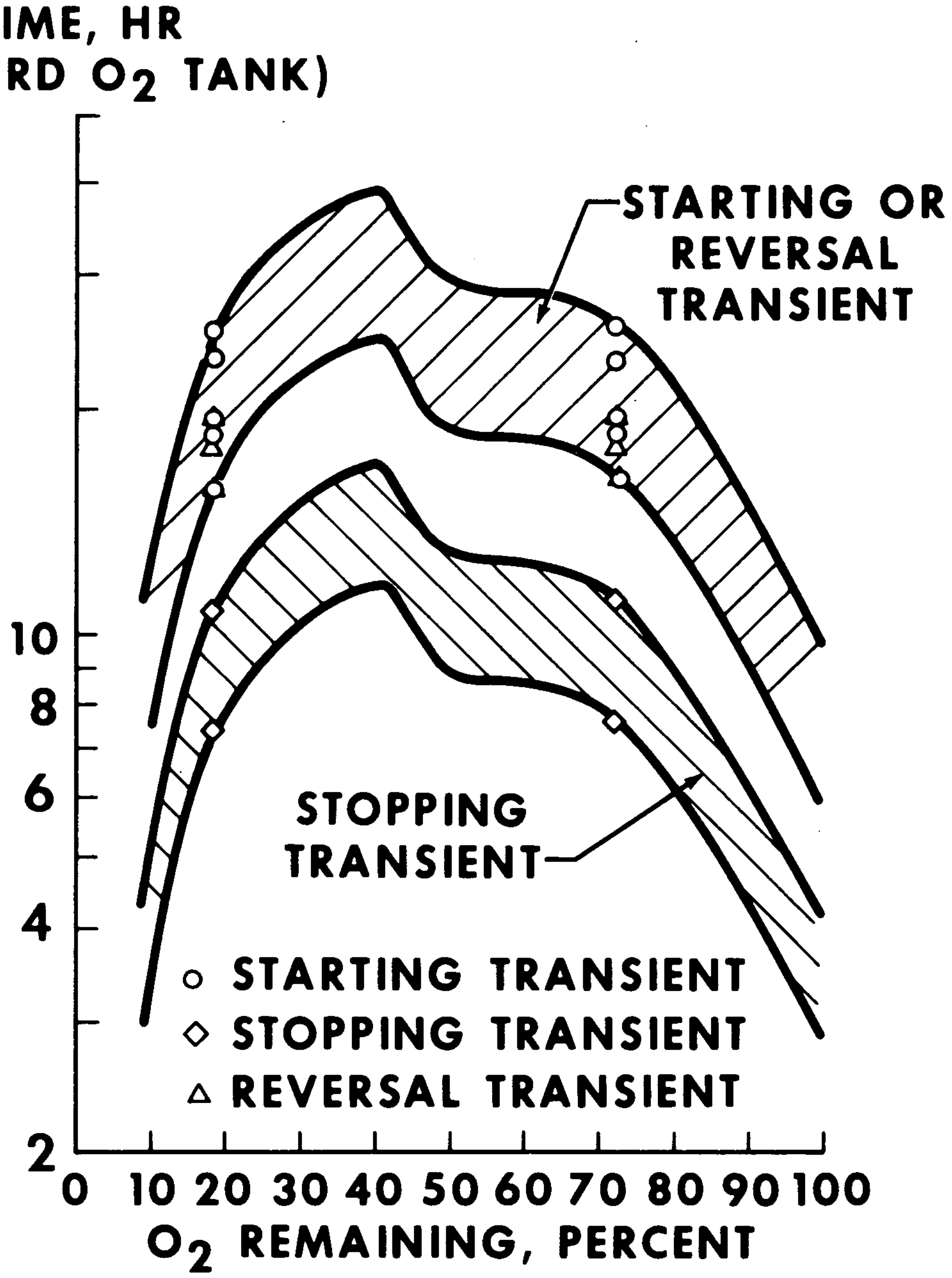

Figure 8.

NASA-S-71-1443-X

TIME TO STEADY STATE

STARTING TRANSIENT

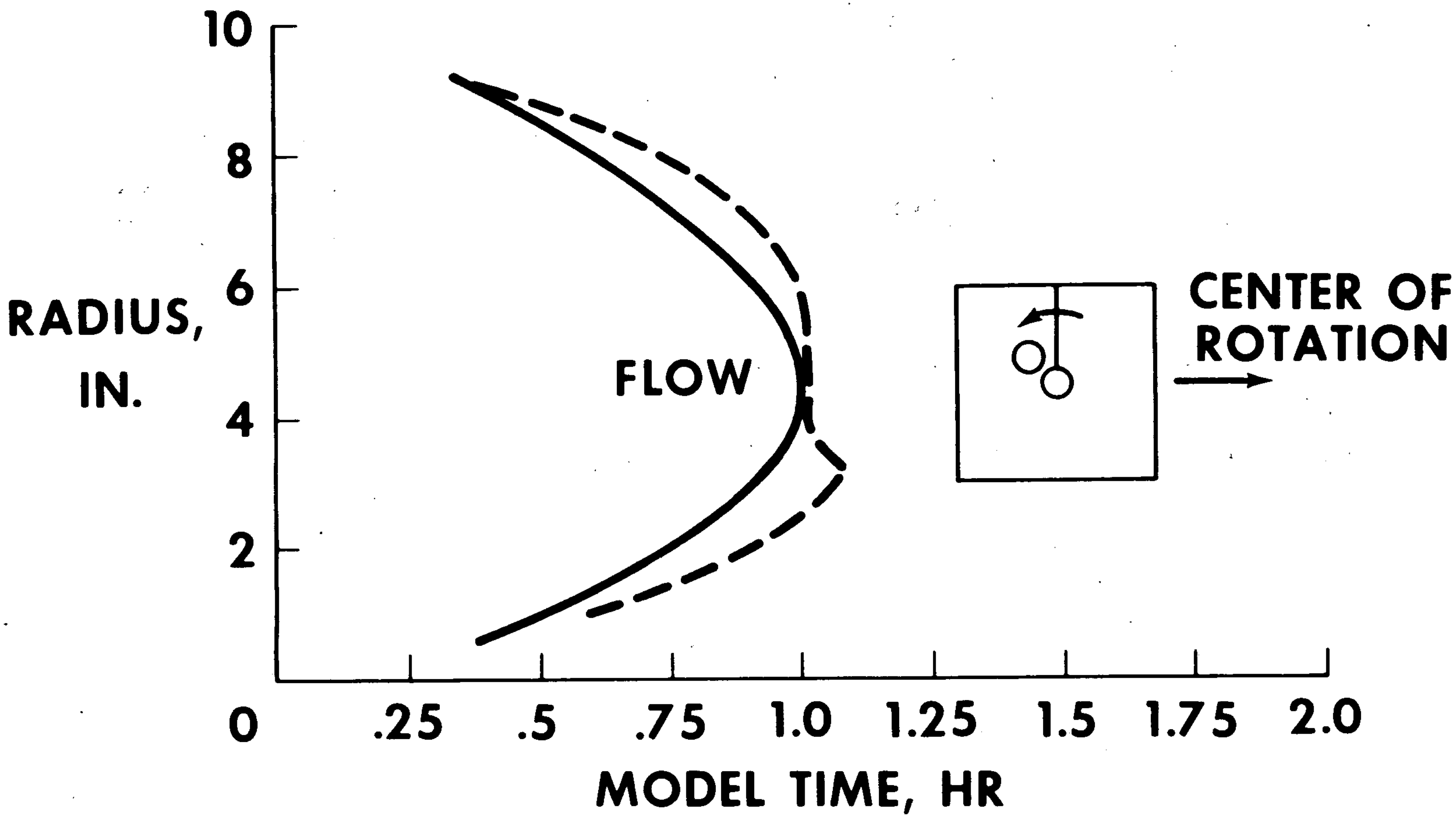

Figure 9.

NASA-S-71-1442-X

TIME TO STEADY STATE

REVERSAL TRANSIENT

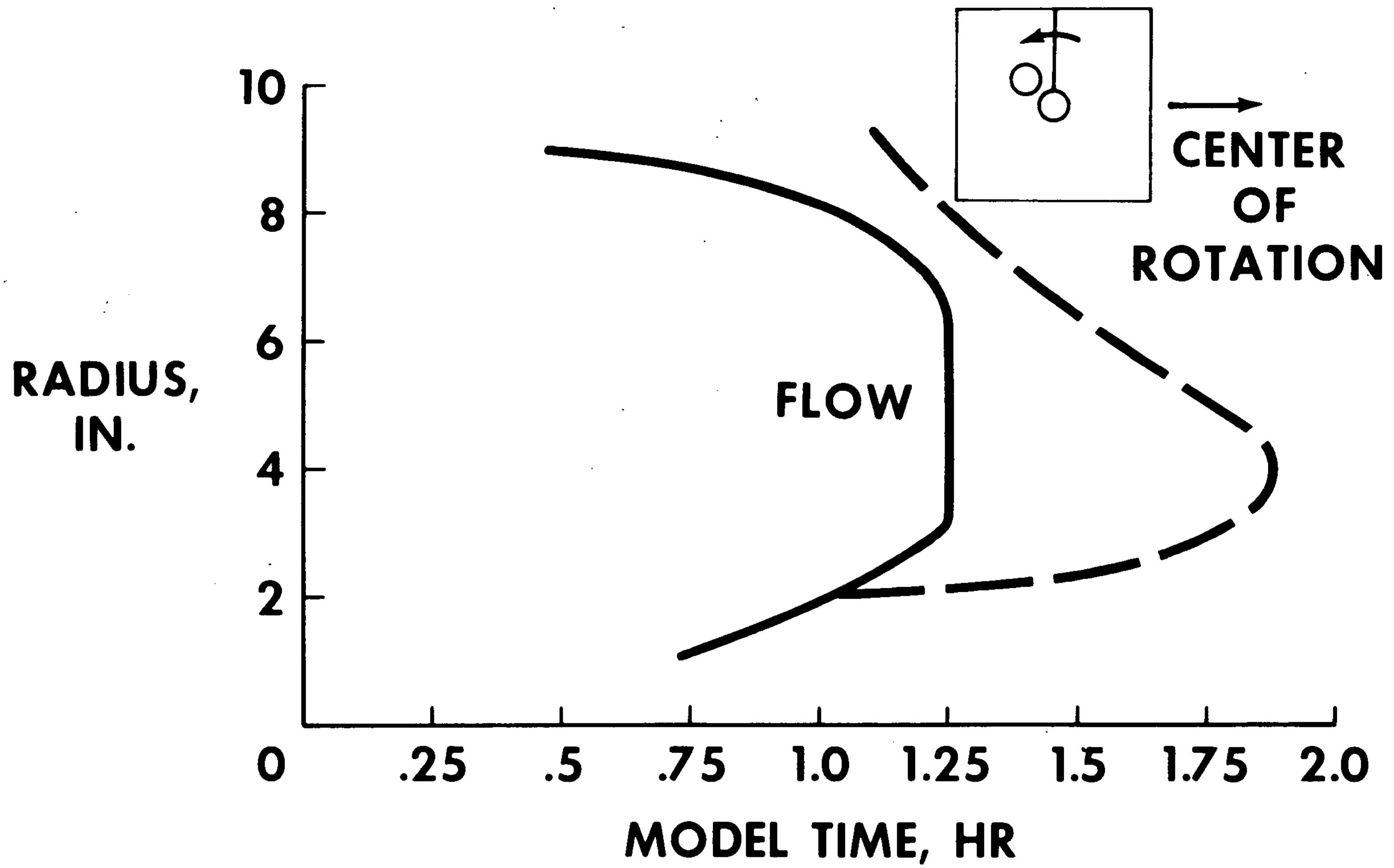

Figure 10.

NASA-S-71-1437-X

TIME TO STEADY STATE

STOPPING TRANSIENT

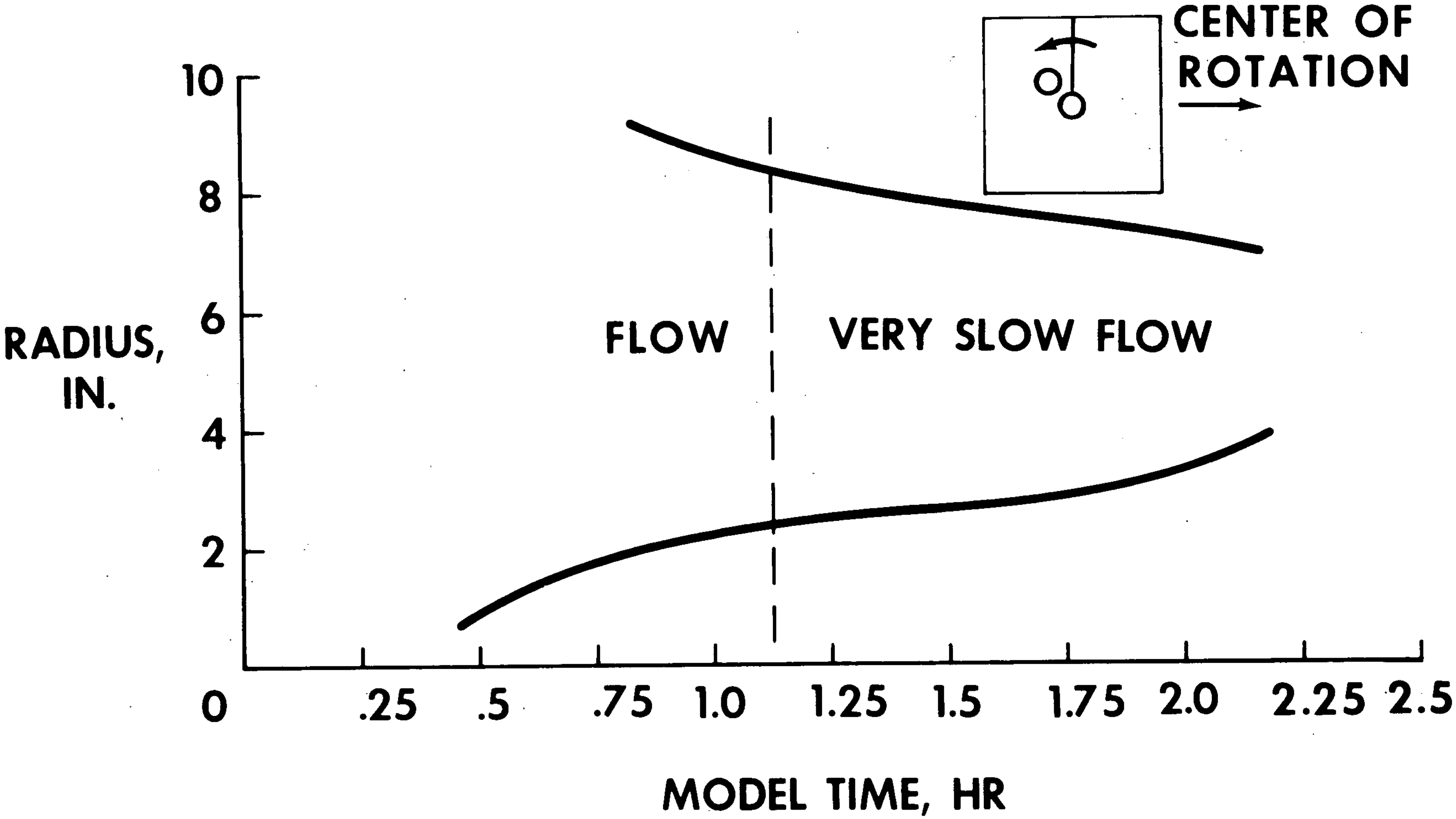

Figure 11.

NASA-S-71-1432-X

TIME FOR O_2 TO COME TO REST ABOUT THE HEATER VS MASS FRACTION OF OXYGEN REMAINING IN TANK

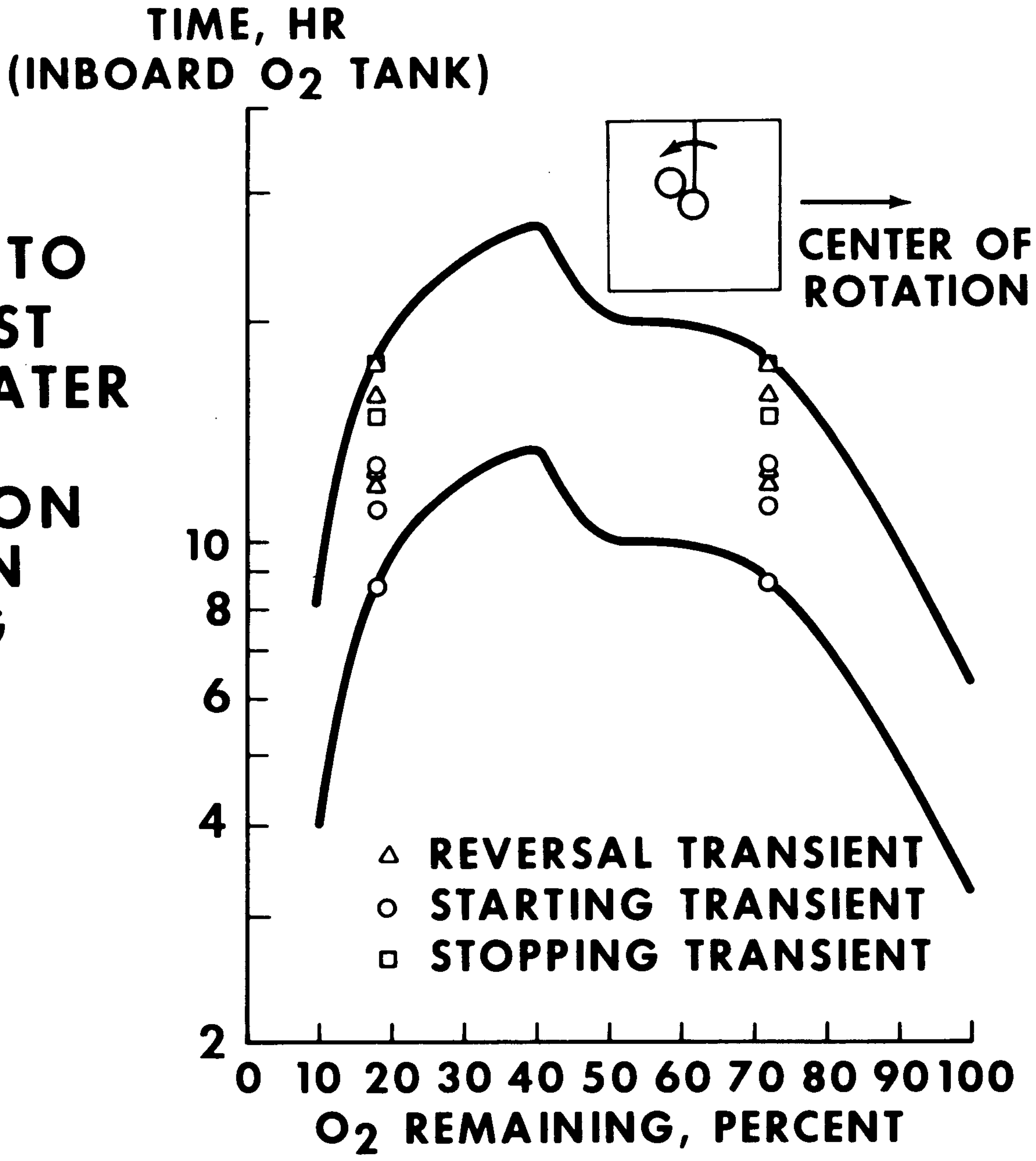

Figure 12.

NASA-S-71-1431-X

TIME TO STEADY STATE

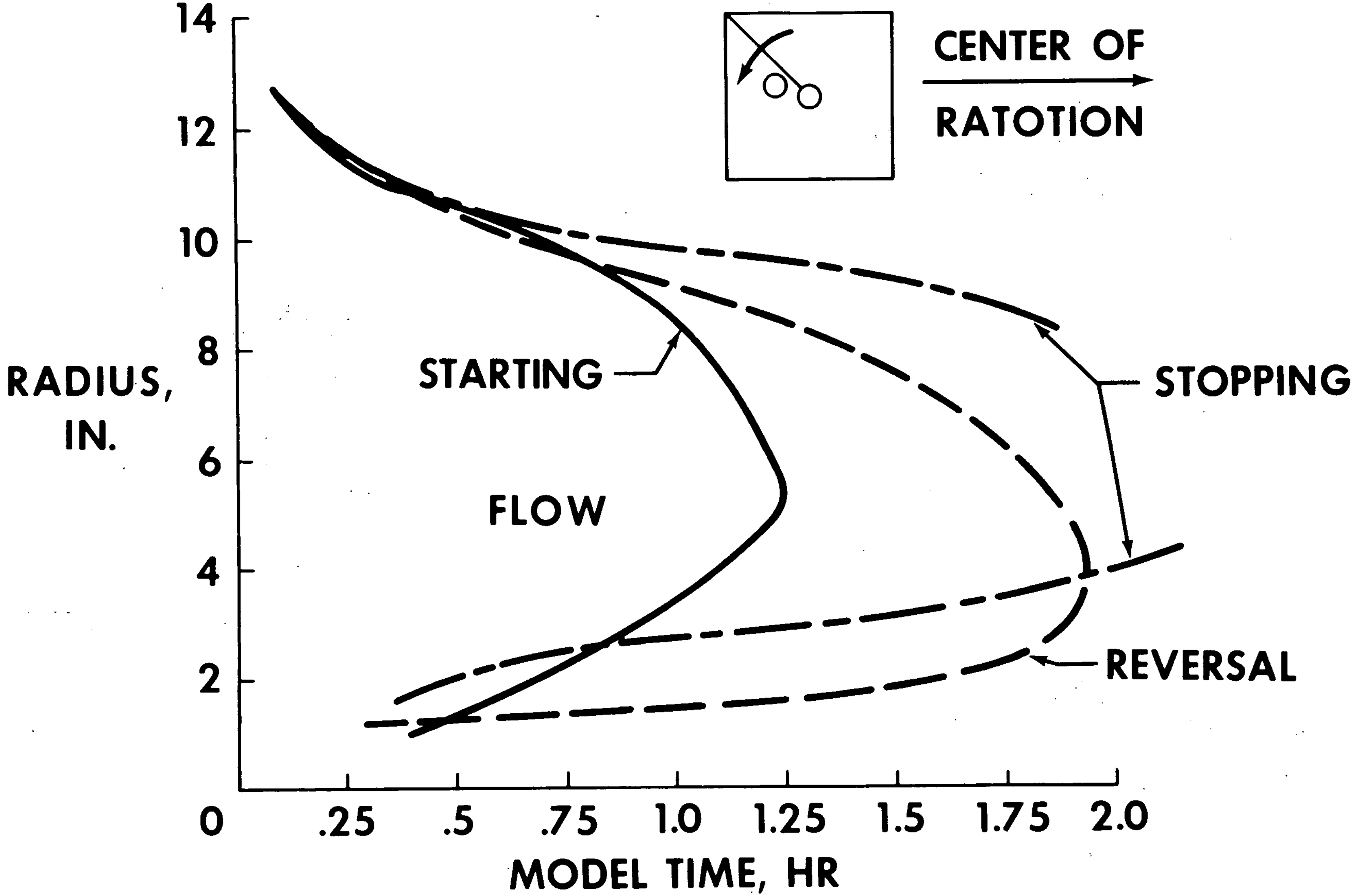

Figure 13.

NASA-S-71-1435-X

TIME FOR O_2 TO COME TO REST ABOUT THE HEATER VS MASS FRACTION OF OXYGEN REMAINING IN TANK

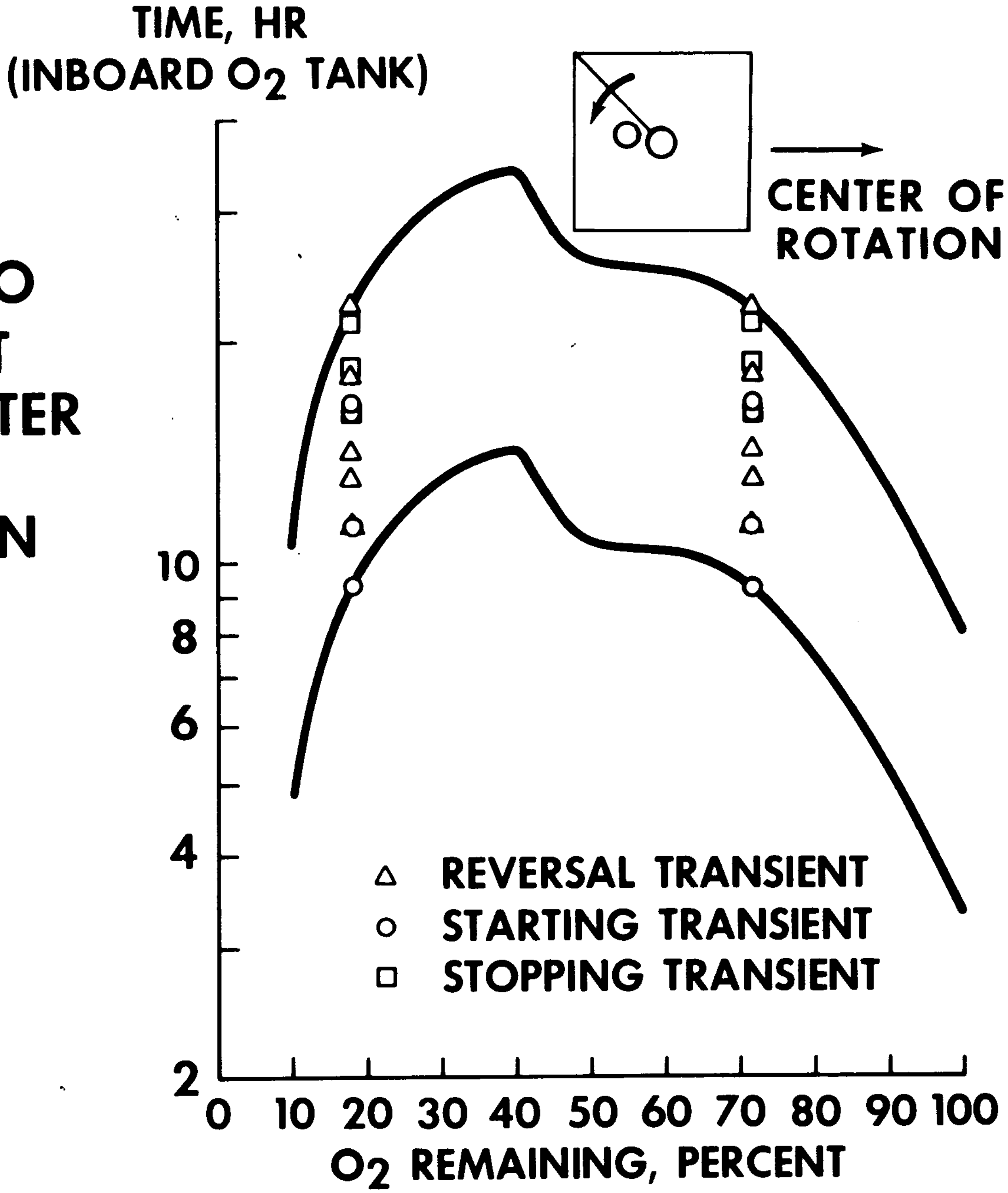

Figure 14.

N72-23799

"A REVIEW OF CRYOGENIC TESTING PERFORMED BY THE THERMOCHEMICAL TEST BRANCH, MANNED SPACECRAFT CENTER IN SUPPORT OF APOLLO 13 AND 14"

By Clarence E. Propp and John M. McGee

NASA Manned Spacecraft Center

ABSTRACT

The Apollo 13 anomaly provided considerable impetus for a variety of types of cryogenic and ignition tests. This presentation will treat the logic of the various test program designs, the test techniques, and their final impact upon the investigation findings. In addition, the presentation will cover several test programs initiated to determine the thermal performance and general performance characteristics of the redesigned Apollo 14 cryogenic storage system.

INTRODUCTION

This paper is a brief summary of the Apollo 13 and Apollo 14 oxygen cryogenic storage system (CSS) tests performed at the Thermochemical Test Area, Manned Spacecraft Center. This area includes five unique facilities which provided the many specialized test environments and fixtures necessary to accomplish the subject test programs. There were 25,000 manhours invested in 30 test programs of which 50% were completed between April 14 and May 22, 1970 in direct support of the Apollo 13 anomaly and the requirements for redesign of the Apollo 14 CSS were made; however, this paper will treat only the test planning logic and the highlights of the more informative tests. The Apollo 13 and Apollo 14 test programs were concerned with ignition and combustion phenomena and the Apollo 14 tests were additionally concerned with determining the operational characteristics of the redesigned CSS.

APOLLO 13 TESTS

The Apollo 13 Anomaly Investigation was a very intense series of test programs and group discussions. The testing was controlled from a single point for the purpose of avoiding redundant and unproductive testing. The control of testing was effective and the pattern which evolved was as described below:

Baseline Tests

These tests were performed for the purpose of basic orientation of the Apollo 13 Review Board, the Observers, and many of the Panel members on the combustion characteristics of the various CSS materials and the operational characteristics of the CSS components and instrumentation.

The materials combustion tests were conducted in high pressure oxygen gas, supercritical oxygen, and subcritical oxygen. There were several informative movies taken during these tests which helped considerably to approximate combustion rates and ignition energy values for teflon wire insulation in 900 psi supercritical oxygen, as well as to establish a graphic understanding of this combustion process.

There were also several test programs conducted for the purpose of characterizing the CSS components and instrumentation in order to more beneficially interpret the data recorded pertinent to the Apollo 13 accident. The TTA test assignments were designed to evaluate the Apollo CSS fluid flow dynamics and its associated valves, pressure transducers, and flowmeter response times. The results of these test programs confirmed that the analysis methods being used on the Apollo 13 data were correct.

At this point, it was evident that combustion of the teflon insulation was a realisitc consideration and the energy released could easily be sufficient to provide the pressure rise rates recorded on the Apollo 13 data. Therefore, it was determined that while ignition and combustion studies continued, an effort to determine the ignition source would be initiated. This included the examination of all aspects of the CSS handling prior to flight.

Simulations of CSS Preflight Servicing

The TTA tests were simulations of the Apollo 13 #2 oxygen tank special detanking procedures which were used by KSC to cope with a detanking problem. This was caused by a displaced inner tank coupling which disallowed simple pressure application for liquid detanking and caused them to detank principally by evaporation. It was suspected that the prolonged and abnormal operation of the tank heaters during detanking was directly related to the ultimate failure. As shown in figure 1, this testing revealed that the heater thermostat switch contacts welded in the closed position. Consequently, heaters were continuously adding energy to the system during the simulated detanking operation which allowed temperatures on the heater probe assembly to rise as high as 1000° F (see figure 2), which is grossly in excess of the

+80° F thermal switch set point. The insulation of the destratification fan motor wires located in this area was severely degraded as shown in figures 3 and 4. This information was very significant for incident reconstruction. As a result of this finding, it was reasonable to postulate that ignition took place somewhere within the heater probe assembly near the degraded fan motor wires after which combustion continued until CSS failure.

Component Level Ignition Studies

This category of tests was designed to deliberately ignite the teflon insulation in a simulated CSS to determine the potential CSS failure modes and to gain a better understanding of system combustion propagation and pressure rise rates. These tests indicated that the flight structural failure occurred within the electrical conduit section between the pressure vessel and the outer shell of the accessory dome. Figure 5 shows the results of these tests. Considerations were now being given to performing a full simulation test using all the flight type hardware possible. However, there were still many reservations concerning the types and quantities of energy releases that could take place after ignition of an "all up" configuration. Therefore, additional tests were performed to determine if there would be gross amounts of energy released from the combustion of metals within the CSS. For these tests, TTA responsibility was primarily the CSS heater/fan motor probe assembly. Every reasonable effort to ignite the fan motors was attempted but no metal combustion was evidenced. Figures 6 and 7 show the results of some of these tests.

Full Simulation O_2 CSS Ignition Test

Subsequently, the "all up" test configuration was established and the test objectives defined. The primary objective was to determine the pressure and temperature time history of the combustion of the teflon wire insulation and the extent of propagation to other materials when the wire insulation was forcibly ignited near the lower fan motor. The test article was a flight configured CSS tanked with approximately 900 psi, -190° F supercritical oxygen. The results of this test were generally as expected. The conduit ruptured 1/4 inch from the pressure vessel (see figure 8) within 58 seconds after ignition. The combustion time history, shown in figure 9, was in agreement with the results obtained from previous component level tests, and was a remarkable facsimile of the Apollo 13 accident time history which occurred within a 75 second period. The difference between one "G" and zero "G" burning rates for the teflon as well as the uncertainty of the exact ignition location easily allows for the 17 seconds difference. The relief valve functioned normally at 1006 psia and the maximum pressure recorded was 1170 psia. As shown in figure 10, post-test inspection of the CSS interior showed that essentially all teflon burned except the lower capacitance probe insulator.

APOLLO 14

Material Ignition and Combustion Tests

During the Apollo 13 investigation, and throughout the resulting Apollo 14 redesign period, the materials test programs continued to provide useful data. The ignition and combustion tests were performed at several MSC locations,* with the TTA responsibility being primarily that of spark ignition studies. Several methods of controlling and measuring spark energy releases were developed, and spark testing was performed over a range of voltages, energies, and specimen types. The test apparatus shown is shown in figure 11, a typical spark ignition device schematic is shown in figure 12, and the results of igniting an aluminum specimen are shown in figure 13. The test results may be generalized as follows:

1. Short term sparking is probable with wire breaks and intermittent shorts and is very difficult to protect against. Normal fusing techniques are too slow to provide adequate protection.

2. Lowering the voltage available at the gap makes it more difficult to transfer spark energy at rates sufficient to cause combustion.

3. Practical values for the spark ignition threshold of materials are very difficult to obtain because they are very dependent on geometries from the viewpoints of ease of sparking, and heat retention properties. That is, sharp points and/or low mass extrusions are more easily ignited than blunt large mass objects.

4. Some ignition threshold values considered useful which were developed by sparking from needle point geometries in an ambient temperature high pressure O_2 environment are 0.25 joules for teflon, approximately 3 joules for poor conducting metals, and somewhat higher energies for good conducting metals.

5. Each design configuration must be independently evaluated to determine its vulnerability to spark ignition.

---

*Flammability Testing Conducted in Support of Apollo 13, by L. J. Leger, Materials Technology Branch, MSC, and R. W. Bricker, Structural Test Branch, MSC.

The Apollo 14 redesigned CSS excluded the destratification fan motors thereby eliminating a potential high energy spark source. In addition, all teflon wire insulation was deleted which eliminated most of the easily ignitable combustible material. The new design incorporated extensive use of stainless steel sheathed, silicone dioxide insulated conductors which provided considerably less vulnerability to damage and combustion than the Apollo 13 installation. All of the elements incorporated in the redesign which would be exposed to oxygen were spark ignition tested under many failure mode simulations. The results were that the Apollo 14 redesign spark tests produced no ignitions when a circuit with resistances and fuse protection like that in the spacecraft was included.

Alternate Destratification Methods

Following the elimination of the destratification fans, two courses of investigation were followed: one, providing a substitute for the loss of the fans, and two, investigating the problems associated with having no destratification devices.

One of the more promising substitutes considered was an external recirculation loop concept. A test was performed to determine the feasibility of using a modified version of the Apollo Environmental Control System (ECS) coolant pump to circulate the fluid to destratify the oxygen in the CSS. Figure 14 shows the disassembled pump. The pump electrical parts were excluded from contact with the fluid by use of a magnetically coupled fluid impeller. In the test setup, the pump was installed such that the oxygen would flow from the vent to the fill line of an Apollo cryogenic storage vessel. For this test an unmodified coolant pump was used, and nitrogen was substituted for oxygen. Various gaseous and supercritical fluid conditions were tested to simulate the full mass quantity spectrum. A normal usage outflow of 1.5 pounds per hour was provided during the test. The feasibility was clearly demonstrated in a low density or 5 pounds per cubic foot test, in which purposely induced stratification was eliminated by operation of the external loop.

To aid in determining the effects of having no destratification devices in the cryogenic storage vessel, tests were performed in which KSC prelaunch tanking procedures were duplicated both with and without heater operation, without the use of destratification fans, and with the vessel in a normal vertical configuration. Following each test, the vessel was agitated to simulate launch vibration; this resulted in a maximum of 10 pounds per square inch decrease from 900 pounds per square inch absolute pressure. These pressure decreases were accompanied by 3° F decreases in indicated temperature and a 2% decrease in indicated quantity.

Additionally, an investigation of stratification at low fill densities was conducted by depleting the cryogenic storage vessel to 35%, establishing normal usage flow and maintaining pressure for 24 hours. The vessel was then agitated to simulate engine firing accelerations and vibrations and no appreciable pressure decay was observed.

The final test in this series was to determine the operational time available when depleting at the maximum expected flowrate to 150 pounds per square inch absolute without the use of heaters and starting at a low fill density (20% full).

The results indicate a time to minimum pressure of 49 hours with the vessel located in a 60° F environment. Even though two phase fluid existed somewhere between 554 and 501 pounds per square inch absolute pressure, it did not cause any operational problems.

Flight Support Tests

To meet a specific Apollo 14 in-flight test objective, it became necessary to determine the best method for filling the newly configured cryogenic storage vessel to approximately 60%. In the first method tested, the vessel was filled with liquid oxygen, dumped to 61% using gaseous oxygen pressure, fully pressurized with ambient temperature gaseous oxygen (quantity increased to 74%), and depleted at one pound per hour for 40.5 hours. During the depletion phase, the pressure decreased below the minimum operational limit and required 5.5 hours to recover although the heaters were on. Figure 15 is a plot of the pressure versus time for this period. The vessel was subsequently agitated but no pressure decay was experienced.

In the second method attempted, the vessel was filled with liquid oxygen, pressurized with heaters, depleted at 1.55 pounds per hour for 63 hours, and further depleted for 44 hours with equilibrium flow to maintain normal pressure. No abnormal pressure decay resulted from depletion flows or from agitation of the vessel.

A third method was implemented whereby the vessel was filled with liquid oxygen, dumped to 51%, pressurized to normal pressure with gaseous oxygen, and maintained at normal pressure by inflow of gaseous oxygen for 10 hours. Agitation produced a pressure decrease of 249 pounds per square inch and subsequent repressurizations with heaters followed by agitations continued to show pressure decreases.

Of the three methods, the second method was chosen since it fit within launch pad operational constraints and produced no instability in the vessel.

CONCLUDING REMARKS

The test programs conducted at the TTA, MSC, in support of the Apollo 13 investigation provided very fast, accurate insight into the cause of the flight anomaly, as well as important guidelines for the Apollo 14 CSS redesign. These test programs also provided the operational information necessary to gain a high confidence level in the redesigned Apollo 14 CSS.

Some specific conclusions from these tests, which are of interest to cryogenic systems designers, are as follows:

1. Electrical circuits included in oxygen storage vessels may be hazardous unless special engineering precautions are taken to limit the availability of electrical energy and/or to provide geometries demonstrated to be safe.

2. Potentially detrimental fluid stratification effects may be minimized by using external loop circulation techniques and/or by special filling and operational methods such as those developed for Apollo 14.

S-70-40850

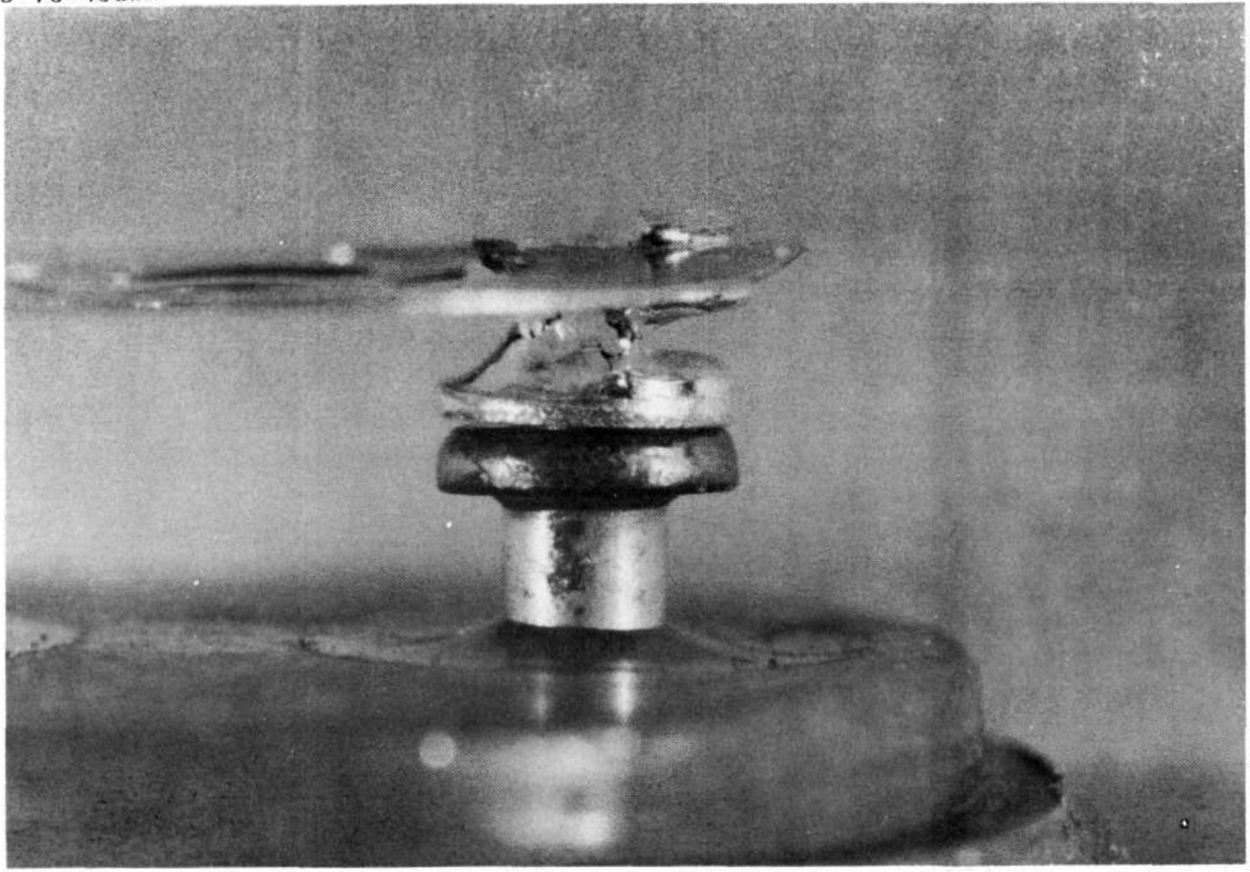

Figure 1.- Welded heater thermostat switch contact

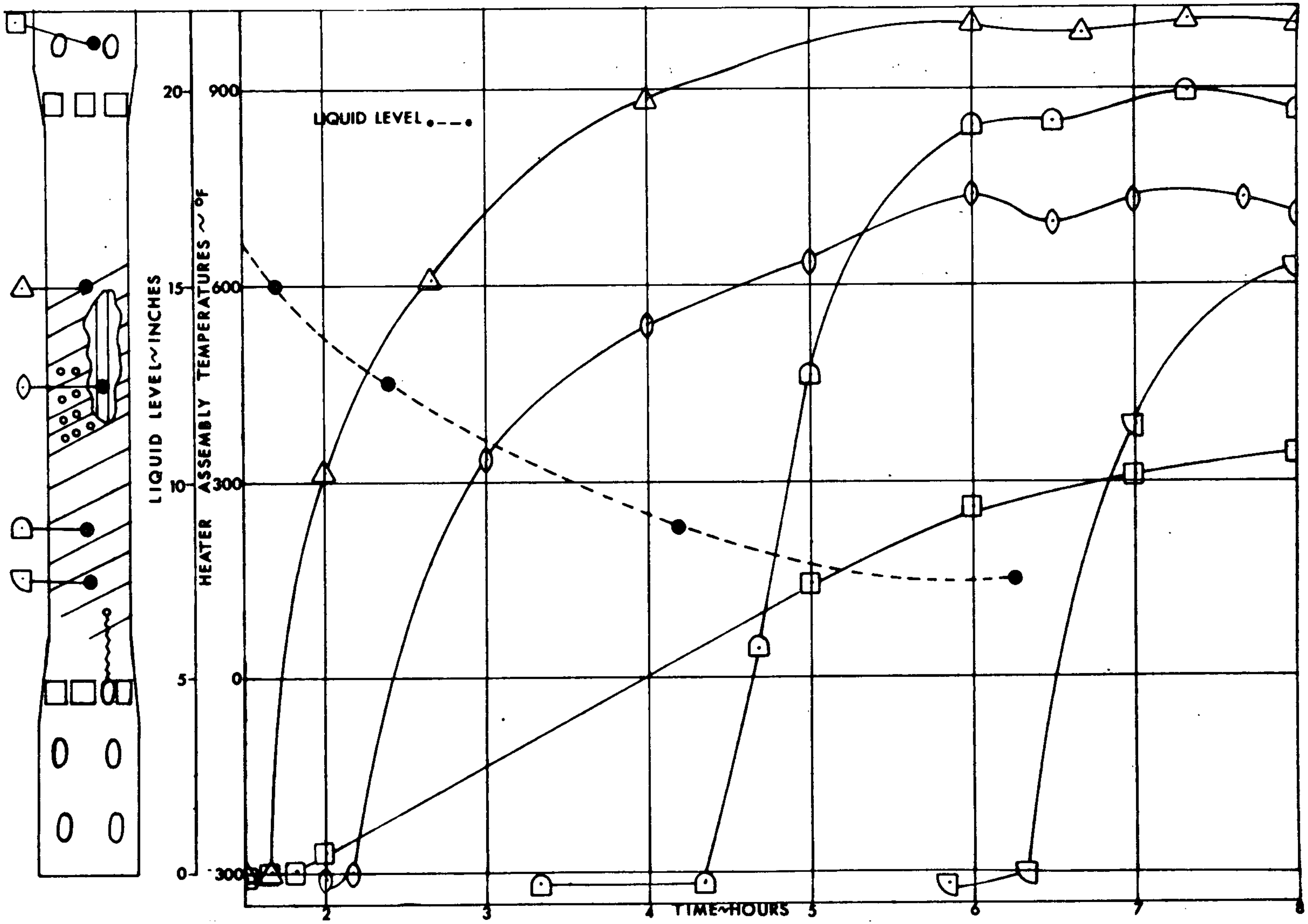

Figure 2.- Detanking heater temperature profile

S-70-40291

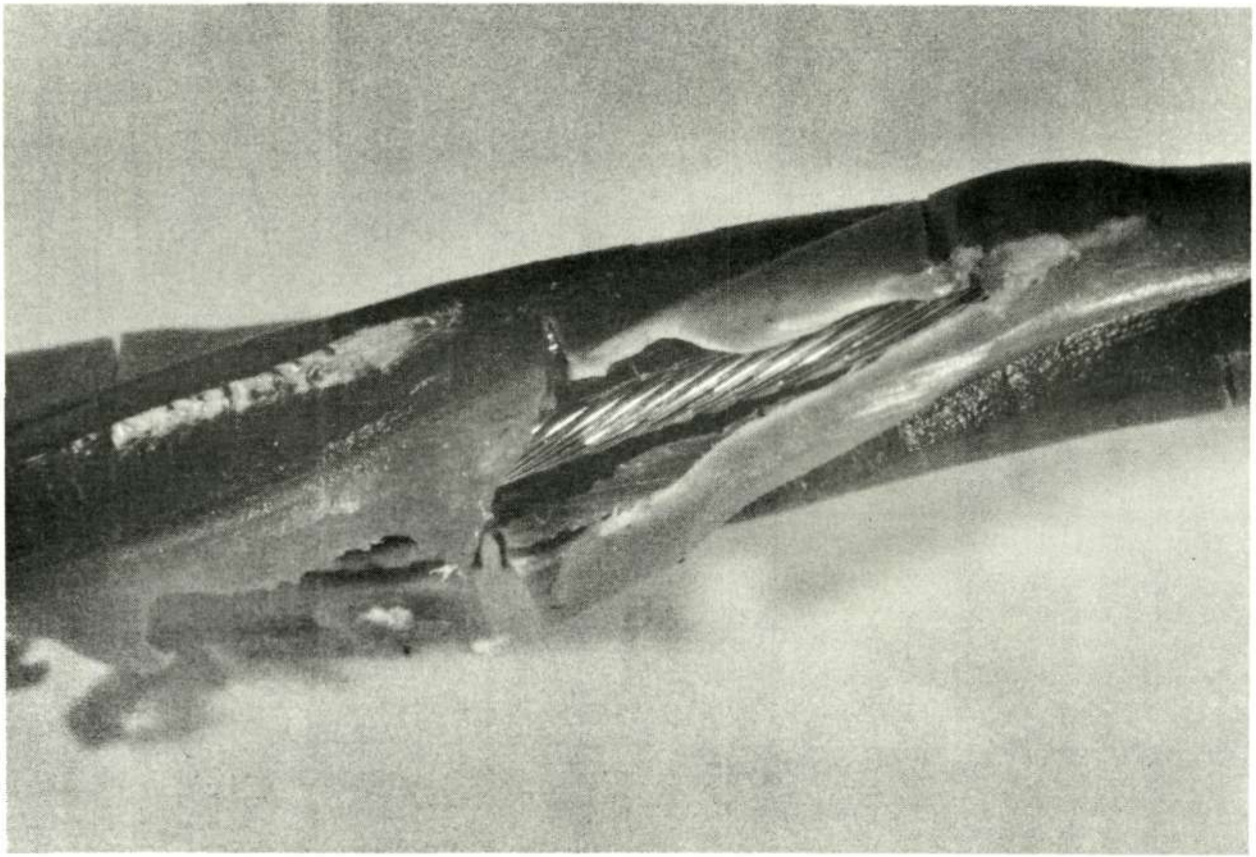

Figure 3.- Most severe degradation to fan motor wire insulation

S-70-40287

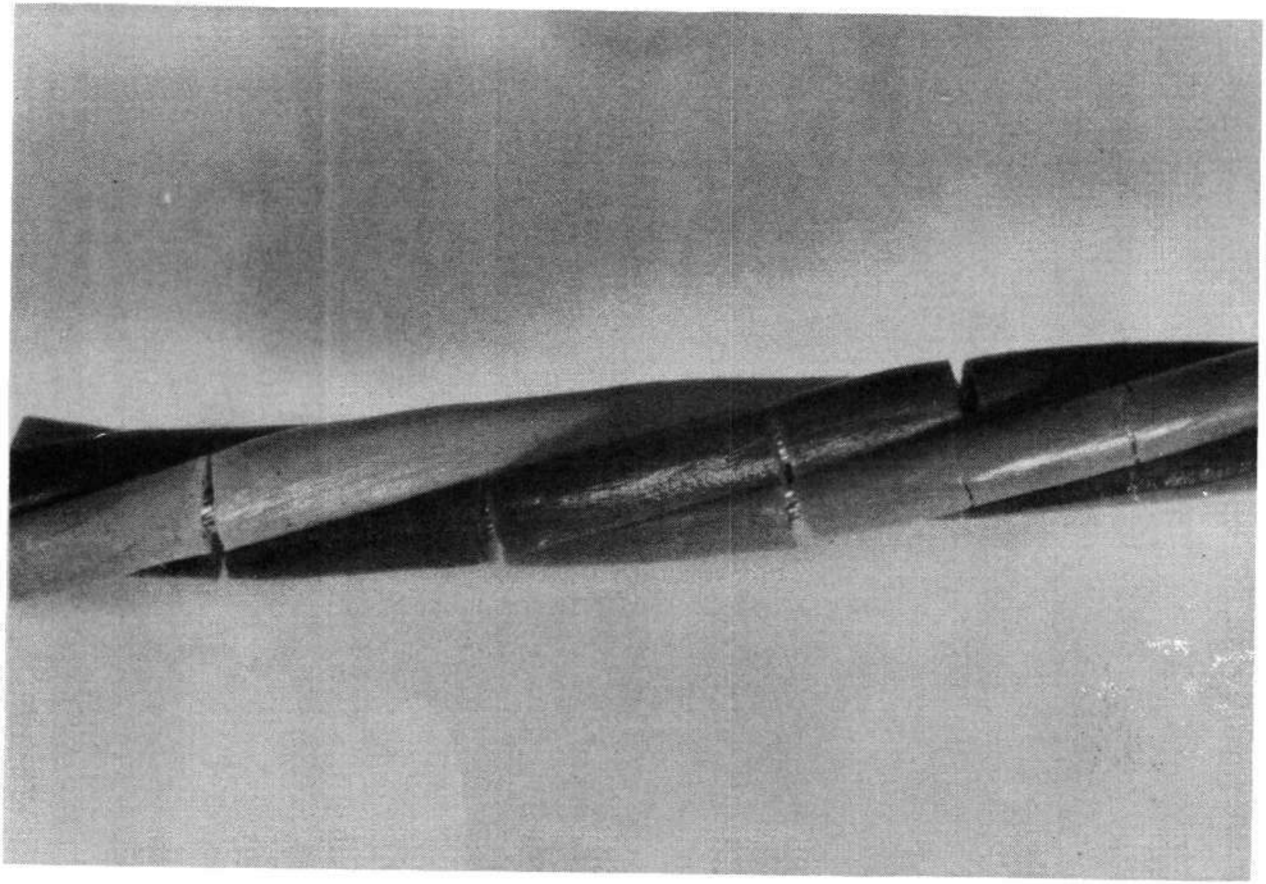

Figure 4.- Average degradation to fan motor wire insulation

S-70-39336

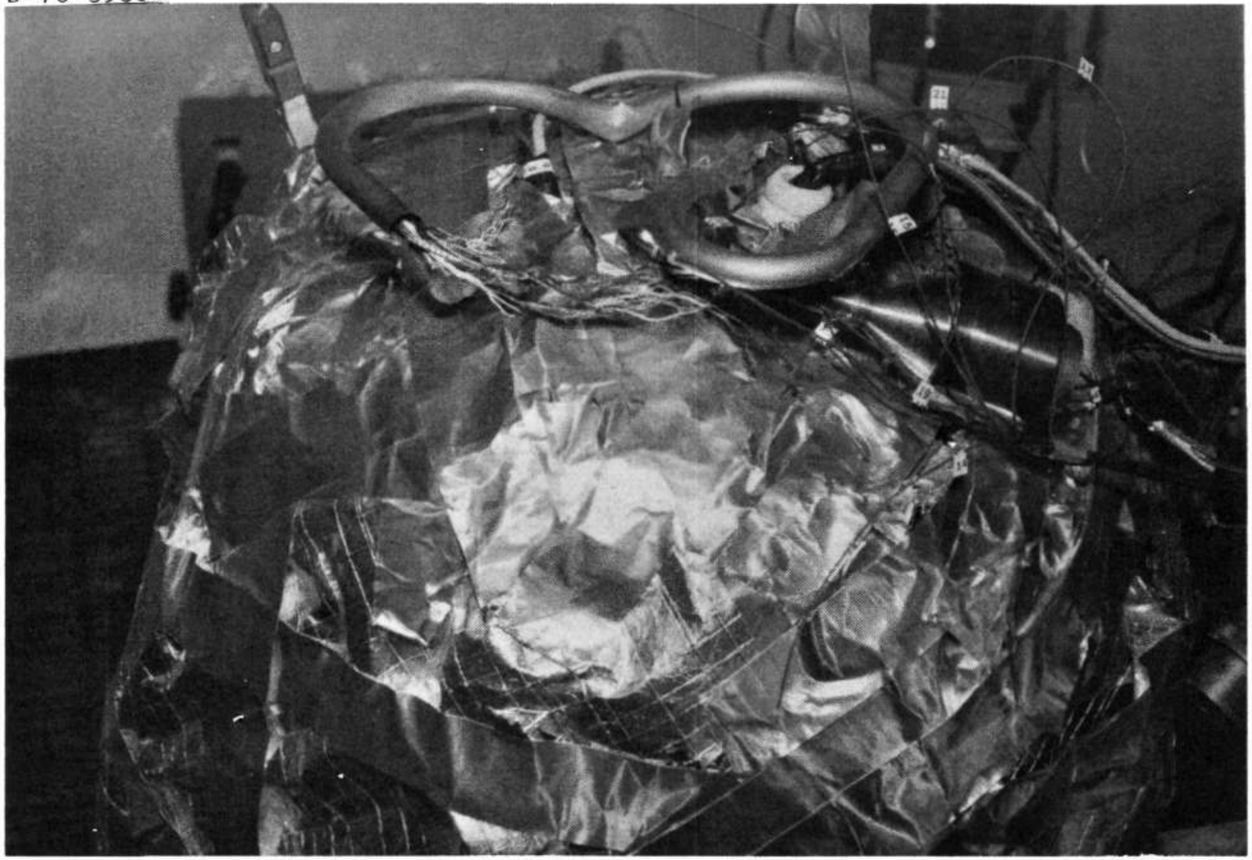

Figure 5.- Electrical conduit after rupture

S-70-40036

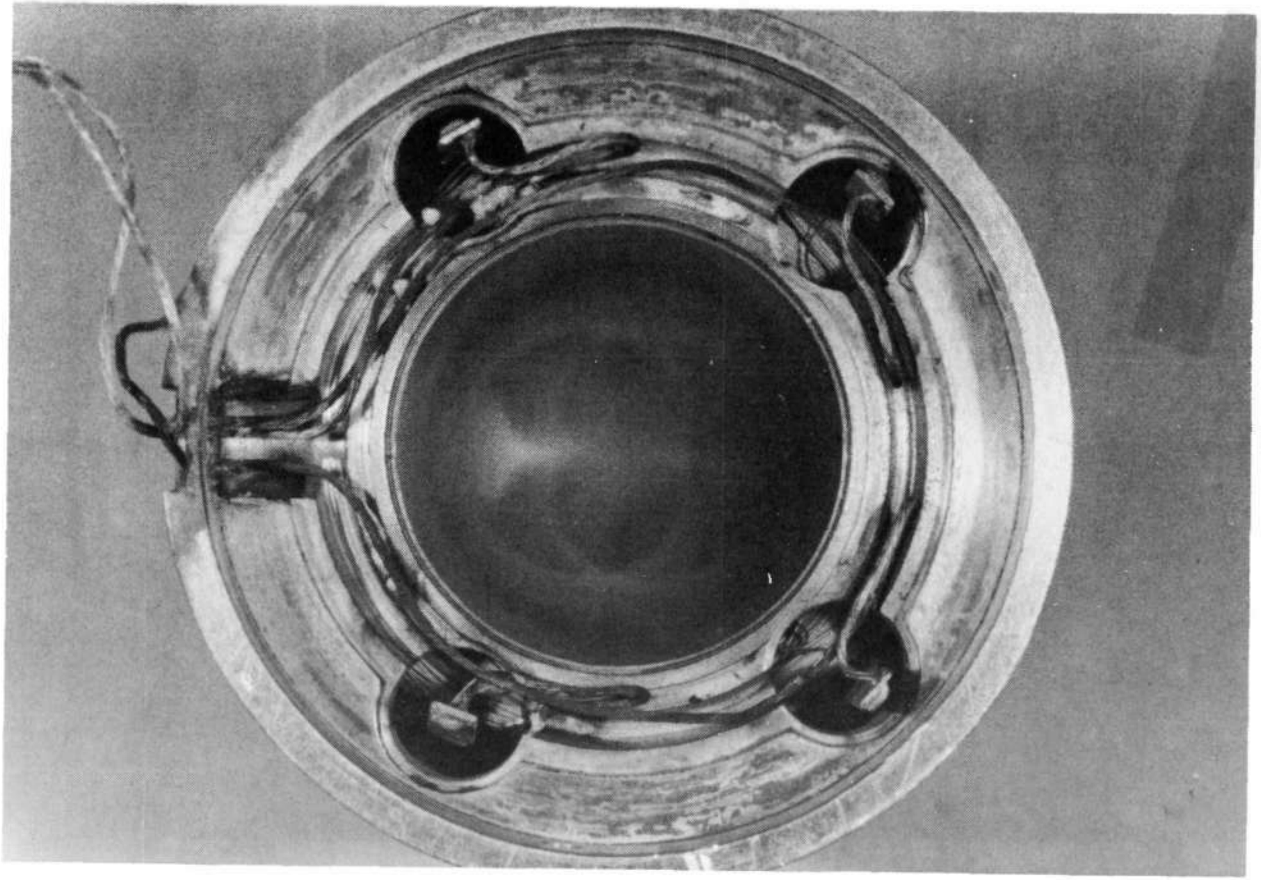

Figure 6.- Fan motor wire and terminal insulation combustion from upward burning

S-70-43325

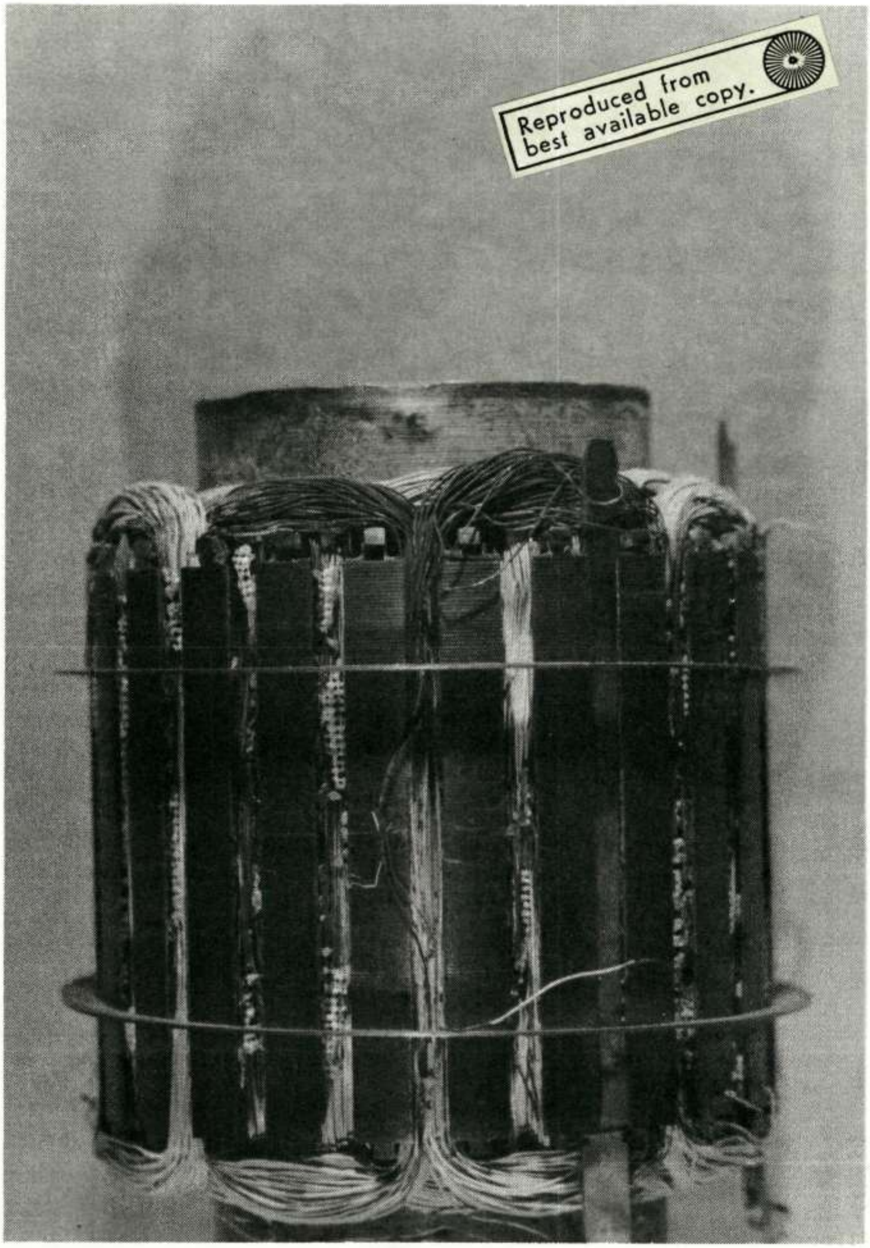

Figure 7.- Fan motor charred stator winding insulation
from upward burning

S-70-41292

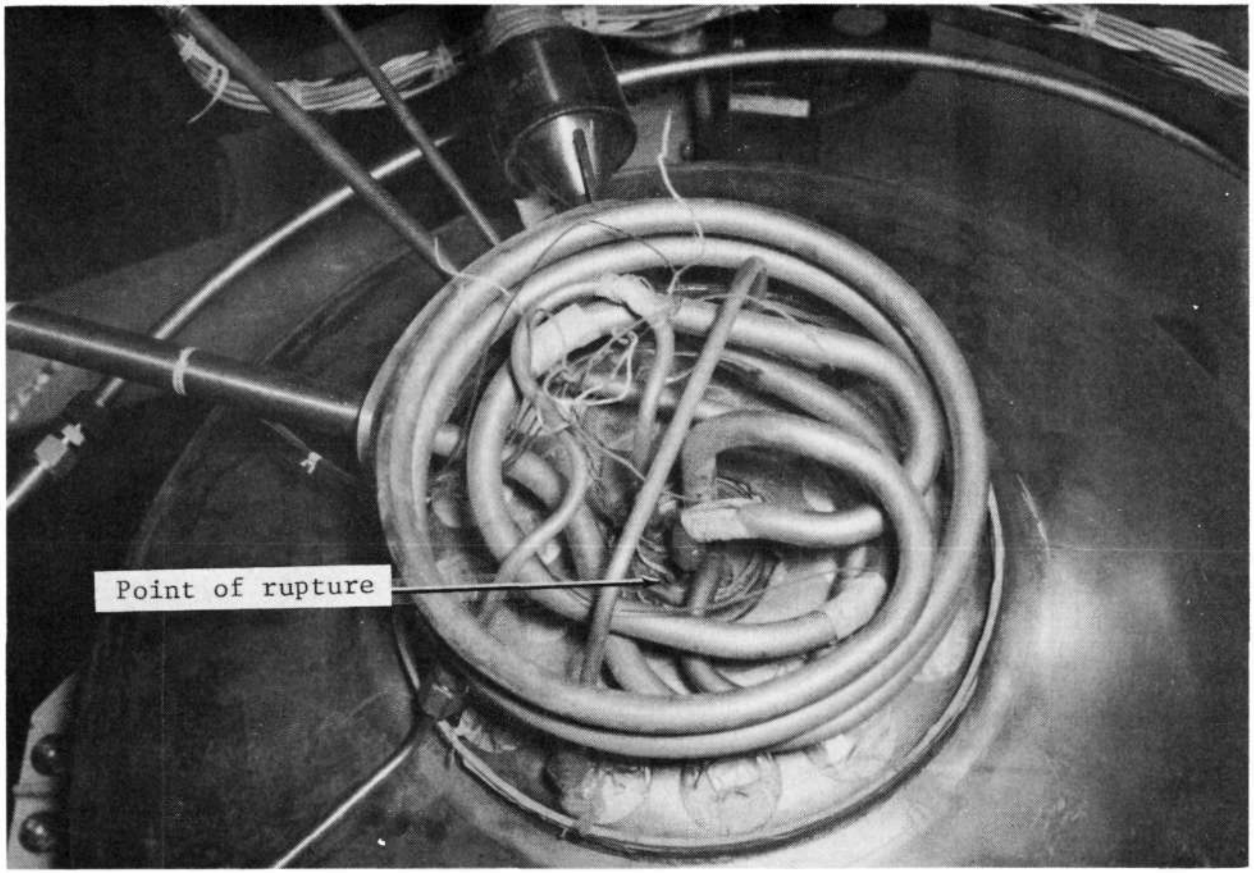

Figure 8.- Electrical conduit rupture after "all up" test

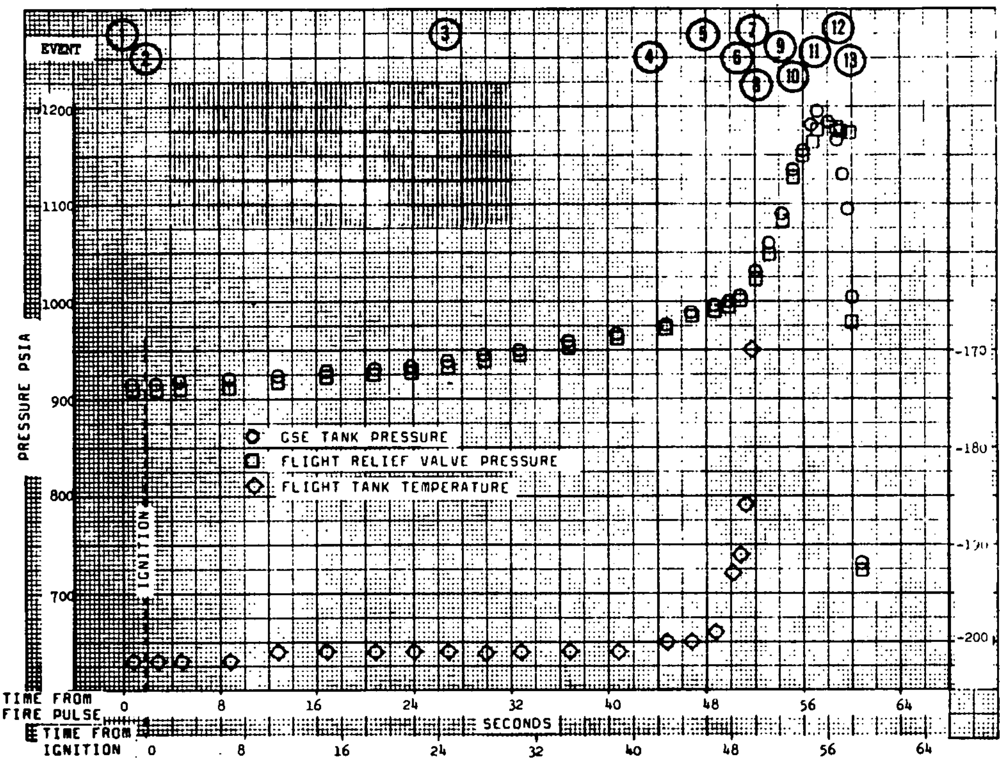

Event number	Event	Time from fire pulse, seconds	Time from ignition, seconds
①	Fire pulse applied to igniter on lower fan motor wires	0.0	-1.99
②	Lower fan motor fuses blown	1.99	0.0
③	Upper fan motor fuses blown	26.70	24.71
④	Wire loop temp. sensor indicated slow temp. rise	43.33	41.34
⑤	Flight position temp. sensor indicated slow temp. rise	47.93	45.94
⑥	Flight relief valve opens at 1006 psia	50.86	48.87
⑦	Wire loop temp. sensor offscale	51.92	49.93
⑧	Flight position temp. sensor offscale	52.03	50.04
⑨	GSE relief valve opens at 1095 psia	54.14	52.15
⑩	GSE relief valve opens at 1129 psia	55.14	53.15
⑪	Maximum tank pressure achieved (1197 psia)	57.03	55.04
⑫	Max. flow thru flight relief valve - 100.2 lb./hr.	59.02	57.03
⑬	Tank rupture at 1134 psia	59.99	58.00

Figure 9.- "All up" test time history

S-70-41327

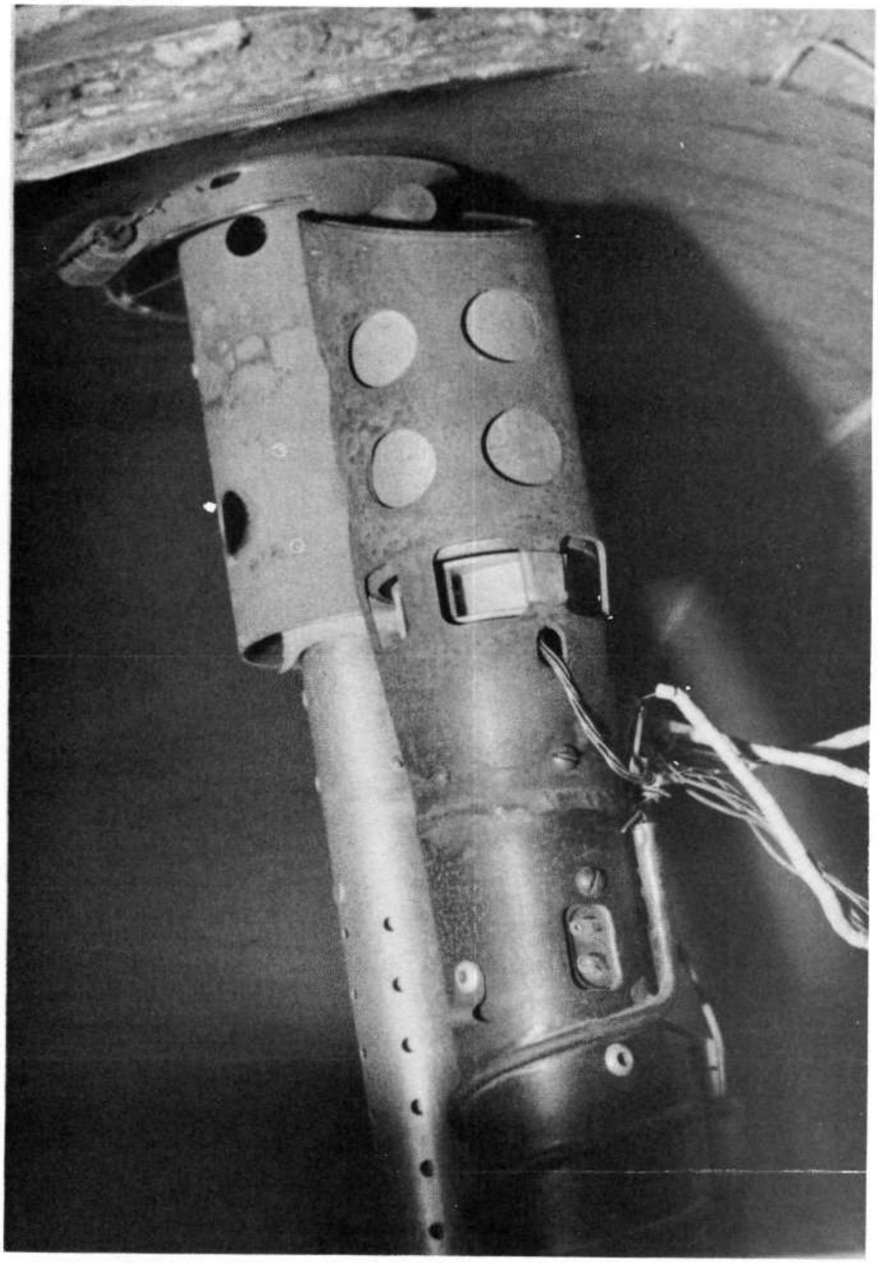

Figure 10.- Top of heater and capacitance probe assembly after "all up" test

S-70-40406

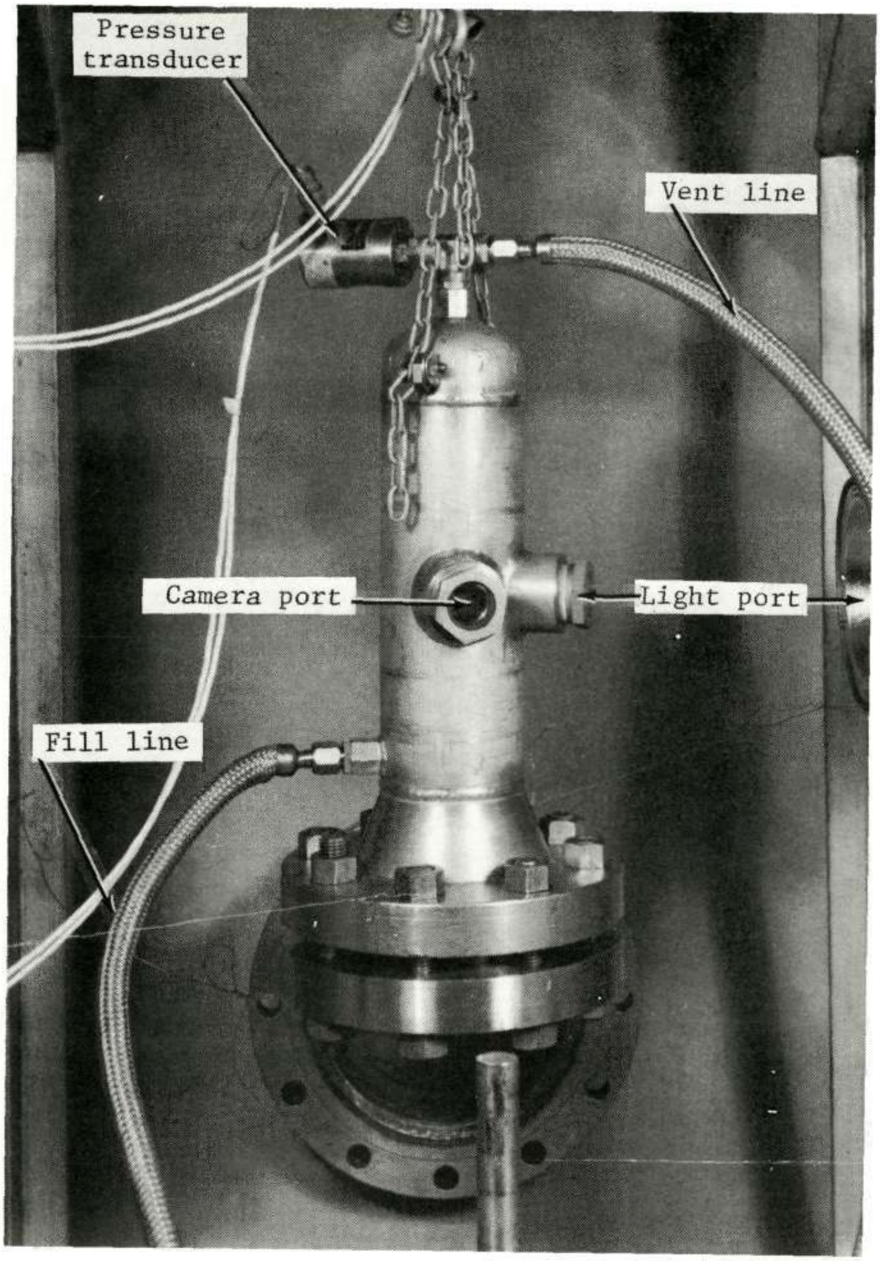

Figure 11.- Supercritical oxygen spark ignition test apparatus

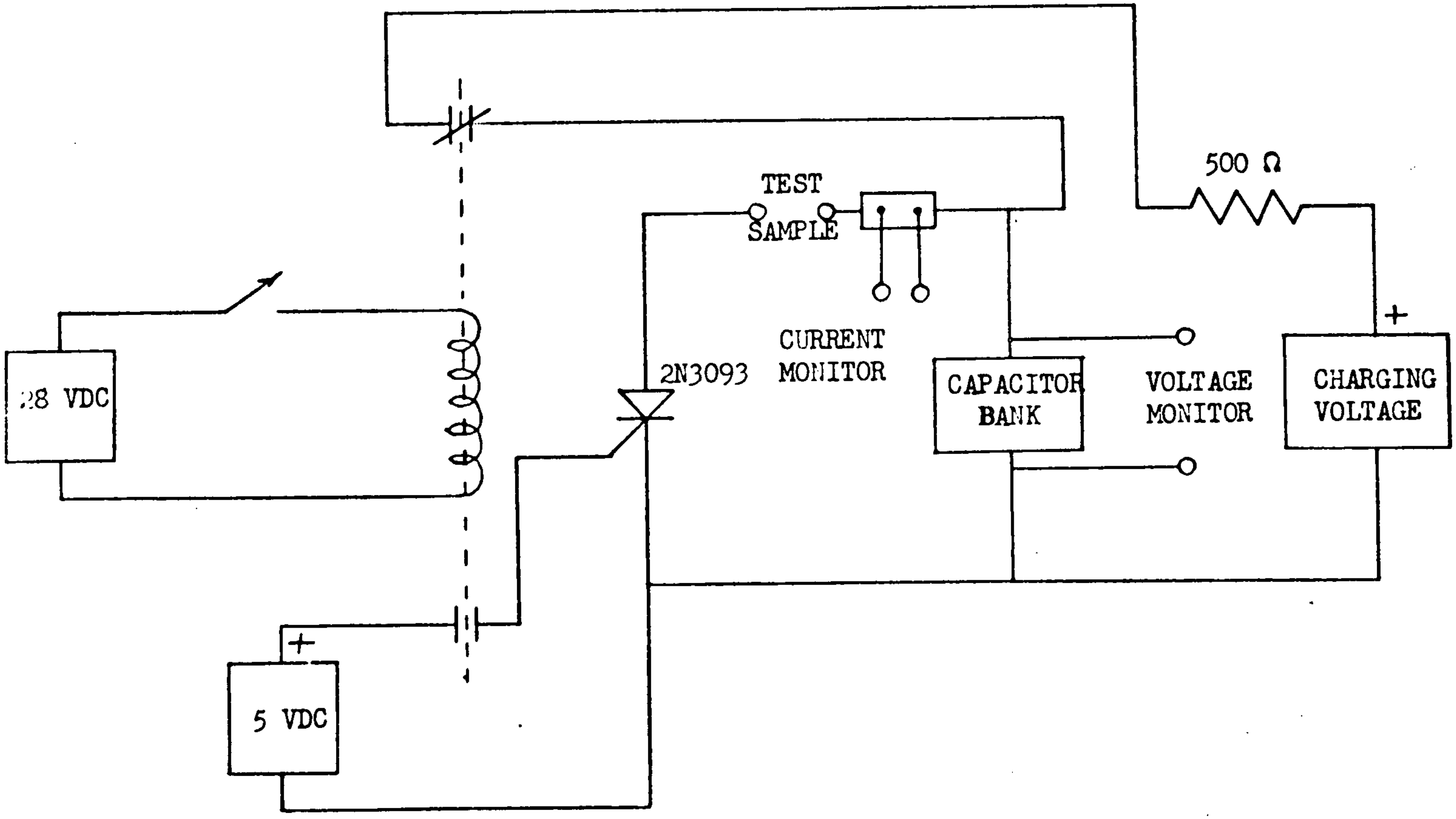

Figure 12.- Capacitor discharge spark ignition test system schematic

S-70-43575

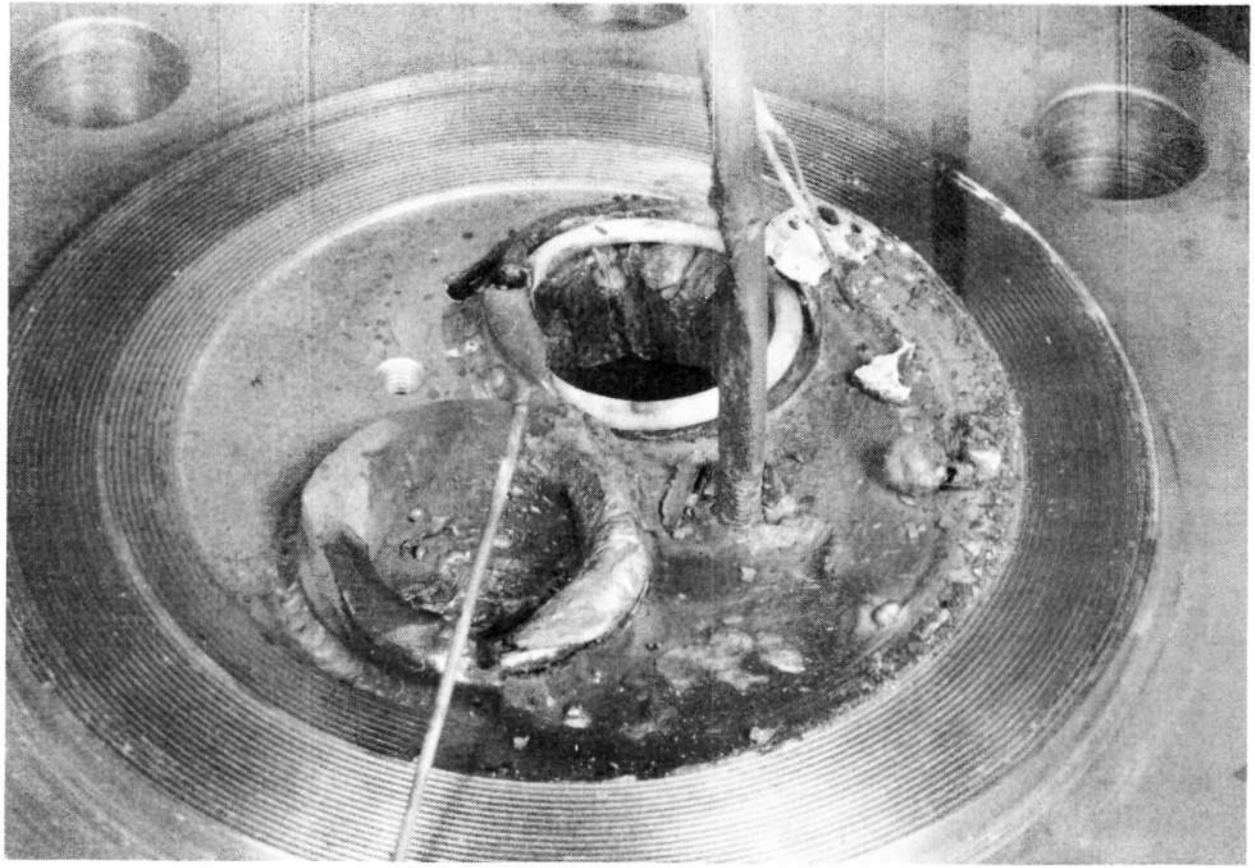

Figure 13.- Results of aluminum burn after spark ignition in a stainless steel test vessel

S-70-47003

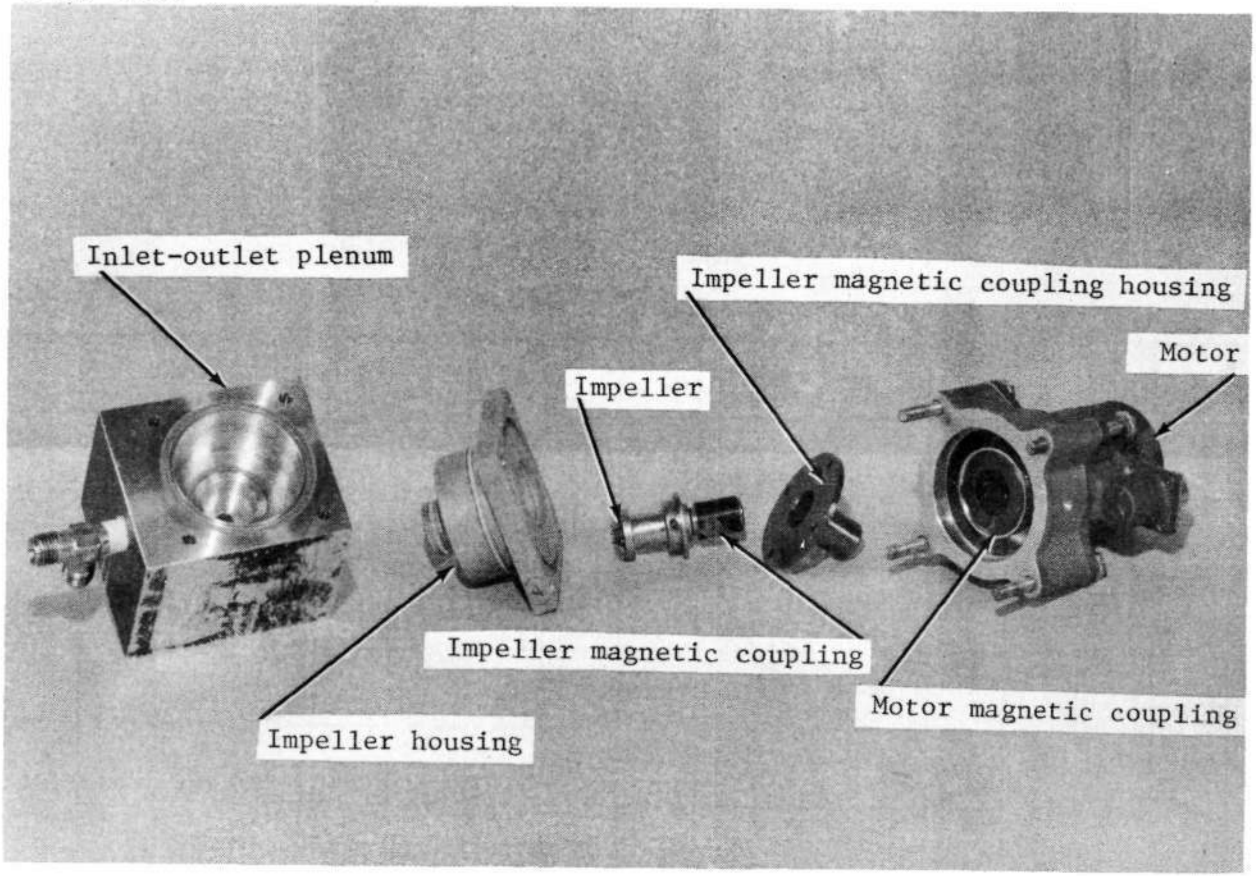

Figure 14.- Disassembled recirculation pump

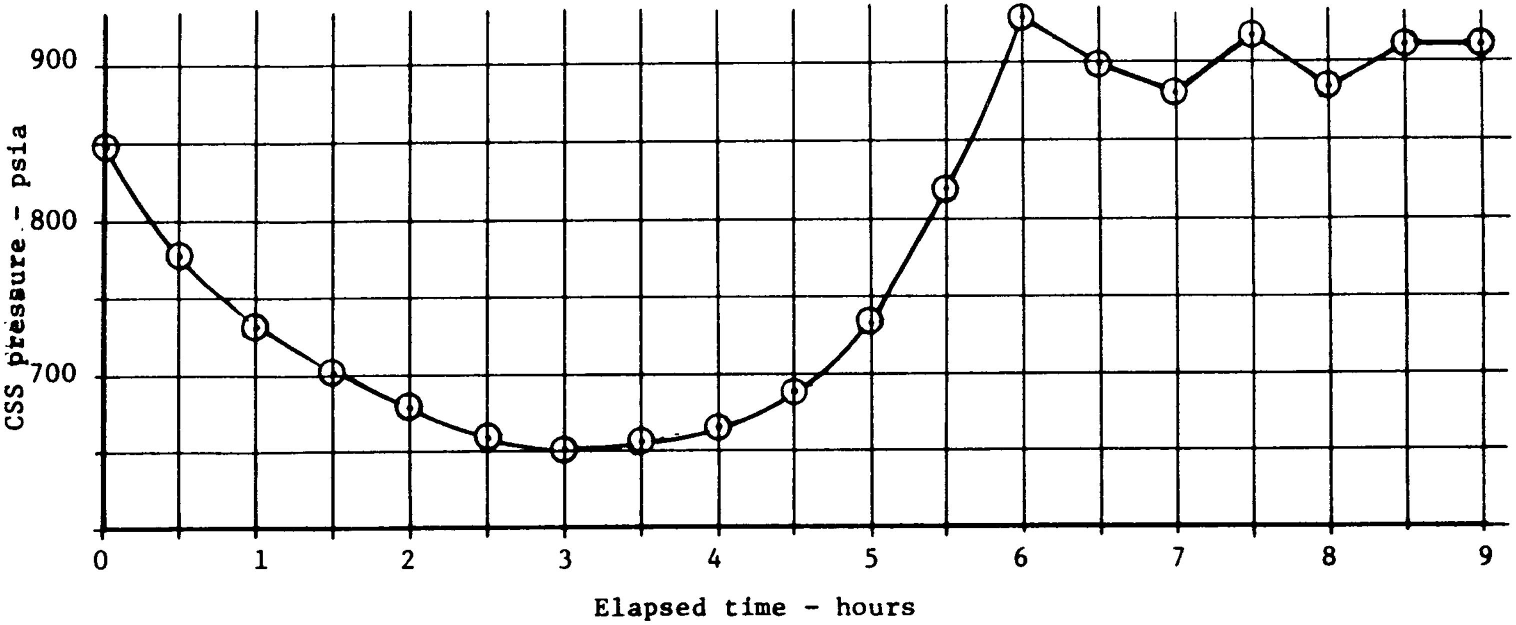

Figure 15.- CSS pressure for 1st partial fill method

N72-23800

FLAMMABILITY TESTING CONDUCTED IN SUPPORT OF APOLLO 13

by

L. J. Leger, Materials Technology Branch, MSC

and

R. W. Bricker, Structural Test Branch, MSC

ABSTRACT

In support of the Apollo 13 investigation of the oxygen tank failure, flame propagation rates were determined for Teflon insulation in cryogenic and ambient temperature oxygen for upward, downward, and zero "g" burns. The propagation rates depended heavily on configuration and varied from 4.8 to 10.9 cm/sec for upward one "g" burns to 0.48 cm/sec for zero "g" burns.

In addition to the flame propagation rates, tests were conducted to determine if Teflon burning in cryogenic oxygen could ignite metals (promoted ignition) with which it came in contact. Tests conducted on various metal alloys used in the oxygen tank indicated that most of the alloys could be ignited by burning Teflon in certain configurations.

After the propagation rates and promoted metal ignitions had been evaluated, a test was conducted on a quantity gauge and wire harness used in the oxygen tank to determine if flame propagation to the tank wall was possible. Propagation of the wire bundle after ignition resulted in a catastrophic failure of the test vessel in the area of the quantity gauge.

INTRODUCTION

Failures of ground oxygen storage and handling systems have been noted frequently in the past. During the trans-lunar phase of the Apollo 13 mission a similar failure occurred in one of the service module compartments; the item that failed was a cryogenic oxygen storage tank which provides oxygen to the crew and fuel cells. The tank consisted of a double-wall, vacuum-jacketed vessel containing a heater, quantity gauge, and two circulating fans, all of which were electrically operated. The tank also contained conductors using polytetrafluoroethylene (Teflon) as insulation and electrical feedthroughs which were all in direct contact with high pressure oxygen. This condition presented a potential problem in that a fire could originate in the electrical system, propagate along the wire insulation, and eventually cause a catastrophic failure of the system.

A major investigation was conducted to explain the tank failure mechanism. It became obvious in the early stages of this investigation that the failure was indeed the result of rapid oxidation inside the tank and that an explanation of the failure would require a study of the flammability properties of tank materials. The probability of ignition of these materials inside the tank and their propagation rates were the object of the study reported herein.

Upward and downward flame propagation rates of the tank electrical insulation were evaluated in both cryogenic and ambient temperature oxygen in one "g" condition at MSC. Zero "g" propagation rates were determined in a zero "g" facility located at Lewis Research Center.

As part of the ignition studies, the promoted ignition (ref. 1) of metals by burning Teflon was investigated. Tests of this type were conducted in both one "g" and zero "g" conditions on a selected number of metal alloys. Spark ignition of the same materials are discussed in another paper of this symposium (ref. 2).

The results of the flame propagation studies and ignition studies were tehn used in testing a flame propagation model for the failed oxygen tank. To evaluate the flame propagation model, a partial configuration of the oxygen tank quantity gauge and fan motor and heater wire bundles was conducted. Results of the partial configuration test, along with the results of the flame propagation and promoted ignition studies, are presented in this paper.

ENVIRONMENTAL TEST CONDITIONS AND IGNITION TECHNIQUE

The tests discussed in this paper were conducted in an oxygen environment at a pressure of 645 ±20 newtons/cm^2 (940 ±30 psia) and at a temperature of -118° ±15°C; these conditions were approximately those in the Apollo 13 oxygen tank at the time of failure. In addition, propagation rates were determined at ambient temperature and at a pressure of 645 ±20 newtons/cm^2, the conditions of the portion of the electrical conduit external to the oxygen tank.

In each test the sample was ignited by wrapping the material with a few turns of 26 gauge nichrome wire, initially applying 5 amps at 28 volts dc for 3 to 5 seconds to provide a localized warmup, and then raising the ignitor power to 10 amps at 28 volts dc until ignition took place (usually a few seconds later).

PROPAGATION RATE TESTS

A study was conducted to measure the upward and downward propagation rates of Teflon insulation (0.03 cm thick) on electrical wires similar to those in the Apollo service module oxygen tank. Inasmuch as the tank was in a zero "g" gravity field at the time of failure, an investigation of propagation rates in this environment was also conducted. Since most of the wires were of different colors, an objective of the study was to determine if the various color pigments used in the Teflon affected propagation rates.

Test Apparatus

One "g" - The chamber (fig. 1) used for the one "g" studies was equipped with a burst disc (2425 newtons/cm^2 burst pressure) oxygen purge, fill and vent lines, thermocouples, ignitor power feedthroughs, and a pressure transducer. The propagation rates of the Teflon insulation were determined by measuring the time necessary for the flame to propagate between two thermocouples 3.7 cm apart. The use of three thermocouples in the propagation path provided additional rate determinations. Details of the test sample, ignitor position, and thermocouple locations are shown in figure 2.

Zero "g" - The zero "g" tests were conducted in the zero "g" facility at Lewis Research Center. Five seconds of zero "g" time were attained during each test. Propagation rates were determined from movies taken during each test by correlating frame speed with travel of the flame along the wire bundle. Figure 3 shows the test specimen and ignitor configuration for the zero "g" tests.

Results

One "g" - The one "g" flame propagation rates for single wires and wire bundles at cryogenic and ambient temperatures are presented in tables I and II. As mentioned previously, insulation with different colors were chosen for the tests; however, there were no significant differences in the propagation rates. The results represent average determinations for different color insulations. Where appropriate, standard deviations of the propagation rates are presented.

Zero "g" - The zero "g" flame propagation rates in cryogenic oxygen for wire bundles are presented in table III. Because of the complexity and cost of the testing, only a limited number of data points were obtained. The data as presented are the rates determined for each zero "g" test.

PROMOTED IGNITION

The objective of this study was to determine if burning Teflon could ignite metal alloys in the configuration (thickness, geometric relationship to fuel, edge condition, etc.) used in the oxygen tank.

Test Apparatus

Various materials and configurations tested in one "g" are shown in figure 4. Only one zero "g" test was conducted; this occurred on configuration 3 of figure 4. The test environment and ignition technique were the same as for the propagation rate studies except that in the promoted ignition tests a small cube of Teflon (1 or 2 gms) was ignited as the fuel to promote ignition of the metals. Test results were evaluated by monitoring temperature and pressure rise during the test and through post test inspection of the metal samples.

Results

Edge contact of 2024 aluminum with the fuel, as shown in configuration 1 of figure 4, did not result in ignition, whereas contact of the Teflon with the flat side of the aluminum (configuration 2) resulted in ignition in three tests. Moving the aluminum away from the Teflon a distance of 1.27 cm, and then of 0.64 cm (configuration 3), resulted in no ignitions for the limited number of tests conducted. Placing silicon steel specimens in contact with the Teflon fuel (configuration 4) resulted in ignition in all three tests conducted. In five tests of 5052 aluminum (configuration 5) conducted in one "g" and in a single zero "g" test, ignition did not occur. In configuration 6 the test specimen consisted of a 2.54 cm length of Inconel X750 electrical conduit containing 18 Teflon insulated wires. In each of three tests the Inconel tube and most of the wiring and insulation were consumed.

PARTIAL CONFIGURATION TEST

The objective of this test was to determine if flames would propagate in a configuration similar to that of the Apollo 13 tank and to determine if the flames would ignite metal components of this configuration.

Test Apparatus

The chamber used for this test was a stainless steel tee equipped with flanges. A camera viewport, electrical and hard line feedthrough, and conduit to the quantity probe interface were installed through the flanges. The chamber, which is shown schematically in figure 5, has a volume of approximately 10 liters. A pressure relief valve was provided which was designed to open at 722 newtons/cm^2. In addition, the test chamber contained a rupture disc to prevent failure of the test chamber in case of pressure relief valve malfunction.

Temperatures were monitored with 5 internal thermocouples, and pressure was measured by use of a pressure transducer. Color motion pictures were taken through the one available viewport at a speed of 24 frames per second. A second camera provided external color motion pictures of the conduit chamber interface, also at 24 frames per second. Three thermocouples were located in the region of the quantity gauge, as shown in figure 5. Two thermocouples measured internal chamber wall temperatures. Three thermocouples were installed on the external surface of the conduit as shown in figure 5 to measure propagation through the conduit.

The two fan motor wire bundles were routed downward to the quantity gauge and penetrated through openings in the quantity gauge to the conduit. All of the wiring (power and instrumentation wires representative of the Apollo tank) was routed through the conduit to a connector which provided the high pressure to ambient pressure interface. The insulation was ignited using the same technique as for the propagation rate studies.

Results

The propagation observed in the motion pictures of the inside of the chamber proceeded vertically downward on the fan motor wire bundle from the ignition site and ignited other wires intersecting its path and eventually reached the upper portion of the quantity gauge. The fire then propagated through the quantity gauge downward to the conduit chamber interface and ignited the metals in this region and burned a large hole in the chamber. The inside diameter of the penetration to the chamber was initially 1.27 cm but was opened up by the oxygen melting, burning, and cutting effect to a final diameter of 4.75 cm. This event occurred in approximately 0.5 second and permitted rapid venting of the high pressure oxygen. Time from ignition through the catastrophic tank burn through was approximately 31 seconds.

Figure 6 shows the pressure history during the test. The initial pressure rise occurred 24 seconds after ignition, and burn through occurred 6.5 seconds later, at which time the pressure decayed to one atmosphere in approximately 0.5 second. Temperature histories of both internal and external portions of the test apparatus are shown in figures 7 and 8.

DISCUSSION OF RESULTS

Propagation Rates

The method employed to determine flame propagation rates in this study is simple to use experimentally but has severe limitations when applied to certain sample configurations. Spurious flames, produced by the burning sample, can in some cases encounter the measuring thermocouple before the main flame front and result in erroneously large rates. These spurious flames are more frequently encountered in upward rate configurations than for other configurations (downward, horizontal) and could be the cause of the large deviations measured for the upward rates in this study. Standard deviations for the downward rates are in the range of 10 to 20% which is within the expected error range for normal variations in the burning process.

During the investigation, it was postulated that color pigments used in the insulation could affect the propagation rates through an interaction between the various pigments (metal oxides) and the polymer at high temperature. However, no differences in the propagation rates for several types of pigmented insulation were noted. The interaction of the polymer with the pigment apparently is not as important as the direct interaction of the polymer with the oxygen to produce COF_2, CF_4, and CO_2, as reported by Duus (ref. 3) for tetrafluoroethylene. Previous unpublished work performed at the MSC indicated that these components are the major products of combustion of Teflon.

The effect of test environment temperature on flame propagation is noticeable in the downward rate determinations. Downward propagation rates at -118°C are only one-half of those at 30°C. Results of 26 and 20 gauge wire upward propagation rates also show a larger rate at 30°C; however, the rates are only approximately one-third larger than those at cryogenic conditions.

Two previous studies, Kimzey (ref. 4) and Andracchio and Aydelott (ref. 5) have reported flame propagation studies of polymeric materials in zero "g". Kimzey found that Teflon was self-extinguishing in a zero "g", 3.4 newtons/cm^2 (5 psia) ambient temperature oxygen environment. These results are in contrast to the propagation rate determination of the present study of 0.48 ±0.25 cm/sec at 632 newtons/cm^2. The difference in these results undoubtly resulted from the different oxygen pressures used. Propagation rates for neoprene, polyurethene, Dacron, and silicone fuels were reported by Kimzey to be approximately 0.2 cm/sec at 3.4 newtons/cm^2 and 0.38 cm/sec at 10.3 newtons/cm^2 (15 psia). Andracchio and Aydelott, reported zero "g" flame propagation rates for thin plates of cellulose acetate of 2.2 to 4.4 cm/sec at 3.4 newtons/cm^2, depending upon the sample thickness used.

Despite the limitations of the propagation rate determinations, there is no apparent reason to believe that the zero "g" rates of Teflon are not representative of rates which could be encountered in oxygen systems of orbiting spacecraft. Any change in the zero "g" environment which could be produced by propulsion maneuvers would produce convection currents and therefore affect the propagation rates. The Teflon propagation rate data apparently constitute a lower bound to the propagation rate of this material in spacecraft oxygen systems.

Promoted Ignition

As mentioned previously, promoted ignition studies were conducted in a manner very similar to the study of Nihart and Smith (ref. 1). The promoting fuel used in their study was neoprene, whereas, in this study Teflon was used exclusively. As in this study, Nihart and Smith were also able to ignite Inconel X750, steels, and aluminum alloys. Effects of sample configuration, as investigated in the present study (and as might be expected), show that thin sections of the alloys are more easily ignited than larger samples.

Partial Configuration Test

Results from the partial configuration test of the quantity gauge and associated wire bundles show that the flame propagation and promoted ignition results are applicable to the configured oxygen tank system. The configuration test film determined the rate of propagation to be approximately 0.67 cm/sec, which is in good agreement with the propagation rate test result of 0.97 cm/sec for this condition. Ignitions of Inconel X750 and stainless steel occurred in the test; again, this effect could be predicted from the promoted ignition results.

CONCLUDING REMARKS

Flame propagation rates for Teflon electrical wire insulation typical of that used in the Apollo 13 cryogenic oxygen tank showed that upward propagation rates are larger than downward rates by approximately a factor of ten. Propagation rates in zero "g" at cryogenic temperature for wire bundles are approximately half of the corresponding one "g" downward rates. A change of temperature from approximately -118°C to 30°C increased the rates by approximately 100% for downward burns and by approximately 30% for upward burns. No effect of insulation color pigment on the flame propagation rates could be detected. The zero "g" Teflon propagation rates apparently constitute a lower bound flame propagation rate for this material applicable to orbiting spacecraft oxygen systems.

Promoted ignition of four metal alloys by burning Teflon showed that ignition and extensive burning occurred for thin sections of silicon steel. Ignition of Inconel X750 and two aluminum alloys occurred for certain configurations, and, once ignited, the test items burned to completion in almost all cases. No ignition of an aluminum alloy occurred in the only zero "g" promoted ignition test conducted. The limited zero "g" data do not permit any conclusions to be drawn for promoted ignition in that environment.

On a partial configuration of the oxygen tank quantity gauge and associated wire bundles, flames propagated along two wire bundles through the upper portion of the quantity gauge and ignited a portion of the conduit-chamber interface. This ignition resulted in a venting of high pressure oxygen over a period of 0.5 sec, during which severe burning of the conduit-chamber interface occurred.

ACKNOWLEDGMENT

The authors wish to express their gratitude to Messrs. Donald A. Petrash and Thomas H. Cochran of Lewis Research Center for conducting the zero "g" tests.

REFERENCES

1. G. J. Nihart, C. P. Smith, Compatibility of Materials with 7500 psi Oxygen, Defense Documentation Center Report AD 608260, 1964.

2. C. E. Propp, J. M. McGee, "A Review of Cryogenic Testing Performed by the Thermochemical Test Branch, MSC, in Support of Apollo 13 and 14," another paper of this symposium.

3. H. C. Duus, Industrial and Engineering Chemistry, 47 #7, p. 1445, 1955.

4. J. H. Kimzey, "Flammability During Weightlessness" NASA TMX-58001, 1966.

5. G. R. Andracchio and J. C. Aydelott, "Comparison of Flame Spreading over Thin Flat Surfaces in Normal Gravity and Weightlessness in an Oxygen Environment," NASA TM X-1992, 1970.

TABLE I. DOWNWARD PROPAGATION RATES

Wire gauge	Pressure, Newtons/cm^2	Temperature, °C	Rate, cm/sec	Number of tests
26 (bundle of four)	670	-118	0.97±0.15	4
26 (individual wires)	666	-118	0.58±0.05	8
22 (individual wires)	690	-118	0.58±0.05	8
22 (coaxial)	650	-118	0.81±0.25	5
20 (individual wires)	653	-118	0.79±0.10	8
26 (individual wires)	678	30	1.55±0.58	6
22 (individual wires)	654	30	1.07±0.13	9
20 (coaxial)	654	30	1.27±0.41	20
20 (individual wires)	662	30	1.37±0.23	4

TABLE II. UPWARD PROPAGATION RATES

Wire gauge	Pressure, Newtons/cm^2	Temperature, °C	Rate, cm/sec	Number of tests
26 (individual wires)	647	-118	5.75	2
22 (individual wires)	659	-118	10.4±5.34	8
20 (coaxial)	650	-118	7.9±2.14	4
20 (individual wires)	650	-118	4.8±2.29	11
26 (individual wires)	664	30	8.9±2.54	4
20 (coaxial)	660	30	10.9±3.81	
22 (individual wires)	662	30	8.6±3.56	10

TABLE III. ZERO "g" PROPAGATION RATES

Test item	Pressure, Newtons/cm^2	Temperature, °C	Rate, cm/sec	Number of tests
Wire bundles: 4 wires clear and white shrink tubing	632	-118	0.48±0.25	6

NASA-S-71-1762-X

APPARATUS FOR PROPAGATION RATE AND PROMOTED IGNITION STUDIES

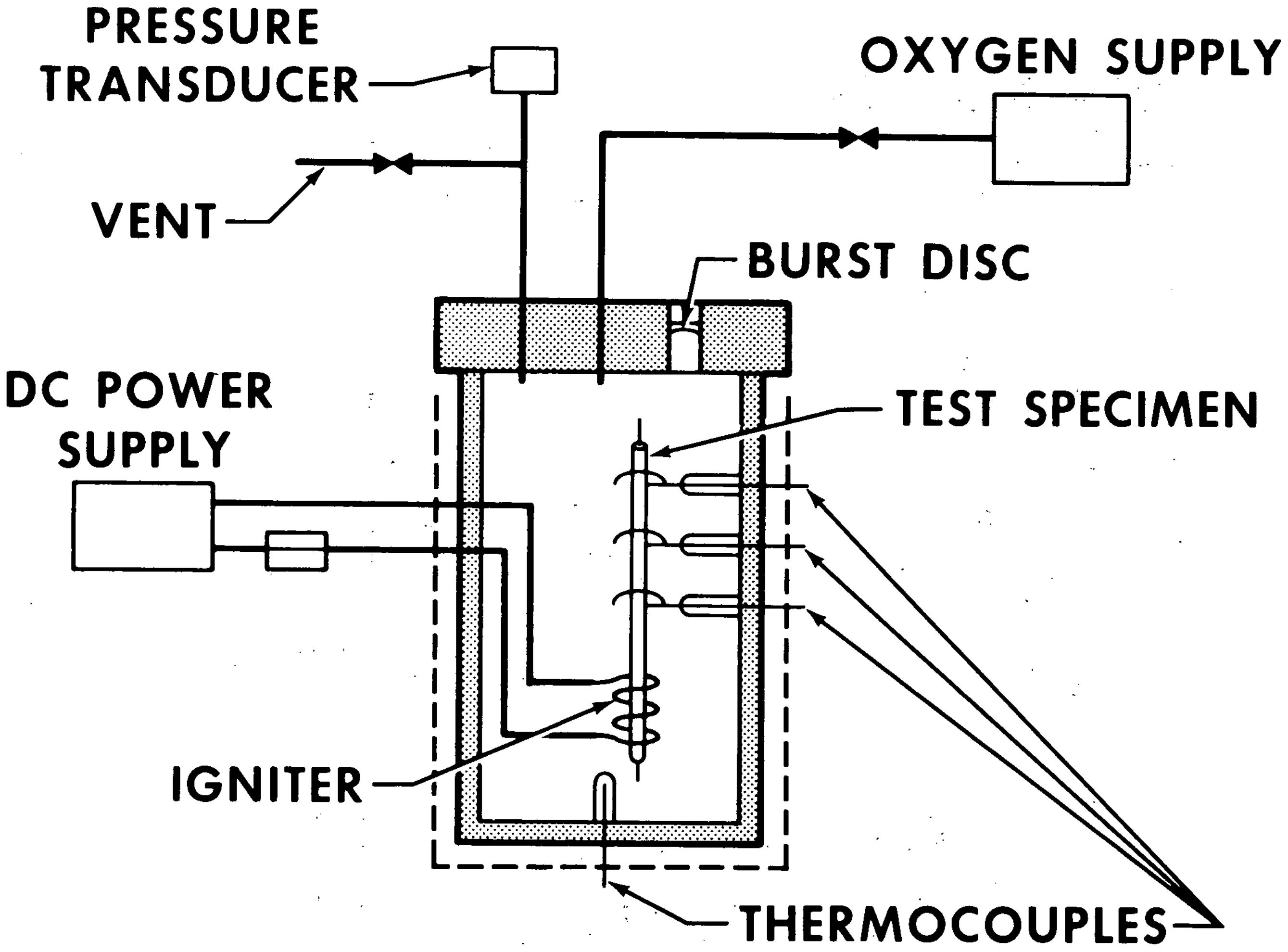

Figure 1.

NASA-S-71-1759-X

PROPAGATION RATE TEST CONFIGURATION

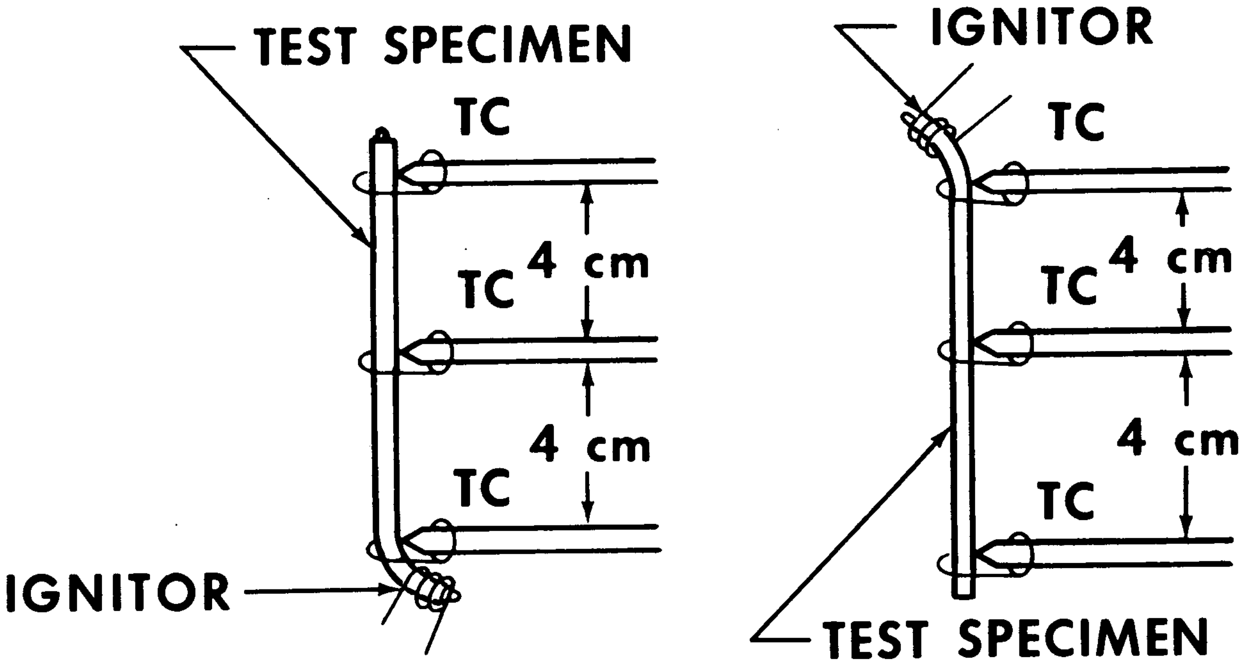

UPWARD PROPAGATION

DOWNWARD PROPAGATION

Figure 2.

NASA-S-71-1786-X

ZERO 'g' FLAME PROPAGATION CONFIGURATION

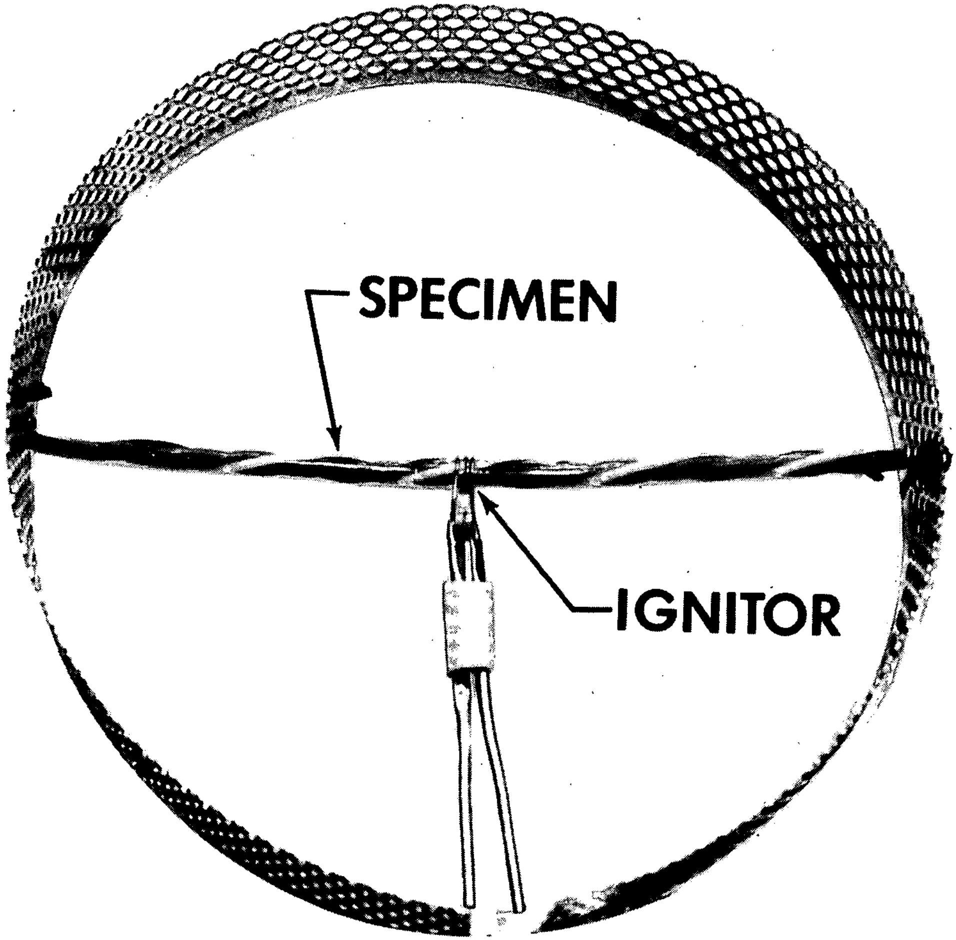

Figure 3.

NASA-S-71-1761-X

PROMOTED IGNITION TEST CONFIGURATIONS

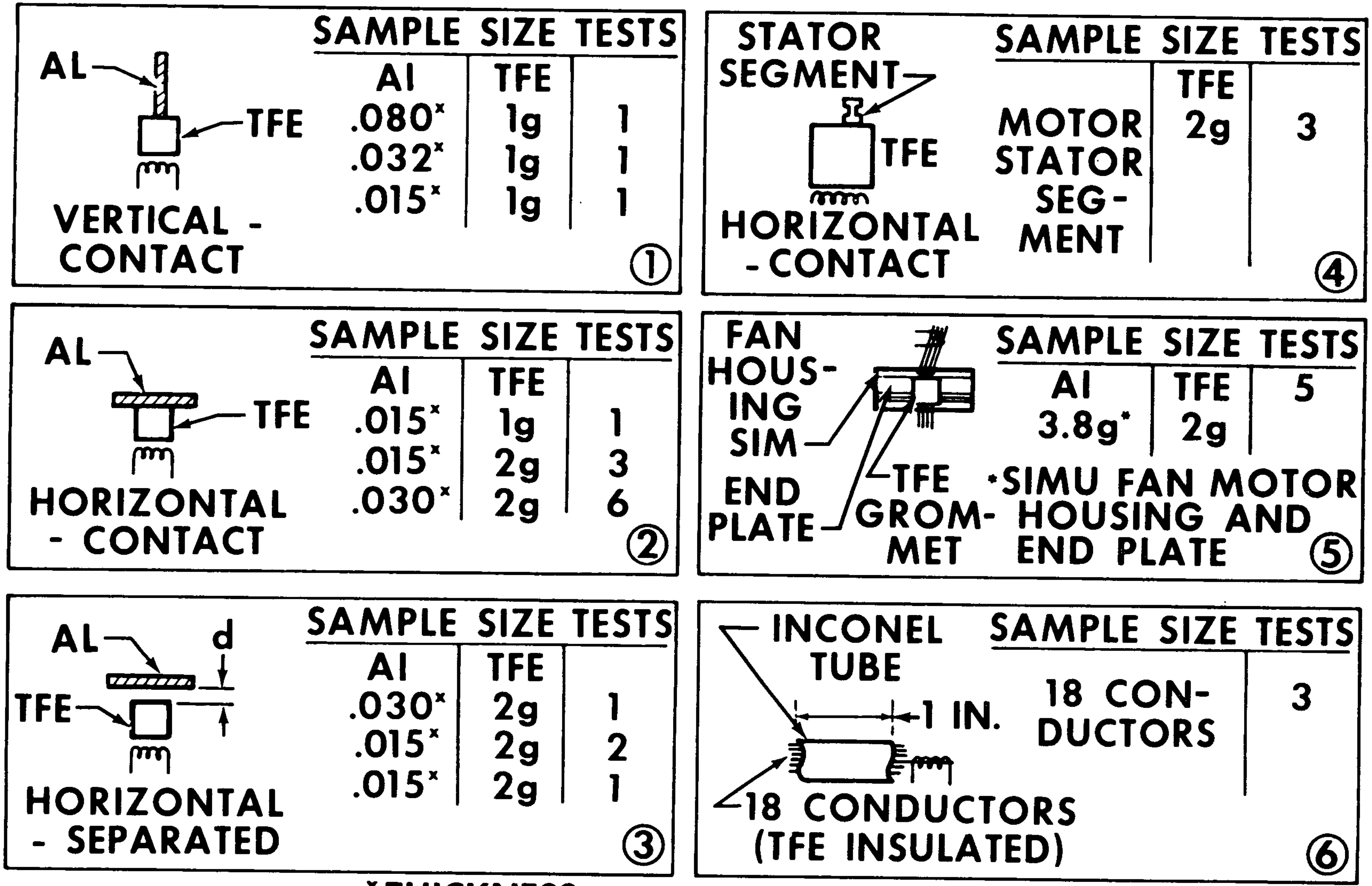

① VERTICAL - CONTACT

SAMPLE SIZE		TESTS
Al	TFE	
.080×	1g	1
.032×	1g	1
.015×	1g	1

② HORIZONTAL - CONTACT

SAMPLE SIZE		TESTS
Al	TFE	
.015×	1g	1
.015×	2g	3
.030×	2g	6

③ HORIZONTAL - SEPARATED

SAMPLE SIZE		TESTS
Al	TFE	
.030×	2g	1
.015×	2g	2
.015×	2g	1

④ HORIZONTAL - CONTACT

SAMPLE SIZE		TESTS
	TFE	
MOTOR STATOR SEGMENT	2g	3

⑤

SAMPLE SIZE		TESTS
Al	TFE	5
3.8g*	2g	

*SIMU FAN MOTOR HOUSING AND END PLATE

⑥

SAMPLE SIZE	TESTS
18 CONDUCTORS	3

×THICKNESS cm

Figure 4.

NASA-S-71-1757-X

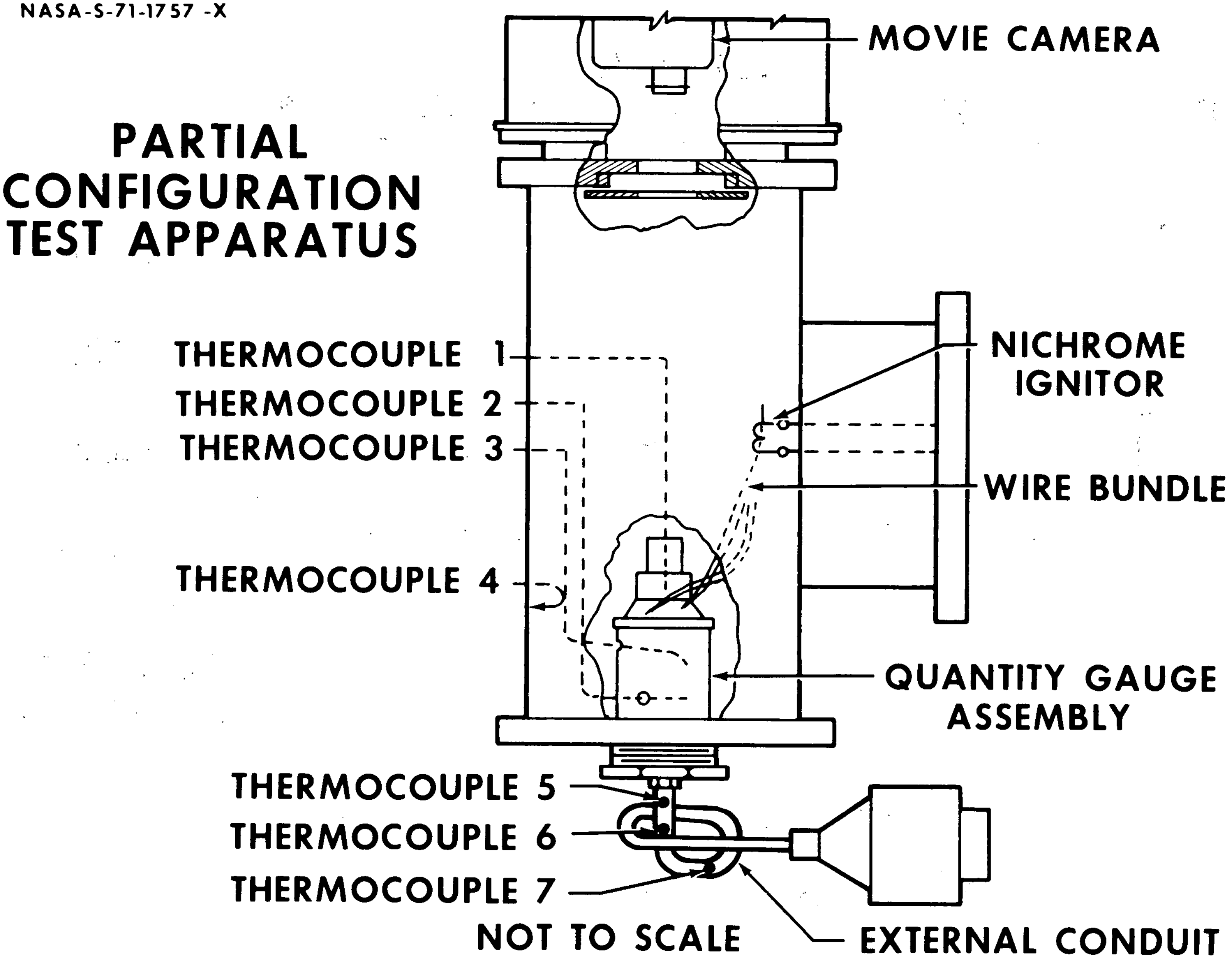

PARTIAL CONFIGURATION TEST APPARATUS

NOT TO SCALE

Figure 5.

NASA-S-71-1760-X

PRESSURE HISTORY OF PARTIAL CONFIGURATION TEST

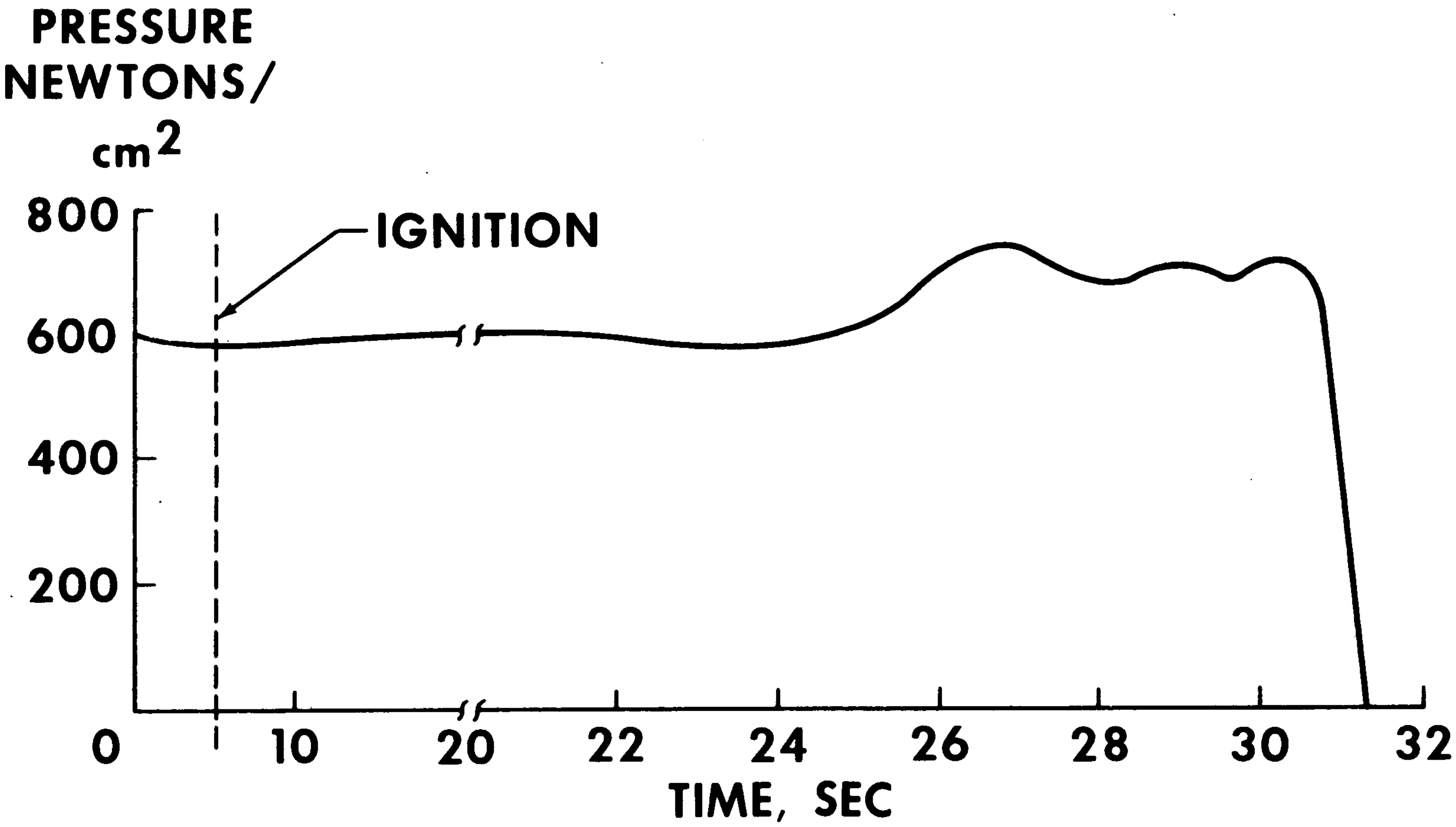

Figure 6.

NASA-S-71-1756-X

TEMPERATURE HISTORY OF QUANTITY GAUGE

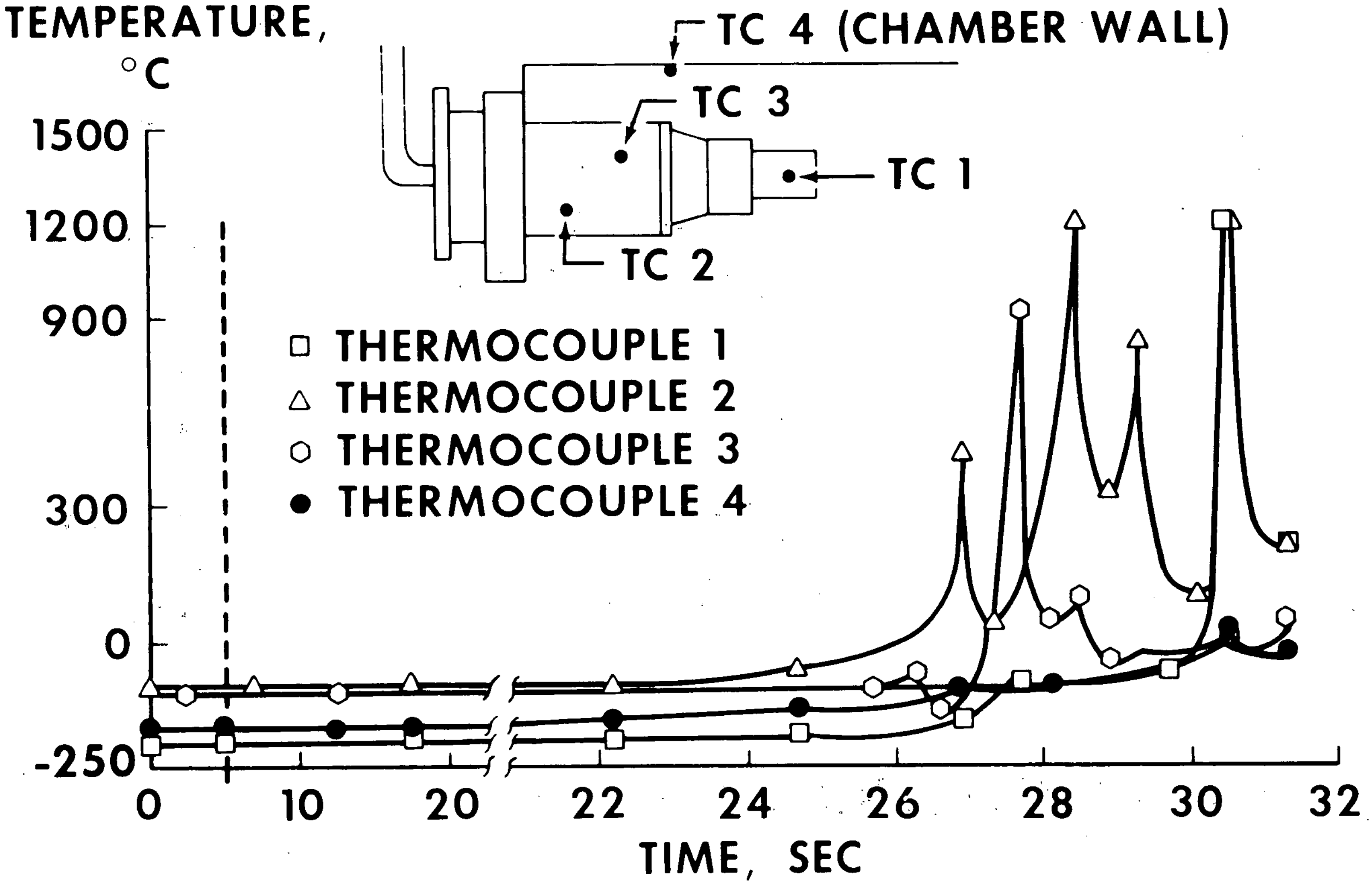

Figure 7.

NASA-S-71-1755-X

TEMPERATURE HISTORY OF EXTERNAL CONDUIT

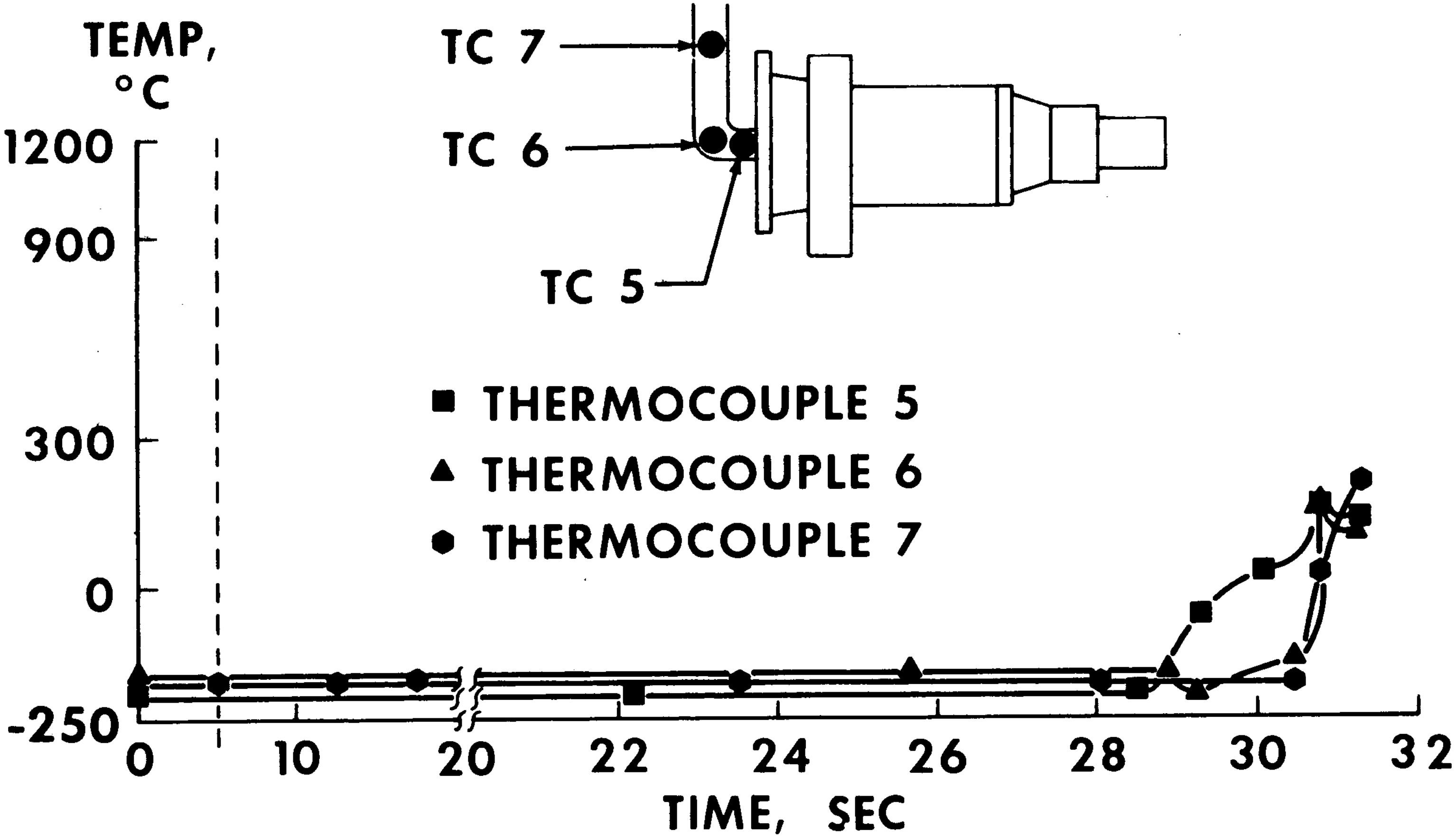

Figure 8.

N72-23801

TESTING AND CONTROL OF MATERIALS USED IN HIGH PRESSURE OXYGEN CRYOGENIC SYSTEMS

by R. P. Segrest
General Electric Company
Apollo and Ground Systems
Houston Programs
Houston, Texas

Introduction

Materials used in the crew bay, in systems interfacing with the crew bay, and in the propellant systems for the Apollo spacecraft are controlled by the Apollo Spacecraft Program Office document, "Apollo Spacecraft Nonmetallic Materials Requirements."(1) The Apollo spacecraft materials requirements for cryogenic oxygen systems are the same as those employed for gaseous oxygen systems (GOX). Tests have been conducted which show flammability testing conditions to be more severe with an atmosphere of ambient temperature GOX than an atmosphere of supercritical oxygen at the same test pressure or liquid (LOX) at ambient pressures.

Modifications were made in Addendum 2 of "Apollo Spacecraft Nonmetallic Materials Requirements" in revising Category D, materials used in greater than 20 psia oxygen, and in adding Category J, materials used in other hazardous fluids, such as propellants. The major revisions to Category D were in extending the existing nonmetallic materials requirements to metals which are normally exposed to the oxygen atmosphere and to all materials, metals and nonmetals, used in the oxygen systems which could be exposed to oxygen as a result of a single barrier failure.

Materials usage for each spacecraft are tracked by the COMAT (Characteristics of Materials) system. This computerized system relates the material to a specific component and lists the quantity used and the test results indicator for the material and/or component. The COMAT system functions to maintain configuration management for all controlled materials in the spacecraft.

Brief discussions of the materials and configurations testing techniques and requirements for the Apollo spacecraft high pressure oxygen systems are presented in the remainder of this paper.

Materials Testing Requirements For High Pressure Oxygen

Metallic Materials

Metallic materials used in high pressure oxygen are required to successfully complete the pneumatic impact test. Metallic materials which are used in dynamic applications such as valve seats are also required to successfully undergo mechanical impact testing.

Nonmetallic Materials

Nonmetallic materials used in high pressure oxygen are required to successfully complete the flash and fire point test, odor test, total organics and carbon monoxide tests, and pneumatic impact test. Nonmetallic materials which are used in dynamic applications also must successfully undergo the mechanical impact testing.

Materials Behind Potential Single Barrier Failures

As previously stated, these above testing requirements apply to materials which are normally exposed to oxygen, as well as those which would be exposed as a result of a single barrier failure. All components are evaluated for the probability of a single barrier failure which would allow oxygen into an enclosed compartment which is not normally a wetted area. The evaluation takes into account such considerations as leakage history, barrier thickness and design, acceptance testing, other spacecraft testing, and burst data. All materials in components which do not have a solid barrier; i.e., those having welded, brazed or mechanical joints, have been tested.

Materials Screening Tests

Only a brief discussion of the materials testing techniques will be presented here. All of the testing described is performed by the Manned Spacecraft Center's White Sands Test Facility and complete descriptions can be found in "Apollo Spacecraft Nonmetallic Materials Requirements."

High Pressure Flash and Fire Point Testing

High pressure flash and fire point testing is performed on all nonmetallic materials in their maximum systems usage pressure. The materials must have a minimum flash point of 400°F and a minimum fire point of 450°F.

Testing is accomplished by placing a half gram sample in the sample cup of the test cell, shown in Figure 1, and adjusting to the proper oxygen pressure. The sample cup is then heated at a rate of 25°F per minute while arcing above the sample for every 4 ± 1 second, 50 ± 20 millijoule spark. The above process is continual to 1000°F or until a flash and/or fire point of the material is obtained. A flash or a fire is detected by a photocell detector and fed into the storage oscilloscope. The high pressure flash and fire point apparatus has a present capability of 50 to 3000 psia. A similar system is employed for flash and fire point testing in pressures less than 50 psia.

Gaseous Oxygen Mechanical Impact Testing

GOX mechanical impact testing is performed on all materials at 1.5 times their maximum system usage pressure. The materials must show no evidence of reaction at that pressure to be acceptable for use in a dynamic application.

The mechanical impact testing apparatus utilizes a modified Army Ballistics Missile Agency impact tester as shown in Figure 2. The basic modifications include using a 7-1/2 pound plummet in lieu of the 20 pound plummet and replacing the anvil with a high-pressure test chamber as shown in Figure 3. All testing for the Apollo Spacecraft Program is done with a 50 foot-pounds per square inch impact which is on the order of six times greater than the highest impact load component used in the Apollo spacecraft.

A clean sample is placed in the sample cup and the system is purged and pressurized with oxygen to the specified test pressure. The pneumatic amplifier chamber is then pressurized with gaseous nitrogen to equalize the pressure on the striker pin. The plummet is then released and the impact energy is transmitted to the specimen through the striker pin. The specimen is then removed and inspected for evidence of a reaction. The mechanical impact system presently has a 7500 psia capability.

Gaseous Oxygen Pneumatic Impact Testing

GOX pneumatic impact testing is performed on all materials at 1.33 times their maximum system usage pressure. Materials must show no evidence of reaction to be acceptable for use in a high pressure oxygen system.

Testing is accomplished in the apparatus diagramed in Figures 4 and 5. A clean sample is placed in the sample cup and the cup is loosely installed into the system. The system is then purged with low pressure oxygen and the sample cup tightened. The system is monitored and pressure, temperature, and valve cycle times are recorded. Testing is accomplished with an automatic sequencer which provides identical pressure cycles. The sequencer first opens the high speed valve (2 milliseconds to full open) for 50 milliseconds. The valve then closes and holds the pressure for 5 seconds before venting down to atmospheric pressure. The pressure-vent sequence is repeated 4 more times per sample before removing and inspecting the sample for evidence of reaction. A high magnitude reaction will also be noted by the temperature readings.

High Pressure Autoignition Testing

High pressure autoignition testing was implemented to supplement the high pressure flash and fire point testing for materials used in higher than 3000 psia systems. Materials are tested at their maximum system usage pressure and must exhibit a minimum autoignition point of 450°F.

Testing is accomplished in an apparatus similar to the flash and fire point apparatus without the arcing equipment and with a thermocouple in lieu of a photocell for detecting a reaction. The sample and chamber preparation for this test is the same as for the flash and fire point testing. The sample is heated at the rate of 25°F per minute until the sample reaches 1000°F or autoignites. The autoignition system is capable of testing to 7500 psia.

Odor Testing

Materials are screened for undesirable odors by an odor panel of five to ten members. A sample equal to five grams per liter of test chamber is placed in the chamber. The chamber is then evacuated to 1 Torr or less and back filled with oxygen to approximately 5 psia. The sample and chamber are then heated inside an oven to 155°F for 72 hours. Next, the chamber is pressurized to one atmosphere with oxygen and sampled. Samples are then diluted with oxygen on a ratio of 29 parts of oxygen to 1 part of sample and 9 parts of oxygen to 1 part of sample. These two dilutions and an undiluted sample are then rated by the panel members on a scale of 0 to 4. A material which has an average rating on the undiluted sample of 2.5 or lower is considered acceptable.

Total Organics and Carbon Monoxide

A sample is prepared and heated for 72 hours as described for the odor testing. Gas samples are taken after the chamber reaches room temperature. The test specimen is then weighed and the gas samples analyzed for total organics and carbon monoxide. Total organics are expressed as pentane equivalents and shall not exceed 100 micrograms per gram of sample and carbon monoxide shall not exceed 25 micrograms per gram of sample for the material to be acceptable.

Test Results

Test results for the mechanical impact test show testing at the service module oxygen tank pressure of 1000 psia GOX to be more severe than testing at the same impact levels in ambient LOX. Tests are currently underway to compare the same materials at the same impact levels in a 1000 psia supercritical oxygen atmosphere.

Approximately 650 materials comprising over 6000 tests have been conducted for certification of the materials used in the current Apollo spacecraft high pressure oxygen systems. Of these tests, more than 90 percent were GOX pneumatic and mechanical impact or high pressure flash and fire point. Testing has indicated that no adverse flammability problem exists with the materials currently used in the Apollo spacecraft oxygen systems. All test data generated by these screening tests in support of the Apollo program are distributed to the Apollo spacecraft contractors in "Materials Test Data for Applications in High Pressure Oxygen and Other Hazardous Fluids," "Material Test Data by Generic Identification," and "Materials Test Data by Manufacturer's Designation." (2) (3) (4)

Configuration Flammability Testing Requirements

Configuration testing is required for all components that have materials associated with an ignition source or that are within one inch of an ignition source. Ignition sources may be either electrical or dynamic impact. Configuration testing may also be required for components which have materials that fail any of the required screening tests.

Configuration Flammability Tests

Configuration testing for the Apollo spacecraft oxygen systems is conducted on both the subassembly and assembly levels. Each configuration test is designed to meet the specific worst case operating conditions of the component. Specific examples of the configuration tests conducted for the service module cryogenics oxygen system are given below.

Subassembly Tests

A good example of a subassembly test is the testing which was conducted on the wiring that is used in the redesigned service module oxygen tank. Current overload and arcing tests were conducted in 1035 psia GOX on both faulted wires, which allow an oxygen path to the conductor, and unfaulted wires and with and without circuit protection.

Early overload testing through the spacecraft circuit protection and under the right conditions of a faulted wire to allow an oxygen path showed a need to enhance the design of the circuit protection with the addition of a 5 ampere fuse for the third heater element of the cryogenic oxygen tanks' heater probes. Faults in the sheath ranged in size from .004 inch to 1/16 of an inch in diameter with ignitions occurring in both extremes. The testing also showed that overloading an unfaulted wire to fusion resulted in the conductor losing continuity in many places while the sheath remained intact with no ignition occurring. Testing through the enhanced circuit protection showed that the cable could not be overloaded or ignited even when faulted. From these tests, it was concluded that ignition would require a multipoint failure mode consisting of a shorted wire, a breakdown of the circuit protection, and a fault to allow an oxygen path to the conductor.

Overload tests were also conducted on the wire in 1035 psia supercritical oxygen. Results from this test showed even a faulted wire without circuit protection would not ignite.

Assembly Tests

A series of tests was conducted on the Service Module oxygen tank heater probe. In one of the tests, a heater element was shorted approximately eight inches from the junction between the copper cold lead and the nichrome heater element. The shorted element had a fault to allow an oxygen path to the nichrome wire. The shorted element was protected by a 5.0 ampere fuse and a 5.0 ampere circuit breaker in series. The heater probe was preheated to various temperatures up to 400°F and a current of 14 amperes at 32 VDC was applied to the shorted element. In all of the tests, the fuse opened in a time ranging from 0.8 second to 2.2 seconds. The test was then repeated twice at 400°F using only the 5 ampere circuit breaker for circuit protection and each time the circuit breaker opened in 1.2 seconds at 14 amperes 32 VDC. Next, the test was repeated without a fuse or a circuit breaker. A current of 14 amperes at 32 VDC was maintained on the shorted wire and maximum steady temperature of 577°F was obtained without fusing or igniting the wire.

In the final test on the heater probe, a new short was made approximately three inches from the cold junction on the same heater element which was previously shorted. No circuit protection was provided. By applying 5.5 amperes to each of the heater elements, the probe was heated to 310°F. Amperage was then dropped to 2 amperes on the shorted wire and then increased to 16 amperes within one second. Current was increased to 17 amperes after 30 seconds. The heater element fused open at 17 amperes without causing ignition.

Other assembly tests were conducted on various Apollo spacecraft oxygen supply systems as required to verify their acceptability prior to Apollo 14.

Findings

Materials and configuration test data have indicated that the best metals available for high pressure oxygen systems are nickel and high nickel base alloys. Stainless steels while being harder to ignite than the softer metals such as aluminum still propagate when ignited. Data to date show that all nonmetallic materials, when supplied with enough energy, will ignite and propagate. All nonmetallic materials which were known to be directly exposed to the high pressure oxygen systems of the Apollo spacecraft have been removed or relocated so as not to be in direct contact with an electrical ignition source. As mentioned previously, test results to date show that an atmosphere of ambient temperature GOX is a more severe testing atmosphere than ambient pressure LOX or supercritical oxygen at the same test pressure as the GOX test pressure.

References

1. Anon.: Apollo Spacecraft Nonmetallic Materials Requirements, MSC-PA-D-67-13, Apollo Spacecraft Program Office, Manned Spacecraft Center.

2. Anon.: Materials Test Data for Applications in High Pressure Oxygen and Other Hazardous Fluids, NB/RT-71-45, Reliability Division, Manned Spacecraft Center.

3. Anon.: Material Test Data by Generic Identification, RPT-X52-32-914D, Reliability Division, Manned Spacecraft Center.

4. Anon.: Material Test Data by Manufacturers Designation, RPT-X52-32-914G, Reliability Division, Manned Spacecraft Center.

WSTF - FLASH AND FIRE POINT TEST APPARATUS AND CONTROL SYSTEM

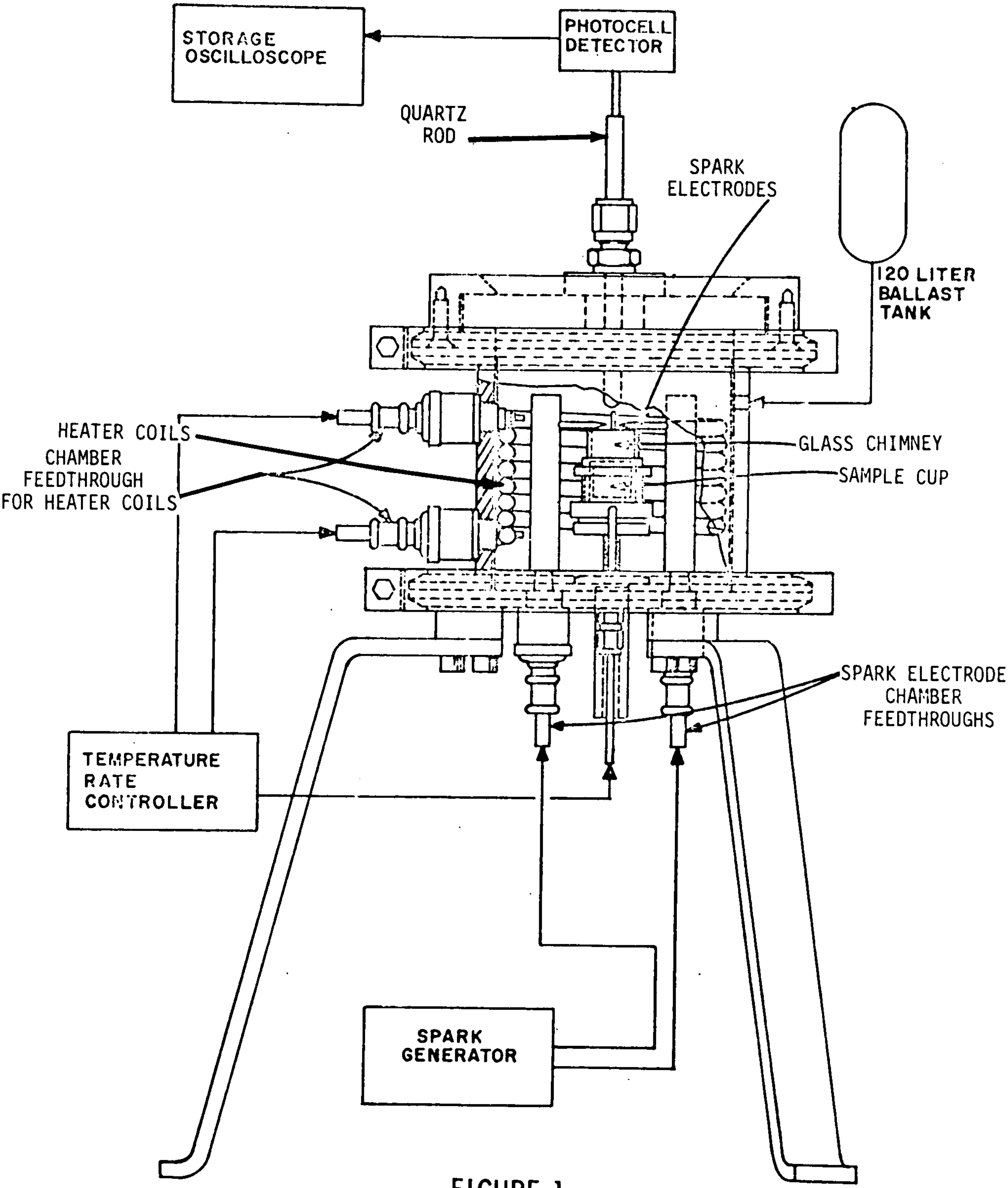

FIGURE 1

WSTF - MECHANICAL IMPACT TEST CHAMBER INSTALLED ON BASIC ABMA TESTER

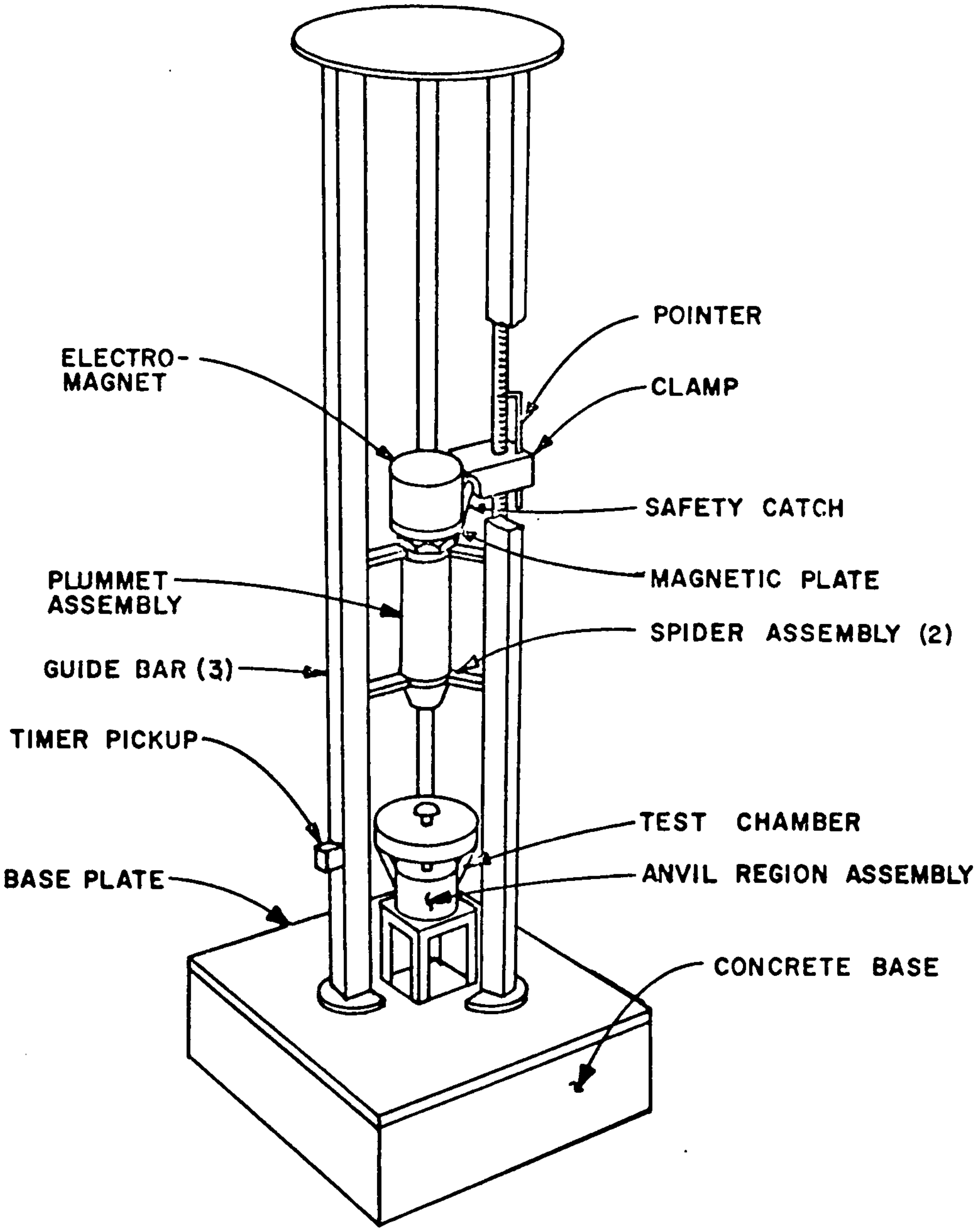

FIGURE 2

WSTF - MECHANICAL IMPACT TEST CHAMBER

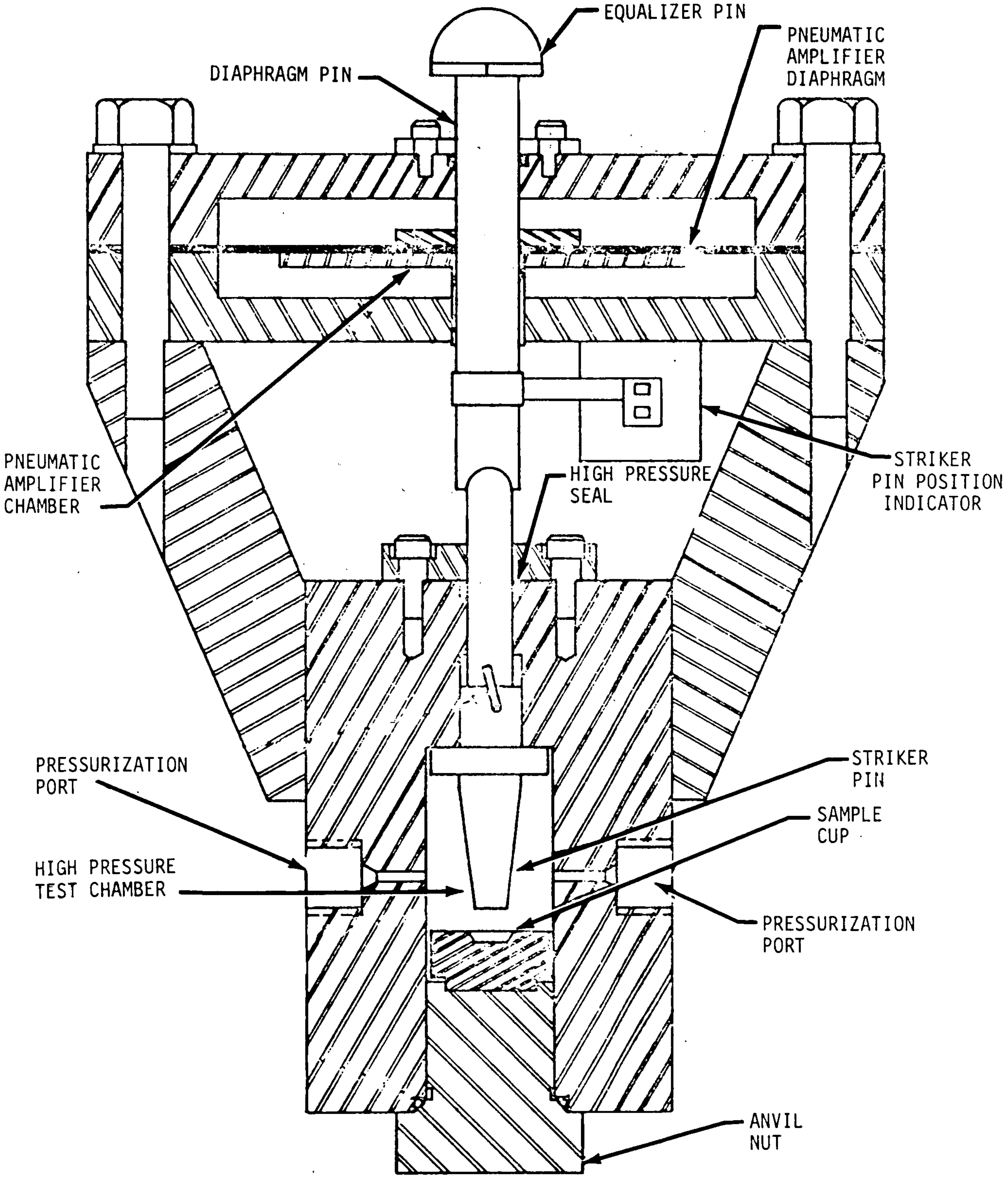

FIGURE 3

WSTF - PNEUMATIC IMPACT TEST SYSTEM

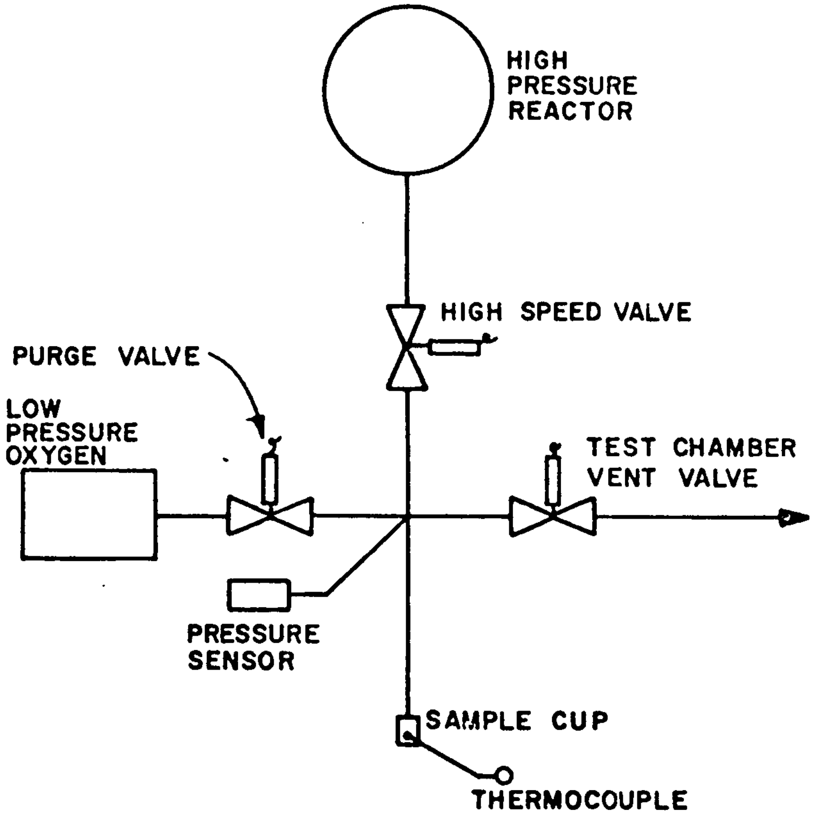

FIGURE 4

WSTF - PNEUMATIC IMPACT TEST SYSTEM

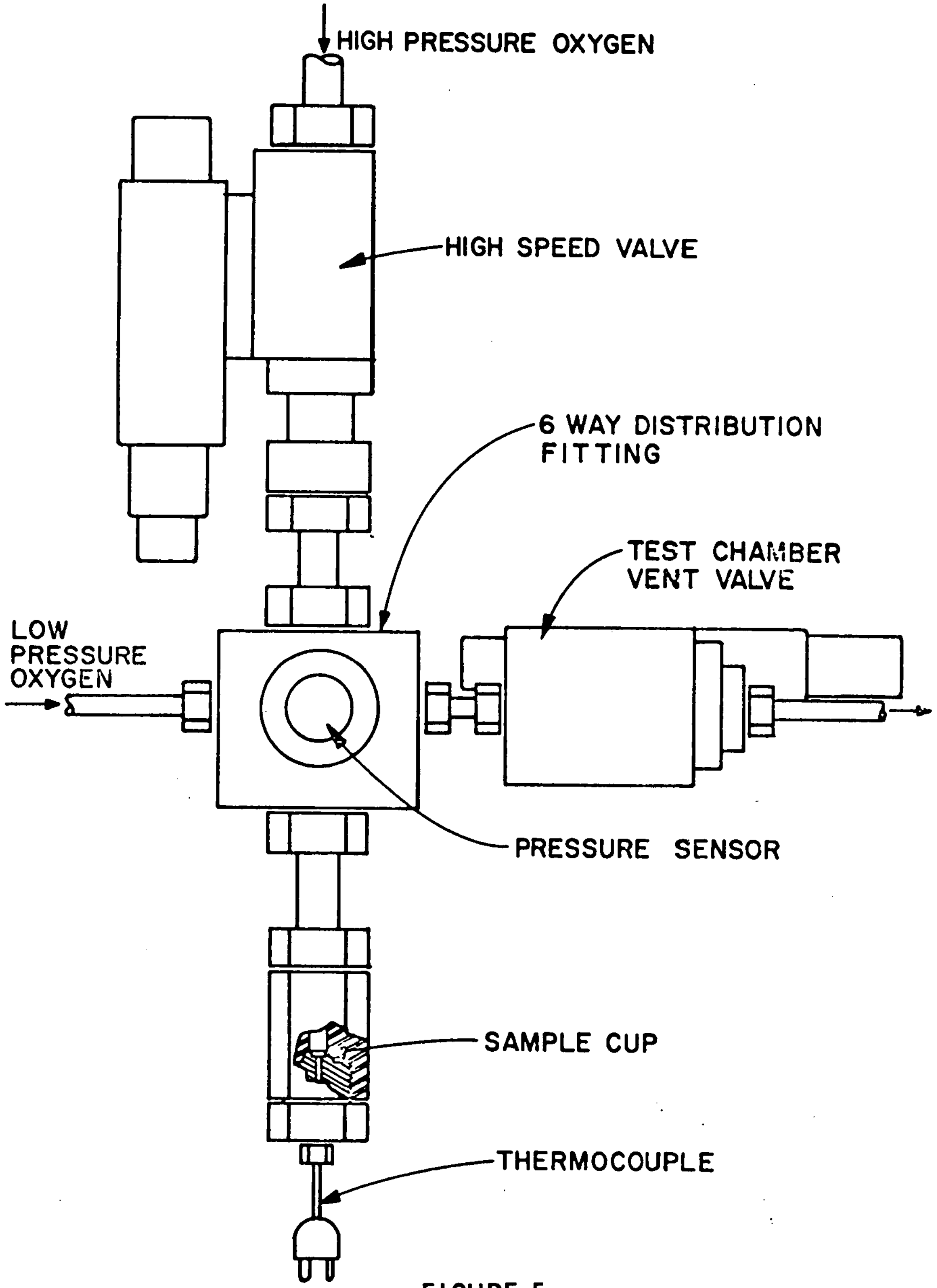

FIGURE 5

N72- 23802

Apollo 14 Flight Support and System Performance

Robert R. Rice
NASA MSC
Houston, Texas

Abstract

The Apollo 13 incident and subsequent oxygen tank redesign for Apollo 14 placed unique requirements on the flight support activity. A major part of this activity was the integration of the various analytical efforts into a single team function. Additionally, the first flight of the redesigned system without an orbital test required an extensive analytical base.

The support team philosophy, objectives, and organization are presented. Various analytical tools that were used during the flight are discussed. Investigations made during the post-flight period are considered and their impact upon subsequent flights shown.

Introduction

There are three major phases of work involved in any flight: preflight, real-time, and post-flight. Because of the cryogenic oxygen system redesign required, those three phases all had their own unique situations and problems which tended to impact each other in more than a normal manner. For this reason, all three phases will be discussed herein--with the preflight discussions being limited to a functional relationship. The paragraphs following introduce the phases.

During the Apollo 14 redesign effort, large contingents of analytical resources were applied to the problem of designing, fabricating, and testing a new cryogenic oxygen system. To provide for adequate communications between the various analytical groups involved, a team approach was thus used. Informal meetings were held during this period so that the team members could present the results of their work and receive feedback to apply to their analyses. As in all flight related programs, the major problem encountered during this effort was the integration of the analyses into the hardware and operational areas. The solutions to this problem are discussed herein and the various end items are presented.

In general, the end result of the analysis effort was a flight support team trained and equipped to respond to the real-time needs of the flight. For example, during the flight, there were several real-time problems that were faced and solved by the team members. Obviously, the training and tools that were used during this time had to be developed prior to the flight. These problems and the methods of solution used will also be discussed.

Once the flight was over, the last phase of work was started--post-flight analysis. For Apollo 14, this was a major task since it basically became a new system evaluation. Therefore, the various items analyzed during this portion of the work are presented to illustrate the requirements for basic system understanding.

The conclusions reached from the three phases of work are presented as concluding remarks to this paper.

Support Team

Pre-Flight

During this effort, there were some twelve identifiable organizational elements involved on the analysis team. The overall coordination of the team was the responsibility of the Power Generation Branch of the Propulsion and Power Division. The major problem faced by the team was that of communications; as mentioned earlier, periodic team meetings were held to facilitate the necessary cross-fertilization between the various efforts.

Since the fan-motors were deleted from the oxygen tanks, the thermal performance of the heater depends to a large extent on the net gravity level. Even though the artificial gravity levels are normally extremely low, natural convection is the predominant mode of heat transfer from the heater to the fluid. Obviously the conditions that dominate these convective processes could not be duplicated in a terrestrial environment; therefore, the adequacy of the design had to be certified by analysis. This then became the major activity of the team: that of insuring that the proposed system would be adequate for the Apollo 14 mission.

There were two main items of interest with respect to the thermal performance of the heater:

1. Maximum temperature reached by the structure (i.e., pressure vessel and heater) during the mission.

2. Maximum expected pressure drop created by stratification effects during the mission.

These items were formally closed prior to the mission with a certification document which contained a condensation of the Analysis Team's findings.

Flight Support

The end result of the analytical effort was to equip the flight support team with the knowledge and resources to make real-time inputs. Figure 1 presents the overall organization that the team functioned under, and as can be seen these activities were concentrated in a support building complex adjacent to the Mission Control Center.

The purpose of the cryogenic support team was to provide a continuous monitoring, analysis, and reporting activity of the cryogenic system. The prime objective of this team was the early detection, evaluation, and reporting of problems or potential problems. A secondary objective was the continuous monitoring, analysis, and reporting of routine system performance.

The general philosophy that was used during the organization of this team was that only those problems that were amenable to rapid solutions could be worked. This restriction had to be observed since a large scale investigation by this team would have destroyed the monitoring capability and left the system vulnerable to additional failures. When problems arose that required large scale efforts, separate teams were called to supply the manpower. In general, the location and organization of these teams were functions of the nature of the particular problem that had to be solved.

The detailed organization of the support team is shown in Figure 2. As can be seen in this figure, the flow of information was basically through the Subsystem Manager's position in the Mission Evaluation Room (MER). As was mentioned earlier, the prime function of the team located in the Backup Support Room (BSR) was that of system monitoring. The procedure used to insure that this was done was to manually plot some thirteen parameters from the real-time displays. This then became the prime data source for the real-time analytical support effort. The required frequency of plotting depended largely upon the system performance. During early parts of the mission, heater cycles occurred at rates of three to four per hour and thus virtually continuous plots were required. Later, when the cycles lengthened, the data points were plotted in about ten minute intervals. This plotting served two purposes:

1. Provided a continuous record of flight performance.

2. Forced an individual to examine the system trends on a rather continuous basis.

As backups to the real-time data, the following items were available to the team:

1. TWX summaries of the flight data on irregular intervals.

2. Polaroid pictures of the displays on ten minute intervals.

3. Tab outputs and plots available on about a twelve-hour turn around basis.

The performance of this support system was such that many real-time inputs were made to the operations team. This type of support team activity was found to be a good solution to the problems of fast response and continuous system surveillance.

In-Flight Analysis

Check Valve Leakage

The first problem noted during the flight was that of a check valve leaking into tank number two. As can be seen in Figure 3, when tank number three's pressure rose, tank number two's pressure would track it. This meant that fluid from tank three was being forced back into tank two. This problem did not affect the overall mission since no fluid was being lost; however, it did affect the cryogenic management and the eventual conduct of the Detailed Test Objective (DTO).

The problem was that as the fluid was forced into tank two, heat energy was also transmitted--thus changing the effective thermal performance of the tank. This would in time affect the individual tank quantity schedule that had been planned prior to flight.

In order to solve this problem, the team members of the Mission Performance and Analysis Division (MPAD) were called upon. The program that they had written prior to flight was modified to include this additional heat and mass transfer into tank two, and the mission quantity schedules were recomputed. As can be seen in Figure 4, the resulting predictions came very close to the actual flight quantities.

It was concluded from this analysis that the leaking check valve would cause no problems during the remainder of the flight and that the DTO could be conducted without modifying the cryo schedule.

Heater Temperatures

The second problem found early in the flight was that the heater temperatures recorded were consistently higher than expected. In order to solve this problem, team members from the Boeing Company, TRW Incorporated, Lockheed Aircraft Corporation, North American Rockwell, Structures and Mechanics Division (SMC), and MPAD were called upon.

The temperature limit of the components inside the pressure vessel was set prior to flight to be 500°F based upon the autoignition temperature of teflon of 700°F. This margin is consistent with margins on flammable materials used in the Command Module. The pressure vessel itself is limited to 200°F based upon fracture mechanics considerations. Preflight analysis indicated that with a maximum heater temperature of 500°F the pressure vessel wall never exceeds this limit. It was known prior to flight that there would be large temperature gradients along the heater and it was felt that the temperature sensor would reflect the temperature of one of the cooler areas of the heater. Using this rationale a limit of 200°F was placed upon the heater sensor indication.

Due to drawing and design changes, the temperature sensor was mislocated in the model by 1.0 to 2.0 inches. This position error occurred at a location where the temperature gradients were as large as 100°F to 300°F per inch. After this was discovered, it was noted that the sensor should and did reflect close to the maximum temperature on the heater. This is shown in Figure 5.

Next, it was found that at various times the heater temperature could lead the sensor indication by as much as 50°F. This was determined by performing a transient analysis of the sensor and heater system.

Using these analyses, it was determined that a safe heater temperature limit could be established as follows:

1.	Heater upper limit	500°F
2.	ΔT between sensor and maximum point	-50°F
3.	Sensor Lag	-50°F
4.	Contingency for instrumentation and analytical errors	-50°F
5.	Final Redline Limit	350°F

Using this rationale, a corrected maximum temperature limit of 350°F was established for the remaining portion of the mission.

Detailed Test Objective Simulation

In view of the new heater temperature work that was done, it was decided to perform the high flow rate test using two heater elements in tank number three (the low density tank). Since all the prior analysis had been performed using three heater elements, the team members of The Boeing Company were called upon to recompute the high flow test predictions. This work was completed prior to the time that the test was to be run, and formed a complete basis for the test monitoring.

The predictions for tank number three along with the test data are shown in Figure 6. As can be seen, the data fell close to the trends predicted. In general, these predictions were such that the support team was able to distinguish between two heater element and three heater element operation.

Real Time Calculations

During the flight, there were many calculations made in an effort to ensure satisfactory system operation. The majority of these calculations involved various methods of establishing the system's thermal performance. Heat leaks were calculated using flow rate averages with the heater off, pressure change rate with the heaters off, and pressure change rate with the heaters on. In general, very little success was obtained using any of these methods to calculate the heat leak. Some of the problems involved with these calculations are as follows:

1. Flow Rate Determination - Since the system does not have individual flow meters for each tank, the flow sharing characteristics must be implied using pressure data, thermal data, and intuition. These methods all leak to large errors when using the resultant flows to calculate heat leaks.

2. Pressure Change Rate - The major problem with this calculation is that the pressure data has a 4 psi bit granularity. This means that a given value of pressure may be as much as 4 psi in error. If the total span of a given cycle is 30 psi, it can be seen that this pressure error represents a very large deviation.

3. System Equilibrium - Since these systems are vapor cooled the thermal performance is a strong function of the flow rate demanded and therefore the flow-sharing characteristics. If a tank has been supplying a large part of the load (i.e., high flow), its vapor cooled shield will be colder than normal. The calculated heat leak into the pressure vessel will then be abnormally low while at the same time another tank will appear abnormally high.

4. Quantity Balance - Finally, with the three tank system, the quantities may be separated by 30% to 40% and each tank will have a different performance based upon its particular fluid state. These heat leaks might at any one time range from 45 Btu/Hr to 20 Btu/Hr.

Post-Flight Analysis

The prime objective of a post-flight analysis is to establish the limits of system performance and to apply these limits to the future Apollo flights. A secondary objective is to reexamine the flight data in detail to insure that no unexplained events go undetected. This type of analysis is done on each flight; however, on Apollo 14, a more detailed analysis than normal was required.

One major decision that had to be made using post-flight analysis was whether or not to install an external recirculation pump on Apollo 15. The various issues involved in this analysis were stratification, quantity gauging accuracy, pressure decay due to stratification, heater temperature limits, crew activity, and extra vehicular activity capability. The data indicated that the quantity gauging accuracy and pressure decays were about the same as those observed on prior flights. As shown in Figure 7, all the observed heater temperatures were within the expected bounds while achieving the demands of Apollo 14. Also, it can be seen that by observing the limits established by this figure, the crew work load could be minimized. Prior ground testing indicated that the system could be operated in the blow-down mode below 20% quantity. Using this data, it was decided that the pumps would not be installed on Apollo 15.

The next major task that was undertaken was to compile a set of data on magnetic computer tapes so that the data could be accessed, used, and plotted. Some thirty-four parameters were stored on these tapes. These included five tank quantities, five tank pressures, five fluid temperatures, three heater temperatures, two bus voltages, three fuel cell currents, six fuel cell flow rates, one environmental control system flow rate, one surge tank pressure, one cabin regulated supply pressure, one cabin pressure, and one oxygen tank manifold pressure. These data were plotted in one second intervals on the Cal-Comp plotter and then distributed to the various team members.

Finally, there were several short studies performed to make sure that the system had performed properly. These studies and their purposes are as follows:

1. Calculated vs Measured Quantities - Using the observed fluid temperatures and pressures in combination with thermodynamic data, densities were calculated. These densities were then used to calculate quantities which are shown compared to the indicated quantities in Figure 8. It should be noted that as the critical region is approached (30% to 50%), this method becomes more inaccurate; however, at the extremes, the method is consistent. This method of quantity determination is shown to be an acceptable backup if it is needed. Also, as part of this effort, these values were compared with Apollo's 11, 12, and 13 to establish the performance of the redesigned sensor. As can be seen in Figure 9, the new sensors are not as accurate as those that were on the old tanks. This was anticipated since the new location of the sensor removes it from initmate contact with the fluid.

2. Tank Energy Balance - This study was performed to establish the overall system energy balance at various times during the mission. This was done to establish whether or not stratification would affect the thermal efficiency of the system. Figure 10 presents the data calculated at various points in the mission. It should be noted that nearly all the data falls within a ten percent band. This is felt to be a remarkable accuracy, considering all of the variables that affect the problem. Also, it is seen that the scatter is random in nature--indicating little or no loss in overall thermal efficiency.

3. Pressure Response Study - This work was performed so that the control characteristics could be established. This information will be used on future flights to aid in system monitoring. During this effort, there were two types of curves developed: heater on time and total cycle time. The results of the tabulation for heater on time are shown in Figure 11. As can be seen in this illustration, exact trends are difficult to observe. Again, this is indicative of a system with many operational variables. The total cycle times are shown in Figure 12; again, exact trends are hard to establish. But, the ranges of times that can be expected for future flights can be observed and also the variation of trend with quantity can be roughed out.

For Apollo 14, there are other analysis efforts that have been done or are in progress. These efforts are very detailed in nature and were in part reported in the other papers. Specifically, these include studies of the "g" levels during various portions of the flight, the heat transfer characteristics of the heater under a variety of conditions, and detailed stratification studies. These studies are not part of normal post-flight evaluation but are typical of those studies that are performed to evaluate specific events of interest.

Conclusions

The system performed basically as was predicted prior to flight and the analytical modes were verified in real-time. In the one case of error--heater temperature--the problem was found to be primarily erroneous heater temperature location input to the model.

It can be concluded that a support team can be organized to respond to real-time flight problems if the members are (1) operationally checked-out and (2) analytical tools are prepared in advance. A corollary to this is that such a large and rather complex team is necessary and can be organized and successfully managed to solve problems of the magnitude of the Apollo 14 cryo system redesign--all in a relatively short time period. Also, it was noted that the parallel nature of many of the studies provided a cross-check of the analytical methods used.

From a technical standpoint, the conclusions are specific and are as follows:

1. The leaking check valve on tank two had little effect on system performance.

2. Large thermal gradients exist on the heater--with the specific temperature profiles being a strong function of gravity level.

3. The location of heater temperature sensors is a critical item on flight systems.

4. The system successfully passed the high-flow test (DTO).

5. The tank quantities can be reasonably calculated from temperature and pressure readings and can be used as a backup to direct quantity readout.

6. Stratification does not affect the thermal efficiency (energy balance) of the system.

7. Tank heat leaks cannot be calculated using present in-flight data.

8. External pumps are not required on Apollo 15.

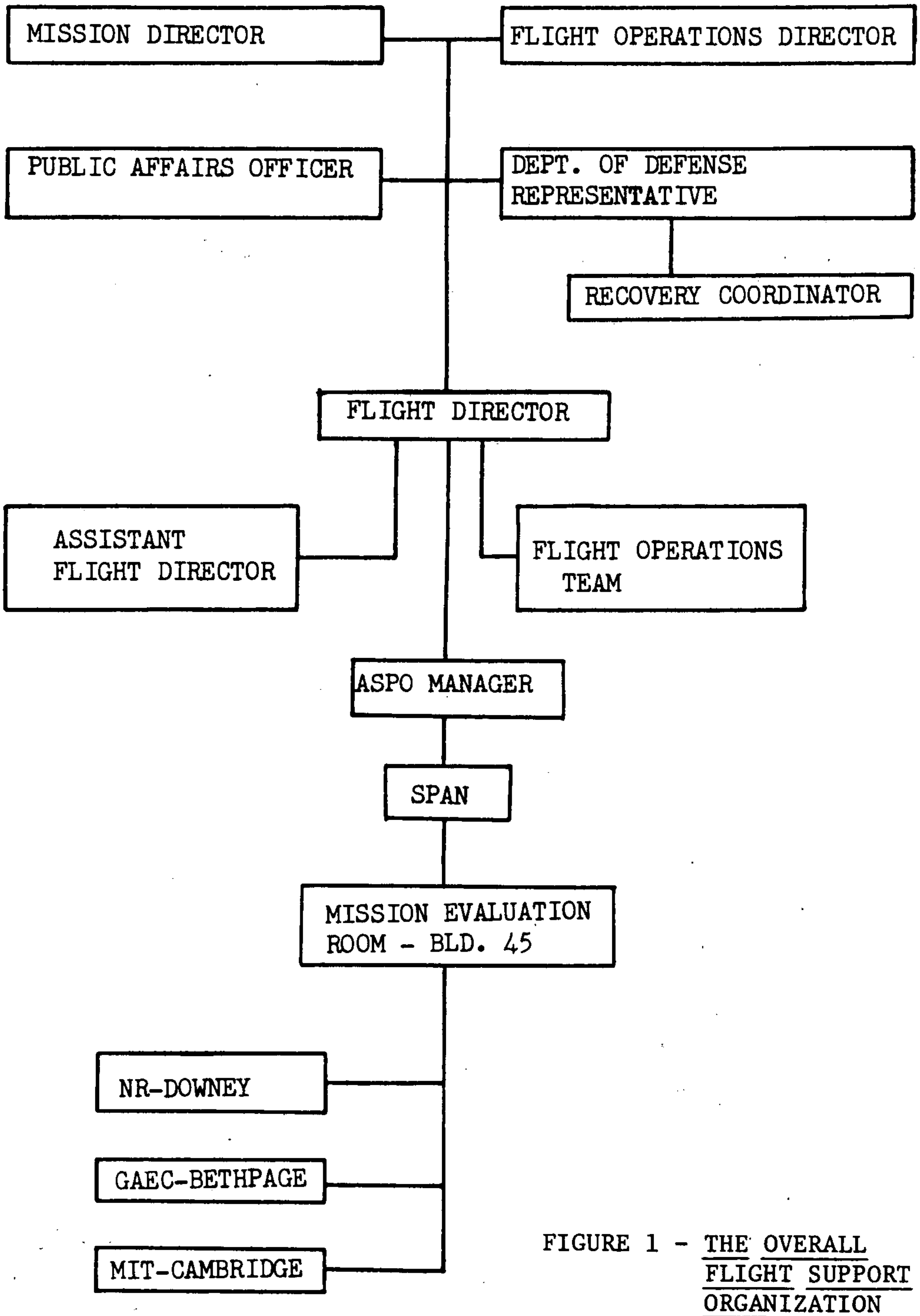

FIGURE 1 - THE OVERALL FLIGHT SUPPORT ORGANIZATION

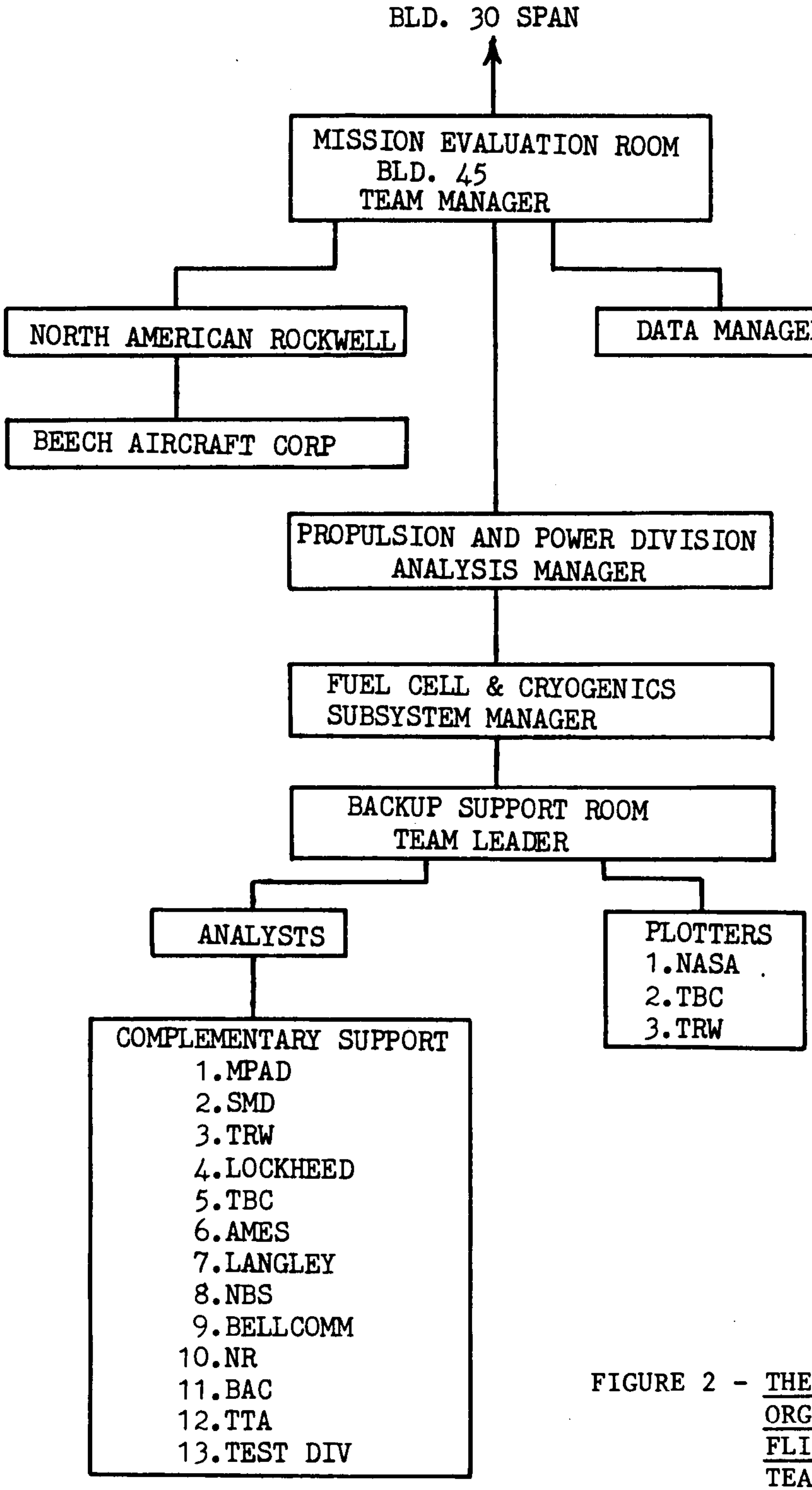

FIGURE 2 - <u>THE DETAILED ORGANIZATION OF THE FLIGHT SUPPORT TEAM</u>

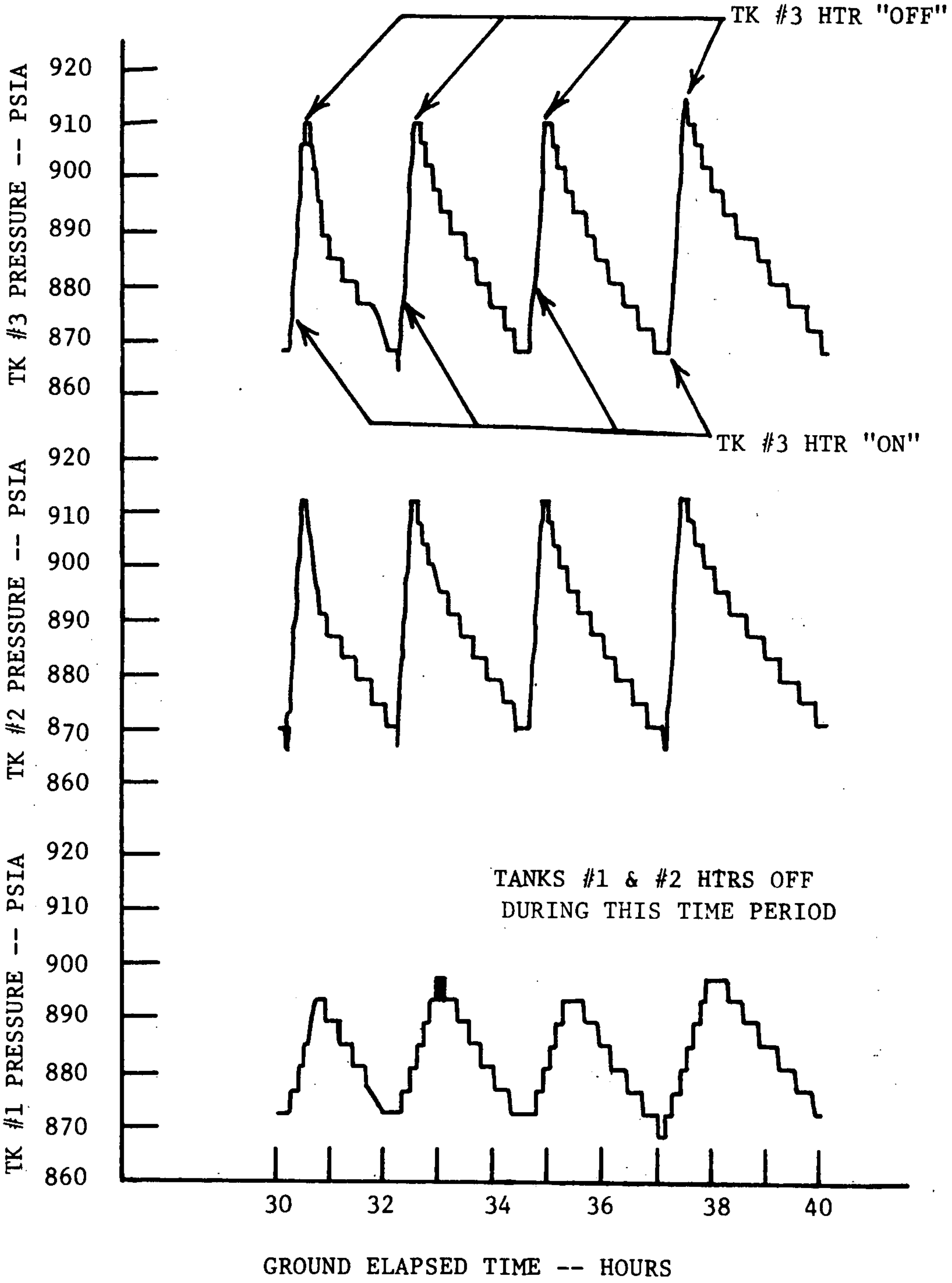

FIGURE 3 - FLIGHT DATA WITH A LEAKING CHECK VALVE

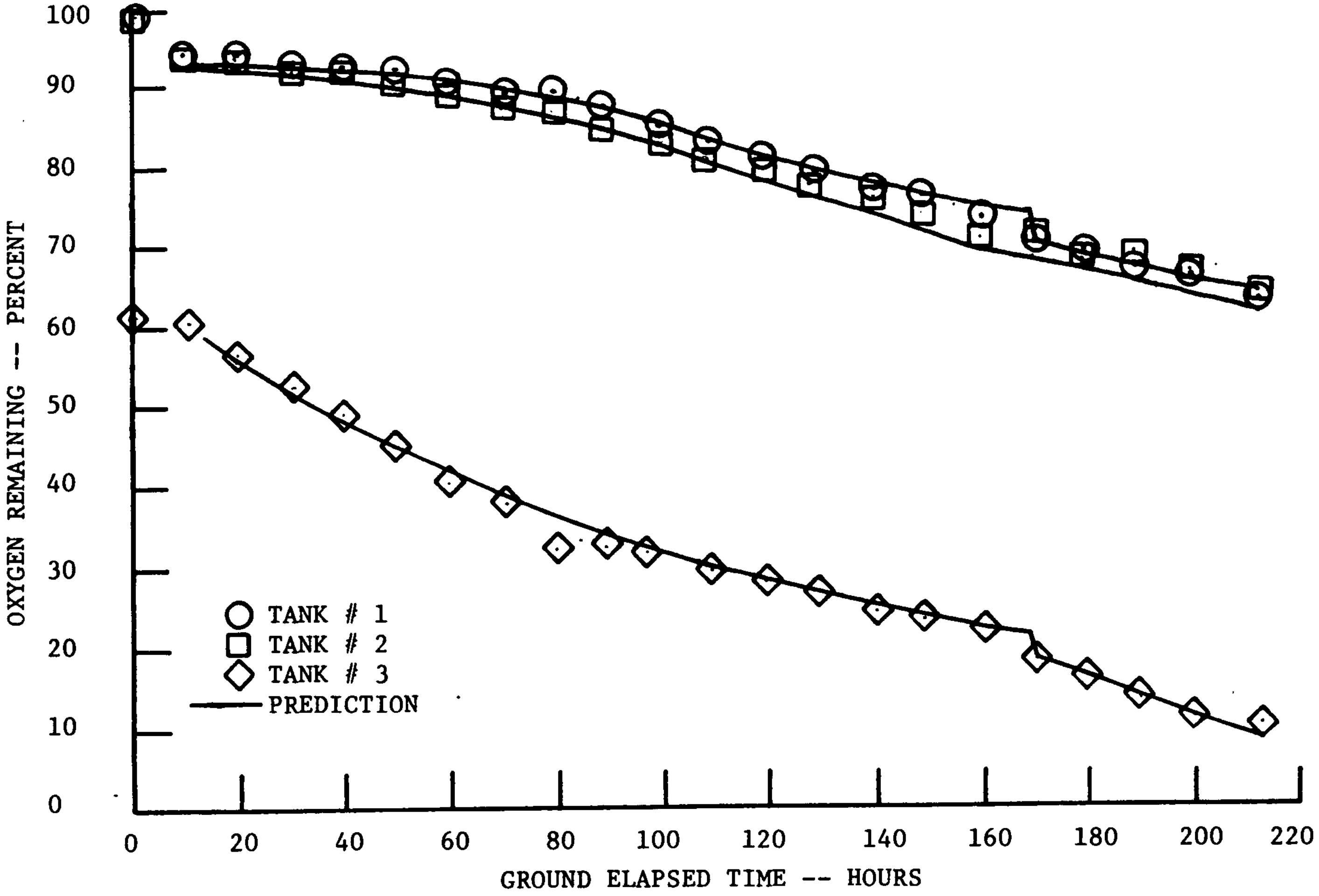

FIGURE 4 - FLIGHT QUANTITY PROFILES COMPARED TO THE PREDICTIONS

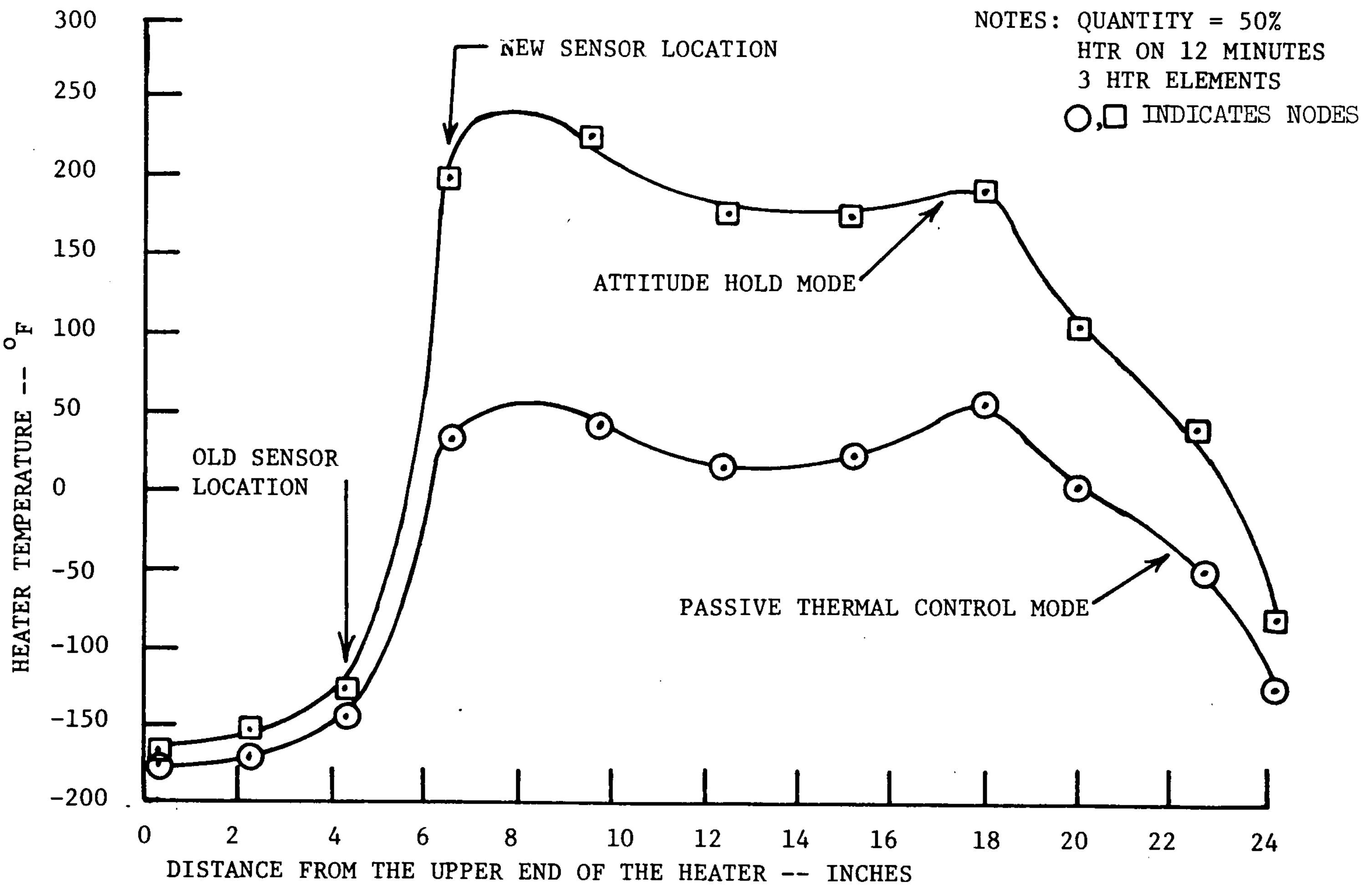

FIGURE 5 - HEATER TEMPERATURE PROFILES

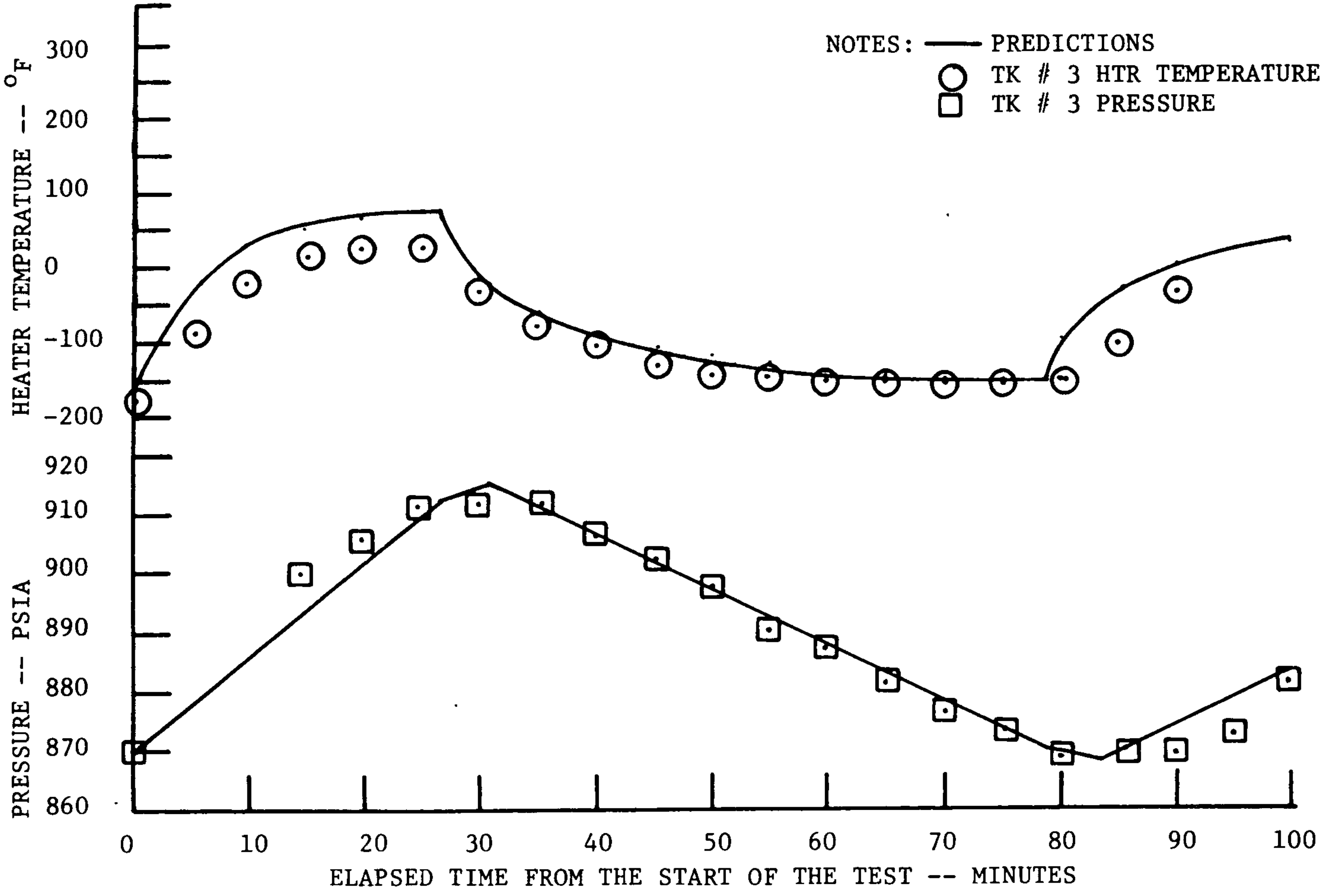

FIGURE 6 - DETAILED TEST OBJECTIVE SIMULATION AND FLIGHT DATA FOR TANK # 3

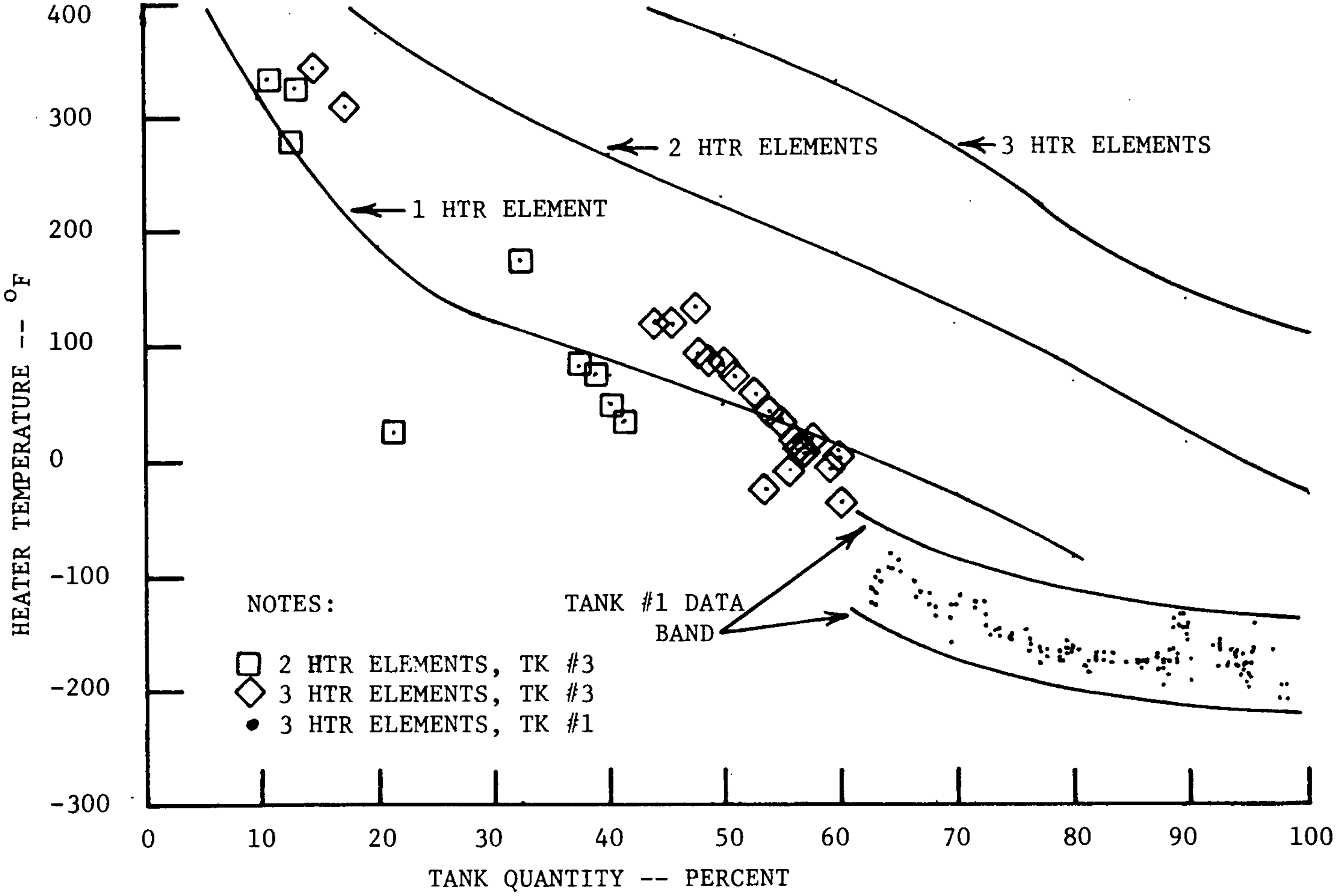

FIGURE 7 - HEATER TEMPERATURES OBSERVED DURING THE FLIGHT COMPARED TO THE MAXIMUM PREDICTED VALUES

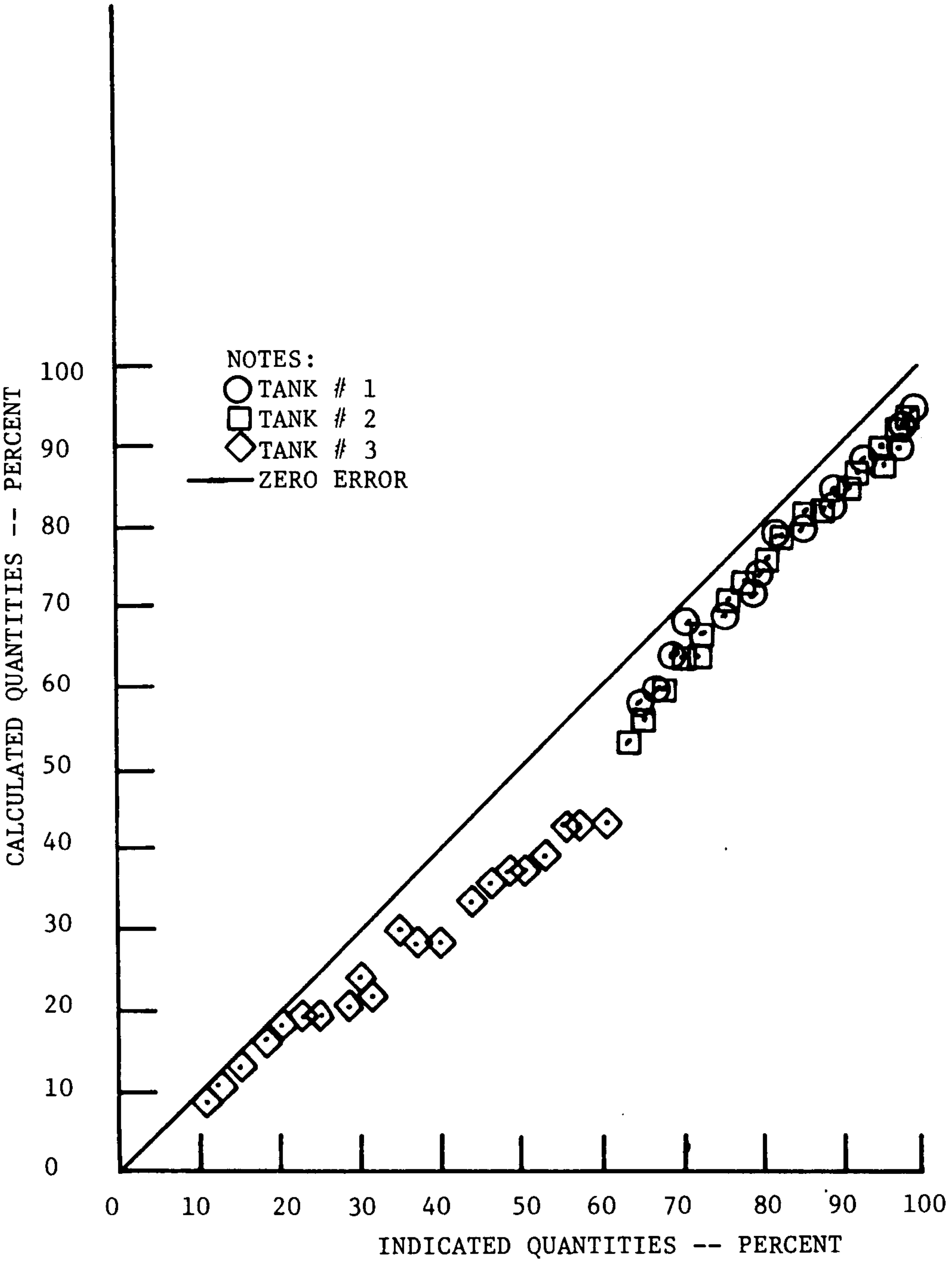

FIGURE 8 - A COMPARISON OF THE CALCULATED AND THE INDICATED QUANTITIES

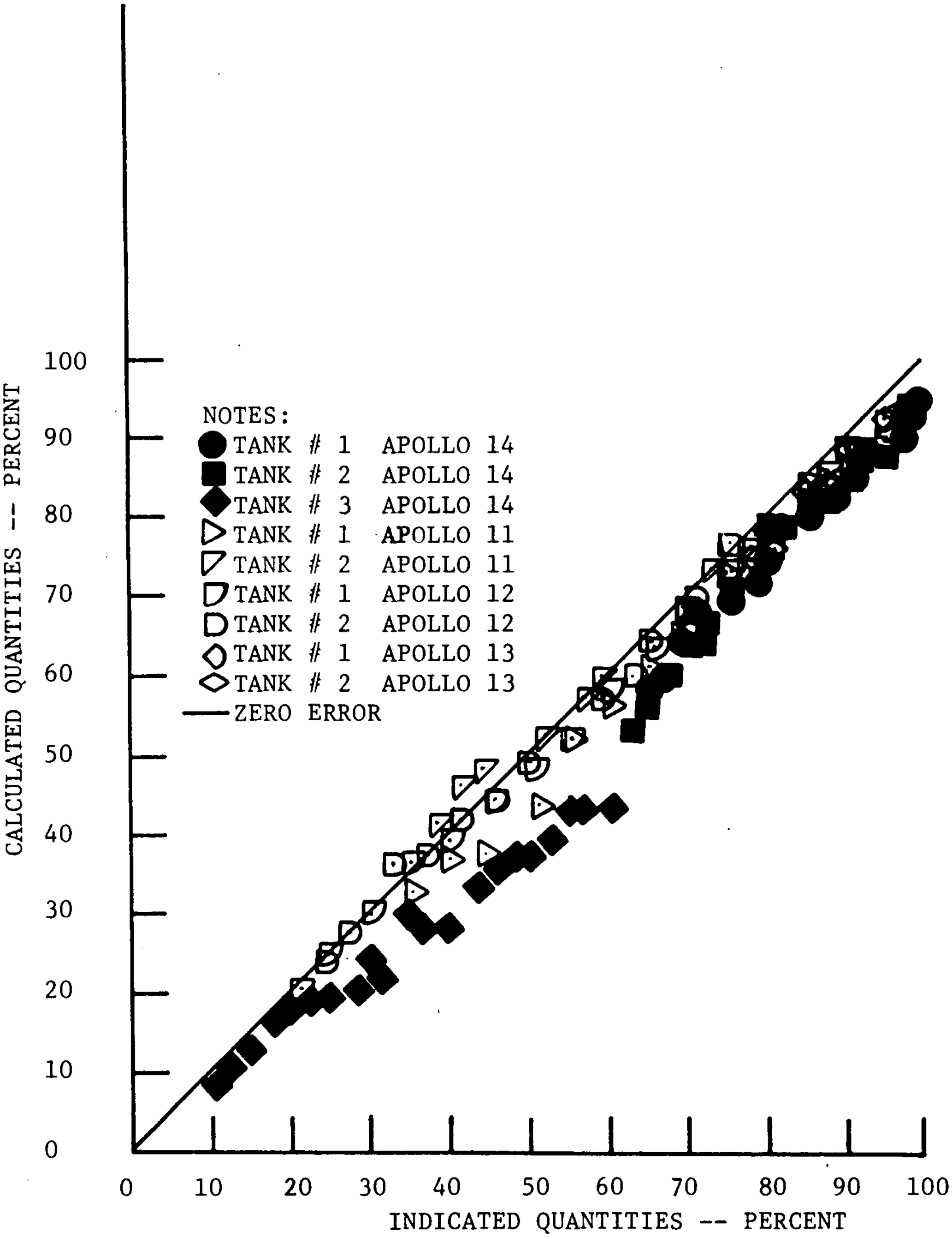

FIGURE 9 - A COMPARISON OF THE CALCULATED AND INDICATED QUANTITIES FROM FOUR APOLLO FLIGHTS

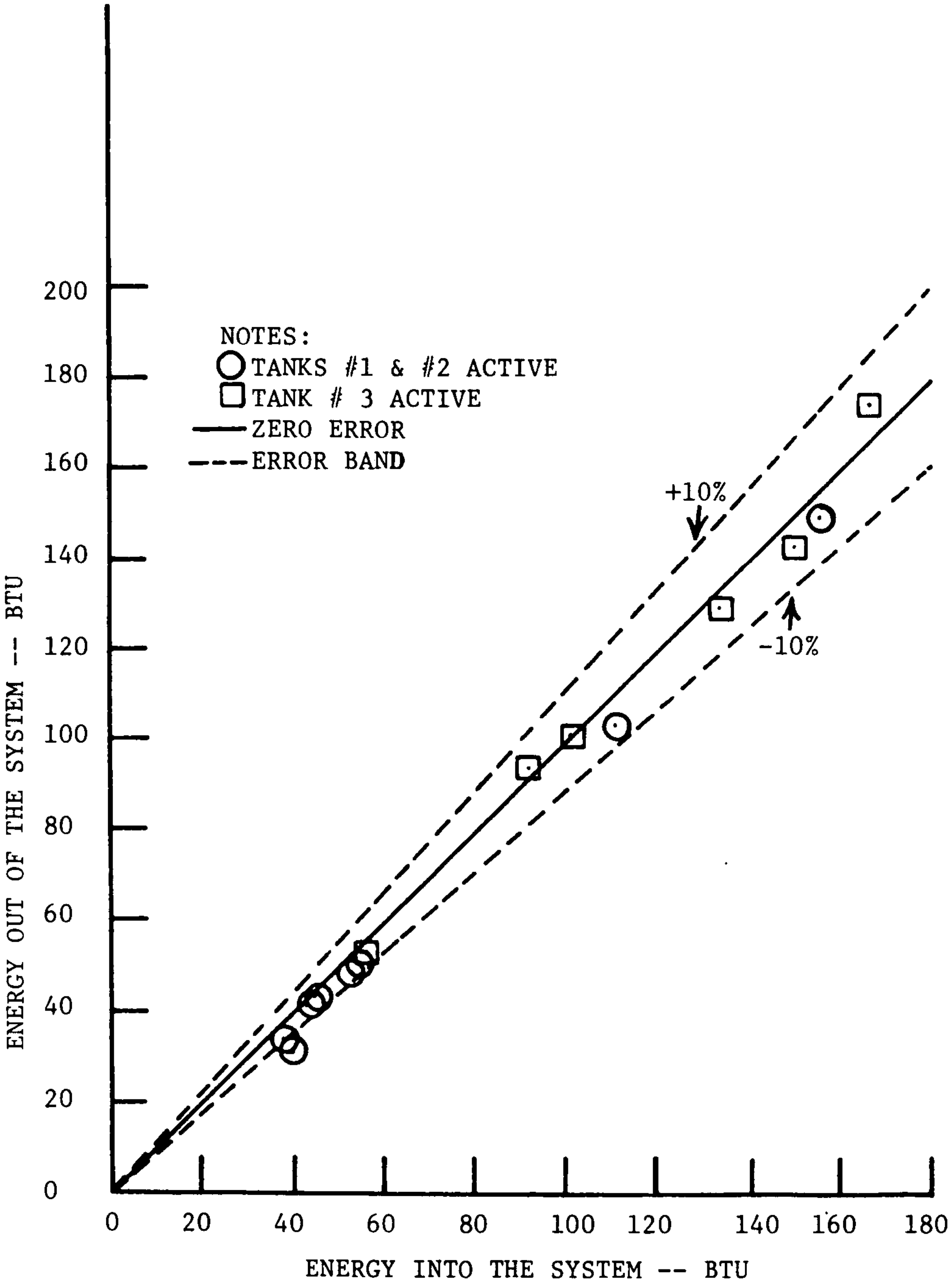

FIGURE 10 - OXYGEN TANK ENERGY BALANCE STUDY

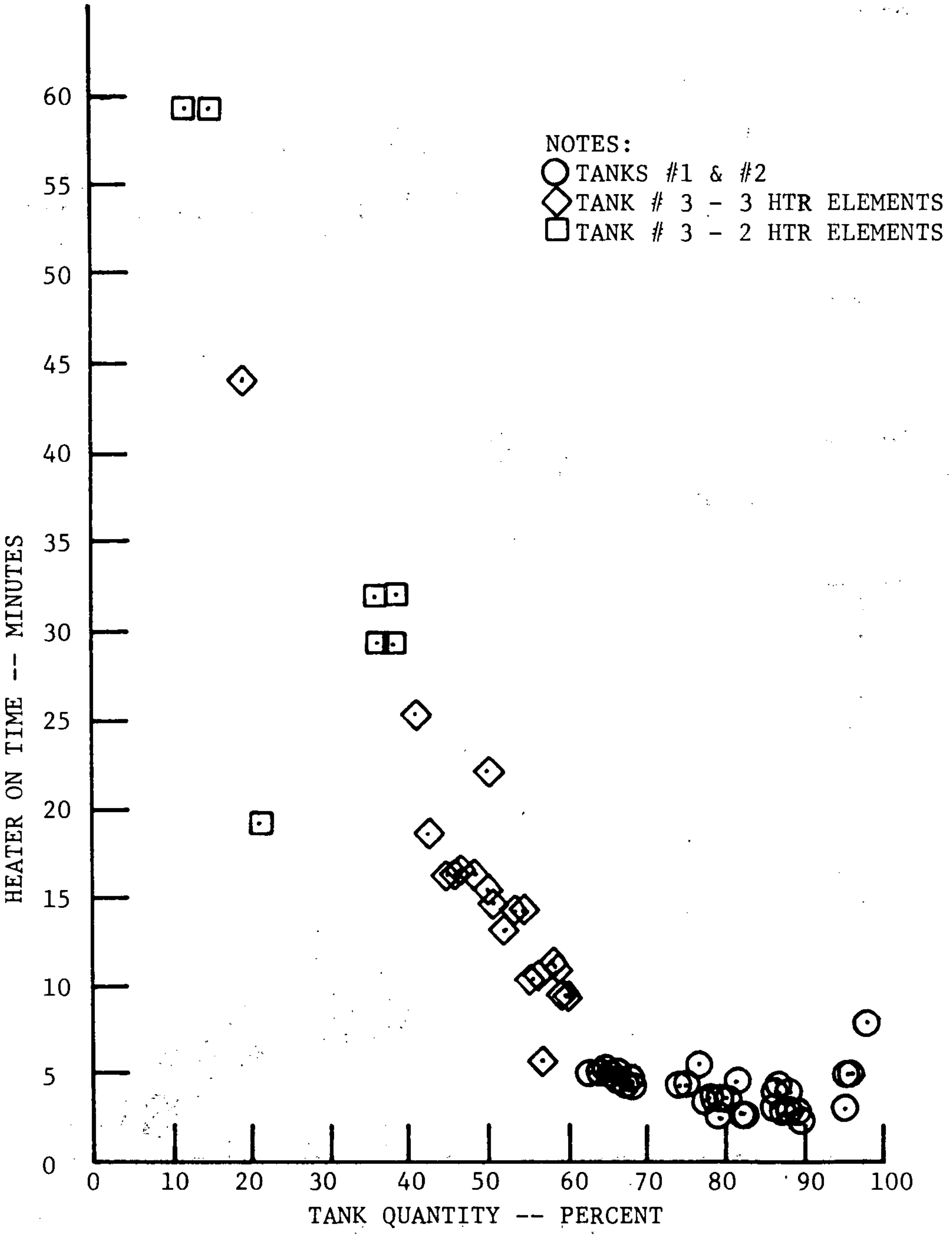

FIGURE 11 - HEATER "ON" TIMES DURING THE MISSION

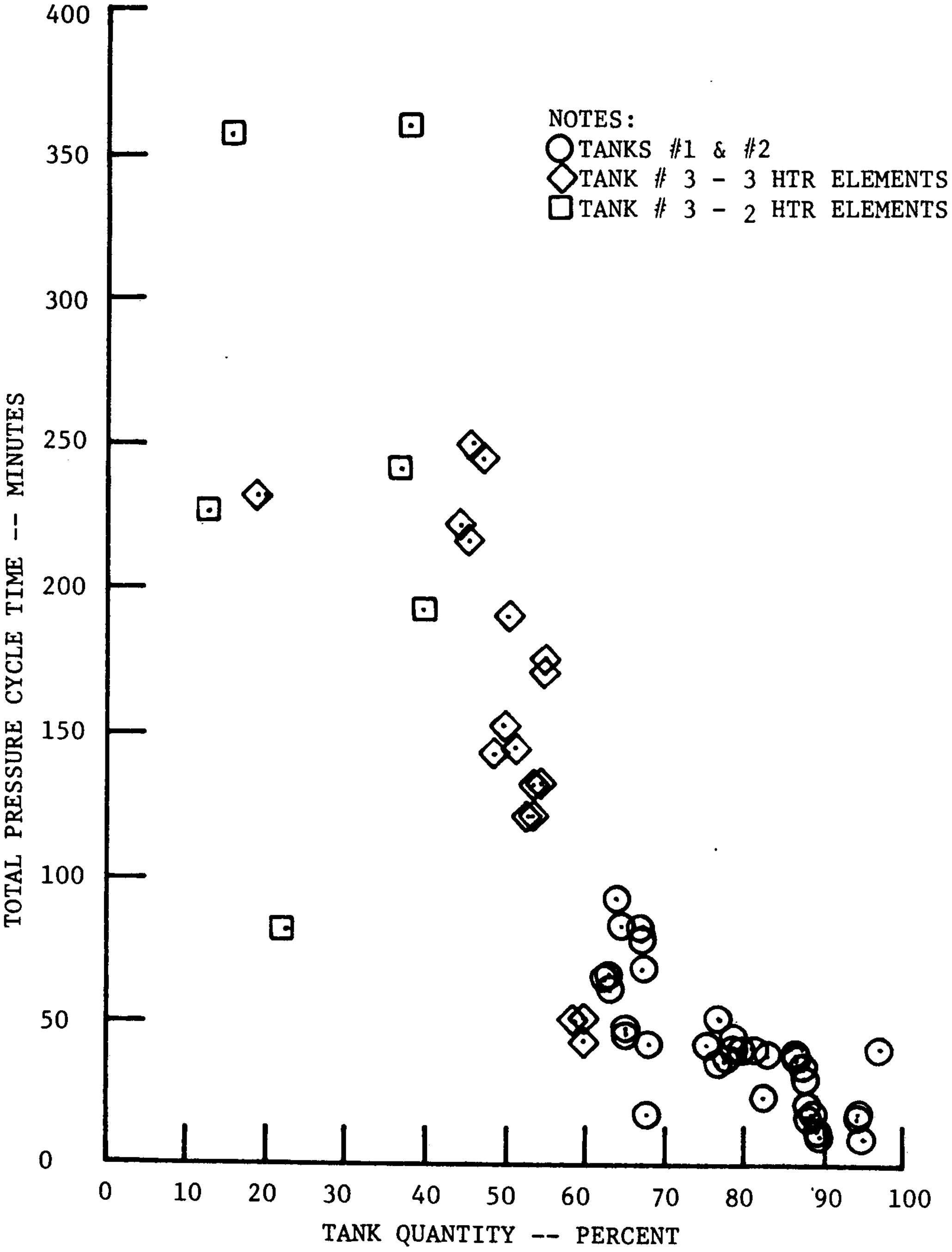

FIGURE 12 - PRESSURE CYCLE TIMES DURING THE MISSION

NASA — MSC — Coml., Houston, Texas